frontiers | Research Topics

The evolution of biomineralization in metazoans

Edited by
Sylvain Marcellini, Melanie Debiais-Thibaud
and Frederic Marin

Published in
Frontiers in Genetics
Frontiers in Ecology and Evolution
Frontiers in Cell and Developmental Biology

ISSN 1664-8714
ISBN 978-2-83251-339-2
DOI 10.3389/978-2-83251-339-2

About Frontiers

Frontiers is more than just an open access publisher of scholarly articles: it is a pioneering approach to the world of academia, radically improving the way scholarly research is managed. The grand vision of Frontiers is a world where all people have an equal opportunity to seek, share and generate knowledge. Frontiers provides immediate and permanent online open access to all its publications, but this alone is not enough to realize our grand goals.

Frontiers journal series

The Frontiers journal series is a multi-tier and interdisciplinary set of open-access, online journals, promising a paradigm shift from the current review, selection and dissemination processes in academic publishing. All Frontiers journals are driven by researchers for researchers; therefore, they constitute a service to the scholarly community. At the same time, the *Frontiers journal series* operates on a revolutionary invention, the tiered publishing system, initially addressing specific communities of scholars, and gradually climbing up to broader public understanding, thus serving the interests of the lay society, too.

Dedication to quality

Each Frontiers article is a landmark of the highest quality, thanks to genuinely collaborative interactions between authors and review editors, who include some of the world's best academicians. Research must be certified by peers before entering a stream of knowledge that may eventually reach the public - and shape society; therefore, Frontiers only applies the most rigorous and unbiased reviews. Frontiers revolutionizes research publishing by freely delivering the most outstanding research, evaluated with no bias from both the academic and social point of view. By applying the most advanced information technologies, Frontiers is catapulting scholarly publishing into a new generation.

What are Frontiers Research Topics?

Frontiers Research Topics are very popular trademarks of the *Frontiers journals series*: they are collections of at least ten articles, all centered on a particular subject. With their unique mix of varied contributions from Original Research to Review Articles, Frontiers Research Topics unify the most influential researchers, the latest key findings and historical advances in a hot research area.

Find out more on how to host your own Frontiers Research Topic or contribute to one as an author by contacting the Frontiers editorial office: frontiersin.org/about/contact

The evolution of biomineralization in metazoans

Topic editors

Sylvain Marcellini — University of Concepcion, Chile
Melanie Debiais-Thibaud — Université de Montpellier, France
Frederic Marin — Délégation Centre-Est (CNRS), France

Citation

Marcellini, S., Debiais-Thibaud, M., Marin, F., eds. (2023). *The evolution of biomineralization in metazoans*. Lausanne: Frontiers Media SA.
doi: 10.3389/978-2-83251-339-2

Table of contents

frontiers | Frontiers in Genetics

TYPE Editorial
PUBLISHED 04 January 2023
DOI 10.3389/fgene.2022.1092695

OPEN ACCESS

EDITED AND REVIEWED BY
Samuel A. Cushman,
United States Department of Agriculture (USDA), United States

*CORRESPONDENCE
Mélanie Debiais-Thibaud,
melanie.debiais-thibaud@umontpellier.fr
Frédéric Marin,
Frederic.Marin@u-bourgogne.fr
Sylvain Marcellini,
smarcellini@udec.cl

SPECIALTY SECTION
This article was submitted to Evolutionary and Population Genetics, a section of the journal Frontiers in Genetics

RECEIVED 08 November 2022
ACCEPTED 16 December 2022
PUBLISHED 04 January 2023

CITATION
Debiais-Thibaud M, Marin F and Marcellini S (2023), Editorial: The evolution of biomineralization in metazoans.
Front. Genet. 13:1092695.
doi: 10.3389/fgene.2022.1092695

Editorial: The evolution of biomineralization in metazoans

Mélanie Debiais-Thibaud[1]*, Frédéric Marin[2]* and Sylvain Marcellini[3]*

[1]Institut des Sciences de l'Evolution de Montpellier, ISEM, Univ Montpellier, CNRS, IRD, EPHE, Montpellier, France, [2]Laboratoire Biogéosciences, UMR CNRS-EPHE 6282, Université de Bourgogne—Franche-Comté, Dijon, France, [3]Laboratory of Development and Evolution (LADE), University of Concepción, Concepción, Chile

KEYWORDS

biomineralisation, evolution, metazoan, corals, mollusks, vertebrates, sponges (porifera)

Editorial on the Research Topic
The evolution of biomineralization in metazoans

Biomineralization refers to the process by which living systems deposit minerals. This process has shaped the face of the Earth over geological time, since the Archean with the appearance of the first stromatolites around 3.5 billion years ago, but particularly with the almost simultaneous emergence of multiple biologically-controlled animal mineralizations - both skeletal and non-skeletal—at the dawn of the Cambrian times, circa 545 million year ago (Knoll, 2003). Metazoan calcium carbonate, calcium phosphate and silica became then major actors of the Earth machine: let us think for a moment that Australia's Great Barrier Reef is the only animal construction visible from space ! Throughout the Phanerozoic times, these three minerals have contributed to maintain Earth homeostasis and, concerning calcium carbonate, to regulate the climate at global scale, by long-term sequestering carbon dioxide (Milliman, 1993).

This Frontiers Research Topic gathers fifteen articles that bring new insights into biomineralization in many metazoan phyla, highlighting both the great diversity of mechanisms as well as some ancient evolutionary events that shaped this important biological process. Figure 1 illustrates the variety of contributions covering a large range of metazoan phyla. Of course, encompassing the whole metazoans was a challenge and some groups are missing in this volume: siliceous sponges for example, but also brachiopods, bryozoans, calcifying annelids, or, among the ecdysozoans, crustaceans. However, the fifteen articles presented here constitute a significant sampling of the research on evolutionary processes that have been driving animal biomineralization for an eon.

Regarding non-bilaterians metazoans, Voigt et al. highlight the evolution of carbonic anhydrases in calcareous sponges (Calcarea), distinguishing the different cellular locations of this enzyme in the two subclasses Calcinea and Calcaronea. For cnidarians, Zaquin et al. show how the skeletal matrix proteins of scleractinian corals result from the independent co-option of ancestral genes predating cnidarian diversification, but also from posterior recruitment of duplicated genes that are species-specific. Finally, Conci et al. review different cellular and molecular aspects of the skeletal biomineralization of another cnidarian clade, Octocorallia,

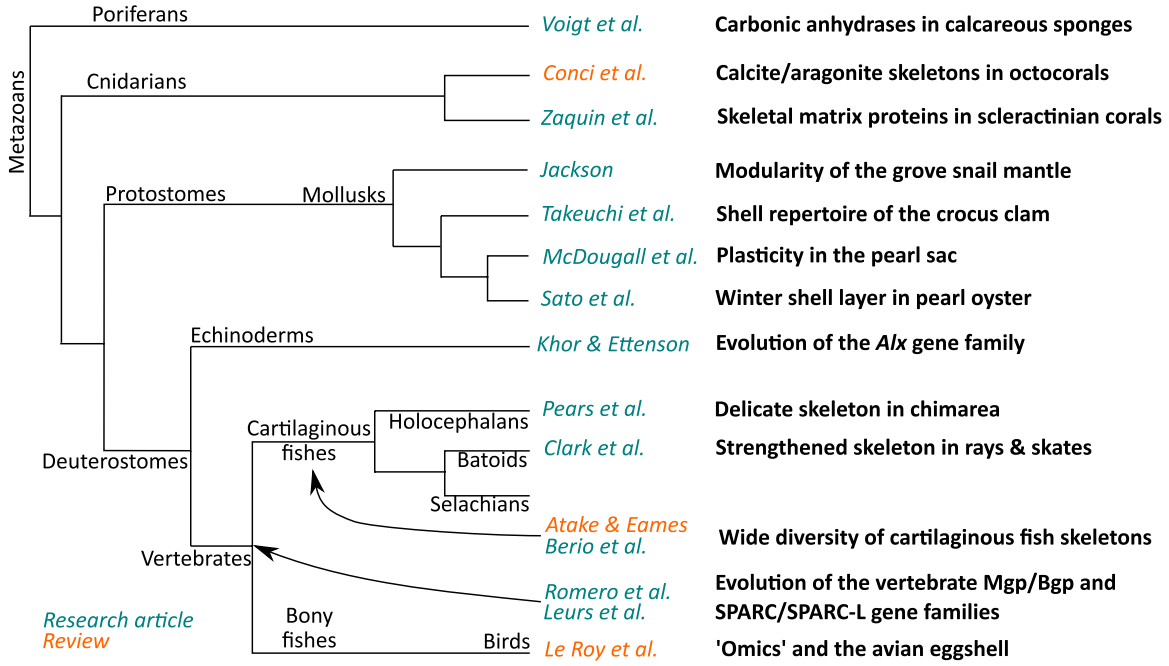

FIGURE 1
The phylogenetic relationships of the 15 contributions of this Research Topic.

which can 'handle' the two calcium carbonate polymorphs, *i.e.*, calcite—the predominant form—but also, more rarely, aragonite.

The four papers covering the protostome world deal with the molecular aspects of shell biomineralization in molluscs, namely, three bivalves and one gastropod. Sato et al. emphasize the seasonal plasticity of the shell, by describing the microstructure of the winter layer and its associated molecular markers, in the shell of the Japanese pearl oyster, while McDougall et al. associate changes in gene expression in the pearl sac to the pearl structural characteristics in the south sea pearl oyster *Pinctada maxima*. Fundamental aspects of shell evolution are examined with the contribution of Takeuchi et al. who identify the complete protein shell repertoire of the Japanese crocus clam. At last, Jackson reveals the modularity and plasticity of the calcifying mantle of the terrestrial grove snail, *Cepaea nemoralis*, by looking at the spatial expression pattern of some key shell-forming genes.

A total of eight articles relate to biomineralisation in the skeleton of deuterostomes, with a major focus on the derived calcium-phosphate based skeleton of vertebrates. In particular, Pears et al. describe in unprecedented detail the delicate mineralisation in the cartilaginous skeleton of Holocephalans, while Clark et al. uncover the various architectures of highly mineralised jaws in batoids (rays). More general aspects of cartilaginous fish skeletal mineralisation are exposed in the review of Atake and Eames and a research article proposed by Berio et al. Specific aspects of skeletal gene evolution are analysed for two vertebrate gene families: *Mgp/Bgp* Leurs et al., and *SPARC/SPARCL* Romero et al., Deuterostomian calcium carbonate-based biomineralizations are not to be outdone, with the contribution of Le Roy et al. on the molecular toolkit for building avian eggshell and with the review of Khor and Ettenson on the skeletal function of Alx homeobox genes in echinoderms and all deuterostomes in general.

While the Research Topic of these research and review articles demonstrates the diversity of biomineralization forms in animals, they also surprisingly underline major genetic variation at all levels of comparisons, from the deepest nodes of metazoans, to more recent divergent groups within vertebrates, molluscs, corals or sponges. We hope that this Research Topic will inspire and encourage the community to further explore this complex and fascinating aspect of animal biology.

Author contributions

All authors listed have made a substantial, direct, and intellectual contribution to the work and approved it for publication.

Conflict of interest

The authors declare that the research was conducted in the absence of any commercial or financial relationships that could be construed as a potential conflict of interest.

Publisher's note

References

Knoll, A. H. (2003). Biomineralization and evolutionary history. *Biominer. Rev. Mineral. Geochem.* 54, 329–356. doi:10.2113/0540329

Milliman, J. D. (1993). Production and accumulation of calcium carbonate in the ocean: Budget of a nonsteady state. *Glob. Biogeochem. Cycles* 7, 927–957. doi:10.1029/93gb02524

frontiers in Genetics

REVIEW
published: 23 November 2020
doi: 10.3389/fgene.2020.569314

Transcription Factors of the Alx Family: Evolutionarily Conserved Regulators of Deuterostome Skeletogenesis

*Jian Ming Khor and Charles A. Ettensohn**

Department of Biological Sciences, Carnegie Mellon University, Pittsburgh, PA, United States

Members of the *alx* gene family encode transcription factors that contain a highly conserved Paired-class, DNA-binding homeodomain, and a C-terminal OAR/Aristaless domain. Phylogenetic and comparative genomic studies have revealed complex patterns of *alx* gene duplications during deuterostome evolution. Remarkably, *alx* genes have been implicated in skeletogenesis in both echinoderms and vertebrates. In this review, we provide an overview of current knowledge concerning *alx* genes in deuterostomes. We highlight their evolutionarily conserved role in skeletogenesis and draw parallels and distinctions between the skeletogenic gene regulatory circuitries of diverse groups within the superphylum.

Keywords: Alx transcription factors, skeletogenesis, chondrogenesis, osteogenesis, deuterostome evolution, neural crest cell, biomineralization, calcification

OPEN ACCESS

Edited by:
Sylvain Marcellini, University of Concepcion, Chile

Reviewed by:
Robert A. Haney, Ball State University, United States
Stephanie Bertrand, UMR7232 Biologie Intégrative des Organismes Marins (BIOM), France

****Correspondence:***
Charles A. Ettensohn
ettensohn@cmu.edu

Specialty section:
This article was submitted to Evolutionary and Population Genetics, a section of the journal Frontiers in Genetics

Received: *03 June 2020*
Accepted: *19 October 2020*
Published: *23 November 2020*

Citation:
Khor JM and Ettensohn CA (2020) Transcription Factors of the Alx Family: Evolutionarily Conserved Regulators of Deuterostome Skeletogenesis. Front. Genet. 11:569314. doi: 10.3389/fgene.2020.569314

INTRODUCTION

Biomineralization, the formation of mineral by living organisms, is an exceptionally widespread phenomenon and is thought to have evolved independently and rapidly in many different metazoan phyla through the deployment of a wide range of biomineralization mechanisms and chemistries. Depending on the type and extent of the mineral components, biomineralized tissues are used for structural support, resource acquisition, and protection. There are three predominant classes of biogenic mineral in metazoans: calcium carbonates, calcium phosphates, and silica. The carbonate and phosphate salts of calcium are widely used as skeletal material by vertebrates and invertebrates, while silica biomineralization is prevalent in sponges (Wang et al., 2010b). The emergence of biomineralization during the Cambrian Explosion, followed by evolutionary modifications of these biomineralization programs, gave rise to the diverse biomineralized structures found in modern metazoans (Knoll, 2003; Zhuravlev and Wood, 2018).

Within the deuterostome superphylum, only vertebrates and echinoderms produce extensive biomineralized skeletal structures. The vertebrate endoskeleton consists primarily of the skull, vertebrae, ribs, and limb bones all of which are composed of matrix proteins (e.g., collagens) and calcium phosphate crystals. Vertebrate biomineralization is predominantly orchestrated by chondrogenic cells (chondrocytes) and osteogenic cells (osteoblasts and osteoclasts). The vertebrate skeleton is formed during early development by cartilage and/or connective tissue membranes, which are subsequently replaced by bony tissues through the process of ossification. There are two forms of ossification, endochondral and intramembranous ossification. Endochondral ossification is associated with the formation of long bones and requires the presence of a hyaline cartilage template formed by chondrocytes (Mackie et al., 2008). During vertebrate embryonic development,

chondrocytes are derived from neural crest cells, somitic mesodermal cells, and lateral plate mesodermal cells (see review by Hirasawa and Kuratani, 2015). Developmental cues signal the cartilage matrix to calcify. This prevents the diffusion of nutrients into the matrix and results in chondrocyte apoptosis, allowing blood vessels to invade the cartilage cavities. Osteoblasts, derived from common osteochondroprogenitor or directly from chondrocytes (Yang et al., 2014), and osteoclasts, derived from erythron-myeloid progenitors (Jacome-Galarza et al., 2019), then transform the calcified cartilage into biomineralized bone (Mackie et al., 2008). During intramembranous ossification, spongy bones are formed when osteoblasts directly deposit biomineral on extracellular sheets of mesenchymal connective tissues (Percival and Richtsmeier, 2013). This process is commonly involved in the formation of flat bones found in the skull, mandible, and clavicles. Whether intramembranous or endochondral ossification arose first during vertebrate evolution remains unclear (Cervantes-Diaz et al., 2017; Wood and Nakamura, 2018; Brazeau et al., 2020).

All adult echinoderms produce calcite-based endoskeletons that consist of the test, teeth, and spines. In most species, the adult form arises from a swimming, feeding larva *via* metamorphosis, and these two life history stages bear little morphological resemblance to one another. In some echinoderm clades, specifically echinoids (sea urchins) and ophiuroids (brittle stars), the feeding larva also possesses an intricate and extensive calcitic endoskeleton, which is first laid down during embryonic development and further elaborated after feeding begins. The founder cells of the embryonic skeletogenic lineage, the large micromeres, arise early in development and are specified by a combination of localized maternal factors and unequal cell division. At the mesenchyme blastula stage, the large micromere descendants undergo an epithelial-to-mesenchyme transition (EMT) and ingress into the blastocoel as primary mesenchyme cells, or PMCs (see reviews by Ettensohn, 2020; McClay et al., 2020). After ingression, PMCs extend filopodia and migrate along the blastocoel wall, gradually adopting a ring-like configuration near the equator of the embryo. As the PMCs migrate, their filopodia fuse, forming a cable-like cytoplasmic strand that connects the cells in a syncytial network. Amorphous calcium carbonate and associated proteins are then secreted into an intercellular space within the cytoplasmic cable, where the biomineral matures and grows, eventually producing the elaborate, branched skeletal elements (spicules) of the larva (Wilt, 2002; McIntyre et al., 2014; Shashikant et al., 2018).

Due to differences in mechanisms underlying axial patterning, developmental timing, and embryological structures, it is often difficult to deduce morphological homology. Although the biomineralized tissues found in different metazoan phyla are not considered homologous in the strictest sense, recent comparative studies have revealed common elements across different biomineralization systems. This has led to the recognition of a possible "biomineralization toolkit;" an ancestral gene regulatory network (GRN) consisting of signaling and gene regulatory pathways that was independently co-opted and fine-tuned for biomineralization in diverse animal taxa. One common regulator of deuterostome skeletogenesis is the Alx transcription factor family, which has been shown to have an ancient, conserved role in this process in both vertebrates and echinoderms. In this review, we examine the current state of knowledge concerning deuterostome *alx* genes, with a focus on their role in skeletogenesis.

PHYLOGENETIC DISTRIBUTION OF *ALX* GENES IN DEUTEROSTOMES

The *alx* gene family encodes Paired-class homeodomain transcription factors that contain a highly conserved DNA-binding homeodomain and a C-terminal Otp, Aristaless, and Rax (OAR) domain, features that are shared by many Paired-class homeodomain proteins. Phylogenetic and comparative genomic studies have revealed considerable variability in the number of *alx* genes in different deuterostomes, pointing to a complex evolutionary pattern of lineage-specific gene duplication and loss (**Figure 1**; adapted from McGonnell et al., 2011; Koga et al., 2016). Hemichordates possess a single *alx* gene (Koga et al., 2016) while echinoderms have two (*alx1* and *alx4*; Ettensohn et al., 2003; Koga et al., 2016). In contrast, humans and mammals possess three *alx* genes (*alx1*/*cart1*, *alx3*, and *alx4*) that arose through two duplication events. Through the course of evolution, one of the paralogues, *alx3*, was lost from amphibian and reptile lineages (McGonnell et al., 2011). Additionally, ray-finned fishes such as zebrafish acquired two paralogues of *alx4*, designated *alx4a* and *alx4b*, as a result of a separate, whole genome duplication event (McGonnell et al., 2011). The lancelets have two *alx* genes. In *Branchiostoma floridae*, these two genes (*Bf-alx1* and *Bf-alx2*) are located close to each other in the genome and have very similar intron-exon organizations. Molecular phylogenetic analysis of Alx proteins indicate that Bf-Alx1 and Bf-Alx2 form a monophyletic group, providing further support for the view that they arose from a lineage-specific gene duplication event (**Figure 1**; Koga et al., 2016).

DEVELOPMENTAL EXPRESSION AND FUNCTION OF *ALX* GENES IN JAWED VERTEBRATES

Members of the *alx* gene family are expressed in several mesenchymal tissues during the embryogenesis of jawed vertebrates (gnathostomes), a group that includes most of the vertebrate species used for developmental studies. These genes are expressed most prominently in distinct but partially overlapping patterns in neural crest-derived craniofacial mesenchyme and in mesenchyme of the limb bud, both of which are sources of cartilage and bone (Zhao et al., 1994; Qu et al., 1997a; ten Berge et al., 1998; Beverdam and Meijlink, 2001). Other sites of embryonic expression have also been reported, including the head mesoderm, sclerotome of the somite (another tissue that produces cartilage and bone), hair follicles, dental papillae of teeth, and parts of the developing urogenital system (Zhao et al., 1994; Hudson et al., 1998; ten Berge et al., 1998; Bothe et al., 2011; Wang et al., 2019).

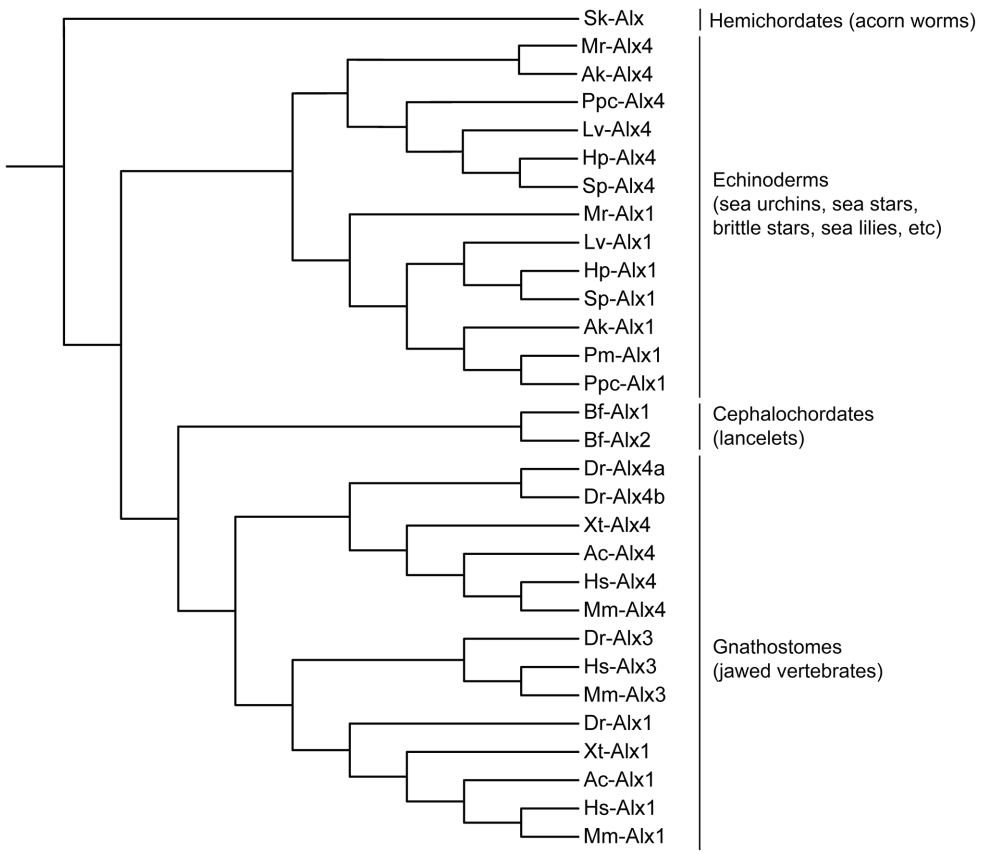

FIGURE 1 | Molecular phylogeny of Alx proteins (adapted from McGonnell et al., 2011; Koga et al., 2016). Branch lengths are arbitrary. Sk, *Saccoglossus kowalevskii* (acorn worm); Lv, *Lytechinus variegatus* (euechinoid sea urchin); Hp, *Hemicentrotus pulcherrimus* (euechinoid sea urchin); Sp, *Strongylocentrotus purpuratus* (euechinoid sea urchin); Mr, *Metacrinus rotundus* (sea lily); Ak, *Amphipholis kochii* (brittle star); Pm, *Patiria miniata* (sea star); Ppc, *Patiria pectinifera* (sea star); Bf, *Branchiostoma floridae* (lancelet); Dr, *Danio rerio* (zebrafish); Xt, *Xenopus tropicalis* (frog); Ac, *Anolis carolinensis* (lizard); Hs, *Homo sapiens* (human); Mm, *Mus musculus* (mouse).

In the developing head, genes of the *alx* family are expressed by neural crest cells, which give rise to cartilages and bones of the skull, jaw, and middle ear, as well as other derivatives (see reviews by Santagati and Rijli, 2003; Noden and Trainor, 2005). Consistent with this pattern of expression, perturbations of *alx* genes commonly result in severe craniofacial malformations, including frontonasal dysplasia and the reduction or malformation of many neural crest-derived skeletal elements (**Table 1**). In mice, loss-of-function mutations of *alx1*/*cart1* or *alx4* also lead to other cranial abnormalities such as anencephaly and lacrimal gland aplasia (Zhao et al., 1996; Garg et al., 2017), although these effects are likely to be secondary consequences of defects in neural crest cells, which provide essential signals that regulate the development of the brain and eye (Zhao et al., 1996; Bhattacherjee et al., 2009; Le Douarin, 2012; Garg et al., 2017). While *alx3*-null mice appear normal, *alx3*/*alx4* double mutant mice exhibit severe frontonasal dysplasia and cranial skeletal defects that are more extreme than those observed in *alx4* mutant mice, revealing non-equivalent but overlapping functions of these highly similar proteins (Beverdam et al., 2001).

During early zebrafish development, the expression of *alx1* alone is detected in migrating neural crest cells, while at later stages, *alx1*, *alx3*, *alx4a*, and *alx4b* exhibit overlapping patterns of expression in the craniofacial mesenchyme (Dee et al., 2013; Wang et al., 2019). *Alx1* is also transiently expressed in the cranial paraxial mesoderm at early developmental stages (Wang et al., 2019). Perturbation of Alx1 expression using antisense morpholino oligonucleotides (MOs) produces severe craniofacial defects in zebrafish, similar to results seen in the mouse, inhibition of *alx3* alone results in no significant craniofacial abnormalities (Dee et al., 2013). In developing frog and chick embryos, both *alx1* and *alx4* are expressed robustly in the craniofacial mesenchyme (Bothe and Dietrich, 2006; McGonnell et al., 2011; Square et al., 2015).

Genes of the *alx* family are also expressed in the mesodermal compartment of the limb buds. At early embryonic stages, these genes are expressed specifically in an anterior, proximal zone while later in development they are also expressed at the distal margin (Qu et al., 1997b). The anterior, proximal zone of expression may include sites where skeletal elements of the shoulder and pelvic girdles (the scapula and pelvis, respectively) form, although this has not been shown directly. The skeletal elements of the limb girdles have complex embryological origins that are only partially understood. The scapula may arise from

TABLE 1 | Summary of expression patterns, mutations, perturbations, and diseases associated with *alx* genes across different deuterostome phyla.

Organism	Gene	Expression Pattern	Reference	Mutation/Perturbation	Disease/Mutational Effect	Reference
Human	*alx1*	n.d.	n.d.	Whole-gene deletion and homozygous homeodomain splice-site mutation (c.531+1G>A)	Frontonasal dysplasia, characterized by microphthalmia and severe facial clefting	Uz et al., 2010
				Reciprocal translocation t(1;12) (p32.1;q21.3) resulting in enhanced gene expression	Microcephaly, language impairment, and mental retardation	Liao et al., 2011
	alx3	n.d.	n.d.	Nonsense (c.543T>A; p.Y191X), frameshift (c.578_581delCTGA; p.T193RfsX137), and splice-site (c.595-2A>T) mutations within homeodomain	Frontonasal dysplasia (frontorhiny)	Twigg et al., 2009
				Nonsense mutation within homeodomain (c.604C>T; p.Q202X), resulting in premature stop	Frontonasal dysplasia (frontorhiny)	Ullah et al., 2018
	alx4	n.d.	n.d.	Deletion and insertion mutation (c.1080_1089delGACCCGGTGC insCTAAGATCTCAACAGAGATG GCAACT; p.D326fsX21), resulting in frameshift and loss of OAR domain	Mild frontonasal dysplasia and enlarge parietal foramina	Bertola et al., 2013
				Deletions (c.385_394del, c.417_418del), point mutation (c.620C>A), and duplication (c.456_465dup)	Enlarged parietal foramina	Mavrogiannis et al., 2006
				Deletion (c.504delT; p.D169X), resulting in premature stop and loss of homeodomain; point mutation in homeodomain (c.815G>C; p.R272P)	Enlarged parietal foramina	Wuyts et al., 2000
				Nonsense mutation (c.793C>T; p. R265X)	Frontonasal dysplasia	Kayserili et al., 2009
				Point mutation (c.653G>A; p.R218Q) in homeodomain nuclear localization signal	Enlarged parietal foramina	Valente et al., 2004
				Deletion (c.291delG; p.Q98SfsX83) resulting in frameshift and premature stop	Frontonasal dysplasia	El-Ruby et al., 2018
				Point mutations (c.19G_T; p.V7F, c.631A>G; p.K211E, c.917C>T; p.P306L)	Nonsyndromic craniosynostosis	Yagnik et al., 2012
Mouse	*alx1*	Craniofacial region (frontonasal head mesenchyme), lateral plate mesoderm, and limb bud mesenchyme	Beverdam and Meijlink, 2001; Zhao et al., 1994	Homozygous null mutant	Acrania and anencephaly	Zhao et al., 1996
	alx3 and *alx4*	Overlapping expression in the craniofacial region (frontonasal head mesenchyme), lateral plate mesoderm, and limb bud mesenchyme. *alx3* is expressed in parts of the developing urogenital system. *alx4* is expressed in hair follicles and dental papillae of teeth.	Qu et al., 1997a; Hudson et al., 1998; ten Berge et al., 1998	Homozygous double *alx3*/*alx4* mutant	Frontonasal dysplasia and preaxial polydactyly	Beverdam et al., 2001
Zebrafish	*alx1*, *alx3*, *alx4a*, and *alx4b*	Overlapping expression in the frontonasal mesenchyme, periocular mesenchyme, mandible arch, and the prospective palate. *alx1* is expressed in the head mesoderm.	Dee et al., 2013; Wang et al., 2019	Knockdown using *alx1* antisense morpholino oligonucleotide	Defective neural crest migration and craniofacial malformations	Dee et al., 2013
				Knockdown using *alx3* antisense morpholino oligonucleotide	No significant effect	Dee et al., 2013

(Continued)

TABLE 1 | Continued

Organism	Gene	Expression Pattern	Reference	Mutation/Perturbation	Disease/Mutational Effect	Reference
Cattle	*alx4*	n.d.	n.d.	Duplication (c.714_734dupTCACCG AGGCCCGCGTGCAG) within the homeodomain	Tibial hemimelia syndrome	Brenig et al., 2015
Cat	*alx1*	n.d.	n.d.	In frame deletion of homeodomain sequences (c.496_507delCTCTCAGGACTG)	Frontonasal dysplasia	Lyons et al., 2016
Frog	*alx1* and *alx4*	Frontal mesenchyme near the eyes	McGonnell et al., 2011	n.d.	n.d.	n.d.
Chicken	*alx1* and *alx4*	Craniofacial region (frontonasal head mesenchyme)	Bothe et al., 2011; McGonnell et al., 2011	n.d.	n.d.	n.d.
Lamprey	*alx*	Trabecular cartilaginous elements near the eye, upper lip mesenchyme and parts of the branchial basket cartilage	Cattell et al., 2011; Kuratani et al., 2016; Square et al., 2017	n.d.	n.d.	n.d.
Lancelet	*alx*	Paraxial mesoderm, pharyngeal arch mesoderm, and gut diverticulum	Meulemans and Bronner-Fraser, 2007	n.d.	n.d.	n.d.
Thin-spined sea urchin	*alx1*	Primary mesenchyme cells in embryos and juvenile skeletogenic centers in late stage larvae	Ettensohn et al., 2003;	Knockdown using *alx1* antisense morpholino oligonucleotide	Loss of skeletogenic cell specification	Ettensohn et al., 2003
			Gao and Davidson, 2008	Overexpression of Alx1 via mRNA microinjection into fertilized eggs	Ectopic activation of the skeletogenic program in mesodermal lineage cells	Ettensohn et al., 2003
	alx4	Primary mesenchyme cells and coelomic mesoderm in embryos	Rafiq et al., 2012; Koga et al., 2016	n.d.	n.d.	n.d.
Pencil urchin	*alx1*	Skeletogenic mesenchyme lineage cells	Erkenbrack and Davidson, 2015	Knockdown using *alx1* antisense morpholino oligonucleotide	Loss of skeletogenic cell specification	Erkenbrack and Davidson, 2015
Sea star	*alx1*	Juvenile skeletogenic centers in late stage larvae	Gao and Davidson, 2008	Overexpression of Alx1 via mRNA microinjection into fertilized eggs	Upregulation of sea star orthologues of sea urchin skeletogenic genes during embryogenesis	Koga et al., 2016
Sea cucumber	*alx1*	Skeletogenic mesenchyme lineage cells	McCauley et al., 2012	Knockdown using *alx1* antisense morpholino oligonucleotide	Loss of skeletogenic cell specification	McCauley et al., 2012
Brittle star	*alx1*	Skeletogenic mesenchyme lineage cells and adult skeletogenic centers in juveniles	Czarkwiani et al., 2013; Koga et al., 2016	n.d.	n.d.	n.d.
Acorn worm	*alx*	Coelomic mesoderm	Koga et al., 2016	n.d.	n.d.	n.d.

n.d., not determined.

three sources: somatic mesoderm of the lateral plate, somite-derived dermamyotome, and neural crest, while the pelvis likely arises from somatic mesoderm and sclerotome (Young et al., 2019). Genetic knockouts in mice have revealed essential and partially redundant roles for *alx1*, *alx3*, and *alx4* in the formation of the superior/anterior portion of the scapula blade (and in the development of the clavicle) and have shown that *alx1* expression in this region is under the direct control of the transcription factors Emx2 and Pbx1 (Kuijper et al., 2005a,b; Capellini et al., 2010). Similarly, compound *alx1*:*alx4* and *alx3*:*alx4* double mutants reveal overlapping roles for these genes in the formation of the pelvic skeleton (Kuijper et al., 2005b; Young et al., 2019). Unlike the neural crest-derived skeleton of the head, the scapula and pelvis both form by endochondral ossification, and defects are observed in both the cartilaginous and bony compartments of these skeletal elements when the function of *alx* family genes is compromised.

A striking developmental consequence of alx4 null mutations is preaxial polydactyly – the formation of one or more supernumerary anterior digits (Forsthoefel, 1963; Qu et al., 1997b). This effect is associated with the formation of an ectopic, anterior zone of polarizing activity (ZPA) in the limb bud and concomitant, anterior expression of *sonic hedgehog* (*shh*; Chan et al., 1995; Qu et al., 1997a,b; Takahashi et al., 1998). At relatively late developmental stages, Shh signaling is required for polydactyly to develop in *alx4*-null mutants, but it has been proposed that *alx4* also plays an earlier, Shh-independent role in anterior-posterior patterning (Kuijper et al., 2005b). The expression domains

of *alx4* and *shh* during limp outgrowth are established, in part, by mutual repression (Kuijper et al., 2005b; Matsubara et al., 2017).

Consistent with the results of experimental gene perturbations, genetic association studies in several vertebrate species have shown that polymorphisms in *alx* genes are associated with phenotypic variations in skeletal development. A genome-wide scan of genetic diversity between two closely related species of Darwin's finches has revealed that polymorphism within the *alx1* gene is strongly associated with beak morphology (Lamichhaney et al., 2015). Linkage analysis and genome-wide association studies have also identified a small 12 bp deletion in the *alx1* gene that is associated with frontonasal dysplasia in Burmese cats (Lyons et al., 2016). Furthermore, variations in the number of repeats in the coding region of *alx4* are quantitatively associated with polydactyly in the Great Pyrenees dog breed (Fondon and Garner, 2004), and a 20 bp duplication in the *alx4* gene is linked to congenital tibial hemimelia (loss or shortening of the tibia) in Gallow cattle (Brenig et al., 2015). Taken together, these findings suggest that an ancient *alx* gene may have constituted a conserved, core element of the ancestral vertebrate skeletogenic GRN and that gene duplication followed by divergence of the paralogs with respect to their developmental expression and/or biochemical properties has produced multiple *alx* family members with overlapping functions.

Considered as a whole, these studies show that members of the vertebrate *alx* gene family play a conserved, prominent role in the development of the cranial and appendicular skeletons. In contrast, they do not appear to mediate the development of the sclerotome-derived, axial skeleton of the trunk (the vertebrae and ribs). Members of the *alx* gene family may also have other, less well-characterized, developmental functions, although some of the effects of mutations in these genes on non-skeletal tissues are likely to be indirect. In the cranial region, it is well-established that *alx*-family genes are expressed robustly and selectively by neural crest cells (Rice et al., 2003; Dee et al., 2013; Garg et al., 2017), a cell population that gives rise to both cartilage and membranous bone. Expression of *alx* family genes is not uniform in all regions of the developing head, however, and it has been hypothesized that this contributes to a regulatory code that controls the region-specific identity of the cranial neural crest (Square et al., 2017). With respect to appendage development, the expression of *alx*-related genes is associated with skeleton-forming potential of mesenchymal cell that will form proximal elements of the limb girdles (clavicle, scapula, and pelvis; Young et al., 2019). The embryological origins and the precise developmental fates of these cells, as well as that of other cells of the developing limb that express *alx*-related genes, are not well-characterized.

DEVELOPMENTAL EXPRESSION OF *ALX* GENES IN OTHER CHORDATES

In basally-derived (jawless) vertebrates and cephalochordates (amphioxus), animals that possess only cartilaginous skeletons, *alx*-family genes are expressed in patterns consistent with a role in skeletogenesis. The single lamprey *alx* gene is expressed at high levels in the trabecular cartilaginous elements near the eye, in a region that may be derived from mesoderm or from the cranial neural crest (Kuratani et al., 2016; Square et al., 2017). Cephalochordates have stiff, acellular pharyngeal endoskeletons that contain fibrillar collagen, and the adult form has a cartilaginous oral skeleton that supports the cirri (Jandzik et al., 2015). Amphioxus lacks a neural crest, and the embryonic cell lineage that produces the oral skeleton has not been identified. One study has examined the expression of *alx*-related genes in cephalochordates and reported expression in the somites and right gut diverticulum at neurula/early larval stages (Meulemans and Bronner-Fraser, 2007). At present, the function of *alx*-related genes in jawless vertebrates and amphioxus has not been explored through gene perturbation studies.

DEVELOPMENTAL EXPRESSION AND FUNCTION OF *ALX* GENES IN ECHINODERMS

In echinoderm clades that form larval skeletons, *alx1* is one of the earliest regulatory genes expressed during development, and it plays a pivotal role in specifying the fate of PMCs, the embryonic skeletogenic cells (Ettensohn et al., 2003; Erkenbrack and Davidson, 2015; Dylus et al., 2016; Shashikant et al., 2018). Transcription of *alx1* can be detected as early as the 56-cell stage specifically in the large micromeres (the progenitors of PMCs), and expression remains restricted to this cell lineage throughout embryogenesis (Ettensohn et al., 2003). Perturbation of Alx1 expression using MOs inhibits PMC specification while overexpression of Alx1 results in ectopic activation of the skeletogenic program in other mesodermal lineages. Furthermore, experimental ablation of PMCs leads to the activation of *alx1* and downstream components of the skeletogenic GRN by non-skeletogenic mesoderm (NSM) cells, which ultimately reform a larval skeleton (Ettensohn et al., 2007). The ectopic activation of *alx1* is essential for NSM cells to acquire skeletogenic properties, although this activation occurs by a mechanism distinct from that which normally operates in the large micromeres (Oliveri et al., 2008; Sharma and Ettensohn, 2011; Ettensohn and Adomako-Ankomah, 2019). Remarkably, the removal of NSM cells *via* microsurgical removal of the archenteron as well as PMCs results in the activation of *alx1* and formation of a skeleton by presumptive endoderm cells (Sharma and Ettensohn, 2011).

The role of *alx1* in the skeletogenic GRN in euechinoid sea urchins has been especially well-characterized (**Figure 2**). Alx1 provides positive inputs into almost half of the ~420 genes that are differentially expressed by PMCs, highlighting the pivotal role of Alx1 in establishing skeletogenic cell identity (Rafiq et al., 2014). A recent chromatin immunoprecipitation sequencing (ChIP-seq) study determined that many of these genes, including both regulatory (i.e., transcription factor-encoding) and effector (i.e., differentiation) genes, are direct targets of *alx1* (Khor et al., 2019). A second transcription factor, Ets1, collaborates with Alx1 in the co-regulation of a large fraction of genes differentially expressed by PMCs (Rafiq et al., 2014), in many cases through a feed-forward mechanism (i.e., Ets1 > Alx1, Ets + Alx1 > effector gene; Yamasu and Wilt, 1999; Amore and Davidson, 2006; Oliveri et al., 2008; Yajima et al., 2010; Shashikant et al., 2018; Khor et al., 2019).

Downstream effector genes that are regulated by Alx1 include those that directly mediate biomineralization (e.g., those that encode secreted spicule matrix proteins that are incorporated into the biomineral) and those that mediate skeletogenesis through signaling pathways and morphogenetic cell behaviors (**Figure 2**).

The *alx1* gene is also expressed specifically in skeletogenic cells of cidaroids (pencil urchins) and holothuroids (sea cucumbers), and is required and for skeletogenesis in these species (McCauley et al., 2012; Erkenbrack and Davidson, 2015). The *alx1* gene is robustly expressed in adult skeletogenic centers, even in sea stars, which lack a larval skeleton (Gao and Davidson, 2008; Czarkwiani et al., 2013; Gao et al., 2015). Comparative studies have revealed many similarities in the gene regulatory programs of skeletogenic cells in the larva and adult (Richardson et al., 1989; Gao and Davidson, 2008; Killian et al., 2010; Czarkwiani et al., 2013; Gao et al., 2015). Hence, it is widely thought that the larval skeleton arose within the echinoderms by co-option of an adult skeletogenic program. Moreover, ectopic expression of sea urchin or sea star *alx1* in sea star embryos is sufficient to activate several sea star orthologs of sea urchin skeletogenic genes (Koga et al., 2016). These findings confirm the critical role that Alx1 plays in establishing skeletogenic identity across all echinoderms at all life history stages, supporting the view that this function was present in the last common ancestor of echinoderms.

Echinoderms also possess a paralog of *alx1*, known as *alx4*. The two genes are directly adjacent to one another in the sea urchin genome, suggesting that they arose through gene duplication. The sister group to echinoderms, the hemichordates, possess a single *alx* gene, suggesting that the gene duplication occurred after the divergence of echinoderms from hemichordates (Koga et al., 2016). The *alx4* gene, like *alx1*, is expressed by skeletogenic PMCs, but *alx4* is also expressed by presumptive coelomic pouch cells at the tip of the archenteron (Rafiq et al., 2012; Koga et al., 2016). The function of *alx4* has not been experimentally determined but it has been proposed to be involved in coelom development as the single *alx* gene in hemichordates is expressed in the coelomic mesoderm. As

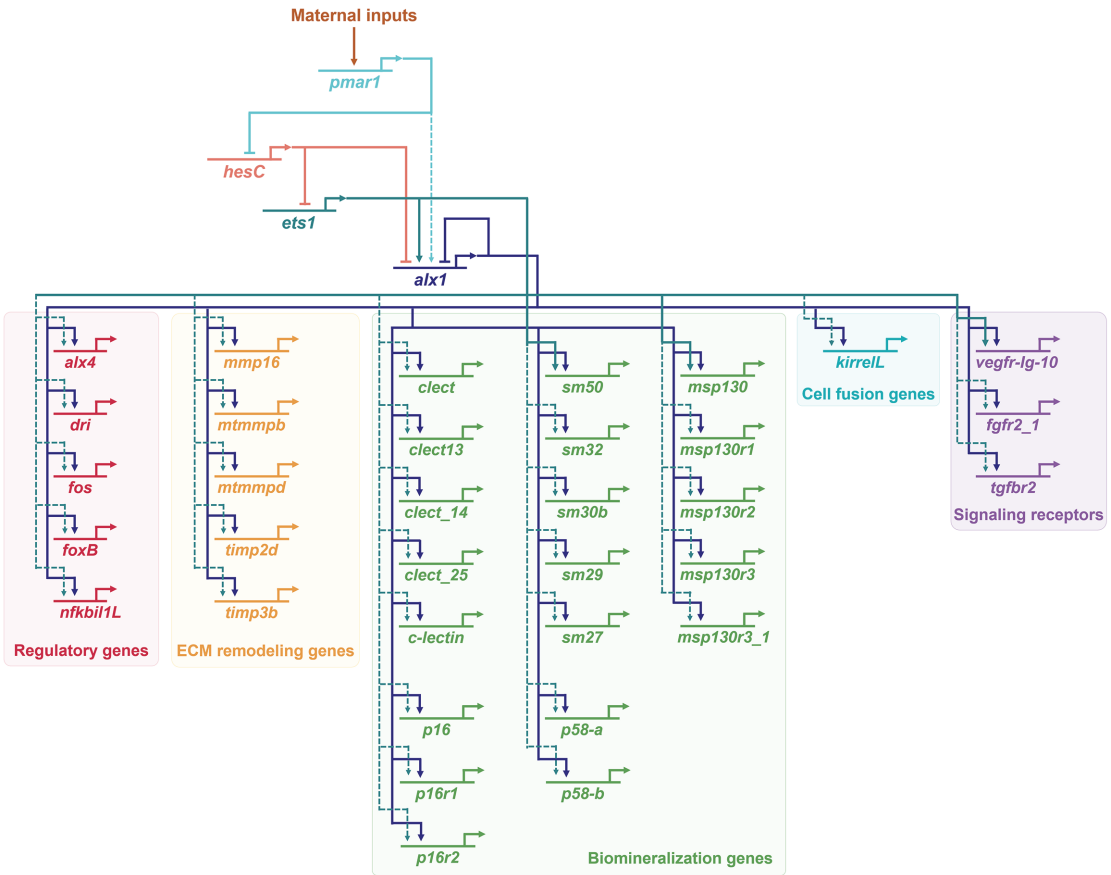

FIGURE 2 | Activation of Alx1 in euechinoids (*S. purpuratus*) and regulatory inputs into primary mesenchyme cell (PMC) effector genes. Only a small number of more than 420 effector genes differentially expressed in PMCs (Rafiq et al., 2014) is shown here. A large subset of effector genes receives regulatory inputs from both Ets1 and Alx1 (Rafiq et al., 2014). Positive regulatory inputs by Ets1 and Alx1 into *msp130*, *sm50*, and *vegf-lg-10* are described in (Oliveri et al., 2008). Direct targets of the sea urchin Alx1 (Khor et al., 2019) define a genetic subcircuit that impinges on almost all aspect of PMC morphogenesis, including directional cell migration, extracellular matrix (ECM) remodeling, cell-cell fusion, and biomineralization. Dashed arrows indicate interactions that may be indirect. For additional information regarding the developmental functions of the specific effector genes shown here, see Shashikant et al. (2018) and references therein.

adult hemichordates possess only small biomineralized elements (Cameron and Bishop, 2012), these observations suggest that *alx1* gained enhanced skeletogenic function in echinoderms secondarily. Structure-function analysis of Alx1 and Alx4 in euechinoid sea urchins has revealed that the gene duplication event permitted the functional specialization of Alx1 through changes in intron-exon organization and the acquisition of a novel protein motif known as the D2 domain (Khor and Ettensohn, 2017). As noted above, a recent genome-wide ChIP-seq study showed that a large part of the embryonic skeletogenic GRN of sea urchins is directly regulated by Alx1, including many morphoeffector genes that are also expressed in adult skeletogenic centers. Hence, a heterochronic shift in *alx1* expression from adult skeletogenic centers to the embryonic skeletogenic cells may have been sufficient to co-opt a substantial subcircuit of biomineralization genes and ultimately transfer skeletogenesis into the embryo (Khor et al., 2019).

A SUITE OF DEUTEROSTOME BIOMINERALIZATION EFFECTOR GENES REGULATED BY *ALX1* IN ECHINODERMS

Studies on vertebrates and echinoderms have identified many examples of closely related genes that mediate biomineralization in both taxa, such as collagens and carbonic anhydrases (see reviews by Veis, 2011; Le Roy et al., 2014). Here, we focus on effector genes that have been identified as direct targets of Alx1 in echinoderms (sea urchins) and that have vertebrate counterparts implicated in chondrogenesis or osteogenesis. Though much is known about the interactions between regulatory genes and signaling pathways in vertebrate neural crest and chondrogenic GRNs (Cole, 2011; Simoes-Costa and Bronner, 2015), direct transcriptional inputs into biomineralization genes that are the downstream effectors of these networks have not been elucidated. Such information will be crucial to definitively assess homology between echinoderm and vertebrate skeletogenic GRNs.

VEGF AND VEGFR

One of the direct targets of sea urchin *alx1* in biomineralizing cells is the vascular endothelial growth factor (VEGF) receptor, *vegfr-Ig-10*, one of the two *vegfr* genes in sea urchins (Duloquin et al., 2007; Rafiq et al., 2014; Khor et al., 2019). During embryonic development, *vegfr-Ig-10* expression is restricted to PMCs, while its ligand, *vegf3* is expressed in the ectoderm specifically in the regions that lie adjacent to two ventro-lateral clusters of PMCs that initiate biomineral formation. MO-based knockdown of Vegf3 or Vegfr-Ig-10 results in the downregulation of skeletogenic genes and lack of embryonic skeleton formation, while ectopic expression of Vegf3 results in supernumerary skeletal elements and irregular branching (Duloquin et al., 2007; Adomako-Ankomah and Ettensohn, 2013). The *vegfr-Ig-10* gene is also expressed in adult skeletogenic centers, even in clades that lack a larval skeleton (Gao and Davidson, 2008; Morino et al., 2012). Other comparative studies in echinoderms have found a strict correlation between the expression of *vegf3*/*vegfr-Ig-10* and the formation of an embryonic skeleton (Duloquin et al., 2007; Morino et al., 2012; Adomako-Ankomah and Ettensohn, 2013; Erkenbrack and Petsios, 2017; Erkenbrack and Thompson, 2019). Remarkably, human VEGFA is able to rescue skeleton formation in sea urchin embryos that lack endogenous Vegf3 expression (Morgulis et al., 2019).

During vertebrate endochondral ossification, the cartilage intermediate is replaced by bone in a process that is partly regulated by the formation of a vascular network (see review by Green et al., 2015). Chondrocytes stimulate vasculogenesis through the secretion of VEGF ligands (Carlevaro et al., 2000). *In vitro* studies show that VEGF ligands (VEGFA, VEGFB, and VEGFC) and VEGF receptors (VEGFR2 and VEGFR3) are expressed by chondrocytes and chondrogenic cells, and autocrine signaling through this pathway regulates morphogenesis and differentiation (Carlevaro et al., 2000; Bluteau et al., 2007). Inhibition of *Vegf* signaling perturbs ossification and bone elongation by promoting chondrocyte proliferation rather than osteoblast differentiation (Gerber et al., 1999; Jacobsen et al., 2008). Mice with conditional deletion of *vegfa* in skeletal lineage cells exhibit thinner bones and decreased skeletal mineralization (Duan et al., 2015). Moreover, conditional deletion of *vegfr2* results in reduced osteogenic differentiation (Duan et al., 2015).

MMPS AND TIMPS

Another class of effector protein common to echinoderm and vertebrate biomineralization consists of matrix remodeling proteins such as matrix metalloproteases (MMPs) and tissue inhibitors of metalloproteinases (TIMPs). MMPs constitute a class of enzymes that function in the degradation of extracellular matrix (ECM) proteins (see review by Rose and Kooyman, 2016). In sea urchins, chemical inhibition of MMPs reversibly blocks spiculogenesis by PMCs *in vivo* and *in vitro* (Roe et al., 1989; Ingersoll and Wilt, 1998). In vertebrates, *mmp-13* (collagenase-3) is expressed specifically in chondrocytes (Tuckermann et al., 2000). Additionally, *in vitro* studies have shown that silencing of *mmp-2* by siRNA disrupts chondrogenic differentiation of mesenchymal stem cells while treatment with a MMP-2 activator stimulates chondrogenesis (Jin et al., 2007). TIMPs have been reported to be the primary endogenous inhibitors of MMPs and are involved in regulating the function of MMPs in many systems (Brew and Nagase, 2010). Overexpression of *timp-3* in mice induces defects in skeletal development and growth (Poulet et al., 2016). In contrast, knockdown of *timp-1* results in upregulated proliferation of mesenchymal stem cells while delaying osteogenic differentiation (Liang et al., 2019).

SLC26

Many members of the solute carrier (SLC) family of membrane transport proteins are differentially expressed in the PMCs

(Rafiq et al., 2014; Barsi et al., 2015). In addition, Alx1 directly regulates the expression of several members of the SLC5 and SLC26 sub-families, including *Slc26a5/1* and *Slc5a11/2* (Rafiq et al., 2014; Khor et al., 2019). While there are data pointing to SLCs that are essential for echinoderm skeletogenesis, mainly *Slc4a10* (Hu et al., 2018) and *Slc26a2/7* (Piacentino et al., 2016), the functions of the proteins that are directly regulated by Alx1 have not been tested. In vertebrates, *Slc26a2*, a sulfate transporter, has been shown to be highly expressed in developing and mature cartilage (Haila et al., 2001). Mice homozygous for mutations in *Slc26a2* exhibit chondrodysplasia, a condition characterized by growth defects and skeletal dysplasia due to reduced chondrocyte proliferation (Forlino et al., 2005). Similarly, mutations in human *Slc26a2* also results in chondrodysplasia (Superti-Furga et al., 1996; Jackson et al., 2012).

FAM20C

One of the direct targets of sea urchin Alx1 is *fam20C*, which encodes a kinase of the FAM20 (family with sequence similarity 20) family (Rafiq et al., 2014; Khor et al., 2019). In vertebrates, members of this family are highly expressed in mineralized tissues, such as teeth and bone (Hao et al., 2007; Wang et al., 2010a). Fam20C is a secreted kinase responsible for the phosphorylation of secreted proteins, many of which are known to be involved in biomineralization (Tagliabracci et al., 2012). Mutations in the human *fam20C* gene cause Raine syndrome, an autosomal recessive disorder characterized by defects in bone development, including microcephaly, cleft palate, and osteosclerosis (Simpson et al., 2007; Rafaelsen et al., 2013; Takeyari et al., 2014; Seidahmed et al., 2015). *In vitro* mutational analyses suggest that Fam20C is involved in the differentiation and mineralization of mouse mesenchymal cells (Hao et al., 2007; Liu et al., 2017), and *fam20C*-null mice exhibit severe biomineralization defects, such as lesions in bones and teeth (Vogel et al., 2012; Wang et al., 2012; Du et al., 2015).

OTOPETRIN

Sea urchin Alx1 also provides positive inputs directly into *otop2L*, the single sea urchin ortholog of the vertebrate *otopetrin* genes (Rafiq et al., 2014; Khor et al., 2019). Otopetrins are multi-pass transmembrane proteins that function as proton channels (Saotome et al., 2019). In vertebrates, these proteins play an essential role in regulating the timing, size, and shape of the developing otoconia, extracellular calcium carbonate biominerals that are required for vestibular functions (Hughes et al., 2004; Sollner et al., 2004; Kim et al., 2010). During mouse and zebrafish embryogenesis, *otop1* is highly expressed in the developing sensory epithelium of the ear (Hurle et al., 2003; Hughes et al., 2004). In zebrafish, MO-based knockdown of Otop1 results in otolith malformations (Hughes et al., 2004; Sollner et al., 2004). Moreover, *otop1* knockout mice also lack otoconia, a phenotype that has been attributed to mis-regulation of intracellular calcium levels (Hughes et al., 2007; Kim et al., 2010). The function of the echinoderm Otop2L protein has not been examined.

ALX GENES AND THE EVOLUTION OF DEUTEROSTOME BIOMINERALIZATION

Among present-day deuterostomes, extensive biomineralized skeletons are found only in echinoderms and vertebrates. It is inherently difficult to reconstruct the underlying evolutionary relationships between the skeletogenic programs of these two groups, which diverged >600 million years ago (Peterson and Eernisse, 2016). It is widely accepted that the ancestral chordate possessed only a cartilaginous skeleton (Rychel et al., 2006; Murdock and Donoghue, 2011; Jandzik et al., 2015; Keating et al., 2018), strongly supporting the view that biomineralized skeletons appeared independently in vertebrates and echinoderms, and therefore, are not homologous in the strictest sense. This does not, of course, resolve the question of whether common embryological and/or genetic mechanisms were deployed to create a biomineralized skeleton in these two groups; i.e., whether skeletogenesis in the two clades is an example of "deep homology" (Shubin et al., 2009). The presence of collagenous pharyngeal cartilage in both cephalochordates and hemichordates supports the view that this was an ancestral feature of deuterostomes that was later lost in echinoderms (Rychel and Swalla, 2007; Jandzik et al., 2015). Moreover, a recent analysis of chondrogenesis in protostomes (horseshoe crabs and cuttlefish) suggests that a more ancient, SoxE and collagen-based chondrogenic gene network was present in the last common ancestor of all Bilateria (Tarazona et al., 2016), providing further support for the view that echinoderm ancestors at one time also possessed cartilage-forming cells. It should be noted that although there is no evidence for definitive cartilage in modern echinoderms, there are mesoderm-derived populations of mesenchymal cells that produce connective tissue containing fibrillar collagen (Suzuki et al., 1997; Whittaker et al., 2006; Goh and Holmes, 2017).

The evolutionary relationships among the skeletogenic cell lineages of vertebrates that express *alx*-related genes and the *alx1*-expressing cells of echinoderms are uncertain. With respect to echinoderms, considerable evidence supports the view that *alx1* arose very early in echinoderm evolution through gene duplication, relatively quickly acquired a robust, biomineralization-related function, and was subsequently co-opted into the early embryo in echinoderm taxa that possess larval skeletons (echinoids and ophiuroids; Khor and Ettensohn, 2017; Shashikant et al., 2018). The biomineralizing cells of the ancestral echinoderm, which were likely of mesodermal origins, expressed *alx1*, *ets1*, *erg*, *vegfr*, and other components of a core skeletogenic program, as well as an assortment of more rapidly evolving biomineralization effector proteins (Gao and Davidson, 2008; Dylus et al., 2018; Erkenbrack and Thompson, 2019; Li et al., 2020). To draw inferences concerning the evolution of *alx* gene expression and function more deeply within Ambulacraria (echinoderms and hemichordates), it will

be important to learn more about the single *alx* gene of hemichordates, including its pattern of expression, gene targets, and role in the formation of the small, calcareous skeletal elements of adult hemichordates (Cameron and Bishop, 2012) and to more precisely determine the embryological origins of the *alx1*-expressing cells of adult echinoderms, which are more relevant to the ancestral echinoderm condition than the more commonly studied larval forms.

In vertebrates, as noted above, the embryonic lineages of cells in the limbs and limb girdles that express *alx1*-related genes have not been mapped precisely, although many of these cells are presumably derived from the somatic layer of the lateral plate mesoderm, a major source of limb skeletal tissue. There is evidence that chondrocytes and osteoblasts of the limb are derived from a common, mesenchymal precursor cell and that the specialization of these two cell types depends upon regulatory functions of *sox9* (a member of a small number of paralogous, *soxE*-family genes in vertebrates) and other sox genes in the chondrogenic lineage, and *runx2* and *osterix* in the osteoblast lineage (Akiyama et al., 2005; Cervantes-Diaz et al., 2017; Lefebvre, 2019; Marín-Llera et al., 2019). Because *alx*-related genes have not been linked directly to the regulatory network that underlies limb skeletogenesis, and because Sox and Runx proteins are not currently known to be associated with skeleton formation in echinoderms, there is presently no obvious similarity between the GRN circuitry that controls skeletal development in the vertebrate limb and the echinoderm skeleton. As noted above, during limb girdle (scapula) development, *alx1* is co-regulated by Emx2 and Pbx1, but the orthologous echinoderm genes have not been studied in detail.

Perhaps the best-characterized cell population in vertebrates that employs *alx*-related genes in biomineralization is the cranial neural crest. There is agreement that a definitive neural crest is found only in vertebrates, but the evolutionary history of this cell population, particularly the origins of the skeletogenic (cranial) compartment, remains a subject of much debate (Jandzik et al., 2015; Rothstein et al., 2018; Cheung et al., 2019; York and McCauley, 2020). Like the program of skeletogenesis in the limb, the formation of cranial neural crest-derived cartilage and bone is believed to progress through the specification of a common osteochondral progenitor, with important contributions by Sox9 and Runx2 in chondrocyte and osteoblast differentiation, respectively (Martik and Bronner, 2017; Dash and Trainor, 2020). The regulatory inputs into *alx*-family genes in the cranial neural crest are unknown, however, and only one direct target (fgf10) has been identified (Garg et al., 2017). Thus, the precise role of *alx*-related genes in the dynamic differentiation program of skeletogenic cranial neural crest cells and their connections to the underlying gene regulatory circuitry remain to be elucidated.

As noted above, in jawless vertebrates and cephalochordates, the expression patterns of *alx*-family genes are consistent with a possible function in the formation of the cartilaginous, pharyngeal skeletons of these animals. A detailed comparison of the expression patterns of *alx*-family genes in lampreys and jawed vertebrates has led to the hypothesis that an expansion of the domain of *alx*-expressing cells may have supported the expansion of the cranial skeleton during vertebrate evolution (Square et al., 2017). With the important caveat that expression data are sparse in these taxa and function studies are lacking, these observations are consistent with the hypothesis that *alx*-related genes were expressed (at least) in the anterior, pharyngeal mesoderm of ancient chordates, in cells that produced pharyngeal cartilage (Kaucka and Adameyko, 2019).

A hypothesis that emerges from these comparative studies is that a rudimentary, ancestral program of chondrogenesis, perhaps deployed in mesenchyme cells derived from embryonic mesoderm, was present in the ancestral deuterostome and provided a suitable gene regulatory system onto which biomineralization-promoting circuitry could be layered. We propose that in echinoderms, gene duplication was followed by the neo-functionalization of *alx1*; i.e., the acquisition of a new role in robustly mediating biomineralization, as reflected by the direct transcriptional inputs this transcription factor provides into a large fraction of biomineralization effector genes (Rafiq et al., 2014; Khor et al., 2019). A similar (and presumably independent) neo-functionalization may have occurred in vertebrates, but the transcriptional targets of vertebrate *alx*-family genes have not been characterized, and therefore, it is not known whether they include effectors of biomineralization. It should be noted that possible signals of evolutionary conservation between echinoderms and vertebrates in this context would likely be obscured by the well-documented, rapid evolution of many biomineralization-related proteins (Kawasaki et al., 2004; Livingston et al., 2006; Marin et al., 2016; McDougall and Degnan, 2018). Presumably, the independent duplication of *alx*-family genes in echinoderms and vertebrates initially involved the sharing and/or duplication of *cis*-regulatory elements among paralogs, as indicated by the overlapping patterns of expression of paralogous *alx*-family genes in both taxa. The recruitment of duplicated, *alx*-related genes to a biomineralization-related function would likely have been facilitated if the ancestral gene was already expressed in an embryonic tissue that produced an extensive extracellular matrix, a prerequisite for the assembly and growth of biomineral (Bolean et al., 2017; Murshed, 2018). In this regard, it will be valuable to characterize more completely in representative deuterostomes the cell lineages that express *alx*-family genes and to better reconstruct the evolutionary relationships among those cell lineages.

AUTHOR CONTRIBUTIONS

JK and CE contributed to the conception of the review and co-wrote the paper. Both the authors contributed to the article and approved the submitted version.

FUNDING

This work was supported by National Science Foundation (IOS-1354973 to C.A.E.).

REFERENCES

Adomako-Ankomah, A., and Ettensohn, C. A. (2013). Growth factor-mediated mesodermal cell guidance and skeletogenesis during sea urchin gastrulation. *Development* 140, 4214–4225. doi: 10.1242/dev.100479

Akiyama, H., Kim, J. -E., Nakashima, K., Balmes, G., Iwai, N., Deng, J. M., et al. (2005). Osteo-chondroprogenitor cells are derived from *Sox9* expressing precursors. *Proc. Natl. Acad. Sci. U. S. A.* 102, 14665–14670. doi: 10.1073/pnas.0504750102

Amore, G., and Davidson, E. H. (2006). *cis*-regulatory control of cyclophilin, a member of the ETS-DRI skeletogenic gene battery in the sea urchin embryo. *Dev. Biol.* 293, 555–564. doi: 10.1016/j.ydbio.2006.02.024

Barsi, J. C., Tu, Q., Calestani, C., and Davidson, E. H. (2015). Genome-wide assessment of differential effector gene use in embryogenesis. *Development* 142, 3892–3901. doi: 10.1242/dev.127746

Bertola, D. R., Rodrigues, M. G., Quaio, C. R. D. C., Kim, C. A., and Passos-Bueno, M. R. (2013). Vertical transmission of a frontonasal phenotype caused by a novel *ALX4* mutation. *Am. J. Med. Genet.* 161, 600–604. doi: 10.1002/ajmg.a.35762

Beverdam, A., Brouwer, A., Reijnen, M., Korving, J., and Meijlink, F. (2001). Severe nasal clefting and abnormal embryonic apoptosis in Alx3/Alx4 double mutant mice. *Development* 128, 3975–3986.

Beverdam, A., and Meijlink, F. (2001). Expression patterns of group-I aristaless-related genes during craniofacial and limb development. *Mech. Dev.* 107, 163–167. doi: 10.1016/S0925-4773(01)00450-6

Bhattacherjee, V., Horn, K. H., Singh, S., Webb, C. L., Pisano, M. M., and Greene, R. M. (2009). CBP/p300 and associated transcriptional co-activators exhibit distinct expression patterns during murine craniofacial and neural tube development. *Int. J. Dev. Biol.* 53, 1097–1104. doi: 10.1387/ijdb.072489vb

Bluteau, G., Julien, M., Magne, D., Mallein-Gerin, F., Weiss, P., Daculsi, G., et al. (2007). VEGF and VEGF receptors are differentially expressed in chondrocytes. *Bone* 40, 568–576. doi: 10.1016/j.bone.2006.09.024

Bolean, M., Simão, A. M. S., Barioni, M. B., Favarin, B. Z., Sebinelli, H. G., Veschi, E. A., et al. (2017). Biophysical aspects of biomineralization. *Biophys. Rev.* 9, 747–760. doi: 10.1007/s12551-017-0315-1

Bothe, I., and Dietrich, S. (2006). The molecular setup of the avian head mesoderm and its implication for craniofacial myogenesis. *Dev. Dyn.* 235, 2845–2860. doi: 10.1002/dvdy.20903

Bothe, I., Tenin, G., Oseni, A., and Dietrich, S. (2011). Dynamic control of head mesoderm patterning. *Development* 138, 2807–2821. doi: 10.1242/dev.062737

Brazeau, M. D., Giles, S., Dearden, R. P., Jerve, A., Ariunchimeg, Y., Zorig, E., et al. (2020). Endochondral bone in an early Devonian 'placoderm' from Mongolia. *Nat. Ecol. Evol.* doi:10.1038/s41559-020-01290-2 [Epub ahead of print]

Brenig, B., Schütz, E., Hardt, M., Scheuermann, P., and Freick, M. (2015). A 20 bp duplication in exon 2 of the aristaless-like homeobox 4 gene (*ALX4*) is the candidate causative mutation for tibial hemimelia syndrome in galloway cattle. *PLoS One* 10:e0129208. doi: 10.1371/journal.pone.0129208

Brew, K., and Nagase, H. (2010). The tissue inhibitors of metalloproteinases (TIMPs): an ancient family with structural and functional diversity. *Biochim. Biophys. Acta* 1803, 55–71. doi: 10.1016/j.bbamcr.2010.01.003

Cameron, C. B., and Bishop, C. D. (2012). Biomineral ultrastructure, elemental constitution and genomic analysis of biomineralization-related proteins in hemichordates. *Proc. Biol. Sci.* 279, 3041–3048. doi: 10.1098/rspb.2012.0335

Capellini, T. D., Vaccari, G., Ferretti, E., Fantini, S., He, M., Pellegrini, M., et al. (2010). Scapula development is governed by genetic interactions of Pbx1 with its family members and with Emx2 via their cooperative control of Alx1. *Development* 137, 2559–2569. doi: 10.1242/dev.048819

Carlevaro, M. F., Cermelli, S., Cancedda, R., and Cancedda, F. D. (2000). Vascular endothelial growth factor (VEGF) in cartilage neovascularization andchondrocyte differentiation: auto-paracrine role during endochondral boneformation. *J. Cell Sci.* 113, 59–69.

Cattell, M., Lai, S., Cerny, R., and Medeiros, D. M. (2011). A New Mechanistic Scenario for the origin and evolution of vertebrate cartilage. *PLoS One* 6:e22474. doi: 10.1371/journal.pone.0022474

Cervantes-Diaz, F., Contreras, P., and Marcellini, S. (2017). Evolutionary origin of endochondral ossification: the transdifferentiation hypothesis. *Dev. Genes Evol.* 227, 121–127. doi: 10.1007/s00427-016-0567-y

Chan, D. C., Laufer, E., Tabin, C., and Leder, P. (1995). Polydactylous limbs in strong's Luxoid mice result from ectopic polarizing activity. *Development* 121, 1971–1978.

Cheung, M., Tai, A., Lu, P. J., and Cheah, K. S. (2019). Acquisition of multipotent and migratory neural crest cells in vertebrate evolution. *Curr. Opin. Genet. Dev.* 57, 84–90. doi: 10.1016/j.gde.2019.07.018

Cole, A. G. (2011). A review of diversity in the evolution and development of cartilage: the search for the origin of the chondrocyte. *Eur. Cells Mater.* 21, 122–129. doi: 10.22203/eCM.v021a10

Czarkwiani, A., Dylus, D. V., and Oliveri, P. (2013). Expression of skeletogenic genes during arm regeneration in the brittle star *Amphiura filiformis*. *Gene Expr. Patterns* 13, 464–472. doi: 10.1016/j.gep.2013.09.002

Dash, S., and Trainor, P. A. (2020). The development, patterning and evolution of neural crest cell differentiation into cartilage and bone. *Bone* 137:115409. doi: 10.1016/j.bone.2020.115409

Dee, C. T., Szymoniuk, C. R., Mills, P. E. D., and Takahashi, T. (2013). Defective neural crest migration revealed by a zebrafish model of Alx1-related frontonasal dysplasia. *Hum. Mol. Genet.* 22, 239–251. doi: 10.1093/hmg/dds423

Du, E. -X., Wang, X. -F., Yang, W. -C., Kaback, D., Yee, S. -P., Qin, C. -L., et al. (2015). Characterization of Fam20C expression in odontogenesis and osteogenesis using transgenic mice. *Int. J. Oral Sci.* 7, 89–94. doi: 10.1038/ijos.2014.67

Duan, X., Murata, Y., Liu, Y., Nicolae, C., Olsen, B. R., and Berendsen, A. D. (2015). Vegfa regulates perichondrial vascularity and osteoblast differentiation in bone development. *Development* 142, 1984–1991. doi: 10.1242/dev.117952

Duloquin, L., Lhomond, G., and Gache, C. (2007). Localized VEGF signaling from ectoderm to mesenchyme cells controls morphogenesis of the sea urchin embryo skeleton. *Development* 134, 2293–2302. doi: 10.1242/dev.005108

Dylus, D. V., Czarkwiani, A., Blowes, L. M., Elphick, M. R., and Oliveri, P. (2018). Developmental transcriptomics of the brittle star *Amphiura filiformis* reveals gene regulatory network rewiring in echinoderm larval skeleton evolution. *Genome Biol.* 19:26. doi: 10.1186/s13059-018-1402-8

Dylus, D. V., Czarkwiani, A., Stångberg, J., Ortega-Martinez, O., Dupont, S., and Oliveri, P. (2016). Large-scale gene expression study in the ophiuroid *Amphiura filiformis* provides insights into evolution of gene regulatory networks. *EvoDevo* 7:2. doi: 10.1186/s13227-015-0039-x

El-Ruby, M., El-Din Fayez, A., El-Dessouky, S. H., Aglan, M. S., Mazen, I., Ismail, N., et al. (2018). Identification of a novel homozygous *ALX4* mutation in two unrelated patients with frontonasal dysplasia type-2. *Am. J. Med. Genet.* 176, 1190–1194. doi: 10.1002/ajmg.a.38655

Erkenbrack, E. M., and Davidson, E. H. (2015). Evolutionary rewiring of gene regulatory network linkages at divergence of the echinoid subclasses. *Proc. Natl. Acad. Sci. U. S. A.* 112, E4075–E4084. doi: 10.1073/pnas.1509845112

Erkenbrack, E. M., and Petsios, E. (2017). A conserved role for VEGF signaling in specification of homologous mesenchymal cell types positioned at spatially distinct developmental addresses in early development of sea urchins. *J. Exp. Zool. B Mol. Dev. Evol.* 328, 423–432. doi: 10.1002/jez.b.22743

Erkenbrack, E. M., and Thompson, J. R. (2019). Cell type phylogenetics informs the evolutionary origin of echinoderm larval skeletogenic cell identity. *Commun. Biol.* 2:160. doi: 10.1038/s42003-019-0417-3

Ettensohn, C. A. (2020). The gene regulatory control of sea urchin gastrulation. *Mech. Dev.* 162:103599. doi: 10.1016/j.mod.2020.103599

Ettensohn, C. A., and Adomako-Ankomah, A. (2019). The evolution of a new cell type was associated with competition for a signaling ligand. *PLoS Biol.* 17:e3000460. doi: 10.1371/journal.pbio.3000460

Ettensohn, C. A., Illies, M. R., Oliveri, P., and De Jong, D. L. (2003). Alx1, a member of the Cart1/Alx3/Alx4 subfamily of paired-class homeodomain proteins, is an essential component of the gene network controlling skeletogenic fate specification in the sea urchin embryo. *Development* 130, 2917–2928. doi: 10.1242/dev.00511

Ettensohn, C. A., Kitazawa, C., Cheers, M. S., Leonard, J. D., and Sharma, T. (2007). Gene regulatory networks and developmental plasticity in the early sea urchin embryo: alternative deployment of the skeletogenic gene regulatory network. *Development* 134, 3077–3087. doi: 10.1242/dev.009092

Fondon, J. W., and Garner, H. R. (2004). Molecular origins of rapid and continuous morphological evolution. *Proc. Natl. Acad. Sci. U. S. A.* 101, 18058–18063. doi: 10.1073/pnas.0408118101

Forlino, A., Piazza, R., Tiveron, C., Torre, S. D., Tatangelo, L., Bonafè, L., et al. (2005). A diastrophic dysplasia sulfate transporter (SLC26A2) mutant mouse: morphological and biochemical characterization of the resulting chondrodysplasia phenotype. *Hum. Mol. Genet.* 14, 859–871. doi: 10.1093/hmg/ddi079

Forsthoefel, P. F. (1963). The embryological development of the effects of strong's luxoid gene in the mouse. *J. Morphol.* 113, 427–451. doi: 10.1002/jmor.1051130307

Gao, F., and Davidson, E. H. (2008). Transfer of a large gene regulatory apparatus to a new developmental address in echinoid evolution. *Proc. Natl. Acad. Sci. U. S. A.* 105, 6091–6096. doi: 10.1073/pnas.0801201105

Gao, F., Thompson, J. R., Petsios, E., Erkenbrack, E., Moats, R. A., Bottjer, D. J., et al. (2015). Juvenile skeletogenesis in anciently diverged sea urchin clades. *Dev. Biol.* 400, 148–158. doi: 10.1016/j.ydbio.2015.01.017

Garg, A., Bansal, M., Gotoh, N., Feng, G. -S., Zhong, J., Wang, F., et al. (2017). Alx4 relays sequential FGF signaling to induce lacrimal gland morphogenesis. *PLoS Genet.* 13:e1007047. doi: 10.1371/journal.pgen.1007047

Gerber, H. -P., Vu, T. H., Ryan, A. M., Kowalski, J., Werb, Z., and Ferrara, N. (1999). VEGF couples hypertrophic cartilage remodeling, ossification and angiogenesis during endochondral bone formation. *Nat. Med.* 5, 623–628. doi: 10.1038/9467

Goh, K., and Holmes, D. (2017). Collagenous extracellular matrix biomaterials for tissue engineering: lessons from the common sea urchin tissue. *Int. J. Mol. Sci.* 18:901. doi: 10.3390/ijms18050901

Green, J. D., Tollemar, V., Dougherty, M., Yan, Z., Yin, L., Ye, J., et al. (2015). Multifaceted signaling regulators of chondrogenesis: implications in cartilage regeneration and tissue engineering. *Genes Dis.* 2, 307–327. doi: 10.1016/j.gendis.2015.09.003

Haila, S., Hästbacka, J., Böhling, T., Karjalainen–Lindsberg, M. -L., Kere, J., and Saarialho–Kere, U. (2001). SLC26A2 (diastrophic dysplasia sulfate transporter) is expressed in developing and mature cartilage but also in other tissues and cell types. *J. Histochem. Cytochem.* 49, 973–982. doi: 10.1177/002215540104900805

Hao, J., Narayanan, K., Muni, T., Ramachandran, A., and George, A. (2007). Dentin matrix protein 4, a novel secretory calcium-binding protein that modulates odontoblast differentiation. *J. Biol. Chem.* 282, 15357–15365. doi: 10.1074/jbc.M701547200

Hirasawa, T., and Kuratani, S. (2015). Evolution of the vertebrate skeleton: morphology, embryology, and development. *Zool. Lett.* 1:2. doi: 10.1186/s40851-014-0007-7

Hu, M. Y., Yan, J. -J., Petersen, I., Himmerkus, N., Bleich, M., and Stumpp, M. (2018). A SLC4 family bicarbonate transporter is critical for intracellular pH regulation and biomineralization in sea urchin embryos. *eLife* 7:e36600. doi: 10.7554/eLife.36600

Hudson, R., Taniguchi-Sidle, A., Boras, K., Wiggan, O., and Hamel, P. A. (1998). Alx-4, a transcriptional activator whose expression is restricted to sites of epithelial-mesenchymal interactions. *Dev. Dyn.* 213, 159–169. doi: 10.1002/(SICI)1097-0177(199810)213:2<159::AID-AJA1>3.0.CO;2-F

Hughes, I., Blasiole, B., Huss, D., Warchol, M. E., Rath, N. P., Hurle, B., et al. (2004). Otopetrin 1 is required for otolith formation in the zebrafish *Danio rerio*. *Dev. Biol.* 276, 391–402. doi: 10.1016/j.ydbio.2004.09.001

Hughes, I., Saito, M., Schlesinger, P. H., and Ornitz, D. M. (2007). Otopetrin 1 activation by purinergic nucleotides regulates intracellular calcium. *Proc. Natl. Acad. Sci. U. S. A.* 104, 12023–12028. doi: 10.1073/pnas.0705182104

Hurle, B., Ignatova, E., Massironi, S. M., Mashimo, T., Rios, X., Thalmann, I., et al. (2003). Non-syndromic vestibular disorder with otoconial agenesis in tilted/mergulhador mice caused by mutations in otopetrin 1. *Hum. Mol. Genet.* 12, 777–789. doi: 10.1093/hmg/ddg087

Ingersoll, E. P., and Wilt, F. H. (1998). Matrix metalloproteinase inhibitors disrupt spicule formation by primary mesenchyme cells in the sea urchin embryo. *Dev. Biol.* 196, 95–106. doi: 10.1006/dbio.1998.8857

Jackson, G. C., Mittaz-Crettol, L., Taylor, J. A., Mortier, G. R., Spranger, J., Zabel, B., et al. (2012). Pseudoachondroplasia and multiple epiphyseal dysplasia: a 7-year comprehensive analysis of the known disease genes identify novel and recurrent mutations and provides an accurate assessment of their relative contribution. *Hum. Mutat.* 33, 144–157. doi: 10.1002/humu.21611

Jacobsen, K. A., Al-Aql, Z. S., Wan, C., Fitch, J. L., Stapleton, S. N., Mason, Z. D., et al. (2008). Bone formation during distraction osteogenesis is dependent on both VEGFR1 and VEGFR2 signaling. *J. Bone Miner. Res.* 23, 596–609. doi: 10.1359/jbmr.080103

Jacome-Galarza, C. E., Percin, G. I., Muller, J. T., Mass, E., Lazarov, T., Eitler, J., et al. (2019). Developmental origin, functional maintenance and genetic rescue of osteoclasts. *Nature* 568, 541–545. doi: 10.1038/s41586-019-1105-7

Jandzik, D., Garnett, A. T., Square, T. A., Cattell, M. V., Yu, J. -K., and Medeiros, D. M. (2015). Evolution of the new vertebrate head by co-option of an ancient chordate skeletal tissue. *Nature* 518, 534–537. doi: 10.1038/nature14000

Jin, E. -J., Choi, Y. -A., Kyun Park, E., Bang, O. -S., and Kang, S. -S. (2007). MMP-2 functions as a negative regulator of chondrogenic cell condensation via down-regulation of the FAK-integrin beta1 interaction. *Dev. Biol.* 308, 474–484. doi: 10.1016/j.ydbio.2007.06.003

Kaucka, M., and Adameyko, I. (2019). Evolution and development of the cartilaginous skull: from a lancelet towards a human face. *Semin. Cell Dev. Biol.* 91, 2–12. doi: 10.1016/j.semcdb.2017.12.007

Kawasaki, K., Suzuki, T., and Weiss, K. M. (2004). Genetic basis for the evolution of vertebrate mineralized tissue. *Proc. Natl. Acad. Sci. U. S. A.* 101, 11356–11361. doi: 10.1073/pnas.0404279101

Kayserili, H., Uz, E., Niessen, C., Vargel, I., Alanay, Y., Tuncbilek, G., et al. (2009). ALX4 dysfunction disrupts craniofacial and epidermal development. *Hum. Mol. Genet.* 18, 4357–4366. doi: 10.1093/hmg/ddp391

Keating, J. N., Marquart, C. L., Marone, F., and Donoghue, P. C. J. (2018). The nature of aspidin and the evolutionary origin of bone. *Nat. Ecol. Evol.* 2, 1501–1506. doi: 10.1038/s41559-018-0624-1

Khor, J. M., and Ettensohn, C. A. (2017). Functional divergence of paralogous transcription factors supported the evolution of biomineralization in echinoderms. *eLife* 6:e32728. doi: 10.7554/eLife.32728

Khor, J. M., Guerrero-Santoro, J., and Ettensohn, C. A. (2019). Genome-wide identification of binding sites and gene targets of Alx1, a pivotal regulator of echinoderm skeletogenesis. *Development* 146:dev180653. doi: 10.1242/dev.180653

Killian, C. E., Croker, L., and Wilt, F. H. (2010). SpSM30 gene family expression patterns in embryonic and adult biomineralized tissues of the sea urchin, *Strongylocentrotus purpuratus*. *Gene Expr. Patterns* 10, 135–139. doi: 10.1016/j.gep.2010.01.002

Kim, E., Hyrc, K. L., Speck, J., Lundberg, Y. W., Salles, F. T., Kachar, B., et al. (2010). Regulation of cellular calcium in vestibular supporting cells by otopetrin 1. *J. Neurophysiol.* 104, 3439–3450. doi: 10.1152/jn.00525.2010

Knoll, A. H. (2003). Biomineralization and evolutionary history. *Rev. Mineral. Geochem.* 54, 329–356. doi: 10.2113/0540329

Koga, H., Fujitani, H., Morino, Y., Miyamoto, N., Tsuchimoto, J., Shibata, T. F., et al. (2016). Experimental approach reveals the role of *alx1* in the evolution of the echinoderm larval skeleton. *PLoS One* 11:e0149067. doi: 10.1371/journal.pone.0149067

Kuijper, S., Beverdam, A., Kroor, C., Brouwer, A., Candille, S., Barsh, G., et al. (2005a). Genetics of shoulder girdle formation: roles of Tbx15 and aristaless-like genes. *Development* 132, 1601–1610. doi: 10.1242/dev.01735

Kuijper, S., Feitsma, H., Sheth, R., Korving, J., Reijnen, M., and Meijlink, F. (2005b). Function and regulation of Alx4 in limb development: complex genetic interactions with Gli3 and Shh. *Dev. Biol.* 285, 533–544. doi: 10.1016/j.ydbio.2005.06.017

Kuratani, S., Oisi, Y., and Ota, K. G. (2016). Evolution of the vertebrate cranium: viewed from hagfish developmental studies. *Zool. Sci.* 33, 229–238. doi: 10.2108/zs150187

Lamichhaney, S., Berglund, J., Almén, M. S., Maqbool, K., Grabherr, M., Martinez-Barrio, A., et al. (2015). Evolution of Darwin's finches and their beaks revealed by genome sequencing. *Nature* 518, 371–375. doi: 10.1038/nature14181

Le Douarin, N. M. (2012). Piecing together the vertebrate skull. *Development* 139, 4293–4296. doi: 10.1242/dev.085191

Le Roy, N., Jackson, D. J., Marie, B., Ramos-Silva, P., and Marin, F. (2014). The evolution of metazoan α-carbonic anhydrases and their roles in calcium carbonate biomineralization. *Front. Zool.* 11:75. doi: 10.1186/s12983-014-0075-8

Lefebvre, V. (2019). Roles and regulation of SOX transcription factors in skeletogenesis. *Curr. Top. Dev. Biol.* 133, 171–193. doi: 10.1016/bs.ctdb.2019.01.007

Li, Y., Omori, A., Flores, R. L., Satterfield, S., Nguyen, C., Ota, T., et al. (2020). Genomic insights of body plan transitions from bilateral to pentameral symmetry in echinoderms. *Commun. Biol.* 3:371. doi: 10.1038/s42003-020-1091-1

Liang, T., Gao, W., Zhu, L., Ren, J., Yao, H., Wang, K., et al. (2019). TIMP-1 inhibits proliferation and osteogenic differentiation of hBMSCs through Wnt/β-catenin signaling. *Biosci. Rep.* 39:BSR20181290. doi: 10.1042/BSR20181290

Liao, H. -M., Fang, J. -S., Chen, Y. -J., Wu, K. -L., Lee, K. -F., and Chen, C. -H. (2011). Clinical and molecular characterization of a transmitted reciprocal translocation t(1;12)(p32.1;q21.3) in a family co-segregating with mental retardation, language delay, and microcephaly. *BMC Med. Genet.* 12:70. doi: 10.1186/1471-2350-12-70

Liu, P., Ma, S., Zhang, H., Liu, C., Lu, Y., Chen, L., et al. (2017). Specific ablation of mouse Fam20C in cells expressing type I collagen leads to skeletal defects and hypophosphatemia. *Sci. Rep.* 7:3590. doi: 10.1038/s41598-017-03960-x

Livingston, B. T., Killian, C. E., Wilt, F., Cameron, A., Landrum, M. J., Ermolaeva, O., et al. (2006). A genome-wide analysis of biomineralization-related proteins in the sea urchin *Strongylocentrotus purpuratus*. *Dev. Biol.* 300, 335–348. doi: 10.1016/j.ydbio.2006.07.047

Lyons, L. A., Erdman, C. A., Grahn, R. A., Hamilton, M. J., Carter, M. J., Helps, C. R., et al. (2016). Aristaless-like homeobox protein 1 (ALX1) variant associated with craniofacial structure and frontonasal dysplasia in Burmese cats. *Dev. Biol.* 409, 451–458. doi: 10.1016/j.ydbio.2015.11.015

Mackie, E. J., Ahmed, Y. A., Tatarczuch, L., Chen, K. -S., and Mirams, M. (2008). Endochondral ossification: how cartilage is converted into bone in the developing skeleton. *Int. J. Biochem. Cell Biol.* 40, 46–62. doi: 10.1016/j.biocel.2007.06.009

Marin, F., Bundeleva, I., Takeuchi, T., Immel, F., and Medakovic, D. (2016). Organic matrices in metazoan calcium carbonate skeletons: composition, functions, evolution. *J. Struct. Biol.* 196, 98–106. doi: 10.1016/j.jsb.2016.04.006

Marín-Llera, J. C., Garciadiego-Cázares, D., and Chimal-Monroy, J. (2019). Understanding the cellular and molecular mechanisms that control early cell fate decisions during appendicular skeletogenesis. *Front. Genet.* 10:977. doi: 10.3389/fgene.2019.00977

Martik, M. L., and Bronner, M. E. (2017). Regulatory logic underlying diversification of the neural crest. *Trends Genet.* 33, 715–727. doi: 10.1016/j.tig.2017.07.015

Matsubara, H., Saito, D., Abe, G., Yokoyama, H., Suzuki, T., and Tamura, K. (2017). Upstream regulation for initiation of restricted Shh expression in the chick limb bud. *Dev. Dyn.* 246, 417–430. doi: 10.1002/dvdy.24493

Mavrogiannis, L. A., Taylor, I. B., Davies, S. J., Ramos, F. J., Olivares, J. L., and Wilkie, A. O. M. (2006). Enlarged parietal foramina caused by mutations in the homeobox genes ALX4 and MSX2: from genotype to phenotype. *Eur. J. Hum. Genet.* 14, 151–158. doi: 10.1038/sj.ejhg.5201526

McCauley, B. S., Wright, E. P., Exner, C., Kitazawa, C., and Hinman, V. F. (2012). Development of an embryonic skeletogenic mesenchyme lineage in a sea cucumber reveals the trajectory of change for the evolution of novel structures in echinoderms. *EvoDevo* 3:17. doi: 10.1186/2041-9139-3-17

McClay, D. R., Warner, J., Martik, M., Miranda, E., and Slota, L. (2020). Gastrulation in the sea urchin. *Curr. Top. Dev. Biol.* 136, 195–218. doi: 10.1016/bs.ctdb.2019.08.004

McDougall, C., and Degnan, B. M. (2018). The evolution of mollusc shells. *Wiley Interdiscip. Rev. Dev. Biol.* 7:e313. doi: 10.1002/wdev.313

McGonnell, I. M., Graham, A., Richardson, J., Fish, J. L., Depew, M. J., Dee, C. T., et al. (2011). Evolution of the Alx homeobox gene family: parallel retention and independent loss of the vertebrate *Alx3* gene. *Evol. Dev.* 13, 343–351. doi: 10.1111/j.1525-142X.2011.00489.x

McIntyre, D. C., Lyons, D. C., Martik, M., and McClay, D. R. (2014). Branching out: origins of the sea urchin larval skeleton in development and evolution. *Genesis* 52, 173–185. doi: 10.1002/dvg.22756

Meulemans, D., and Bronner-Fraser, M. (2007). Insights from amphioxus into the evolution of vertebrate cartilage. *PLoS One* 2:e787. doi: 10.1371/journal.pone.0000787

Morgulis, M., Gildor, T., Roopin, M., Sher, N., Malik, A., Lalzar, M., et al. (2019). Possible cooption of a VEGF-driven tubulogenesis program for biomineralization in echinoderms. *Proc. Natl. Acad. Sci. U. S. A.* 116, 12353–12362. doi: 10.1073/pnas.1902126116

Morino, Y., Koga, H., Tachibana, K., Shoguchi, E., Kiyomoto, M., and Wada, H. (2012). Heterochronic activation of VEGF signaling and the evolution of the skeleton in echinoderm pluteus larvae. *Evol. Dev.* 14, 428–436. doi: 10.1111/j.1525-142X.2012.00563.x

Murdock, D. J. E., and Donoghue, P. C. J. (2011). Evolutionary origins of animal skeletal biomineralization. *Cells Tissues Organs* 194, 98–102. doi: 10.1159/000324245

Murshed, M. (2018). Mechanism of bone mineralization. *Cold Spring Harb. Perspect. Med.* 8:a031229. doi: 10.1101/cshperspect.a031229

Noden, D. M., and Trainor, P. A. (2005). Relations and interactions between cranial mesoderm and neural crest populations: neural crest populations. *J. Anat.* 207, 575–601. doi: 10.1111/j.1469-7580.2005.00473.x

Oliveri, P., Tu, Q., and Davidson, E. H. (2008). Global regulatory logic for specification of an embryonic cell lineage. *Proc. Natl. Acad. Sci. U. S. A.* 105, 5955–5962. doi: 10.1073/pnas.0711220105

Percival, C. J., and Richtsmeier, J. T. (2013). Angiogenesis and intramembranous osteogenesis. *Dev. Dyn.* 242, 909–922. doi: 10.1002/dvdy.23992

Peterson, K. J., and Eernisse, D. J. (2016). The phylogeny, evolutionary developmental biology, and paleobiology of the deuterostomia: 25 years of new techniques, new discoveries, and new ideas. *Org. Divers. Evol.* 16, 401–418. doi: 10.1007/s13127-016-0270-x

Piacentino, M. L., Zuch, D. T., Fishman, J., Rose, S., Speranza, E. E., Li, C., et al. (2016). RNA-Seq identifies SPGs as a ventral skeletal patterning cue in sea urchins. *Development* 143, 703–714. doi: 10.1242/dev.129312

Poulet, B., Liu, K., Plumb, D., Vo, P., Shah, M., Staines, K., et al. (2016). Overexpression of TIMP-3 in chondrocytes produces transient reduction in growth plate length but permanently reduces adult bone quality and quantity. *PLoS One* 11:e0167971. doi: 10.1371/journal.pone.0167971

Qu, S., Li, L., and Wisdom, R. (1997a). Alx-4: cDNA cloning and characterization of a novel paired-type homeodomain protein. *Gene* 203, 217–223. doi: 10.1016/S0378-1119(97)00497-6

Qu, S., Niswender, K. D., Ji, Q., Meer, R.van der, Keeney, D., and Magnuson, M. A. (1997b). Polydactyly and ectopic ZPA formation in Alx-4 mutant mice. *Development* 124, 3999–4008.

Rafaelsen, S. H., Raeder, H., Fagerheim, A. K., Knappskog, P., Carpenter, T. O., Johansson, S., et al. (2013). Exome sequencing reveals FAM20c mutations associated with fibroblast growth factor 23-related hypophosphatemia, dental anomalies, and ectopic calcification. *J. Bone Miner. Res.* 28, 1378–1385. doi: 10.1002/jbmr.1850

Rafiq, K., Cheers, M. S., and Ettensohn, C. A. (2012). The genomic regulatory control of skeletal morphogenesis in the sea urchin. *Development* 139, 579–590. doi: 10.1242/dev.073049

Rafiq, K., Shashikant, T., McManus, C. J., and Ettensohn, C. A. (2014). Genome-wide analysis of the skeletogenic gene regulatory network of sea urchins. *Development* 141, 950–961. doi: 10.1242/dev.112763

Rice, R., Rice, D. P. C., Olsen, B. R., and Thesleff, I. (2003). Progression of calvarial bone development requires Foxc1 regulation of Msx2 and Alx4. *Dev. Biol.* 262, 75–87. doi: 10.1016/S0012-1606(03)00355-5

Richardson, W., Kitajima, T., Wilt, F., and Benson, S. (1989). Expression of an embryonic spicule matrix gene in calcified tissues of adult sea urchins. *Dev. Biol.* 132, 266–269. doi: 10.1016/0012-1606(89)90222-4

Roe, J. L., Park, H. R., Strittmatter, W. J., and Lennarz, W. J. (1989). Inhibitors of metalloendoproteases block spiculogenesis in sea urchin primary mesenchyme cells. *Exp. Cell Res.* 181, 542–550. doi: 10.1016/0014-4827(89)90110-9

Rose, B. J., and Kooyman, D. L. (2016). A tale of two joints: the role of matrix metalloproteases in cartilage biology. *Dis. Markers* 2016:4895050. doi: 10.1155/2016/4895050

Rothstein, M., Bhattacharya, D., and Simoes-Costa, M. (2018). The molecular basis of neural crest axial identity. *Dev. Biol.* 444, S170–S180. doi: 10.1016/j.ydbio.2018.07.026

Rychel, A. L., Smith, S. E., Shimamoto, H. T., and Swalla, B. J. (2006). Evolution and development of the chordates: collagen and pharyngeal cartilage. *Mol. Biol. Evol.* 23, 541–549. doi: 10.1093/molbev/msj055

Rychel, A. L., and Swalla, B. J. (2007). Development and evolution of chordate cartilage. *J. Exp. Zool. B Mol. Dev. Evol.* 308, 325–335. doi: 10.1002/jez.b.21157

Santagati, F., and Rijli, F. M. (2003). Cranial neural crest and the building of the vertebrate head. *Nat. Rev. Neurosci.* 4, 806–818. doi: 10.1038/nrn1221

Saotome, K., Teng, B., Tsui, C. C., Lee, W. -H., Tu, Y. -H., Kaplan, J. P., et al. (2019). Structures of the otopetrin proton channels Otop1 and Otop3. *Nat. Struct. Mol. Biol.* 26, 518–525. doi: 10.1038/s41594-019-0235-9

Seidahmed, M. Z., Alazami, A. M., Abdelbasit, O. B., Al Hussein, K., Miqdad, A. M., Abu-Sa'da, O., et al. (2015). Report of a case of Raine syndrome and literature review. *Am. J. Med. Genet. A* 167, 2394–2398. doi: 10.1002/ajmg.a.37159

Sharma, T., and Ettensohn, C. A. (2011). Regulative deployment of the skeletogenic gene regulatory network during sea urchin development. *Development* 138, 2581–2590. doi: 10.1242/dev.065193

Shashikant, T., Khor, J. M., and Ettensohn, C. A. (2018). From genome to anatomy: the architecture and evolution of the skeletogenic gene regulatory network of sea urchins and other echinoderms. *Genesis* 56:e23253. doi: 10.1002/dvg.23253

Shubin, N., Tabin, C., and Carroll, S. (2009). Deep homology and the origins of evolutionary novelty. *Nature* 457, 818–823. doi: 10.1038/nature07891

Simoes-Costa, M., and Bronner, M. E. (2015). Establishing neural crest identity: a gene regulatory recipe. *Development* 142, 242–257. doi: 10.1242/dev.105445

Simpson, M. A., Hsu, R., Keir, L. S., Hao, J., Sivapalan, G., Ernst, L. M., et al. (2007). Mutations in FAM20C are associated with lethal osteosclerotic bone dysplasia (Raine syndrome), highlighting a crucial molecule in bone development. *Am. J. Hum. Genet.* 81, 906–912. doi: 10.1086/522240

Sollner, C., Schwarz, H., Geisler, R., and Nicolson, T. (2004). Mutated otopetrin 1 affects the genesis of otoliths and the localization of Starmaker in zebrafish. *Dev. Genes Evol.* 214, 582–590. doi: 10.1007/s00427-004-0440-2

Square, T., Jandzik, D., Cattell, M., Coe, A., Doherty, J., and Medeiros, D. M. (2015). A gene expression map of the larval *Xenopus laevis* head reveals developmental changes underlying the evolution of new skeletal elements. *Dev. Biol.* 397, 293–304. doi: 10.1016/j.ydbio.2014.10.016

Square, T., Jandzik, D., Romášek, M., Cerny, R., and Medeiros, D. M. (2017). The origin and diversification of the developmental mechanisms that pattern the vertebrate head skeleton. *Dev. Biol.* 427, 219–229. doi: 10.1016/j.ydbio.2016.11.014

Superti-Furga, A., Rossi, A., Steinmann, B., and Gitzelmann, R. (1996). A chondrodysplasia family produced by mutations in the diastrophic dysplasia sulfate transporter gene: genotype/phenotype correlations. *Am. J. Med. Genet.* 63, 144–147. doi: 10.1002/(SICI)1096-8628(19960503)63:1<144::AID-AJMG25>3.0.CO;2-N

Suzuki, H. R., Reiter, R. S., D'Alessio, M., Di Liberto, M., Ramirez, F., Exposito, J. -Y., et al. (1997). Comparative analysis of fibrillar and basement membrane collagen expression in embryos of the sea urchin, *Strongylocentrotus purpuratus*. *Zool. Sci.* 14, 449–454. doi: 10.2108/zsj.14.449

Tagliabracci, V. S., Engel, J. L., Wen, J., Wiley, S. E., Worby, C. A., Kinch, L. N., et al. (2012). Secreted kinase phosphorylates extracellular proteins that regulate biomineralization. *Science* 336, 1150–1153. doi: 10.1126/science.1217817

Takahashi, M., Tamura, K., Buscher, D., Masuya, H., Yonei-Tamura, S., Matsumoto, K., et al. (1998). The role of Alx-4 in the establishment of anteroposterior polarity during vertebrate limb development. *Development* 125, 4417–4425.

Takeyari, S., Yamamoto, T., Kinoshita, Y., Fukumoto, S., Glorieux, F. H., Michigami, T., et al. (2014). Hypophosphatemic osteomalacia and bone sclerosis caused by a novel homozygous mutation of the FAM20C gene in an elderly man with a mild variant of Raine syndrome. *Bone* 67, 56–62. doi: 10.1016/j.bone.2014.06.026

Tarazona, O. A., Slota, L. A., Lopez, D. H., Zhang, G., and Cohn, M. J. (2016). The genetic program for cartilage development has deep homology within Bilateria. *Nature* 533, 86–89. doi: 10.1038/nature17398

ten Berge, D., Brouwer, A., El Bahi, S., Guénet, J. -L., Robert, B., and Meijlink, F. (1998). Mouse Alx3: an aristaless-like homeobox gene expressed during embryogenesis in ectomesenchyme and lateral plate mesoderm. *Dev. Biol.* 199, 11–25. doi: 10.1006/dbio.1998.8921

Tuckermann, J. P., Pittois, K., Partridge, N. C., Merregaert, J., and Angel, P. (2000). Collagenase-3 (MMP-13) and integral membrane protein 2a (Itm2a) are marker genes of chondrogenic/osteoblastic cells in bone formation: sequential temporal, and spatial expression of Itm2a, alkaline phosphatase, MMP-13, and osteocalcin in the mouse. *J. Bone Miner. Res.* 15, 1257–1265. doi: 10.1359/jbmr.2000.15.7.1257

Twigg, S. R. F., Versnel, S. L., Nürnberg, G., Lees, M. M., Bhat, M., Hammond, P., et al. (2009). Frontorhiny, a distinctive presentation of frontonasal dysplasia caused by recessive mutations in the ALX3 homeobox gene. *Am. J. Hum. Genet.* 84, 698–705. doi: 10.1016/j.ajhg.2009.04.009

Ullah, A., Umair, M., E-Kalsoom, U., Shahzad, S., Basit, S., and Ahmad, W. (2018). Exome sequencing revealed a novel nonsense variant in *ALX3* gene underlying frontorhiny. *J. Hum. Genet.* 63, 97–100. doi: 10.1038/s10038-017-0358-y

Uz, E., Alanay, Y., Aktas, D., Vargel, I., Gucer, S., Tuncbilek, G., et al. (2010). Disruption of ALX1 causes extreme microphthalmia and severe facial clefting: expanding the spectrum of autosomal-recessive ALX-related frontonasal dysplasia. *Am. J. Hum. Genet.* 86, 789–796. doi: 10.1016/j.ajhg.2010.04.002

Valente, M., Valente, K. D., Sugayama, S. S. M., and Kim, C. A. (2004). Malformation of cortical and vascular development in one family with parietal foramina determined by an *ALX4* homeobox gene mutation. *AJNR Am. J. Neuroradiol.* 25, 1836–1839.

Veis, A. (2011). Organic matrix-related mineralization of sea urchin spicules, spines, test and teeth. *Front. Biosci.* 16, 2540–2560. doi: 10.2741/3871

Vogel, P., Hansen, G. M., Read, R. W., Vance, R. B., Thiel, M., Liu, J., et al. (2012). Amelogenesis imperfecta and other biomineralization defects in *Fam20a* and *Fam20c* null mice. *Vet. Pathol.* 49, 998–1017. doi: 10.1177/0300985812453177

Wang, X., Hao, J., Xie, Y., Sun, Y., Hernandez, B., Yamoah, A. K., et al. (2010a). Expression of FAM20C in the osteogenesis and odontogenesis of mouse. *J. Histochem. Cytochem.* 58, 957–967. doi: 10.1369/jhc.2010.956565

Wang, H., Holland, P. W. H., and Takahashi, T. (2019). Gene profiling of head mesoderm in early zebrafish development: insights into the evolution of cranial mesoderm. *EvoDevo* 10:14. doi: 10.1186/s13227-019-0128-3

Wang, X., Wang, S., Li, C., Gao, T., Liu, Y., Rangiani, A., et al. (2012). Inactivation of a novel FGF23 regulator, FAM20C, leads to hypophosphatemic rickets in mice. *PLoS Genet.* 8:e1002708. doi: 10.1371/journal.pgen.1002708

Wang, X., Wiens, M., Schröder, H. C., Hu, S., Mugnaioli, E., Kolb, U., et al. (2010b). Morphology of sponge spicules: silicatein a structural protein for bio-silica formation. *Adv. Eng. Mater.* 12, B422–B437. doi: 10.1002/adem.200980042

Whittaker, C. A., Bergeron, K. -F., Whittle, J., Brandhorst, B. P., Burke, R. D., and Hynes, R. O. (2006). The echinoderm adhesome. *Dev. Biol.* 300, 252–266. doi: 10.1016/j.ydbio.2006.07.044

Wilt, F. H. (2002). Biomineralization of the spicules of sea urchin embryos. *Zool. Sci.* 19, 253–261. doi: 10.2108/zsj.19.253

Wood, T. W. P., and Nakamura, T. (2018). Problems in fish-to-tetrapod transition: genetic expeditions into old specimens. *Front. Cell Dev. Biol.* 6:70. doi: 10.3389/fcell.2018.00070

Wuyts, W., Cleiren, E., Homfray, T., Rasore-Quartino, A., Vanhoenacker, F., and Van Hul, W. (2000). The ALX4 homeobox gene is mutated in patients with ossification defects of the skull (foramina parietalia permagna, OMIM 168500). *J. Med. Genet.* 37, 916–920. doi: 10.1136/jmg.37.12.916

Yagnik, G., Ghuman, A., Kim, S., Stevens, C. G., Kimonis, V., Stoler, J., et al. (2012). ALX4 gain-of-function mutations in nonsyndromic craniosynostosis. *Hum. Mutat.* 33, 1626–1629. doi: 10.1002/humu.22166

Yajima, M., Umeda, R., Fuchikami, T., Kataoka, M., Sakamoto, N., Yamamoto, T., et al. (2010). Implication of HpEts in gene regulatory networks responsible for specification of sea urchin skeletogenic primary mesenchyme cells. *Zool. Sci.* 27, 638–646. doi: 10.2108/zsj.27.638

Yamasu, K., and Wilt, F. H. (1999). Functional organization of DNA elements regulating SM30alpha, a spicule matrix gene of sea urchin embryos. *Dev. Growth Differ.* 41, 81–91. doi: 10.1046/j.1440-169x.1999.00407.x

Yang, L., Tsang, K. Y., Tang, H. C., Chan, D., and Cheah, K. S. E. (2014). Hypertrophic chondrocytes can become osteoblasts and osteocytes in endochondral bone formation. *Proc. Natl. Acad. Sci. U. S. A.* 111, 12097–12102. doi: 10.1073/pnas.1302703111

York, J. R., and McCauley, D. W. (2020). The origin and evolution of vertebrate neural crest cells. *Open Biol.* 10:190285. doi: 10.1098/rsob.190285

Young, M., Selleri, L., and Capellini, T. D. (2019). Genetics of scapula and pelvis development: an evolutionary perspective. *Curr. Top. Dev. Biol.* 132, 311–349. doi: 10.1016/bs.ctdb.2018.12.007

Zhao, Q., Behringer, R. R., and de Crombrugghe, B. (1996). Prenatal folic acid treatment suppresses acrania and meroanencephaly in mice mutant for the Cart1 homeobox gene. *Nat. Genet.* 13, 275–283. doi: 10.1038/ng0796-275

Zhao, G. -Q., Eberspaecher, H., Seldin, M. F., and de Crombrugghe, B. (1994). The gene for the homeodomain-containing protein Cart-1 is expressed in cells that have a chondrogenic potential during embryonic development. *Mech. Dev.* 8, 245–254. doi: 10.1016/0925-4773(94)90063-9

Zhuravlev, A. Y., and Wood, R. A. (2018). The two phases of the Cambrian Explosion. *Sci. Rep.* 8:16656. doi: 10.1038/s41598-018-34962-y

Conflict of Interest: The authors declare that the research was conducted in the absence of any commercial or financial relationships that could be construed as a potential conflict of interest.

frontiers in Genetics

ORIGINAL RESEARCH
published: 26 November 2020
doi: 10.3389/fgene.2020.571694

Mineralization of the *Callorhinchus* Vertebral Column (Holocephali; Chondrichthyes)

Jacob B. Pears[1], Zerina Johanson[2], Kate Trinajstic[1], Mason N. Dean[3]* and Catherine A. Boisvert[1]*

[1] School of Molecular and Life Sciences, Curtin University, Perth, WA, Australia, [2] Department of Earth Sciences, Natural History Museum, London, United Kingdom, [3] Department of Biomaterials, Max Planck Institute of Colloids and Interfaces, Potsdam, Germany

Members of the Chondrichthyes (Elasmobranchii and Holocephali) are distinguished by their largely cartilaginous endoskeletons, which comprise an uncalcified core overlain by a mineralized layer; in the Elasmobranchii (sharks, skates, rays) most of this mineralization takes the form of calcified polygonal tiles known as tesserae. In recent years, these skeletal tissues have been described in ever increasing detail in sharks and rays, but those of Holocephali (chimaeroids) have been less well-studied, with conflicting accounts as to whether or not tesserae are present. During embryonic ontogeny in holocephalans, cervical vertebrae fuse to form a structure called the synarcual. The synarcual mineralizes early and progressively, anteroposteriorly and dorsoventrally, and therefore presents a good skeletal structure in which to observe mineralized tissues in this group. Here, we describe the development and mineralization of the synarcual in an adult and stage 36 elephant shark embryo (*Callorhinchus milii*). Small, discrete, but irregular blocks of cortical mineralization are present in stage 36, similar to what has been described recently in embryos of other chimaeroid taxa such as *Hydrolagus*, while in *Callorhinchus* adults, the blocks of mineralization are more irregular, but remain small. This differs from fossil members of the holocephalan crown group (*Edaphodon*), as well as from stem group holocephalans (e.g., Symmorida, *Helodus*, Iniopterygiformes), where tesserae are notably larger than in *Callorhinchus* and show similarities to elasmobranch tesserae, for example with respect to polygonal shape.

Keywords: Holocephali, *Callorhinchus*, tesserae, mineralization, evolution, stem group Holocephali

OPEN ACCESS

Edited by:
Sylvain Marcellini, University of Concepcion, Chile

Reviewed by:
Brian Frank Eames, University of Saskatchewan, Canada
Fidji Berio, Université de Lyon, France

****Correspondence:***
Zerina Johanson
z.johanson@nhm.ac.uk
Mason N. Dean
Mason.Dean@mpikg.mpg.de

Specialty section:
This article was submitted to Evolutionary and Population Genetics, a section of the journal Frontiers in Genetics

Received: *11 June 2020*
Accepted: *30 October 2020*
Published: *26 November 2020*

Citation:
Pears JB, Johanson Z, Trinajstic K, Dean MN and Boisvert CA (2020) Mineralization of the Callorhinchus Vertebral Column (Holocephali; Chondrichthyes). Front. Genet. 11:571694. doi: 10.3389/fgene.2020.571694

INTRODUCTION

During ontogeny, most vertebrate skeletons are initially composed predominantly of hyaline cartilage and largely replaced by bone via endochondral ossification (Hall, 1975, 2005). In contrast, chondrichthyans, including elasmobranchs (sharks, skates, rays, and relatives) and holocephalans (chimaeroids) do not develop osseous skeletons, having secondarily lost the ability to produce endoskeletal bone (Coates et al., 1998; Dean and Summers, 2006; Ryll et al., 2014; Debiais-Thibaud, 2019; Brazeau et al., 2020). Instead, the chondrichthyan endoskeleton remains primarily composed

of hyaline-like cartilage, with elasmobranchs developing a comparatively thin outer layer of cortical mineralization over most of their skeleton during ontogeny (Hall, 2005; Egerbacher et al., 2006; Dean et al., 2009, 2015; Seidel et al., 2016, 2019b; Atake et al., 2019; Debiais-Thibaud, 2019). This mineralized tissue begins as small separated islets near the cartilage surface, which gradually grow via mineral accretion to fill the intervening spaces, eventually forming a cortex of abutting polygonal tiles called tesserae (Dean and Summers, 2006; Dean et al., 2009, 2015; Seidel et al., 2016, 2019b). These tiles cover the uncalcified cartilage core and are themselves overlain by a distal fibrous perichondrium (Dean and Summers, 2006; Dean et al., 2009, 2015). This mosaic of uncalcified cartilage, tesserae and perichondrium is called tessellated cartilage and comprises most of the cranial and postcranial skeleton (Kemp and Westrin, 1979; Dean and Summers, 2006; Seidel et al., 2016, 2017a).

Tessellated cartilage is therefore a major component of the skeleton and is currently believed to be a synapomorphy for the entire chondrichthyan group (e.g., Maisey et al., 2019, 2020, but see comments therein regarding morphological and histological disparity in stem-chondrichthyans). Contemporary examination of extant chondrichthyan mineralized skeletons and their tissues, however, have almost exclusively focused on sharks (Kemp and Westrin, 1979; Peignoux-Deville et al., 1982; Clement, 1986, 1992; Bordat, 1987, 1988; Egerbacher et al., 2006; Eames et al., 2007; Enault et al., 2016) and rays (Dean et al., 2009; Claeson, 2011; Seidel et al., 2016, 2017a,b; Criswell et al., 2017a,b). In contrast, mineralized skeletal tissues of extant chimaeroids (Holocephali) have been largely ignored, since the descriptions of vertebral development and morphology in the late nineteenth to mid-twentieth centuries (Hasse, 1879; Schauinsland, 1903; Dean, 1906); fossil holocephalans have faced similar neglect (but see Moy-Thomas, 1936; Patterson, 1965; Maisey, 2013). This has led to contradictory descriptions of chimaeroid tissues (Lund and Grogan, 1997; Grogan and Lund, 2004; Pradel et al., 2009), prompting calls for more research (Eames et al., 2007; Dean et al., 2015; Enault et al., 2016). Notably, recent examination of chimaeroid mineralized skeletal tissues identified tesseral structures in the vertebral column (synarcual) and Meckel's cartilage of *Chimaera* and *Hydrolagus* (both Family Chimaeridae; Finarelli and Coates, 2014; Debiais-Thibaud, 2019; Seidel et al., 2019a, 2020) and in the fin skeleton of *Callorhinchus* (Family Callorhinchidae; Maisey et al., 2020), seemingly refuting the view that extant chimaeroids lack tessellated cartilage.

In order to address this controversy, and determine whether tessellated cartilage is indeed a shared character among cartilaginous fishes, we performed a correlated, multi-technique examination of mineralization in the skeletal tissue of *Callorhinchus*, focusing on the synarcual of the elephant shark (*Callorhinchus milii*). The synarcual is a fused element in the anterior vertebral column (Claeson, 2011; Johanson et al., 2013, 2015, 2019; VanBuren and Evans, 2017) and is one of the better anatomical structures for mineralized tissue characterization, being formed early in development and also mineralizing early (Johanson et al., 2015, 2019). Whilst no developmental series of synarcual mineralization in *C. milii* has yet been published, two observations from the only study of its development (Johanson et al., 2015) suggest its spatial pattern. The formation of the cartilages that comprise the synarcual of *C. milii* occurs anteroposteriorly. Micro-CT analysis of an adult sample, from the same study, suggested an anterior-to-posterior/dorsal-to-ventral mineralization front. Accordingly, we assume that antero-dorsal mineralized tissues in *C. milii* are more advanced developmentally than ventro-posterior mineralized tissues, which appears to be reflected in the histological data examined here. We report the presence of a layer of mineralization in the *Callorhinchus* embryo, maintained in adults, comprising small, irregularly shaped units, but lacking many of the characteristics of tesserae in the elasmobranchs. To provide phylogenetic context we also examined mineralized tissues in fossil members of the Callorhinchidae (*Edaphodon*; Nelson et al., 2006), as well as stem-group holocephalan taxa (e.g., *Cladoselache*, *Cobelodus*, *Helodus*, Iniopterygiformes; Coates et al., 2017, 2018; Dearden et al., 2019; Frey et al., 2019). The tesserae in these stem-group holocephalans are larger than in *Callorhinchus*, and more similar in shape to polygonal elasmobranch tesserae. Thus, the evolution of skeletal mineralization in Chondrichthyes may have involved a progressive reduction of mineralization in the Holocephali, relative to the elasmobranchs.

MATERIALS AND METHODS

Histological Sections of *Callorhinchus milii* Synarcual

To gain insight into the development of mineralized tissues, stained slides of the synarcual from a sectioned embryo of an elephant shark (*Callorhinchus millii*; section thickness ∼30 μm; Life Sciences Department, Natural History Museum, London) were examined by light microscopy using an Olympus BX51 compound microscope and Olympus DP70 camera and management software. These slides were prepared sometime during the 1980s and no information aside from the species was recorded with the slides. They are presumed to be stained with haematoxylin and eosin. The animal is estimated to represent stage 36 [near hatching, based on the calculated size of the individual (110–135 mm; Didier et al., 1998)]. This developmental stage is ideal to study mineralization as it is small enough to section but mature enough to show mineralization. As noted, given that holocephalan synarcuals are known to mineralize first anterodorsally and that mineralization subsequently progresses in a posteroventral fashion (Johanson et al., 2015), this provides ontogenetic information on how mineralization develops, in one individual. Location of hard tissue was confirmed by micro-CT scanning of the sections.

Adult *Callorhinchus milii*

Two adult females of *C. milii* were captured by rod and reel from Western Port Bay, Victoria, Australia (Permits: RP1000, RP 1003, and RP1112) with the authorization and direction of the Monash University Animal Ethics Committee (Permit: MAS-ARMI-2010-01) and kept according to established husbandry

methods (Boisvert et al., 2015). These specimens died in captivity and were frozen.

Scanning Electron Microscopy

The synarcual of one of these adult *C. milii* specimens was dissected out and either small layers of mineralized tissue or cross sections of the vertebrae were collected. Samples were macerated in a trypsin solution (0.25 g Trypsin Sigma T-7409 Type II-S from porcine pancreas in 100 mL 10%PBS) and warmed in a 38°C water bath. Samples were extracted from the solution every hour to remove macerated flesh and fascia using scalpels, needles and forceps. This was repeated until sufficient flesh had been removed to observe the mineralized surface. To prevent distortion, samples were placed between Teflon blocks before being air-dried until firm. Cross sections were embedded in a Struers CitoVac using Struers EpoFix Resin and EpoFix Hardener mixed in a 50:6 weight ratio and polished using a Struers Tegramin-30. All samples were given a 3 nm conductive coating of pure platinum using a Cressington 208HR sputter coater. Samples were imaged using a TESCAN MIRA3 XMU variable pressure field emission scanning electron microscope (VP-FESEM) using backscatter mode (voltage: 15 kv; working distance: 6–15 mm; Tescan Mira3 VP-FESEM instrumentation, John de Laeter Centre, Curtin University). The synarcual from the remaining adult specimen (Johanson et al., 2015; **Figure 7**) was dissected out, defleshed by immersion in 36°C water and removal of muscle and fascia with needles and forceps, and imaged using a FEI Quanta 650 FEG SEM in secondary electron mode (voltage: 10 kv; working distance: 14.7 mm). Through this method mineralized tissues can be easily distinguished from soft tissue through differences in backscatter signal.

Macrophotography, CT-Scanning

Five fossil holocephalans from the Earth Sciences Department, NHM (NHMUK PV P) were chosen to represent extinct taxa, phylogenetically important with respect to the Callorhinchidae and crown-group holocephalans (Coates et al., 2017, 2018; Frey et al., 2019). These comprised: *Cladoselache* (NHMUK PV P.9285), *Cobelodus* (NHMUK PV P.62281a), *Sibirhynchus* (NHMUK PV P.62316b), *Edaphodon* (NHMUK PV P.10343), and *Helodus* (NHMUK PV P.8212). One specimen preserving mineralized cartilage was chosen from each taxon, and photographed using a Canon EOS 600D camera, EOS Utility. Five to ten images of each specimen were taken at different focal depths and the resultant image stack imported into Helicon Focus (v. 6.8.0) to create images with high depth of focus. These specimens were also photographed using a Zeiss Axio Zoom microscope with camera to provide closeup images; tesseral width was determined using the measurement function in the Zen Pro 2 software accompanying the Axio Zoom microscope (**Supplementary Info Table 1**).

The second adult *Callorhinichus milii* synarcual was CT-scanned (Johanson et al., 2015) using an X-Tek HMX ST CT scanner (Image and Analysis Centre, NHM; *kv* = 165; μA = 175; no filter applied; 3142 projections; resolution = 36.9μm), and rendered using the programs Drishti[1] and Avizo[2]. Subsequently, the synarcual was air-dried and photographed using the Zeiss Axio Zoom microscope to illustrate tesseral shape.

RESULTS

Histology

General Morphology

The axial skeleton of chondrichthyans typically includes a series of cartilages dorsal and ventral to the notochord, and in the elasmobranchs, centra associated with the notochord (e.g., Dean, 1895; Gadow and Abbott, 1895; Goodrich, 1930; Compagno, 1977; Criswell et al., 2017b). Mineralization of the axial skeleton takes a variety of forms, recently summarized by Debiais-Thibaud (2019), with the dorsal and ventral cartilages (i.e., neural and haemal arches) of most species, as well as the outer centrum, composed of tessellated cartilage (Dean and Summers, 2006; Dean et al., 2009; Criswell et al., 2017b; Johanson et al., 2019). Most of the spool-shaped vertebral centrum comprises areolar mineralization, with substantial variation in patterns of mineralization between elasmobranch species (Ridewood, 1921; Dean and Summers, 2006; Porter et al., 2007). Holocephalans also possess dorsal and ventral cartilages (e.g., Dean, 1895; Johanson et al., 2013, 2015), but centra do not develop (Gadow and Abbott, 1895; Goodrich, 1909). Instead, the notochord is surrounded by a fibrous chordal sheath, which contains many calcified rings, except in the Callorhinchidae, where these rings are absent (Goodrich, 1909; Patterson, 1965; Didier, 1995). Holocephalans, unlike many elasmobranchs, possess a synarcual, which is the focus of the following description.

In the *Callorhinchus* embryo examined (stage 36), several tissue layers concentrically surround the notochord. Most proximal is a thin basophilic membrane, the elastic interna, adherent to the outside of the notochord (**Figures 1A–D**, nc, el.int). Distal to this membrane is a thick (∼665 μm) fibrous sheath (**Figures 1A,B**, fb.sh), which is largely composed of spindle shaped cells (**Figures 1C,D**). Abutting the sheath dorsally and ventrally are separate bilateral pairs of cartilages, the basidorsals and basiventrals, respectively (**Figures 1B,D**, bv, bd). Immediately dorsal to the sheath is the spinal cavity, containing the spinal cord, which is surrounded ventrolaterally by the basidorsal cartilages and dorsally by the neural arch cartilage (**Figure 1B**, sp.c, sp.cd, bd, na). Spinal nerves are also visible in section, with the dorsal root exiting the neural tube toward the dorsal root ganglion situated lateral to the vertebral column (**Figures 1A,B**, d.rt, d.rt.g). The hyaline cartilages associated with the vertebral column—the neural arch, basidorsals and basiventrals— fuse anteriorly to form the synarcual, which surrounds the majority of the fibrous sheath and spinal cavity, while maintaining foramina for the dorsal root (**Figure 1A**).

In these histological slides, areas of mineralization, verified via CT imaging, are limited to the superficial regions of

[1]https://github.com/AjayLimaye/drishti

[2]https://www.fei.com/software/avizo3d/

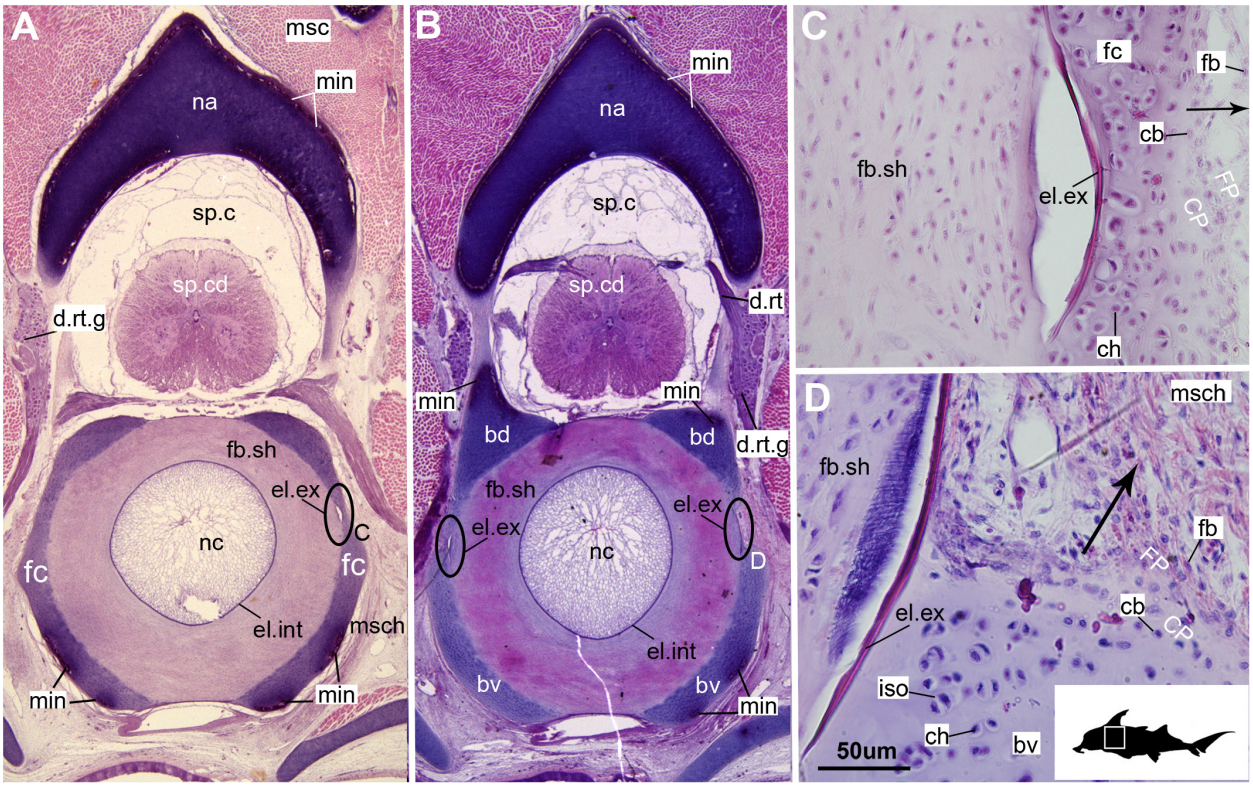

FIGURE 1 | Histological sections through the synarcual (anterior fused vertebrae) of a stage 36 embryo of *Callorhinchus milii* (Holocephali; Callorhinchidae). **(A,B)** Section showing neural arch surrounding the spinal cord and basidorsal and basiventral arches surrounding the notochord. **(C)** closeup of region indicated in **(A)**; **(D)** closeup of region indicated in **(B)**. Black s in **(C,D)** indicate direction of appositional growth of the basiventral cartilage. bd, basidoral; bv, basiventral; cb, chondroblast; ch, chondrocyte; CP, perichondrium including chondroblast cells; d.rt, dorsal root of the spinal nerve; d.rt.g, dorsal root ganglion of the spinal nerve; el. ex, elastica externa; el.int, elastica interna; fb, fibroblasts; fb.sh, fibrous sheath surrounding the notochord; fc, fused cartilage; FP, perichondrium including fibroblast cells; iso, isogenous group of chondrocytes; min, mineralization; msc, musculature; msch, mesenchymal cells; na, neural arch; nc, notochord; sp.c, spinal cavity; sp.cd, spinal cord. Black silhouette of *C. millii* indicates approximate region shown in the figure.

the vertebral column-associated cartilages (**Figures 1**, **2**, min). These mineralized tissues are bordered externally by a fibrous perichondrium and a thin, cell-rich layer of cartilage (**Figures 2**, **3**, FP, SC), similar to the suprateseral cartilage intervening between tesserae and perichondrium in the stingray *Urobatis halleri* (Seidel et al., 2017a).

Cellular Aspects

Cells within the neural arch, basidorsal and basiventral cartilages can be categorized with respect to morphology, and distribution within the cartilage. Chondrocytes located proximally inside the cartilage (**Figures 2A,B**, **3A**, IN, ch) are generally similar in terms of cell morphology and density: ≥200 μm from the periphery, cells are sparsely distributed within the cartilage matrix, with most being ovoid in shape and located in open circular spaces identified as lacunae (diameter: ∼15 μm). Chondrocytes often occur in pairs (isogenous groups), indicative of recent mitotic activity (**Figures 2A,B**, **3A**, ch; Kheir and Shaw, 2009). This proximal region (≥200 μm from the periphery) of cartilage also contains relatively greater quantities of empty lacunae compared to the more peripheral cartilage (**Figures 2A,B**, **3A**, el). Closer to the periphery, within 100–200 μm of the outer edge, and immediately proximal to mineralized tissue, chondrocytes are clustered within a distinct layer (**Figures 2**, **3B**, CPL) and appear uniformly ovoid. This area displays a greater variation in cell size, as it contains many smaller chondrocytes (diameter: 5–10 μm) and fewer empty lacunae compared to the interior. In addition, this area contains notably more isogenous groups relative to the interior, which may indicate higher rates of chondrocyte proliferation (**Figures 2A,B**, **3B,E**, iso; Kheir and Shaw, 2009). In some regions, mineralization is absent at the periphery; in these areas, cell distribution and morphology are more similar to the interior (**Figure 3A**).

Mineralization

The layer of mineralization varies in its completeness in the vertebral elements, but typically appears discontinuous, broken into individual acellular units; we identify these units as tesserae, although they are not entirely similar to the tesserae of sharks and rays (discussed further below). In the neural arches, more dorsally, the distribution of mineralized tissue is more complete, extending along almost the entire periphery, excluding only the ventro-mesial concave part of the arch (**Figures 2C**, **4B**). Within the basiventrals, mineralized tissue is also found near

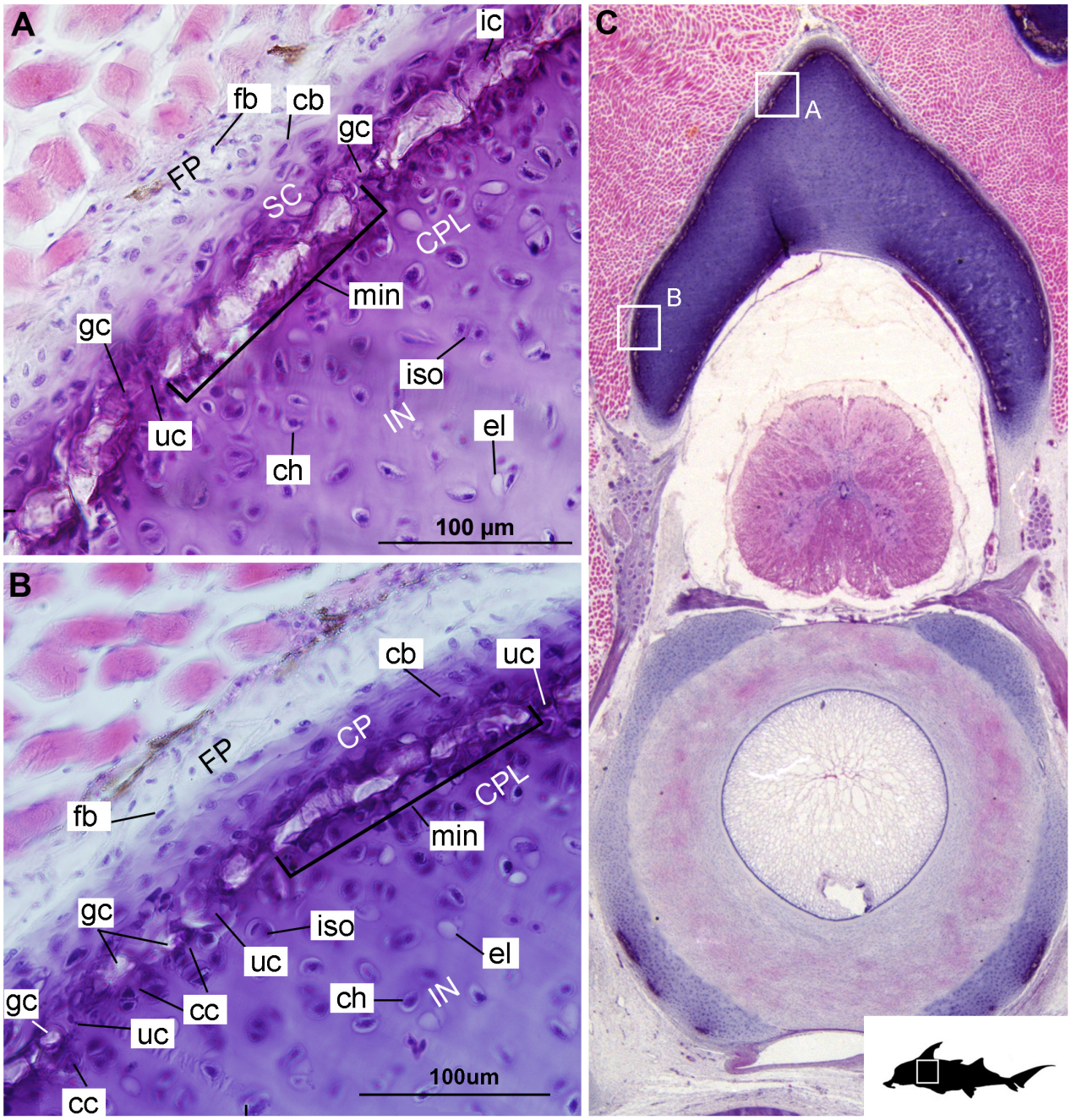

FIGURE 2 | Histological section through the anterior synarcual (anterior fused vertebrae) of a stage 36 embryo of *Callorhinchus milii* (Holocephali; Callorhinchidae). **(A,B)** Closeups showing perichondrium, cartilage, and mineralization in the neural arch; **(C)** overview of section with locations of closeup views indicated by white squares. Abbreviations: As in **Figure 1**, also cc, clustered chondrocytes CPL, chondrocyte proliferative layer; el, empty chondrocyte lacunae; gc, calcification globule; ic, chondrocyte that is being engulfed or has been incorporated; uc, uncalcified cartilage; IN, internal cartilage; SC, supratesseral/mineral cartilage. Black silhouette of *C. millii* indicates approximate region shown in the figure.

the periphery, but by comparison to the neural arches, is only patchily distributed (**Figures 3**, **4**), with individual units more variable and irregular in shape (**Figures 3B,E**, **4**, min). In the neural arches, these units are more rectangular and flatter (**Figures 2A,B**, **5A,B**, **6**). Nevertheless, mineralized tissues in all vertebral elements lack a regular geometry and any differentiation into inner and outer regions. Additionally, beyond being limited to the cartilage periphery beneath the fibrous perichondrium, these tissues lack obvious patterning, reflecting the lack of a regular geometric shape to the individual units.

The least developed forms of tissue mineralization, which are located in the more posterior vertebrae, take the form

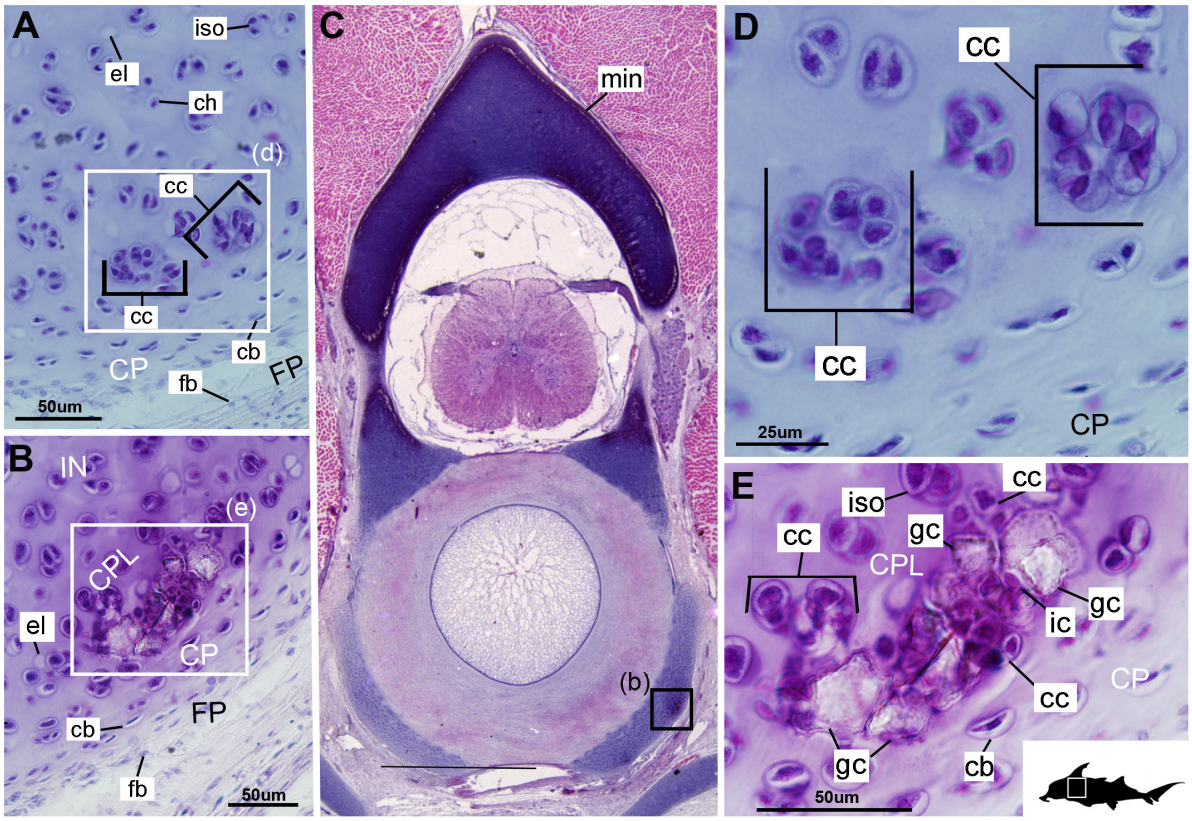

FIGURE 3 | Histological sections through the posterior synarcual (anterior fused vertebrae) of a stage 36 embryo of *Callorhinchus milii* (Holocephali; Callorhinchidae). **(A,B)** Closeups showing initial mineralization in a basiventral and clustered chondrocytes in the same location in the preceding section; **(C)** overview with location of closeup view of initial mineralization indicated by a black square; **(D,E)** close ups of **(A,B)** locations indicated by white squares. Abbreviations: As in previous figures, also dm, developing mineralization. Black silhouette of *C. millii* indicates approximate region shown in the figure.

of small islands of calcification (≤25 μm width) situated amongst concentrated clusters of chondrocytes beneath the perichondrium (**Figures 3A,D**, **5B**, cc, FP, gc). More developed tesserae in the posterior vertebrae are smaller (50–100 μm) and more regularly separated by regions of unmineralized cartilage (**Figures 4F**, **5A,B**, min, uc), reflecting their earlier developmental stage. Unlike the more developed acellular units in the anterior vertebrae (**Figures 2A,B**, min) some units in the posterior vertebrae appear to contain vital chondrocytes (**Figures 3F**, **5A**, ic).

Scanning Electron Microscopy (SEM)

In planar views of the external surface of the synarcual of adult *Callorhinchus milii*, the mineralized layer appears to comprise a tessellated surface of irregular tiles that are separated by (∼5 μm) thin strips of uncalcified cartilage (**Figures 7A,B** min, uc). These tesserae do not have a uniform shape or size, ranging from 50 to 150 μm in width (**Figure 7B** and **Supplementary Figure 1**).

In transverse view, the mineralized tissue forms a single layer of tesserae, tightly arranged units of irregular blocks separated by very thin (<5 μm) strips of uncalcified cartilage (**Figure 7C**, min, SC, IN, uc). In this perspective, the tesserae are 30–50 μm thick and 30–150 μm wide (**Figure 7C**). Some cracking of the mineralization during sample preparation is visible, but individual tesserae can be identified by comparing and matching Liesegang lines between adjacent fragments (**Figure 7C**, ll, f). Liesegang lines are concentric, wave-like patterns of varying mineral density visible in the mineralized tissue, and are particularly prominent near the lateral margins of the mineralized units (**Figures 7C,D**, ll).

Spheroidal mineralized regions, surrounded by Liesegang lines and approximately the size and shape of chondrocytes also permeate the tesserae (**Figure 7D**, ch). These are likely calcified (micropetrotic) cells, are variously sized (∼1–5 μm), and appear to be organized in clusters (isogenous groups), suggesting some have either been calcified during mitosis or immediately after mitosis, but before interstitial growth separated the cells in an isogenous groups (Seidel et al., 2016, 2017b, 2019c; **Figure 7D**, ch, iso).

Mineralization in Stem Holocephali and Fossil Callorhinchidae

Following recent phylogenetic reviews (Coates et al., 2017, 2018; Dearden et al., 2019; Frey et al., 2019), several taxa that were previously resolved as stem group chondrichthyans (basal to the clade Elasmobranchii + Holocephali; Pradel et al., 2011) are now

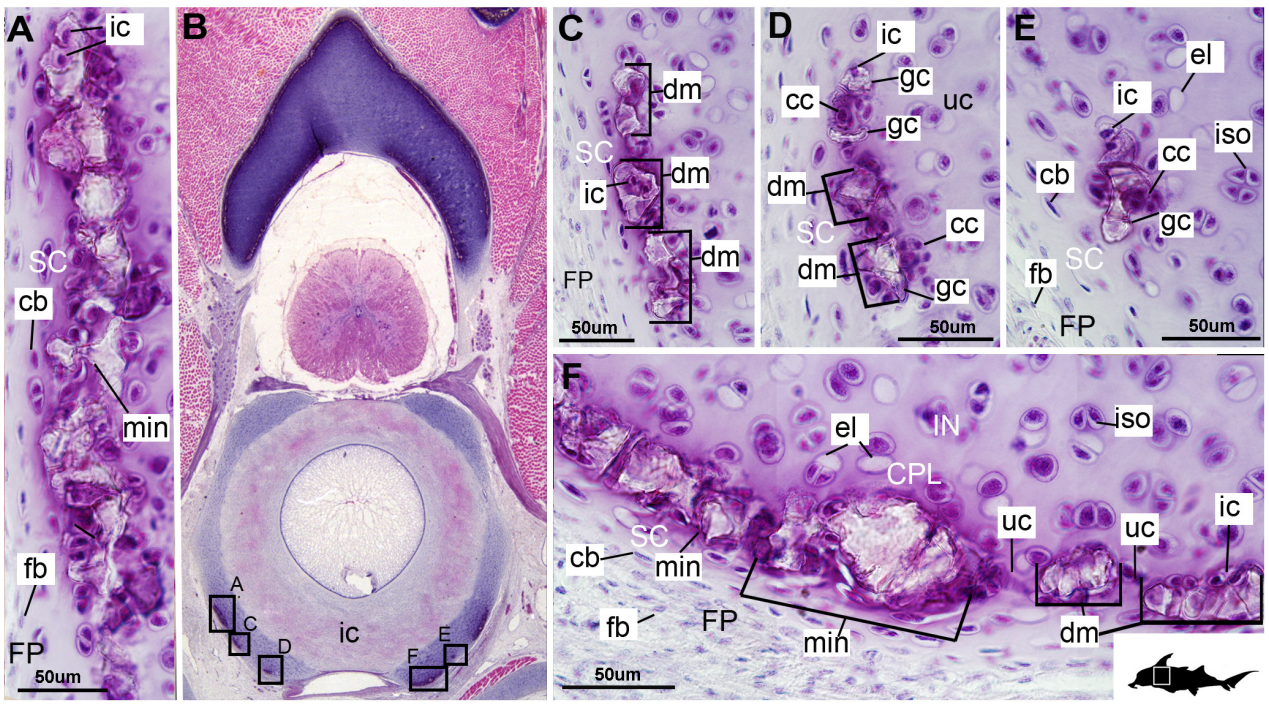

FIGURE 4 | Histological section through the anterior synarcual (anterior fused vertebrae) of a stage 36 embryo of *Callorhinchus milii* (Holocephali; Callorhinchidae). **(A,C–F)** Closeups showing perichondrium, cartilage, and mineralization in basiventrals; **(B)** overview of section through the neural arch with locations of closeup views indicated by black squares. Abbreviations: As in previous figures. Black silhouette of *C. millii* indicates approximate region shown in the figure.

resolved as stem holocephalans. These taxa join more crownward stem holocephalans including the Iniopterygiformes (Zangerl and Case, 1973), *Helodus* (Moy-Thomas, 1936), *Kawichthys*, *Debeerius*, and *Chondrenchelys*, the latter being the sister taxon to the crown group Holocephali (chimaeroids) (**Figure 8**). Tessellated calcified cartilage has been variously identified among these stem-group Holocephali: this includes taxa assigned to the Symmoriida, such as *Dwykaselachus* (Coates et al., 2017: extended data **Figure 1D**), *Ozarcus* (Pradel et al., 2014), *Cladoselache* ("minute granular calcifications," Dean, 1894; **Figures 9A,B**), *Akmonistion* ("prismatic calcified cartilage," Coates and Sequeira, 2001), *Damocles* and *Falcatus* (Lund and Grogan, 1997), also present in *Cobelodus* (**Figure 9B**). In all these taxa, the tessellated layer is comprised of recognizable polygonal units, although in *Cladoselache*, the edges of the units appear less regular, and were referred to as "zig-zag tesserae" (Maisey et al., 2020). This may represent the presence of mineralized "spokes" extending between the tesserae (Maisey et al., 2020; **Figure 9B**, arrows): spokes are hypermineralized tissue regions associated with points of contact between elasmobranch tesserae, often represented externally by lobulated extensions along tesseral margins (Seidel et al., 2016; Atake et al., 2019; Jayasankar et al., 2020; **Figure 10**). Such structural extensions, suggestive of mineralized spokes, are even more clearly present in *Cobelodus* (**Figure 9C**, arrows).

In the more crownward stem holocephalans, comparable polygonal tesserae are also present, including in *Kawichthys* ("tesserate prismatic calcified cartilage," Pradel et al., 2011) and the Iniopterygiformes ("calcified cartilage prisms," Zangerl and Case, 1973), represented by *Sibirhynchus* in **Figure 9D**. Particularly small tesserae (**Supplementary Info Table 1**) are present in *Helodus* ("minute tesserae," Moy-Thomas, 1936; **Figure 9G**), and *Chondrenchelys* ("tessellated calcified cartilage," Finarelli and Coates, 2014; **Figure 7B**). There appears to be more variation in the shape of these polygons, and signs of mineralized spokes are less apparent in these taxa, but this may be due to postmortem distortion. With respect to the fossil taxa assigned to the Callorhinchidae (crown group Holocephali), mineralized tissue units in *Edaphodon* appear to maintain a polygonal shape, compared to the stem holocephalans just described (**Figures 9E,F**). The width of tesserae in these fossil taxa was measured (**Supplementary Info Table 1**) for comparison to the size of mineralized units in adult *Callorhinchus* (50–150 μm, as noted above); the tesserae of all fossil taxa were notably larger than in *Callorhinchus*, discussed further below.

DISCUSSION

Cartilage Growth and Cellular Aspects

The cartilages in the histological series examined here exhibit tissue and cellular morphologies that suggest mechanisms of growth and cell death were occurring in these tissues. The perichondria of the cartilages, for example, most notably the basidorsals and basiventrals, display a gradient of cell morphology that may explain one of the means by which

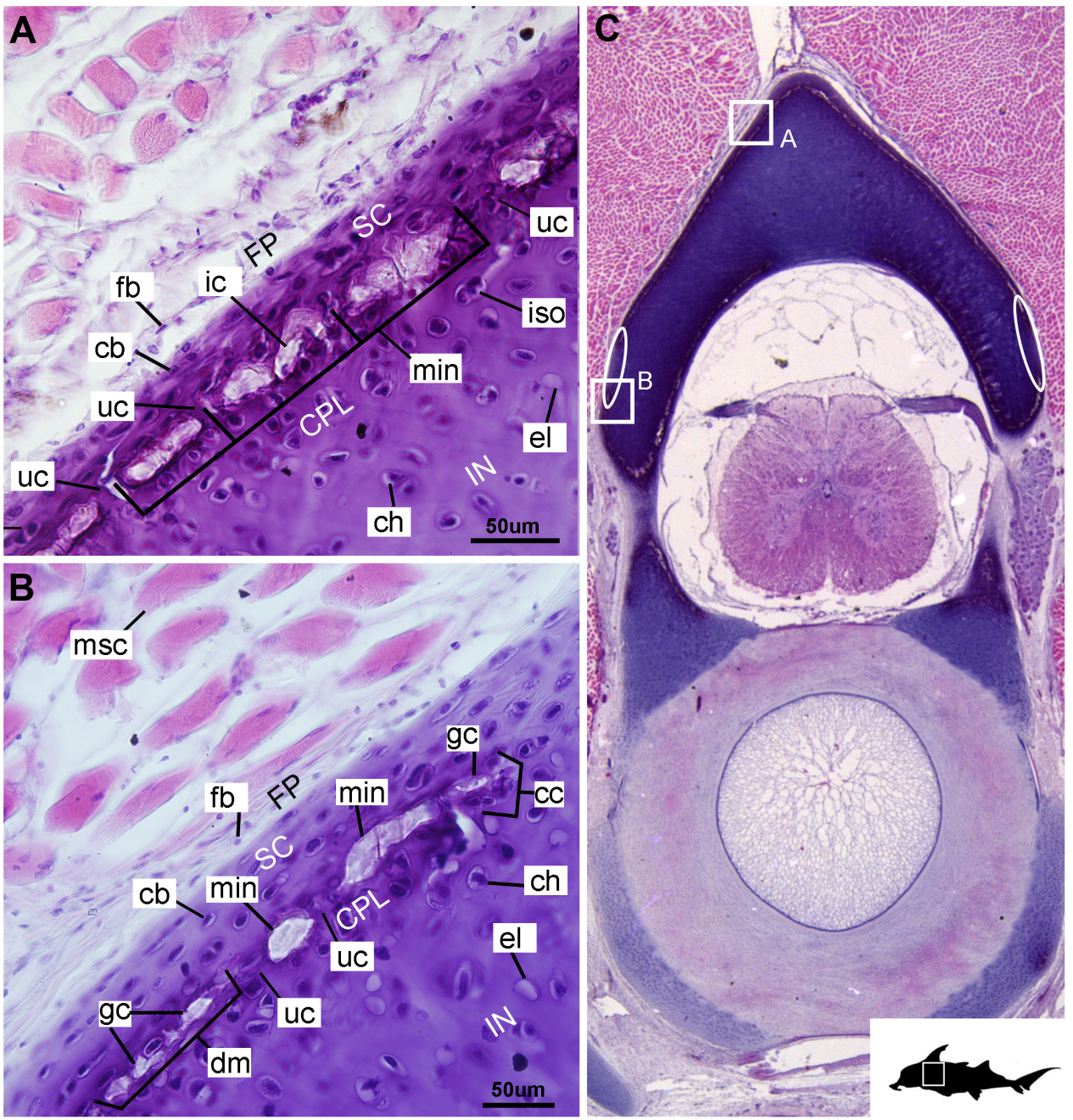

FIGURE 5 | Histological section through the posterior synarcual (anterior fused vertebrae) of a stage 36 embryo of *Callorhinchus milii* (Holocephali; Callorhinchidae). **(A,B)** Closeups showing perichondrium, cartilage, and mineralization in the neural arch; **(C)** overview of section with locations of closeup views indicated by white squares. Abbreviations: As in previous figures, also ellipses indicating areas not yet mineralized. Black silhouette of *C. millii* indicates approximate region shown in the figure.

these cartilaginous tissues grow. From the perichondrium through to the suprateseral cartilage, there is a transition in cellular morphology from fibroblast cells in the perichondrium, differentiating to chondroblasts in the suprateseral cartilage, and then to chondrocytes in the main body of the cartilage, suggesting a potential progressive differentiation of cell type between regions, as described in Genten et al. (2009; **Figures 1C,D**, **2A,B**, CP, FP, fb, cb, ch). This is suggestive of appositional growth, in which newly differentiated chondrocytes deposit matrix at the cartilage margins. Interstitial growth, that is, growth through chondrocyte mitosis and matrix deposition increasing the size of the cartilage element from within, also appears to be occurring as evidenced by the presence of isogenous groups (groups of recently divided chondrocytes, e.g., **Figures 1B–D**, **2A,B**, iso;

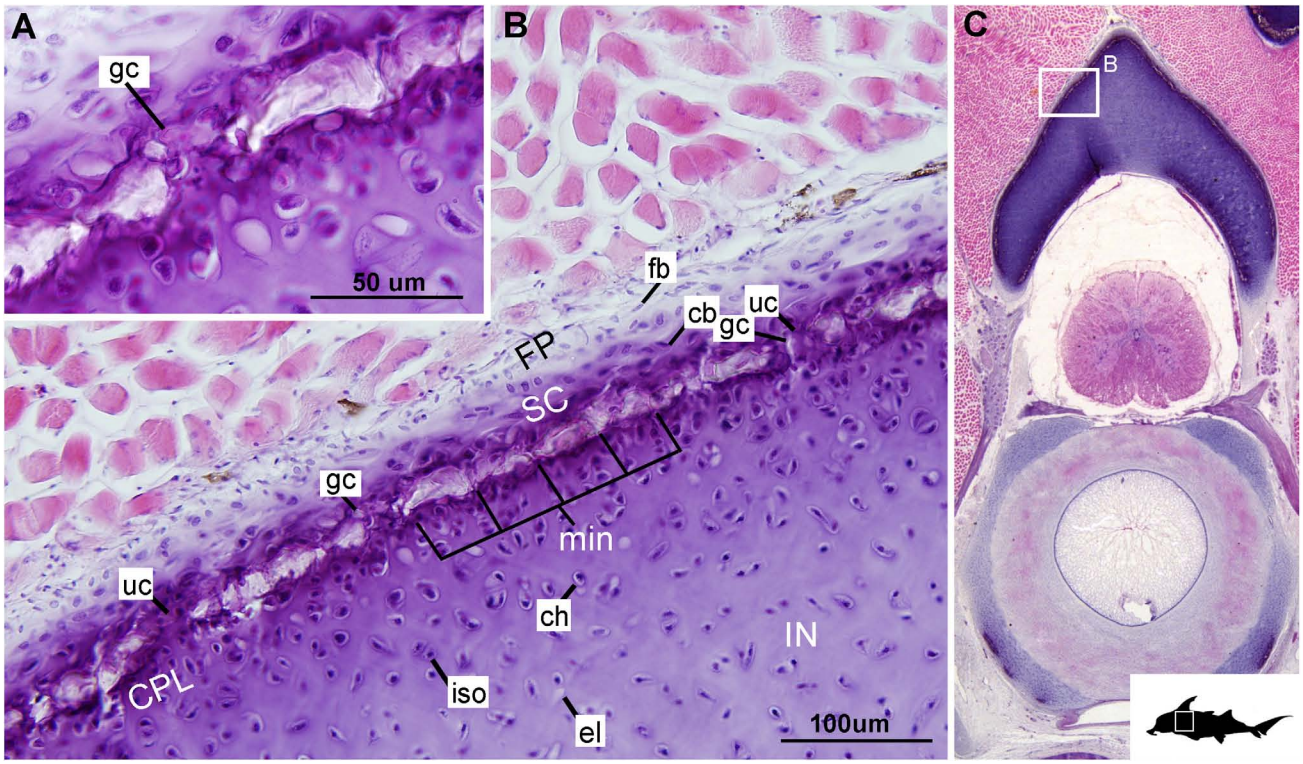

FIGURE 6 | Histological section through the synarcual (anterior fused vertebrae) of a stage 36 embryo of *Callorhinchus milii* (Holocephali; Callorhinchidae). **(A,B)** Closeups showing the potential formation of new mineralization foci between already existing units; **(C)** overview of section through the neural arch with locations of closeup views indicated by white squares. Abbreviations: as in previous figures. Black silhouette of *C. millii* indicates approximate region shown in the figure.

Hall, 2005; Kheir and Shaw, 2009). Both processes seem to be involved in the formation of the synarcual. In several sections, the basidorsal and basiventral cartilages are still separate (e.g., **Figure 1B**), but show marginal regions suggestive of appositional and interstitial growth, which continues until these unite to form the synarcual (**Figures 1B–D**, black arrows suggesting direction of growth). Both modes of growth have similarly been speculated to be involved in the growth and development of the metapterygium in elasmobranchs (Marconi et al., 2020).

Regarding cell death, empty lacunae are found throughout the cartilages examined here, but they appear in greater numbers more proximally (>200 μm from the periphery) (**Figures 2A,B**, **3A**, el). This may indicate either an artifact of sectioning or chondroptosis (chondrocyte apoptosis; Roach et al., 2004), although the latter in vertebrates is normally associated with chondrocyte hypertrophy, which has not been observed in chondrichthyans (Dean et al., 2015; Seidel et al., 2017b; but see Debiais-Thibaud (2019) for a summary of contrary opinions).

Mineralized Tissue Development

Currently, the ultrastructure and ontogeny of mineralized endoskeletal tissues of chimaeroids is poorly described, with previous work only providing a broad overview of developmental trajectories, such as observations that mineralization in the vertebral skeleton (in the synarcual) progresses from anterior to posterior and dorsal to ventral, demonstrated by a recognizable mineralization front in a micro-CT scan of a *Callorhinchus milii* adult (Johanson et al., 2015; **Figures 11A,B**, white arrowheads). The series described above in the stage 36 embryo goes beyond this to capture fine histological detail related to the progression of this mineralization.

The development of mineralized tissue described here for *C. milii* shares some similarities with the development of elasmobranch tesserae (Seidel et al., 2016; Debiais-Thibaud, 2019). Tesserae in elasmobranchs such as the batoid ray *Urobatis halleri* initially develop as patches of globular mineralization interposing within clusters of flattened, subperichondral chondrocytes (at a distance from the perichondrium). These chondrocytes become entombed by the growth of these mineralized inter-chondrocyte septa, apparently by mineral accretion (Dean et al., 2009; Seidel et al., 2016). The morphologies associated with this accretion and entombment process in elasmobranchs (e.g., the size and shape of mineralized septae) are similar to those we observed in *C. milii*, suggesting a similar inception and progression of mineralization (**Figures 4C,D**, **5A,B**). Through development of *U. halleri*, the mineralized septae continue to grow and engulf chondrocytes, eventually forming discrete, but abutting tesserae, which contain vital chondrocytes and closely border the perichondrium (Seidel et al., 2016; also in

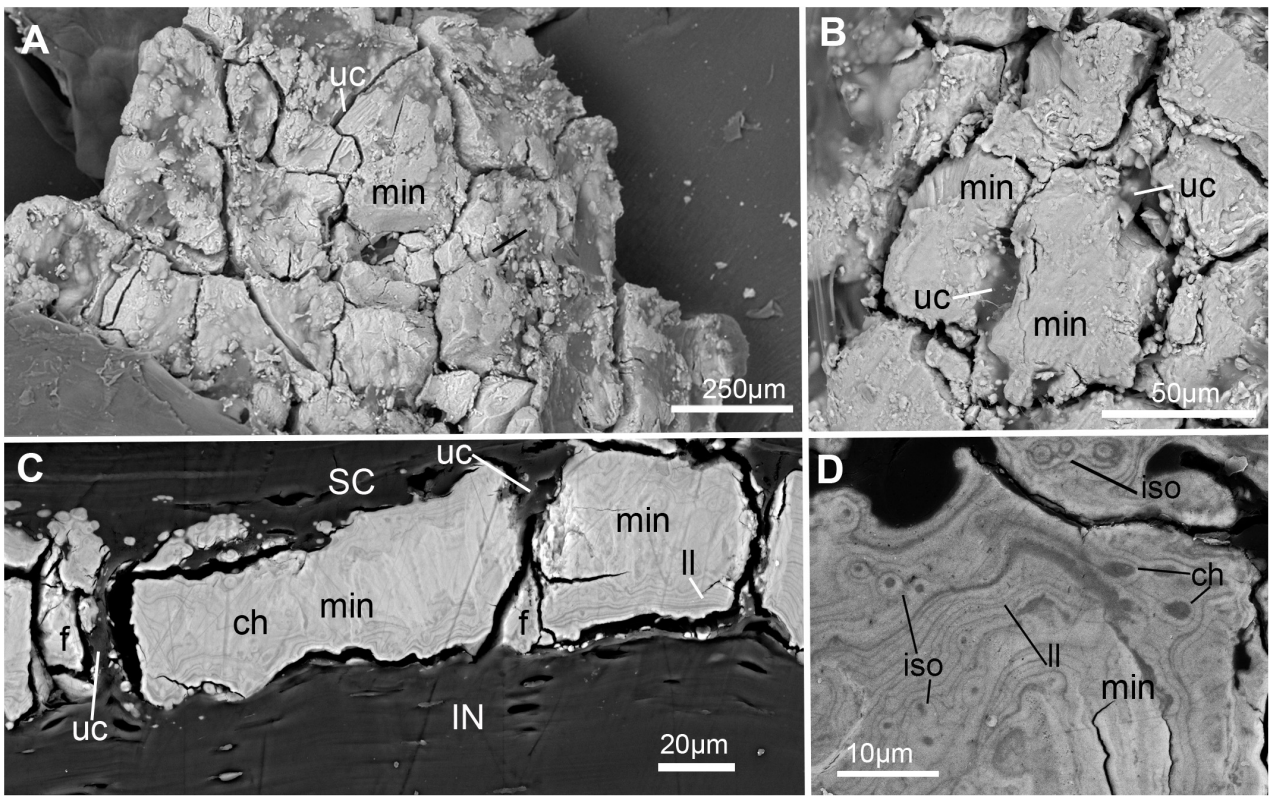

FIGURE 7 | SEM images of mineralization from the synarcual (anterior fused vertebrae) of an adult *Callorhinchus milii* (Holocephali; Callorhinchidae). **(A)** Overview of tesselated mineralization from a planar perspective; **(B)** close up of mineralization from a planar perspective; **(C)** mineralization from a transverse perspective; **(D)** close up of mineralization surface in transverse perspective; Note brightness and contrast of **(C,D)** have been altered to more clearly visualize morphology. Abbreviations: As in previous Figures, also f, fragments ll, Liesegang lines.

the batoid *Raja clavata*, Debiais-Thibaud, 2019). In a general sense, elasmobranch tesserae are not dissimilar to some of the developing units of mineralization in *C. milii* (**Figure 4F**, dm, ic), which also border the perichondrium, grow via calcification of surrounding cartilage matrix and, at least early in development, contain chondrocytes which appear to be vital. Additionally, mineralized tissues in *C. milii* appear to be overlain by a distinct layer of uncalcified cartilage, beneath the perichondrium (**Figure 2A**, SC). This resembles the thin layer of "supratesseral uncalcified cartilage" intervening between tesserae and perichondrium in elasmobranchs such as *U. halleri* and *Scyliorhinus canicula* (Kemp and Westrin, 1979; Bordat, 1988; Egerbacher et al., 2006; Enault et al., 2015; Seidel et al., 2016, 2017a; Debiais-Thibaud, 2019).

Despite these similarities, however, mineralization in adult *C. milii* appears to result in a distinct form of tessellated calcified cartilage. From a planar perspective, the mineralized tissue comprises a more irregular mosaic of tesserae than typically seen in elasmobranchs, with near-abutting calcified tiles separated by uncalcified cartilage (**Figures 7A,B**, min, uc; **Supplementary Figure 1**). From a transverse perspective, these tesserae are similar to those of the embryo, arranged as a single layer of tightly arranged units separated by very thin strips of uncalcified cartilage and sandwiched between a supratesseral layer and internal uncalcified cartilage (**Figures 7C,D**, min, uc, SC, IN). From this perspective, the tesserae of *C. milii* most closely resemble the tesserae of the sevengill shark (*Notorynchus cepedianus*) in terms of their arrangement, being very tightly organized and separated by minimal uncalcified cartilage, while also lacking vital chondrocytes; however, they are not comparable in size, being ∼19–57% of the size (Seidel et al., 2016). This is notable, as the Hexanchiformes, to which *N. cepedianus* belongs, are considered one of the most primitive of modern selachian groups (Barnett et al., 2012; Tanaka et al., 2013; da Cunha et al., 2017). However, despite this resemblance, it is likely that this tissue organization does not represent a plesiomorphic trait given the morphology of the skeletal tissues of stem holocephalans such as *Cobelodus* (see section "Mineralised Tissue Development"). It may be that this similarity is an example of evolutionary convergence resulting from common environmental factors. Both *C. milii* and *N. cepedianus* are both known to inhabit lower depths, 200–500 m, respectively (Last and Stevens, 2009; Buglass et al., 2020). This particular skeletal morphology could potentially be beneficial for coping with the conditions of these deep waters. Some osteichthyan fish that also lack swim bladders and inhabit mesopelagic waters (100–1,000 m in depth), have been thought to adapt to the consequences of hydrostatic pressure of these depths through a combination of light "poorly developed" skeletons and

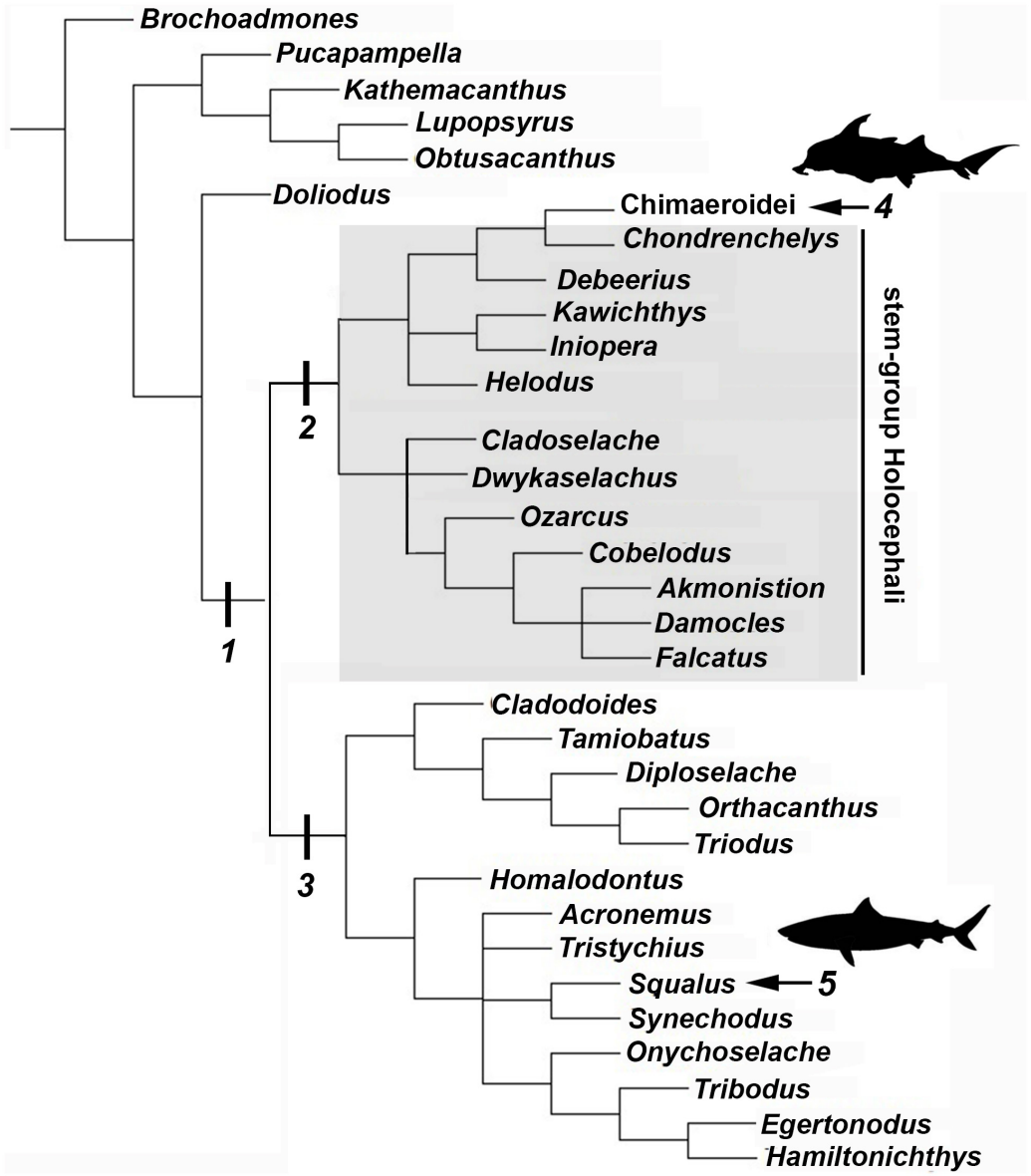

FIGURE 8 | Chondricthyan phylogeny (after Coates et al., 2018). 1, Crown–group Chondrichthyes (Holocephali + Elasmobranchii); 2, Holocephali; 3, Elasmobranchii; 4, Crown–group Holocephali; 5, Crown–group Elasmobranchii.

"watery" bodies (high water content) to assist with buoyancy and the metabolic costs of locomotion (Blaxter et al., 1971; Blaxter, 1980). Indeed, the scant data on the skeletal biology of deeper-water elasmobranchs (*Somniosus*, *Hexanchus*, *Notorhynchus*) suggests mineralization is greatly reduced, even in adult animals, with tessellation absent or only patchily distributed on skeletal elements (Dean et al., 2015; Seidel et al., 2016; Maisey et al., 2020). Whilst cartilaginous fish are known to control buoyancy through the use of oil-filled livers (Bone and Roberts, 1969; Gleiss et al., 2017), adaptations of the skeletons of these organisms to their environment have never been thoroughly examined. Whether the ostensible convergence in the taxa discussed here is related to common environmental factors could be confirmed by further investigation into the skeletal tissues and ecophysiology of other deep-sea chondrichthyans.

Despite similarities in the early stages of development between elasmobranch and *C. milii* tesserae (e.g., with early growth surrounding vital chondrocytes; **Figures 3B**, **4E**, **5B**), the tesserae of *C. milii* differ significantly from those elasmobranchs, and particularly batoids, in terms of size and ultrastructure. The tesserae observed in the stage 36 embryo and adult *C. milii* (**Figures 2**, **4** and **Supplementary Figure 1**, min) are much smaller compared to most elasmobranch tesserae that have been examined (Seidel et al., 2016; **Figure 10**, t), generally being less than 50 μm thick and ranging from 50 to 150 μm in width (**Figures 2A**, **7C**), comparable in size to the ∼100 μm

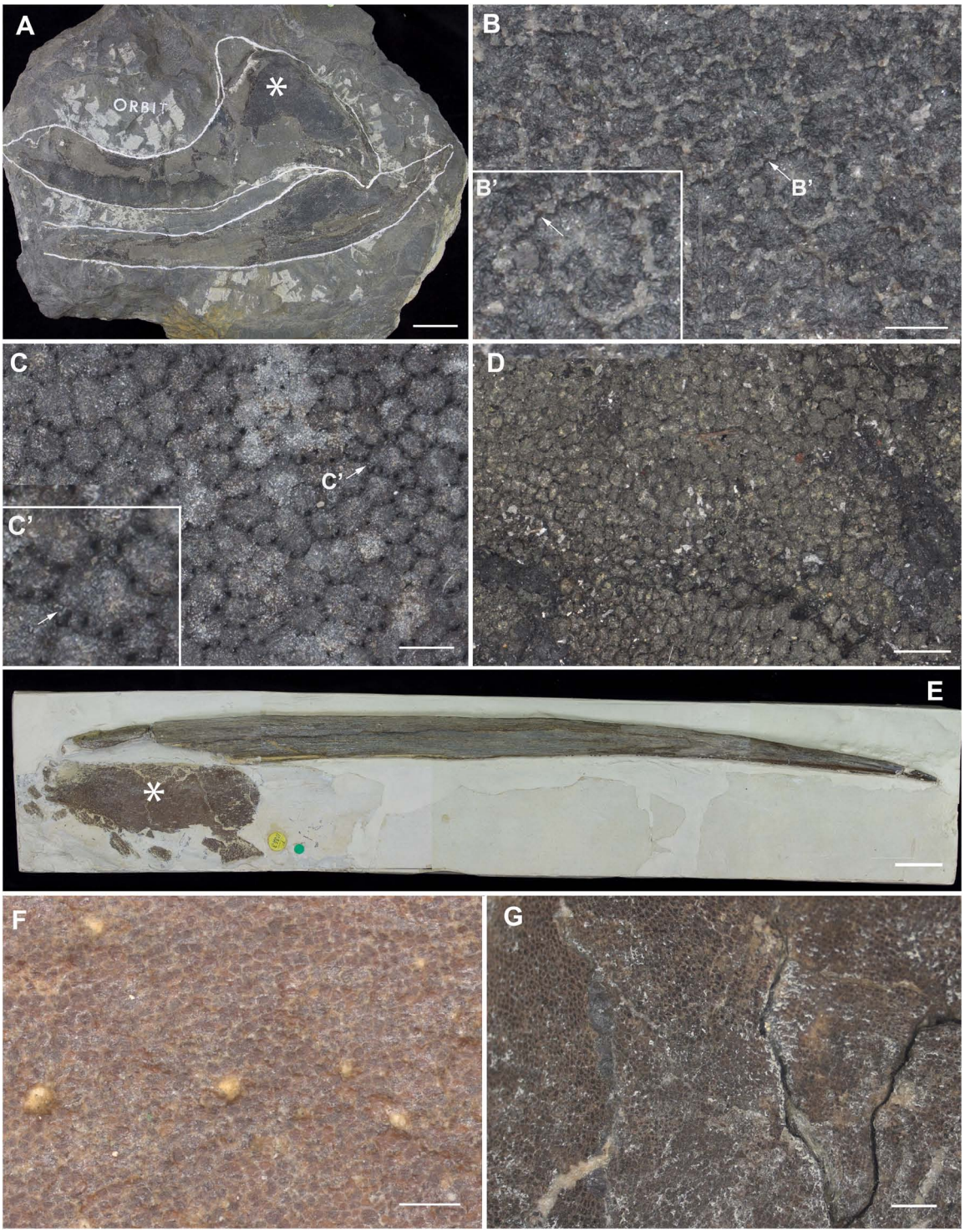

FIGURE 9 | Mineralized cartilage in stem Holocephali and crown group Holocephali (**Figure 8**). **(A)** NHMUK PV P.9285, *Cladoselache*, stem Holocephali, palatoquadrate, and Meckel's cartilage; asterisk indicates area shown in **(B)**, anterior to the left; **(B)** polygonal mineralization (tesserae), with irregular margins; **(B')** closeup of tessera, white arrow indicates contact along the tesseral margin which may represent "spokes" characterizing elasmobranch tesserae; **(C)** NHMUK PV P.62281a, *Cobelodus*, stem Holocephali, cranium, more regular polygonal mineralization (tesserae); **(C')** closeup of tessera, white arrow indicates "spokes" more similar to those in elasmobranch tesserae; **(D)** NHMUK PV P.62316b, *Sibirhynchus*, stem Holocephali, cranium, polygonal mineralization (tesserae); **(E,F)** NHMUK PV P.10343, *Edaphodon*, Family Callorhinchidae, crown group Holocephali (**Figures 8**, **2**), **(E)** dorsal fin endoskeletal support (with dorsal fin spine, anterior to left), asterisk indicates area shown in **(F)**, anterior to the left; **(F)** closeup showing polygonal mineralization (tesserae); **(G)** NHMUK PV P.8212, *Helodus*, cranium, polygonal mineralization. See **Supplementary Info Table 1** for tessera sizes in these taxa.

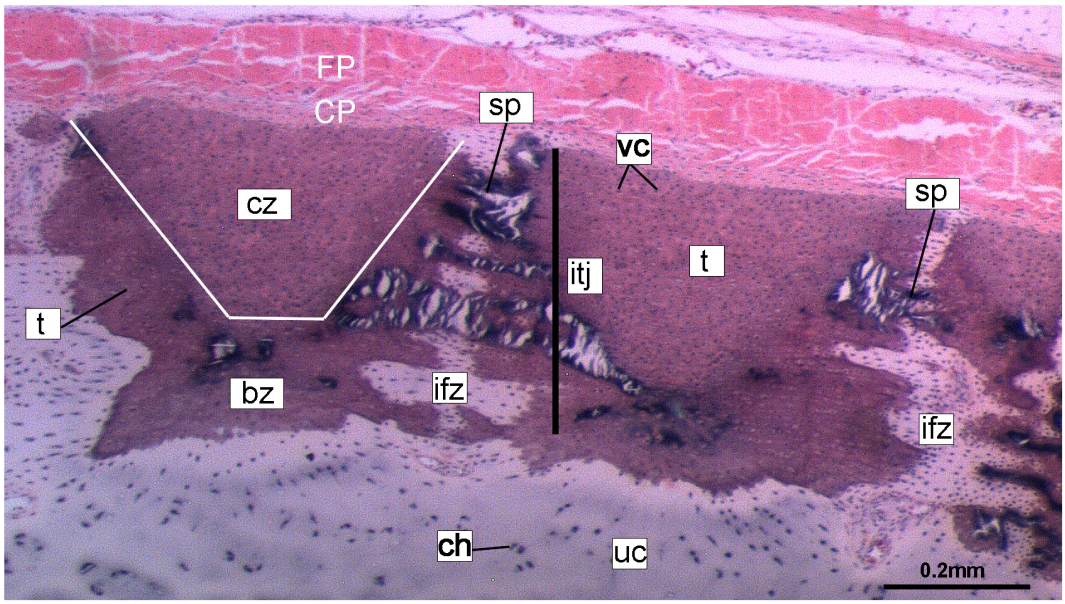

FIGURE 10 | Histological section of tessellated cartilage of a batoid ray (*Raja*). Abbreviations: as in previous Figures also bz, body zone; CP, chondrogenic perichondrium cz, cap zone; ifz, intertesseral fibrous zone; itj, intertesseral joint; FP, fibrous perichondrium; sp., spoke; t, tesserae; vc, vital chondrocytes.

tesserae of the catshark *Scyliorhinus* (Egerbacher et al., 2006; Seidel et al., 2016; Debiais-Thibaud, 2019). Additionally, *C. milii* tesserae display no internal regionalization into the cap and body zones (regions in elasmobranch tesserae delineated by cell shape and collagen type, **Figure 10**, bz, cz; Kemp and Westrin, 1979; Seidel et al., 2016; Chaumel et al., 2020), with no differences observed between the surfaces closer to the fibrous perichondrium, and surfaces surrounded by hyaline cartilage (e.g., **Figures 6A**, **7C**). *Callorhinchus milii* tesserae also apparently lack the intertesseral joints and mineralized spokes characteristic of elasmobranch tesserae (**Figure 10**, itj, sp.; Seidel et al., 2016), as well as the Sharpey's fibers that extend from the perichondrium into the tesserae cap zone in elasmobranchs (e.g., Kemp and Westrin, 1979; Peignoux-Deville et al., 1982; Clement, 1992; Summers, 2000; Seidel et al., 2017a). With respect to growth, the presence of Liesegang lines parallel to tesseral edges (**Figures 7C,D**, **ll**) suggests calcification in *C. milii* accretes at the margins of tesserae (**Figures 2–5**, min, dm, gc) in the same manner as elasmobranch tesserae. Additionally and/or alternatively, *C. milii* tesserae may grow through the development and fusion of new, smaller mineralization foci between existing tesserae (e.g., **Figure 6A**). Indeed, the irregular and less concentric arrangement of Liesegang lines in *C. milii* tesserae relative to those in elasmobranchs may be indicative of a more multimodal and/or haphazard form of growth, perhaps explaining the varied shape of the observed tesserae (**Figure 7**).

As noted, chondrocytes appear to be engulfed during mineralization in *C. milii* (**Figures 3B,E**, **4E**) and may be vital in early stages (**Figures 4C,D,F**, **5**, dm, ic). However, more developed tesserae in embryos and adults appear to be acellular (**Figures 2**, **4A**, **6**, min), with internal ultrastructures suggesting previously entombed chondrocytes died and underwent micropetrosis, calcifying their lacunae (**Figure 7D**, ch). Although similar morphological suggestion of micropetrosis has been observed in elasmobranch tesserae (Seidel et al., 2016, 2017b, 2019c), the indication of cell death accompanying mineralization to yield completely acellular tesserae is a major difference to most elasmobranch tesserae (Seidel et al., 2017a; Debiais-Thibaud, 2019; **Figure 10**). The absence of vital chondrocytes in the tesserae of *C. milii* may have important implications for their maintenance. In batoids, chondrocytes entombed in tesserae (**Figure 10**) remain vital in uncalcified lacunar spaces and form passages linking adjacent chondrocyte lacunae, similar to the canalaculi found in bone (Dean et al., 2010; Seidel et al., 2016; Chaumel et al., 2020). These chondrocytes and the networks they form are thought to have important functions with regard to maintaining the endoskeleton by communicating information about the mechanical environment in a manner similar to osteocytes in bone (Dean et al., 2010; Seidel et al., 2016; Chaumel et al., 2020). Thus, vital chondrocytes are absent in the mineralized tissues of the adult and the anterior older (anterior) regions of the synarcual, suggesting that these are lost during ontogeny, along with their associated putative mechanosensory networks, and that these functions are either absent or achieved through alternative means.

Chimaeroid Endoskeleton: Form Across Phylogeny

The limited literature available on chimaeroid skeletal biology offers conflicting descriptions of the endoskeletal mineralization: tessellated calcified cartilage akin to that of elasmobranchs (Hasse, 1879; Seidel et al., 2019b), smooth superficial sheets of continuous calcified cartilage formed from the fusion of

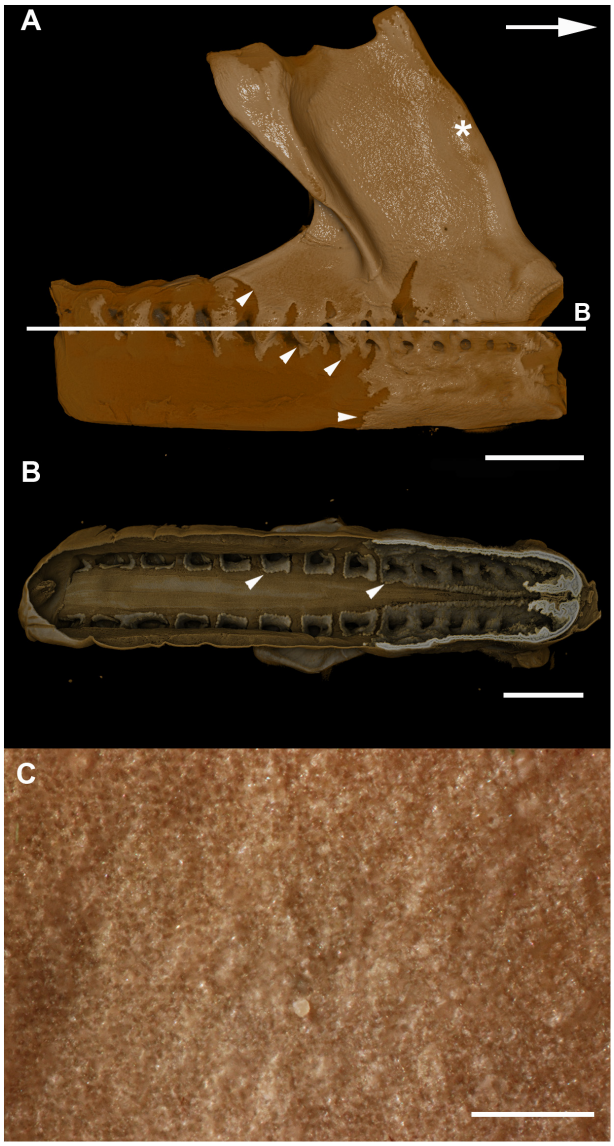

FIGURE 11 | (A,B) micro–CT scan of a synarcual from an adult *Callorhinchus milii* (Holocephali; Callorhinchidae). **(A)** synarcual, lateral view; **(B)** coronal section (virtual) through synarcual; **(C)** macrophotograph of lateral synarcual surface showing mineralization with a granular appearance. **Figures 11A,B** from Johanson et al. (2015). Usage permitted under CC BY licensing.

tesserae during ontogeny (Lund and Grogan, 1997; Grogan and Lund, 2004; Pradel et al., 2009; Grogan et al., 2015), or a granular texture (*Hydrolagus*, Finarelli and Coates, 2014). Recent histological data from the synarcual of a sub-adult (20 cm) *Hydrolagus* illustrates two forms of mineralized tissue (Debiais-Thibaud, 2019: 116): (1) small ($\leq$50 μm) subperichondral tissues "reminiscent of globular mineralization" at the periphery of the vertebral body and neural arch, that appear to follow a tessellated pattern, and (2) a more irregular form of globular mineralization deep within the vertebral body surrounding the fibrous chordal sheath.

Based on these few recent reported data on chimaeroid mineralization, tesserae in *C. milii* seem to share similarities with those of *Hydrolagus*. In both taxa, mineralization is tessellated and limited to the periphery of structures composed of hyaline cartilage, including the neural arches, basidorsals and basiventrals (vertebral body), though *C. milii* lacks the second deeper layer of globular mineralization (Debiais-Thibaud, 2019; **Figure 6**.1). The mineralized tissues of *Hydrolagus* also take the form of small, irregular acellular units, lacking clear separation into upper cap and lower body zones (Seidel et al., 2016; Debiais-Thibaud, 2019). Likewise, in *Chimaera*, mineralization more clearly takes the form of tesserae, although differences with respect to the more developed batoid tesserae have been described (Seidel et al., 2019a).

These few recent descriptions of mineralization in modern chimaeroids, including that provided here for *C. millii*, indicate that these taxa neither possess sheets of continuous calcified cartilage, nor a granular texture (Lund and Grogan, 1997; Grogan and Lund, 2004; Pradel et al., 2009; Finarelli and Coates, 2014). Instead they appear to support more historical claims (Hasse, 1879) that these organisms possess tesselated skeletal tissues, though contrary to these sources, these are distinctly different from most elasmobranch tesserae. These discrepant accounts may arise from the tissue arrangements; in taxa such as *C. milii* the tesserae are very tightly arranged, being separated by very thin portions of uncalcified cartilage, which may give the impression that the surface comprises a sheet. The tesserae themselves are covered in a type of fascia (see Materials and Methods, above), which could account for the observations of a granular texture.

Given the quality, available perspectives, and challenging surrounding matrices of many fossil specimens, the identification of useful morphological correlates for identifying tesseral ultrastructures is vital for understanding tesseral evolution and comparing modern and extinct forms. Recently, Maisey et al. (2020) provided a detailed description of the evolution of tesserae in the total group Chondrichthyes, which includes taxa known as acanthodians (Zhu et al., 2013; Coates et al., 2017, 2018; Dearden et al., 2019; Frey et al., 2019). Notably, certain acanthodian taxa, resolved closer to the base of the Chondrichthyes showed "subtesselate calcified cartilage," where the mineralized layer was broken by fissures, but these did not extend through the layer. More crownward, Maisey et al. (2020) outlined the appearance of various components of the tesserae, for example, the intertesseral joint system in the stem-chondrichthyans *Pucapampella* and *Gladbachus*, and division of the tesserae into cap and body zones in the latter.

As well, the mineralized meshwork visible on jaw cartilages of *Gladbachus* (Coates et al., 2018; **Supplementary Figure 2F**), echoes a distinct stellate tesseral morphology that has been observed in modern batoid fishes (*Leucoraja erinacea*, *Bathyraja eatonii*, *Urobatis halleri*), termed "trabecular tesserae" by Atake et al. (2019), and which has been shown to be associated with tesserae with a dominant spoke component (i.e., where non-spoke regions of tesserae have been reduced; Jayasankar et al.,

2020). This meshwork tissue morphology was also visible when observing the chondral aspect (the "underside") of the tesseral layer in skates, even in polygonal tesserae (Atake et al., 2019; **Figures 1H,I**). The association of this meshwork morphology with tesseral spokes and its observation in *Gladbachus* suggests that the stellate/trabecular tesseral morphology and the presence of spokes may be plesiomorphic for the Chondrichthyes and that polygonal tesserae were acquired later in the group (Atake et al., 2019). Although the structural complexity of tesserae is increasingly well-understood (Dean and Summers, 2006; Dean et al., 2009, 2010; Seidel et al., 2016, 2017a, 2019c), it is also increasingly clear that tesserae have had a complex evolutionary history, including the stepwise acquisition of characters.

By comparison, it appears that the Holocephali is characterized by a progressive loss of tesseral features. In a series of stem holocephalans, cartilage mineralization in what are presumed to be adults occurs as small polygonal units that are very similar among disparate taxa (**Figure 9**). The polygonal shape is more comparable to tesserae in the Elasmobranchii, including the suggested presence of mineralized spokes at tesseral joints in taxa such as *Cobelodus* and potentially *Cladoselache* (**Figures 9A–C**; Maisey et al., 2020). In contrast, polygonal tesserae are more irregular in shape, and spokes appear absent, in more crownward taxa, including *Edaphodon* (Callorhinchidae), a member of the crown group Holocephali. In these features, the tissues of crownward taxa bear the closest resemblance to those of *C. milii* (Callorhinchidae), however, tesserae in *C. milii* are more irregular in shape and much smaller than the irregular polygonal tesserae of *Edaphodon* (**Figure 11C**, **Supplementary Info Table 1**). The apparent loss of characteristics such as spokes and intertesseral joints in the skeletal tissues of crown holocephalans, may be related to their relatively irregular shape and organization. It could potentially be the case that features such as joints and spokes are important in or are a result of the formation of the regular polygonal geometry of tesserae. The presence of shape and structural features in some of the fossil taxa examined that echo those in modern elasmobranch tesserae suggests that substantial changes have occurred in mineralization in living chimaeroids, with a loss of many characteristics of tesserae seen in other chondrichthyans.

CONCLUSION

Whilst tessellated cartilage has been suggested to be a shared characteristic of chondrichthyan endoskeletons (e.g., Maisey et al., 2020), the data presented here indicate that this type of mineralization has been significantly modified within the holocephalans. The mineralized layer of the endoskeleton of *Callorhinchus milii* (Family Callorhinchidae) consists of tightly arranged, irregularly shaped tesserae, also present in *Hydrolagus* (Family Chimaeridae). These tesserae in *Callorhinchus* and *Hydrolagus* differ in many respects from most shark and ray tesserae, being smaller and simpler, lacking features such as distinct cap and body zones, mineralized spokes between the tesserae and retention of lacunae housing vital chondrocytes. Nevertheless some similarities in development are present, such as the inter-chondrocyte septa that surround the chondrocytes early in the development of the tesserae, described above in *Callorhinchus* and the ray *Urobatis* (Dean et al., 2009; Seidel et al., 2016). Tesserae in sharks such as *Notorynchus* may also lack some features seen in other elasmobranchs (Debiais-Thibaud, 2019; **Figure 6**.3; Seidel et al., 2016; **Figure 11A**). Tesserae in stem group holocephalans, as well as in fossil relatives of *Callorhinchus* such as *Edaphodon*, within the Family Callorhinchidae (**Figure 9F**), also appear to possess the polygonal shape more characteristic of ray tesserae with these being larger and better developed than the tesserae of adult *Callorhinchus*. Thus it appears that these smaller units may be the characteristic mineralized structure in extant holocephalans, representing a reduction of mineralization occurring separately within the Callorhinchidae and Chimaeridae, and within the Elasmobranchii.

DATA AVAILABILITY STATEMENT

The raw data supporting the conclusions of this article will be made available by the authors, without undue reservation, to any qualified researcher.

ETHICS STATEMENT

Ethical review and approval from Curtin University was not required for the animal study because specimens of *Callorhinchus milii* were collected near Melbourne several years ago, and CB now works at Curtin University, Perth. She collected these specimens under the following permits: RP1000, RP 1003, and RP1112, with the authorization and direction of the Monash University Animal Ethics Committee (Permit: MAS-ARMI-2010-01). So it's not necessary for them to approve this particular study, as they approved the initial collection with the appropriate permits.

AUTHOR CONTRIBUTIONS

ZJ, CB, and JP conceived this project and contributed data to the project from fossil and extant holocephalans. All authors contributed to interpretation of the data and writing of the manuscript.

FUNDING

JP and CB were funded by the Curtin University Faculty of Science and Engineering Research and Development Committee Small Grant, CB was funded by the Curtin Research fellowship, and JP was funded by the Australian Government Research Training Program Scholarship (AGRTP). The John de Laeter

Centre was funded by the Australian Research Council (ARC LE130100053).

ACKNOWLEDGMENTS

We would like to thank Ollie Crimmen and James MacLaine (NHM Life Sciences Department) for providing access to the slides of the *Callorhinchus* embryo and Innes Claxworthy (NHM Core Research Labs) for SEM imaging of the *Callorhinchus* adult. We would also like to acknowledge Elaine Miller and the John de Laeter Centre at Curtin University for expert advice, assistance, and service in the imaging of *Callorhinchus* embryo tissues, and the Curtin Faculty of Science and Engineering, School of Molecular and Life Sciences and Centre of Health and Innovation Research for support. We would also like to thank Alan Pradel and John Maisey for discussion of tesserae in fossil chondrichthyans.

SUPPLEMENTARY MATERIAL

The Supplementary Material for this article can be found online at: https://www.frontiersin.org/articles/10.3389/fgene.2020.571694/full#supplementary-material

Supplementary Figure 1 | SEM images of mineralization from the synarcual (anterior fused vertebrae) of the second adult *Callorhinchus milii* (Holocephali; Callorhinchidae). **(A)** Tesselated mineralization from a planar perspective; **(B)** close up of mineralization from a planar perspective.

Supplementary Table 1 | Holocephali tesserae size (microns).

REFERENCES

Atake, O. J., Cooper, D. M., and Eames, B. F. (2019). Bone-like features in skate suggest a novel elasmobranch synapomorphy and deep homology of trabecular mineralization patterns. *Acta Biomater.* 84, 424–436. doi: 10.1016/j.actbio.2018.11.047

Barnett, A., Braccini, J. M., Awruch, C. A., and Ebert, D. A. (2012). An overview on the role of Hexanchiformes in marine ecosystems: biology, ecology and conservation status of a primitive order of modern sharks. *J. Fish Biol.* 80, 966–990. doi: 10.1111/j.1095-8649.2012.03242.x

Blaxter, J. H. S. (1980). "The effect of hydrostatic pressure on fishes," in *Environmental Physiology of Fishes*, ed. M. A. Ali (Boston: Springer), 369–386. doi: 10.1007/978-1-4899-3659-2_13

Blaxter, J. H. S., Wardle, C. S., and Roberts, B. L. (1971). Aspects of the circulatory physiology and muscle systems of deep-sea fish. *J. Mar. Biol. Assoc. U.K.* 51, 991–1006. doi: 10.1017/s0025315400018105

Boisvert, C. A., Martins, C. L., Edmunds, A. G., Cocks, J., and Currie, P. (2015). Capture, transport, and husbandry of elephant sharks (*Callorhinchus milii*) adults, eggs, and hatchlings for research and display. *Zoo Biol.* 34, 94–98. doi: 10.1002/zoo.21183

Bone, Q., and Roberts, B. L. (1969). The density of elasmobranchs. *J. Mar. Biol. Assoc. U.K.* 49, 913–937. doi: 10.1017/s0025315400038017

Bordat, C. (1987). Etude ultrastructurale de l'os des vertèbres du Sélacien *Scyliorhinus canicula* L. *Can. J. Zool.* 65, 1435–1444. doi: 10.1139/z87-226

Bordat, C. (1988). Les cartilages calcifiés de la petite roussette (*Scyliorhinus canicula* L., Chondrichthyens): histologie et ultrastructure. *Can. J. Zool.* 66, 1432–1445. doi: 10.1139/z88-210

Brazeau, M. D., Giles, S., Dearden, R. P., Jerve, A., Ariunchimeg, Y., Zorig, E., et al. (2020). Endochondral bone in an Early Devonian 'placoderm' from Mongolia. *Nat. Ecol. Evol.* 4, 1477–1484. doi: 10.1038/s41559-020-01290-2

Buglass, S., Nagy, S., Ebert, D., Sepa, P., Turchik, A., Bell, K. L., et al. (2020). First records of the seven-gilled *Notorynchus cepedianus* and six-gilled *Hexanchus griseus* sharks (Chondrichthyes: Hexanchiformes: Hexanchidae) found in the Galápagos Marine Reserve. *J. Fish Biol.* 97, 926–929. doi: 10.1111/jfb.14447

Chaumel, J., Schotte, M., Bizzarro, J., Zaslansky, P., Fratzl, P., Baum, D., et al. (2020). Co–aligned chondrocytes: zonal morphological variation and structured arrangement of cell lacunae in tessellated cartilage. *Bone* 134:115264. doi: 10.1016/j.bone.2020.115264

Claeson, K. M. (2011). The synarcual cartilage of batoids with emphasis on the synarcual of Rajidae. *J. Morphol.* 272, 1444–1463. doi: 10.1002/jmor.10996

Clement, J. (1986). *Development, Structure and Composition of Chondrichthyan Skeletal Tissues*. Ph.D. thesis, University of London, London.

Clement, J. (1992). Re–examination of the fine structure of endoskeletal mineralization in Chondrichthyans: implications for growth, ageing and calcium homeostasis. *Mar. Freshw. Res.* 43, 157–181. doi: 10.1071/mf9920157

Coates, M. I., Finarelli, J. A., Sansom, I. J., Andreev, P. S., Criswell, K. E., Tietjen, K., et al. (2018). An early chondrichthyan and the evolutionary assembly of a shark body plan. *Proc. Biol. Sci.* 285:20172418. doi: 10.1098/rspb.2017.2418

Coates, M. I., Gess, R. W., Finarelli, J. A., Criswell, K. E., and Tietjen, K. (2017). A symmoriiform chondrichthyan braincase and the origin of chimaeroid fishes. *Nature* 541, 208–211. doi: 10.1038/nature20806

Coates, M. I., and Sequeira, S. E. K. (2001). A new stethacanthid chondrichthyan from the lower Carboniferous of Bearsden, Scotland. *J. Vertebr. Paleontol.* 21, 438–459. doi: 10.1671/0272-4634(2001)021[0438:anscft]2.0.co;2

Coates, M. I., Sequeira, S. E. K., Sansom, I., and Smith, M. (1998). Spines and tissues of ancient sharks. *Nature* 396, 729. doi: 10.1038/25467

Compagno, L. J. (1977). Phyletic relationships of living sharks and rays. *Am. Zool.* 17, 303–322. doi: 10.1093/icb/17.2.303

Criswell, K. E., Coates, M. I., and Gillis, J. A. (2017a). Embryonic development of the axial column in the little skate, *Leucoraja erinacea*. *J. Morphol.* 278, 300–320. doi: 10.1002/jmor.20637

Criswell, K. E., Coates, M. I., and Gillis, J. A. (2017b). Embryonic origin of the gnathostome vertebral skeleton. *Proc. Biol. Sci.* 284:20172121. doi: 10.1098/rspb.2017.2121

da Cunha, D., da Silva Rodrigues-Filho, L. F., and de Luna Sales, J. B. (2017). *A Review of the Mitogenomic Phylogeny of the Chondrichthyes*. Available online at: https://www.intechopen.com/books/chondrichthyes-multidisciplinary-approach/a-review-of-the-mitogenomic-phylogeny-of-the-chondrichthyes (accessed February 20, 2020).

Dean, B. (1894). Contributions to the morphology of *Cladoselache* (*Cladodus*). *J. Morphol.* 9, 87–114. doi: 10.1002/jmor.1050090103

Dean, B. (1895). *Fishes, Living and Fossil. An Outline of Their Forms and Probable Relationships*. New York, NY: Macmillan and Co.

Dean, B. (1906). *Chimaeroid Fishes and their Development*. Washington, DC: Carnegie Institution of Washington.

Dean, M. N., Ekstrom, L., Monsonego-Ornan, E., Ballantyne, J., Witten, P. E., Riley, C., et al. (2015). Mineral homeostasis and regulation of mineralization processes in the skeletons of sharks, rays and relatives (Elasmobranchii). *Semin. Cell Dev. Biol.* 46, 51–67. doi: 10.1016/j.semcdb.2015.10.022

Dean, M. N., Mull, C. G., Gorb, S. N., and Summers, A. P. (2009). Ontogeny of the tessellated skeleton: insight from the skeletal growth of the round stingray *Urobatis halleri*. *J. Anat.* 215, 227–239. doi: 10.1111/j.1469-7580.2009.01116.x

Dean, M. N., Socha, J., Hall, B., and Summers, A. P. (2010). Canaliculi in the tessellated skeleton of cartilaginous fishes. *J. Appl. Ichthyol.* 26, 263–267. doi: 10.1111/j.1439-0426.2010.01417.x

Dean, M. N., and Summers, A. P. (2006). Mineralized cartilage in the skeleton of chondrichthyan fishes. *Zoology* 109, 164–168. doi: 10.1016/j.zool.2006.03.002

Dearden, R. P., Stockey, C., and Brazeau, M. D. (2019). The pharynx of the stem–chondrichthyan *Ptomacanthus* and the early evolution of the gnathostome gill skeleton. *Nat. Commun.* 10:2050.

Debiais-Thibaud, M. (2019). "The Evolution of Endoskeletal Mineralisation in Chondrichthyan Fish," in *Evolution and Development of Fishes*, eds Z. Johanson, C. Underwood, and M. Richter (Cambridge: Cambridge University Press), 110–125. doi: 10.1017/9781316832172.007

Didier, D. A. (1995). Phylogenetic systematics of extant chimaeroid fishes (Holocephali, Chimaeroidei). *Am. Mus. Novit.* 3119, 1–86. doi: 10.1016/j.cretres.2013.09.011

Didier, D. A., LeClair, E. E., and Vanbuskirk, D. R. (1998). Embryonic staging and external features of development of the chimaeroid fish, *Callorhinchus milii* (Holocephali, Callorhinchidae). *J. Morphol.* 236, 25–47. doi: 10.1002/(sici)1097-4687(199804)236:1<25::aid-jmor2>3.0.co;2-n

Eames, B. F., Allen, N., Young, J., Kaplan, A., Helms, J. A., and Schneider, R. A. (2007). Skeletogenesis in the swell shark *Cephaloscyllium ventriosum*. *J. Anat.* 210, 542–554. doi: 10.1111/j.1469-7580.2007.00723.x

Egerbacher, M., Helmreich, M., Mayrhofer, E., and Böck, P. (2006). Mineralisation of the hyaline cartilage in the small–spotted dogfish *Scyliorhinus canicula* L. *Scripta Med.* 79, 199–212.

Enault, S., Adnet, S., and Debiais-Thibaud, M. (2016). Skeletogenesis during the late embryonic development of the catshark *Scyliorhinus canicula* (Chondrichthyes; Neoselachii). *MorphoMuseum* 1:e2. doi: 10.18563/m3.1.4.e2

Enault, S., Muñoz, D. N., Silva, W. T., Borday-Birraux, V., Bonade, M., Oulion, S., et al. (2015). Molecular footprinting of skeletal tissues in the catshark *Scyliorhinus canicula* and the clawed frog *Xenopus tropicalis* identifies conserved and derived features of vertebrate calcification. *Front. Genet.* 6:283. doi: 10.3389/fgene.2015.00283

Finarelli, J. A., and Coates, M. I. (2014). *Chondrenchelys problematica* (Traquair, 1888) redescribed: a Lower Carboniferous, eel–like holocephalan from Scotland. *Earth Environ. Sci. Trans. R. Soc. Edinb.* 105, 35–59. doi: 10.1017/s1755691014000139

Frey, L., Coates, M. I., Ginter, M., Hairapetian, V., Rücklin, M., Jerjen, I., et al. (2019). The early elasmobranch *Phoebodus*: phylogenetic relationships, ecomorphology and a new time–scale for shark evolution. *Proc. Biol. Sci.* 286:20191336. doi: 10.1098/rspb.2019.1336

Gadow, H. F., and Abbott, E. (1895). XVIII. On the evolution of the vertebral column of fishes. *Proc. R. Soc. Lond.* 56, 296–299. doi: 10.1098/rspl.1894.0117

Genten, F., Terwinghe, E., and Danguy, A. (2009). *Atlas of Fish Histology*. Boca Raton, FL: CRC Press.

Gleiss, A. C., Potvin, J., and Goldbogen, J. A. (2017). Physical trade-offs shape the evolution of buoyancy control in sharks. *Proc. Biol. Sci.* 284:20171345. doi: 10.1098/rspb.2017.1345

Goodrich, E. (1909). *A Treatise on Zoology. Part IX, Vertebrata Craniata (first Fasicle: Cyclostomes and Fishes)*. London: Adam & Charles Black.

Goodrich, E. (1930). *Studies on the Structure & Development of Vertebrates*. London: Macmillan.

Grogan, E. D., and Lund, R. (2004). "The origin and relationships of early Chondrichthyes," in *Biology of Sharks and their Relatives*, eds J. C. Carrier, J. A. Musick, and M. R. Heithaus (Boca Raton, FL: CRC Press), 22–61.

Grogan, E. D., Lund, R., and Greenfest-Allen, E. (2015). "The origin and relationships of early chondrichthyans," in *Biology of Sharks and Their Relatives*, eds J. C. Carrier, J. A. Musick, and M. R. Heithaus (Boca Raton, FL: CRC Press).

Hall, B. K. (1975). Evolutionary consequences of skeletal differentiation. *Am. Zool.* 15, 329–350. doi: 10.1093/icb/15.2.329

Hall, B. K. (2005). *Bones and Cartilage: Developmental and Evolutionary Skeletal Biology*. San Diego, CA: Academic Press.

Hasse, C. (1879). *Das näturliche System der Elasmobranchier auf Grundlage des Baues und der Entwicklung ihrer Wirbelsäule: eine morphologische und paläontologische Studie*. London: Forgotten Books.

Jayasankar, A. K., Seidel, R., Hosny, A., Weaver, J. C., Fratzl, P., Chen, J., et al. (2020). Multi–scale modeling and mechanical performance characterization of stingray skeleton–inspired tessellations. *J. Mech. Phys. Solids* 138:103906. doi: 10.1016/j.jmps.2020.103906

Johanson, Z., Boisvert, C., Maksimenko, A., Currie, P., and Trinajstic, K. (2015). Development of the synarcual in the elephant sharks (Holocephali; Chondrichthyes): implications for vertebral formation and fusion. *PLoS One* 10:e0135138. doi: 10.1371/journal.pone.0135138

Johanson, Z., Fraser, G., Martin, K., and James, K. (2019). The synarcual of the Little Skate, *Leucoraja erinacea*: novel development among the vertebrates. *Front. Ecol. Evol.* 7:12. doi: 10.3389/fevo.2019.00012

Johanson, Z., Trinajstic, K., Carr, R., and Ritchie, A. (2013). Evolution and development of the synarcual in early vertebrates. *Zoomorphology* 132, 95–110. doi: 10.1007/s00435-012-0169-9

Kemp, N. E., and Westrin, S. K. (1979). Ultrastructure of calcified cartilage in the endoskeletal tesserae of sharks. *J. Morphol.* 160, 75–101. doi: 10.1002/jmor.1051600106

Kheir, E., and Shaw, D. (2009). Hyaline articular cartilage. *Orthop. Trauma* 23, 450–455. doi: 10.1016/j.mporth.2009.01.003

Last, P. R., and Stevens, J. D. (2009). *Sharks and Rays of Australia. CSIRO Marine and Atmospheric Research*, 2nd Edn. Melbourne: CSIRO Publishing.

Lund, R., and Grogan, E. D. (1997). Relationships of the Chimaeriformes and the basal radiation of the Chondrichthyes. *Rev. Fish Biol. Fish.* 7, 65–123.

Maisey, J. G. (2013). The diversity of tessellated calcification in modern and extinct chondrichthyans. *Rev. Paléobiol.* 32, 355–371.

Maisey, J. G., Denton, J. S. S., Burrow, C., and Pradel, A. (2020). Architectural and ultrastructural features of tessellated calcified cartilage in modern and extinct chondrichthyan fishes. *J. Fish Biol.* 2020, 1–23. doi: 10.1111/jfb.14376

Maisey, J. G., Janvier, P., Pradel, A., Denton, J. S. S., Bronson, A., Miller, R., et al. (2019). "*Doliodus* and Pucapampellids," in *Evolution and Development of Fishes*, eds Z. Johanson, C. Underwood, and M. Richter (Cambridge: Cambridge University Press), 87–109. doi: 10.1017/9781316832172.006

Marconi, A., Hancock-Ronemus, A., and Gillis, J. A. (2020). Adult chondrogenesis and spontaneous cartilage repair in the skate, *Leucoraja erinacea*. *eLife* 9:e53414.

Moy-Thomas, J. A. (1936). On the structure and affinities of the Carboniferous cochliodont *Helodus simplex*. *Geol. Mag.* 73, 488–503. doi: 10.1017/s0016756800095212

Nelson, J. S., Grande, T. G., and Wilson, M. V. H. (2006). *Fishes of the World. Fifth Edition*. Hoboken, NJ: Wiley.

Patterson, C. (1965). The phylogeny of the chimaeroids. *Phil. Trans. Roy. Soc. London. Ser. B. Biol. Sci.* 249, 101–219. doi: 10.1098/rstb.1965.0010

Peignoux-Deville, J., Lallier, F., and Vidal, B. (1982). Evidence for the presence of osseous tissue in dogfish vertebrae. *Cell Tissue Res.* 222, 605–614.

Porter, M. E., Koob, T. J., and Summers, A. P. (2007). The contribution of mineral to the material properties of vertebral cartilage from the smooth–hound shark *Mustelus californicus*. *J. Exp. Biol.* 210, 3319–3327. doi: 10.1242/jeb.006189

Pradel, A., Maisey, J. G., Tafforeau, P., and Janvier, P. (2009). An enigmatic gnathostome vertebrate skull from the Middle Devonian of Bolivia. *Acta Zool.* 90, 123–133. doi: 10.1111/j.1463-6395.2008.00350.x

Pradel, A., Tafforeau, P., Maisey, J. G., and Janvier, P. (2011). A new Paleozoic Symmoriiformes (Chondrichthyes) from the Late Carboniferous of Kansas (USA) and cladistic analysis of early chondrichthyans. *PLoS One* 6:e24938. doi: 10.1371/journal.pone.0024938

Pradel, P., Maisey, J. G., Tafforeau, P., Mapes, R. H., and Mallatt, J. (2014). A Palaeozoic shark with osteichthyan–like branchial arches. *Nature* 509, 608–611. doi: 10.1038/nature13195

Ridewood, W. (1921). VIII.—On the calcification of the vertebral centra in sharks and rays. *Philos. Trans. R. Soc. Lond. B* 210, 311–407. doi: 10.1098/rstb.1921.0008

Roach, H. I., Aigner, T., and Kouri, J. B. (2004). Chondroptosis: a variant of apoptotic cell death in chondrocytes? *Apoptosis* 9, 265–277. doi: 10.1023/b:appt.0000025803.17498.26

Ryll, B., Sanchez, S., Haitina, T., Tafforeau, P., and Ahlberg, P. E. (2014). The genome of Callorhinchus and the fossil record: a new perspective on SCPP gene evolution in gnathostomes. *Evol. Dev.* 16, 123–124. doi: 10.1111/ede.12071

Schauinsland, H. H. (1903). Beiträge zur Entwicklungsgeschichte und Anatomie der Wirbeltiere. I. *Sphenodon, Callorhynchus, Chameleo*. *Zoologica* 39, 1–98.

Seidel, R., Blumer, M., Chaumel, J., Amini, S., and Dean, M. N. (2020). Endoskeletal mineralization in chimaera and a comparative guide to tessellated cartilage in chondrichthyan fishes (sharks, rays and chimaera). *J. R. Soc. Interface* 17:20200474. doi: 10.1098/rsif.2020.0474

Seidel, R., Blumer, M., Pechriggl, E.-J., Lyons, K., Hall, B. K., Fratzl, P., et al. (2017a). Calcified cartilage or bone? Collagens in the tessellated endoskeletons of cartilaginous fish (sharks and rays). *J. Struct. Biol.* 200, 54–71. doi: 10.1016/j.jsb.2017.09.005

Seidel, R., Blumer, M., Zaslansky, P., Knötel, D., Huber, D. R., Weaver, J. C., et al. (2017b). Ultrastructural, material and crystallographic description of endophytic masses–A possible damage response in shark and ray tessellated calcified cartilage. *J. Struct. Biol.* 198, 5–18. doi: 10.1016/j.jsb.2017.03.004

Seidel, R., Chaumel, J., Blumer, M., Herbert, A., Moreno-Jimenez, I., Summers, A. P., et al. (2019a). "Mineralization in Chimaera Cartilage: tessellated but not Tesserae?," in *Proceedings of the Society for Integrative and Comparative Biology, Annual Meeting*, Vol. 2-214, Tampa, FL, 363.

Seidel, R., Jayasankar, A., Shahar, R., and Dean, M. N. (2019b). "Multiscale architectures of fish bone and tessellated cartilage and their relation to function," in *Architectured Materials in Nature and Engineering*, Vol. 282, eds Y. Estrin, Y. Bréchet, J. W. C. Dunlop, and P. Fratzl (New York, NY: Springer), 329–353. doi: 10.1007/978-3-030-11942-3_11

Seidel, R., Roschger, A., Li, L., Bizzarro, J. J., Zhang, Q., Yin, J., et al. (2019c). Mechanical properties of stingray tesserae: high-resolution correlative analysis of mineral density and indentation moduli in tessellated cartilage. *Acta Biomater.* 96, 421–435. doi: 10.1016/j.actbio.2019.06.038

Seidel, R., Lyons, K., Blumer, M., Zaslansky, P., Fratzl, P., Weaver, J. C., et al. (2016). Ultrastructural and developmental features of the tessellated endoskeleton of elasmobranchs (sharks and rays). *J. Anat.* 229, 681–702. doi: 10.1111/joa.12508

Summers, A. P. (2000). Stiffening the stingray skeleton–an investigation of durophagy in myliobatid stingrays (Chondrichthyes, Batoidea, Myliobatidae). *J. Morph.* 243, 113–126. doi: 10.1002/(SICI)1097-4687(200002)243:2<113::AID-JMOR1>3.0.CO;2-A

Tanaka, K., Shiina, T., Tomita, T., Suzuki, S., Hosomichi, K., Sano, K., et al. (2013). Evolutionary relations of Hexanchiformes deep–sea sharks elucidated by whole mitochondrial genome sequences. *BioMed Res. Int.* 2013: 147064.

VanBuren, C. S., and Evans, D. C. (2017). Evolution and function of anterior cervical vertebral fusion in tetrapods. *Biol. Rev. Camb. Philos. Soc.* 92, 608–626. doi: 10.1111/brv.12245

Zangerl, R., and Case, G. R. (1973). Iniopterygia: a new order of Chondrichthyan fishes from the Pennsylvanian of North America. *Fieldiana Geol. Mem.* 6, 1–67.

Zhu, M., Yu, X., Ahlberg, P. E., Choo, B., Lu, J., Qiao, T., et al. (2013). A Silurian placoderm with osteichthyan-like marginal jaw bones. *Nature* 502, 188–193. doi: 10.1038/nature12617

Conflict of Interest: The authors declare that the research was conducted in the absence of any commercial or financial relationships that could be construed as a potential conflict of interest.

frontiers in Genetics

ORIGINAL RESEARCH
published: 08 January 2021
doi: 10.3389/fgene.2020.597459

Pearl Sac Gene Expression Profiles Associated With Pearl Attributes in the Silver-Lip Pearl Oyster, *Pinctada maxima*

Carmel McDougall[1,2], Felipe Aguilera[1†], Ali Shokoohmand[2], Patrick Moase[3] and Bernard M. Degnan[1]**

[1] Centre for Marine Science, School of Biological Sciences, The University of Queensland, St. Lucia, QLD, Australia, [2] Australian Rivers Institute, Griffith University, Nathan, QLD, Australia, [3] Clipper Pearls and Autore Pearling, Broome, WA, Australia

OPEN ACCESS

Edited by:
Frederic Marin,
Délégation Centre-Est (CNRS), France

Reviewed by:
Michio Suzuki,
The University of Tokyo, Japan
Peter J. Prentis,
Queensland University of Technology, Australia

***Correspondence:**
Bernard M. Degnan
b.degnan@uq.edu.au
Carmel McDougall
c.mcdougall@griffith.edu.au

†Present address:
Felipe Aguilera,
Departamento de Bioquímica y Biología Molecular, Facultad de Ciencias Biológicas, Universidad de Concepción, Concepción, Chile

Specialty section:
This article was submitted to Evolutionary and Population Genetics, a section of the journal Frontiers in Genetics

Received: 21 August 2020
Accepted: 07 December 2020
Published: 08 January 2021

Citation:
McDougall C, Aguilera F, Shokoohmand A, Moase P and Degnan BM (2021) Pearl Sac Gene Expression Profiles Associated With Pearl Attributes in the Silver-Lip Pearl Oyster, Pinctada maxima. Front. Genet. 11:597459. doi: 10.3389/fgene.2020.597459

Pearls are highly prized biomineralized gemstones produced by molluscs. The appearance and mineralogy of cultured pearls can vary markedly, greatly affecting their commercial value. To begin to understand the role of pearl sacs—organs that form in host oysters from explanted mantle tissues that surround and synthesize pearls—we undertook transcriptomic analyses to identify genes that are differentially expressed in sacs producing pearls with different surface and structural characteristics. Our results indicate that gene expression profiles correlate with different pearl defects, suggesting that gene regulation in the pearl sac contributes to pearl appearance and quality. For instance, pearl sacs that produced pearls with surface non-lustrous calcification significantly down-regulate genes associated with cilia and microtubule function compared to pearl sacs giving rise to lustrous pearls. These results suggest that gene expression profiling can advance our understanding of processes that control biomineralization, which may be of direct value to the pearl industry, particularly in relation to defects that result in low value pearls.

Keywords: ***Pinctada maxima*, pearl, pearl quality, nacre, biomineralization, CEL-Seq**

INTRODUCTION

Pearls are stunning and structurally complex biominerals fabricated by a wide range of molluscs (Strack, 2006; Southgate and Lucas, 2008; McDougall et al., 2013b). Some species produce pearls composed of nacre (mother-of-pearl), and many of these species have been used for the production of cultured pearls, resulting in a valuable aquaculture industry (Australian Bureau of Agricultural and Resource Economics and Sciences [ABARES], 2018).

Cultured saltwater pearl production involves two oysters: a donor and a host. Small pieces of the mantle—the organ responsible for shell formation in molluscs—are excised from the donor oyster and surgically inserted into the gonad of the host, along with a spherical bead known as the nucleus (Taylor and Strack, 2008). Over time, the explanted mantle grows around the nucleus to form a continuous epithelial layer, the pearl sac (Taylor and Strack, 2008; McDougall et al., 2013b). The pearl sac first secretes an organic layer onto the surface of the nucleus (Taylor and Strack, 2008). This is followed by the deposition of successive layers of calcium carbonate, first prismatic and then nacreous, although a large degree of variation can be observed in individual pearls (Cuif et al., 2008, 2011; Mariom et al., 2019). This structural

layering is similar to that observed within the pearl oyster shell that also consists of three layers; an outer organic-rich layer (the periostracum), a middle prismatic layer of calcite, and an inner nacreous layer of aragonite. These similarities have led to the generalized assertion that pearls are essentially inverted shells (Farn, 1986; Taylor and Strack, 2008).

The formation of pearls and shells by similar processes is evident at the molecular level. The proteinaceous component of adult pearl oyster (*Pinctada*) shells is complex, comprising over 80 individual shell matrix proteins (SMPs), many of which are specific to particular shell layers (Joubert et al., 2010; Marie et al., 2012; Liu et al., 2015). Gene expression analysis of pearl sacs has revealed that pearl formation also involves many of these previously identified SMPs (Wang et al., 2009; Inoue et al., 2010; McGinty et al., 2012; Zhan et al., 2013; Le Luyer et al., 2019); however, pearl sac specific isoforms of known biomineralization genes have also been reported (Kinoshita et al., 2011). Temporal transcriptomic analysis has further revealed that SMPs associated with the prismatic shell layer are up-regulated in the early stages of pearl formation, whereas those associated with the nacreous shell layer are up-regulated later (Mariom et al., 2019), suggesting that the molecular process of pearl formation largely recapitulates that observed in the shell.

From a commercial perspective, the ideal pearl is round, highly lustrous (shiny), of a pleasing color, and has an unblemished surface (Southgate and Lucas, 2008). However, many cultured pearls do not have these characteristics. For pearl oysters, seeding experiments have provided some insights into the underlying causes of some of the undesirable characteristics commonly found in pearls, and have indicated ways in which they might be avoided. For example, pearl shape is influenced by the skill of the grafting technician, and improvements can be made by modification of seeding techniques (Ky et al., 2015). Likewise, there is some evidence that luster (**Figures 1A,B**) and color can be improved by careful selection of donor oysters (Ky et al., 2014, 2019; Zhifeng et al., 2014; McDougall et al., 2016a; Blay et al., 2017). Surface blemishes, or defects, continue to be a problem for the pearl industry, despite some research indicating that these defects can, in some cases, be associated with particular host characteristics such as overall growth rate (McDougall et al., 2016a), or nacre deposition rate (Blay et al., 2014).

Given that molecular processes within the pearl sac ultimately regulate pearl formation, several studies have investigated potential links between pearl quality and gene expression. Inoue et al. (2010) assessed the expression levels of six candidate SMPs in pearl sacs that produced low- or high-quality pearls, assessed by the proportion of the pearl surface that displayed no defects. One gene (*msi31*) was found to be consistently up-regulated in high quality pearls. In a similar approach, Blay et al. (2018) determined the expression levels of eight candidate genes, representing both prismatic and nacreous SMPs, in pearl sacs. They found that three of the prismatic SMPs were up-regulated in sacs that produced pearls with low surface quality, whereas PIF (characterized as a nacreous SMP) was up-regulated in pearls with high surface quality (in this case, pearls with over 10 pits, bumps, or scratches were determined to have low surface quality). While these studies demonstrate that correlative differences can be observed between gene expression and pearl quality, differing expression of SMPs is likely to be a result of abnormal upstream processes, rather than the root cause.

In a recent study, Le Luyer et al. (2019) performed whole transcriptome analysis to compare gene expression between pearl sacs producing pearls of differing quality. The study revealed few genes (16) that were up-regulated in high quality pearls, compared to 246 up-regulated in low quality pearls. Again, an association between prismatic layer SMPs and poor pearl

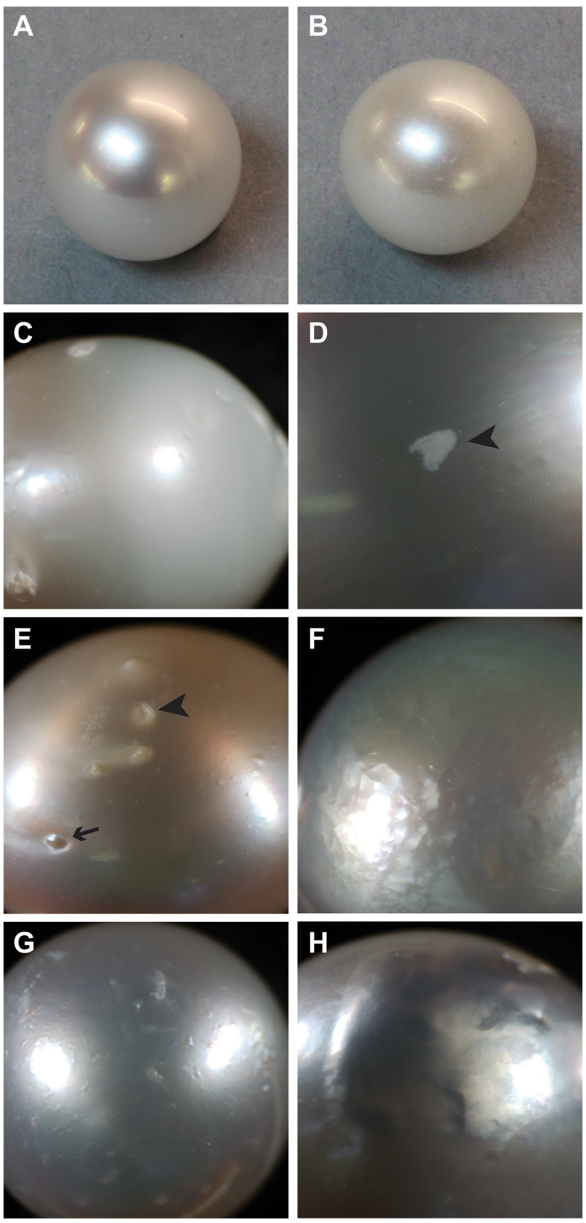

FIGURE 1 | Examples of surface characteristics of pearls. **(A)** High luster, note sharp reflection. **(B)** Low luster. **(C)** Major calcification, note opaque appearance on right half of pearl. **(D)** Localized calcification (arrowhead). **(E)** Spots, both raised (arrow) and depressed (arrowhead). **(F)** Hammer. **(G,H)** Underskin.

quality was detected. Although the study was not able to determine specific mechanisms that control pearl quality, the results did suggest a potential role for transposable elements, and potentially alternative splicing of biomineralization genes, on pearl characteristics.

The different ways in which pearl "quality" is determined may explain why the causes of poor pearl quality remain elusive. There are a number of different kinds of defects (McDougall et al., 2016a), and each type may have a different underlying cause. "Luster" describes the "shine" of the pearl, with high-luster pearls having a mirror-like reflectance and low-luster pearls appearing dull and are deemed low quality. Luster is ultimately determined by the thickness of the brick-like nacre tablets, with particular thicknesses inducing a phase-shift in reflected light that produces an iridescence effect (Simkiss and Wada, 1980). Poor luster can also be caused by a defect known within the industry as "calcification." The term "calcification" is clearly a misnomer, as the entire pearl is clearly calcified, however, within the pearling industry, the term refers to the presence of white or opaque (non-lustrous) areas on the pearl surface (**Figures 1C,D**). In freshwater pearls, a similar defect is caused by the deposition of vaterite rather than aragonite (Ma and Lee, 2006; Bourrat et al., 2012); however, it is not known how this shift is mediated. Other pearls possess "spots" on their external surface, these can be either raised or depressed, and can often be associated with localized calcification (**Figure 1E**). In some cases, areas of the pearl surface have a golf ball-like appearance, known as "hammer" (**Figure 1F**), and in other cases, the pearl surface is bumpy or wrinkly, a condition known as "underskin" (**Figures 1G,H**). It is unknown whether any of these defects have similar underlying causes, and therefore the pooling of pearls with these qualities into a single "low quality" category possibly leads to low power for the detection of the underlying causes of these disparate defects.

Here, we utilize a low-input RNA-Seq method (CEL-Seq2) to evaluate gene expression in 28 individual pearl sacs from *Pinctada maxima*. The method was originally derived for gene expression analysis within single cells (Hashimshony et al., 2012, 2016), but has also been applied to multi-celled samples such as individual embryos and larvae (Anavy et al., 2014; Levin et al., 2016; Say and Degnan, 2020). Analysis of genes that are differentially expressed between these pearl sacs reveals that each investigated character or defect is associated with a distinct molecular signature, and, therefore, that these defects likely have different underlying causes. We predict that further investigation of the mechanistic causes of these particular defects will not only point the pearling industry toward possible methods for their prevention, but will also reveal fundamental principles about the biomineralization process that may be applicable across other biocalcifying taxa.

MATERIALS AND METHODS

Transcriptome Sequencing

Pinctada maxima adult mantle, juvenile mantle, and pearl sac tissues (six individuals per tissue) were provided by Clipper Pearls, Broome, Western Australia. Tissues were dissected, immediately placed in RNAlater (Sigma–Aldrich), and stored at 4°C overnight before transportation and long-term storage at −20°C. Sampled mantle tissue consisted of all mantle zones, i.e., both edge and pallial. Pearl sacs were initially dissected along with surrounding gonad tissue, and were further dissected to isolate the pearl sac epithelium away from other tissues after storage in RNAlater. RNA extractions were performed separately for each individual mantle or pearl sac sample. Extractions were performed using 1 mL of TRI Reagent (Sigma–Aldrich) as per the manufacturer's instructions, using 1-bromo-3-chloropropane for phase separation, and 0.25 mL of isopropanol and 0.25 mL of high salt precipitation solution (0.8 M sodium citrate and 1.2 M sodium chloride) for precipitation. RNA from each sample was pooled in equimolar amounts for each sample type (adult mantle, juvenile mantle, and pearl sac) and quality was checked on a Bioanalyzer (Agilent). RNA was sent to Macrogen (Seoul, Korea) for library preparation using a TruSeq Stranded mRNA Sample Prep Kit (Illumina) and sequencing on a HiSeq2000 to generate between 60 and 70 million 100 bp paired-end reads per library. A transcriptome assembly was performed using reads from all three libraries (adult mantle, juvenile mantle, and pearl sac) using Trinity v. 2014-04-13, with quality trimming via Trimmomatic and normalization of reads. Resulting transcripts were annotated using Trinotate pipeline 3.1.1[1] (Bryant et al., 2017) via similarity searching against Swissprot by BLAST (Altschul et al., 1990), Pfam (Finn et al., 2016) by hmmscan (Finn et al., 2011), and by association with Gene Ontology terms (Ashburner et al., 2000).

Pearl Sac Sampling

Sampling was conducted during standard harvesting operations of a cohort of pearls (24 months post seeding; originally seeded within a 2-day period by a single technician) by Clipper Pearls Pty Ltd., Broome, Western Australia. Harvesting operations were observed and pearls with varying qualities identified. These pearls were extracted, individually bagged, numbered, and graded by a single expert pearl grader at Autore Pearls Pty Ltd., utilizing a modification of the Autore pearl grading and classification system known as the Autore Five S's™ South Sea Pearl Classification Guide (trademark and copyright held by Autore Pearls Pty Ltd.) (Pearlautore International Pty Ltd,, 2006; McDougall et al., 2016b). Host characteristics including shell dorso-ventral height, anterior–posterior width, and sex at harvest (either male, female, or non-reproductive) were recorded at time of harvest. Pearl weight was calculated as the final weight of the pearl in momme (1 momme = 3.75 g), minus the average weight of the inserted nucleus. After pearls were harvested, a clean nucleus was inserted into the pearl sac, which was then dissected from the animal and stored in RNAlater™ (Ambion) overnight at 4°C before long-term storage at −20°C.

Gene Expression Analysis

For extraction of pearl sac epithelia, samples were placed in a petri dish containing RNAlater™ and dissected open to reveal the embedded nucleus. The nucleus was removed, and surrounding pearl sac tissue peeled away from the surrounding tissue using

[1]https://github.com/Trinotate/Trinotate.github.io/wiki

TABLE 1 | Characteristics of pearls selected for this study.

Pearl ID	Luster	Spots	Hammer	Underskin	Calcification	Pearl weight (momme)	Host sex at harvest
1	A	Yes	No	No	No	0.45	Male
2	C	Yes	No	No	No	0.35	Non-reproductive
3	C	Yes	No	No	No	0.25	Non-reproductive
4	C/D	Yes	No	Yes	Yes	0.30	Male
5	A	Yes	Yes	No	Yes	0.55	Male
6	A	No	No	No	No	0.50	Non-reproductive
7	A	No	No	No	No	0.70	Male
8	A	Yes	No	No	Yes	0.45	Non-reproductive
9	C	Yes	Yes	Yes	No	0.55	Male
10	A	Yes	No	No	No	0.30	Male
11	B	No	No	No	No	0.40	Non-reproductive
12	C	Yes	No	No	Yes	0.45	Non-reproductive
13	A	Yes	No	No	No	0.40	Non-reproductive
14	C	Yes	No	Yes	No	0.20	Male
15	C	Yes	No	No	No	0.30	Non-reproductive
16	A	Yes	No	No	No	0.50	Male
17	A	Yes	No	No	No	0.55	Male
18	C	Yes	No	No	Yes	0.65	Male
19	A	No	No	Yes	No	0.85	Non-reproductive
20	B	No	No	No	No	0.75	Non-reproductive
21	A	Yes	No	No	Yes	0.35	Non-reproductive
22	A	No	No	No	No	0.80	Male
23	C	Yes	No	No	Yes	0.15	Male
24	C	Yes	No	Yes	No	0.70	Male
25	A	Yes	No	No	No	0.45	Female
26	C	Yes	No	No	No	0.35	Male
27	A	Yes	No	No	No	0.70	Male
28	C/D	Yes	No	Yes	Yes	0.30	Non-reproductive

fine forceps. Any adhering non-epithelial tissue (displaying distinct fluffy texture) was removed before the pearl sac tissue was placed into TRI Reagent® (Sigma–Aldrich). RNA extractions were performed according to the manufacturer's instructions.

Individual sequencing of pearl sac transcriptomes was performed using the CEL-Seq2 protocol (Hashimshony et al., 2016), which utilizes early sample barcoding, 3' end-tagging, and the inclusion of 6 nt unique molecule identifiers (UMIs) to generate high-sensitivity transcriptomes from low input starting material. 25 ng RNA and 0.5 μl ERCC spike-in (1:10,000 dilution) were added to the initial RNA/primer/ERCC/dNTP mix for each sample. Paired-end sequencing was performed on a HiSeq 2500 (rapid run mode), with a 15 bp read 1 and a 55 bp read 2. Transcript counts were generated using the CEL-Seq2 pipeline (Hashimshony et al., 2016), modified to accommodate a 55 bp read 2, to use the –norc and –a commands during BOWTIE mapping, and to perform counting using a "fake".gtf file. This was generated using faSize and the following command: cat P_maxima_transcriptome_Sizes.fa | awk '{print $1"\tPinctada\texon\t1\t"$2"\t\.\t\ + \t.\tgene_id \""$1"\""}' > Pinctada_transcriptome_Fake.gtf. UMI counts were converted to transcript numbers following the binomial method outlined in previous studies (Grün et al., 2014). Transcripts with very low counts (less than 30 reads across all 28 samples after transformation) were removed from the dataset entirely. Transcript isoforms with very similar counts across all samples were collapsed using the "collapseRows" and "connectivityBasedCollapsing" function within the WGCNA program in R.

Differential gene expression analysis was performed for each pearl attribute (luster, weight, spots, underskin, and calcification) using DESeq2 (v 1.16.1) (Love et al., 2014) using an adjusted *p*-value cut-off of 0.05. For the analysis of luster, the two pearls exhibiting "B" grade luster were excluded from the analysis. Transcript counts (normalized using blind variance stabilizing transformation in DESeq2) were used to generate heatmaps for visualization of differentially expressed genes using the packages pheatmap version 1.0.12 (Kolde, 2012) and RColorBrewer version 1.1-2 (Neuwirth, 2011) in R version 3.5.1 (R Core Team,, 2014). Expression was scaled by row z-scores for visualization. Analysis for functional over-representation within differentially expressed transcripts was performed using hypergeometric tests of "biological process" gene ontology categories within the BiNGO plugin (Maere et al., 2005) of Cytoscape (Shannon et al., 2003), along with the Trinotate annotation of the *P. maxima* transcriptome as a reference and a *p*-value (Benjamini–Hochberg FDR correction) cut-off of 0.01.

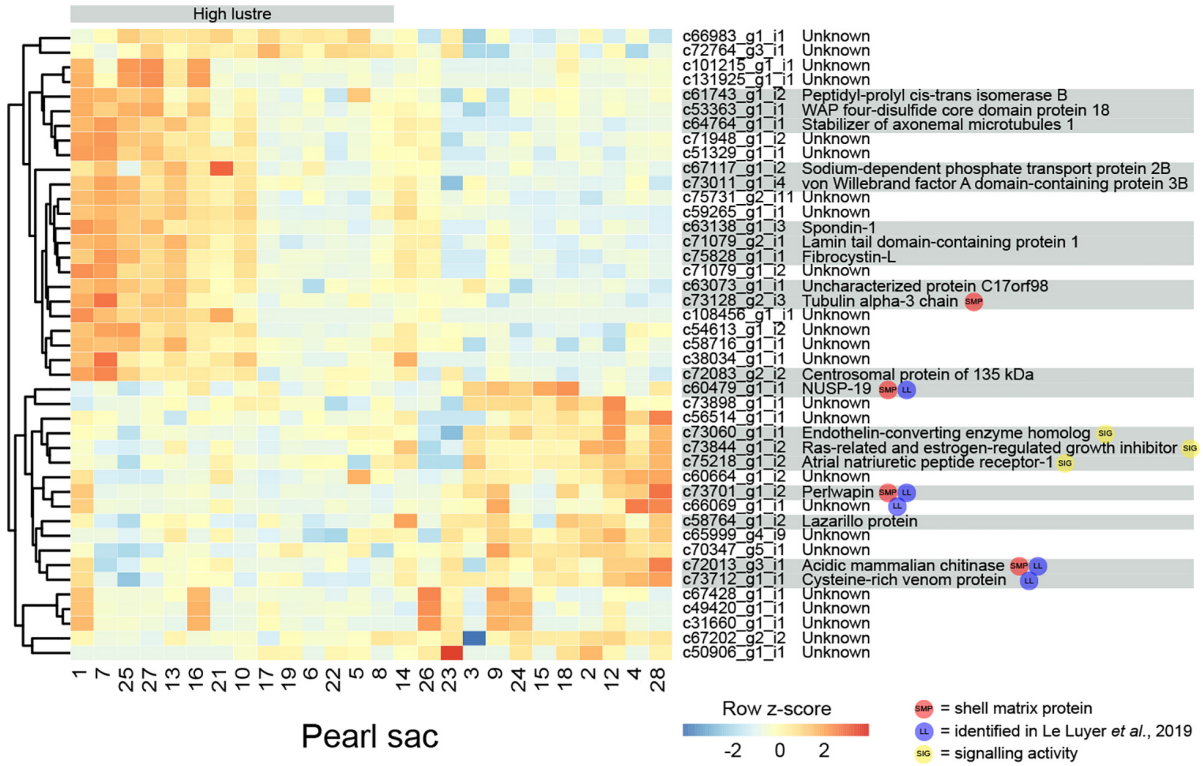

FIGURE 2 | Heatmap of significantly differentially expressed transcripts associated with luster quality. The number at the bottom of each column corresponds to the pearl sac that produced the pearl displayed in **Supplementary Figure S1**. Transcripts are displayed as horizontal rows and are clustered by similarity of expression profiles, represented by the dendrogram to the left of the heatmap. Red indicates higher expression, and pearl sacs producing high luster pearls (A grade) are shown on the left of the heatmap, as indicated by the gray bar. Transcript annotations are indicated to the right of the heatmap.

Differentially expressed transcripts were further investigated to determine whether they (i) were likely to encode SMPs based upon similarity to proteins that had previously been identified from molluscan shells, (ii) possibly had regulatory roles (specifically, whether they were likely to have transcription regulatory or signaling activity), or (iii) whether they had similarity to transcripts that had been associated with pearl quality in a previous study (Le Luyer et al., 2019). Similarity to SMPs was ascertained by performing BLASTP searches against an in-house database of published proteins that had previously been identified from the shells of other mollusc species (Marie et al., 2010, 2011, 2012, 2013b, 2017; Bédouet et al., 2012; Mann et al., 2012, 2018; Pavat et al., 2012; Zhang et al., 2012; Mann and Jackson, 2014; Gao et al., 2015; Liao et al., 2015, 2019; Liu et al., 2015; Arivalagan et al., 2016; Upadhyay et al., 2016; Le Pabic et al., 2017; Shimizu et al., 2018), using an e-value cut-off of $1e^{-10}$. Reciprocal BLAST searches were then performed against the parent taxon of the top BLAST hit in NCBI to provide evidence for transcript homology. As many SMPs possess repetitive, low complexity domains (Sudo et al., 1997; Jackson et al., 2010; Marie et al., 2010; McDougall et al., 2013a, 2016b), BLASTP searches were conducted without filtering for low-complexity regions and without compositional adjustment. Potential transcription factor or signaling activity was ascertained by searching GO term annotations for GO:0003700 (DNA-binding transcription factor activity), or for the phrase "signal." Finally, comparisons were made between the differentially expressed transcripts identified here and those identified in the study by Le Luyer et al. (2019). As the sequence data from the Le Luyer manuscript were not available at the time of writing, the top BLAST hits to the Le Luyer transcripts (**Supplementary Table S2** in Le Luyer et al., 2019) were downloaded and used in reciprocal BLAST searches.

Phylogenetic Analyses

To provide support to computational annotation, alignments of transcripts of interest and related sequences were performed and edited within AliView (Larsson, 2014). Maximum likelihood phylogenetic analyses were conducted using RAxML version 8.2.11 (Stamatakis, 2014), with automatic model selection and 100 rapid bootstrap inferences. Resulting phylogenetic trees were visualized in FigTree (Rambaut, 2006).

RESULTS AND DISCUSSION

Transcriptome Sequencing and Assembly

To obtain a comprehensive transcriptome to facilitate investigation into *P. maxima* biomineralization, sequencing was performed for three libraries (adult mantle, juvenile mantle,

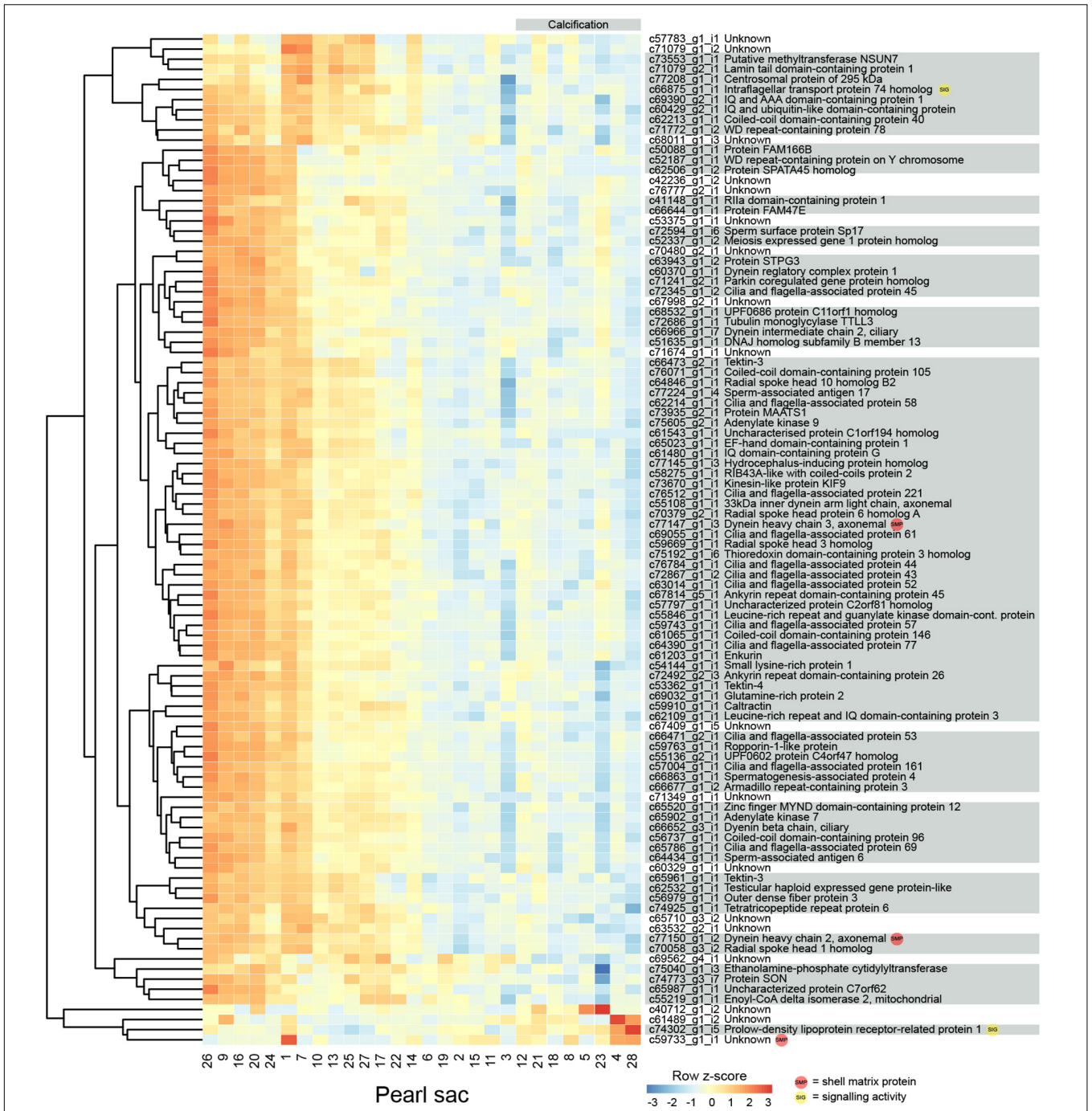

FIGURE 3 | Heatmap of the 100 most significant calcification-associated differentially expressed transcripts. Transcripts are displayed as horizontal rows and are clustered by similarity of expression profiles. Red indicates higher expression, and pearl sacs producing pearls with calcification are shown on the right of the plot, as indicated by the gray bar. Transcript annotations are indicated on the right.

and pearl sac; six individuals in each library) on an Illumina HiSeq 2000. Reads from all three libraries were used to construct a combined transcriptome assembly, consisting of 185,077 transcripts, with a contig N50 of 1740 bp. Raw sequences and assembled transcripts are publicly available under NCBI BioProject PRJNA636870.

Characteristics of Selected Pearls

Standard pearl harvesting operations were observed and 28 pearls and their corresponding pearl sacs were selected for sampling based upon pearl appearance. The characteristics of the selected pearls are outlined in **Table 1**, and photographs of the pearls can be found in **Supplementary Figure S1**. Gene expression in each

TABLE 2 | The 10 most highly enriched biological processes of transcripts differentially expressed between sacs producing calcified and uncalcified pearls.

Biological process	GO accession	Adjusted *P*-value
Cilium organization	0044782	3.56E-34
Cilium assembly	0060271	1.49E-31
Microtubule-based process	0007017	8.03E-30
Plasma membrane bounded cell projection assembly	0120031	5.52E-29
Cell projection assembly	0030031	7.38E-29
Microtubule-based movement	0007018	1.66E-26
Organelle assembly	0070925	2.12E-25
Cell projection organization	0030030	1.01E-23
Axoneme assembly	0035082	1.33E-19
Plasma membrane bounded cell projection organization	0120036	1.30E-18

pearl sac was assessed using CEL-Seq2, with a resulting average sequencing depth of 6.4 million reads per sample (ranging from 461,492 to 14,789,883 reads), and an average mapping rate of 67% (ranging from 62 to 72%). Genes that were significantly differentially expressed in pearl sacs producing pearls with different characteristics were identified using DESeq2. Only two pearls were found that exhibited "hammer" on their surface, therefore this defect was not analyzed further.

Luster

Pearl luster is graded on a scale of A-D, with A grade pearls possessing greater luster. 43 transcripts are found to be significantly differentially expressed between pearl sacs producing high (A) and low (C or C/D) luster pearls, of which 19 have associated Swissprot annotations (**Figure 2** and **Supplementary Table S1**). No specific biological process is over-represented in this dataset, most likely due to the low number of annotated transcripts.

Four differentially expressed transcripts are found to be highly similar to reported SMPs via reciprocal BLAST searches. Three are found to be down-regulated in high luster pearl sacs: c60479_g1_i1, which exhibits similarity to *Pinctada margaritifera* NUSP-19 (Marie et al., 2012); c72013_g3_i1, which is annotated as "acidic mammalian chitinase" and possesses similarity to SMPs found in nine bivalve species and in *Sepia officalis* cuttlebone; and c73701_g1_i2, which is annotated as perlwapin, a known SMP from abalone shells that inhibits calcium carbonate crystal growth *in vitro* (Treccani et al., 2006). The other transcript, c73128_g2_i3 (annotated as "tubulin alpha-3 chain"), is up-regulated in high luster pearl sacs. This alpha tubulin is almost identical at the amino acid level to proteins isolated from *Perna viridis* (99% similarity) and *Crassostrea gigas* (60% similarity) shells (Zhang et al., 2012; Liao et al., 2019). A number of intracellular proteins, including tubulins, have been detected within shells; however, it has been suggested that their presence is due to contamination of biominerals by cellular remains, i.e., that they are not true components of the organic matrix of shells (Marie et al., 2013a). Aside from putative SMPs, other differentially expressed genes exhibited similarity with genes that have been implicated in biomineralization in other species, for example, peptidyl-prolyl *cis-trans* isomerase (cyclophilin) (Amore and Davidson, 2006; Jackson et al., 2010) and spondin (Kinoshita et al., 2011; Funabara et al., 2014). Furthermore, five of the differentially expressed transcripts are detected in the pearl quality study by Le Luyer et al. (2019), including perlwapin, NUSP19, chitinase, "cysteine-rich venom protein" (c73712_g1_i1) and an unannotated transcript (c66069_g1_i1).

Three transcripts that are likely to have signaling functions and may be components of a genetic regulatory network that affects luster are co-expressed (**Figure 2**; c73060_g1_i1, annotated as endothelin-converting enzyme homolog; c73844_g1_i2, annotated as Ras-related and estrogen-regulated growth inhibitor; and c75218_g1_i2, annotated as atrial natriuretic peptide receptor-1). Although the functions of these signaling proteins are unstudied in molluscs and may differ from those in vertebrates (Grandchamp et al., 2019), the co-expression of these genes suggests that the regulatory interplay between these proteins (i.e., hydrolysis of atrial natriuretic peptide and regulation of Ras proteins by endothelin-converting enzyme (Foschi et al., 1997; Johnson et al., 1999) may be conserved.

Calcification

Eight pearls have some degree of calcification, and 315 transcripts are significantly differentially expressed between these pearls and those without the defect (**Figure 3** displays the 100 most significant transcripts, see **Supplementary Table S2** for the full list). 207 of these transcripts have Swissprot annotations, and 14 are similar to known SMPs. These include c72013_g3_i1, the transcript annotated as mammalian acidic chitinase that is also differentially expressed in the luster analysis, three unannotated transcripts, five transcripts with similarity to dynein proteins, and a number of other transcripts with similarity to intracellular proteins such as beta tubulin, pyruvate kinase, arginine kinase, and histone H3 (**Supplementary Table S2**). Three differentially expressed transcripts have similarity with transcripts associated with pearl quality in the study by Le Luyer et al. (2019), including two unannotated transcripts (c67849_g1_i1 and c72382_g1_i1), and a transcript annotated as metalloproteinase inhibitor 3 (c70381_g2_i1). A number of genes with potential signaling functions are differentially expressed (**Supplementary Table S2**), and one transcript (c58003_g1_i1) encoding the transcription factor forkhead box J1 (FoxJ1) is down-regulated in pearls with calcification (**Supplementary Table S2** and **Supplementary Figure S2**). This result is congruent with the recent identification of *FoxJ1* as a candidate regulatory gene for expression of nacre-associated SMPs in the clam *Laternula elliptica* (Sleight et al., 2020).

Genes that are differentially expressed between sacs producing calcified and non-calcified pearls are enriched for genes involved in 96 biological processes (**Supplementary Table S3**, 10 most highly significant shown in **Table 2**), and many of these were associated with cilia or microtubule function, suggesting cellular cytoskeletal elements contribute to pearl formation and quality. Given that pearl sacs are located within the gonad of the host animal, we considered the possibility that this result could be due to sperm contamination from male gonads. This is unlikely to be the case, as the eight calcified pearls were obtained from four male hosts and four hosts that were reproductively inactive,

FIGURE 4 | Heatmap of underskin-associated differentially expressed transcripts. Transcripts are displayed as horizontal rows and are clustered by similarity of expression profiles. Red indicates higher expression, and pearl sacs producing pearls with underskin are shown on the left of the plot, as indicated by the gray bar. One transcript was able to be annotated, indicated on the far right.

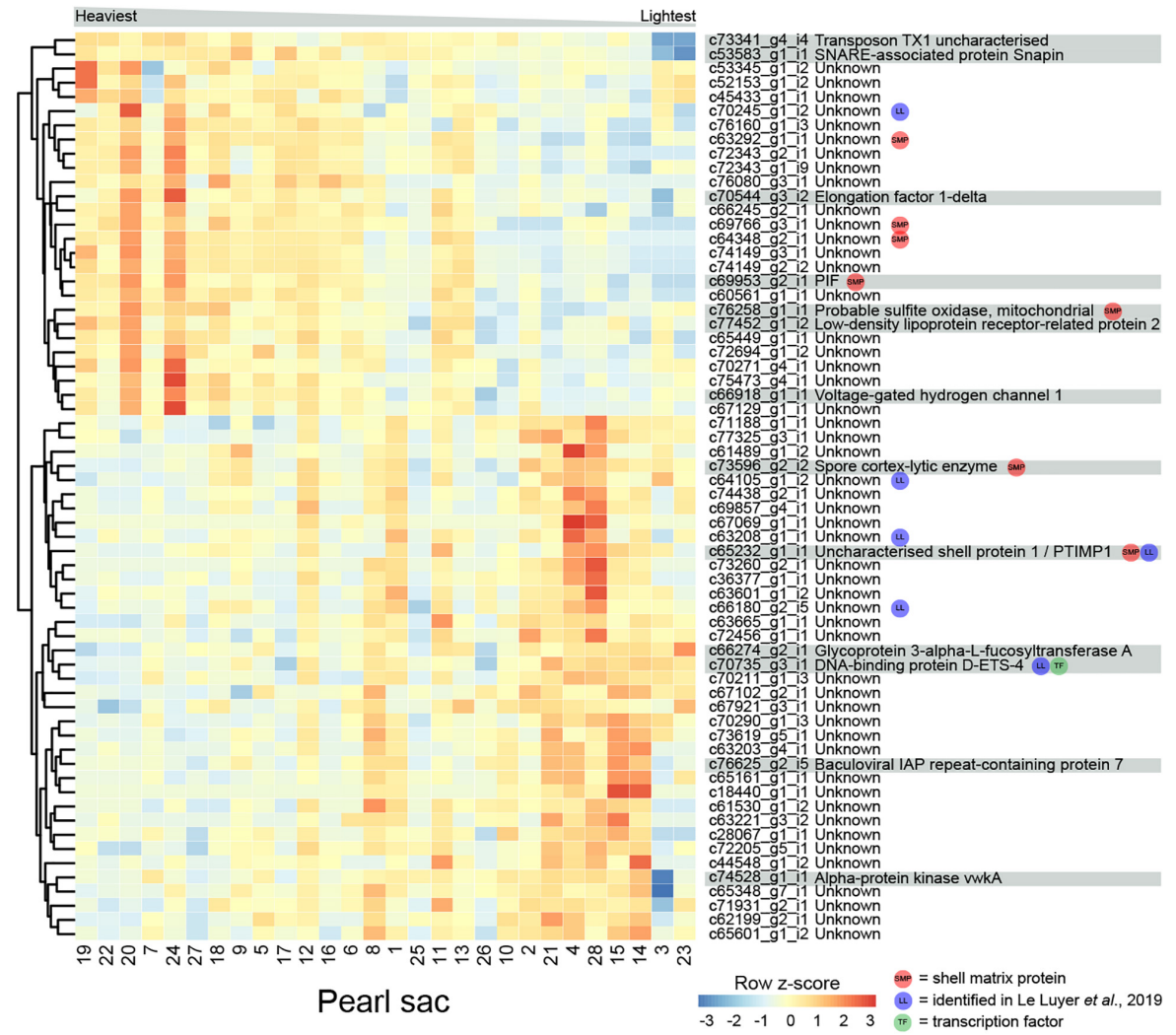

FIGURE 5 | Heatmap of weight-associated differentially expressed transcripts. Transcripts are displayed as horizontal rows and are clustered by similarity of expression profiles. Red indicates higher expression, and pearl sacs producing heavier pearls are shown on the left of the plot, as indicated by the gray bar. Transcript annotations are indicated on the far right.

and hosts producing non-calcified pearls had a similar sex distribution (**Table 1**).

The mantles of several different bivalves are known to be ciliated in different regions, including the larval and adult mantle of *Nodipecten nodosus* (Audino et al., 2015), and the inner mantle epithelium and folds of *Velesunio ambiguus* and *Hyridella depressa* (Colville and Lim, 2003). Ciliated mantle cells are also present in primary cell cultures from the bivalve clam *Paphia malabarica* (Dessai, 2012). In *P. margaritifera*, cilia are present in the epithelium of the inner fold, the periostracal groove, and the outer fold, and cells within the mantle pallial have "short protruding cell processes" (Jabbour-Zahab et al., 1992). There are conflicting reports of cilia within pearl sacs. Some reports indicate that cilia may be present in the early stages of pearl sac

TABLE 3 | Multi-trait differentially expressed transcripts.

Transcript	Annotation	Luster (low)	Calcification	Underskin	Weight (low)
c61489_g1_i2	–		↑	↑	↑
c71079_g1_i2	Lamin tail domain-containing protein 1	↓	↓		
c71079_g2_i1	–	↓	↓		
c71948_g1_i2	–	↓	↓		
c63138_g1_i3	Spondin-1	↓	↓		
c49420_g1_i1	–	↑	↓		
c53363_g1_i1	WAP four-disulfide core domain protein 18	↓	↓		
c67428_g1_i1	–	↑	↓		
c75828_g1_i1	Fibrocystin-L	↓	↓		
c72013_g3_i1	Acidic mammalian chitinase	↑	↑		
c101215_g1_i1	–	↓		↓	
c66069_g1_i1	–	↑		↑	
c63208_g1_i1	WAP domain containing			↑	↑

Arrows indicate an up- and down-regulated gene expression in relation to each pearl quality trait.

formation but not in later stages (Chatchavalvanich et al., 2010; Cochennec-Laureau et al., 2010), whereas others report variation in the presence or absence of cilia and the possible influence of the grafting process in this trait (Kishore and Southgate, 2015, 2016). Intriguingly, Dix (1973) reported that sacs producing nacreous pearls consist of a single, non-ciliated layer of epithelial cells, whereas a sac producing a "periostracal" (brown, organic layer) pearl consist of tall, ciliated epithelial cells. While no "periostracal" pearl sacs were investigated in this study, our findings are consistent with those of Dix (1973) and suggest a role for ciliation in nacre deposition. The association between cellular differentiation and the biomineralization of different calcium carbonate polymorphs has already been proposed for molluscs (Sud et al., 2002; Jolly et al., 2004; Jackson et al., 2006, 2007; McDougall et al., 2011; Marie et al., 2012) and bryozoans (Jacob et al., 2019).

Underskin

Four transcripts are significantly differentially expressed in pearl sacs that produced pearls with and without underskin (n = 6; **Figure 4** and **Supplementary Table S4**). Only one of these transcripts, c52227_g1_i2, produced significant BLAST or Pfam hits, displaying similarity to arthropod hemocyte protein-glutamine gamma-glutamyltransferase. It is down-regulated in pearl sacs that yield pearls with underskin defects. Hemocyte protein-glutamine gamma-glutamyltransferase (transglutaminases) have been implicated in the immune response of the Pacific oyster *C. gigas* (Gueguen et al., 2003; Hart et al., 2016), suggesting that the underskin defect may be related to infection within the pearl sac. One of the unannotated transcripts (c66069_g1_i1) was likely also identified as being associated with pearl quality in the study by Le Luyer et al. (2019).

Spots

In this study, only six pearls did not possess at least one "spot." Despite the prevalence of this defect, no transcripts are significantly differentially expressed between pearl sacs producing pearls with and without spotting. We note that there is a large degree of variation associated with this defect, i.e., spots can either be raised or depressed, and either nacreous or opaque (**Figure 1**). Each type of spot may have a differing underlying cause, and it is possible that combining this defect into a single category has masked underlying gene expression differences.

Pearl Weight

The weight of deposited pearl material in this study varied between 0.15 and 0.85 momme (0.56 and 3.19 g). 64 transcripts are significantly differentially expressed in relation to pearl weight (**Figure 5** and **Supplementary Table S5**). Of these, 14 can be annotated. There are no functional categories over-represented within the differentially expressed genes.

Seven transcripts encode proteins with similarity to previously identified SMPs (**Supplementary Table S5**). c69953_g2_i1 encodes PIF, a protein that is cleaved into two components; Pif 80, an acidic protein that is involved in aragonite crystal formation, and Pif 97 that binds to chitin, in *P. fucata* (Suzuki et al., 2009, 2013). A second transcript encodes a homolog of "uncharacterized shell protein 1," originally isolated from *P. margaritifera* shell (Joubert et al., 2010). Two other transcripts (c73596_g2_i2, annotated as "spore cortex-lytic enzyme," and c76258_g1_i1, annotated as "probable sulfite oxidase," mitochondrial) are similar to proteins isolated from *C. gigas* shell (Zhang et al., 2012), and the other three have similarity to uncharacterized SMPs. Six of the differentially expressed transcripts, including "uncharacterized shell protein 1," were also likely identified by Le Luyer et al. (2019) (**Supplementary Table S5**).

One gene that was over-expressed in pearls with lower weights encodes an ETS4/PDEF transcription factor (**Supplementary Figure S3**). The ETS family of transcription factors play a wide range of roles in metazoans, including in neural development, vasculogenesis, hematopoiesis (Sharrocks, 2001; Yagi et al., 2003), and the regulation of spiculogenesis in sea urchins (Davidson et al., 2002). PDEF regulates the specification of secretory cells in vertebrates (Chen et al., 2009). It is possible that this transcription factor affects pearl development via the specification of particular biomineralization cell types.

Proteins predicted from other differentially expressed transcripts are similar to a range of proteins involved in general metabolism, including sulfite oxidase, voltage-gated hydrogen channel protein, and elongation factor 1-delta (**Figure 5**). These transcripts have higher expression in heavier pearls, possibly indicating overall higher metabolism in the corresponding pearl sacs.

Multi-Character Differentially Expressed Transcripts

In total, 13 genes are significantly differentially expressed for more than one pearl characteristic (**Table 3**). Nine of the 43 genes that are differentially expressed between sacs producing pearls with high or low luster are also differentially expressed in association with calcification. Except for two genes, the expression levels of these multi-character transcripts correlate with high calcification and low luster pearls, suggesting an association between these traits. However, it is worth noting that pearls with high calcification are likely to be deemed to have a low luster, especially if the calcified proportion of the surface is high.

The other traits share very few differentially expressed genes, and no differentially expressed transcripts are shared between sacs producing pearls of differing luster and differing pearl weights. The lack of overlap in differentially expressed transcripts between all the pearl characteristics demonstrates that each is underpinned by unique transcriptional profiles.

Previous studies have investigated pearl sac gene expression in relation to pearl quality; however, in these studies, quality has generally been expressed as "high" or "low" without distinguishing between defect types. We expect that our "multi-character" genes are more likely to be uncovered by studies using a broader quality classification system. Three of the multi-character transcripts, c63208_g1_i1 (WAP-domain containing), c66069_g1_i1 (unannotated), and c72013_g3_i1 (chitinase), appear to have also been identified as quality-associated transcripts by Le Luyer et al. (2019). Notably, none of the well-studied SMPs that have previously been associated with pearl quality (e.g., MSI60, aspein, prismalin, or any shematrins) (Inoue et al., 2011a,b; Blay et al., 2018) are identified to be associated with any of the pearl quality characteristics investigated here.

CONCLUSION

This study reveals that unique transcriptional profiles in pearl sacs underlie different pearl characteristics. These transcriptional profiles not only indicate possible causative mechanisms of particular pearl defects or undesirable traits, but also reveal hitherto unrecognized processes linked to biomineralization, for example, the potential role of ciliation and cytoskeletal elements. A number of known SMPs were differentially expressed in pearls displaying different traits, and further analysis of the role of these proteins will likely reveal their functional role across different shell polymorphs, i.e., in calcite or nacre, and how these are associated with particular pearl defects. The analysis of gene expression within sacs producing pearls with different characteristics also provides evidence for the involvement of the transcription factors FoxJ1 and ETS4 in biomineralization, providing candidates for the regulation of nacre formation and specification of biomineralization cell types in molluscs.

DATA AVAILABILITY STATEMENT

The datasets generated for this study can be found under NCBI BioProject PRJNA636870.

AUTHOR CONTRIBUTIONS

CM, PM, and BD conceived of the study. CM performed molecular work, bioinformatics and data analysis, and drafted the manuscript with contribution from all other authors. FA performed the transcriptome assembly and assisted with bioinformatic analysis. AS compiled the dataset of published SMP proteins and assisted with bioinformatic analysis. All authors have read and approved the final manuscript.

FUNDING

This research was funded by an Australian Research Council Linkage Grants LP0990280 and LP130100086 to BD and PM.

ACKNOWLEDGMENTS

The authors would like to acknowledge Kerry Roper for assistance with the CEL-Seq2 protocol, Selene L. Fernandez-Valverde for assistance with bioinformatics, and staff at Clipper Pearls Pty Ltd. and Autore Pearls Pty Ltd. for assisting with pearl culture and grading.

SUPPLEMENTARY MATERIAL

The Supplementary Material for this article can be found online at: https://www.frontiersin.org/articles/10.3389/fgene.2020.597459/full#supplementary-material

Supplementary Figure 1 | Photographs of pearls extracted for the pearl sacs used in this study (PDF).

Supplementary Figure 2 | Maximum likelihood phylogenetic analysis of the *Pinctada maxima* FoxJ1 protein (PDF).

Supplementary Figure 3 | Maximum likelihood phylogenetic analysis of the *Pinctada maxima* ETS4/PDEF protein (PDF).

Supplementary Table 1 | Transcripts differentially expressed between sacs producing high vs low lustre pearls.

Supplementary Table 2 | Transcripts differentially expressed between sacs producing pearls with 'calcification' and those without.

Supplementary Table 3 | Gene Ontology 'Biological Process' enrichments within calcification-associated differentially expressed transcripts.

Supplementary Table 4 | Transcripts differentially expressed between sacs producing pearls with 'underskin' and those without.

Supplementary Table 5 | Transcripts differentially expressed between sacs producing pearls with different weights.

REFERENCES

Altschul, S. F., Gish, W., Miller, W., Myers, E. W., and Lipman, D. J. (1990). Basic local alignment search tool. *J. Mol. Biol.* 215, 403–410.

Amore, G., and Davidson, E. H. (2006). *cis*-Regulatory control of cyclophilin, a member of the ETS-DRI skeletogenic gene battery in the sea urchin embryo. *Dev. Biol.* 293, 555–564. doi: 10.1016/j.ydbio.2006.02.024

Anavy, L., Levin, M., Khair, S., Nakanishi, N., Fernandez-Valverde, S. L., Degnan, B. M., et al. (2014). BLIND ordering of large-scale transcriptomic developmental timecourses. *Development* 141, 1161–1166. doi: 10.1242/dev.105288

Arivalagan, J., Marie, B., Sleight, V. A., Clark, M. S., Berland, S., and Marie, A. (2016). Shell matrix proteins of the clam, *Mya truncata*: roles beyond shell formation through proteomic study. *Mar. Genomics* 27, 69–74. doi: 10.1016/j.margen.2016.03.005

Ashburner, M., Ball, C. A., Blake, J. A., Botstein, D., Butler, H., Cherry, J. M., et al. (2000). Gene ontology: tool for the unification of biology. *Nat. Genet.* 25, 25–29.

Audino, J. A., Marian, J. E. A. R., Wanninger, A., and Lopes, S. G. B. C. (2015). Mantle margin morphogenesis in *Nodipecten nodosus* (Mollusca: Bivalvia): new insights into the development and the roles of bivalve pallial folds. *BMC Dev. Biol.* 15:22. doi: 10.1186/s12861-015-0074-9

Australian Bureau of Agricultural and Resource Economics and Sciences [ABARES], (2018). *Australian Fisheries and Aquaculture Statistics 2017*. Canberra, NSW: Australian Bureau of Agricultural and Resource Economics and Sciences.

Bédouet, L., Marie, A., Berland, S., Marie, B., Auzoux-Bordenave, S., Marin, F., et al. (2012). Proteomic strategy for identifying mollusc shell proteins using mild chemical degradation and trypsin digestion of insoluble organic shell matrix: a pilot study on *Haliotis tuberculata*. *Mar. Biotechnol.* 14, 446–458. doi: 10.1007/s10126-011-9425-0

Blay, C., Planes, S., and Ky, C.-L. (2017). Donor and recipient contribution to phenotypic traits and the expression of biomineralisation genes in the pearl oyster model *Pinctada margaritifera*. *Sci. Rep.* 7:2696.

Blay, C., Planes, S., and Ky, C.-L. (2018). Cultured pearl surface quality profiling by the shell matrix protein gene expression in the biomineralised pearl sac tissue of *Pinctada margaritifera*. *Mar. Biotechnol.* 20, 490–501. doi: 10.1007/s10126-018-9811-y

Blay, C., Sham-Koua, M., Vonau, V., Tetumu, R., Cabral, P., and Ky, C. (2014). Influence of nacre deposition rate on cultured pearl grade and colour in the black-lipped pearl oyster *Pinctada margaritifera* using farmed donor families. *Aquac. Int.* 22, 937–953. doi: 10.1007/s10499-013-9719-5

Bourrat, X., Qiao, L., Feng, Q., Angellier, M., Dissaux, A., Beny, J.-M., et al. (2012). Origin of growth defects in pearl. *Mater. Charact.* 72, 94–103. doi: 10.1016/j.matchar.2012.07.010

Bryant, D. M., Johnson, K., DiTommaso, T., Tickle, T., Couger, M. B., Payzin-Dogru, D., et al. (2017). A tissue-mapped axolotl de novo transcriptome enables identification of limb regeneration factors. *Cell Rep.* 18, 762–776. doi: 10.1016/j.celrep.2016.12.063

Chatchavalvanich, K., Nagachinda, A., Kovitvadhi, U., Kovitvadhi, S., Thongpan, A., and Meejui, O. (2010). Histological development of pearl-sac formation in Thai freshwater mussels. *Kasetsart J. Nat. Sci.* 44, 202–209.

Chen, G., Korfhagen, T. R., Xu, Y., Kitzmiller, J., Wert, S. E., Maeda, Y., et al. (2009). SPDEF is required for mouse pulmonary goblet cell differentiation and regulates a network of genes associated with mucus production. *J. Clin. Invest.* 119, 2914–2924.

Cochennec-Laureau, N., Montagnani, C., Saulnier, D., Fougerouse, A., Levy, P., and Lo, C. (2010). A histological examination of grafting success in pearl oyster *Pinctada margaritifera* in French Polynesia. *Aquat. Living Resour.* 23, 131–140.

Colville, A., and Lim, R. (2003). Microscopic structure of the mantle and palps in the freshwater mussels *Velesunio ambiguus* and *Hyridella depressa* (Bivalvia: Hyriidae). *Molluscan Res.* 23, 1–20. doi: 10.1007/978-3-319-23534-9_1

Cuif, J. P., Ball, A. D., Dauphin, Y., Farre, B., Nouet, J., Perez-Huerta, A., et al. (2008). Structural, mineralogical, and biochemical diversity in the lower part of the pearl layer of cultivated seawater pearls from Polynesia. *Microsc. Microanal.* 14, 405–417. doi: 10.1017/s1431927608080859

Cuif, J.-P., Dauphin, Y., Howard, L., Nouet, J., Rouzière, S., and Salomé, M. (2011). Is the pearl layer a reversed shell? A re-examination of the theory of pearl formation through physical characterizations of pearl and shell developmental stages in *Pinctada margaritifera*. *Aquat. Living Resour.* 24, 411–424. doi: 10.1051/alr/2011149

Davidson, E. H., Rast, J. P., Oliveri, P., Ransick, A., Calestani, C., Yuh, C.-H., et al. (2002). A genomic regulatory network for development. *Science* 295, 1669–1678. doi: 10.1126/science.1069883

Dessai, S. N. (2012). Primary culture of mantle cells of bivalve mollusc, *Paphia malabarica*. *In Vitro Cell. Dev. Biol. Anim.* 48, 473–477. doi: 10.1007/s11626-012-9538-4

Dix, T. G. (1973). Histology of the mantle and pearl sac of the pearl oyster *Pinctada maxima* (Lamellibranchia). *J. Malacol. Soc. Aust.* 2, 365–375. doi: 10.1080/00852988.1973.10673862

Farn, A. E. (1986). *Pearls. Natural, Cultured and Imitation*. London: Butterworths Gem Books.

Finn, R. D., Clements, J., and Eddy, S. R. (2011). HMMER web server: interactive sequence similarity searching. *Nucleic Acids Res.* 39, W29–W37.

Finn, R. D., Coggill, P., Eberhardt, R. Y., Eddy, S. R., Mistry, J., Mitchell, A. L., et al. (2016). The Pfam protein families database: towards a more sustainable future. *Nucleic Acids Res.* 44, 279–285.

Foschi, M., Chari, S., Dunn, M. J., and Sorokin, A. (1997). Biphasic activation of p21ras by endothelin-1 sequentially activates the ERK cascade and phosphatidylinositol 3-kinase. *EMBO J.* 16, 6439–6451. doi: 10.1093/emboj/16.21.6439

Funabara, D., Ohmori, F., Kinoshita, S., Koyama, H., Mizutani, S., Ota, A., et al. (2014). Novel genes participating in the formation of prismatic and nacreous layers in the pearl oyster as revealed by their tissue distribution and RNA interference knockdown. *PLoS One* 9:e84706. doi: 10.1371/journal.pone.0084706

Gao, P., Liao, Z., Wang, X.-X., Bao, L.-F., Fan, M.-H., Li, X.-M., et al. (2015). Layer-by-layer proteomic analysis of *Mytilus galloprovincialis* shell. *PLoS One* 10:e0133913. doi: 10.1371/journal.pone.0133913

Grandchamp, A., Tahir, S., and Monget, P. (2019). Natriuretic peptides appeared after their receptors in vertebrates. *BMC Evol. Biol.* 19:215. doi: 10.1186/s12862-019-1517-x

Grün, D., Kester, L., and van Oudenaarden, A. (2014). Validation of noise models for single-cell transcriptomics. *Nat. Methods* 11, 637–640. doi: 10.1038/nmeth.2930

Gueguen, Y., Cadoret, J.-P., Flament, D., Barreau-Roumiguière, C., Girardot, A.-L., Garnier, J., et al. (2003). Immune gene discovery by expressed sequence tags generated from hemocytes of the bacteria-challenged oyster, *Crassostrea gigas*. *Gene* 303, 139–145. doi: 10.1016/s0378-1119(02)01149-6

Hart, C. E., Lauth, M. J., Hunter, C. S., Krasny, B. R., and Hardy, K. M. (2016). Effect of 4-nonylphenol on the immune response of the Pacific oyster *Crassostrea gigas* following bacterial infection with *Vibrio campbellii*. *Fish Shellfish Immunol.* 58, 449–461. doi: 10.1016/j.fsi.2016.09.054

Hashimshony, T., Senderovich, N., Avital, G., Klochendler, A., de Leeuw, Y., Anavy, L., et al. (2016). CEL-Seq2: sensitive highly-multiplexed single-cell RNA-Seq. *Genome Biol.* 17:77.

Hashimshony, T., Wagner, F., Sher, N., and Yanai, I. (2012). CEL-Seq: single-cell RNA-Seq by multiplexed linear amplification. *Cell Rep.* 2, 666–673. doi: 10.1016/j.celrep.2012.08.003

Inoue, N., Ishibashi, R., Ishikawa, T., Atsumi, T., Aoki, H., and Komaru, A. (2010). Gene expression patterns and pearl formation in the Japanese pearl oyster (*Pinctada fucata*): a comparison of gene expression patterns between the pearl sac and mantle tissues. *Aquaculture* 308, S68–S74.

Inoue, N., Ishibashi, R., Ishikawa, T., Atsumi, T., Aoki, H., and Komaru, A. (2011a). Gene expression patterns in the outer mantle epithelial cells associated with pearl sac formation. *Mar. Biotechnol.* 13, 474–483. doi: 10.1007/s10126-010-9318-7

Inoue, N., Ishibashi, R., Ishikawa, T., Atsumi, T., Aoki, H., and Komaru, A. (2011b). Comparison of expression patterns of shell matrix protein genes in the mantle tissues between high- and low-quality pearl-producing recipients of the pearl oyster, *Pinctada fucata*. *Zool. Sci.* 28, 32–36. doi: 10.2108/zsj.28.32

Jabbour-Zahab, R., Chagot, D., Blanc, F., and Grizel, H. (1992). Mantle histology, histochemistry and ultrastructure of the pearl oyster *Pinctada margaritifera* (L.). *Aquat. Living Resour.* 5, 287–298. doi: 10.1051/alr:1992027

Jackson, D. J., McDougall, C., Green, K., Simpson, F., Wörheide, G., and Degnan, B. M. (2006). A rapidly evolving secretome builds and patterns a sea shell. *BMC Biol.* 4:40. doi: 10.1186/1741-7007-4-40

Jackson, D. J., McDougall, C., Woodcroft, B., Moase, P., Rose, R. A., Kube, M., et al. (2010). Parallel evolution of nacre building gene sets in molluscs. *Mol. Biol. Evol.* 27, 591–608. doi: 10.1093/molbev/msp278

Jackson, D. J., Wörheide, G., and Degnan, B. M. (2007). Dynamic expression of ancient and novel molluscan shell genes during ecological transitions. *BMC Evol. Biol.* 7:160. doi: 10.1186/1471-2148-7-160

Jacob, D. E., Ruthensteiner, B., Trimby, P., Henry, H., Martha, S. O., Leitner, J., et al. (2019). Architecture of *Anoteropora latirostris* (Bryozoa, Cheilostomata) and implications for their biomineralization. *Sci. Rep.* 9:11439.

Johnson, G. D., Stevenson, T., and Ahn, K. (1999). Hydrolysis of peptide hormones by endothelin-converting enzyme-1: a comparison with neprilysin. *J. Biol. Chem.* 274, 4053–4058. doi: 10.1074/jbc.274.7.4053

Jolly, C., Berland, S., Milet, C., Borzeix, S., Lopez, E., and Doumenc, D. (2004). Zonal localization of shell matrix proteins in mantle of *Haliotis tuberculata* (Mollusca, Gastropoda). *Mar. Biotechnol.* 6, 541–551. doi: 10.1007/s10126-004-3129-7

Joubert, C., Piquemal, D., Marie, B., Manchon, L., Pierrat, F., Zanella-Cléon, I., et al. (2010). Transcriptome and proteome analysis of *Pinctada margaritifera* calcifying mantle and shell: focus on biomineralization. *BMC Genomics.* 11:613. doi: 10.1186/1471-2164-11-613

Kinoshita, S., Wang, N., Inoue, H., Maeyama, K., Okamoto, K., Nagai, K., et al. (2011). Deep sequencing of ESTs from nacreous and prismatic layer producing tissues and a screen for novel shell formation-related genes in the pearl oyster. *PLoS One* 6:e21238. doi: 10.1371/journal.pone.0021238

Kishore, P., and Southgate, P. C. (2015). Development and function of pearl-sacs grown from regenerated mantle graft tissue in the black-lip pearl oyster, *Pinctada margaritifera* (Linnaeus, 1758). *Fish Shellfish Immunol.* 45, 567–573. doi: 10.1016/j.fsi.2015.05.008

Kishore, P., and Southgate, P. C. (2016). A detailed description of pearl-sac development in the black-lip pearl oyster, *Pinctada margaritifera* (Linnaeus 1758). *Aquac. Res.* 47, 2215–2226. doi: 10.1111/are.12674

Kolde, R. (2012). *pheatmap: Pretty Heatmaps. R package version 1.0.8.* Available online at http://CRAN.R-project.org/package=pheatmap (accessed February 2, 2020).

Ky, C., Blay, C., Sham-Koua, M., Lo, C., and Cabral, P. (2014). Indirect improvement of pearl grade and shape in farmed *Pinctada margaritifera* by donor "oyster" selection for green pearls. *Aquaculture* 432, 154–162. doi: 10.1016/j.aquaculture.2014.05.002

Ky, C.-L., Blay, C., Broustal, F., Sham Koua, M., and Planes, S. (2019). Relationship of the orange tissue morphotype with shell and pearl colouration in the mollusc *Pinctada margaritifera*. *Sci. Rep.* 9:5114.

Ky, C.-L., Nakasai, S., Molinari, N., and Devaux, D. (2015). Influence of grafter skill and season on cultured pearl shape, circles and rejects in *Pinctada margaritifera* aquaculture in Mangareva lagoon. *Aquaculture* 435, 361–370. doi: 10.1016/j.aquaculture.2014.10.014

Larsson, A. (2014). AliView: a fast and lightweight alignment viewer and editor for large data sets. *Bioinformatics* 30, 3276–3278. doi: 10.1093/bioinformatics/btu531

Le Luyer, J., Auffret, P., Quillien, V., Leclerc, N., Reisser, C., Vidal-Dupiol, J., et al. (2019). Whole transcriptome sequencing and biomineralization gene architecture associated with cultured pearl quality traits in the pearl oyster, *Pinctada margaritifera*. *BMC Genomics* 20:111. doi: 10.1186/s12864-019-5443-5

Le Pabic, C., Marie, A., Marie, B., Percot, A., Bonnaud-Ponticelli, L., Lopez, P. J., et al. (2017). First proteomic analyses of the dorsal and ventral parts of the *Sepia officinalis* cuttlebone. *J. Proteomics* 150, 63–73. doi: 10.1016/j.jprot.2016.08.015

Levin, M., Anavy, L., Cole, A. G., Winter, E., Mostov, N., Khair, S., et al. (2016). The mid-developmental transition and the evolution of animal body plans. *Nature* 531, 637–641.

Liao, Z., Bao, L.-F., Fan, M.-H., Gao, P., Wang, X.-X., Qin, C.-l, et al. (2015). In-depth proteomic analysis of nacre, prism, and myostracum of *Mytilus* shell. *J. Proteomics*122, 26–40. doi: 10.1016/j.jprot.2015.03.027

Liao, Z., Jiang, Y.-t, Sun, Q., Fan, M.-H., Wang, J.-x, and Liang, H.-y (2019). Microstructure and in-depth proteomic analysis of *Perna viridis* shell. *PLoS One* 14:e0219699. doi: 10.1371/journal.pone.0219699

Liu, C., Li, S., Kong, J., Liu, Y., Wang, T., Xie, L., et al. (2015). In-depth proteomic analysis of shell matrix proteins of *Pinctada fucata*. *Sci. Rep.* 5:17269.

Love, M. I., Huber, W., and Anders, S. (2014). Moderated estimation of fold change and dispersion for RNA-seq data with DESeq2. *Genome Biol.* 15:550.

Ma, H. Y., and Lee, I.-S. (2006). Characterization of vaterite in low quality freshwater-cultured pearls. *Mater. Sci. Eng. C* 26, 721–723. doi: 10.1016/j.msec.2005.09.109

Maere, S., Heymans, K., and Kuiper, M. (2005). BiNGO: a cytoscape plugin to assess overrepresentation of gene ontology categories in biological networks. *Bioinformatics* 21, 3448–3449. doi: 10.1093/bioinformatics/bti551

Mann, K., Cerveau, N., Gummich, M., Fritz, M., Mann, M., and Jackson, D. J. (2018). In-depth proteomic analyses of *Haliotis laevigata* (greenlip abalone) nacre and prismatic organic shell matrix. *Proteome Sci.* 16:11.

Mann, K., Edsinger-Gonzales, E., and Mann, M. (2012). In-depth proteomic analysis of a mollusc shell: acid-soluble and acid-insoluble matrix of the limpet *Lottia gigantea*. *Proteome Sci.* 10:28. doi: 10.1186/1477-5956-10-28

Mann, K., and Jackson, D. J. (2014). Characterization of the pigmented shell-forming proteome of the common grove snail *Cepaea nemoralis*. *BMC Genomics.* 15:249. doi: 10.1186/1471-2164-15-249

Marie, B., Arivalagan, J., Mathéron, L., Bolbach, G., Berland, S., Marie, A., et al. (2017). Deep conservation of bivalve nacre proteins highlighted by shell matrix proteomics of the Unionoida *Elliptio complanata* and *Villosa lienosa*. *J. R. Soc. Interface* 14:20160846. doi: 10.1098/rsif.2016.0846

Marie, B., Jackson, D. J., Ramos-Silva, P., Zanella-Cléon, I., Guichard, N., and Marin, F. (2013b). The shell-forming proteome of *Lottia gigantea* reveals both deep conservations and lineage-specific novelties. *FEBS J.* 280, 214–232. doi: 10.1111/febs.12062

Marie, B., Joubert, C., Tayalé, A., Zanella-Cléon, I., Belliard, C., Piquemal, D., et al. (2012). Different secretory repertoires control the biomineralization processes of prism and nacre deposition of the pearl oyster shell. *Proc. Natl. Acad. Sci. U.S.A.* 109, 20986–20991. doi: 10.1073/pnas.1210552109

Marie, B., Marie, A., Jackson, D. J., Dubost, L., Degnan, B. M., Milet, C., et al. (2010). Proteomic analysis of the organic matrix of the abalone *Haliotis asinina* calcified shell. *Proteome Sci.* 8:54. doi: 10.1186/1477-5956-8-54

Marie, B., Ramos-Silva, P., Marin, F., and Marie, A. (2013a). Proteomics of CaCO3 biomineral-associated proteins: how to properly address their analysis. *Proteomics* 13, 3109–3116. doi: 10.1002/pmic.201300162

Marie, B., Trinkler, N., Zanella-Cleon, I., Guichard, N., Becchi, M., Paillard, C., et al. (2011). Proteomic identification of novel proteins from the calcifying shell matrix of the manila clam *Venerupis philippinarum*. *Mar. Biotechnol.* 13, 955–962. doi: 10.1007/s10126-010-9357-0

Mariom, Take, S., Igarashi, Y., Yoshitake, K., Asakawa, S., Maeyama, K., et al. (2019). Gene expression profiles at different stages for formation of pearl sac and pearl in the pearl oyster *Pinctada fucata*. *BMC Genomics* 20:240. doi: 10.1186/s12864-019-5579-3

McDougall, C., Aguilera, F., and Degnan, B. M. (2013a). Rapid evolution of pearl oyster shell matrix proteins with repetitive, low-complexity domains. *J. R. Soc. Interface* 10:20130041. doi: 10.1098/rsif.2013.0041

McDougall, C., Aguilera, F., Moase, P., Lucas, J. S., and Degnan, B. M. (2013b). Pearls. *Curr. Biol.* 23, R671–R673.

McDougall, C., Green, K., Jackson, D. J., and Degnan, B. M. (2011). Ultrastructure of the mantle of the gastropod *Haliotis asinina* and mechanisms of shell regionalization. *Cells Tissues Organs* 194, 103–107. doi: 10.1159/000324213

McDougall, C., Moase, P., and Degnan, B. M. (2016a). Host and donor influence on pearls produced by the silver-lip pearl oyster, *Pinctada maxima*. *Aquaculture.* 450, 313–320. doi: 10.1016/j.aquaculture.2015.08.008

McDougall, C., Woodcroft, B. J., and Degnan, B. M. (2016b). The widespread prevalence and functional significance of silk-like structural proteins in metazoan biological materials. *PLoS One* 11:e0159128. doi: 10.1371/journal.pone.0159128

McGinty, E. L., Zenger, K. R., Jones, D. B., and Jerry, D. R. (2012). Transcriptome analysis of biomineralisation-related genes within the pearl sac: host and donor oyster contribution. *Mar. Genomics* 5, 27–33. doi: 10.1016/j.margen.2011.08.006

Neuwirth, E. (2011). *RColorBrewer. R Package Version 1.1-2.* Available online at https://cran.r-project.org/package=RColorBrewer (accessed February 2, 2020).

Pavat, C., Zanella-Cléon, I., Becchi, M., Medakovic, D., Luquet, G., Guichard, N., et al. (2012). The shell matrix of the pulmonate land snail *Helix aspersa maxima*. *Comp. Biochem. Phys. B* 161, 303–314. doi: 10.1016/j.cbpb.2011.12.003

Pearlautore International Pty Ltd, (2006). *Autore's Five S's South Sea Cultured Pearl Classification Guide*. Sydney, NSW: Pearlautore International Pty Ltd.

R Core Team, (2014). *R: A Language and Environment for Statistical Computing*. Vienna: R Foundation for Statistical Computing.

Rambaut, A. (2006). *FigTree. 1.1.1*. Edinburgh: University of Edinburgh.

Say, T. E., and Degnan, S. M. (2020). Molecular and behavioural evidence that interdependent photo- and chemo-sensory systems regulate larval settlement in a marine sponge. *Mol. Ecol.* 29, 247–261. doi: 10.1111/mec.15318

Shannon, P., Markiel, A., Ozier, O., Baliga, N. S., Wang, J. T., Ramage, D., et al. (2003). Cytoscape: a software environment for integrated models of biomolecular interaction networks. *Genome Res.* 13, 2498–2504. doi: 10.1101/gr.1239303

Sharrocks, A. D. (2001). The ETS-domain transcription factor family. *Nat. Rev. Mol. Cell Biol.* 2, 827–837.

Shimizu, K., Kimura, K., Isowa, Y., Oshima, K., Ishikawa, M., Kagi, H., et al. (2018). Insights into the evolution of shells and love darts of land snails revealed from their matrix proteins. *Genome Biol. Evol.* 11, 380–397. doi: 10.1093/gbe/evy242

Simkiss, K., and Wada, K. (1980). Cultured pearls – commercialised biomineralisation. *Endeavour* 4, 32–37. doi: 10.1016/0160-9327(80)90107-6

Sleight, V. A., Antczak, P., Falciani, F., and Clark, M. S. (2020). Computationally predicted gene regulatory networks in molluscan biomineralisation identify extracellular matrix production and ion transportation pathways. *Bioinformatics* 36, 1326–1332.

Southgate, P. C., and Lucas, J. S. (2008). *The Pearl Oyster*. Amsterdam: Elsevier.

Stamatakis, A. (2014). RAxML version 8: a tool for phylogenetic analysis and post-analysis of large phylogenies. *Bioinformatics* 30, 1312–1313. doi: 10.1093/bioinformatics/btu033

Strack, E. (2006). *Pearls*. Stuttgart: Rühle-Diebener-Verlag.

Sud, D., Poncet, J., Saihi, A., Lebel, J., Doumenc, D., and Boucaud-Camou, E. (2002). A cytological study of the mantle edge of *Haliotis tuberculata* L. (Mollusca, Gastropoda) in relation to shell structure. *J. Shellfish Res.* 21, 201–210.

Sudo, S., Fujikawa, T., Nagakura, T., Ohkubo, T., Sakaguchi, K., Tanaka, M., et al. (1997). Structures of mollusc shell framework proteins. *Nature* 387, 563–564. doi: 10.1038/42391

Suzuki, M., Iwashima, A., Kimura, M., Kogure, T., and Nagasawa, H. (2013). The molecular evolution of the pif family proteins in various species of mollusks. *Mar. Biotechnol.* 15, 145–158. doi: 10.1007/s10126-012-9471-2

Suzuki, M., Saruwatari, K., Kogure, T., Yamamoto, Y., Nishimura, T., Kato, T., et al. (2009). An acidic matrix protein, Pif, is a key macromolecule for nacre formation. *Science* 325, 1388–1390. doi: 10.1126/science.1173793

Taylor, J., and Strack, E. (2008). "Pearl production," in *The Pearl Oyster*, eds P. C. Southgate, and J. S. Lucas, (Amsterdam: Elsevier), 273–302. doi: 10.1016/b978-0-444-52976-3.00008-5

Treccani, L., Mann, K., Heinemann, F., and Fritz, M. (2006). Perlwapin, an abalone nacre protein with three four-disulfide core (whey acidic protein) domains, inhibits the growth of calcium carbonate crystals. *Biophys. J.* 91, 2601–2608. doi: 10.1529/biophysj.106.086108

Upadhyay, A., Thiyagarajan, V., and Tong, Y. (2016). Proteomic characterization of oyster shell organic matrix proteins (OMP). *Bioinformation* 12, 266–278. doi: 10.6026/97320630012266

Wang, N., Kinoshita, S., Riho, C., Maeyama, K., Nagai, K., and Watabe, S. (2009). Quantitative expression analysis of nacreous shell matrix protein genes in the process of pearl biogenesis. *Comp. Biochem. Physiol. B Biochem. Mol. Biol.* 154, 346–350. doi: 10.1016/j.cbpb.2009.07.012

Yagi, K., Satou, Y., Mazet, F., Shimeld, S. M., Degnan, B., Rokhsar, D., et al. (2003). A genomewide survey of developmentally relevant genes in *Ciona intestinalis*. *Dev. Genes Evol.* 213, 235–244. doi: 10.1007/s00427-003-0322-z

Zhan, X., Gu, Z., Yu, C., Wen, H., Shi, Y., and Wang, A. (2013). Expressed sequence tags 454 sequencing and biomineralization gene expression for pearl sac of the pearl oyster, *Pinctada fucata martensii*. *Aquac. Res.* 46, 745–758. doi: 10.1111/are.12227

Zhang, G., Fang, X., Guo, X., Li, L., Luo, R., Xu, F., et al. (2012). The oyster genome reveals stress adaptation and complexity of shell formation. *Nature* 490, 49–54.

Zhifeng, G., Fengshao, H., Hai, W., Kai, G., Xin, Z., Yaohua, S., et al. (2014). Contribution of donor and host oysters to the cultured pearl colour in *Pinctada martensii*. *Aquac. Res.* 45, 1126–1132. doi: 10.1111/are.12052

Conflict of Interest: PM was employed by the company Clipper Pearls Pty Ltd. and Autore Pearls Pty Ltd. (Broome, WA, Australia) during the study.

The remaining authors declare that the research was conducted in the absence of any commercial or financial relationships that could be construed as a potential conflict of interest.

frontiers in Genetics

ORIGINAL RESEARCH
published: 02 February 2021
doi: 10.3389/fgene.2021.618517

Evolution of Protein-Mediated Biomineralization in Scleractinian Corals

Tal Zaquin[1†], Assaf Malik[1†], Jeana L. Drake[1], Hollie M. Putnam[2] and Tali Mass[1]*

[1] Department of Marine Biology, The Leon H. Charney School of Marine Sciences, University of Haifa, Haifa, Israel,
[2] Department of Biological Sciences, University of Rhode Island, Kingston, RI, United States

While recent strides have been made in understanding the biological process by which stony corals calcify, much remains to be revealed, including the ubiquity across taxa of specific biomolecules involved. Several proteins associated with this process have been identified through proteomic profiling of the skeletal organic matrix (SOM) extracted from three scleractinian species. However, the evolutionary history of this putative "biomineralization toolkit," including the appearance of these proteins' throughout metazoan evolution, remains to be resolved. Here we used a phylogenetic approach to examine the evolution of the known scleractinians' SOM proteins across the Metazoa. Our analysis reveals an evolutionary process dominated by the co-option of genes that originated before the cnidarian diversification. Each one of the three species appears to express a unique set of the more ancient genes, representing the independent co-option of SOM proteins, as well as a substantial proportion of proteins that evolved independently. In addition, in some instances, the different species expressed multiple orthologous proteins sharing the same evolutionary history. Furthermore, the non-random clustering of multiple SOM proteins within scleractinian-specific branches suggests the conservation of protein function between distinct species for what we posit is part of the scleractinian "core biomineralization toolkit." This "core set" contains proteins that are likely fundamental to the scleractinian biomineralization mechanism. From this analysis, we infer that the scleractinians' ability to calcify was achieved primarily through multiple lineage-specific protein expansions, which resulted in a new functional role that was not present in the parent gene.

Keywords: skeleton evolution, co-option, SOM proteins, stony corals, phylogenetic analysis

OPEN ACCESS

Edited by:
Melanie Debiais-Thibaud, Université de Montpellier, France

Reviewed by:
Marcos Barbeitos, Federal University of Paraná, Brazil
Paul Simion, University of Namur, Belgium

***Correspondence:**
Tali Mass
tmass@univ.haifa.ac.il

[†] These authors have contributed equally to this work

Specialty section:
This article was submitted to Evolutionary and Population Genetics, a section of the journal Frontiers in Genetics

Received: *17 October 2020*
Accepted: *08 January 2021*
Published: *02 February 2021*

Citation:
Zaquin T, Malik A, Drake JL, Putnam HM and Mass T (2021) Evolution of Protein-Mediated Biomineralization in Scleractinian Corals. Front. Genet. 12:618517. doi: 10.3389/fgene.2021.618517

INTRODUCTION

Scleractinian corals (commonly known as stony or hard corals) are foundation species in the tropical marine ecosystem (Moberg and Folke, 1999). One of their most important roles is reef formation through their ability to create a rigid aragonite exoskeleton by the process of biomineralization. These exoskeletons are valuable as they provide the ecological framework that supports high rates of primary production and permits extensive biological diversity in coral reef ecosystems (Veron et al., 2009), as well as serving as a large reservoir of biogenic calcium carbonate in the ocean (Cohen and McConnaughey, 2003). Scleractinians are among the oldest

biomineralizing Metazoa, likely appearing in the late Ordovician (∼445 Million years ago), and becoming highly diverse (Stolarski et al., 2011; Drake et al., 2020). They are represented by different morphologies and spatial distribution (Veron, 2000), and show distinct molecular evolution, with the order split into two major clades, known as the Complexa (complex corals) and Robusta (robust corals) (Romano and Palumbi, 1996; Kitahara et al., 2010; Ying et al., 2018), named for the extent of skeletal calcification-specific patterns of corallite wall construction. While the process of biomineralization in scleractinians has long been studied (reviewed by Drake et al., 2020), its biomolecular mechanisms have only recently begun to be revealed (reviewed by Murdock, 2020), coinciding with advances in genomics and protein identification.

The "biomineralization toolkit" is the collective term for the many specific lipids, polysaccharides, and proteins both documented and hypothesized to be involved in the formation of the biomineral at various stages of an organism's life history, some of which may become embedded in its skeleton (Livingston et al., 2006). Those organic molecules which are retained in the skeleton (the skeletal organic matrix, SOM) directly mediate and regulate the process by which many organisms from across all kingdoms of life form biominerals (Lowenstam and Weiner, 1989; Mann, 2001; Knoll, 2003), with the resulting biominerals exhibiting characteristics different from their abiogenic counterparts (Weiner, 2003; Gal et al., 2015). Out of all the SOM molecules, the most intensively studied are the proteins (Evans, 2019; Clark, 2020; Erwin, 2020; Murdock, 2020). Proteomic studies have shown that different lineages use sets of proteins with similar functional categories, including matrix formers, nucleation assisters, signalers, and remodelers to form their skeletal structure (Marin et al., 2016; Evans, 2019). Although the SOM proteins from distant organisms share common properties (Evans, 2019), each taxon-specific suite appears to have evolved independently through convergent and co-option evolution, resulting in varying contributions by lineage- and species-specific novel proteins, which exhibit contrasting rates of conservation between and within lineages (Drake et al., 2014).

In scleractinians, numerous SOM-related characteristics have been studied (Tambutté et al., 2011), yet only a few proteomic profiling experiments have been conducted, and then solely for tropical species. Extensive proteomic studies using species-specific genomes and transcriptomes include those of *Stylophora pistillata* (Drake et al., 2013; Peled et al., 2020), *Acropora millepora* (Ramos-Silva et al., 2013), and *Acropora digitifera* (Takeuchi et al., 2016), which, when combined, revealed over 100 SOM protein, hence members of the "biomineralization toolkit." Similar to previous examinations of various metazoan lineages, scleractinian SOM proteins appear to share functional roles in carbohydrate-binding and catalytic activities (Ramos-Silva and Marin, 2015). Notably, the most extensively studied SOM proteins in scleractinians are the aspartic acid-rich proteins which assist in mineral nucleation and modification (Lowenstam and Weiner, 1989; Marin and Luquet, 2008; Mass et al., 2013; Gavriel et al., 2018; Laipnik et al., 2019), and α-carbonic anhydrases that play a role in both carbon supply and concentration (Bertucci et al., 2013; Zoccola et al., 2016). However, many scleractinian SOM proteins do not contain known functional domains and remain to be functionally characterized. Furthermore, out of all the known scleractinian SOM proteins, only a few were found to be shared between the three species (Takeuchi et al., 2016; Peled et al., 2020). The identification and characterization of the suite of scleractinian SOM proteins to date has led to the hypothesis that the proteins underlying scleractinian skeleton formation developed through stepwise evolution, supplementing proteins that are conserved across Metazoa with scleractinian-specific and species-specific novel proteins (Ramos-Silva et al., 2013; Takeuchi et al., 2016).

While useful for initial studies, most of the analyses that examined SOM protein diversity across taxa were carried out using heuristic methods of sequence similarity scores (e.g., BLAST), which estimates the phylogenetic relationships between a set of genes by the premise that higher-scoring sequence pairs are likely to have diverged more recently compared to their lower-scoring counterparts (Fitch, 1970; Lafond et al., 2018; Emms and Kelly, 2019). As a preliminary examination, sequence similarity can aid in determining homologous gene groups and are useful for function-related applications (Doyle et al., 2010; Paps and Holland, 2018; Richter et al., 2018); yet, the lack of a phylogenetic analysis based on a species tree limits our understanding of the proteins' origin and evolutionary dynamics, as sequence duplication can result in a high sequence differentiation and subsequently leads to overlooking orthologous sequences (Lafond et al., 2018). To date, Bhattacharya et al. (2016) have published the most intensive phylogenetic study of the previously known scleractinian biomineralization proteins. The authors provided the basis for understanding scleractinian genomic evolutionary information, revealing mechanisms for scleractinians to adapt to changing environments while maintaining the ability to calcify. Recent advances in genome and transcriptome sequencing and the production of more gene databases are increasing our ability to provide a higher resolution comparison of SOM proteins and therefore, a better understanding of their evolutionary dynamics. This will allow extrapolation of the occurrence of the scleractinian "core biomineralization toolkit," that is, the biomineralization-related proteins that are shared across scleractinian species and, as such, have a fundamental role in the skeleton formation process across the order. While at first glance, the most straightforward method may be to sequence more scleractinian skeletal proteomes, in practice, direct proteomic analyses are often incomplete and time-consuming (Marin et al., 2016; Aguilera et al., 2017; Peled et al., 2020); predictions based on transcriptomic and genomic data, therefore, become essential. However, on their own, such predictions can result in redundancies and overestimations, while at the same time overlooking potential gene candidates due to unresolved and incomplete genomes and transcriptomes (Eisenhaber, 2013; Sinha et al., 2018). Therefore, it is essential to combine both approaches, based on both proteins and DNA/RNA sequencing, to generate a more holistic picture of SOM protein evolution.

Here, we used a phylogenetic approach of the known scleractinian SOM proteins to study their evolution across the metazoan tree of life. As we have used the orthology/paralogy

relationships for each protein in one species at a time, our results are independent for each lineage, providing a robust evaluation of their evolution. Our results reveal part of the "core biomineralization toolkit" across scleractinians, comprised of multiple proteins sharing an evolutionary history across distinct species. Since orthologous genes are more likely to share a biological function (Fang et al., 2010; Gabaldón and Koonin, 2013; Altenhoff et al., 2019), our approach might allow us to extrapolate the occurrence of proteins that play a fundamental role in the skeleton formation across scleractinians. However, the major fraction of each species SOM proteins were found to be independently co-opted into their own "biomineralization toolkit" from genes that evolved before the emergence of scleractinians. These were coupled with scleractinian-specific gene family expansions resulting in each scleractinian lineage and species having a unique set of SOM proteins.

MATERIALS AND METHODS

Scleractinian SOM Protein Orthogroup and Gene Tree Reconciliation

Our phylogenetic analysis was based on 43 annotated genomes spanning the metazoan kingdom (**Supplementary Table 1**), with the addition of seven Fungi species and two choanoflagellate species as the outgroups. The outgroups were selected in order to consider the Opisthokonta evolution. More specifically, the Fungi kingdom was included as scleractinians were found to share a complete histidine biosynthesis pathway, which is unique across the Metazoa (Ying et al., 2018), indicating that the consideration of fungi outgroup may be critical. Furthermore, the Choanoflagellata class was also included as it is considered to be the sister group of the Metazoa (King et al., 2008; Schalchian-Tabrizi et al., 2008). The complete dataset includes rigid skeleton/shell forming and non-forming taxa, including representation of major marine calcifying phyla (Mollusca, Echinodermata, Arthropoda, and Cnidaria) as we sought to group the known scleractinian SOM proteins (Drake et al., 2013; Ramos-Silva et al., 2013; Takeuchi et al., 2016; Peled et al., 2020) into their respective orthogroups. An orthogroup is defined as a set of genes descended from a single gene in the last common ancestor of all the species being considered. We limited our database of known scleractinian SOM proteins to studies for which the skeletal proteomes were sequenced against annotated genomes from the same species, limiting us to representatives of scleractinian SOM proteins from *A. digitifera, A. millepora,* and *S. pistillata*. We decided to use a larger proportion of species from the cnidarian phylum and more particularly, within the scleractinian order, as they are the focus of this study. The annotated genomes in the analysis are comprised of datasets with a median BUSCO score of 90.05% (Seppey et al., 2019; **Supplementary Table 1**). To infer the scleractinian SOM orthogroups, we clustered all the protein-coding sequences from our entire database using OrthoFinder 2.2.7 (Emms and Kelly, 2015, 2019), to give a total of ∼16,000 orthogroups. After identifying all orthogroups from each sequence in our known SOM protein dataset, we aligned the sequences in each orthogroup separately using MAFFT (Katoh and Standley, 2013), followed by the removal of sequences and regions based on inconsistencies in the consensus alignment; sequences with both fewer than thirty aligned amino acids and less than 50% of the sequence aligned columns with <2 aligned sequences were removed. Gene trees were constructed in IQ-TREE (Nguyen et al., 2015) using the best-fitted model (LG) and discrete Gamma distribution of four rates across site categories (Resulting trees can be found in **Supplementary File 1**). To infer pairwise orthology relationships and to reconstruct the sequences' evolutionary histories, the gene trees were further rooted and reconciled via the Orthofinder2 pipeline, using the rooted species tree with the topology presented in **Figure 1A**, which is based on the current knowledge of animal phylogeny (Laumer et al., 2019; Fernández and Gabaldón, 2020). Then we selected orthogroups that include known SOM proteins of *A. digitifera, A. millepora,* and *S. pistillata*. Lastly, the known scleractinian SOM protein orthogroups were used for downstream analyses.

As data acquired from *de novo* transcriptomes are highly fragmented and can lead to misinterpretation of downstream analysis (Emms and Kelly, 2015), we did not include any transcriptomic data sets as part of the Orthofinder2 pipeline. However, the ability to produce a calcium carbonate rigid skeleton is not unique to the scleractinian order within Cnidaria, with several taxa, including hydrozoans and octocorals, demonstrating this ability. Therefore, to further identify common molecular traits between extant taxa, we searched for the known scleractinian SOM proteins putative orthologs in the transcriptome of a representative species, the blue octocoral *Heliopora coerulea* (Guzman et al., 2018) using Conditional Reciprocal Best BLAST 0.6.6 (CRB-BLAST) (Aubry et al., 2014), that performs complementary BLAST alignments between query and target sequences. Sequences with more than a single hit across query and target of the same scleractinian species, were removed.

Scleractinian SOM Protein Orthogroup Gain and Duplication Patterns

We based our analysis on Dollo's parsimony (Farris, 1977) and phylostratigraphic profiling (Domazet-Lošo et al., 2007) to infer the likely phylogenetic origin of each known scleractinian SOM gene family. Dollo's parsimony, implemented in COUNT 9.1106 (Csûös, 2010), is modeled on Dollo's law (Dollo, 1893) that argues the statistical improbability of an organism to transition into a different state. It leads to a substantial simplification of evolutionary scenarios as it assumes that genes, which have been lost during evolution in a particular lineage, are unlikely to be regained. This heuristic approach enables us to map the scleractinian SOM proteins to the species tree based on the most phylogenetically distant lineage present in their representative orthogroup and to determine if SOM protein gains are the product of a lineage-specific evolution rather than the co-option of pre-existing genes into a skeleton formation role. If an SOM protein was reported as not having an orthogroup, we assigned it as a species-specific protein.

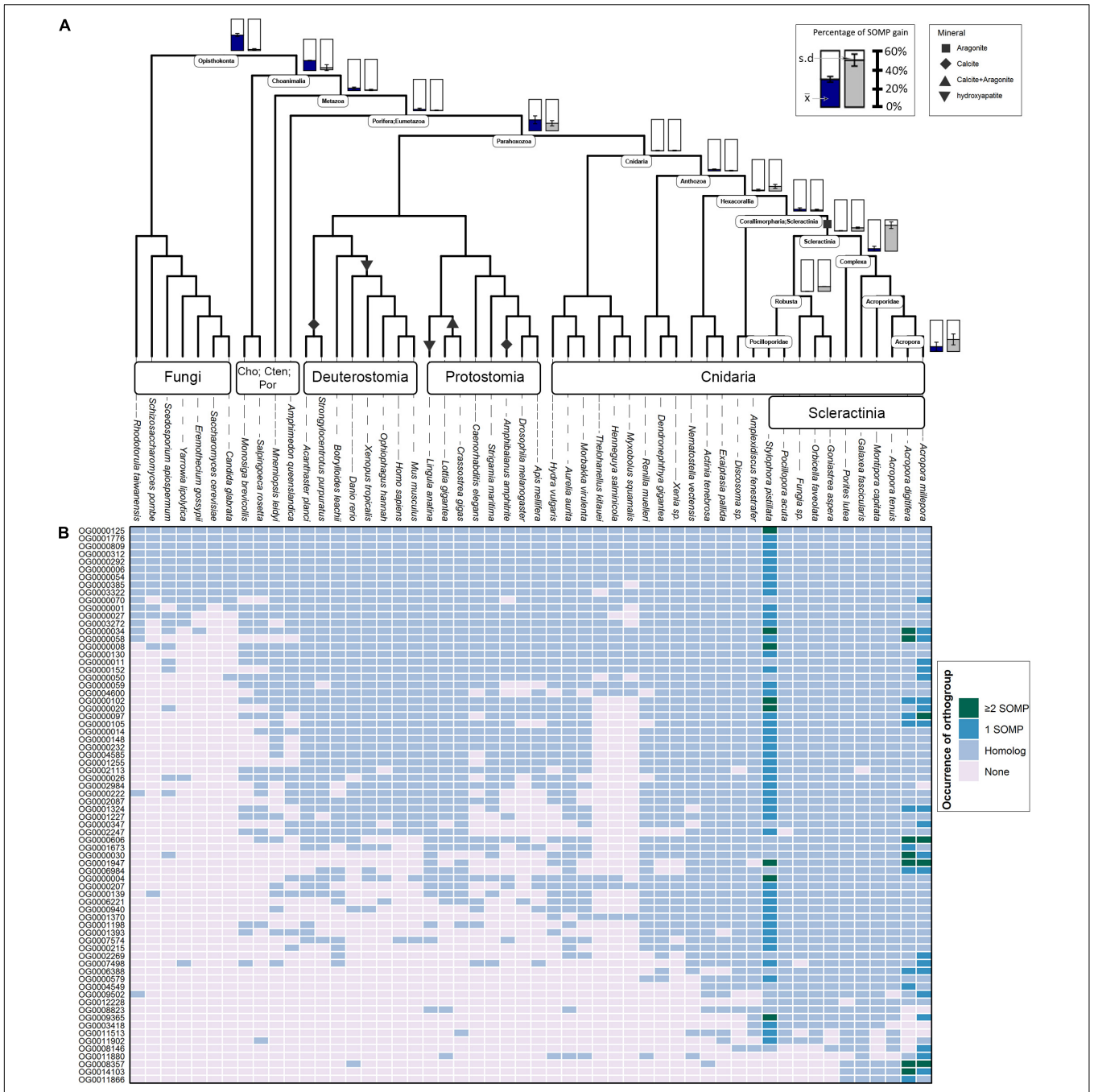

FIGURE 1 | Evolutionary origin of SOM proteins (SOMP) and duplication rates across animal taxa. **(A)** In the species tree, each internal node represents an ancestral lineage, where tips represent extant species. Accordingly, blue-filled bars near specific internal nodes represent the percentage of known SOM proteins that were gained in a specific ancestral lineage, based on our results. Similarly, the gray-filled bar represents the percentage of known SOM proteins that evolved from a protein whose last duplication occurred at specific ancestral species. Bottom-right bars represent gain at extant species. The mean ($\bar{x}$) and standard deviation (s.d.) values are indicated in each bar graph. Black shapes symbolize the different mineral phases of the species that form a rigid skeleton or shell. **(B)** The heatmap describes the occurrences of each known SOM protein from *Stylophora pistillata*, *Acropora digitifera,* and *A. millepora* across the different orthogroups and their coding sequence homologs among all species in this study. For a comprehensive list of the SOM proteins found in each orthogroup, see **Supplementary Table 2**.

Gene duplication rates were calculated using the phylogenetic birth-and-death model implemented in COUNT 9.1106 (Csûös, 2010). Specifically, the rate model was calculated and optimized under the gain-loss–duplication model with the Poisson distribution at the root. The variation rate across families was set to 4:1:1:4 gamma categories for the edge length, the loss rate, gain rate, and the duplication rate, respectively. The convergence criteria applied were set to 100 rounds for the optimization

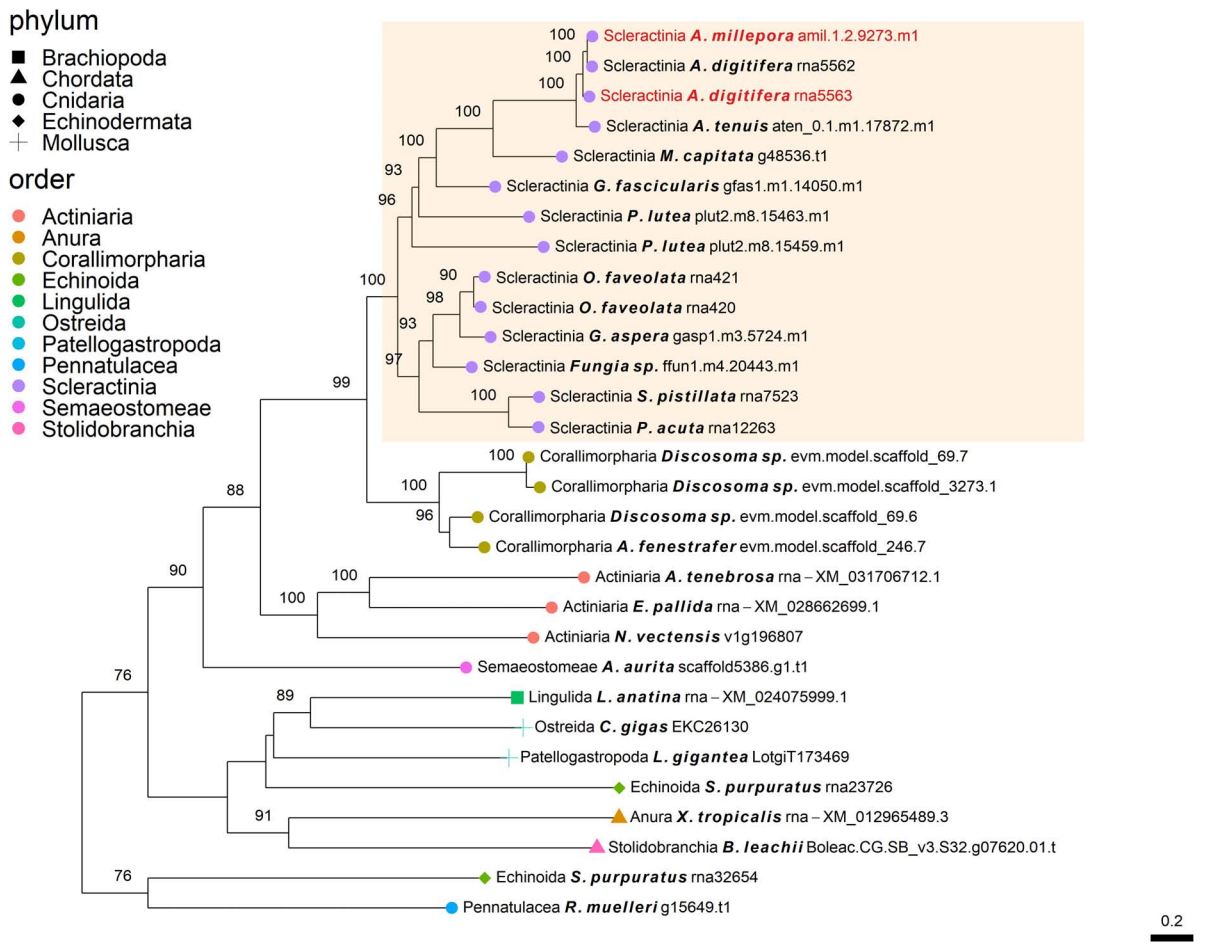

FIGURE 2 | Rooted gene tree of polycystin-like proteins (OG0006984) representing the independent co-option of orthologous proteins into the SOM of the Acroporidae species. Node points represent the phylum (shape) and order (color). Tips that are labeled red indicate the occurrence of scleractinian known SOM proteins. The highlighted cluster represents a "Scleractinia branch." Node support values indicate percentage bootstrap values. Only values above 75 are indicated.

TABLE 1 | Known coral SOM proteins in "Scleractinia branches."

Orthogroup	Orthogroup description	SOM protein occurrences in "Scleractinia branch"	Size of "Scleractinia branch"	SOM protein density in "Scleractinian branch"
OG0000020	Trypsin	2	4	0.5
OG0000030	Uncharacterized SOM protein 5	3	40	0.075
OG0000034*	Properdin	3	11	0.273
OG0000058*	Pikachurin-like	5	33	0.152
OG0000097*	MAM and LDL-receptor domain-containing proteins	3	11	0.273
OG0000102*	Protocadherin	2	16	0.125
OG0000105*	ZP domain-containing proteins	3	16	0.186
OG000606*	Galaxin-2	5	18	0.278
OG0001324*	Hephestin	3	18	0.167
OG0001947*	Aspartic acid-rich proteins	6	23	0.261
OG0006984	Polycystin-like proteins	2	22	0.091
OG0009365	Uncharacterized SOM protein 8	2	11	0.182

The list represents only "Scleractinia branches" with at least two scleractinian known SOM proteins and their density in the branch. Asterisks symbolize "Scleractinia branches" that contain SOM proteins from species of both the complex and robust scleractinian clades.

rounds with a likelihood threshold of 0.1. This model is based on the assumption that the primary mechanism of gene gain in eukaryotes is genomic duplications, while the possibility of gene gain through horizontal gene transfer (HGT) between different

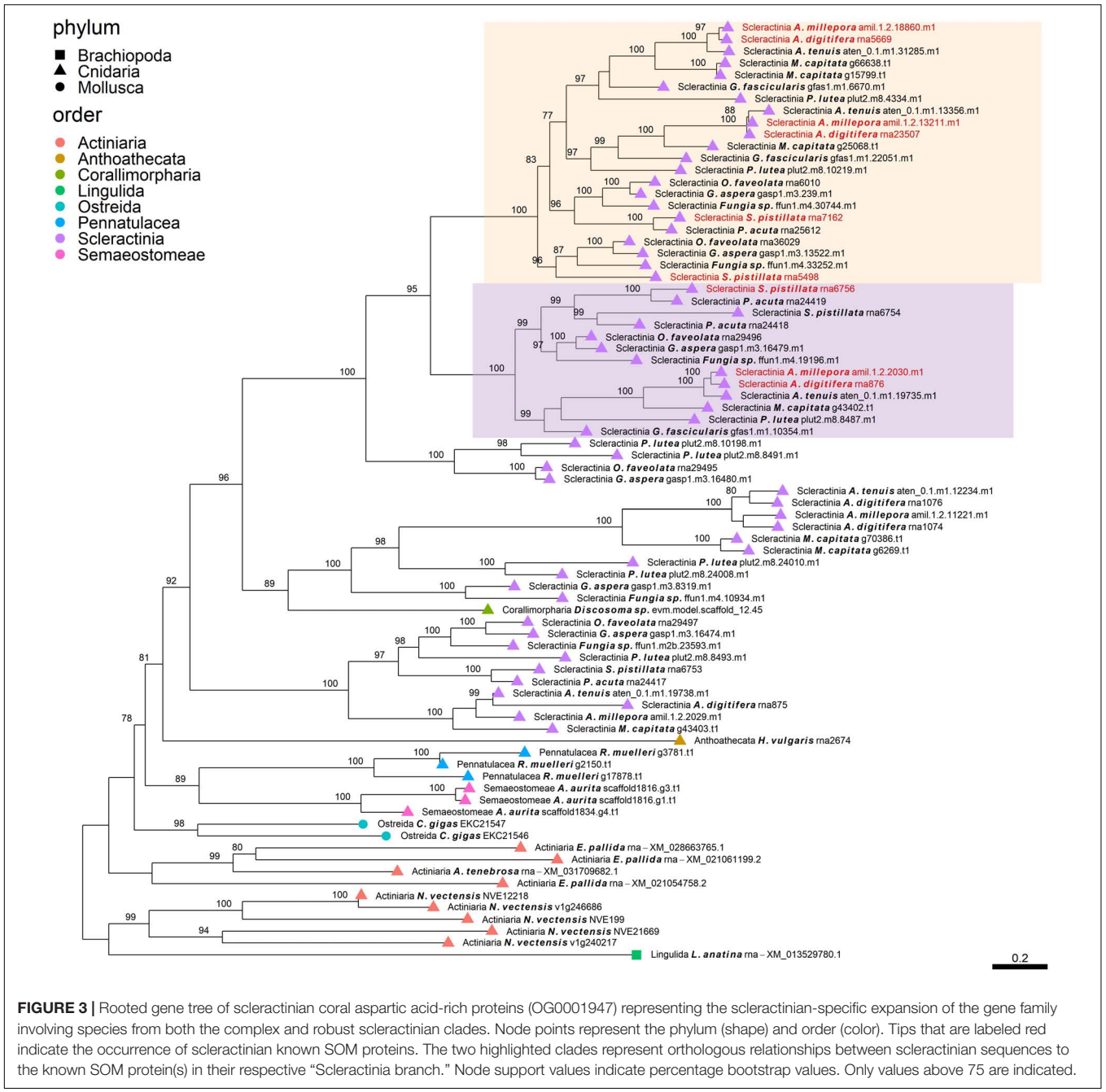

FIGURE 3 | Rooted gene tree of scleractinian coral aspartic acid-rich proteins (OG0001947) representing the scleractinian-specific expansion of the gene family involving species from both the complex and robust scleractinian clades. Node points represent the phylum (shape) and order (color). Tips that are labeled red indicate the occurrence of scleractinian known SOM proteins. The two highlighted clades represent orthologous relationships between scleractinian sequences to the known SOM protein(s) in their respective "Scleractinia branch." Node support values indicate percentage bootstrap values. Only values above 75 are indicated.

nodes of the gene tree is less likely (Csûrös and Miklós, 2006). However, as our methodological approach centered around using gene phylogenies to infer pairwise orthology and paralogy relationships for all genes in the analysis, it is robust to the effect of HGT, genome completeness and variable genome size (Huerta-Cepas et al., 2014; Emms and Kelly, 2015, 2019).

SOM-Enriched Branches and Permutation Test Method

In each rooted gene tree (see above), we first detected "Scleractinia branches," namely: groups of proteins that evolved from a single protein that existed in the last common ancestor of complex/robust scleractinians. For each scleractinian branch, we calculated the following values: (1) the total number of proteins in that branch, PN; (2) the number of SOM proteins known from previous studies (Drake et al., 2013; Ramos-Silva et al., 2013; Takeuchi et al., 2016; Peled et al., 2020) in that branch, pn; and (3) SOM protein density, pn/PN, if at least one known SOM protein was observed, otherwise density = 0. Our analysis tested whether known scleractinian SOM proteins evolved independently as opposed to having evolved from an SOM-related protein that existed in the most recent common ancestor of scleractinia. We compared our observed "Scleractinia

FIGURE 4 | Rooted gene tree of metal transport proteins (OG0001324) representing the scleractinian-specific expansion of the gene family. Node points represent the phylum (shape) and order (color). Tips that are labeled red indicate the occurrence of scleractinian known SOM proteins. The highlighted cluster represents a "Scleractinia branch." Node support values indicate percentage bootstrap values. Only values above 75 are indicated.

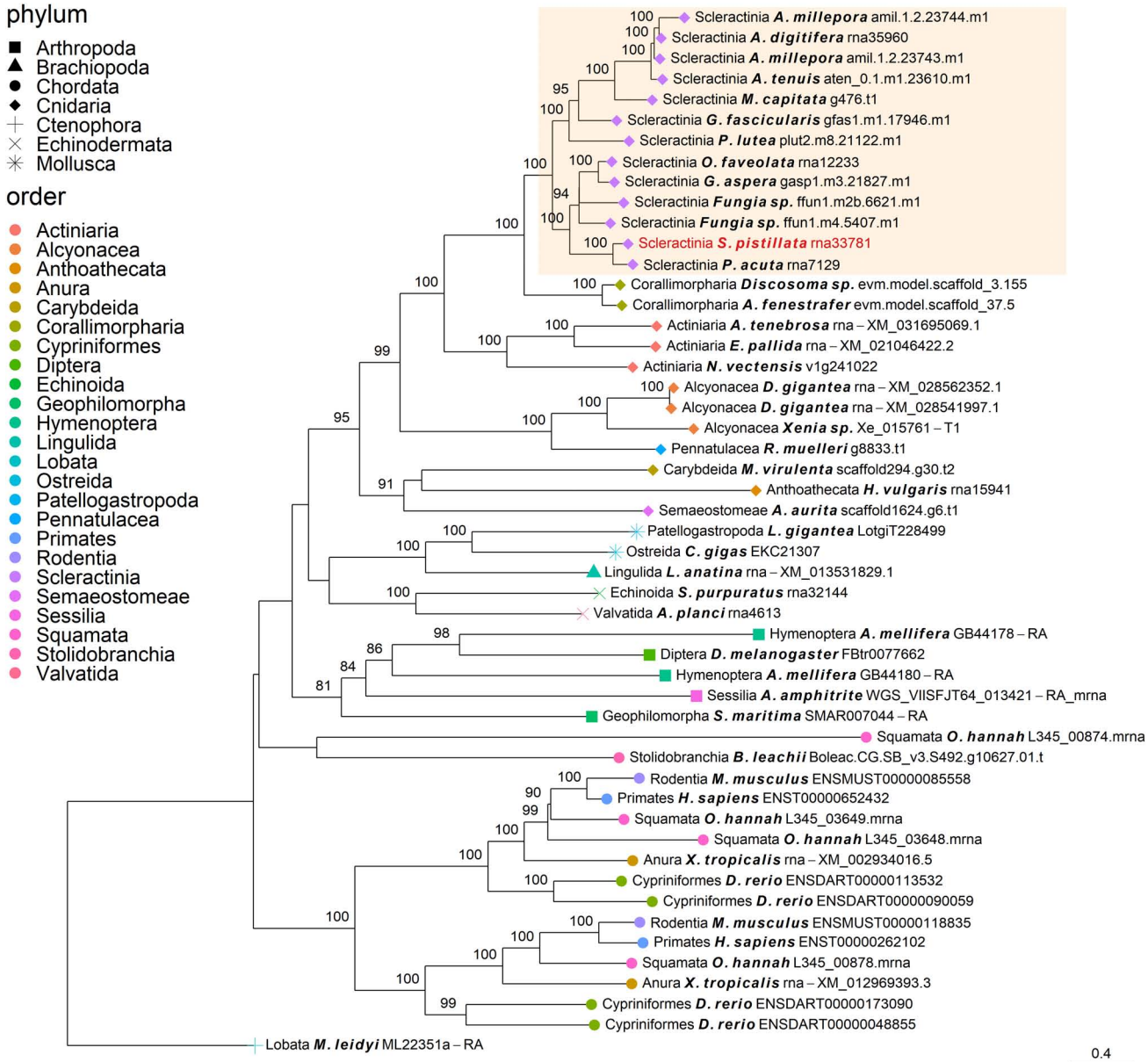

FIGURE 5 | Rooted gene tree of CAP-Gly domain-containing proteins (OG0004585) representing the independent co-option of a single *S. pistillata* protein into the SOM. Node points represent the phylum (shape) and order (color). Tips that are labeled red indicate the occurrence of known SOM proteins. The highlighted cluster represents a "Scleractinia branch." Node support values indicate percentage bootstrap values. Only values above 75 are indicated.

branches" SOM protein density to an expected density obtained by randomly selecting (n1) *S. pistillata*, (n2) *A. digitifera*, and (n3) *A. millepora* proteins (where n1, 2, 3 are equal to the counts of respective observed SOM proteins). The comparison was conducted using a permutation test ($n = 1{,}000$ sums), where a *P*-value was defined as the proportion of cases where the observed sum of density is smaller than the expected sum. We also repeated this test where density = 1 is assigned if species from both the complex and robust scleractinian clade are found in a cluster, and otherwise density = 0.

RESULTS

Scleractinian SOM Protein Evolutionary History

Using OrthoFinder2, 123 known scleractinian SOM proteins were clustered in 72 different orthogroups (i.e., all genes descended from a single gene belonging to the last common ancestor of the tested species). The identification of known scleractinian SOM proteins was based on previously published

scleractinian SOM proteomes (**Figure 1B** and **Supplementary Table 2**). The majority of the orthogroups, 54 out of 72, were found to include known SOM proteins from a single species, while twelve orthogroups contain two species and seven orthogroups are represented by all three species (**Figure 1B** and **Supplementary Table 1**). In fourteen orthogroups, we have identified the occurrence of scleractinian known SOM protein paralogs (that is, proteins which separated by a duplication event), from one or more species (**Figure 1B** and **Supplementary Table 2**). Although most orthogroups included known SOM proteins from a single species, we identified orthologs of those proteins across most scleractinian species with a mean of 67.5 (±1.78) orthogroups per scleractinian species (**Figure 1B**).

Gene gain can involve the co-option of pre-existing molecular traits to serve a new functional role as well as the evolution of lineage-specific genes, through a multiple "birth" model (True and Carroll, 2002; Choi and Kim, 2006; McLennan, 2008; Mello et al., 2018). As such, we evaluated these two categories using a phylostratigraphic approach. We observed an unbalanced gene distribution, where 76% of the SOM proteins are descendants of genes that were gained before the cnidarian diversification (**Figure 1A** and **Supplementary Table 3**). In our analysis, we found only a single scleractinian-specific orthogroup (OG0012228), representing species from both the robust and complex scleractinian clades. This orthogroup contains the *S. pistillata* SOM protein "Coral Acid-Rich Protein 2" (**Supplementary Figure 1**), which was observed to have an essential role in the early life stages of scleractinians (Mass et al., 2016; Akiva et al., 2018). However, ∼60% of the SOM proteins, found in the different orthogroups, emerged during the scleractinian evolution due to gene family expansion (**Figure 1A** and **Supplementary Table 3**). Simultaneously, 10.53 and 7.41% of the known SOM proteins from *S. pistillata* and *A. millepora*, respectively, were not found in any a specific orthogroup (**Supplementary Table 2**), suggesting a species-specific evolution.

Calculation of duplication rates across the tested orthogroups (**Supplementary Table 3**) shows high rates at the Opisthokonta and Choanimalia branches, followed by low rates at the subsequent branches leading to the known SOM proteins' species (**Supplementary Figure 2**).

Using CRB-BLAST, 21 distinct transcripts from the massive aragonite skeleton forming octocoral, *H. coerulea*, were identified to be putative orthologs of 27 scleractinian known biomineralization proteins, spanning 20 orthogroups (**Supplementary Table 4**). All identified *H. coerulea* transcripts were present in orthogroups with the phylogenetic origin at the metazoan branch or earlier (**Figure 1B**). Furthermore, in all of the respective orthogroups, at least two other non-rigid skeleton forming octocoral species were identified (**Figure 1B**). In five instances, the *H. coerulea* transcripts were identified as putative orthologs of more than a single species in the same orthogroup. Those orthogroups include putative enzymes, transporters, and acidic proteins, suggesting functional conservation across lineages. However, due to limitations of the transcriptomic dataset, the evolutionary relationship between sequences was not resolved. Our understanding of the evolutionary dynamics that guide the biomineralization gene repertoire evolution will increase through the growth in annotated genomic datasets.

Identification of Species-Specific vs. Scleractinian-Conserved SOM Protein Evolution

In the 72 gene trees tested, we detected multiple "Scleractinia branches," namely: groups of scleractinian genes that evolved from a single gene copy of the most recent common ancestor of scleractinians. Subsequently, we identified known SOM proteins in *S. pistillata* (Drake et al., 2013; Peled et al., 2020), *A. digitifera* (Takeuchi et al., 2016), and *A. millepora* (Ramos-Silva et al., 2013) within each "Scleractinia branch." Accordingly, in 12 "Scleractinia branches," we observed the cross-species conservation of more than a single known SOM protein (**Figure 2** and **Table 1**). Moreover, in eight "Scleractinia branches," known SOM proteins from both the complex and robust scleractinian clades were identified (**Figures 3**, **4** and **Table 1**). A permutation test revealed that this clustering pattern is non-random ($p < 0.001$), with a significantly higher SOM protein density per cluster than expected (**Table 1** and **Supplementary Figure 2**). Overall, these results indicate that the evolution of SOM-related functions emerged in the last common ancestor of scleractinians.

DISCUSSION

The mineralized skeleton is a paramount innovation, appearing simultaneously across phyla during the Cambrian Explosion (Murdock and Donoghue, 2011; Erwin, 2020; Murdock, 2020). Currently, there is growing evidence that many animal taxa inherited sets of ancestral genes that were then independently co-opted to guide skeleton formation (Murdock, 2020). Here, we sought to examine the evolutionary history of scleractinian biomineralization proteins across the metazoan tree of life to determine how modern stony corals evolved to form one of the most significant biostructures on Earth (Veron et al., 2009).

Determining the age of the SOM proteins by phylostratigraphy (**Figure 1A**) indicates that each scleractinian species' "biomineralization toolkit" has a similar age profile, characterized by progressively descending gene gain toward the tip of the tree. The most substantial proportion of genes for which orthogroups were found, appear to have evolved over 700 million years ago, before the cnidarian diversification, through extensive expansions of gene families. Of these ancestral genes, 96% of orthogroups contain at least one species that does not form a rigid skeleton (**Figure 1B**). The evidence that the scleractinian SOM proteins have an ancient origin and are shared between rigid skeleton forming and non-forming taxa further supports the hypothesis that the "biomineralization toolkit" evolved by the differential independent co-option of genes that had unrelated skeleton forming functions (Erwin, 2020).

The independent co-option of ancient genes is not only restricted to between-lineage relationships, but is also evident in the same lineage, with taxa utilizing a unique set of proteins with similar functional patterns (Evans, 2019). For example, mollusks

have been found to express in their mantle a species-specific unique set of genes that evolved before their evolutionary origins (Aguilera et al., 2017). This tendency for different species to use a separate set of ancient genes that converge toward the same results is also found in stony corals. Orthogroup OG0006984 (**Figure 2**), was found to include polycystin-like sequences, having calcium binding sites (Rastogi and Liberles, 2005). This gene family has an evolutionary origin going back at least to the Parahoxozoa lineage. Although the SOM proteins were found to be orthologous to sequences from all three scleractinian species with a published SOM proteome, only the Acroporidae family proteins has been identified in the skeleton. In addition, solely an *S. pistillata* known SOM protein was identified in the CAP-Gly orthogroup (OG0004585, **Figure 5**) which contain genes that are involved in the transport of vesicles along the cytoskeletal network (Riehemann and Sorg, 1993). Similarly to the polycystin orthogroup, the known SOM protein shares a 1:1 orthology to sequences from the scleractinian species with a published SOM proteome yet, was only identified in the *S. pistillata*'s skeleton. It is noteworthy that this example can be a result of the identification of different protein sets by the use of diverse protein extraction methods, which can lead not only to different yield but also different content of proteins as the various methods are biased toward their own properties (Marin et al., 2016; Klont et al., 2018; Peled et al., 2020). For example, mechanical filtration is biased toward hydrophobic proteins, while acetone precipitation increase the identification of hydrophilic proteins (Thongboonkerd et al., 2002). As such, the use of multiple extraction methods to retrieve SOM proteins makes it difficult to fully compare across species, likely leading to underestimation of the SOM protein repertoire.

Species-specific novel proteins are those with no orthologous relationship outside the species of interest. This class of proteins was also found to contribute to the scleractinian SOM protein assemblage, although to a lesser extent than the co-option of pre-existing molecular traits (**Figure 1A** and **Supplementary Table 2**). While the variability in their detection is high between our species of interest, as discussed above, it could also be caused by underestimation due to different extraction methods. In mollusks, species-specific proteins have been suggested to play a considerable role in physiological adaptations to environmental changes (Arivalagan et al., 2016) and in the formation of the numerous shell morphologies and properties (Kocot et al., 2016). However, to date, our knowledge of the functional roles of most SOM proteins in scleractinians is still lacking. Therefore, the clarification of novel biomineralization proteins from different species, combined with experimental functional validation, is still required to elucidate their significance.

Gene duplication events play a crucial role in the emergence of novel genes (Singh and Bansal, 2019), and are thought to have contributed to the evolution of morphological and physiological diversity (True and Carroll, 2002; Kondrashov, 2012; Lallemand et al., 2020). The high rates of duplications that occurred before the metazoan diversification (**Supplementary Figure 2**) suggest that both ancient duplications and the retention of duplicated genes have contributed to the expansion of the gene families. This allowed the emergence of novel functions and possibly promoting the specific evolution of scleractinian SOM proteins. The mechanisms that may lead to gene duplications in scleractinian lineages include tandem duplications, transposable elements, retrotransposition and transduplication, and segmental duplications (Lallemand et al., 2020). Duplicated genes can acquire novel functions, namely, undergoing neofunctionalization and subfunctionalization, where paralogs may carry complementary functions (Thongboonkerd et al., 2002). As we further explain here, it seems that the scleractinian SOM protein evolution is characterized by the gain of SOM-specific genes, supporting a neofunctionalization model.

Despite the many scleractinian SOM protein gene families that appear to be orthologous to diverse phyla, the evolution of scleractinian-specific SOM lineages and their neofunctionalization seem to be the primary force (**Figure 1A**). For example, the aspartic acid-rich gene family (**Figure 3**) is represented by several known SOM proteins from all three scleractinian species with sequenced skeletal proteomes. While known coral SOM proteins in this orthogroup have several orthologous sequences across the cnidarian, molluscan and brachiopod phyla, the orthogroup expansion resulted in the speciation of two distinct scleractinian-specific clusters, each with its own unique last common ancestor (i.e., being spread across the robust and complex clades). A similar example can be found for the metal transport gene tree family (**Figure 4**), where the various scleractinian SOM proteins share diverse orthologous relationships across many phyla, nonetheless converging into a scleractinian-specific branch. Although the scleractinian "biomineralization toolkit" bound in the skeleton seems to differ between species, the presence of multiple orthologs to known SOM proteins seems to indicate that SOM-related functionality emerged in the last common ancestor of scleractinia (**Table 1**). As such, these known SOM orthologs retained a fundamental role in biomineralization and are therefore conserved across scleractinian species.

Going further, we propose that for distinct scleractinian species whose skeletal proteomes have not yet been sequenced, the likelihood of orthologous genes to known SOM proteins found under specific "Scleractinia branches," will be further identified upon proteomic profiling. Subsequently, the ability to have SOM-related gene markers will increase our capability to predict corals' response to changing environments, without the need to perform proteomic analysis on a large number of coral species. However, we acknowledge that our predictions should be taken with certain caveats. While proteomic data representing both the complex and robust scleractinian clades are available, our resolution may be limited, as very few scleractinian species possess a published SOM proteome profile relative to the ∼1,600 known scleractinian species (WoRMS, 2020). Consequently, we are likely missing groups of SOM proteins conserved across species and affiliated with specific growth forms, life strategies and habitats. As such, we suggest that the type of analysis used here will become more robust with the addition of a diverse representation of scleractinian SOM proteomes that will further help identify the "core biomineralization toolkit" across, and between, the scleractinian order.

Altogether, our results clarify the differing evolutionary dynamics of the scleractinian corals' "biomineralization toolkit" as illustrated in **Supplementary Figure 4**. First, we provide further evidence that the evolution of a subset of biomineralization proteins in scleractinians is through a stepwise process (Ramos-Silva et al., 2013; Takeuchi et al., 2016; Murdock, 2020). This is evident by the presence of pre-existing genes shared by an assortment of skeleton forming and non-forming taxa. It suggests that gene co-option played an integral role in the initial development of an extracellular organic matrix in the last common ancestor of the scleractinian order. Second, the differential independent co-option, through gene duplications, followed by sub and neofunctionalization to form lineage-specific proteins and construct species-specific organic matrix frameworks, can have a significant role in distinct skeleton morphology between species. Third, this would supplement the contribution of novel species-specific proteins, crucially allowing organismal plasticity and adaptation to environmental change. While the presence of such lineage- and species-specific key innovations appears to have crucial roles, our results emphasize the importance of the evolutionary dynamics through gene duplications, although the mechanism remains to be revealed.

DATA AVAILABILITY STATEMENT

The datasets presented in this study can be found in online repositories. The names of the repository/repositories and accession number(s) can be found below: https://github.com/OOassafOO/gene-set-overrepresentation-in-trees.

AUTHOR CONTRIBUTIONS

TZ, AM, and TM designed the study. TZ and AM analyzed the data. All authors wrote the manuscript and approved it.

FUNDING

This project was received funding from the European Research Council (ERC) under the European Union's Horizon 2020 Research and Innovation Programme (grant agreement no. 755876 to TM) and from the Israeli Binational Science Foundation (BSF 2016321 to HP and TM). JD was supported by the Zuckerman STEM Leadership Program. Computations presented in this work were performed on the Hive computer cluster at the University of Haifa, which is partly funded by ISF grant 2155/15.

ACKNOWLEDGMENTS

We thank Dr. R. Almuly, M. Morgulis, and Dr. M. Lalzar for helpful discussions, which informed the ideas presented here.

SUPPLEMENTARY MATERIAL

The Supplementary Material for this article can be found online at: https://www.frontiersin.org/articles/10.3389/fgene.2021.618517/full#supplementary-material

REFERENCES

Aguilera, F., McDougall, C., Degnan, B. M., and Irwin, D. (2017). Co-option and de novo gene evolution underlie molluscan shell diversity. *Mol. Biol. Evol.* 34, 779–792. doi: 10.1093/molbev/msw294

Akiva, A., Neder, M., Kahil, K., Gavriel, R., Pinkas, I., Goobes, G., et al. (2018). Minerals in the pre-settled coral *Stylophora pistillata* crystallize via protein and ion changes. *Nat. Commun.* 9:1880. doi: 10.1038/s41467-018-04285-7

Altenhoff, A. M., Glover, N. M., and Dessimoz, C. (2019). *Inferring orthology and paralogy in Methods in Molecular Biology*.Totowa: Humana Press Inc. 149–175. doi: 10.1007/978-1-4939-9074-0_5

Arivalagan, J., Yarra, T., Marie, B., Sleight, V. A., Duvernois-Berthet, E., Clark, M. S., et al. (2016). Insights from the shell proteome: biomineralization to adaptation. *Mol. Biol. Evol.* 34, 66–77. doi: 10.1093/molbev/msw219

Aubry, S., Kelly, S., Kümpers, B. M. C., Smith-Unna, R. D., and Hibberd, J. M. (2014). Deep evolutionary comparison of gene expression identifies parallel recruitment of trans-factors in two independent origins of C_4 photosynthesis. *PLoS Genet.* 10:1004365. doi: 10.1371/journal.pgen.1004365

Bertucci, A., Moya, A., Tambutté, S., Allemand, D., Supuran, C. T., and Zoccola, D. (2013). Carbonic anhydrases in anthozoan corals-A review. *Bioorg. Med. Chem.* 21, 1437–1450. doi: 10.1016/j.bmc.2012.10.024

Bhattacharya, D., Agrawal, S., Aranda, M., Baumgarten, S., Belcaid, M., Drake, J. L., et al. (2016). Comparative genomics explains the evolutionary success of reef-forming corals. *Elife* 5, 1–26. doi: 10.7554/eLife.13288

Choi, I. G., and Kim, S. H. (2006). Evolution of protein structural classes and protein sequence families. *Proc. Natl. Acad. Sci. U. S. A.* 103, 14056–14061. doi: 10.1073/pnas.0606239103

Clark, M. S. (2020). Molecular mechanisms of biomineralization in marine invertebrates. *J. Exp. Biol.* 223:jeb206961. doi: 10.1242/jeb.206961

Cohen, A. L., and McConnaughey, T. A. (2003). Geochemical perspectives on coral mineralization. *Rev. Mineral. Geochem.* 54, 151–187. doi: 10.2113/0540151

Csûös, M. (2010). Count: evolutionary analysis of phylogenetic profiles with parsimony and likelihood. *Bioinformatics* 26, 1910–1912. doi: 10.1093/bioinformatics/btq315

Csûrös, M., and Miklós, I. (2006). "A probabilistic model for gene content evolution with duplication, loss, and horizontal transfer," in *Research in Computational Molecular Biology*, eds A. Apostolico, C. Guerra, S. Istrail, P. A. Pevzner, and M. Waterman (Heidelberg: Springer Berlin Heidelberg), 206–220.

Dollo, L. (1893). The laws of evolution. *Bull. Soc. Bel. Geol. Paleontol.* 7, 164–166.

Domazet-Lošo, T., Brajković, J., and Tautz, D. (2007). A phylostratigraphy approach to uncover the genomic history of major adaptations in metazoan lineages. *Trends Genet.* 23, 533–539.

Doyle, M. A., Gasser, R. B., Woodcroft, B. J., Hall, R. S., and Ralph, S. A. (2010). Drug target prediction and prioritization: using orthology to predict essentiality in parasite genomes. *BMC Genomics* 11:1–14.

Drake, J. L., Mass, T., and Falkowski, P. G. (2014). The evolution and future of carbonate precipitation in marine invertebrates: witnessing extinction or documenting resilience in the Anthropocene? *Elem. Sci. Anthr.* 2:000026. doi: 10.12952/journal.elementa.000026

Drake, J. L., Mass, T., Haramaty, L., Zelzion, E., Bhattacharya, D., and Falkowski, P. G. (2013). Proteomic analysis of skeletal organic matrix from the stony coral *Stylophora pistillata*. *Proc. Natl. Acad. Sci.* 110, 3788–3793. doi: 10.1073/pnas.1301419110

Drake, J. L., Mass, T., Stolarski, J., Von Euw, S., Schootbrugge, B., and Falkowski, P. G. (2020). How corals made rocks through the ages. *Glob. Chang. Biol.* 26, 31–53. doi: 10.1111/gcb.14912

Eisenhaber, F. (2013). *"Prediction of protein function," in Discovering Biomolecular Mechanisms with Computational Biology*. Boston, MA: Springer US, 39–54. doi: 10.1007/0-387-36747-0_4

Emms, D. M., and Kelly, S. (2015). OrthoFinder: solving fundamental biases in whole genome comparisons dramatically improves orthogroup inference accuracy. *Genome Biol.* 16:157. doi: 10.1186/s13059-015-0721-2

Emms, D. M., and Kelly, S. (2019). OrthoFinder: phylogenetic orthology inference for comparative genomics. *Genome Biol.* 20:238. doi: 10.1186/s13059-019-1832-y

Erwin, D. H. (2020). The origin of animal body plans: a view from fossil evidence and the regulatory genome. *Development* 147:dev182899. doi: 10.1242/dev.182899

Evans, J. S. (2019). The biomineralization proteome: protein complexity for a complex bioceramic assembly process. *Proteomics* 2019:1900036. doi: 10.1002/pmic.201900036

Fang, G., Bhardwaj, N., Robilotto, R., and Gerstein, M. B. (2010). Getting started in gene orthology and functional analysis. *PLoS Comput. Biol.* 6:e1000703–e1000703. doi: 10.1371/journal.pcbi.1000703

Farris, J. S. (1977). Phylogenetic analysis under Dollo's law. *Syst. Biol.* 26, 77–88. doi: 10.1093/sysbio/26.1.77

Fernández, R., and Gabaldón, T. (2020). Gene gain and loss across the metazoan tree of life. *Nat. Ecol. Evol.* 4:1069–x. doi: 10.1038/s41559-019-1069-x

Fitch, W. M. (1970). Distinguishing homologous from analogous proteins. *Syst. Zool.* 19, 99–113.

Gabaldón, T., and Koonin, E. V. (2013). Functional and evolutionary implications of gene orthology. *Nat. Rev. Genet.* 14, 360–366. doi: 10.1038/nrg3456

Gal, A., Weiner, S., and Addadi, L. (2015). A perspective on underlying crystal growth mechanisms in biomineralization: solution mediated growth versus nanosphere particle accretion. *Cryst. Eng. Comm* 17, 2606–2615. doi: 10.1039/c4ce01474j

Gavriel, R., Nadav-Tsubery, M., Glick, Y., Yarmolenko, A., Kofman, R., Keinan-Adamsky, K., et al. (2018). The coral protein CARP3 acts from a disordered mineral surface film to divert aragonite crystallization in favor of Mg-calcite. *Adv. Funct. Mater.* 28:1707321. doi: 10.1002/adfm.201707321

Guzman, C., Shinzato, C., Lu, T. M., and Conaco, C. (2018). Transcriptome analysis of the reef-building octocoral, *Heliopora coerulea*. *Sci. Rep.* 8, 1–11. doi: 10.1038/s41598-018-26718-5

Huerta-Cepas, J., Capella-Gutiérrez, S., Pryszcz, L. P., Marcet-Houben, M., and Gabaldón, T. (2014). PhylomeDB v4: Zooming into the plurality of evolutionary histories of a genome. *Nucleic Acids Res.* 42, D897–D902. doi: 10.1093/nar/gkt1177

Katoh, K., and Standley, D. M. (2013). MAFFT multiple sequence alignment software version 7: improvements in performance and usability. *Mol. Biol. Evol.* 30, 772–780. doi: 10.1093/molbev/mst010

King, N., Westbrook, M. J., Young, S. L., Kuo, A., Abedin, M., Chapman, J., et al. (2008). The genome of the choanoflagellate Monosiga brevicollis and the origin of metazoans. *Nature* 451, 783–788. doi: 10.1038/nature06617

Kitahara, M. V., Cairns, S. D., Stolarski, J., Blair, D., and Miller, D. J. (2010). A comprehensive phylogenetic analysis of the Scleractinia (Cnidaria, Anthozoa) based on mitochondrial CO1 sequence data. *PLoS One* 5:e11490. doi: 10.1371/journal.pone.0011490

Klont, F., Bras, L., Wolters, J. C., Ongay, S., Bischoff, R., Halmos, G. B., et al. (2018). Assessment of sample preparation bias in mass spectrometry-based proteomics. *Anal. Chem.* 90, 5405–5413. doi: 10.1021/acs.analchem.8b00600

Knoll, A. H. (2003). Biomineralization and evolutionary history. *Rev. Mineral. Geochem.* 54, 329–356. doi: 10.2113/0540329

Kocot, K. M., Aguilera, F., McDougall, C., Jackson, D. J., and Degnan, B. M. (2016). Sea shell diversity and rapidly evolving secretomes: insights into the evolution of biomineralization. *Front. Zool.* 13:23. doi: 10.1186/s12983-016-0155-z

Kondrashov, F. A. (2012). Gene duplication as a mechanism of genomic adaptation to a changing environment. *Proc. R. Soc. B Biol. Sci.* 279, 5048–5057. doi: 10.1098/rspb.2012.1108

Lafond, M., Meghdari Miardan, M., and Sankoff, D. (2018). Accurate prediction of orthologs in the presence of divergence after duplication. *Bioinformatics* 34, i366–i375.

Laipnik, R., Bissi, V., Sun, C. Y., Falini, G., Gilbert, P. U. P. A., and Mass, T. (2019). Coral acid rich protein selects vaterite polymorph in vitro. *J. Struct. Biol.* 209, 107431. doi: 10.1016/j.jsb.2019.107431

Lallemand, T., Leduc, M., Landčs, C., Rizzon, C., and Lerat, E. (2020). An overview of duplicated gene detection methods: Why the duplication mechanism has to be accounted for in their choice. *Genes* 11:1046. doi: 10.3390/genes11091046

Laumer, C. E., Fernández, R., Lemer, S., Combosch, D., Kocot, K. M., Riesgo, A., et al. (2019). Revisiting metazoan phylogeny with genomic sampling of all phyla. *Proc. R. Soc. B Biol. Sci.* 286:20190831. doi: 10.1098/rspb.2019.0831

Livingston, B. T., Killian, C. E., Wilt, F., Cameron, A., Landrum, M. J., Ermolaeva, O., et al. (2006). A genome-wide analysis of biomineralization-related proteins in the sea urchin *Strongylocentrotus purpuratus*. *Dev. Biol.* 300, 335–348. doi: 10.1016/j.ydbio.2006.07.047

Lowenstam, H. A., and Weiner, S. (1989). *On biomineralization*. Oxford: Oxford University Press on Demand.

Mann, S. (2001). *Biomineralization: principles and concepts in bioinorganic materials chemistry*. Oxford: Oxford University Press on Demand.

Marin, F., and Luquet, G. (2008). *Unusually acidic proteins in biomineralization in Handbook of Biomineralization*. Germany: Wiley-VCH Verlag GmbH, 273–290. doi: 10.1002/9783527619443.ch16

Marin, F., Bundeleva, I., Takeuchi, T., Immel, F., and Medakovic, D. (2016). Organic matrices in metazoan calcium carbonate skeletons: composition, functions, evolution. *J. Struct. Biol.* 196, 98–106. doi: 10.1016/j.jsb.2016.04.006

Mass, T., Drake, J. L., Haramaty, L., Kim, J. D., Zelzion, E., Bhattacharya, D., et al. (2013). Cloning and characterization of four novel coral acid-rich proteins that precipitate carbonates *in vitro*. *Curr. Biol.* 23, 1126–1131. doi: 10.1016/j.cub.2013.05.007

Mass, T., Putnam, H. M., Drake, J. L., Zelzion, E., Gates, R. D., Bhattacharya, D., et al. (2016). Temporal expression pattern of biomineralization proteins during early development in the stony coral *Pocillopora damicornis*. *Proc. R. Soc. B Biol. Sci.* 2016:283.

McLennan, D. A. (2008). The concept of co-option: Why evolution often looks miraculous. *Evol. Educ. Outreach* 1, 247–258. doi: 10.1007/s12052-008-0053-8

Mello, C. V., Lovell, P. V., and Wirthlin, M. (2018). *Discovery of novel genes and other lineage-specific features through comparative genomics in Molecular-Genetic and Statistical Techniques for Behavioral and Neural Research*. 225–241. Amsterdam: Elsevier Inc., doi: 10.1016/B978-0-12-804078-2.00010-6

Moberg, F., and Folke, C. (1999). Ecological goods and services of coral reef ecosystems. *Ecol. Econ.* 29, 215–233. doi: 10.1016/S0921-8009(99)00009-9

Murdock, D. J. E. (2020). The 'biomineralization toolkit' and the origin of animal skeletons. *Biol. Rev.* 2020:brv.12614. doi: 10.1111/brv.12614

Murdock, D. J. E., and Donoghue, P. C. J. (2011). Evolutionary origins of animal skeletal biomineralization. *Cells Tissues Organs* 194, 98–102. doi: 10.1159/000324245

Nguyen, L.-T., Schmidt, H. A., Von Haeseler, A., and Minh, B. Q. (2015). IQ-TREE: a fast and effective stochastic algorithm for estimating maximum-likelihood phylogenies. *Mol. Biol. Evol.* 32, 268–274.

Paps, J., and Holland, P. W. H. (2018). Reconstruction of the ancestral metazoan genome reveals an increase in genomic novelty. *Nat. Commun.* 9, 1–8.

Peled, Y., Drake, J. L., Malik, A., Almuly, R., Lalzar, M., Morgenstern, D., et al. (2020). Optimization of skeletal protein preparation for LC–MS/MS sequencing yields additional coral skeletal proteins in Stylophora pistillata. *BMC Mater.* 2:8. doi: 10.1186/s42833-020-00014-x

Ramos-Silva, P., and Marin, F. (2015). Proteins as functional units of biocalcification – an overview. *Key Eng. Mater.* 672, 183–190. doi: 10.4028/www.scientific.net/KEM.672.183

Ramos-Silva, P., Kaandorp, J., Huisman, L., Marie, B., Zanella-Cléon, I., Guichard, N., et al. (2013). The skeletal proteome of the coral *Acropora millepora*: the evolution of calcification by co-option and domain shuffling. *Mol. Biol. Evol.* 30, 2099–2112. doi: 10.1093/molbev/mst109

Rastogi, S., and Liberles, D. A. (2005). Subfunctionalization of duplicated genes as a transition state to neofunctionalization. *BMC Evol. Biol.* 5:28. doi: 10.1186/1471-2148-5-28

Richter, D. J., Fozouni, P., Eisen, M. B., and King, N. (2018). Gene family innovation, conservation and loss on the animal stem lineage. *Elife* 7:e34226.

Riehemann, K., and Sorg, C. (1993). Sequence homologies between four cytoskeleton-associated proteins. *Trends Biochem. Sci.* 18, 82–83. doi: 10.1016/0968-0004(93)90159-K

Romano, S. L., and Palumbi, S. R. (1996). Evolution of scleractinian corals inferred from molecular systematics. *Science* 271, 640–642. doi: 10.1126/science.271.5249.640

Schalchian-Tabrizi, K., Minge, M. A., Espelund, M., Orr, R., Ruden, T., Jakobsen, K. S., et al. (2008). Multigene phylogeny of Choanozoa and the origin of animals. *PLoS One* 3:0002098. doi: 10.1371/journal.pone.0002098

Seppey, M., Manni, M., and Zdobnov, E. M. (2019). *BUSCO: Assessing genome assembly and annotation completeness in Methods in Molecular Biology*. Totowa: Humana Press Inc., 227–245. doi: 10.1007/978-1-4939-9173-0_14

Singh, T. R., and Bansal, A. (2019). *"Phylogenetic analysis: gene duplication and speciation," in Encyclopedia of Bioinformatics and Computational Biology*. Amsterdam: Elsevier, 965–974. doi: 10.1016/B978-0-12-809633-8.20176-3

Sinha, S., Eisenhaber, B., and Lynn, A. M. (2018). *"Predicting protein function using homology-based methods," in Bioinformatics: Sequences, Structures, Phylogeny*. Berlin: Springer, 289–305.

Stolarski, J., Kitahara, M. V., Miller, D. J., Cairns, S. D., Mazur, M., and Meibom, A. (2011). The ancient evolutionary origins of Scleractinia revealed by azooxanthellate corals. *BMC Evol. Biol.* 11:316. doi: 10.1186/1471-2148-11-316

Takeuchi, T., Yamada, L., Shinzato, C., Sawada, H., and Satoh, N. (2016). Stepwise evolution of coral biomineralization revealed with genome-wide proteomics and transcriptomics. *PLoS One* 11:0156424. doi: 10.1371/journal.pone.0156424

Tambutté, S., Holcomb, M., Ferrier-Pagès, C., Reynaud, S., Tambutté, É, Zoccola, D., et al. (2011). Coral biomineralization: from the gene to the environment. *J. Exp. Mar. Bio. Ecol.* 408, 58–78. doi: 10.1016/j.jembe.2011.07.026

Thongboonkerd, V., Mcleish, K. R., Arthur, J. M., and Klein, J. B. (2002). Proteomic analysis of normal human urinary proteins isolated by acetone precipitation or ultracentrifugation. *Kidney Int.* 62:1461-1469. doi: 10.1111/j.1523-1755.2002.kid565.x

True, J. R., and Carroll, S. B. (2002). Gene co-option in physiological and morphological evolution. *Annu. Rev. Cell Dev. Biol.* 18, 53–80. doi: 10.1146/annurev.cellbio.18.020402.140619

Veron, J. E. N. (2000). *Corals of the world*. Australia: Australian Institute of Marine Science.

Veron, J. E. N., Hoegh-Guldberg, O., Lenton, T. M., Lough, J. M., Obura, D. O., Pearce-Kelly, P., et al. (2009). The coral reef crisis: the critical importance of $<$350 ppm CO_2. *Mar. Pollut. Bull.* 58, 1428–1436. doi: 10.1016/J.MARPOLBUL.2009.09.009

Weiner, S. (2003). An overview of biomineralization processes and the problem of the vital effect. *Rev. Mineral. Geochemistry* 54, 1–29. doi: 10.2113/0540001

WoRMS, E. B. (2020). *World register of marine species (WoRMS)*.Belgium:World register of marine species.

Ying, H., Cooke, I., Sprungala, S., Wang, W., Hayward, D. C., Tang, Y., et al. (2018). Comparative genomics reveals the distinct evolutionary trajectories of the robust and complex coral lineages. *Genome Biol.* 19, 1–24. doi: 10.1186/s13059-018-1552-8

Zoccola, D., Innocenti, A., Bertucci, A., Tambutté, Ć, Supuran, C., Tambutté, S., et al. (2016). Coral carbonic anhydrases: regulation by ocean acidification. *Mar. Drugs* 14:109. doi: 10.3390/md14060109

Conflict of Interest: The authors declare that the research was conducted in the absence of any commercial or financial relationships that could be construed as a potential conflict of interest.

frontiers in Genetics

ORIGINAL RESEARCH
published: 05 February 2021
doi: 10.3389/fgene.2021.622400

Mantle Modularity Underlies the Plasticity of the Molluscan Shell: Supporting Data From *Cepaea nemoralis*

*Daniel J. Jackson**

Department of Geobiology, Georg-August University of Göttingen, Göttingen, Germany

Molluscs have evolved the capacity to fabricate a wide variety of shells over their 540+ million-year history. While modern sequencing and proteomic technologies continue to expand the catalog of molluscan shell-forming proteins, a complete functional understanding of how any mollusc constructs its shell remains an ambitious goal. This lack of understanding also constrains our understanding of how evolution has generated a plethora of molluscan shell morphologies. Taking advantage of a previous expression atlas for shell-forming genes in *Lymnaea stagnalis*, I have characterized the spatial expression patterns of seven shell-forming genes in the terrestrial gastropod *Cepaea nemoralis*, with the aim of comparing and contrasting their expression patterns between the two species. Four of these genes were selected from a previous proteomic screen of the *C. nemoralis* shell, two were targeted by bioinformatics criteria designed to identify likely shell-forming gene products, and the final one was a clear homolog of a peroxidase sequence in the *L. stagnalis* dataset. While the spatial expression patterns of all seven *C. nemoralis* genes could be recognized as falling into distinct zones within the mantle tissue similar to those established in *L. stagnalis*, some zones have apparently been modified. These similarities and differences hint at a modularity to the molluscan mantle that may provide a mechanistic explanation as to how evolution has efficiently generated a diversity of molluscan shells.

Keywords: biomineralization, plasticity, modularity, *Cepaea nemoralis*, shell formation, evolution, mantle, mollusc

OPEN ACCESS

Edited by:
Frederic Marin,
Délégation Centre-Est (CNRS), France

Reviewed by:
Robert A. Haney,
Ball State University, United States
Feng Zhang,
Chinese Academy of Agricultural Sciences (CAAS), China

***Correspondence:**
Daniel J. Jackson
djackso@uni-goettingen.de

Specialty section:
This article was submitted to Evolutionary and Population Genetics, a section of the journal Frontiers in Genetics

Received: *28 October 2020*
Accepted: *04 January 2021*
Published: *05 February 2021*

Citation:
Jackson DJ (2021) Mantle Modularity Underlies the Plasticity of the Molluscan Shell: Supporting Data From Cepaea nemoralis. Front. Genet. 12:622400. doi: 10.3389/fgene.2021.622400

INTRODUCTION

Animals fabricate a spectacular variety of biomineralized structures that serve almost all conceivable biological functions. From predation (Dietl and Vega, 2008), defense (Edgell et al., 2008), reproduction (Lodi and Koene, 2016) and vision (Aizenberg and Hendler, 2004), to navigation (Söllner et al., 2003), locomotion (Wilkinson, 2008) and buoyancy control (Greenwald and Ward, 2010), the evolution of the ability to precisely control the assembly of mineralized structures was a milestone in the rise of complex life (Murdock, 2020). From a molecular and cellular perspective, a complete understanding of the biomineralization process in any animal model remains elusive. Related to this incomplete functional understanding is a dearth of knowledge regarding the way in which evolution modifies

the mechanisms of biomineralization to generate structures that fulfill different biological requirements. This is perhaps exemplified no better than within the phylum Mollusca. Shelled molluscs, and in particular gastropods, have evolved an impressive diversity of shells over the last 540+ million years. The evolutionary plasticity of the shell is likely one of the reasons molluscs have diversified so extensively, allowing them to occupy almost every ecological niche on the planet. Despite this, and the long-standing scientific and cultural fascination we have for molluscan shells (Sakalauskaite et al., 2019; Marin, 2020), a plausible and widely accepted hypothesis that can explain how evolution has generated this shelled diversity remains elusive.

Molluscs employ a variety of proteins (and other important biomolecules such as polysaccharides and lipids) to construct (primarily) calcified shells. Despite their paucity in the mature biomineral (often < 5% w/w), these biomolecules significantly influence many features of the shell including, but not restricted to, the crystallography (for example whether aragonite or calcite is deposited; Arroyo-Loranca et al., 2020), the mechanical properties (increased fracture resistance; Meyers et al., 2009) and pigmentation (Williams, 2017). The importance of these molecules has seen many proteomic, transcriptomic and genomic screens of conchiferans (shelled molluscs) aimed at the identification and comparison of their shell-forming protein repertoires (Joubert et al., 2010; Berland et al., 2011; Marie et al., 2011; Sleight et al., 2016; Yarra et al., 2016; Wang et al., 2017; Le Luyer et al., 2019; Malachowicz and Wenne, 2019; Xu et al., 2019). To this end, we previously surveyed and characterized the shell-forming proteome of the freshwater gastropod *Lymnaea stagnalis* (Herlitze et al., 2018). In that work we were able to spatially map the expression patterns of more than 30 shell-forming genes in developmental stages and in the adult shell-forming mantle tissue. This allowed us to recognize a modularity to the adult mantle tissue of *L. stagnalis*. We hypothesized that this modularity may be a key feature of all molluscan mantle tissues that would allow for the efficient modification and evolution of distinct regions within the mantle tissue to generate shells with novel features; for example increasing the thickness of the nacreous layer independently of the outer pigmented periostracum, or to modify the crystallographic orientation of nacre tablets independently of the prismatic layer. To further explore this idea of a modular organization of the shell-forming mantle tissue I have characterized the spatial expression patterns of seven major shell-forming genes in the terrestrial gastropod *Cepaea nemoralis*, a representative of a clade of molluscs that have received relatively little attention in terms of the molecular biology of biomineralization. These seven genes include a set of four previously identified shell-forming genes (Mann and Jackson, 2014), and three additional typical shell-forming genes. By comparing their spatial expression patterns with our previous results for *L. stagnalis* (Herlitze et al., 2018). I observe both striking similarities and differences. These observations provide further support for the notion that the molluscan mantle tissue can be subdivided into morphological modules (Eble et al., 2005; Esteve-Altava, 2016, 2017). This hypothetical framework provides a platform from which testable hypothesis of molluscan shell evolution can be built and tested.

MATERIALS AND METHODS

Animals and *in situ* Hybridization Preparation

Juvenile *C. nemoralis* (recognized by the absence of the terminal pigmented lateral stripe in the shell) were collected from the surrounds of Göttingen in the spring of 2020. Juveniles were collected as they were assumed to be relatively rapidly depositing shell material and therefore to be expressing shell-forming genes. Total RNA was extracted from the mantle tissue of several individuals using Qiazol (Qiagen #79306) as a Trizol substitute. RNA integrity was observed via denaturing gel electrophoresis and quantified using a Nanodrop spectrophotometer. Complementary DNA (cDNA) was synthesized by first combining 1 μg of total RNA with 5 μL of 10 μM oligodT primer in a 10 μL volume and heating to 70°C for 10 min. To this mixture 5 μL of MMLV-RT buffer, 1 μL of 10 mM dNTPs, 8 μL of nuclease-free water and 1 μL Promega's MMLV-RT H^- point mutant (#M3682) was added, mixed and then incubated at 42°C for 90 min. This cDNA was used as template DNA in PCRs with primers designed to amplify 4 shell-forming genes previously identified in Mann and Jackson (2014), and 2 Glycine-rich shell forming genes, similar to the Shematrin gene family known to play a role in shell formation in oysters (Yano et al., 2006) and also an "animal heme dependent peroxidase" gene product that is a likely ortholog to *Lstag-sfc-5* that we previously studied in *L. stagnalis* (Herlitze et al., 2018). Details of the primers used to amplify these genes and PCR amplicon lengths are provided in **Supplementary File 1**. PCR products were cloned and confirmed by Sanger sequencing using procedures described in Herlitze et al. (2018). For *in situ* hybridization (ISH) a range of size classes (approximately 10–15 mm shell length) were studied to minimize the potential influence of age-specific gene expression patterns. Prior to fixation for ISH the shells of juvenile snails were gently cracked to allow for a more complete and rapid penetration of the fixative. Juvenile snails were fixed in 3.7% formaldehyde in PBSTw (1× PBS buffer with 0.1% Tween20) for 1 h at room temperature. After 30 min the fixative solution was renewed. Fixed snails were subsequently washed several times with PBSTw, and then dehydrated through an increasing EtOH series. Animals were given three washes in 100% EtOH and stored at −20°C. ISH was performed on at least 10 individuals for each gene.

Paraffin Embedding, Sectioning, ISH, and Histology

Tissue preparation and ISH was broadly performed as described in Herlitze et al. (2018). Individuals selected for ISH were brought to room temperature and the shell was gently removed with a scalpel and tweezers while submerged in 100% ethanol. Once de-shelled each individual was cut sagittally using a razor blade such that two approximately equal halves (a left and right side) were produced. These halves were then further dehydrated in 100% ethanol for 1 h at room temperature to ensure all remaining water was displaced, and then incubated in xylene at room temperature overnight with gentle rocking. The next day tissue pieces were

given a rinse with fresh xylene and then placed into molten paraffin which was allowed to perfuse the tissue for 24 h. The opposing halves of several individuals were then arranged in an embedding cassette such that the left and right half would be located next to each other, and the paraffin was allowed to set. Sections (12 μm thick) were then taken and collected onto polysine slides (Roth #ET10.1) and allowed to dry at 37°C overnight. Sections were de-waxed with 3× 10-min washes in xylene, and then re-hydrated through a descending ethanol series. Slides were then installed into an Intavis (now CEM) InSituPro Vsi liquid handling robot. An outline of the steps performed by the InSituPro follows: All slides received 2× 5-min washes of PBSTw before being treated with 0.1 U/mL Proteinase-K (NEB #P8107) diluted in PBSTw for 10 min at room temperature. Proteinase-K digestion was stopped with 2× 5-min washes of 0.2% glycine in PBSTw and 2× 5-min washes of PBSTw. Reactive amino groups were acetylated first with 1× 5-min wash of 1% (v/v) triethanolamine (TEA) in PBS, then with 2× 5-min washes of 1% TEA + 0.3% acetic anhydride (AA). These solutions were subsequently washed out with 2× 5-min washes of PBSTw. Tissue sections were then brought into hybridization buffer (5× SSC; 5 mM EDTA; 50% formamide; 100 μg/mL heparin; 0.1% Tween; 100 μg/mL salmon sperm; 1× Denhardt's) with 2× 5-min washes at room temperature, followed by an elevation in temperature to 50°C for 30 min. Riboprobes were then added and the slides were brought to 75°C for 20 min to allow the probe and target to denature, followed by an 18 h incubation at 50°C. Excess probe was washed out at 50°C with one wash each of 4× (4× SSC, 50% formamide, 0.1% Tween), 2× (2× SSC, 50% formamide, 0.1% Tween) and 1× (1× SSC, 50% formamide, 0.1% Tween) wash solutions. Slides were brought into 1× SSC + 0.1% Tween and to room temperature before being rinsed 2× with PBSTw. Non-specifically bound riboprobe was digested with a single wash of 0.2 μg/mL RNAse A (NEB #T3018) in PBSTw followed by 2× PBSTw washes. Slides were brought into maleic acid buffer (MAB = 0.1M maleic acid; 0.15M NaCl; pH 7.5) with a 10-min wash, and were then blocked in 2% block (Roche #11 096 176 001) dissolved in MAB for 1 h at room temperature. Anti-Digoxigenin-AP, Fab fragments (Roche #11093274910) diluted 1/5,000 in 2% block was then applied and incubated at room temperature for 8 h. Excess antibody was washed out with 15× 15 min washes of PBSTw before tissue sections were brought into alkaline phosphatase color development buffer (AP = 0.1M NaCl; 0.1M Tris; pH 9.5). Slides were then removed from the InSituPro and 200 μL of color development solution (AP + 50 mM MgCl2 + 450 μg/mL NBT + 175 μg/mL BCIP) was applied manually to each slide and monitored for color development. Once the signal intensity was deemed adequate, the color reaction was stopped with several washes in water. Slides were finally mounted in an aqueous resin (Roth #2848) and imaged with a Zeiss StereoV8 and Axio ImagerM2.

De-waxed paraffin sections of *L. stagnalis* were also prepared (as described above) and stained simultaneously with *C. nemoralis* sections using Giemsa (Roth #T862.1). Briefly, a working stock of Giemsa stain was prepared by taking 600 μL of stock solution into 50 mL of distilled water. Sections were stained overnight at room temperature, rinsed briefly in distilled water, differentiated with 0.5% aqueous acetic acid for less than 30 s, washed in tap water for 10 min and mounted in an aqueous medium with DAPI.

Sequence Alignments and Phylogenetic Analysis

All peroxidase sequences with similarity to Lstag_sfc_5 (Herlitze et al., 2018) were extracted from both the *L. stagnalis* genome (submitted to NCBI) and a re-assembly of our previously reported *C. nemoralis* transcriptome (Mann and Jackson, 2014) using tBLASTn. *C. nemoralis* sequences with similarity to Lstag_sfc_22 (Herlitze et al., 2018) were identified using tBLASTn. The best match (Cnem_R27072766) was aligned to Lstag_sfc_22 using Seaview v. 4.7 with default parameters (Gouy et al., 2010) and the resulting alignment submitted to MView[1]. Other sequences with similarity to Cnem_R27072766 were identified from SwissProt, GenBank's nr database and the *L. stagnalis* genome using tBLASTn. Protein sequences were aligned using Seaview (as above) and conserved regions were identified using Gblocks (Talavera and Castresana, 2007). See the **Supplementary Material** for both the complete and Gblock-ed peroxidase (**Supplementary Files 2, 3**) and chitin-binding periotrophin-A alignments (**Supplementary Files 4, 5**). Phylogenetic analyses were performed with MrBayes v. 3.2.7a (Ronquist et al., 2012) with the following parameters: lset rates = gamma; prset aamodelpr = mixed; mcmcp nruns = 4, ngen = 2,000,000, nchains = 4, savebrlens = yes temp = 0.2 stoprule = yes stopval = 0.005. This number of generations was adequate for the stop value to be reached and the convergence diagnostic (Potential Scale Reduction Factor) was 1.000 for both analyses.

RESULTS

Sequence Features

Four of the seven genes investigated here were previously identified by proteomic work on shells of *C. nemoralis* (Mann and Jackson, 2014). In that previous work 59 gene products accounted for > 90% of all identifiable peptides in the shell of *C. nemoralis*. Here, four of these gene products (R27072837, R27072766, R27073283, and R27075188) which accounted for a total of almost 40% of the shell-protein content (Mann and Jackson, 2014), were cloned and studied further. The remaining three genes were selected from an assembly of *C. nemoralis* transcriptome data (Mann and Jackson, 2014) because they either had features indicative of a role in shell-formation with a distinctive expression pattern (glycine-rich-2 and -3 have unusually high glycine contents and are expressed in zone 3 of the *L. stagnalis* mantle) or provided a clear example of an ortholog to a shell-forming gene previously spatially characterized in the mantle tissue of *L. stagnalis* (Herlitze et al., 2018). All seven of the derived protein sequences possess a signal sequence and are therefore likely to be secreted from the mantle tissue (**Supplementary Files 6–8**).

[1]https://www.ebi.ac.uk/Tools/msa/mview/

R27072766 (Chitin Binding Periotrophin-A Domain)

Cepaea nemoralis contig R27072766 is 2,716 nucleotides long and encodes an open reading frame (ORF) of 727 amino acid residues. BLASTp searches against SwissProt returned sequences with significant similarity to several shell-associated proteins from bivalves implicated in the formation of nacre (**Supplementary File 9**) including Pif (Suzuki et al., 2009). A search for conserved domains revealed a clear chitin binding periotrophin-A domain (**Figure 1** and **Supplementary File 10**). Searching the Cnem-R27072766 sequence against the *L. stagnalis* transcriptome reported in Herlitze et al. (2018) returned Lstag_sfc_22 as the top hit. A phylogenetic analysis of all of these sequences grouped the *C. nemoralis* R27072766 and *L. stagnalis* jg75923.t1 sequences (along with a *Biomphalaria glabrata*) sequence with strong support (**Figure 2**), indicating that our proteomic screen of the *C. nemoralis* shell (Mann and Jackson, 2014) identified the ortholog of Lstag_sfc_22, a protein identified by our proteomic screen of the *L. stagnalis* shell (Herlitze et al., 2018).

Peroxidase

Cepaea nemoralis contig R37577449 is 2,200 nucleotides long, contains an "animal haem dependent peroxidase" domain (**Figure 3** and **Supplementary File 10**) and shares sequence similarity with a diverse range of peroxidases from vertebrates and invertebrates (**Supplementary File 9**). There are a number of peroxidase-domain containing contigs in both the *C. nemoralis* transcriptome and the *L. stagnalis* genome (**Supplementary File 11**), however, a phylogenetic analysis revealed that *Cnem*_R37577449 was more closely related to *Lsta_jg27188.t1* [the gene model for the previously

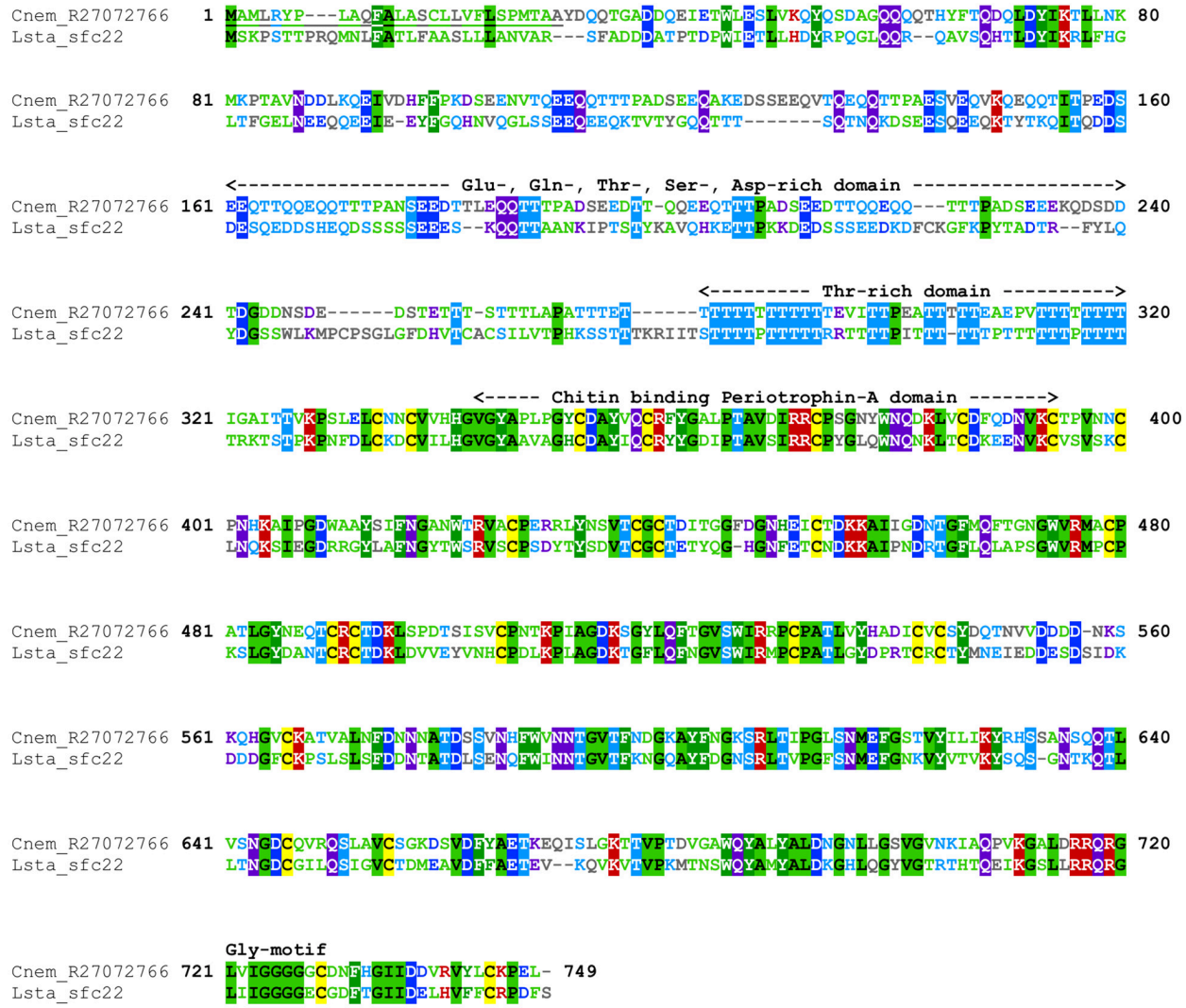

FIGURE 1 | Annotated alignment of Cnem-R27072766 and Lstag-sfc_22. These orthologous shell-forming proteins (see **Figure 2**) each possess a signal sequence (underlined) and domains rich in Glu, Gln, Thr, Ser, and Asp. The locations of 24 Cys residues are conserved, and the chitin binding domain displays a high degree of sequence conservation. Cnem-R27072766 was identified from a proteomic screen of the *C. nemoralis* shell (Mann and Jackson, 2014) and Lstag_sfc_22 was identified from a proteomic screen of the *L. stagnalis* shell (Herlitze et al., 2018).

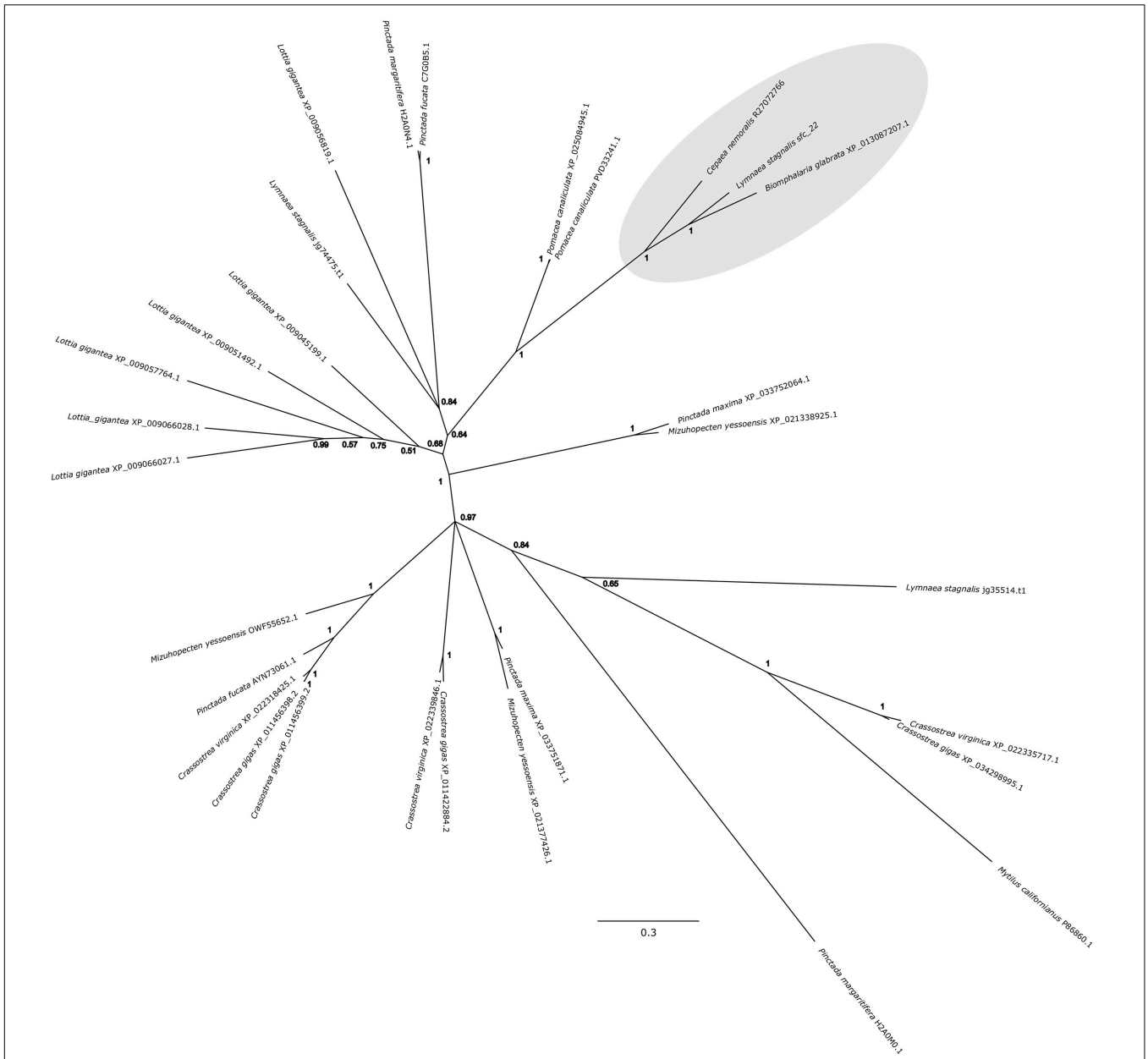

FIGURE 2 | Bayesian phylogenetic analysis of homologous chitin binding Periotrophin-A sequences. The tree presented here is midpoint rooted and posterior probabilities for each node are indicated. The previously studied peroxidase sequence from *L. stagnalis* Lsta_sfc_22 (see Herlitze et al., 2018) and the *C. nemoralis* peroxidase sequence reported here, Cnem-R27072766, along with a sequence from *Biomphalaria glabrata* are highlighted in gray. See **Supplementary Files 4, 5** for the aligned sequences used to generate this phylogeny.

reported Lstag_sfc_5 in Herlitze et al. (2018)] than to any other sequence (**Figure 4**).

Glycine-Rich-2 and -3

A screen of a previous *C. nemoralis* mantle transcriptome assembly (Mann and Jackson, 2014) for ORFs that possess a signal sequence and mature protein sequences with anomalous amino acid contents revealed several secreted glycine-rich contigs. Two of these were cloned and apparently possess glycine contents of >50% and high tyrosine contents (13.1 and 19.2%), however, it must be noted that *Cnem*-gly-rich-2 (339 nucleotides long) is apparently not full length as a stop codon could not be identified (**Figure 5** and **Supplementary Files 7, 8**). This sequence was nonetheless selected for further characterization because of the extremely glycine-rich domain evident at the amino-terminus of the secreted protein.

Novel Genes R27072837, R27073283, and R27075188

Cnem-R27072837 (2,379 nucleotides), Cnem-R27073283 (1,878 nucleotides) and Cnem-R27075188 (1,827 nucleotides) encode

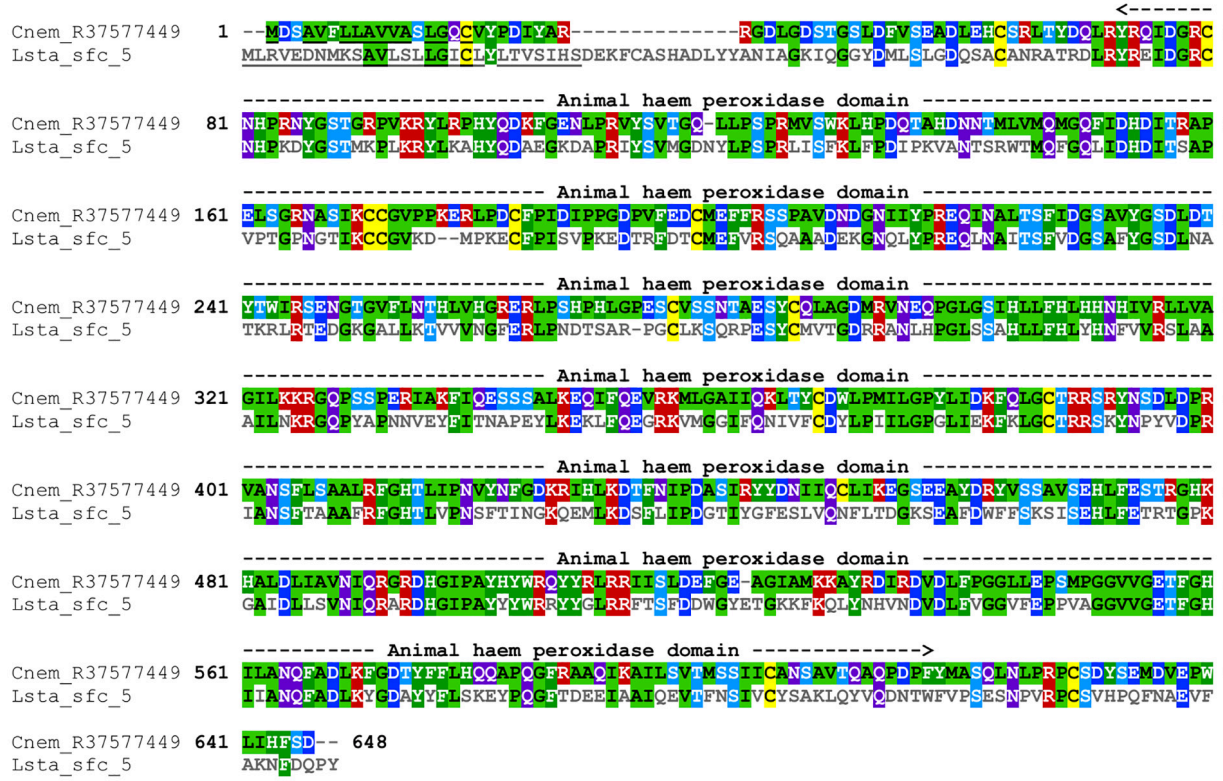

FIGURE 3 | Annotated alignment of Cnem-R37577449 and Lsta_sfc_5. These orthologous shell-forming proteins (see **Figure 4**) each possess a signal sequence (underlined), and conserved "Animal haem peroxidase" domains (see **Supplementary File 10**). Cnem-R37577449 was identified from a proteomic screen of the *C. nemoralis* shell (Mann and Jackson, 2014) and Lstag_sfc_5 was identified from a proteomic screen of the *L. stagnalis* shell (Herlitze et al., 2018).

proteins that were previously identified in a proteomic screen of the *C. nemoralis* shell (Mann and Jackson, 2014). None of the translated products of these genes possessed recognizable domains or shared similarity with sequences in the SwissProt database (however, these sequences did return hits against the nr database that were strictly gastropod, see **Supplementary File 12**). Cnem-R27072837 is notable as it was previously identified as being the most abundant recognizable protein in the shell of *C. nemoralis* (Mann and Jackson, 2014) accounting for more than 26% (by iBaq abundance) of all identifiable proteins. The mature (secreted) protein is also predicted to have unusually high glycine (12.4%) and proline (20.7%) contents (**Supplementary Files 6, 8**). Cnem-R27072837 and Cnem-R27075188 are also likely orthologs to proteins we previously identified in a proteomic screen of the *L. stagnalis* shell [Lsta_sfc_27 and Lsta_sfc_20, respectively, see **Supplementary Files 13, 14**; (Herlitze et al., 2018)]. While Cnem-R27073283 has a likely ortholog in the *L. stagnalis* genome (jg37438.t1) we have not yet studied the expression pattern of that gene in *L. stagnalis*.

Comparative Histology

Giemsa stained paraffin sections of *C. nemoralis* and *L. stagnalis* tissue sections revealed broad similarities and subtle differences in the arrangement of cells within the mantle tissue of each species (**Figure 6**). While zone 5 of the mantle (the proximal, squamous epithelium that covers most of the animal) appears to be largely similar between the two species (**Figures 6E,E'**), the distal-most leading edge of the mantle that is comprised of zones 1–4 and is responsible for the growth of the shell at its very edge, revealed clear differences. Perhaps the most noticeable difference was in the morphology of the belt (zones 2 and 3; **Figures 6C,D'**). In *C. nemoralis* the darkly stained belt appears to be comprised of cells that are not oriented in any appreciable way. The nuclei of these cells are not located basally, and the cells themselves do not have a classic columnar morphology (**Figure 6D**). In contrast, the belt of *L. stagnalis* is comprised of tall columnar cells with the nucleus clearly basal to the cell (**Figure 6D'**). In addition, in *C. nemoralis* at the base of the periostracal groove (which is responsible for the secretion of the periostracum) there is a population of cells with basally located nuclei that is not apparent in *L. stagnalis* (*cf.* **Figures 6D,D'**).

ISH

All seven of the genes studied here gave consistent, clear and distinct expression patterns in the mantle tissue of all of the *C. nemoralis* individuals investigated. The four genes that were previously identified by a proteomic screen of the *C. nemoralis* shell (updated contig names R27072837, R27072766, R27073283, R27075188) are all within the top 8 most abundant proteins identified within the *C. nemoralis* shell, with contig R27072837

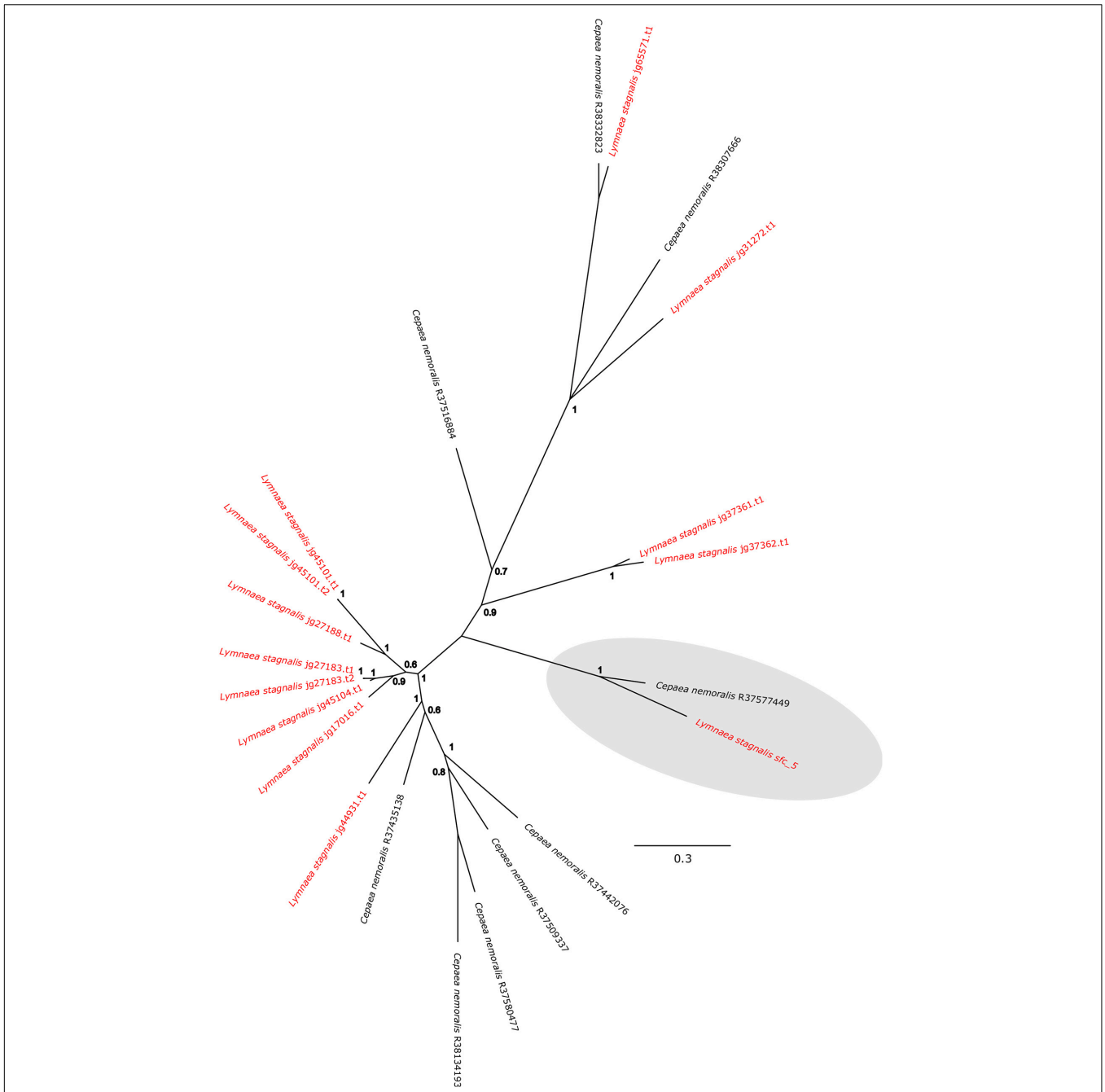

FIGURE 4 | Bayesian phylogenetic analysis of *L. stagnalis* and *C. nemoralis* peroxidase sequences. The tree presented here is midpoint rooted and all *L. stagnalis* sequences are highlighted in red. Posterior probabilities for each node are indicated and the previously studied peroxidase sequence from *L. stagnalis* Lsta_sfc_5 (see Herlitze et al., 2018) and the *C. nemoralis* peroxidase sequence reported here Cnem-R37577449 are highlighted in gray. See **Supplementary Files 2, 3** for the aligned sequences used to generate this phylogeny.

```
Cnem_Gly_rich2    1 MYKTVLVVAFIAAAVLTVQGGCYGGGGLGLGGVIVGGLGGYGGGYGGGYCRQGVALTVAQPLVVGGYGGGYCSGYGGGYGG 81

Cnem_R37432942    1 MYKPVAVLMLVATLSMSAEAIVGGYGIGFPGYGLGIGKYGYGGYGIGGLGLGGLGYGVGGYGYGLGGYGYGLGGAGYGLGGIGVGYGIGGIYGKGLYY* 98
```

FIGURE 5 | Sequence features of *C. nemoralis* glycine-rich proteins expressed in the mantle. These contigs were identified from a *C. nemoralis* mantle transcriptome after searching for translations that gave proteins with a detectable signal sequence and high glycine contents. For each sequence the signal sequence is underlined. Note that Cnem-Gly-rich 2 is apparently not full-length.

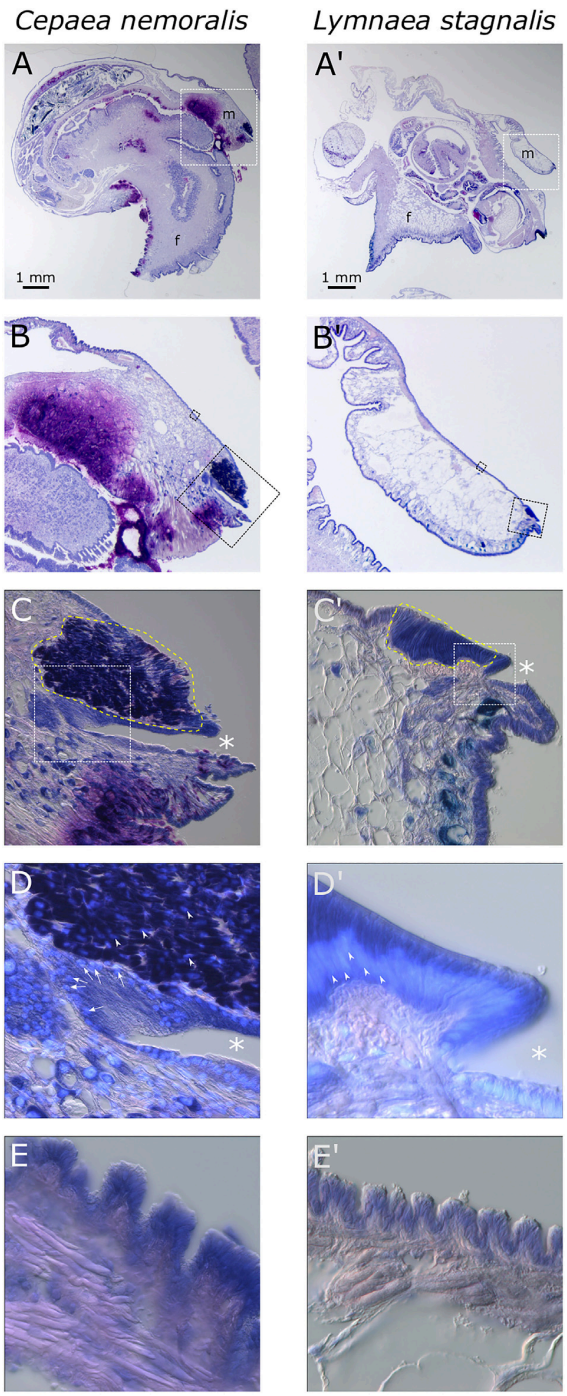

FIGURE 6 | Comparison of *C. nemoralis* and *L. stagnalis* mantle morphologies. Giemsa stained paraffin sections of juvenile snails of each species reveal similarities and differences in some of the main feature so the mantle tissue. **(A,A')** An overview of representative sections of each species and the location of the mantle tissue in relation to the rest of the body. The white dashed boxes indicate the magnified region shown in **(B,B')**. **(B,B')** The edge of the mantle tissue where new shell material is deposited. The black dashed boxes indicate the magnified region shown in **(C,C',E,E')**. **(C,C')** The mantle edge and the periostracal groove (indicated by asterisks) contains the distinctive "belt" region (yellow dashed outline). The white dashed boxes *(Continued)*

FIGURE 6 | Continued
indicate the magnified regions shown in **(D,D')**. **(D,D')** Magnified view of the periostracal groove (indicated by asterisks) and the belt. In *C. nemoralis* a histologically distinct population of cells at the base of the periostracal groove possess basal nuclei (stained sky blue with DAPI and indicated with white arrows). Nuclei in the belt in *C. nemoralis* are not basally oriented (white arrow heads in **D**). In *L. stagnalis* nuclei in belt cells are clearly basally oriented (white arrow heads in **D'**) and the cells themselves are distinctly columnar. **(E,E')** Proximal regions of the mantle epithelia in zone 5 appear broadly similar between the two species.

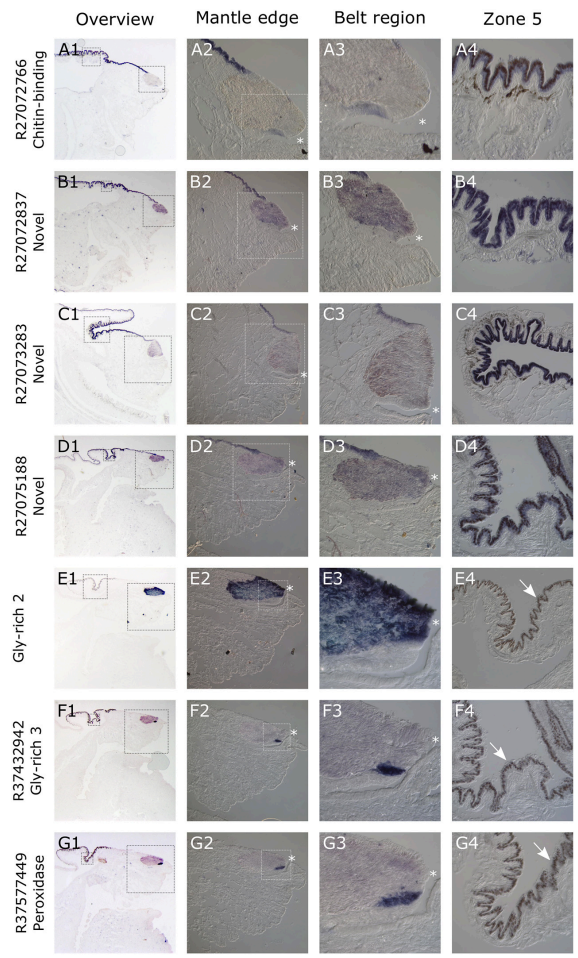

FIGURE 7 | Overview of *C. nemoralis* and *L. stagnalis* mantle tissue and ISH of seven shell-forming genes in *C. nemoralis* juvenile mantle tissue sections. The first image in each row provides an overview of the staining pattern for each gene, with dashed boxes indicating regions that are magnified in columns 2 and 4. The dashed box regions in all column 2 panels are magnified in column 3. For Cnem-glycine-rich-2 and -3 and Cnem_R37577449, the lack of expression in zone 5 reveals naturally brown pigmented mantle epithelium (white arrows in E4–G4). For all panels a dark blue color can be interpreted as the result of alkaline phosphatase activity (i.e., ISH signal). The opening of the periostracal groove is indicated by a white asterisk in columns 2 and 3.

as the most abundant accounting for more than 25% of the identifiable protein content of the shell (Mann and Jackson, 2014). All four of these genes are expressed exclusively in

zone 5 of the mantle (**Figures 7A1–D4**). Cnem-R27072766, which is the ortholog of Lstag_sfc_22 (Herlitze et al., 2018) and possesses a chitin binding Periotrophin-A domain, appears to have a homologous expression pattern to *Lstag_sfc_22* in zone 5. The three genes bioinformatically targeted for characterization due to their likely role in molluscan shell-formation, (glycine-rich 2 and 3) and Cnem_R37577449 (peroxidase) due to its orthology with Lstag_sfc5 (Herlitze et al., 2018), were all expressed within zones 1–4 (**Figures 7D1–G4**). Glycine-rich 2 was broadly expressed throughout the "belt" region (zones 2–4) while glycine-rich 3 and the peroxidase homolog were restricted to zone 1 and appear to be spatially co-expressed (**Figures 7F1–G4**).

DISCUSSION

The catalog of proteins involved in molluscan shell-formation continues to grow at an exponential rate, and many exciting discoveries continue to be made based on high-throughput sequence analyses of the shell itself, the mantle tissue and the genomes of various molluscs (Zhang et al., 2012; Kocot et al., 2016; McDougall et al., 2016; Aguilera et al., 2017; Der Sarkissian et al., 2020; Marin, 2020). Due to the general lack of *in vivo* gene manipulation assays for most molluscan models, additional insight into the functions of these genes (many of which share little to no sequence similarity with non-molluscan species) can be gained by characterizing their spatial expression patterns (Nederbragt et al., 2002; Jackson et al., 2006; Grande and Patel, 2008; Samadi and Steiner, 2009). With this approach we previously characterized the expression patterns of 31 genes identified from a proteomic screen of the *L. stagnalis* shell (Herlitze et al., 2018). In that previous work, coupled with a previous histological analysis of *L. stagnalis* mantle tissue (Timmermans, 1969), we were able to categorize the spatial expression patterns of those 31 genes into five distinct domains (Herlitze et al., 2018). The striking modularity of those expression domains led us to hypothesize that this may be a general feature of the molluscan mantle that facilitates the evolution of new shell morphologies. The expression patterns of the seven *C. nemoralis* genes I investigated here (four of which are orthologs to *L. stagnalis* shell-forming genes) provides an opportunity to explore this hypothesis further. While *L. stagnalis* and *C. nemoralis* are both pulmonates, as respective representatives of the families Lymnaeidae and Helicidae they share an ancestor that lived ∼200 million years ago (Teasdale, 2017) placing this comparison in context.

As a first step toward characterizing the architecture of the *C. nemoralis* mantle on a molecular level, I cloned four genes that give rise to some of the most abundant proteins we previously detected in the *C. nemoralis* shell (Mann and Jackson, 2014). Three of these genes (Cnem_R27072837, Cnem_R27073283, and Cnem_R27075188) have no recognizable domains and share no sequence similarity with SwissProt sequences, while Cnem_R27072766 contains a chitin binding Periotrophin-A domain, shares sequence similarity with other molluscan shell-forming proteins and is the ortholog of Lsta_sfc_22 (**Figure 2** and **Supplementary File 9**; Herlitze et al., 2018). Interestingly all four of these abundant genes were expressed in zone 5 of the *C. nemoralis* mantle (**Figure 7**), as was *Lsta_sfc_22* in *L. stagnalis* (Herlitze et al., 2018). While similar molluscan shell-forming genes (notably Pif from *Pinctada fucata*) have been associated with the production of nacre (Suzuki et al., 2009), neither *L. stagnalis* nor *C. nemoralis* construct nacre and so the functions of Cnem_R27072766 and Lsta_sfc_22 remain unknown. Nonetheless it is a striking reminder that oysters and pulmonates do share such similar downstream effector genes in their biomineralization toolkits, along with other proteins such as carbonic anhydrases, tyrosinases and peroxidases (Zhang et al., 2006; Hohagen and Jackson, 2013; Le Roy et al., 2014; Liu et al., 2014; Herlitze et al., 2018). The similarity in the spatial expression patterns of *Lsta_sfc_22* and *Cnem_R27072766* (both within zone 5), and their clear orthology (**Figure 2**), also supports the overall approach of comparing two mantle tissues separated by ∼200 million years of evolution (Teasdale, 2017). In addition, two of these 4 genes I selected from our previous proteomic analysis of the *C. nemoralis* shell (Cnem_R27072837 and Cnem_R27075188) also appear to have orthologs in the set of *L. stagnalis* shell-forming proteins we previously identified (Lsta_sfc_27 and Lsta_sfc_20, respectively; Herlitze et al., 2018, #91913). Cnem_R27072837 was the most abundant protein we could identify in the shell of *C. nemoralis* (Mann and Jackson, 2014) and it is expressed exclusively in zone 5 (**Figure 7**). This protein has high and exclusive sequence similarity with Lsta_sfc_27 (**Supplementary File 13**; Herlitze et al., 2018) and is therefore likely to be the ortholog of this protein. Lsta_sfc_27 is also exclusively expressed in zone 5 (Herlitze et al., 2018). In contrast, Cnem_R27075188 which also has a very high sequence similarity with Lsta_sfc_20 (**Supplementary File 14**) is expressed exclusively in zone 5 (**Figure 7**), while *Lsta_sfc_20* is expressed in zone 4 (Herlitze et al., 2018), a subtle but noticeable difference. BLASTp searches against SwissProt revealed no similar sequences to Cnem_R27075188 (**Supplementary File 9**), while searches against nr only returned gastropod sequences (**Supplementary File 12**) suggesting that this is a lineage restricted gene.

Secreted, glycine-rich proteins are typical members of molluscan shell-forming proteomes (Yano et al., 2006; Herlitze et al., 2018) and may provide similar mechanical properties to the shell as silk proteins do for spider silk (McDougall et al., 2016). In addition, certain shell-forming proteins are known to possess distinct domains rich in glycine (for example Lustrin (Shen et al., 1997), and Nacrein (Miyamoto et al., 1996)]. As we previously reported the spatial expression patterns for several of these genes in *L. stagnalis* (Herlitze et al., 2018), all of which were restricted to zone 3, I was interested to identify potential orthologous glycine-rich shell-forming genes in *C. nemoralis*. I searched the *C. nemoralis* mantle transcriptome and was able to identify several secreted glycine-rich genes expressed in the mantle tissue. I then cloned and determined the spatial expression patterns for two of these. In *L. stagnalis* the "belt" zone (a narrow zone of high columnar cells that is continuous with a low columnar epithelium, which covers the remaining outer surface of the mantle as described by Timmermans (1969) encompasses zones 2 and 3. All three of the glycine-rich genes we previously studied

in *L. stagnalis* were exclusively expressed in zone 3 of the belt (Herlitze et al., 2018). While assigning homology to regions of the mantle between species should currently be done with caution, if we assume these high columnar cells in the anterior region of the mantles of *C. nemoralis* and *L. stagnalis* are homologous "belts," then there are significant differences in the expression of the two glycine-rich genes I studied here: *Cnem_Gly-rich-2* was exclusively expressed throughout the belt (zones 2 and 3), while *Cnem_Gly-rich-3* (Cnem_R37432942) was exclusively expressed outside of the belt in the periostracal groove in zone 1 (**Figure 7**). The remaining problem in this comparison of glycine-rich genes between *C. nemoralis* and *L. stagnalis* is the question of homology between the genes themselves. Sequences such as these that are so biased in composition cannot be confidently homologized without additional information, for example gene synteny (Vakirlis et al., 2020) that would require at least a draft quality genome assembly for each species. Nonetheless, one might provisionally assume that such extreme glycine-rich proteins may be serving similar functions in the shells of their respective species, and the observed differences in their spatial expression patterns would therefore impart observable differences to their shells. Due to these uncertainties I also studied another protein for which the question of homology was clear. Lsta_sfc_5 was identified in the shell of *L. stagnalis* and has a peroxidase domain (Herlitze et al., 2018). I searched the *C. nemoralis* transcriptome for similar sequences, and although I was able to identify more than a dozen peroxidase-like sequences (**Supplementary File 11**) Cnem_R37577449 was clearly the ortholog of Lsta_sfc_5 (**Figure 4**). In *L. stagnalis* mantle tissue *Lsta_sfc_5* is exclusively expressed in zones 1 and 2, a relatively broad expression domain that partly includes the belt (Herlitze et al., 2018). In contrast *Cnem_R37577449* is expressed in the mantle tissue of *C. nemoralis* in a relatively restricted pattern in zone 1 that is distal to the belt (**Figure 7**). This expression domain apparently overlaps that of *Cnem_Gly-rich-3* (Cnem_R37432942; **Figure 7**). While the precise functions of

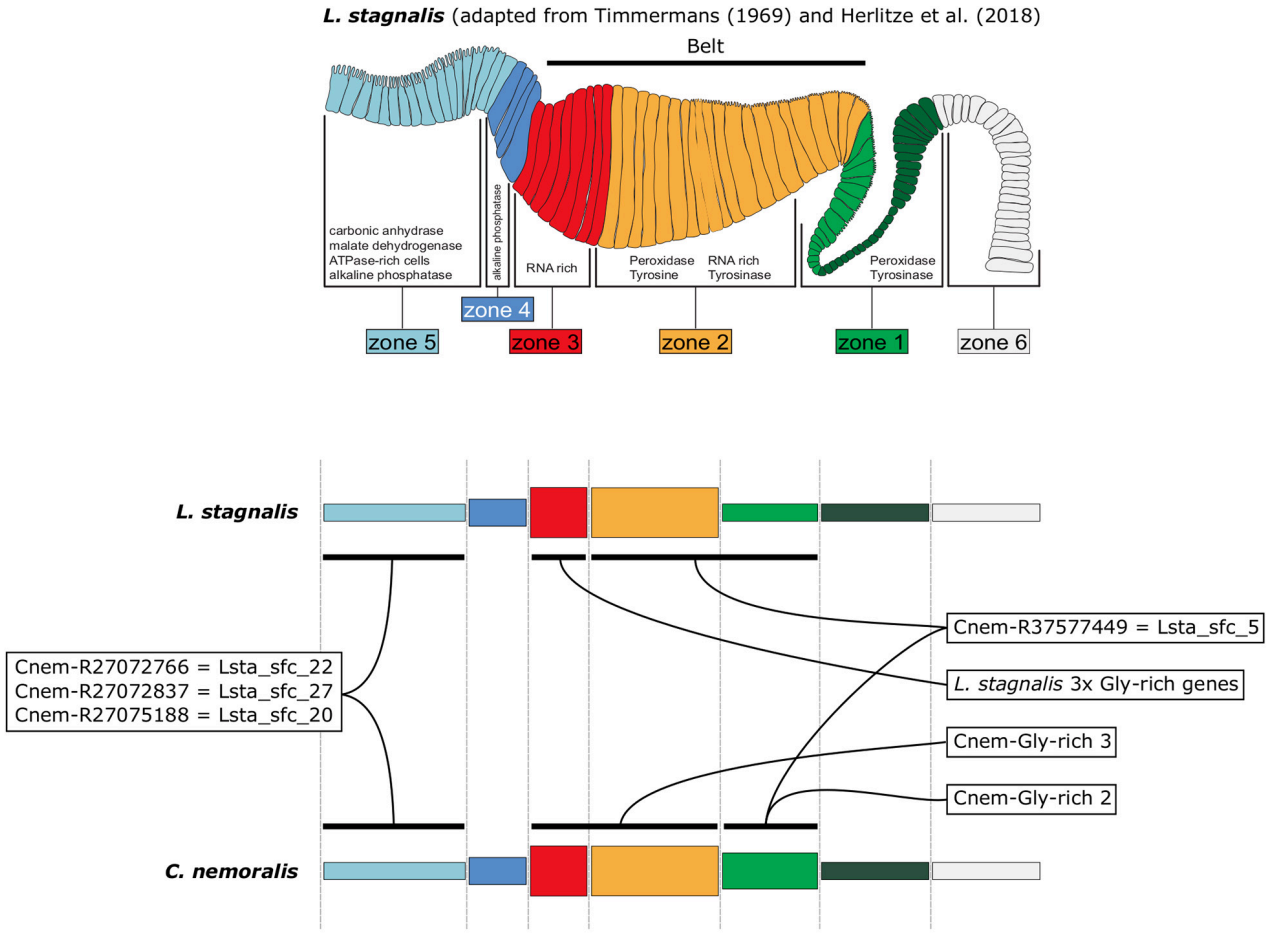

FIGURE 8 | A schematic representation of *L. stagnalis* and *C. nemoralis* mantle tissues and orthologous shell-forming gene expression patterns highlights the modularity of the molluscan mantle. The uppermost panel is adapted from Herlitze et al. (2018) and indicates the main mantle zones that Timmermans described in her histological examination of *L. stagnalis* mantle tissue (Timmermans, 1969). Domains of enzymatic activity are shown and correlate well with cases where we were able to locate the gene expression of responsible genes (for example peroxidase activity was detected in zones 1 and 2 and this is where we observed the expression of Lsta_sfc_5, a peroxidase homolog). A more highly schematized representation of the mantle is presented in the lower panels, and facilitates the comparison of orthologous shell-forming genes. Note the differences in the expression of the peroxidase orthologs (*Cnem-R37577449* and *Lsta_sfc_5*) and the glycine-rich genes.

these enzymes in the mantle tissues of molluscs are not accurately known, these significant differences in spatial expression patterns could be expected to influence the overall structure of the mature biomineral. Specific gene function analyses are required to verify this hypothesis. In addition to a larger collection of shell-forming gene expression patterns from more diverse species, draft genome sequences would allow for deeper inspection of the loci that encode these genes, and would allow for the identification of orthologous *cis*-regulatory elements (CREs) that presumably drive shell-forming gene expression in zones 1–5. The identification of "mantle-zone-specific" CREs would lend strong support to the model of mantle modularity we previously proposed (Herlitze et al., 2018). In this regard a comprehensive study of such CREs across the Gastropoda (and beyond) would be a stimulating exercise.

By characterizing the spatial expression patterns of the *C. nemoralis* genes I have studied here, and comparing them with those we previously studied in *L. stagnalis* (Herlitze et al., 2018), a conceptually appealing modularity to the molluscan mantle presents itself. When the expression patterns of orthologous shell-forming genes are compared on a highly schematized representation of the mantle (**Figure 8**) it appears as though the spatial regulation of certain genes have been significantly modified, most noticeably *Cnem-R37577449 cf. Lsta_sfc_5* (homologs of a peroxidase gene) and the glycine rich genes. Others (*Cnem-R27072766 cf. Lsta_sfc_22, Cnem-R27072837 cf. Lsta_sfc_27*, and *Cnem-R27075188 cf. Lsta_sfc_20*) appear to have been largely conserved over their ∼200 million years of independent evolution (Teasdale, 2017). While these intriguing observations require further investigation and an expansion of the comparative gene-expression datasets, I propose that this apparent modularity to the mantle tissue would have greatly facilitated the evolution of novel molluscan shell types. With the growing availability of conchiferan genomes, coupled with advanced sequencing methods such as single cell RNASeq and the development of gene-editing methods for more diverse species, it will be possible to rigorously test this hypothesis, and to gain further insight into the mechanisms by which evolution has generated the diversity of molluscan shells we admire today.

DATA AVAILABILITY STATEMENT

The datasets presented in this study can be found in online repositories. The names of the repository/repositories and accession number(s) can be found in the article/**Supplementary Material**.

AUTHOR CONTRIBUTIONS

DJ performed the lab work, sequence analyses, wrote and drafted the manuscript.

FUNDING

This work was funded by Deutsche Forschungsgemeinschaft (DFG) grant DJ 2108/6-1 (Project Number 387855163) to DJ.

ACKNOWLEDGMENTS

I gratefully acknowledge Aodhan, Graham, Johanna, and Nicolas Cerveau for assistance in collecting the *C. nemoralis* used in this work, and to Nicolas Cerveau for constructive discussions during the preparation of this manuscript and for preparing the *L. stagnalis* tissue for sectioning.

SUPPLEMENTARY MATERIAL

The Supplementary Material for this article can be found online at: https://www.frontiersin.org/articles/10.3389/fgene.2021.622400/full#supplementary-material

REFERENCES

Aguilera, F., McDougall, C., and Degnan, B. M. (2017). Co-Option and de novo gene evolution underlie molluscan shell diversity. *Mol. Biol. Evol.* 34, 779–792. doi: 10.1093/molbev/msw294

Aizenberg, J., and Hendler, G. (2004). Designing efficient microlens arrays: lessons from Nature. *J. Mat. Chem.* 14, 2066–2072. doi: 10.1039/B402558J

Arroyo-Loranca, R. G., Hernandez-Saavedra, N. Y., Hernandez-Adame, L., and Rivera-Perez, C. (2020). Ps19, a novel chitin binding protein from *Pteria sterna* capable to mineralize aragonite plates in vitro. *PLoS One.* 15:e0230431. doi: 10.1371/journal.pone.0230431.s004

Berland, S., Marie, A., Duplat, D., Milet, C., Sire, J. Y., and Bédouet, L. (2011). Coupling proteomics and transcriptomics for the identification of novel and variant forms of mollusk shell proteins: a study with *P. margaritifera*. *ChemBioChem.* 12, 950–961. doi: 10.1002/cbic.201000667

Der Sarkissian, C., Möller, P., Hofman, C. A., Ilsøe, P., Rick, T. C., Schiøtte, T., et al. (2020). Unveiling the ecological applications of ancient DNA From Mollusk Shells. *Front. Ecol. Evol.* 8:37. doi: 10.3389/fevo.2020.00037

Dietl, G. P., and Vega, F. J. (2008). Specialized shell-breaking crab claws in Cretaceous seas. *Biol. Lett.* 4, 290–293. doi: 10.1098/rsbl.2008.0031

Eble, G. J., Callebaut, W., and Rasskin-Gutman, D. (2005). "Morphological modularity and macroevolution: conceptual and empirical aspects," in *Modularity: Understanding the Development and Evolution of Natural Complex Systems*, eds W. Callebut and D. Rasskin-Gutman (Cambridge, MA: MIT Press), 221–239.

Edgell, T. C., Brazeau, C., Grahame, J. W., and Rochette, R. (2008). Simultaneous defense against shell entry and shell crushing in a snail faced with the predatory shorecrab *Carcinus maenas*. *Mar. Ecol. Prog. Ser.* 371, 191–198. doi: 10.3354/meps07698

Esteve-Altava, B. (2016). In search of morphological modules: a systematic review. *Biol. Rev.* 92, 1332–1347. doi: 10.1007/s11692-008-9034-7

Esteve-Altava, B. (2017). Challenges in identifying and interpreting organizational modules in morphology. *J. Morphol.* 278, 960–974. doi: 10.1002/jmor.20690

Gouy, M., Guindon, S., and Gascuel, O. (2010). SeaView Version 4: a multiplatform graphical user interface for sequence alignment and phylogenetic tree building. *Mol. Biol. Evol.* 27, 221–224. doi: 10.1093/molbev/msp259

Grande, C., and Patel, N. H. (2008). Nodal signalling is involved in left-right asymmetry in snails. *Nature* 457, 1007–1011. doi: 10.1038/nature07603

Greenwald, L., and Ward, P. D. (2010). "Buoyancy in *Nautilus*," in *Nautilus*. Topics in Geobiology, eds W. B. Saunders and N. H. Landman (Dordrecht: Springer), 547–560.

Herlitze, I., Marie, B., Marin, F., and Jackson, D. J. (2018). Molecular modularity and asymmetry of the molluscan mantle revealed by a gene expression atlas. *GigaScience* 7:giy056. doi: 10.1093/gigascience/giy056

Hohagen, J., and Jackson, D. J. (2013). An ancient process in a modern mollusc: early development of the shell in Lymnaea stagnalis. *BMC Dev. Biol.* 13:27. doi: 10.1186/1471-213X-13-27

Jackson, D. J., McDougall, C., Green, K., Simpson, F., Worheide, G., and Degnan, B. M. (2006). A rapidly evolving secretome builds and patterns a sea shell. *BMC Biol.* 4:40. doi: 10.1186/1741-7007-4-40

Joubert, C., Piquemal, D., Marie, B., Manchon, L., Pierrat, F., Zanella-Cleon, I., et al. (2010). Transcriptome and proteome analysis of *Pinctada margaritifera* calcifying mantle and shell: focus on biomineralization. *BMC Genomics* 11:613. doi: 10.1186/1471-2164-11-613

Kocot, K. M., Aguilera, F., McDougall, C., Jackson, D. J., and Degnan, B. M. (2016). Sea shell diversity and rapidly evolving secretomes: insights into the evolution of biomineralization. *Front. Zool.* 13:23. doi: 10.1186/s12983-016-0155-z

Le Luyer, J., Auffret, P., Quillien, V., Leclerc, N., Reisser, C., Vidal-Dupiol, J., et al. (2019). Whole transcriptome sequencing and biomineralization gene architecture associated with cultured pearl quality traits in the pearl oyster, *Pinctada margaritifera*. *BMC Genomics* 20:111. doi: 10.1186/s12864-019-5443-5

Le Roy, N., Jackson, D. J., and Marie, B. (2014). The evolution of metazoan α-carbonic anhydrases and their roles in calcium carbonate biomineralization. *Front. Zool* 11:75. doi: 10.1186/s12983-014-0075-8

Liu, D., Kong, L., and Chen, Z. (2014). Detection of endogenous peroxidase and phenoloxidase in the mantle and liver of the clam *Ruditapes philippinarum*. *J. Chem. Pharma. Res.* 6, 1861–1864.

Lodi, M., and Koene, J. M. (2016). The love-darts of land snails: integrating physiology, morphology and behaviour. *J. Molluscan. Stud.* 82, 1–10. doi: 10.1093/mollus/eyv046

Malachowicz, M., and Wenne, R. (2019). Mantle transcriptome sequencing of Mytilus spp. and identification of putative biomineralization genes. *PeerJ.* 6:e6245. doi: 10.7717/peerj.6245

Mann, K., and Jackson, D. J. (2014). Characterization of the pigmented shell-forming proteome of the common grove snail *Cepaea nemoralis*. *BMC Genomics* 15:249. doi: 10.1186/1471-2164-15-249

Marie, B., Trinkler, N., Zanella-Cleon, I., Guichard, N., Becchi, M., Paillard, C., et al. (2011). Proteomic identification of novel proteins from the calcifying shell matrix of the manila clam *Venerupis Philippinarum*. *Mar. Biotechnol.* 13, 955–962. doi: 10.1007/s10126-010-9357-0

Marin, F. (2020). Mollusc shellomes: past, present and future. *J. Struct. Biol.* 212:107583. doi: 10.1016/j.jsb.2020.107583

McDougall, C., Woodcroft, B. J., and Degnan, B. M. (2016). The widespread prevalence and functional significance of silk-like structural proteins in metazoan biological materials. *PLoS One* 11:e0159128. doi: 10.1371/journal.pone.0159128

Meyers, M. A., Lim, C. T., Li, A., Nizam, B. R. H., Tan, E. P. S., Seki, Y., et al. (2009). The role of organic intertile layer in abalone nacre. *Mat. Sci. Eng. C.* 29, 2398–2410. doi: 10.1016/j.msec.2009.07.005

Miyamoto, H., Miyashita, T., Okushima, M., Nakano, S., Morita, T., and Matsushiro, A. (1996). A carbonic anhydrase from the nacreous layer in oyster pearls. *Proc. Natl. Acad. Sci. U.S.A.* 93, 9657–9660. doi: 10.1073/pnas.93.18.9657

Murdock, D. J. E. (2020). The 'biomineralization toolkit' and the origin of animal skeletons. *Biol. Rev.* 95, 1372–1392. doi: 10.1111/brv.12614

Nederbragt, A., van Loon, A. E., and Dictus, W. (2002). Expression of *Patella vulgata* orthologs of engrailed and dpp-BMP2/4 in adjacent domains during molluscan shell development suggests a conserved compartment boundary mechanism. *Dev. Biol.* 246, 341–355. doi: 10.1006/dbio.2002.0653

Ronquist, F., Teslenko, M., Van Der Mark, P., Ayres, D. L., Darling, A., Höhna, S., et al. (2012). MrBayes 3.2: efficient Bayesian phylogenetic inference and model choice across a large model space. *Syst. Biol.* 61, 539–542. doi: 10.1093/sysbio/sys029

Sakalauskaite, J., Andersen, S. H., Biagi, P., Borrello, M. A., Cocquerez, T., Colonese, A. C., et al. (2019). 'Palaeoshellomics' reveals the use of freshwater mother-of-pearl in prehistory. *eLife* 8:e45644. doi: 10.7554/eLife.45644

Samadi, L., and Steiner, G. (2009). Involvement of Hox genes in shell morphogenesis in the encapsulated development of a top shell gastropod (*Gibbula varia* L.). *Dev. Genes. Evol.* 219, 523–530. doi: 10.1007/s00427-009-0308-6

Shen, X., Belcher, A., Hansma, P. K., Stucky, G. D., and Morse, D. (1997). Molecular cloning and characterization of lustrin A, a matrix protein from shell and pearl nacre of *Haliotis rufescens*. *J. Biol. Chem.* 272, 32472–32481. doi: 10.1074/jbc.272.51.32472

Sleight, V. A., Thorne, M. A. S., Peck, L. S., Arivalagan, J., Berland, S., Marie, A., et al. (2016). Characterisation of the mantle transcriptome and biomineralisation genes in the blunt-gaper clam, *Mya truncata*. *Mar. Gen.* 27, 47–55. doi: 10.1016/j.margen.2016.01.003

Söllner, C., Burghammer, M., Busch-Nentwich, E., Berger, J., Schwarz, H., Riekel, C., et al. (2003). Control of crystal size and lattice formation by starmaker in otolith biomineralization. *Science* 302:282. doi: 10.1126/science.1088443

Suzuki, M., Saruwatari, K., Kogure, T., Yamamoto, Y., Nishimura, T., Kato, T., et al. (2009). An acidic matrix protein, Pif, is a key macromolecule for nacre formation. *Science* 325, 1388–1390. doi: 10.1126/science.1173793

Talavera, G., and Castresana, J. (2007). Improvement of phylogenies after removing divergent and ambiguously aligned blocks from protein sequence alignments. *Syst. Biol.* 56, 564–577. doi: 10.1080/10635150701472164

Teasdale, L. C. (2017). *Phylogenomics of the Pulmonate Land Snails*.University of Melbourne, Melbourne. [dissertation].

Timmermans, L. P. M. (1969). Studies on shell formation in molluscs. *Neth. J. Zool* 19, 413–523.

Vakirlis, N., Carvunis, A.-R., and McLysaght, A. (2020). Synteny-based analyses indicate that sequence divergence is not the main source of orphan genes. *eLife* 9:e53500. doi: 10.7554/eLife.53500

Wang, X., Liu, Z., and Wu, W. (2017). Transcriptome analysis of the freshwater pearl mussel (*Cristaria plicata*) mantle unravels genes involved in the formation of shell and pearl. *Mol. Genet. Genom.* 292, 343–352. doi: 10.1007/s00438-016-1278-9

Wilkinson, M. T. (2008). Three-dimensional geometry of a pterosaur wing skeleton, and its implications for aerial and terrestrial locomotion. *Zool J. Linn. Soc.* 154, 27–69. doi: 10.1111/j.1096-3642.2008.00409.x

Williams, S. T. (2017). Molluscan shell colour. *Biol. Rev.* 92, 1039–1058. doi: 10.1111/brv.12268

Xu, M., Huang, J., Shi, Y., Zhang, H., and He, M. (2019). Comparative transcriptomic and proteomic analysis of yellow shell and black shell pearl oysters, *Pinctada fucata martensii*. *BMC Genomics* 20:469. doi: 10.1186/s12864-019-5807-x

Yano, M., Nagai, K., Morimoto, K., and Miyamoto, H. (2006). Shematrin: a family of glycine-rich structural proteins in the shell of the pearl oyster Pinctada fucata. *Comp. Biochem. Physiol. B.* 144, 254–262. doi: 10.1016/j.cbpb.2006.03.004

Yarra, T., Gharbi, K., Blaxter, M., Peck, L. S., and Clark, M. S. (2016). Characterization of the mantle transcriptome in bivalves: *Pecten maximus, Mytilus edulis* and *Crassostrea gigas*. *Mar. Gen.* 27, 9–15. doi: 10.1016/j.margen.2016.04.003

Zhang, C., Xie, L., Huang, J., Chen, L., and Zhang, R. (2006). A novel putative tyrosinase involved in periostracum formation from the pearl oyster (*Pinctada fucata*). *Biochem. Biophys. Res. Commun.* 342, 632–639. doi: 10.1016/j.bbrc.2006.01.182

Zhang, G., Fang, X., Guo, X., Li, L., Luo, R., Xu, F., et al. (2012). The oyster genome reveals stress adaptation and complexity of shell formation. *Nature* 490, 49–54. doi: 10.1038/nature11413

Conflict of Interest: The author declares that the research was conducted in the absence of any commercial or financial relationships that could be construed as a potential conflict of interest.

The handling editor declared a past co-authorship with one of the authors DJ.

frontiers in Ecology and Evolution

REVIEW
published: 19 February 2021
doi: 10.3389/fevo.2021.623774

The Biology and Evolution of Calcite and Aragonite Mineralization in Octocorallia

*Nicola Conci[1], Sergio Vargas[1] and Gert Wörheide[1,2,3]**

[1] Department of Earth and Environmental Sciences, Ludwig-Maximilians-Universität, Munich, Germany, [2] SNSB - Bayerische Staatssammlung für Paläontologie und Geologie, Munich, Germany, [3] GeoBio-Center LMU, Ludwig-Maximilians-Universität, Munich, Germany

Octocorallia (class Anthozoa, phylum Cnidaria) is a group of calcifying corals displaying a wide diversity of mineral skeletons. This includes skeletal structures composed of different calcium carbonate polymorphs (aragonite and calcite). This represents a unique feature among anthozoans, as scleractinian corals (subclass Hexacorallia), main reef builders and focus of biomineralization research, are all characterized by an aragonite exoskeleton. From an evolutionary perspective, the presence of aragonitic skeletons in Octocorallia is puzzling as it is observed in very few species and has apparently originated during a Calcite sea (i.e., time interval characterized by calcite-inducing seawater conditions). Despite this, octocorals have been systematically overlooked in biomineralization studies. Here we review what is known about octocoral biomineralization, focusing on the evolutionary and biological processes that underlie calcite and aragonite formation. Although differences in research focus between octocorals and scleractinians are often mentioned, we highlight how strong variability also exists between different octocoral groups. Different main aspects of octocoral biomineralization have been in fact studied in a small set of species, including the (calcitic) gorgonian *Leptogorgia virgulata* and/or the precious coral *Corallium rubrum.* These include descriptions of calcifying cells (scleroblasts), calcium transport and chemistry of the calcification fluids. With the exception of few histological observations, no information on these features is available for aragonitic octocorals. Availability of sequencing data is also heterogeneous between groups, with no transcriptome or genome available, for instance, for the clade Calcaxonia. Although calcite represents by far the most common polymorph deposited by octocorals, we argue that studying aragonite-forming could provide insight on octocoral, and more generally anthozoan, biomineralization. First and foremost it would allow to compare calcification processes between octocoral groups, highlighting homologies and differences. Secondly, similarities (exoskeleton) between *Heliopora* and scleractinian skeletons, would provide further insight on which biomineralization features are driven by

OPEN ACCESS

Edited by:
Frederic Marin,
Délégation Centre-Est (CNRS), France

Reviewed by:
Philippe Ganot,
Centre Scientifique de Monaco, Monaco
Felipe Aguilera,
University of Concepcion, Chile

***Correspondence:**
Gert Wörheide
woerheide@lmu.de

Specialty section:
This article was submitted to Evolutionary and Population Genetics, a section of the journal Frontiers in Ecology and Evolution

Received: *30 October 2020*
Accepted: *01 February 2021*
Published: *19 February 2021*

Citation:
Conci N, Vargas S and Wörheide G (2021) The Biology and Evolution of Calcite and Aragonite Mineralization in Octocorallia. Front. Ecol. Evol. 9:623774. doi: 10.3389/fevo.2021.623774

skeleton characteristics (shared by scleractinians and aragonitic octocorals) and those driven by taxonomy (shared by octocorals regardless of skeleton polymorph). Including the diversity of anthozoan mineralization strategies into biomineralization studies remains thus essential to comprehensively study how skeletons form and evolved within this ecologically important group of marine animals.

Keywords: octocorallia, biomineralization, aragonite, evolutionary biology, calcite

INTRODUCTION

Biomineralization refers to the process by which organisms produce minerals. The ability to form biomineral structures is taxonomically widespread and has evolved multiple times during the Earth's history, including twenty independent origins within Metazoa and four within plants (Knoll, 2003). Biominerals serve a wide variety of biological functions including, among others, body support, defense against predation, navigation (Frankel et al., 1997) and (in plants) the regulation of photosynthesis and ion concentration (He et al., 2014 for review). Many groups of marine invertebrates (e.g., sponges, molluscs, and echinoderms) produce biominerals and among these, anthozoan coral (Cnidaria: Anthozoa) calcium carbonate biomineralization holds an extreme ecological significance, as it forms the 3D-framework of one of the most biodiverse ecosystems on the planet, coral reefs. Within Anthozoa, calcifying corals are found in two distinctive clades: the order Scleractinia (subclass Hexacorallia) and the subclass Octocorallia (**Figure 1f**). Scleractinian corals currently are the major contributors to reef accretion, and have thus been the focus of biomineralization research over the years (e.g., Tambutté et al., 2011; Falini et al., 2015). On the other hand, calcium carbonate ($CaCO_3$) production in octocorals, commonly referred to as *soft corals,* is often modest and can be of several orders of magnitude lower compared to scleractinians (Smith and Kinsey, 1976; Herrán et al., 2017; Edinger et al., 2019). Despite this, some octocoral species (primarily the order Helioporacea) can significantly contribute to reef formation (Zann and Bolton, 1985) and can become the main reef builders within different habitats (Shaish et al., 2010; Yasuda et al., 2012). Octocorals can also exhibit higher resilience to environmental conditions, enabling them to outperform and replace scleractinians after events such as coral bleaching, pollution and *Acanthaster* outbreaks (Nishishira, 1974; Stobart et al., 2005; Ruzicka et al., 2013). Moreover, from a biomineralogical perspective, octocorals are more diverse than scleractinians, as they have evolved a wide range of different biomineralization strategies. These include the production of skeletal structures composed of different calcium carbonate polymorphs (aragonite and calcite) and of organic components (Gorgonin). On the other hand, all modern scleractinian species are characterized by the production of aragonite skeletons only.

In light of this, octocorals represent an interesting target for biomineralization research. Yet they remain marginally studied. One of the main questions surrounding octocoral calcification is whether the morphological and compositional diversity of their skeletons is related to differences in the cellular and molecular mechanisms employed by them for biomineralization. As in other animal groups, calcification in Octocorallia is a *biologically controlled* process, in which the precipitation mineral is not a byproduct of metabolic processes (*biologically induced mineralization*), but is rather under strict physiologic control (Lowenstam, 1981; Mann, 1983). In general, biological control can be broadly subdivided into two main processes, namely, the regulation of ion (e.g., calcium) transport and concentration at the calcification sites (Kingsley and Watabe, 1985; Watabe and Kingsley, 1992; Bertucci et al., 2013), and the secretion of an organic matrix into the mineral fraction of the skeleton (Weiner et al., 1983). The composition of organic matrix in octocorals is of particular interest, as it has been shown—in other calcifying taxa—that it regulates *in vitro* precipitation of different $CaCO_3$ polymorphs (Goffredo et al., 2011; Laipnik et al., 2019). Despite this, little is known about skeleton formation in octocorals, especially whether these animals have (and how they evolved) the ability to control the formation of different $CaCO_3$ polymorphs. Finally, furthering our knowledge on octocoral calcification would also allow to obtain comparative information on the biomineralization strategies of two different groups of calcifying corals, and better understand how biomineralization evolved within the Anthozoa.

In this review, we examine the research status of calcite and aragonite biomineralization in octocorals. After introducing Octocorallia and highlighting the diversity of their skeletons, we summarize what is known about the evolutionary histories of biomineralization in octocorals, with a focus on polymorph diversity. We then surveyed available information on the cellular and molecular processes responsible for the formation of different skeletons. The aim was to (1) highlight the numerous current knowledge gaps characterizing octocoral biomineralization (especially pertaining to aragonite-forming species), and (2) propose novel potential approaches and/or research avenues to gain insight on the molecular mechanisms underlying such skeleton diversity.

OCTOCORALS: *SOFT* BIOMINERALIZERS

The cnidarian subclass Octocorallia represents a group of marine benthic organisms, currently comprising more than 3,400 described valid species (Williams and Cairns, 2015). They inhabit all marine habitats, but do mostly occur in either shallow tropical or deep sea environments. Around 75% of octocoral species have been described from waters below 50 m and the deepest specimen to date was recorded at 6,400 m depth (Roberts et al.,

2009; Zapata Guardiola and López González, 2012). They are globally distributed, albeit very few species are cosmopolitan, with the highest diversity occurring in the Indo-Pacific region (Williams and Cairns, 2013; Pérez et al., 2016). Octocorals represent important marine community members and can increase habitats' spatial complexity (Quattrini et al., 2014). In deep sea environments, for example, octocorals can occur at high densities and sustain biodiverse ecosystems by providing substratum and shelter to other organisms like fishes (Caley and St John, 1996), or nudibranchs, crustaceans, and echinoderms (Krieger and Wing, 2002; Mortensen and Buhl-Mortensen, 2005; De Clippele et al., 2015). As observed in scleractinians, octocoral can also establish symbiotic relationships (obligate or facultative) with photosynthetic microalgae (zooxanthellae) or be non-symbiotic (Fabricius and Alderslade, 2001). This octocoral-algae association is considered mutualistic: the symbiont obtains inorganic nutrients from the coral, while the host receives in turn organic compounds, the products of photosynthesis. Primary productivity is nonetheless usually low, and octocorals often rely also on heterotrophy (e.g., suspension feeding, prey capture) (Sorokin, 1991; Fabricius and Klumpp, 1995; Ribes et al., 1998).

With the sole exception of members of the genus *Taiaroa* (Bayer and Muzik, 1976), octocorals are colonial, and consist of multiple polyps embedded and interconnected by tissue (coenenchyme). Octocoral colonies can be morphologically very distinct and exhibit a wide range of forms from encrusting to arborescent (**Figures 1a–e**). Nevertheless, polyps are always characterized by an eightfold symmetry (i.e., they possess eight tentacles and eight internal mesenteries). This represents the synapomorphy of the group and separates Octocorallia from all remaining anthozoan taxa, in which a sixfold symmetry is present. In octocorals, polyp tentacles are also often characterized by lateral branched structures called pinnulae. This does however not constitute an octocoral synapomorphy as species with smooth tentacles have also been described (Alderslade and McFadden, 2007). Biomineralization is also not shared by all octocorals, and species lacking any mineral structure have been described in different groups (Alderslade and Mcfadden, 2011; Benayahu et al., 2017; Lau and Reimer, 2019b).

Taxonomically, Octocorallia is currently divided into three orders: Helioporacea, Pennatulacea, and Alcyonacea (Bayer, 1981b). The first two are grouped based on well-defined characters: the presence of an aragonite skeleton (Helioporacea) and the oozoid, a differentiated polyp that ensures attachment to the substratum (Pennatulacea). Order Alcyonacea is subsequently divided into six sub-ordinal groups based on their skeleton characteristics: Alcyoniina, Holaxonia, Stolonifera, Calcaxonia, Scleraxonia, and Protoalcyonacea (Grasshoff, 1999; Fabricius and Alderslade, 2001). Molecular phylogenetic studies of Octocorallia, however, have repeatedly shown that these groups are artificial and should be abandoned. For example, the analysis McFadden et al. (2006) found the suborders Stolonifera, Alcyoniina, and Scleraxonia polyphyletic. Polyphyly for Scleraxonia was also observed in Sánchez et al. (2003a), while Alcyoniina and Calcaxonia appeared paraphyletic.

DIVERSITY AND COMPOSITION OF OCTOCORAL SKELETONS

Compared to modern scleractinians, which all produce massive aragonitic exoskeletons, octocorals have evolved a diverse array of skeletal structures. In the vast majority of species, the skeletal elements consist of multiple micro- or millimetric calcareous structures called sclerites, which occur embedded within the animal tissues. The overall sclerite morphology (e.g., spicule, spindle, rod, plate) (Devictor and Morton, 2010) and the different types of ornamentations can differ sensibly between species (**Figure 2**) and have been thus used extensively for species delimitation (Bayer, 1981a; Fabricius and Alderslade, 2001; Tentori and van Ofwegen, 2011). Molecular phylogenies have confirmed the taxonomic value of sclerite morphology to some extent, despite also highlighting instances of homoplasy (Sánchez et al., 2003b; Vargas et al., 2010c, 2014; Ament-Velásquez et al., 2016; Poliseno et al., 2017). Morphological plasticity linked to environmental conditions (Prada et al., 2008) and predation (West, 1997) has also been reported. Intraspecific variability is also present and different sclerite types and abundance can be observed within single individuals (Van Alstyne et al., 1992; Vargas et al., 2010a,b). In some species, different sclerite morphologies appear to correlate with their different localization (e.g., polyp, base) within the animal body (Williams, 1986, 1992; Alderslade, 2000; Tentori and van Ofwegen, 2011). Sclerites are found embedded within the mesoglea—a collagen-like substance between the ectodermal and endodermal layers (Barzansky and Lenhoff, 1974)—of the coenenchyme (tissue connecting the polyps) and/or the polyp (Fabricius and Alderslade, 2001).

Mineralogy: Octocoral sclerites are all composed of $CaCO_3$ in the form of high-magnesium calcite. More detailed compositional analyses have been obtained for the sclerites of Mediterranean gorgonians and precious corals. In the former, magnesium concentrations ranged between 1.4 and 2.2% (Weinbauer and Vellmirov, 1995). Slightly higher values (2.1–3.0%) have been found in *C. rubrum* (Family Corallidae), although variability in magnesium content both within single sclerites, individuals and between colonies was reported (Weinbauer et al., 2000). Strontium is another common component of octocoral sclerites and its concentration values in gogonians can range between 0.1 and 0.2% (Weinbauer and Vellmirov, 1995). Incorporated amounts of magnesium and strontium have been extensively used to reconstruct paleoclimatic conditions. For example, the concentration of magnesium in octocoral sclerites is positively correlated with seawater temperature (Weinbauer and Vellmirov, 1995; Yoshimura et al., 2011), although in *C. rubrum* this correlation appears not to hold when colonies are exposed to large temperature fluctuations (Vielzeuf et al., 2013). Finally, several trace elements have been detected in the sclerites of *C. rubrum* including lithium, iron, zinc and barium (Vielzeuf et al., 2013, 2018).

In some octocoral groups a mineral axial skeleton is deposited alongside sclerites. The axis provides support to the colony and can be entirely composed of biogenic calcite or be a combination of scleroproteins (collectively referred

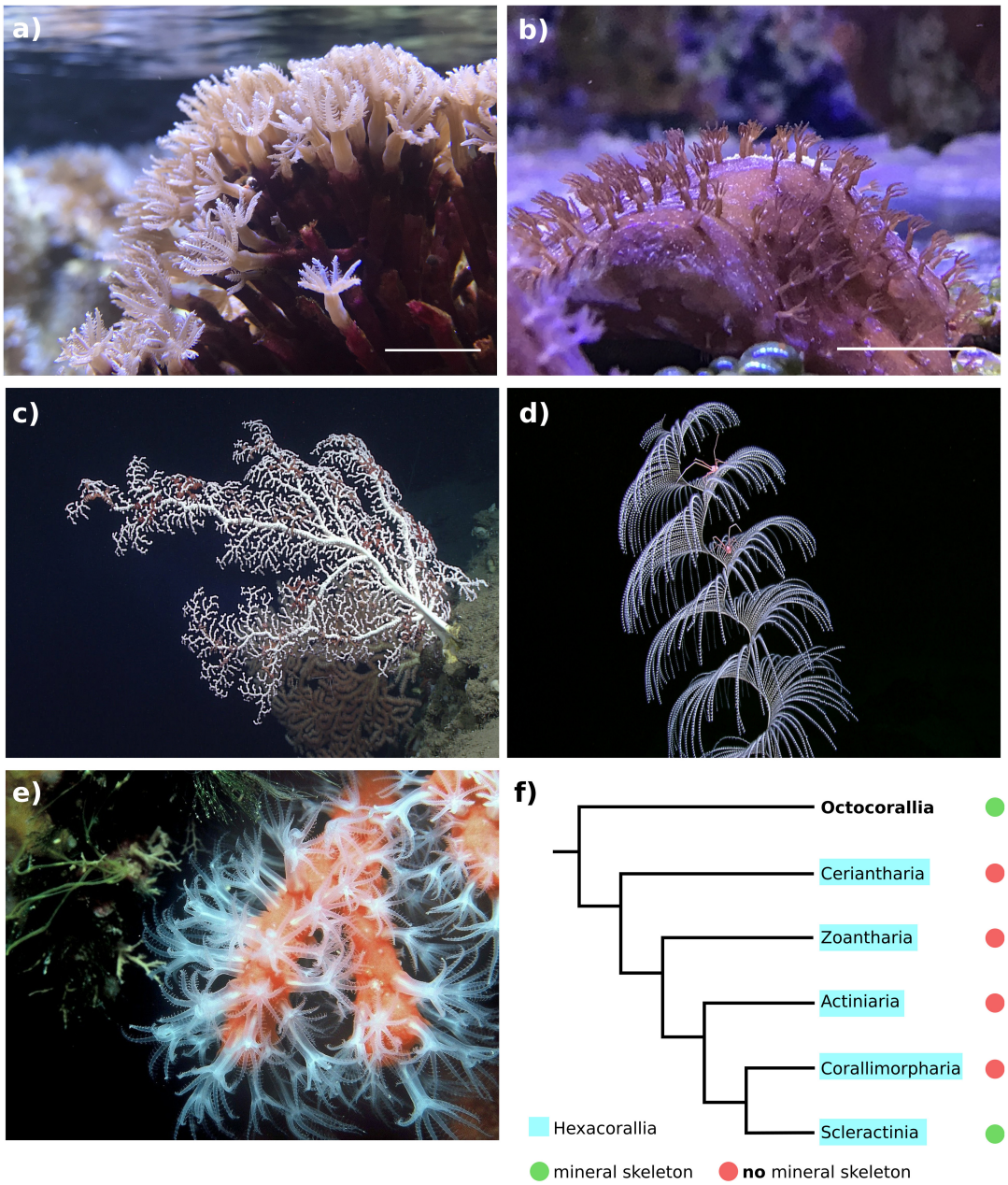

FIGURE 1 | (a) *Tubipora musica* (order Stolonifera) (scale bar: 1 cm). **(b)** *Heliopora coerulea* (order Helioporacea) (scale bar: 1 cm). **(c)** *Paragorgia* sp. (order Alcyonacea). **(d)** *Iridogorgia* sp. (order Alcyonacea). **(e)** *Corallium rubrum* (order Alcyonacea). **(f)** Phylogenetic tree of class Anthozoa highlighting presence-absence patterns of mineral skeletons. We based the Anthozoa phylogenetic tree on Kayal et al. (2018). Here, Ceriantharia was found as sister taxon to other members of Hexacorallia. This has been recently corroborated in a phylogenomic analysis by McFadden et al. (2021). However, an alternative tree topology puts Ceriantharia as sister to remaining Anthozoa (Stampar et al., 2014). Pictures credit: **(a,b)** Department of Earth and Environmental Science, Ludwig-Maximilians-Universität München, **(c)** NOAA Office of Ocean Exploration and Research, Deep Connections 2019, and **(d)** NOAA Okeanos Explorer Program, Gulf of Mexico 2012 Expedition.

to as gorgonin; Bayer, 1981b) and calcite. Axial skeletons can arise from different calcification mechanisms that often entail the fusion of sclerites. In the precious coral *Corallium rubrum*, for example, sclerites at the tips of colony branches fuse to form the core of the axis, which is secondarily thickened by subsequent deposition of mineral layers (Allemand, 1993; Debreuil et al., 2012). In *C. johnsoni* however, the axial skeleton appears to be devoid of scleritic material (Lawniczak, 1987). In Octocorallia, different biomineralization strategies could have thus evolved within genera. In the family Ellisellidae, sclerites forming the axial core are often markedly different from those found in the coenenchyme (Devictor and Morton, 2010). Alternatively, sclerites can also assemble into reticulate structures (e.g., *Melithaea*) (Cuif, 2016). In octocorals

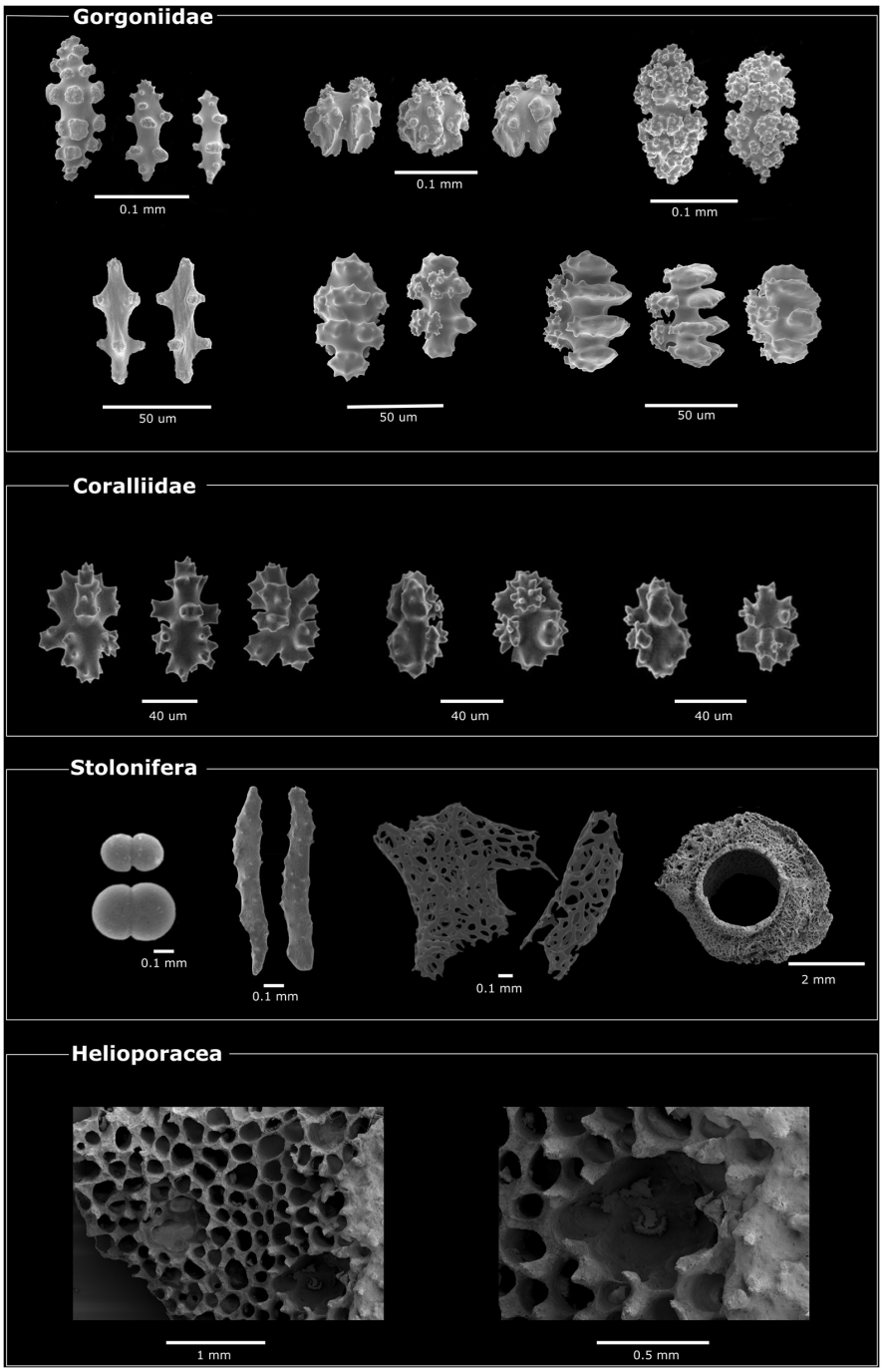

FIGURE 2 | Overview of skeletal structures present in different octocoral clades. Images acquired by scanning electron microscopy (SEM). Images sources: Gorgoniidae from Horvath (2019), Corallidae from Simpson and Watling (2011) (Cambridge Press©, reproduced with permission of copyright holder), Stolonifera from Lau et al. (2019) and personal image, Helioporacea (personal images). Image from Conci (2020).

producing proteinaceous skeletons, the axis can be reinforced with endogenous/biogenic (high magnesium calcite) or non-endogenous (calcite, aragonite, or amorphous $CaCO_3$) minerals (Lewis et al., 1992). Amounts and origin of the axis mineral fraction can differ between groups. In Calcaxonia, large amounts of non-scleritic or scleritic calcite are present, while members of the suborder Holaxonia are characterized by small quantities of embedded calcium carbonate (Bayer and Macintyre, 2001). In bamboo corals (Family Isididae), the proteinaceous and mineral fractions of the axial skeleton are arranged to form an alternation of flexible joints and rigid mineral internodes (Noé and Dullo, 2006).

Exceptions to the "*calcite rule*" are members of Order Helioporacea, in which a trabecular skeleton of fibrous aragonite is present (Hill, 1960). In the genus *Heliopora* and *Nanipora*, only aragonite is observed, while in the genus *Epiphaxum* calcite sclerites are formed alongside the aragonitic skeleton (Lozouet and Molodtsova, 2008; Miyazaki and Reimer, 2015). However, compared to the high-magnesium calcite of sclerites, the magnesium content found in *Heliopora's* aragonite skeleton is lower (ca. 0.5 mol%) (Velimirov, 1980).

Finally, hydroxyapatite ($Ca_{10}(PO_4)6(OH)_2$) has also been detected in some gorgonians and currently represent the only possible instance of likely biologically produced calcium phosphate in cnidarians (Macintyre et al., 2000).

EVOLUTIONARY HISTORY OF OCTOCORAL BIOMINERALIZATION

The origin of Octocorallia and the evolutionary relationships between different skeletal structures, notably between aragonite skeletons and calcite structures (sclerites and axis), remain largely elusive. This is in part caused by the poor preservation (Cope, 2005) and challenging identification (Deflandre-Rigaud, 1957; Kocurko and Kocurko, 1992) of octocoral skeletal elements in the fossil record, and the current lack of robust phylogenetic analyses for Octocorallia (but see Quattrini et al., 2020).

The earliest putative octocoral fossils currently date back to the Ediacaran (Glaessner, 1985). A putative Cambrian bryozoan fossil (genus *Pywackia*) (Landing et al., 2010) was later re-classified as an octocoral (Ausich and Babcock, 1998; Taylor et al., 2013), although this claim has been questioned (Landing et al., 2015). Earliest undisputed specimens of the group currently date back to the Ordovician, and belong to the gorgonian genus *Petilavenula* (Cope, 2005). Paleozoic (Silurian) octocoral fossils also include examples of a spiculite, a type of calcareous rock composed of cemented sclerites (Bengtson, 1981). Other octocoral groups appeared in the fossil record during the Cretaceous period (**Figure 3**). These include sea pens (order Pennatulacea) (Reich and Kutscher, 2011) and precious corals (family Coralliidae) (Schlagintweit and Gawlick, 2009). The oldest fossil specimens of aragonitic *Heliopora* and *Epiphaxum* species also date back to the Creataceous (Eguchi, 1948; Colgan, 1984; Lozouet and Molodtsova, 2008). A recent time-calibrated molecular phylogenetic analysis has corroborated the hypothesis of a Cretaceous origin for helioporaceans, while the proposed origin of pennatulaceans was pushed back to the Carboniferous (Quattrini et al., 2020).

The emergence of aragonitic skeletons during the Cretaceous is of evolutionary interest, as it lies in apparent disagreement with the calcite-inducing conditions (i.e., low magnesium-calcium molar ratio, or *m*Mg:*m*Ca) experienced by marine calcifiers during that time (Hardie, 1996; Lowenstein et al., 2001). The *m*Mg:*m*Ca of seawater has been hypothesized to represent one of the main drivers of selective inorganic precipitation of $CaCO_3$ polymorphs, with lower (<2) and higher (>2) values promoting the formation of calcite and aragonite, respectively (Morse et al., 1997; Balthasar and Cusack, 2015). Variations in *m*Mg:*m*Ca during the last 500 Mya have created an alternation between aragonite and calcite-favoring environments (referred to as the so-called "Aragonite-" and "Calcite Seas"), and have been shown to correlate with shifts in the skeleton polymorph produced by major calcificiers (Hardie, 1996; Stanley and Hardie, 1998; Knoll, 2003).

Aragonitic scleractinian corals, for example, represent the main reef framework-builders today (*m*Mg:*m*Ca ca. 5.2) and were responsible for reef formation during the Triassic Aragonite Sea (Stanley, 1981). They were, however, replaced by calcitic rudists (class Bivalvia, phylum Mollusca) during the Cretaceous, when Calcite Sea conditions prevailed (Scott, 1988). In addition to driving shifts in the composition of reef building communities, the seawater *m*Mg:*m*Ca appears to have also influenced the polymorph initially adopted by different organisms (Porter, 2010).

Aragonitic octocorals represent one of the very few exceptions to these patterns, as they appear to have evolved the ability to deposit aragonite skeletons during a Calcite Sea interval (Porter, 2010). On one hand, this could be explained by a currently incomplete fossil record. Aragonite-forming octocorals might have appeared earlier during aragonite-favoring conditions. This would, however, imply an extensive gap in the fossil record. On the other hand, precipitation of aragonite could have been promoted by other environmental variables. During the Cretaceous, several seawater properties differed compared to today's conditions. These include higher seawater temperatures (above 32°C at low latitudes) in shallow marine habitats (Schouten et al., 2003; Bice et al., 2006), lower pH (Zeebe, 2001) and lower sulfate (SO_4^{2-}) concentrations (Algeo et al., 2015). Among these, higher seawater temperatures have been shown to promote the co-precipitation of aragonite, alongside calcite, even at *m*Mg:*m*Ca < 1 (Balthasar and Cusack, 2015). The warm surface temperature characterizing the shallow environments inhabited by *H. coerulea* during the Cretaceous (Zann and Bolton, 1985), might thus have enabled this species to deposit its aragonitic skeleton. A similar scenario has also been proposed to explain the appearance of aragonitic brachiopod shells in the Silurian and Ordovician (Balthasar et al., 2011; Balthasar and Cusack, 2015).

Inferences on the evolution of octocoral biomineralization are furthermore hampered by the current lack of robust phylogenies for Octocorallia. The most comprehensive analysis, published by McFadden et al. (2006), identified two major clades (Holaxonia + Alcyoniina and Pennatulacea + Calcaxonia) plus a third clade consisting of genus *Anthomastus* and the precious coral *Corallium ducale*. The blue coral *H. coeruela* formed a clade with sea pens and calcaxonians. The hypothesis of a close evolutionary relationship between aragonitic octocorals (genera *Heliopora* and *Nanipora*) was later corroborated by Miyazaki and Reimer (2015) using different molecular markers. In another phylogeny, based on mitochondrial protein-coding genes, *H. coerulea* was, however, retrieved as sister to the rest of Octocorallia (Kayal et al., 2013). Nonetheless, the latter study aimed at resolving evolutionary relationships between Cnidaria major clades, and included a smaller taxon sampling of octocorals. In any case, no mitochondrial or nuclear

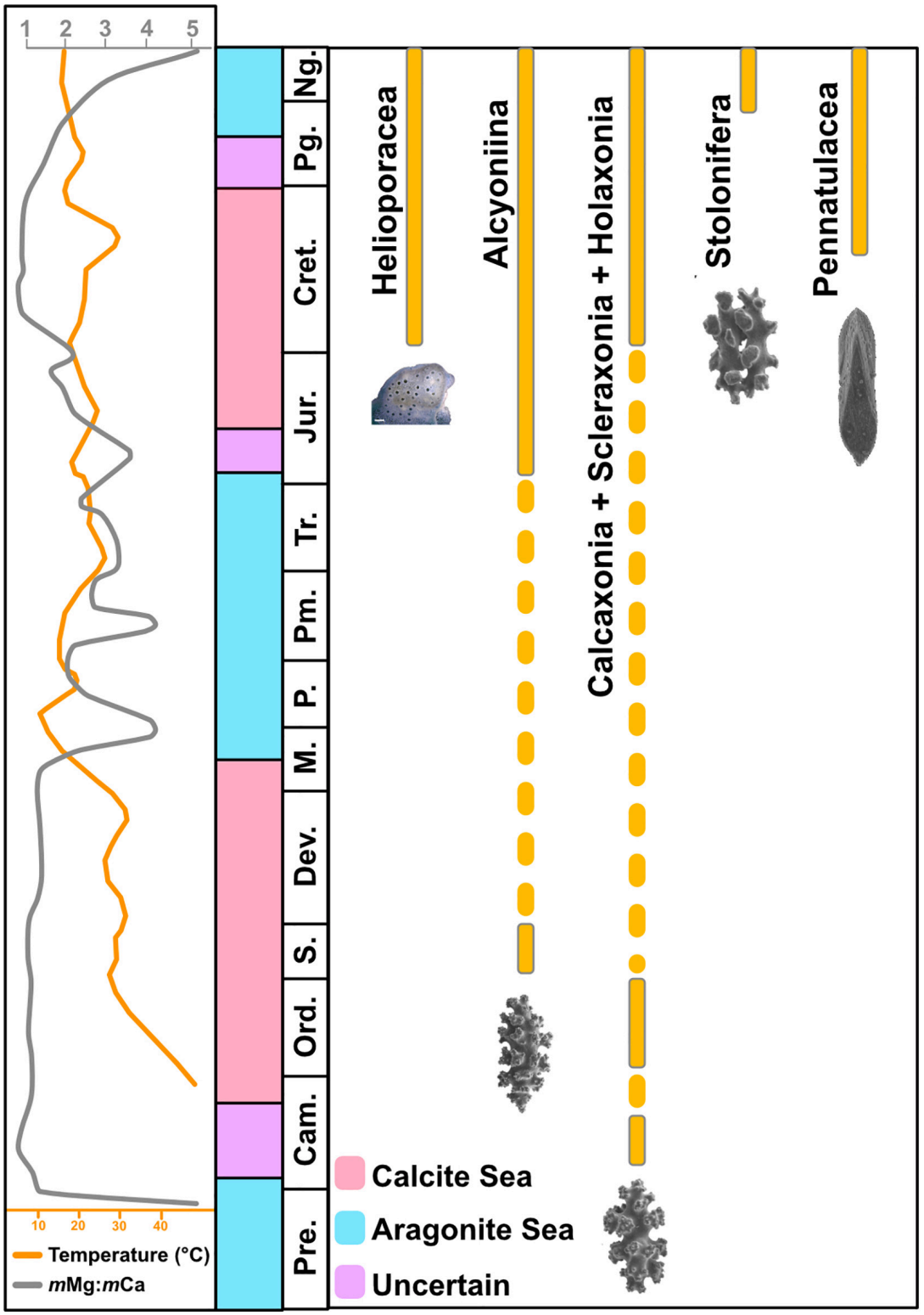

FIGURE 3 | Current fossil record of different octocoral taxa and concurrent environmental conditions (magnesium-calcium molar ratio, *m*Mg:*m*Ca, and sea surface water temperature) during the last 500 Mya. Fossil record based on Reich (2009). Seawater surface temperature and *m*Mg:*m*Ca based on Song et al. (2019) and Hardie (1996), respectively. Skeleton images: Helioporacea (Gert Wörheide), Alcyoniina (McFadden and Ofwegen, 2017) (Magnolia Press© reproduced with permission of copyright holder), Holaxonia (Dautova, 2019), Stolonifera (Lau et al., 2018) and Pennatulacea (Williams, 2015). Pre, Precambrian; Cam, Cambrian; Ord, Ordovician; S, Silurian; Dev, Devonian; M, Mississippian; P, Pennsylvanian; Pm, Permian; Tr, Triassic; Jur, Jurassic; Cret, Cretaceous; Pg, Plaeogene; Ng, Neogene.

marker have proved effective in resolving deep phylogenetic relationships between octocoral clades to date. This suggests that octocorals might have undergone a rapid radiation. Because phylogenomic analyses with larger taxon sampling to reconstruct the evolutionary history between octocoral groups are currently lacking, there clearly is the need for increased transcriptome and genome sequencing efforts to fill this knowledge gap (Rokas et al., 2005; McFadden et al., 2010). Nonetheless, some sequencing data is already available for some species and octocorals have been included in broader phylogenomic and phylotranscriptomic analyses to assess evolutionary relationships between cnidarian (Zapata et al., 2015; Kayal et al., 2018) or metazoan (Simion et al., 2017) groups. Several octocoral transcriptomes have been sequenced in the last few years and three genomes were released in the last 2 years (**Table 1**).

The majority of sequencing datasets is derived from octocorals of the suborder Holaxonia, while for other groups the number of species with a sequenced transcriptome/genome is extremely limited. To date, to the best of our knowledge, no data is available for Calcaxonia. Despite the recent increase in availability of octocoral *omic* resources, dozens of genera remain to be sequenced before phylogenomic (or phylotranscriptomic) analyses, with taxon samplings equivalent to previous studies (e.g., 103 species included in McFadden et al., 2006), can be conducted. In this light, research efforts aimed at resolving the origin and evolution of octocorals should (1) focus on filling the gap in terms of availability of data for calcaxonian octocorals and (2) examine existing phylogenies to prioritize the sequencing of taxa belonging to unresolved clades.

SCLEROBLASTS: THE OCTOCORAL CALCIFYING CELLS

Biological control over biomineralization often entails specialized cell types carrying out skeleton formation. For example, cells forming the scleractinian aboral ectoderm (or calicoblastic layer) or the outer epithelium of the molluscan mantle are, respectively, responsible for the deposition of skeletons or shells, respectively (Saleuddin, 1977; Johnston, 1980; Jolly et al., 2004). In octocorals, sclerites are produced by calcifying cells called scleroblasts. These cells likely originate in the ectodermal layer (Hickson, 1895; Woodland, 1905; Bayer and Owre, 1967; Watabe and Kingsley, 1992) and from there migrate into the mesoglea. Scleroblasts can exhibit varying morphological states, which appear to be correlated with different developmental stages of sclerite formation (Watabe and Kingsley, 1992). Based on histological and electron microscopy observations, a two step growth model for sclerite development has been proposed, involving an intracellular and a possible extracellular formation phase (see Watabe and Kingsley, 1992, for a review). Several authors provided a description of scleroblasts associated with different maturation stages in different octocorals, for example *Leptogorgia virgulata* (Kingsley and Watabe, 1982), *Sinularia* (Jeng et al., 2011), pennatulaceans (Dunkelberger and Watabe, 1974), and the precious coral *C. rubrum* (Grillo et al., 1993). An entirely intracellular growth model was initially proposed for the sea pen *Renilla reniformis* (Dunkelberger and Watabe, 1974), but later observations revealed the presence of an additional extracellular growth phase also in this octocoral species (Watabe, 1981).

Sclerite deposition appears to initially occur within a series of vacuoles present in the cytoplasm of scleroblasts (Watabe and Kingsley, 1992). Secretion of an organic matrix (discussed in the following section) into these vacuoles precedes mineral deposition and continues throughout sclerite formation (Kingsley and Watabe, 1982). The function of these organic matrices apparently is to provide a scaffold for mineral deposition (Lowenstam and Weiner, 1989). During the *intracellular* phase, scleroblasts are characterized by a prominent nucleus and their cytoplasm is rich in vesicles and mitochondria (Kingsley and Watabe, 1982; Grillo et al., 1993; **Figure 4.1a**). At this stage, scleroblasts are not solitary in the mesoglea but they instead form cell aggregates (Grillo et al., 1993). As sclerites grow, vacuoles occupy an increasingly larger space within the scleroblast, while the nucleus and cytoplasm are now restricted to the periphery of the cell (Watabe and Kingsley, 1992; **Figure 4.1b**). These changes are followed by the extrusion of the sclerite into the mesoglea (**Figure 4.1c**). A detailed description of the transition between the intracellular and extracellular phase has been provided for *L. virgulata* by Kinglsey and Watanabe (1982). These authors have shown that the extrusion of sclerites involves the fusion of the cell plasma membrane with the vacuole containing the sclerite. The maturation stage at which the sclerites become extracellular appears to vary between species. In *L. virgulata*, for example, the emergence of sclerites from the scleroblasts occurs at a late growth stage, and sclerites already exhibit their characteristic wart-like branching structures (Kingsley et al., 1987). In the gorgonian *Pseudoplexaura flagellosa,* on the other hand, crystals are extruded and they eventually aggregate into sclerites extracellularly (Goldberg and Benayahu, 1987). Once extracellular, sclerites can be enveloped by different scleroblasts, which are in contact by means of pseudopod-like extensions (Grillo et al., 1993). In *C. rubrum* for instance, two scleroblasts joined by septate junctions surround growing sclerites in the mesoglea (Le Goff et al., 2017; **Figure 4.2**). One or more scleroblasts associated with

TABLE 1 | Number of octocoral genomes and transcriptome publicly available.

Taxon	Genome	Transcriptome	Species in McFadden et al. (2006)
Alcyoniina	2	3	37
Calcaxonia			12
Helioporacea		1	1
Holaxonia	1	8	29
Pennatulacea	1	2	10
Scleraxonia		2	7
Stolonifera		3	7

Number indicates number of species with at least one transcriptome and/or genome sequenced. Numbers are compared to taxon sampling in McFadden et al. (2006). Numbers based on NCBI Sequence Read Archive (SRA), NCBI Transcriptome Shotgun Assembly (TSA) Database and the Cnidarian Blast Database available at http://data.centrescientifique.mc (Karako-Lampert et al., 2014). Assignment of species to subordinal groups based on the World Register of Marine Species. All databases last accessed on 21.08.2020.

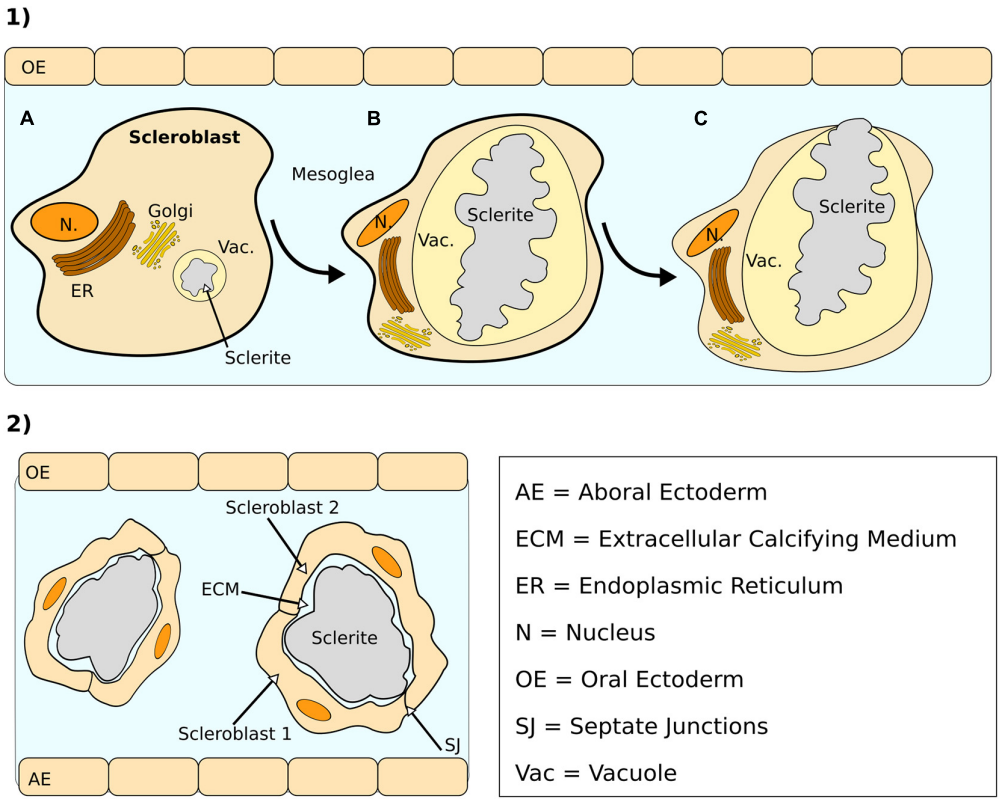

FIGURE 4 | (1) Different sclerite growth phases in *Leptogorgia virgulata*: (a) early intracellular deposition in a vacuole, (b) latest stage of intracellular deposition, and (c) transition between intracellular and extracellular stage by expulsion from vacuole/cell into the mesogloea. During the latter, vacuole and cell membrane fuse together and the sclerite is extruded from the scleroblasts (based on Watabe and Kingsley, 1992). **(2)** Extracellular growth of a sclerite in *Corallium rubrum*. Two scleroblasts—connected by septate junctions (SJ) envelop a single sclerite, surrounded by an extracellular calcifying medium (based on Le Goff et al., 2017).

single sclerites have also been observed in *Swiftia exserta* (Menzel et al., 2015).

In *Sinularia* species, an additional cementation phase takes place at the base of the colony, where mature sclerites are fused together by amorphous calcium carbonate (Jeng et al., 2011). Sclerite fusion is also observed among different stoloniferous octocoral species (Lau and Reimer, 2019a).

Less is known about the cells responsible for the growth of axial skeletons. A description of the epithelial cells responsible for the axis annular growth in *C. rubrum* has, however, been provided by Grillo et al. (1993). These authors did not report any observable differences between the cells enveloping the axial skeleton and the scleroblasts found in the mesoglea. Based on this, they proposed that these cells constitute actual scleroblasts and that sclerite-forming cells might be the result of calcifying epithelium fragmentation.

Information about calcifying cells in aragonite-forming octocorals is extremely limited but the presence of a calcifying epithelium in *H. coerulea* was already reported in an early observation (Moseley, 1876). Calcifying cells in *H. coerulea* were originally defined as "mesodermic" (Moseley, 1876), but were later described as of ectodermal origin (Bourne and Lankester, 1895). The latter authors also reported an increase in size and granule content during the diversification of calcifying (calicoblastic) cells from epithelial cells. The calcifying epithelium of *H. coerulea* was later further characterized by Le Tissier (1991), who noted the presence of vesicles in the cytoplasm of calicoblastic cells found in areas of active skeleton deposition. However, whether these cells can be classified as "scleroblasts" (homologous to those characterizing calcitic species) is not currently known. In fact, although it appears that both aragonite and calcite skeletons in Octocorallia are deposited by specialized ectodermal calcifying cells, possible differences in cytological characteristics and gene expression patterns between "calcite-forming scleroblasts" and aragonite-forming cells have not been investigated.

Biological Control I: Skeleton Organic Matrix

Octocoral sclerites and skeletons are biocomposite materials formed by a mineral ($CaCO_3$) and an organic fraction. The latter is also referred to as the *skeleton organic matrix* (SkOM). In scleractinian corals, SkOM quantities can range between 0.3 and 2% of the total dried skeleton weight (Constantz and Weiner, 1988; Allemand et al., 1994; Cuif et al., 2004; Goffredo et al., 2011; Ramos-Silva et al., 2013). Higher amounts have been reported in Octocorallia. In gorgonians, the SkOM

represents between 1 and 5% of the skeleton weight (Silberberg et al., 1972; Kingsley and Watabe, 1983). However, a sensibly lower value (ca. 0.04%) was later obtained for the octocoral *Sinularia* sp. (Rahman et al., 2013). Precisely quantifying organic materials occluded within coral skeletal structures is, however, a challenging task. Following skeleton/sclerites decalcification, SkOM isolation requires a series of washing steps that can contribute to loss of low-molecular weight components from the sample, which in turn can lead to underestimations of SkOM amounts (Puverel et al., 2007; Allemand et al., 2011). Compositionally, the SkOM consists of a diverse mixture of different macromolecules. Major components of both octocoral and scleractinian matrices include proteins (Fukuda et al., 2003; Ramos-Silva et al., 2013), both mono- and polysaccharides (Goldberg, 2001; Naggi et al., 2018; Takeuchi et al., 2018) and lipids (Farre et al., 2010; Reggi et al., 2016). In the gorgonian *Eugorgia ampla*, lipids can represent ca. 60% of the SkOM and are followed in abundance by proteins (Fox et al., 1969). In *Corallium* species, for example, proteins constitute ca. 0.01% of the total skeleton weight (Debreuil et al., 2011). Among carbohydrates, glucose, galactose, galactosamine, and mannose were the most represented in the sclerites of *Pseudoplexaura* (Goldberg, 1988). Additional studies have also focused on the pigments responsible for the coloration of skeletal elements in gorgonians (carotenoids) (Leverette et al., 2008), *H. coerulea* (biliverdin IXa) (Rüdiger et al., 1968; Hongo et al., 2017) and precious corals (canthaxanthin) (Merlin and Delé-Dubois, 1986; Cvejic et al., 2007; Bracco et al., 2016).

One property of the octocoral SOM, shared by many different calcifying organisms (Puverel et al., 2005; Marin and Luquet, 2007; Mann et al., 2010), is the abundance of proteins highly enriched in acidic (isoelectric point < 4.5) amino acids, primarily aspartic acid (Watabe and Kingsley, 1992; Rahman and Oomori, 2009). One possible biological reason being the proposed interaction of carboxylic groups, found in the side chain of aspartic acid, interacting with calcium ions (Weiner and Hood, 1975). The mechanisms underlying SkOM regulation over coral calcification remain, however, elusive, and no functional information is currently available. The first octocoral skeletal protein to be characterized was extracted from the sclerites of *C. rubrum*, and named scleritin (Debreuil et al., 2012). This occurred almost a decade after the isolation of the first skeletal protein (galaxin) from a scleractinian skeleton (Fukuda et al., 2003). Scleritin does not possess any known protein domain and appears solely expressed by scleroblasts found in the mesoglea, but not by the cells in calcifying epithelium forming the axial skeleton (Debreuil et al., 2012). As previously mentioned, the latter have been classified as composed of scleroblasts, due to the absence of morphological differences with the mesogleal sclerite-producing cells (Grillo et al., 1993). However, the expression pattern of scleritin suggests that cells involved in these two calcification processes (i.e., sclerite formation and axial skeleton deposition) employ different proteins and are thus characterized by different gene expression profiles. Another extracellular protein (ECMP-67), with the ability to regulate $CaCO_3$ polymorphism *in vitro,* was also isolated from the sclerites of *Lobophytum crassum* (Rahman et al., 2011).

Over the years, different coral SkOM components - including proteins, polysaccharides and lipids—have been in fact shown to promote the formation of different calcium carbonate polymorphs *in vitro* (Rahman and Oomori, 2009; Reggi et al., 2016; Naggi et al., 2018; Laipnik et al., 2019). However, whether these molecules possess the same properties *in vivo* remains to be determined. More recently, the advent of mass spectroscopy coupled with transcriptomics has enabled researchers to shift from the analysis of single proteins to the characterization of whole skeletal proteomes. This allowed to describe the "skeletogenic proteins" (Jackson et al., 2007), "skeletome" (Ramos-Silva et al., 2013) or "biomineralization toolkits" (Drake et al., 2013) in different calcifying organisms. This approach was recently applied to obtain the first proteomes found in octocoral skeletons and sclerites and provide a comparative analysis of octocorals producing aragonite (*H. coerulea*) and calcite (*Tubipora musica* and *S.* cf. *cruciata*) (Conci et al., 2020). An extremely low overlap was reported between aragonite and calcite-producing species, pointing to different protein repertoires being used by species forming different polymorphs. The only instance of a shared protein was a carbonic anhydrase homolog to CruCA-4. This protein was originally described, alongside other five carbonic anhydrases, in *C. rubrum* and found overexpressed in tissues enriched in calcifying cells (Le Goff et al., 2016). Carbonic anhydrases (CAs) are a superfamily of enzymes responsible for catalyzing the interconversion between carbon dioxide (CO_2) and bicarbonate (HCO_3^-) (Supuran, 2008), and are commonly found in different animal skeletons, including scleractinian corals (Miyamoto et al., 1996; Mann et al., 2008; Ramos-Silva et al., 2013; Mann, 2015). In anthozoan corals, CAs can regulate the concentration of HCO_3^- in calcification spaces (see Bertucci et al., 2013 for a review). Scleritin was identified in the organic matrix of both *T. musica* and *S.* cf. *cruciata*, but not in the aragonitic *H. coerulea (Conci et al., 2020)*, consistent with the hypothesis of its involvement in sclerite formation. Nonetheless, despite not being secreted into the skeleton, scleritin homologs are actively being expressed in *H. coerulea* (Conci et al., 2019). This could point on one hand to *H. coerulea* scleritin playing a different role (not requiring secretion into the skeleton) in calcification. Alternatively, the protein could hold an unrelated function and could have been recruited for biomineralization by octocorals producing calcite sclerites. In this light, comparison of the characteristics and function of calcification-related proteins in both aragonite and calcite-forming octocorals could highlight differences between groups and detect co-option events of proteins for biomineralization.

Biological Control II: Ion Transport and Regulation

For $CaCO_3$ precipitation to occur, different physio-chemical conditions have to be reached within the calcification spaces. One critical parameter is the saturation state (Ω) of the solution with respect to a certain $CaCO_3$ polymorph ($\Omega_{Aragonite}$ or $\Omega_{Calcite}$). This value is calculated as the ratio of Ca^{2+} and CO_3^{2-} ion activity products to the stoichiometric solubility product of aragonite or calcite (Morse and Mackenzie, 1990). At Ω = 1

solid mineral and seawater are in equilibrium, while at $\Omega > 1$ and $\Omega < 1$ precipitation and dissolution, respectively, occur. The saturation state is also intimately linked to the pH of the solution as this can influence the availability of CO_3^{2-} ions. It has been suggested that corals might be able to modulate the composition of their calcifying fluids, with respect to seawater, to promote $CaCO_3$ precipitation and enhance calcification. In scleractinian corals for example, Ω_{Ar} of calcifying fluids can be on average around 12 (DeCarlo et al., 2017) and display diurnal cyclic variability (DeCarlo et al., 2019). This value is sensibly higher compared to seawater in reef environments (Ω_{Ar} ca. 3) (Mongin et al., 2016).

Several chemical parameters of the calcifying fluids have been studied in scleractinian corals (Cai et al., 2016; Comeau et al., 2017; Sevilgen et al., 2019), while information on octocorals is very limited. This is partly due to the presence of additional tissue layers preventing direct access to the calcification space (Le Goff et al., 2017). Information on the pH of calcifying fluids (pH_{cf}) in both coral groups is however available. In scleractinian corals, pH_{cf} is higher compared to the pH_{sw}, but increases in seawater acidity appear to cause declines in the pH of calcifying fluids (Venn et al., 2013; Holcomb et al., 2014). Contrarily, early analyses in *C. rubrum* (based on boron isotopic analysis) did not detect the presence of significant pH upregulation between seawater and the pH_{cf} of the axial skeleton (McCulloch et al., 2012). This was later corroborated by pH-sensitive dye-based measurements showing that sclerites and axis growth occur at a pH of 7.97 ± 0.15 and 7.89 ± 0.09, respectively (Le Goff et al., 2017). In the same study however, pH_{cf} was found more alkaline compared to the cytoplasm of calcifying cells, which implies—as in scleractinians (Zoccola et al., 2004)—the active proton removal from calcification spaces, possibly operated by a Ca^{2+}-ATPase (Le Goff et al., 2017). Measurements for sclerites were obtained during the extracellular phase (i.e., sclerites enveloped by two scleroblasts), while no information is currently available for pH of the calcifying medium within scleroblasts vacuoles (i.e., intracellular stage).

Analysis was then conducted at normal pH_{sw} values. Whether *C. rubrum* is able to maintain pH homeostasis under seawater acidification conditions has not been determined. Differences in pH regulation between scleractinian skeletons and octocoral sclerites could be related to the different localization or composition (aragonite vs. calcite) of the skeletal structures. For example, the cells and/or mesoglea surrounding octocoral sclerites could buffer the effects of seawater chemistry. Surrounding tissues have, for instance, been proposed to act as a protective barrier against the effects of ocean acidification (OA) in octocorals (discussed in the next section; Gabay et al., 2014). However, the multi-step (intracellular and extracellular) growth model of octocoral sclerites previously described, opens to the possibility that sclerites could experience different environments—in terms of calcifying fluids chemistry and their interaction with seawater—during their formation.

Ocean acidification also appears to impact $CaCO_3$ polymorphs differently, with calcite being apparently less affected (although depending on magnesium content) (Ries et al., 2009). A possible approach to further elucidate pH_{cf} regulation mechanisms in octocorals could be the characterization of calcifying fluids pH in *H. coerulea,* for which no information is currently available. Such analysis could determine, on one hand, whether the absence of pH_{cf} regulation is indeed a common trait among Octocorallia, independently of the characteristics of the mineral structures (calcite sclerites/axis vs. aragonite skeleton). Alternatively, aragonitic octocorals could exhibit pH_{cf} increases as observed in scleractinian, pointing to pH upregulation representing a required feature for aragonite deposition in both coral groups.

Within the calcification space, calcium concentration in scleractinians is not necessarily higher compared to seawater, but some species can modulate calcium levels in response to decreases in seawater pH (DeCarlo et al., 2018). For octocorals, to the best of our knowledge, no information has been obtained. Calcium transport to calcification sites has been studied in *Leptogorgia virgulata* and a general model of calcium transfer has nonetheless been provided by Watabe and Kingsley (1992). Transport of Ca^{2+} during the intracellular growth of sclerites in octocorals represents a multi-step process (**Figure 5**). To reach the calcification space, calcium first diffuses from seawater into the outer epithelial cells and is actively extruded into the mesoglea. Studies involving specific transporters inhibitors have highlighted the action of Ca^{2+}-ATPases during this step, while Na^{+}-K^{+} exchangers don't appear to be involved (Kingsley and Watabe, 1984). Once in the mesoglea, the majority of calcium ions reach the axis epithelium and are incorporated into the axial skeleton, while others diffuse into the scleroblasts. Inside calcifying cells, calcium is transported inside electron-dense bodies (Kingsley and Watabe, 1985) to the calcifying vacuoles where sclerites form (Kingsley and Watabe, 1982). Both the membrane of scleroblasts and calcium-transporting vesicles exhibit signs of Ca^{2+}-ATPases activity (Kingsley and Watabe, 1984).

The origin and transport of carbon (CO_2 and HCO_3^{-}) has also been investigated in *L. virgulata* (Lucas and Knapp, 1997). In this species, carbonic anhydrase represented the major carbon source followed by bicarbonate. Inhibition of carbonic anhydrases caused significant declines in incorporation rates of both dissolved and metabolically produced CO_2, pointing to an important role of these enzymes in the regulation of carbon availability. Carbonic anhydrases, for example, have been proposed to operate on the membrane of calcifying vacuoles and electron-dense bodies (Kingsley and Watabe, 1987; Lucas and Knapp, 1996) and the aforementioned presence of CruCA-4 homologs inside octocoral skeletons confirms the presence of these enzymes within the calcifying medium (Conci et al., 2020).

ANTHROPOGENIC THREATS TO OCTOCORAL BIOMINERALIZATION

The effects of anthropic stressors on the ability of marine organisms to calcify have been the topic of a number of studies. In corals, for example, changes in calcification rates and growth have been studied in relation to different stressors, such as seawater temperature (Howe and Marshall, 2002;

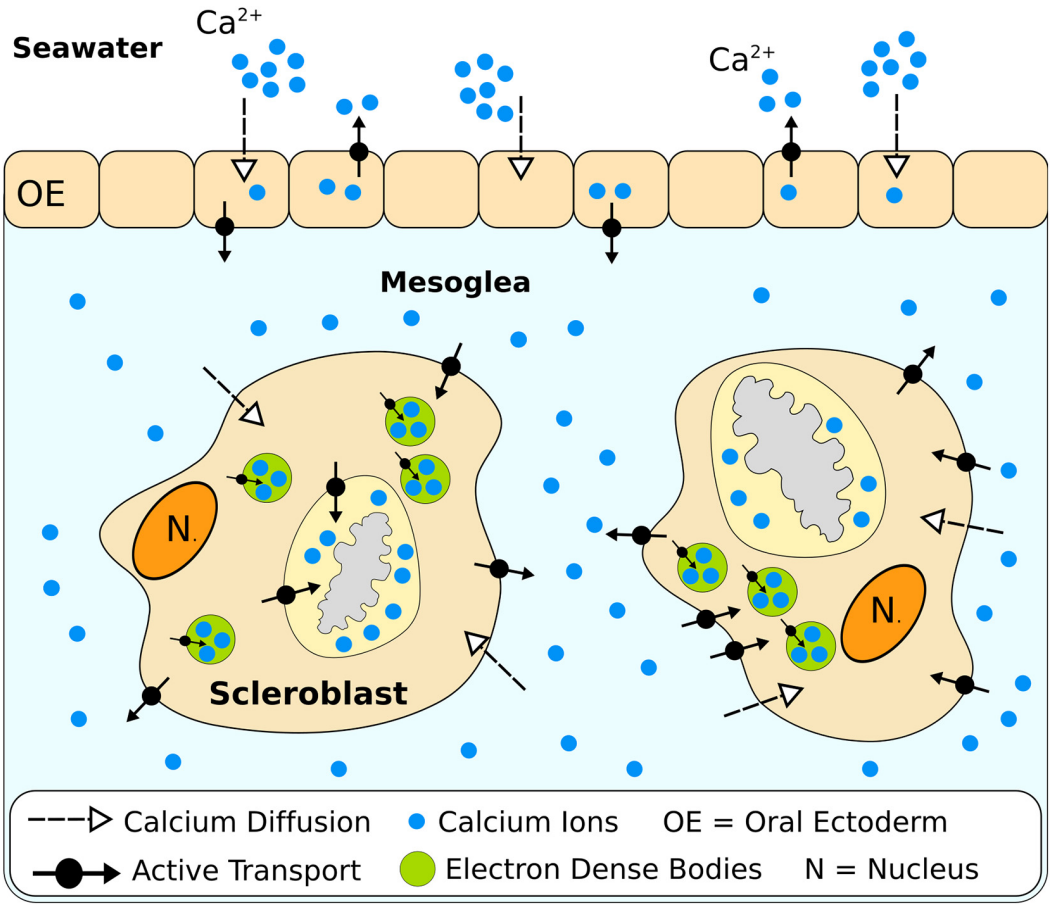

FIGURE 5 | Proposed model of calcium transport from seawater to growing sclerites in *Leptogorgia virgulata* (based on Watabe and Kingsley, 1992).

Marshall and Clode, 2004), pollution (Spencer Davies, 1990; Biscéré et al., 2015) and turbidity (Kendall et al., 1985; Browne, 2012).

However, particular focus has been dedicated to study the effects of the so-called "ocean acidification" (OA), i.e., the decrease in sea surface water pH caused by the increase in the atmospheric carbon dioxide (CO_2) concentration (Hoegh-Guldberg et al., 2007; Solomon et al., 2007). Ocean acidification linked detrimental effects on biomineralization have been reported for multiple marine groups including calcifying algae (Kuffner et al., 2008), scleractinian corals (Marubini et al., 2003; Hoegh-Guldberg et al., 2007; Mollica et al., 2018) and molluscs (Comeau et al., 2009; Gazeau et al., 2013). Research has however also highlighted several instances of resilience to ocean acidification, highlighting species-specific responses to low pH (Cross et al., 2015a,b; González-Pech et al., 2017; Lenz and Edmunds, 2017).

Octocorals appear to exhibit varying responses to ocean acidification. An inverse correlation between calcification rates and pCO_2 have been reported for *Eunicea flexuosa* when exposed to a pH range of 8.1 and 7.1 (Gómez et al., 2015). Contrarily, in another study no changes in branch extension and sclerite structure could be observed in the same species at pH 7.75 compared to control values (pH 8.1) (Enochs et al., 2016). Lower pH (7.6 and 7.3) had no effects on polyp weight and protein content in different octocorals nor in chlorophyll abundance ordensity of its symbiotic algae (Gabay et al., 2013). One possible explanation behind octocoral resilience could be the location inside the mesoglea of their sclerites with the surrounding tissues acting as a protective barrier (Gabay et al., 2014). A similar scenario has also been proposed for the organic layers protecting mollusc shells against dissolution (Rodolfo-Metalpa et al., 2011). From an ecological perspective, different tolerance to changing environmental conditions is of importance as it can determine which species will thrive or decline under future conditions, and cause profound changes in marine communities composition (Fabricius et al., 2011). And shifts from stony (more vulnerable) to soft coral (more resistant)-dominated environments have already been observed (Inoue et al., 2013).

DISCUSSION

Octocorals (Cnidaria: Anthozoa) represent a group of benthic marine organisms that have evolved a wide variety

of biomineralization strategies. The composite biomaterials produced by these organisms include structures composed of different calcium carbonate ($CaCO_3$) polymorphs (aragonite and calcite). From an evolutionary perspective, the presence of aragonite skeletons in Octocorallia is puzzling as it is observed in an extremely low number of species in a single clade, the Helioporacea. Apparently, this occurrence represents one of the very few instances of aragonite formation originating during a Calcite Sea interval (Porter, 2010). Despite the diversity of their skeletal elements, octocorals have only been marginally studied for biomineralization research. This has been partially caused by their low contribution to $CaCO_3$ production and reef formation (Smith and Kinsey, 1976; Herrán et al., 2017; Edinger et al., 2019) compared to scleractinian corals, the other group of calcifying anthozoans and main reef builders in today's oceans. Additionally, octocoral species often inhabit deeper marine habitats compared to scleractinians (Roberts et al., 2009), which can hinder field observation and the collection of specimens for follow-up studies. With the aim to identify current knowledge gaps and propose possible future research approaches, here we reviewed the research status of octocoral biomineralization. We focused and compared what is known about the evolutionary, cellular and molecular processes underlying different octocoral skeletons, with a focus on $CaCO_3$ polymorph (i.e., aragonite and calcite) diversity.

Although differences in research output between scleractinian and octocoral calcification are often mentioned, we highlighted how differences—both in terms of data availability and scientific knowledge—exist with respect to the process of biomineralization between different octocoral groups. Several mechanisms and features of octocoral biomineralization, such as the characteristics of the calcifying cells (e.g., scleroblasts) or Ca^{2+} transport, have mostly been investigated in species depositing calcite. Although calcite represents by far the most commonly deposited polymorph in octocorals, studying aragonite formation provides the opportunity to further our understanding on multiple aspects of the origin and evolution of octocoral and scleractinian biomineralization. Firstly, differences between aragonite and calcite formation are not necessarily limited to skeleton polymorphism. In fact, calcite and aragonite-forming species also differ in terms of other calcification-related properties, such as the composition of the organic matrix proteome (Conci et al., 2020) and possibly the type and characteristics of calcifying cells and epithelia. With the exception of early descriptions from the late nineteenth century (e.g., Bourne and Lankester (1895), no study has in fact focused on the calcifying cells of aragonitic octocorals. In addition, the different localization of calcitic and aragonitic structures (i.e., surrounded by tissue or not) could also entail the different regulation of the chemistry and pH of the calcification fluids, as observed between scleractinians (Venn et al., 2013; Holcomb et al., 2014) and *Corallium rubrum* (Le Goff et al., 2017). In fact, the scleractinian-like characteristics of helioporacean skeletons (i.e., aragonite exoskeleton), provide the unique opportunity to compare aragonite formation between Octocorallia and Scleractinia, and in turn determine which biomineralization features are driven by phylogeny (i.e., properties shared by octocorals producing different polymorphs) and which are instead related to the characteristics of the skeleton (i.e., properties shared by aragonitic octocorals and scleractinians). So far, this research avenue has not been fully explored, but at present the data at hand suggest that the aragonitic *Heliopora coerulea* employs a different biomineralization strategy compared to both calcitic octocorals and scleractinians. The only aspect for which information is currently available for all three groups concerns the composition of the skeleton proteomes. Their analyses have shown that very few proteins found in the skeleton of *Heliopora coerulea* are also found in other calcifying corals, irrespective of whether those are of calcite or aragonite (Ramos-Silva et al., 2013; Conci et al., 2020).

Difference in research focus and information availability are not limited to calcite vs. aragonite species, but can also be observed within the former. The majority of information for calcite-forming octocorals has been obtained from a small set of species, including the gorgonian *Leptogorgia virgulata* and the precious coral *Corallium rubrum*. This includes (1) the current knowledge on ion sources and transport needed for calcification, (2) detailed description of scleroblasts, and (3) both mechanisms of intracellular and extracellular formation of sclerites. Although extremely informative, a research approach focusing on very few "model species" may lead to an underestimation of the diversity of biomineralization strategies exhibited by different octocoral groups. The possible presence of substantial differences in sclerites and/or skeleton formation that can also occur even within a single genus (e.g., *Corallium*) (Lawniczak, 1987), requires extensive comparative analyses instead.

In the light of this, a possible step could be to taxonomically widen the generation of—*omic* resources, optimized to encompass a broad diversity of octocoral skeletal structures. The simultaneous presence, within Octocorallia, of calcite, aragonite and aragonite + calcite skeletons represents an ideal scenario to compare gene repertories across species producing different polymorphs, and compare those with scleractinian corals. Moreover, in addition to the aforementioned need for DNA sequencing data from the Calcaxonia, sequencing projects for skeleton-lacking octocorals (e.g., genus *Phenganax*) (Alderslade and Mcfadden, 2011) would also be beneficial, as they would allow to detect differences in the molecular mechanisms of biomineralization between calcifying and non-calcifying octocorals. The increase in the availability of octocoral genomes and transcriptomes would then in turn allow to progressively conduct more taxonomically comprehensive phylogenetic analysis, and resolve deep evolutionary relationships between clades, and ultimately how biomineralization in Octocorallia evolved.

AUTHOR CONTRIBUTIONS

NC wrote the manuscript. SV and GW edited the manuscript. All authors contributed to the discussion.

REFERENCES

Alderslade, P. (2000). Four new genera of soft corals (Coelenterata: octocorallia), with notes on the classification of some established taxa. *Zool. Meded.* 74, 237–249.

Alderslade, P., and McFadden, C. S. (2007). Pinnule-less polyps: a new genus and new species of Indo-Pacific Clavulariidae and validation of the soft coral genus *Acrossota* and the family Acrossotidae (Coelenterata: octocorallia). *Zootaxa* 1400, 27–44. doi: 10.11646/zootaxa.1400.2

Alderslade, P., and Mcfadden, C. S. (2011). A new sclerite-free genus and species of Clavulariidae (Coelenterata: octocorallia). *Zootaxa* 3104, 64–68. doi: 10.11646/zootaxa.3104.1.6

Algeo, T. J., Luo, G. M., Song, H. Y., Lyons, T. W., and Canfield, D. E. (2015). Reconstruction of secular variation in seawater sulfate concentrations. *Biogeosciences* 12, 2131–2151. doi: 10.5194/bg-12-2131-2015

Allemand, D. (1993). The biology and skeletogenesis of the Mediterranean Red Coral: a review. *Precious Corals Octocorals Res.* 2, 19–39.

Allemand, D., Cuif, J. P., Watabe, N., Oishi, M., and Kawaguchi, T. (1994). The organic matrix of skeletal structures of the Mediterranean red coral, *Corallium rubrum*. *Bull. Inst. Océanogr.* 14, 129–139.

Allemand, D., Tambutté, É, Zoccola, D., and Tambutté, S. (2011). "Coral calcification, cells to reefs," in *Coral Reefs: An Ecosystem in Transition*, eds Z. Dubinksy and N. Stambler (Dordrecht: Springer), 119–150. doi: 10.1007/978-94-007-0114-4_9

Ament-Velásquez, S. L., Breedy, O., Cortés, J., Guzman, H. M., Wörheide, G., and Vargas, S. (2016). Homoplasious colony morphology and mito-nuclear phylogenetic discordance among Eastern Pacific octocorals. *Mol. Phylogenet. Evol.* 98, 373–381. doi: 10.1016/j.ympev.2016.02.023

Ausich, W. I., and Babcock, L. E. (1998). The phylogenetic position of *Echmatocrinus brachiatus*, a probable octocoral from the Burgess Shale. *Palaeontology* 41, 193–202.

Balthasar, U., and Cusack, M. (2015). Aragonite-calcite seas—Quantifying the gray area. *Geology* 43, 99–102. doi: 10.1130/g36293.1

Balthasar, U., Cusack, M., Faryma, L., Chung, P., Holmer, L. E., Jin, J., et al. (2011). Relic aragonite from ordovician–silurian brachiopods: implications for the evolution of calcification. *Geology* 39, 967–970. doi: 10.1130/g32269.1

Barzansky, B., and Lenhoff, H. M. (1974). On the chemical composition and developmental role of the mesoglea of *Hydra*. *Integr. Comp. Biol.* 14, 575–581. doi: 10.1093/icb/14.2.575

Bayer, F. M. (1981a). *Bibliography of Octocorallia 1469-1977. Seminarios de Biologia Marinha*. Rio de Janeiro: Academia Brasileira de Ciências, 29–102.

Bayer, F. M. (1981b). Key to the genera of Octocorallia exclusive of Pennatulacea (Coelenterata: anthozoa), with diagnosis of new taxa. *Proc. Biol. Soc. Washington* 94, 902–947.

Bayer, F. M., and Macintyre, I. G. (2001). The mineral component of the axis and holdfast of some gorgonacean octocorals (Coelenteratea: anthozoa), with specieal reference to the family Gorgoniidae. *Proc. Biol. Soc. Washington* 114, 309–345.

Bayer, F. M., and Muzik, K. M. (1976). A new solitary octocoral, *Taiaroa tauhou* gen. et sp. nov. (Coelenterata: protoalcyonaria) from New Zealand. *J. R. Soc. N. Z.* 6, 499–515. doi: 10.1080/03036758.1976.10421488

Bayer, F. M., and Owre, H. B. (1967). *The Free Living Lower Invertebrates*. New York, NY: The Mcmillan CO.

Benayahu, Y., McFadden, C. S., and Shoham, E. (2017). Search for mesophotic octocorals (Cnidaria, Anthozoa) and their phylogeny: I. A new sclerite-free genus from Eilat, northern Red Sea. *ZooKeys* 680, 1–11. doi: 10.3897/zookeys.680.12727

Bengtson, S. (1981). Atractosella, a silurian alcyonacean octocoral. *J. Paleontol.* 55, 281–294.

Bertucci, A., Moya, A., Tambutté, S., Allemand, D., Supuran, C. T., and Zoccola, D. (2013). Carbonic anhydrases in anthozoan corals—A review. *Bioorg. Med. Chem.* 21, 1437–1450. doi: 10.1016/j.bmc.2012.10.024

Bice, K. L., Birgel, D., Meyers, P. A., Dahl, K. A., Hinrichs, K.-U., and Norris, R. D. (2006). A multiple proxy and model study of Cretaceous upper ocean temperatures and atmospheric CO2 concentrations : cretaceous multiple proxy study. *Paleoceanography* 21:A2002.

Biscéré, T., Rodolfo-Metalpa, R., Lorrain, A., Chauvaud, L., Thébault, J., Clavier, J., et al. (2015). Responses of two scleractinian corals to cobalt pollution and ocean acidification. *PLoS One* 10:e0122898. doi: 10.1371/journal.pone.0122898

Bourne, G. C., and Lankester, E. R. (1895). IX. On the structure and affinities of <Heliopora coerulea, Pallas. With some observations on the structure of *Xenia* and *Heteroxenia*. *Philos. Trans. R. Soc. Lond. (B)* 186, 455–483. doi: 10.1098/rstb.1895.0009

Bracco, S., Fumagalli, P., Fusi, P., Santambrogio, C., Rolandi, V., and Brajkovic, A. (2016). Identification of the chromophores in *Corallium rubrum* gem quality corals by HPLC/UV, ESI-MS and 1H NMR spectroscopy. *Period. Mineral.* 85, 83–93.

Browne, N. K. (2012). Spatial and temporal variations in coral growth on an inshore turbid reef subjected to multiple disturbances. *Mar. Environ. Res.* 77, 71–83. doi: 10.1016/j.marenvres.2012.02.005

Cai, W.-J., Ma, Y., Hopkinson, B. M., Grottoli, A. G., Warner, M. E., Ding, Q., et al. (2016). Microelectrode characterization of coral daytime interior pH and carbonate chemistry. *Nat. Commun.* 7:11144.

Caley, M. J., and St John, J. (1996). Refuge availability structures assemblages of tropical reef fishes. *J. Anim. Ecol.* 65, 414–428. doi: 10.2307/5777

Colgan, M. W. (1984). "The cretaceous coral *Heliopora* (Octocorallia, Coenothecalia)—a common indo-pacific reef builder," in *Living Fossils*, eds N. Eldredge and S. M. Stanley (New York, NY: Springer New York), 266–271. doi: 10.1007/978-1-4613-8271-3_33

Comeau, S., Gorsky, G., Jeffree, R., Teyssié, J.-L., and Gattuso, J.-P. (2009). Impact of ocean acidification on a key Arctic pelagic mollusc (*Limacina helicina*). *Biogeosciences* 6, 1877–1882. doi: 10.5194/bg-6-1877-2009

Comeau, S., Tambutté, E., Carpenter, R. C., Edmunds, P. J., Evensen, N. R., Allemand, D., et al. (2017). Coral calcifying fluid pH is modulated by seawater carbonate chemistry not solely seawater pH. *Proc. Biol. Sci.* 284:20161669. doi: 10.1098/rspb.2016.1669

Conci, N. (2020). *Molecular Biomineralization of Octocoral Skeletons: Calcite Versus Aragonite*. Dissertation, LMU München, Munich.

Conci, N., Lehmann, M., Vargas, S., and Wörheide, G. (2020). Comparative proteomics of octocoral and scleractinian skeletomes and the evolution of coral calcification. *Genome Biol. Evol.* 12, 1623–1635. doi: 10.1093/gbe/evaa162

Conci, N., Wörheide, G., and Vargas, S. (2019). New non-bilaterian transcriptomes provide novel insights into the evolution of coral skeletomes. *Genome Biol. Evol.* 11, 3068–3081. doi: 10.1093/gbe/evz199

Constantz, B., and Weiner, S. (1988). Acidic macromolecules associated with the mineral phase of scleractinian coral skeletons. *J. Exp. Zool.* 248, 253–258. doi: 10.1002/jez.1402480302

Cope, J. C. W. (2005). OCTOCORALLIAN AND HYDROID FOSSILS FROM THE LOWER ORDOVICIAN OF WALES. *Palaeontology* 48, 433–445. doi: 10.1111/j.1475-4983.2005.00455.x

Cross, E. L., Peck, L. S., and Harper, E. M. (2015a). Ocean acidification does not impact shell growth or repair of the Antarctic brachiopod *Liothyrella uva* (Broderip, 1833). *J. Exp. Mar. Bio. Ecol.* 462, 29–35. doi: 10.1016/j.jembe.2014.10.013

Cross, E. L., Peck, L. S., Lamare, M. D., and Harper, E. M. (2015b). No ocean acidification effects on shell growth and repair in the New Zealand brachiopod *Calloria inconspicua* (Sowerby, 1846). *ICES J. Mar. Sci.* 73, 920–926. doi: 10.1093/icesjms/fsv031

Cuif, J.-P. (2016). "Calcification in the cnidaria through time: an overview of their skeletal patterns from individual to evolutionary viewpoints," in *The Cnidaria, Past, Present and Future: The world of Medusa and Her Sisters*, eds S. Goffredo and Z. Dubinsky (Cham: Springer International Publishing), 163–179. doi: 10.1007/978-3-319-31305-4_11

Cuif, J.-P., Dauphin, Y., Berthet, P., and Jegoudez, J. (2004). Associated water and organic compounds in coral skeletons: quantitative thermogravimetry coupled to infrared absorption spectrometry. *Geochem. Geophys. Geosyst.* 5:Q11011.

Cvejic, J., Tambutté, S., Lotto, S., Mikov, M., Slacanin, I., and Allemand, D. (2007). Determination of canthaxanthin in the red coral (*Corallium rubrum*) from Marseille by HPLC combined with UV and MS detection. *Mar. Biol.* 152, 855–862. doi: 10.1007/s00227-007-0738-5

Dautova, T. N. (2019). New species of deep-water *Calcigorgia* gorgonians (Anthozoa: octocorallia) from the Sea of Okhotsk, with a re-diagnosis and a taxonomic review of the genus. *Eur. J. Taxon.* 549, 1–27. doi: 10.5852/ejt.2019.549

De Clippele, L. H., Buhl-Mortensen, P., and Buhl-Mortensen, L. (2015). Fauna associated with cold water gorgonians and sea pens. *Cont. Shelf Res.* 105, 67–78. doi: 10.1016/j.csr.2015.06.007

Debreuil, J., Tambutté, E., Zoccola, D., Deleury, E., Guigonis, J.-M., Samson, M., et al. (2012). Molecular cloning and characterization of first organic matrix protein from sclerites of red coral, *Corallium rubrum*. *J. Biol. Chem.* 287, 19367–19376. doi: 10.1074/jbc.m112.352005

Debreuil, J., Tambutté, S., Zoccola, D., Segonds, N., Techer, N., Marschal, C., et al. (2011). Specific organic matrix characteristics in skeletons of *Corallium* species. *Mar. Biol.* 158, 2765–2774. doi: 10.1007/s00227-011-1775-7

DeCarlo, T. M., Comeau, S., Cornwall, C. E., and McCulloch, M. T. (2018). Coral resistance to ocean acidification linked to increased calcium at the site of calcification. *Proc. Biol. Sci.* 285:20180564. doi: 10.1098/rspb.2018.0564

DeCarlo, T. M., D'Olivo, J. P., Foster, T., Holcomb, M., Becker, T., and McCulloch, M. T. (2017). Coral calcifying fluid aragonite saturation states derived from Raman spectroscopy. *Biogeosciences* 14, 5253–5269. doi: 10.5194/bg-14-5253-2017

DeCarlo, T. M., Ross, C. L., and McCulloch, M. T. (2019). Diurnal cycles of coral calcifying fluid aragonite saturation state. *Mar. Biol.* 166:28.

Deflandre-Rigaud, M. (1957). A classification of fossil alcyonarian sclerites. *Micropaleontology* 3, 357–366. doi: 10.2307/1484441

Devictor, S. T., and Morton, S. L. (2010). Identification guide to the shallow water (0–200 m) octocorals of the South Atlantic Bight. *Zootaxa* 2599, 1–62. doi: 10.11646/zootaxa.2599.1.1

Drake, J. L., Mass, T., Haramaty, L., Zelzion, E., Bhattacharya, D., and Falkowski, P. G. (2013). Proteomic analysis of skeletal organic matrix from the stony coral *Stylophora pistillata*. *Proc. Natl. Acad. Sci. U.S.A.* 110, 3788–3793. doi: 10.1073/pnas.1301419110

Dunkelberger, D. G., and Watabe, N. (1974). An ultrastructural study on spicule formation in the pennatulid colony *Renilla reniformis*. *Tissue Cell* 6, 573–586. doi: 10.1016/0040-8166(74)90001-9

Edinger, E., Baker, K., Bélanger, D., Greeley, K., de Moura Neves, B., Sherwood, O., et al. (2019). Estimating calcium carbonate production by Northwest Atlantic octocorals. *Geophys. Res. Abstr.* 21.

Eguchi, M. (1948). Fossil helioporidae from Japan and the South Sea Islands. *J. Paleontol.* 22, 362–364.

Enochs, I. C., Manzello, D. P., Wirshing, H. H., Carlton, R., and Serafy, J. (2016). Micro-CT analysis of the Caribbean octocoral *Eunicea flexuosa* subjected to elevated pCO2. *ICES J. Mar. Sci.* 73, 910–919. doi: 10.1093/icesjms/fsv159

Fabricius, K., and Alderslade, P. (2001). *Soft Corals and Sea Fans: A Comprehensive Guide to the Tropical Shallow Water Genera of the Central-West Pacific, the Indian Ocean and the Red Sea*. Cape Cleveland, QLD: Australian Institute of Marine Science.

Fabricius, K. E., and Klumpp, D. W. (1995). Widespread mixotrophy in reef-inhabiting soft corals:the influence of depth, and colony expansion and contraction on photosynthesis. *Mar. Ecol. Prog. Ser.* 125, 195–204. doi: 10.3354/meps125195

Fabricius, K. E., Langdon, C., Uthicke, S., Humphrey, C., Noonan, S., De'ath, G., et al. (2011). Losers and winners in coral reefs acclimatized to elevated carbon dioxide concentrations. *Nat. Clim. Chang.* 1, 165–169. doi: 10.1038/nclimate1122

Falini, G., Fermani, S., and Goffredo, S. (2015). Coral biomineralization: a focus on intra-skeletal organic matrix and calcification. *Semin. Cell Dev. Biol.* 46, 17–26. doi: 10.1016/j.semcdb.2015.09.005

Farre, B., Cuif, J.-P., and Dauphin, Y. (2010). Occurrence and diversity of lipids in modern coral skeletons. *Zoology* 113, 250–257. doi: 10.1016/j.zool.2009.11.004

Fox, D. L., Smith, V. E., Grigg, R. W., and MacLeod, W. D. (1969). Some structural and chemical studies of the microspicules in the fan-coral *Eugorgia ampla* verrill. *Comp. Biochem. Physiol.* 28, 1103–1114. doi: 10.1016/0010-406x(69)90550-7

Frankel, R. B., Bazylinski, D. A., Johnson, M. S., and Taylor, B. L. (1997). Magneto-aerotaxis in marine coccoid bacteria. *Biophys. J.* 73, 994–1000. doi: 10.1016/s0006-3495(97)78132-3

Fukuda, I., Ooki, S., Fujita, T., Murayama, E., Nagasawa, H., Isa, Y., et al. (2003). Molecular cloning of a cDNA encoding a soluble protein in the coral exoskeleton. *Biochem. Biophys. Res. Commun.* 304, 11–17. doi: 10.1016/s0006-291x(03)00527-8

Gabay, Y., Benayahu, Y., and Fine, M. (2013). Does elevatedpCO2affect reef octocorals? *Ecol. Evol.* 3, 465–473. doi: 10.1002/ece3.351

Gabay, Y., Fine, M., Barkay, Z., and Benayahu, Y. (2014). Octocoral tissue provides protection from declining oceanic pH. *PLoS One* 9:e91553. doi: 10.1371/journal.pone.0091553

Gazeau, F., Parker, L. M., Comeau, S., Gattuso, J.-P., O'Connor, W. A., Martin, S., et al. (2013). Impacts of ocean acidification on marine shelled molluscs. *Mar. Biol.* 160, 2207–2245. doi: 10.1007/s00227-013-2219-3

Glaessner, M. F. (1985). *The Dawn of Animal Life: A Biohistorical Study*. Cambridge: CUP Archive.

Goffredo, S., Vergni, P., Reggi, M., Caroselli, E., Sparla, F., Levy, O., et al. (2011). The skeletal organic matrix from Mediterranean coral *Balanophyllia europaea* influences calcium carbonate precipitation. *PLoS One* 6:e22338. doi: 10.1371/journal.pone.0022338

Goldberg, W. M. (1988). Chemistry, histochemistry and microscopy of the organic matrix of spicules from a gorgonian coral. *Histochemistry* 89, 163–170. doi: 10.1007/bf00489919

Goldberg, W. M. (2001). Acid polysaccharides in the skeletal matrix and calicoblastic epithelium of the stony coral *Mycetophyllia reesi*. *Tissue Cell* 33, 376–387. doi: 10.1054/tice.2001.0191

Goldberg, W. M., and Benayahu, Y. (1987). Spicule formation in the gorgonian coral *Pseudoplexaura flagellosa*. 1: demonstration of intracellular and extracellular growth and the effect of ruthenium red during decalcification. *Bull. Mar. Sci.* 40, 287–303.

Gómez, C. E., Paul, V. J., Ritson-Williams, R., Muehllehner, N., Langdon, C., and Sánchez, J. A. (2015). Responses of the tropical gorgonian coral *Eunicea fusca* to ocean acidification conditions. *Coral Reefs* 34, 451–460. doi: 10.1007/s00338-014-1241-3

González-Pech, R. A., Vargas, S., Francis, W. R., and Wörheide, G. (2017). Transcriptomic resilience of the montipora digitata holobiont to low pH. *Front. Mar. Sci.* 4:403. doi: 10.3389/fmars.2017.00403

Grasshoff, M. (1999). *The Shallow Water Gorgonians of New Caledonia and Adjacent Islands:(Coelenterata: Octocorallia)*. Frankfurt: Senckenbergische Naturforschende Gesellschaft.

Grillo, M.-C., Goldberg, W. M., and Allemand, D. (1993). Skeleton and sclerite formation in the precious red coral *Corallium rubrum*. *Mar. Biol.* 117, 119–128. doi: 10.1007/bf00346433

Hardie, L. A. (1996). Secular variation in seawater chemistry: an explanation for the coupled secular variation in the mineralogies of marine limestones and potash evaporites over the past 600 m.y. *Geology* 24, 279–283. doi: 10.1130/0091-7613(1996)024<0279:svisca>2.3.co;2

He, H., Veneklaas, E. J., Kuo, J., and Lambers, H. (2014). Physiological and ecological significance of biomineralization in plants. *Trends Plant Sci.* 19, 166–174. doi: 10.1016/j.tplants.2013.11.002

Herrán, N., Narayan, G. R., Reymond, C. E., and Westphal, H. (2017). Calcium carbonate production, coral cover and diversity along a distance gradient from stone town: a case study from Zanzibar, Tanzania. *Front. Mar. Sci.* 4:412. doi: 10.3389/fmars.2017.00412

Hickson, S. J. (1895). The anatomy of *Alcyonium digitatum*. *Q. J. Microsc. Sci.* 37, 343–388.

Hill, D. (1960). Possible intermediates between Alcyonaria and Tabulata, Tabulata and Rugosa and Rugosa and Hexacoralla. *21st. Rept. Intern. Geol. Congr.* 22, 51–58.

Hoegh-Guldberg, O., Mumby, P. J., Hooten, A. J., Steneck, R. S., Greenfield, P., Gomez, E., et al. (2007). Coral reefs under rapid climate change and ocean acidification. *Science* 318, 1737–1742.

Holcomb, M., Venn, A. A., Tambutté, E., Tambutté, S., Allemand, D., Trotter, J., et al. (2014). Coral calcifying fluid pH dictates response to ocean acidification. *Sci. Rep.* 4:5207.

Hongo, Y., Yasuda, N., and NagaI, S. (2017). Identification of genes for synthesis of the blue pigment, biliverdin IXα, in the blue coral *Heliopora coerulea*. *Biol. Bull.* 232, 71–81. doi: 10.1086/692661

Horvath, E. A. (2019). A review of gorgonian coral species (Cnidaria, Octocorallia, Alcyonacea) held in the santa barbara museum of natural history research collection: focus on species from Scleraxonia, Holaxonia, Calcaxonia - Part III: suborder holaxonia continued, and suborder Calcaxonia. *Zookeys* 860, 183–306.

Howe, S. A., and Marshall, A. T. (2002). Temperature effects on calcification rate and skeletal deposition in the temperate coral, *Plesiastrea versipora* (Lamarck). *J. Exp. Mar. Bio. Ecol.* 275, 63–81. doi: 10.1016/s0022-0981(02)00213-7

Inoue, S., Kayanne, H., Yamamoto, S., and Kurihara, H. (2013). Spatial community shift from hard to soft corals in acidified water. *Nat. Clim. Chang.* 3, 683–687. doi: 10.1038/nclimate1855

Jackson, D. J., Macis, L., Reitner, J., Degnan, B. M., and Wörheide, G. (2007). Sponge paleogenomics reveals an ancient role for carbonic anhydrase in skeletogenesis. *Science* 316, 1893–1895. doi: 10.1126/science.1141560

Jeng, M.-S., Huang, H.-D., Dai, C.-F., Hsiao, Y.-C., and Benayahu, Y. (2011). Sclerite calcification and reef-building in the fleshy octocoral genus *Sinularia* (Octocorallia: alcyonacea). *Coral Reefs* 30, 925–933. doi: 10.1007/s00338-011-0765-z

Johnston, I. S. (1980). The ultrastructure of skeletogenesis in hermatypic corals. *Int. Rev. Cytol.* 67, 171–214. doi: 10.1016/s0074-7696(08)62429-8

Jolly, C., Berland, S., Milet, C., Borzeix, S., Lopez, E., and Doumenc, D. (2004). Zona localization of shell matrix proteins in mantle of *Haliotis tuberculata* (Mollusca, Gastropoda). *Mar. Biotechnol.* 6, 541–551. doi: 10.1007/s10126-004-3129-7

Karako-Lampert, S., Zoccola, D., Salmon-Divon, M., Katzenellenbogen, M., Tambutté, S., Bertucci, A., et al. (2014). Transcriptome analysis of the scleractinian coral *Stylophora pistillata*. *PLoS One* 9:e88615. doi: 10.1371/journal.pone.0088615

Kayal, E., Bentlage, B., Sabrina Pankey, M., Ohdera, A. H., Medina, M., Plachetzki, D. C., et al. (2018). Phylogenomics provides a robust topology of the major cnidarian lineages and insights on the origins of key organismal traits. *BMC Evol. Biol.* 18:68. doi: 10.1186/s12862-018-1142-0

Kayal, E., Roure, B., Philippe, H., Collins, A. G., and Lavrov, D. V. (2013). Cnidarian phylogenetic relationships as revealed by mitogenomics. *BMC Evol. Biol.* 13:5. doi: 10.1186/1471-2148-13-5

Kendall, J. J., Powell, E. N., Connor, S. J., Bright, T. J., and Zastrow, C. E. (1985). Effects of turbidity on calcification rate, protein concentration and the free amino acid pool of the coral *Acropora cervicornis*. *Mar. Biol.* 87, 33–46. doi: 10.1007/bf00397003

Kingsley, R. J., Bernhardt, A. M., Wilbur, K. M., and Watabe, N. (1987). Scleroblast cultures from the gorgonian *Leptogorgia virgulata* (Lamarck) (Coelenterata: gorgonacea). *In Vitro Cell. Dev. Biol.* 23, 297–302. doi: 10.1007/bf02623713

Kingsley, R. J., and Watabe, N. (1982). Ultrastructural investigation of spicule formation in the gorgonian *Leptogorgia virgulata* (Lamarck) (Coelenterata: gorgonacea). *Cell Tissue Res.* 223, 325–334. doi: 10.1007/bf01258493

Kingsley, R. J., and Watabe, N. (1983). Analysis of proteinaceous components of the organic matrices of spicules from the gorgonian *Leptogorgia virgulata*. *Comp. Biochem. Physiol. Part B Comp. Biochem.* 76, 443–447. doi: 10.1016/0305-0491(83)90273-0

Kingsley, R. J., and Watabe, N. (1984). Calcium uptake in the gorgonian *Leptogorgia virgulata*. The effects of atpase inhibitors. *Comp. Biochem. Physiol. A Physiol.* 79, 487–491. doi: 10.1016/0300-9629(84)90551-6

Kingsley, R. J., and Watabe, N. (1985). An autoradiographic study of calcium transport in spicule formation in the gorgonian *Leptogorgia virgulata* (Lamarck) (Coelenterata: gorgonacea). *Cell Tissue Res.* 239, 305–310.

Kingsley, R. J., and Watabe, N. (1987). Role of carbonic anhydrase in calcification in the gorgonian *Leptogorgia virgulata*. *J. Exp. Zool.* 241, 171–180. doi: 10.1002/jez.1402410203

Knoll, A. H. (2003). Biomineralization and evolutionary history. *Rev. Mineral. Geochem.* 54, 329–356. doi: 10.1515/9781501509346-016

Kocurko, M. J., and Kocurko, D. J. (1992). Fossil octocorallia of the red bluff formation. *Lower Oligocene Mississippi. J. Paleontol.* 66, 594–602. doi: 10.1017/s0022336000024458

Krieger, K. J., and Wing, B. L. (2002). Megafauna associations with deepwater corals (*Primnoa* spp.) in the Gulf of Alaska. *Hydrobiologia* 471, 83–90.

Kuffner, I. B., Andersson, A. J., Jokiel, P. L., Rodgers, K. S., and Mackenzie, F. T. (2008). Decreased abundance of crustose coralline algae due to ocean acidification. *Nat. Geosci.* 1, 114–117. doi: 10.1038/ngeo100

Laipnik, R., Bissi, V., Sun, C.-Y., Falini, G., Gilbert, P. U. P. A., and Mass, T. (2019). Coral acid rich protein selects vaterite polymorph in vitro. *J. Struct. Biol.* 209:107431. doi: 10.1016/j.jsb.2019.107431

Landing, E., Antcliffe, J. B., Brasier, M. D., and English, A. B. (2015). Distinguishing Earth's oldest known bryozoan (Pywackia, late Cambrian) from pennatulacean octocorals (Mesozoic–Recent). *J. Paleontol.* 89, 292–317. doi: 10.1017/jpa.2014.26

Landing, E., English, A., and Keppie, J. D. (2010). Cambrian origin of all skeletalized metazoan phyla—Discovery of Earth's oldest bryozoans (Upper Cambrian, southern Mexico). *Geology* 38, 547–550. doi: 10.1130/g30870.1

Lau, Y. W., and Reimer, J. D. (2019a). A first phylogenetic study on stoloniferous octocorals off the coast of Kota Kinabalu, Sabah, Malaysia, with the description of two new genera and five new species. *Zookeys* 872, 127–158. doi: 10.3897/zookeys.872.36288

Lau, Y. W., and Reimer, J. D. (2019b). Zooxanthellate, sclerite-free, and pseudopinnuled octocoral *Hadaka nudidomus* gen. nov. et sp. nov. (Anthozoa, octocorallia) from mesophotic reefs of the Southern Ryukyus Islands. *Diversity* 11:176. doi: 10.3390/d11100176

Lau, Y. W., Stokvis, F. R., Imahara, Y., and Reimer, J. D. (2019). The stoloniferous octocoral, *Hanabira yukibana*, gen. nov., sp. nov., of the southern Ryukyus has morphological and symbiont variation. *Contrib. Zool.* 88, 54–77. doi: 10.1163/18759866-20191355

Lau, Y. W., Stokvis, F. R., van Ofwegen, L. P., and Reimer, J. D. (2018). Stolonifera from shallow waters in the north-western Pacific: a description of a new genus and two new species within the Arulidae (Anthozoa, Octocorallia). *Zookeys* 790, 1–19.

Lawniczak, A. (1987). Les modalités de croissance de l'axe calcaire chez *Corallium johnsoni*. *Senckenb. Marit.* 19, 149–161.

Le Goff, C., Ganot, P., Zoccola, D., Caminiti-Segonds, N., Allemand, D., and Tambutté, S. (2016). Carbonic anhydrases in cnidarians: novel perspectives from the octocorallian *Corallium rubrum*. *PLoS One* 11:e0160368. doi: 10.1371/journal.pone.0160368

Le Goff, C., Tambutté, E., Venn, A. A., Techer, N., Allemand, D., and Tambutté, S. (2017). In vivo pH measurement at the site of calcification in an octocoral. *Sci. Rep.* 7:11210.

Le Tissier, M. D. (1991). The nature of the skeleton and skeletogenic tissues in the Cnidaria. *Hydrobiologia* 216, 397–402. doi: 10.1007/978-94-011-3240-4_57

Lenz, E. A., and Edmunds, P. J. (2017). Branches and plates of the morphologically plastic coral *Porites rus* are insensitive to ocean acidification and warming. *J. Exp. Mar. Bio. Ecol.* 486, 188–194. doi: 10.1016/j.jembe.2016.10.002

Leverette, C. L., Warren, M., Smith, M.-A., and Smith, G. W. (2008). Determination of carotenoid as the purple pigment in *Gorgonia ventalina* sclerites using Raman microscopy. *Spectrochim. Acta A Mol. Biomol. Spectrosc.* 69, 1058–1061. doi: 10.1016/j.saa.2007.07.018

Lewis, J. C., Barnowski, T. F., and Telesnicki, G. J. (1992). Characteristics of carbonates of gorgonian axes (coelenterata, octocorallia). *Biol. Bull.* 183, 278–296. doi: 10.2307/1542215

Lowenstam, H. A. (1981). Minerals formed by organisms. *Science* 211, 1126–1131. doi: 10.1126/science.7008198

Lowenstam, H. A., and Weiner, S. (1989). *On Biomineralization*, New York, NY: Oxford University Press, 144–167.

Lowenstein, T. K., Timofeeff, M. N., Brennan, S. T., Hardie, L. A., and Demicco, R. V. (2001). Oscillations in Phanerozoic seawater chemistry: evidence from fluid inclusions. *Science* 294, 1086–1088. doi: 10.1126/science.1064280

Lozouet, P., and Molodtsova, T. (2008). Filling a gap: the first occurrences of *Epiphaxum* (Cnidaria: helioporacea: lithotelestidae) in the eocene, oligocene and miocene. *Palaeontology* 51, 241–250. doi: 10.1111/j.1475-4983.2007.00744.x

Lucas, J. M., and Knapp, L. W. (1996). Biochemical characterization of purified carbonic anhydrase from the octocoral *Leptogorgia virgulata*. *Mar. Biol.* 126, 471–477. doi: 10.1007/bf00354629

Lucas, J. M., and Knapp, L. W. (1997). A physiological evaluation of carbon sources for calcification in the octocoral *Leptogorgia virgulata* (Lamarck). *J. Exp. Biol.* 200, 2653–2662.

Macintyre, I. G., Bayer, F. M., Logan, M. A. V., and Skinner, H. C. W. (2000). Possible vestige of early phosphatic biomineralization in gorgonian octocorals (Coelenterata). *Geology* 28, 455–458. doi: 10.1130/0091-7613(2000)028<0455:pvoepb>2.3.co;2

Mann, K. (2015). The calcified eggshell matrix proteome of a songbird, the zebra finch (*Taeniopygia guttata*). *Proteome Sci.* 13:29.

Mann, K., Poustka, A. J., and Mann, M. (2008). The sea urchin (*Strongylocentrotus purpuratus*) test and spine proteomes. *Proteome Sci.* 6:22. doi: 10.1186/1477-5956-6-22

Mann, K., Wilt, F. H., and Poustka, A. J. (2010). Proteomic analysis of sea urchin (*Strongylocentrotus purpuratus*) spicule matrix. *Proteome Sci.* 8:33. doi: 10.1186/1477-5956-8-33

Mann, S. (1983). "Mineralization in biological systems," in *Inorganic Elements in Biochemistry* Structure and Bonding, eds P. H. Connett, H. Folłmann, M. Lammers, S. Mann, J. D. Odom, and K. E. Wetterhahn (Berlin: Springer Berlin Heidelberg), 125–174. doi: 10.1007/bfb0111320

Marin, F., and Luquet, G. (2007). "Unusually acidic proteins in biomineralization," in *Handbook of Biomineralization*, ed. E. Buerlein (Weinheim: Wiley-VCH Verlag GmbH), 273–290. doi: 10.1002/9783527619443.ch16

Marshall, A. T., and Clode, P. (2004). Calcification rate and the effect of temperature in a zooxanthellate and an azooxanthellate scleractinian reef coral. *Coral Reefs* 23, 218–224. doi: 10.1007/s00338-004-0369-y

Marubini, F., Ferrier-Pages, C., and Cuif, J.-P. (2003). Suppression of skeletal growth in scleractinian corals by decreasing ambient carbonate-ion concentration: a cross-family comparison. *Proc. Biol. Sci.* 270, 179–184. doi: 10.1098/rspb.2002.2212

McCulloch, M., Trotter, J., Montagna, P., Falter, J., Dunbar, R., Freiwald, A., et al. (2012). Resilience of cold-water scleractinian corals to ocean acidification: boron isotopic systematics of pH and saturation state up-regulation. *Geochim. Cosmochim. Acta* 87, 21–34. doi: 10.1016/j.gca.2012.03.027

McFadden, C. S., France, S. C., Sánchez, J. A., and Alderslade, P. (2006). A molecular phylogenetic analysis of the Octocorallia (Cnidaria: anthozoa) based on mitochondrial protein-coding sequences. *Mol. Phylogenet. Evol.* 41, 513–527. doi: 10.1016/j.ympev.2006.06.010

McFadden, C. S., and Ofwegen, L. P. V. (2017). Revisionary systematics of the endemic soft coral fauna (Octocorallia: alcyonacea: alcyoniina) of the agulhas bioregion, South Africa. *Zootaxa* 4363, 451–488. doi: 10.11646/zootaxa.4363.4.1

McFadden, C. S., Quattrini, A. M., Brugler, M. R., Cowman, P. F., Dueñas, L. F., Kitahara, M. V., et al. (2021). Phylogenomics, origin and diversification of anthozoans (*Phylum Cnidaria*). *Syst. Biol.* syaa103. doi: 10.1093/sysbio/syaa103

McFadden, C. S., Sánchez, J. A., and France, S. C. (2010). Molecular phylogenetic insights into the evolution of Octocorallia: a review. *Integr. Comp. Biol.* 50, 389–410. doi: 10.1093/icb/icq056

Menzel, L. P., Tondo, C., Stein, B., and Bigger, C. H. (2015). Histology and ultrastructure of the coenenchyme of the octocoral Swiftia exserta, a model organism for innate immunity/graft rejection. *Zoology* 118, 115–124. doi: 10.1016/j.zool.2014.09.002

Merlin, J. C., and Delé-Dubois, M. L. (1986). Resonance Raman characterization of polyacetylenic pigments in the calcareous skeleton. *Comp. Biochem. Physiol. Part B Comp. Biochem.* 84, 97–103. doi: 10.1016/0305-0491(86)90277-4

Miyamoto, H., Miyashita, T., Okushima, M., Nakano, S., Morita, T., and Matsushiro, A. (1996). A carbonic anhydrase from the nacreous layer in oyster pearls. *Proc. Natl. Acad. Sci. U.S.A.* 93, 9657–9660. doi: 10.1073/pnas.93.18.9657

Miyazaki, Y., and Reimer, J. D. (2015). A new genus and species of octocoral with aragonite calcium-carbonate skeleton (Octocorallia, helioporacea) from Okinawa, Japan. *Zookeys* 511, 1–23.

Mollica, N. R., Guo, W., Cohen, A. L., Huang, K.-F., Foster, G. L., Donald, H. K., et al. (2018). Ocean acidification affects coral growth by reducing skeletal density. *Proc. Natl. Acad. Sci. U.S.A.* 115, 1754–1759. doi: 10.1073/pnas.1712806115

Mongin, M., Baird, M. E., Tilbrook, B., Matear, R. J., Lenton, A., Herzfeld, M., et al. (2016). The exposure of the great barrier reef to ocean acidification. *Nat. Commun.* 7:10732.

Morse, J. W., and Mackenzie, F. T. (1990). *Geochemistry of Sedimentary Carbonates*. Amsterdam: Elsevier.

Morse, J. W., Wang, Q., and Tsio, M. Y. (1997). Influences of temperature and Mg:Ca ratio on CaCO3 precipitates from seawater. *Geology* 25, 85–87. doi: 10.1130/0091-7613(1997)025<0085:iotamc>2.3.co;2

Mortensen, P. B., and Buhl-Mortensen, L. (2005). Morphology and growth of the deep-water gorgonians Primnoa resedaeformis and *Paragorgia arborea*. *Mar. Biol.* 147, 775–788. doi: 10.1007/s00227-005-1604-y

Moseley, H. N. (1876). On the structure and relations of the alcyonarian *Heliopora caerulea* with some account of the anatomy of a species of *Sarcophyton*, notes on the structure of species of the genera *Millepora*, *Pocillopora*, and *Stylaster*, and remarks on the affinities of certain palaeozoic corals. *Philos. Trans. R. Soc. Lond.* 166, 91–129. doi: 10.1098/rstl.1876.0004

Naggi, A., Torri, G., Iacomini, M., Colombo Castelli, G., Reggi, M., Fermani, S., et al. (2018). Structure and function of stony coral intraskeletal polysaccharides. *ACS Omega* 3, 2895–2901. doi: 10.1021/acsomega.7b02053

Nishishira, M. (1974). Human interference with the coral community and Acanthaster infestation of Okinawa. *Proc. 2nd Int. Coral Reef Symp.* 1974, 577–590.

Noé, S. U., and Dullo, W.-C. (2006). Skeletal morphogenesis and growth mode of modern and fossil deep-water isidid gorgonians (Octocorallia) in the West Pacific (New Zealand and Sea of Okhotsk). *Coral Reefs* 25, 303–320. doi: 10.1007/s00338-006-0095-8

Pérez, C. D., de Moura Neves, B., Cordeiro, R. T., Williams, G. C., and Cairns, S. D. (2016). "Diversity and distribution of octocorallia," in *The Cnidaria, Past, Present and Future: The world of Medusa and her sisters*, eds S. Goffredo and Z. Dubinsky (Cham: Springer International Publishing), 109–123. doi: 10.1007/978-3-319-31305-4_8

Poliseno, A., Feregrino, C., Sartoretto, S., Aurelle, D., Wörheide, G., McFadden, C. S., et al. (2017). Comparative mitogenomics, phylogeny and evolutionary history of Leptogorgia (Gorgoniidae). *Mol. Phylogenet. Evol.* 115, 181–189. doi: 10.1016/j.ympev.2017.08.001

Porter, S. M. (2010). Calcite and aragonite seas and the de novo acquisition of carbonate skeletons. *Geobiology* 8, 256–277. doi: 10.1111/j.1472-4669.2010.00246.x

Prada, C., Schizas, N. V., and Yoshioka, P. M. (2008). Phenotypic plasticity or speciation? A case from a clonal marine organism. *BMC Evol. Biol.* 8:47. doi: 10.1186/1471-2148-8-47

Puverel, S., Houlbrèque, F., Tambutté, E., Zoccola, D., Payan, P., Caminiti, N., et al. (2007). Evidence of low molecular weight components in the organic matrix of the reef building coral, *Stylophora pistillata*. *Comp. Biochem. Physiol. A Mol. Integr. Physiol.* 147, 850–856. doi: 10.1016/j.cbpa.2006.10.045

Puverel, S., Tambutté, E., Pereira-Mouriès, L., Zoccola, D., Allemand, D., and Tambutté, S. (2005). Soluble organic matrix of two Scleractinian corals: partial and comparative analysis. *Comp. Biochem. Physiol. B Biochem. Mol. Biol.* 141, 480–487. doi: 10.1016/j.cbpc.2005.05.013

Quattrini, A. M., Etnoyer, P. J., Doughty, C., English, L., Falco, R., Remon, N., et al. (2014). A phylogenetic approach to octocoral community structure in the deep Gulf of Mexico. *Deep Sea Res. Part 2 Top. Stud. Oceanogr.* 99, 92–102. doi: 10.1016/j.dsr2.2013.05.027

Quattrini, A. M., Rodríguez, E., Faircloth, B. C., Cowman, P. F., Brugler, M. R., Farfan, G. A., et al. (2020). Palaeoclimate ocean conditions shaped the evolution of corals and their skeletons through deep time. *Nat Ecol Evol.* 4, 1531–1538. doi: 10.1038/s41559-020-01291-1

Rahman, M. A., and Oomori, T. (2009). In vitro regulation of CaCO3 crystal growth by the highly acidic proteins of calcitic sclerites in soft coral, *Sinularia polydactyla*. *Connect. Tissue Res.* 50, 285–293. doi: 10.3109/03008200802714933

Rahman, M. A., Oomori, T., and Wörheide, G. (2011). Calcite formation in soft coral sclerites is determined by a single reactive extracellular protein. *J. Biol. Chem.* 286, 31638–31649. doi: 10.1074/jbc.m109.070185

Rahman, M. A., Shinjo, R., Oomori, T., and Wörheide, G. (2013). Analysis of the proteinaceous components of the organic matrix of calcitic sclerites from the soft coral *Sinularia* sp. *PLoS One* 8:e58781. doi: 10.1371/journal.pone.0058781

Ramos-Silva, P., Kaandorp, J., Huisman, L., Marie, B., Zanella-Cléon, I., Guichard, N., et al. (2013). The skeletal proteome of the coral *Acropora millepora*: the evolution of calcification by co-option and domain shuffling. *Mol. Biol. Evol.* 30, 2099–2112. doi: 10.1093/molbev/mst109

Reggi, M., Fermani, S., Samorì, C., Gizzi, F., Prada, F., Dubinsky, Z., et al. (2016). Influence of intra-skeletal coral lipids on calcium carbonate precipitation. *CrystEngComm* 18, 8829–8833. doi: 10.1039/c6ce01939k

Reich, M. (2009). "A critical review of octocorallian fossil record (Cnidaria: anthozoa)," in *Proceedings of the International Conference on the Cambrian Explosion–Walcott*, eds M. R. Smith, L. J. O'Brien, and J. B. Caron (Toronto: Burgess Shale Consortium).

Reich, M., and Kutscher, M. (2011). Sea pens (Octocorallia: pennatulacea) from the late cretaceous of northern Germany. *J. Paleontol.* 85, 1042–1051. doi: 10.1666/10-109.1

Ribes, M., Coma, R., and Gili, J.-M. (1998). Heterotrophic feeding by gorgonian corals with symbiotic zooxanthella. *Limnol. Oceanogr.* 43, 1170–1179. doi: 10.4319/lo.1998.43.6.1170

Ries, J. B., Cohen, A. L., and McCorkle, D. C. (2009). Marine calcifiers exhibit mixed responses to CO2-induced ocean acidification. *Geology* 37, 1131–1134. doi: 10.1130/g30210a.1

Roberts, J. M., Murray Roberts, J., Wheeler, A., Freiwald, A., and Cairns, S. (2009). *Cold Water Corals: The Biology and Geology of Deep-Sea Coral Habitats*. Cambridge: Cambridge University Press.

Rodolfo-Metalpa, R., Houlbrèque, F., Tambutté, É, Boisson, F., Baggini, C., Patti, F. P., et al. (2011). Coral and mollusc resistance to ocean acidification adversely affected by warming. *Nat. Clim. Chang.* 1, 308–312. doi: 10.1038/nclimate1200

Rokas, A., Krüger, D., and Carroll, S. B. (2005). Animal evolution and the molecular signature of radiations compressed in time. *Science* 310, 1933–1938. doi: 10.1126/science.1116759

Rüdiger, W., Klose, W., Vuillaume, M., and Barbier, M. (1968). On the structure of pterobilin, the blue pigment ofPieris brassicae. *Experientia* 24, 1000–1000. doi: 10.1007/bf02138705

Ruzicka, R. R., Colella, M. A., Porter, J. W., Morrison, J. M., Kidney, J. A., Brinkhuis, V., et al. (2013). Temporal changes in benthic assemblages on Florida Keys reefs 11 years after the 1997/1998 El Niño. *Mar. Ecol. Prog. Ser.* 489, 125–141.

Saleuddin, A. S. M. (1977). Ultrastructural studies on the formation of the periostracum inHelix aspersa (Mollusca). *Calcif. Tissue Res.* 22, 49–65. doi: 10.1007/bf02010346

Sánchez, J. A., Lasker, H. R., and Taylor, D. J. (2003a). Phylogenetic analyses among octocorals (Cnidaria): mitochondrial and nuclear DNA sequences (lsu-rRNA, 16S and ssu-rRNA, 18S) support two convergent clades of branching gorgonians. *Mol. Phylogenet. Evol.* 29, 31–42. doi: 10.1016/s1055-7903(03)00090-3

Sánchez, J. A., McFadden, C. S., France, S. C., and Lasker, H. R. (2003b). Molecular phylogenetic analyses of shallow-water Caribbean octocorals. *Mar. Biol.* 142, 975–987. doi: 10.1007/s00227-003-1018-7

Schlagintweit, F., and Gawlick, H.-J. (2009). The incertae sedis Carpathoporella Dragastan, 1995, from the lower cretaceous of albania: skeletal elements (sclerites, internodes/branches, holdfasts) of colonial octocorals. *Facies* 55, 553–573. doi: 10.1007/s10347-009-0185-5

Schouten, S., Hopmans, E. C., Forster, A., van Breugel, Y., Kuypers, M. M. M., and Sinninghe Damsteì, J. S. (2003). Extremely high sea-surface temperatures at low latitudes during the middle Cretaceous as revealed by archaeal membrane lipids. *Geology* 31, 1069–1072. doi: 10.1130/g19876.1

Scott, R. W. (1988). Evolution of late Jurassic and early Cretaceous reef biotas. *Palaios* 3, 184–193. doi: 10.2307/3514529

Sevilgen, D. S., Venn, A. A., Hu, M. Y., Tambutté, E., de Beer, D., Planas-Bielsa, V., et al. (2019). Full in vivo characterization of carbonate chemistry at the site of calcification in corals. *Sci Adv* 5:eaau7447. doi: 10.1126/sciadv.aau7447

Shaish, L., Levy, G., Katzir, G., and Rinkevich, B. (2010). Coral reef restoration (bolinao, philippines) in the face of frequent natural catastrophes. *Restor. Ecol.* 18, 285–299. doi: 10.1111/j.1526-100x.2009.00647.x

Silberberg, M. S., Ciereszko, L. S., Jacobson, R. A., and Smith, E. C. (1972). Evidence for a collagen-like protein within spicules of coelenterates. *Comp. Biochem. Physiol. Part B Comp. Biochem.* 43, 323–332. doi: 10.1016/0305-0491(72)90291-x

Simion, P., Philippe, H., Baurain, D., Jager, M., Richter, D. J., Di Franco, A., et al. (2017). A large and consistent phylogenomic dataset supports sponges as the sister group to all other animals. *Curr. Biol.* 27, 958–967. doi: 10.1016/j.cub.2017.02.031

Simpson, A., and Watling, L. (2011). Precious corals (Coralliidae) from northwestern Atlantic Seamounts. *J. Mar. Biol. Assoc. U. K.* 91, 369–382. doi: 10.1017/s002531541000086x

Smith, S. V., and Kinsey, D. W. (1976). Calcium carbonate production, coral reef growth, and sea level change. *Science* 194, 937–939. doi: 10.1126/science.194.4268.937

Solomon, S., Manning, M., Marquis, M., Qin, D., Chen, Z., Avery, K. B., et al. (2007). *Climate Change 2007: The Physical Science Basis: Working Group I Contribution to the Fourth Assessment Report of the IPCC*. Cambridge: Cambridge Univ. Press.

Song, H., Wignall, P. B., Song, H., Dai, X., and Chu, D. (2019). Seawater temperature and dissolved oxygen over the past 500 million years. *J. Earth Sci.* 30, 236–243. doi: 10.1007/s12583-018-1002-2

Sorokin, Y. I. (1991). Biomass, metabolic rates and feeding of some common reef zoantharians and octocorals. *Mar. Freshw. Res.* 42, 729–741. doi: 10.1071/mf9910729

Spencer Davies, P. (1990). A rapid method for assessing growth rates of corals in relation to water pollution. *Mar. Pollut. Bull.* 21, 346–348. doi: 10.1016/0025-326x(90)90797-c

Stampar, S. N., Maronna, M. M., Kitahara, M. V., Reimer, J. D., and Morandini, A. C. (2014). Fast-evolving mitochondrial DNA in Ceriantharia: a reflection of hexacorallia paraphyly? *PLoS One* 9:e86612. doi: 10.1371/journal.pone.0086612

Stanley, G. D. Jr. (1981). Early history of scleractinian corals and its geological consequences. *Geology* 9, 507–511. doi: 10.1130/0091-7613(1981)9<507:ehosca>2.0.co;2

Stanley, S. M., and Hardie, L. A. (1998). Secular oscillations in the carbonate mineralogy of reef-building and sediment-producing organisms driven by tectonically forced shifts in seawater chemistry. *Palaeogeogr. Palaeoclimatol. Palaeoecol.* 144, 3–19. doi: 10.1016/s0031-0182(98)00109-6

Stobart, B., Teleki, K., Buckley, R., Downing, N., and Callow, M. (2005). Coral recovery at aldabra atoll, seychelles: five years after the 1998 bleaching event. *Philos. Trans. A Math. Phys. Eng. Sci.* 363, 251–255. doi: 10.1098/rsta.2004.1490

Supuran, C. T. (2008). Carbonic anhydrases–an overview. *Curr. Pharm. Des.* 14, 603–614.

Takeuchi, T., Plasseraud, L., Ziegler-Devin, I., Brosse, N., Shinzato, C., Satoh, N., et al. (2018). Biochemical characterization of the skeletal matrix of the massive coral, *Porites australiensis*–The saccharide moieties and their localization. *J. Struct. Biol.* 203, 219–229. doi: 10.1016/j.jsb.2018.05.011

Tambutté, S., Holcomb, M., Ferrier-Pagès, C., Reynaud, S., Tambutté, É, Zoccola, D., et al. (2011). Coral biomineralization: from the gene to the environment. *J. Exp. Mar. Bio. Ecol.* 408, 58–78. doi: 10.1016/j.jembe.2011.07.026

Taylor, P. D., Berning, B., and Wilson, M. A. (2013). Reinterpretation of the cambrian "bryozoan" *Pywackia* as an octocoral. *J. Paleontol.* 87, 984–990. doi: 10.1666/13-029

Tentori, E., and van Ofwegen, L. P. (2011). Patterns of distribution of calcite crystals in soft corals sclerites. *J. Morphol.* 272, 614–628. doi: 10.1002/jmor.10942

Van Alstyne, K. L., Wylie, C. R., Paul, V. J., and Meyer, K. (1992). Antipredator defenses in tropical pacific soft corals (coelenterata: alcyonacea). I. sclerites as defenses against generalist carnivorous fishes. *The Biological Bulletin* 182, 231–240. doi: 10.2307/1542116

Vargas, S., Breedy, O., and Guzman, H. M. (2010a). The phylogeny of *Pacifigorgia* (coelenterata, octocorallia, gorgoniidae): a case study of the use of continuous characters in the systematics of the octocorallia. *Zoosystema* 32, 5–18. doi: 10.5252/z2010n1a1

Vargas, S., Breedy, O., Siles, F., and Guzman, H. M. (2010b). How many kinds of sclerite? Towards a morphometric classification of gorgoniid microskeletal components. *Micron* 41, 158–164. doi: 10.1016/j.micron.2009.08.009

Vargas, S., Eitel, M., Breedy, O., and Schierwater, B. (2010c). Molecules match morphology: mitochondrial DNA supports bayer's lytreia – bebryce – heterogorgia (alcyonacea : octocorallia) clade hypothesis. *Invertebr. Syst.* 24:23. doi: 10.1071/is09033

Vargas, S., Guzman, H. M., Breedy, O., and Wörheide, G. (2014). Molecular phylogeny and DNA barcoding of tropical eastern Pacific shallow-water gorgonian octocorals. *Mar. Biol.* 161, 1027–1038. doi: 10.1007/s00227-014-2396-8

Velimirov, B. (1980). growth aspects and magnesium carbonate concentrations of the reef building octocoral *Heliopora coerulea* (pallas) after transplantation. *Mar. Ecol.* 1, 155–168. doi: 10.1111/j.1439-0485.1980.tb00217.x

Venn, A. A., Tambutté, E., Holcomb, M., Laurent, J., Allemand, D., and Tambutté, S. (2013). Impact of seawater acidification on pH at the tissue–skeleton interface and calcification in reef corals. *Proc. Natl. Acad. Sci. U.S.A.* 110, 1634–1639. doi: 10.1073/pnas.1216153110

Vielzeuf, D., Gagnon, A. C., Ricolleau, A., Devidal, J.-L., Balme-Heuze, C., Yahiaoui, N., et al. (2018). Growth kinetics and distribution of trace elements in precious corals. *Front. Earth Sci. Chin.* 6:167. doi: 10.3389/feart.2018.00167

Vielzeuf, D., Garrabou, J., Gagnon, A., Ricolleau, A., Adkins, J., Günther, D., et al. (2013). Distribution of sulphur and magnesium in the

red coral. *Chem. Geol.* 355, 13–27. doi: 10.1016/j.chemgeo.2013.07.008

Watabe, N. (1981). Crystal growth of calcium carbonate in the invertebrates. *Prog. Cryst. Growth Charact. Mater.* 4, 99–147. doi: 10.1016/0146-3535(81)90050-2

Watabe, N., and Kingsley, R. J. (1992). "Calcification in octocorals," in *Hard Tissue Mineralization and Demineralization*, eds S. Suga and N. Watabe (Tokyo: Springer Japan), 127–147. doi: 10.1007/978-4-431-68183-0_9

Weinbauer, M. G., Brandstätter, F., and Velimirov, B. (2000). On the potential use of magnesium and strontium concentrations as ecological indicators in the calcite skeleton of the red coral (*Corallium rubrum*). *Mar. Biol.* 137, 801–809. doi: 10.1007/s002270000432

Weinbauer, M. G., and Vellmirov, B. (1995). Calcium, magnesium and strontium concentrations in the calcite sclerites of Mediterranean gorgonians (coelenterata: octocorallia). *Estuar. Coast. Shelf Sci.* 40, 87–104. doi: 10.1016/0272-7714(95)90015-2

Weiner, S., and Hood, L. (1975). Soluble protein of the organic matrix of mollusk shells: a potential template for shell formation. *Science* 190, 987–989. doi: 10.1126/science.1188379

Weiner, S., Traub, W., and Lowenstam, H. A. (1983). "Organic matrix in calcified exoskeletons," in *Biomineralization and Biological Metal Accumulation*, eds P. Westbroek and E. W. de Jong (Dordrecht: Springer), 205–224. doi: 10.1007/978-94-009-7944-4_18

West, J. M. (1997). Plasticity in the sclerites of a gorgonian coral: tests of water motion. *Light Level Damage Cues. Biol. Bull.* 192, 279–289. doi: 10.2307/1542721

Williams, G. C. (1986). *Morphology, Systematics, and Variability of the Southern African Soft Coral Alcyonium Variabile (J. Stuart Thomson, 1921)(Octocorallia, Alcyoniidae)*. Gardens: South African Museum.

Williams, G. C. (1992). The alcyonacea of southern Africa. stoloniferous octocorals and soft corals. *Ann. S. Afr. Mus.* 100, 249–358.

Williams, G. C. (2015). A new genus and species of pennatulacean octocoral from equatorial West Africa (Cnidaria, Anthozoa, Virgulariidae). *Zookeys* 546, 39–50. doi: 10.3897/zookeys.546.6344

Williams, G. C., and Cairns, S. D. (2013). *Biodiversity Myth Busters, Octocoral Research Center*. Available online at: http://researcharchive.calacademy.org/research/izg/Biodiversity%20Myth%20Busters%202.html (accessed March 9, 2015).

Williams, G. C., and Cairns, S. D. (2015). *Systematic List of Valid Octocoral Genera, Octocoral Research Center*. Available online at: http://researcharchive.calacademy.org/research/izg/OCTOCLASS.htm (accessed March 9, 2015).

Woodland, W. (1905). Memoirs: studies in spicule formation: I.–spicule formation in *Alcyonium digitatum*; with remarks on the histology. *J. Cell Sci.* 2, 283–304.

Yasuda, N., Abe, M., Takino, T., Kimura, M., Lian, C., Nagai, S., et al. (2012). Large-scale mono-clonal structure in the north peripheral population of blue coral, *Heliopora coerulea*. *Mar. Genomics* 7, 33–35. doi: 10.1016/j.margen.2012.02.001

Yoshimura, T., Tanimizu, M., Inoue, M., Suzuki, A., Iwasaki, N., and Kawahata, H. (2011). Mg isotope fractionation in biogenic carbonates of deep-sea coral, benthic foraminifera, and hermatypic coral. *Anal. Bioanal. Chem.* 401, 2755–2769. doi: 10.1007/s00216-011-5264-0

Zann, L. P., and Bolton, L. (1985). The distribution, abundance and ecology of the blue coral *Heliopora coerulea* (Pallas) in the Pacific. *Coral Reefs* 4, 125–134. doi: 10.1007/bf00300871

Zapata, F., Goetz, F. E., Smith, S. A., Howison, M., Siebert, S., Church, S. H., et al. (2015). Phylogenomic analyses support traditional relationships within cnidaria. *PLoS One* 10:e0139068. doi: 10.1371/journal.pone.0139068

Zapata Guardiola, R., and López González, P. J. (2012). Revision and redescription of the species previously included in the genus *Amphilaphis* studer and wright in studer, 1887 (Octocorallia: primnoidae). *Sci. Mar.* 76, 357–380. doi: 10.3989/scimar.03278.18b

Zeebe, R. E. (2001). Seawater pH and isotopic paleotemperatures of cretaceous oceans. *Palaeogeogr. Palaeoclimatol. Palaeoecol.* 170, 49–57. doi: 10.1016/s0031-0182(01)00226-7

Zoccola, D., Tambutté, E., Kulhanek, E., Puverel, S., Scimeca, J.-C., Allemand, D., et al. (2004). Molecular cloning and localization of a PMCA P-type calcium ATPase from the coral *Stylophora pistillata*. *Biochim. Biophys. Acta* 1663, 117–126. doi: 10.1016/j.bbamem.2004.02.010

Conflict of Interest: The authors declare that the research was conducted in the absence of any commercial or financial relationships that could be construed as a potential conflict of interest.

frontiers in Genetics

ORIGINAL RESEARCH
published: 10 March 2021
doi: 10.3389/fgene.2021.620659

Evolution of Matrix Gla and Bone Gla Protein Genes in Jawed Vertebrates

Nicolas Leurs[1], Camille Martinand-Mari[1], Stéphanie Ventéo[2], Tatjana Haitina[3] and Mélanie Debiais-Thibaud[1]**

[1] ISEM, CNRS, IRD, EPHE, Univ. Montpellier, Montpellier, France, [2] Institute for Neurosciences of Montpellier, Saint Eloi Hospital, Inserm UMR 1051, Univ. Montpellier, Montpellier, France, [3] Department of Organismal Biology, Uppsala University, Uppsala, Sweden

Matrix Gla protein (Mgp) and bone Gla protein (Bgp) are vitamin-K dependent proteins that bind calcium in their γ-carboxylated versions in mammals. They are recognized as positive (Bgp) or negative (Mgp and Bgp) regulators of biomineralization in a number of tissues, including skeletal tissues of bony vertebrates. The Mgp/Bgp gene family is poorly known in cartilaginous fishes, which precludes the understanding of the evolution of the biomineralization toolkit at the emergence of jawed vertebrates. Here we took advantage of recently released genomic and transcriptomic data in cartilaginous fishes and described the genomic loci and gene expression patterns of the Mgp/Bgp gene family. We identified three genes, Mgp1, Mgp2, and Bgp, in cartilaginous fishes instead of the single previously reported Mgp gene. We describe their genomic loci, resulting in a dynamic evolutionary scenario for this gene family including several events of local (tandem) duplications, but also of translocation events, along jawed vertebrate evolution. We describe the expression patterns of *Mgp1*, *Mgp2*, and *Bgp* in embryonic stages covering organogenesis in the small-spotted catshark *Scyliorhinus canicula* and present a comparative analysis with Mgp/Bgp family members previously described in bony vertebrates, highlighting ancestral features such as early embryonic, soft tissues, and neuronal expressions, but also derived features of cartilaginous fishes such as expression in fin supporting fibers. Our results support an ancestral function of Mgp in skeletal mineralization and a later derived function of Bgp in skeletal development that may be related to the divergence of bony vertebrates.

Keywords: Gla protein, osteocalcin, shark, skeleton, evo-devo, biomineralization, bglap

OPEN ACCESS

Edited by:
Susana Seixas,
University of Porto, Portugal

Reviewed by:
Shigehiro Kuraku,
RIKEN Center for Biosystems Dynamics Research (BDR), Japan
Vincent Laizé,
University of Algarve, Portugal

****Correspondence:***
Mélanie Debiais-Thibaud
melanie.debiais-thibaud@umontpellier.fr
Tatjana Haitina
tatjana.haitina@ebc.uu.se

Specialty section:
This article was submitted to Evolutionary and Population Genetics, a section of the journal Frontiers in Genetics

Received: *23 October 2020*
Accepted: *08 February 2021*
Published: *10 March 2021*

Citation:
Leurs N, Martinand-Mari C, Ventéo S, Haitina T and Debiais-Thibaud M (2021) Evolution of Matrix Gla and Bone Gla Protein Genes in Jawed Vertebrates. Front. Genet. 12:620659. doi: 10.3389/fgene.2021.620659

INTRODUCTION

Vertebrates display a range of skeletal tissues that are biomineralized through the regulation of calcium phosphate crystal deposition (Janvier, 1996; Donoghue and Sansom, 2002; Omelon et al., 2009), except in the extant cyclostome group (agnathan fishes: lampreys and hagfishes) where the skeletal units are made of cartilage with no detection of calcium precipitates (Yao et al., 2011; Ota et al., 2013). Several vitamin K-dependent (VKD) proteins were shown to be involved in skeletal

tissue mineralization in jawed vertebrates (reviewed in Bordoloi et al., 2018; Wen et al., 2018). Of these, Mgp (matrix Gla protein) and Bgp (bone Gla protein, bglap, and osteocalcin) display consistent similarities in their sequences and were considered to belong to the same gene family (Laizé et al., 2005; Cancela et al., 2014). Both these proteins display a Gla domain characterized by the ability to undergo γ-carboxylation of several glutamate residues, resulting in a putative ability of the protein to bind calcium (reviewed in Yáñez et al., 2012).

Expression of the *Mgp* and *Bgp* genes in mouse first appeared spatially exclusive, with *Bgp* expressed uniquely in osteoblasts or osteocytes but also in odontoblasts, while *Mgp* expression was restricted to hypertrophic chondrocytes (Ikeda et al., 1992; D'Errico et al., 1997). More recent data support the expression of *Mgp* in other skeletal cells, including osteoblasts and osteoclasts (Coen et al., 2009). *Mgp* was also shown to be largely expressed in many soft tissues such as kidney, lung, heart, and spleen (Fraser and Price, 1988). Mgp was shown to act as an inhibitor of several processes both in skeletal and soft tissues: calcium precipitation in hyaline cartilage and human vascular smooth muscle cells (Luo et al., 1997; Schurgers et al., 2007; reviewed by Wen et al., 2018), and also dentin or bone matrices mineralization and osteoclast differentiation (Kaipatur et al., 2008; Zhang et al., 2019). The Bgp protein, on the other hand, seems to function in two ways, either in its carboxylated form by regulating hydroxyapatite crystal growth in skeletal tissues or in its non-carboxylated form by potentially acting as a circulating hormone that may be involved in energy metabolism and other functions (Diegel et al., 2020). Focusing on their skeletal functions, the data gathered from mammals indicate that Bgp is involved in the regulation, both positive and negative, of biomineralization processes in bone tissues, while Mgp is an inhibitory protein for these biomineralization processes (reviewed in Wen et al., 2018).

The evolutionary history of the Mgp/Bgp gene family has been discussed for more than two decades, particularly in relation to the evolution of a mineralized skeleton in vertebrates (Rice et al., 1994; Cancela et al., 2001, 2014; Pinto et al., 2001; Simes et al., 2003; Laizé et al., 2005; Gavaia et al., 2006; Viegas et al., 2013). The search for *Mgp* and *Bgp* genes in a variety of bony vertebrates led to the identification of two *Bgp* copies in several teleost fishes [the most recently identified being named *OC2* (Laizé et al., 2005; Cancela et al., 2014; Cavaco et al., 2014)] and also in some tetrapods [amphibians and sauropsids, where the recently identified duplicate was named *OC3* (Cancela et al., 2014)] while *Mgp* was, until now, only found to be present as a single gene (Cancela et al., 2014). The hypothesis was raised that *Mgp* and *Bgp* genes originated from an ancestral gene after the two whole-genome duplications in vertebrates (Laizé et al., 2005) and that more recent events of duplication of *Bgp* occurred more recently and independently in the bony fish and the tetrapod lineages (Cancela et al., 2014). Cartilaginous fishes, e.g., sharks (selachians), skates and rays (batoids), and holocephalans, are crucial in this issue as their lineage diverged from bony fishes more than 450 million years ago and they display a skeleton devoid of bone tissue but made of hyaline and mineralized cartilage (Janvier, 1996). Several authors have previously described the presence of a *Mgp* gene in two shark species, the school shark *Galeorhinus galeus* (Rice et al., 1994) and the blue shark *Prionace glauca* (Ortiz-Delgado et al., 2006) for which they showed high conservation with tetrapod for (i) the Mgp amino-acid motifs which are critical for post-translational modifications [serine phosphorylation and glutamate γ-carboxylation (Price et al., 1994; Ortiz-Delgado et al., 2006)]; (ii) *Mgp* expression pattern and Mgp sites of accumulation [vertebral cartilage, endothelium, kidney, heart (vascular endothelia and smooth muscle), and dentinal matrix (Ortiz-Delgado et al., 2006)]. Previous studies have not identified any sequence that would be homologous to *Bgp* in cartilaginous fish genomes (Cancela et al., 2014).

The current explosion of genomic data, including in the cartilaginous fish lineage, allows the better description of gene complement and gene expression in this *Mgp*/*Bgp* family. Here we collect transcriptomic and genomic data from different jawed vertebrates, including several cartilaginous fishes where we identify an unknown diversity of *Mgp*/*Bgp* sequences and their genomic loci. We describe their gene expression patterns in embryonic stages of the small-spotted catshark *Scyliorhinus canicula* and uncover highly conserved but also previously unknown sites of expression.

MATERIALS AND METHODS

Collection of *Mgp*/*Bgp* Sequences in the Genomes and Transcriptomes of Chondrichthyans

Synteny Analyses

Matrix Gla protein and bone Gla protein sequences for human, mouse, and zebrafish were collected from GenBank and were used to screen locally assembled small-spotted catshark (*Scyliorhinus canicula*) and thornback ray (*Raja clavata*) transcriptomic data (Debiais-Thibaud et al., 2019) as well as the most recently assembled genome for *S. canicula* (sScyCan1.1, GCA_902713615.1), using TBLASTN. Additional cDNA sequences were obtained by screening accessible transcriptomic data collected by the SkateBase project[1] [little skate *Leucoraja erinacea* transcriptome (Contig Build-2, GEO:GSM643957) and small-spotted catshark transcriptome (GEO:GSM643958)] using TBLASTN. Small-spotted catshark, little skate, and thornback ray sequences were then used to screen other databases for elephant shark genome assembly (GCA_000165045.2 Callorhinchus_milii-6.1.3) (Venkatesh et al., 2014) and whale shark genome *Rhincodon typus* (GCA_001642345.2 ASM164234v2) (Tan et al., 2019). Thornback ray, small-spotted catshark, and little skate cDNA sequences were used to map synteny on the thorny skate *Amblyraja radiata* and the smalltooth sawfish *Pristis pectinata* draft assembled genomes using TBLASTN [data accessed from, and analyzed in agreement with, Vertebrate Genome Project (Rhie et al., 2020), PriPec2.pri, GCA_009764475.1]. Syntenic genes in chondrichthyans are

[1] http://skatebase.org/

Ddx47 (elephant shark XM_007909802.1 in GenBank; thorny skate ENSARAT00005031107 in Ensembl Rapid Release) and *Erp27* (elephant shark XM_007909813.1 in GenBank; thorny skate ENSARAT00005031079 in Ensembl Rapid Release). Synteny data in bony fish genomes were extracted from the Ensembl database for selected genomes [human genome assembly: (GRCh38.p10); mouse *Mus musculus* (GRCm38.p6); chicken *Gallus gallus* (GRCg6a); tropical clawed frog *Xenopus tropicalis* (Xenopus_tropicalis_v9.1); elephant shark *Callorhinchus milii* (Callorhinchus_milii-6.1.3); gar *Lepisosteus oculatus* (LepOcu1); zebrafish *Danio rerio* (GRCz10); Chinese softshell turtle *Pelodiscus sinensis* (PelSin_1.0); central bearded dragon *Pogona vitticeps* (pvi1.1); reedfish *Erpetoichthys calabaricus* (fErpCal1.1); Asian bonytongue *Scleropages formosus* (fSclFor1.1)] and from NCBI for the caecilian *Microcaecilia unicolor* (aMicUni1.1).

Phylogenetic Reconstruction

Protein sequences for all identified Mgp and Bgp genes from the different chondrichthyan species together with sequences from osteichthyan species were used for phylogenetic tree reconstruction. These protein sequences are preproteins as they are obtained from the translation of either the cDNA sequence or of a predicted gene from available genomes. All sequences used in this study are detailed with IDs and origin in the **Supplementary Material 1**. Sequences were aligned using MAFFT (Katoh et al., 2002; Katoh and Standley, 2013) using standard parameters (**Supplementary Material 2**). Because a large proportion of the sequences is predicted from genomes and may include false exons, this alignment was then cleaned using HmmCleaner with standard parameters (option "–large") to remove low similarity segments (Di Franco et al., 2019). Our final alignment used for subsequent phylogenetic reconstruction was 129 amino-acid long and is available in the **Supplementary Material 3**. Phylogenetic analyses were performed on the amino-acid alignment to infer the evolutionary history of these genes. This data set was used to reconstruct gene phylogenies in Maximum Likelihood using IQ-TREE 1.6.1 (Nguyen et al., 2015) under the JTT + I + G4 evolution model for amino-acid data. Node support was estimated by performing a thousand ultra-fast (UF) bootstrap replicates (Hoang et al., 2017) and single branch tests (SH-aLRT; Guindon et al., 2010).

Protein Domain Description

Conservation of protein domains was evaluated by mapping previously identified functional regions (Laizé et al., 2005) onto the aligned sequences of human, mouse, chicken, zebrafish, elephant shark, and small-spotted catshark Mgp or Bgp proteins. Additional motif recognition was validated on the small-spotted catshark and elephant shark protein sequences with InterPro (Finn et al., 2017), SMART (Letunic et al., 2021), and FIMO version 5.3.0 (Grant et al., 2011).

Reconciliation Between the Gene Phylogeny and Species Phylogeny

Evolutionary scenario for gene duplication/loss was built minimizing the duplication and loss score with standard parameters in Treerecs (Comte et al., 2020), using contracted versions of the gene and species trees (**Supplementary Material 4**).

In situ Hybridization and Histology

Identified small-spotted catshark *Mgp1*, *Mgp2*, and *Bgp* cDNA sequences were used to design the following primers (sequences are given in the 5′-3′ orientation): Fw TCACAGATTCACACTCGCTG and Rv GGCCGAACCAGAGC TGCTG amplifying 702 bp for *Mgp1*; Fw CCGATCTCAC AAACTGAGCT and Rv CACAGACTGCAGCAAATAGT amplifying 817 bp for *Mgp2*; Fw CCAGAGAAGATGATGG TCCT and Rv GGGGAATTAACAGAGTCGTC amplifying 675 bp for *Bgp*. Sequences were amplified from cDNA reverse-transcribed from total RNA extractions of a mix of embryonic stages. These PCR products were ligated into the pGEM-T easy vector using the TA cloning kit (Promega). Inserts with flanking T7 and SP6 sites were amplified using M13F/M13R primers and sequenced to verify the amplicon sequence and orientation, and these PCR products were then used as templates for the synthesis of antisense DIG riboprobes [3 µl reaction, 100–200 ng PCR product, DIG RNA labeling mix (Roche) with either T7 or SP6 (depending on the amplicon orientation) RNA polymerase (Promega), following manufacturer's instructions]. Before *in situ* hybridization, all DIG-labeled riboprobes were purified on MicroSpin G50 column (GE Healthcare). The obtained expression patterns were different for each probe, excluding detectable cross-hybridization between Mgp1/Mgp2/Bgp probes, so we did not use sense probes as negative control.

Whole embryos of either 6 cm total length, 7.7 cm total length, or 9 cm long hatchlings, were euthanized in buffered tricaïne, eviscerated and fixed for 48 h in 4% paraformaldehyde in 1× phosphate-buffered saline (PBS) solution at 4 °C, rinsed in PBS 1× for an hour, and then transferred in 50% ethanol (EtOH)-PBS 1×, 75% EtOH-PBS 1×, and three successive bathes of 100% EtOH before storage at −20°C in EtOH 100%. We then sampled (i) the lower jaw (hatchling) and (ii) transversal slices in the posterior zone of the branchial arches to allow visualization of gene expression in, respectively, (i) teeth and the Meckel's cartilage; and (ii) abdominal vertebrae, pectoral fin, or branchial rays. Experiments of *in situ* hybridization were performed on 14 µm thick cryosections of the chosen samples that had been progressively transferred back to PBS 1×, then equilibrated in sucrose 30% for 24 h before being transferred and frozen in Tissue-Tek® O.C.T.™ (Sakura Finetek France SAS). Consecutive cryosections were distributed on 10 successive slides to a maximum of 6–8 sections per slide and were stored at −20°C. *In situ* hybridization on sections was performed as described previously (Enault et al., 2015) with stringent conditions of hybridization at 70°C. *In situ* hybridization results were taken with Hamamatsu NanoZoomer 2.0-HT Slide Scanner (Montpellier RIO Imaging facility, INM Optique) with a 40× objective.

Histological staining (Hematoxylin-Eosine-Saffran) was performed at the local histology platform (RHEM platform

at IRCM, Montpellier) on 7 μm paraffin sections of non-demineralized samples on a histology automaton.

RNA Isolation and qPCR Analysis

Early embryos (three or four for each stage) were collected from embryonic stages 18–32 (Ballard et al., 1993), with stage 32 embryos <3.5 cm total length. Total RNA was isolated with ReliaPrep RNA tissue Miniprep system according to the supplier's instructions (Promega), and their quality was verified on a Bioanalyzer 2100 instrument (Agilent): 500 ng of total RNA were used for cDNA preparation performed by Superscript II reverse transcriptase (Invitrogen) with an oligodT primer.

For quantitative PCR, 1:20 dilution of each cDNA was run in triplicate on a 384-well plate for each primer pair by using thermal cycling parameters: 95°C for 2 min, 95°C for 10 s, 68°C for 10 s, 72°C for 10 s (45 cycles), and an additional step 72°C for 10 min performed on a Light Cycler 480 with the SensiFAST SYBR No-ROX kit (Meridian Bioscience) (qPHD UM2/GenomiX Platform, Montpellier – France). Results were normalized with the expression of two reference genes *Eef1a* and *Rpl8* [previously used in elasmobranch fishes (O'Shaughnessy et al., 2015; Onimaru et al., 2016)] by geometric mean, and data were further analyzed with the Light Cycler 480 software 1.5.1.

We used Primer 3.0 to design all the sets of forward and reverse primers to amplify selected genes (sequences are given in the 5′-3′ orientation): Fw TCGGGAGGAGAGATGCACAT and Rv TGCCACCAAAGTATCTGCCA amplifying 183 bp for *Mgp1*; Fw CCTGATTCTGCTGTGCCTGT and Rv TTTTCCATAGGC CGCCATGT amplifying 277 bp for *Mgp2*; Fw TGATGGT CCTTTCCTCGGGA and Rv TGGTATCCAATCCTGTTTGC CA amplifying 180 bp for *Bgp*; Fw GGTGTGGGTGAATTT GAAGC and Rv TTGTCACCATGCCAACCAGA amplifying 245 bp for *Eef1a*; Fw TTCATTGCAGCGGAGGGAAT and Rv TCAATACGACCACCACCAGC amplifying 302 bp for *Rpl8*.

The expression data obtained were compared over time to test if any gene was differentially expressed in time with a one-way ANOVA. A Shapiro–Wilk normality test was applied on the log transformed data, and for each gene the null hypothesis of normality was kept ($P > 0.05$). We tested for heteroscedasticity of variance between developmental stages, and the null hypothesis had to be rejected only for the Bgp gene ($P < 0.05$), even after log transformation. Note that we are very constrained by an unbalanced protocol (different number of observations in each developmental stage) and small sample size, which limits statistical power.

Embryo Collection and Ethics Statement

Embryos of the small-spotted catshark *S. canicula* originated from a Mediterranean population of adult females housed at Station Méditerranéenne de l'Environnement Littoral, Sète, France. Handling of small-spotted catshark embryos followed all institutional, national, and international guidelines [European Communities Council Directive of September 22, 2010 (2010/63/UE)]: no further approval by an ethics committee was necessary as the biological material is embryonic and no live experimental procedures were carried out. Embryos were raised in seawater tanks at 16–18 °C and euthanized by overdose of tricaine (MS222, Sigma) at appropriate stages (Ballard et al., 1993; Enault et al., 2016).

RESULTS

Evolution of the Mgp/Bgp Gene Complement in Jawed Vertebrates

Three transcripts were identified as Mgp or Bgp genes in the small-spotted catshark transcriptome and named after their position in the phylogenetic reconstruction: *Mgp1*, *Mgp2*, and *Bgp* (**Figure 1**). To perform this reconstruction, we screened other available cartilaginous fish genomes as well as the genomes of several bony fishes by reciprocal blasts to recover a maximum of Mgp/Bgp sequences in the jawed vertebrate clade. The produced alignment was 129 amino acid long after HmmCleaner (alignment available as **Supplementary Material 3**). The major limitation on the analysis of this phylogeny was the lack of an outgroup: no potential Mgp/Bgp sequence could be identified in the available genomic and transcriptomic sequences for cyclostome species (e.g., lamprey or hagfish), and there is currently no identified closely related gene family in jawed vertebrates. Both Mgp and Bgp clades in bony fishes were monophyletic and had a closest monophyletic group made of cartilaginous fish sequences (see **Supplementary Material 5** for the unrooted tree), which made us place the putative root of this tree as resulting in **Figure 1**, leading to one Mgp and one Bgp clade for jawed vertebrates. This choice implies that one ancestral Bgp and one ancestral Mgp genes were already present in the last common ancestor of extant jawed vertebrates, as previously suggested (Laizé et al., 2005).

In this phylogenetic reconstruction, two cartilaginous fish genes were identified as duplicated copies grouping together as the sister group to a single *Mgp* copy in bony fishes (UF-bootstrap and SH-aLRT support reach acceptable values at this chondrichthyan node, although they are lower than for other deep nodes): the two chondrichthyan copies were named *Mgp1* and *Mgp2* (**Figure 1**). In the Bgp clade, cartilaginous fish sequences were monophyletic and strongly supported by the SH-aLRT statistic and UF-bootstrap, with only one Bgp gene in each species, whereas bony fish sequences grouped into two sister clades, suggesting two osteichthyans Bgp paralogs well supported by the UF-bootstraps and SH-aLRT (**Figure 1**). One of these bony fish paralogs is best known as the *osteocalcin*/*Bgp* gene product in all screened actinopterygians and sarcopterygians (also previously named *OC1*; Cancela et al., 2014). To account for the different nature of the described paralogs, we will further identify this clade as Bgp1: although our phylogenetic reconstruction leads to little resolution within this clade, its monophyly is very robust in the tree (SH-aLRT = 99.4; UFboot = 100). The second osteichthyan Bgp paralog is herein named Bgp2: it includes sequences found only in lissamphibians and sauropsids (including birds). This *Bgp2* gene is predicted but most frequently not annotated in the Ensembl or NCBI databases (for *Chrysemys*, the kiwi bird and the tiger snake) or named *Mgp-like* in *Pogona, osteocalcin-like* in *Xenopus laevis* and other lissamphibians, *osteocalcin* in *X. tropicalis* or *osteocalcin 3*

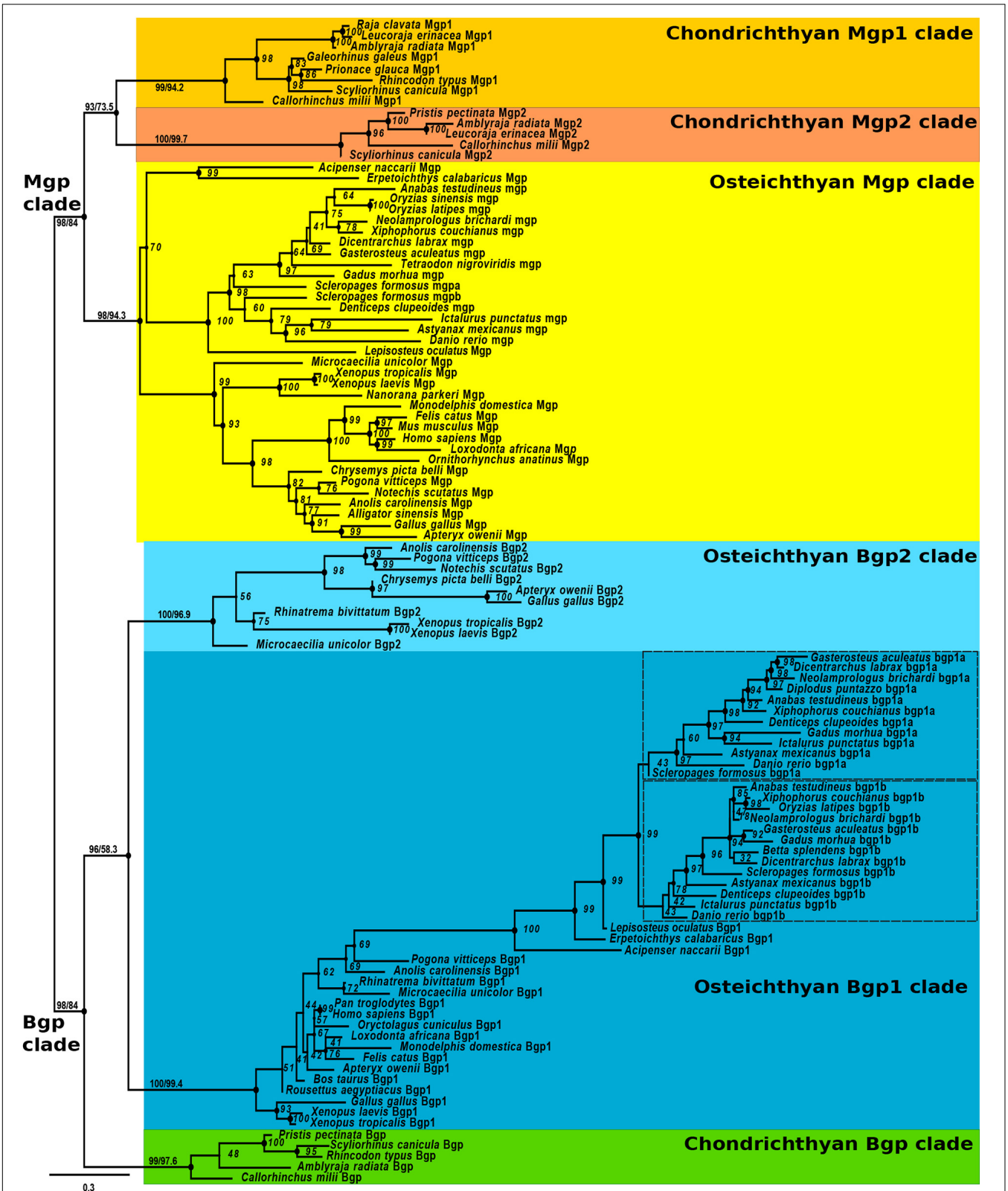

FIGURE 1 | Maximum likelihood phylogenetic tree based on Bgp and Mgp amino-acid sequences (107 sequences, 129 positions) with JTT + I + G4 evolution model in IQ-TREE. Node support was evaluated with 1000 ultra-fast bootstrap replicates (shown on all nodes) and SH-aLRT (UFbootstrap/SH-aLRT), shown only on deeper nodes. Colored boxes indicate osteichthyan and chondrichthyan monophyletic clades. See text for gene name nomenclature.

in the chicken [see all references to the extracted sequences in **Supplementary Material 1**; this paralog has also previously been named *OC3* (Cancela et al., 2014)]. As a consequence, this topology suggests an event of duplication of an ancestral bony fish *Bgp* gene leading to these *Bgp1* and *Bgp2* paralogs (**Figure 1**). Another event of duplication is deduced from the two sister clades observed within teleost fishes in the Bgp1 group: this and synteny data (see below) support these paralogs to originate from the teleost-specific whole-genome duplication (Amores et al., 1998), so we followed the accepted gene nomenclature and named them bgp1a (usually annotated *bglap* or *osteocalcin* in public databases) and bgp1b [previously named *OC2* (Cancela et al., 2014), or *bglap-like* in databases, see **Supplementary Material 1**].

Genomic Organization of the Mgp and Bgp Genes in Jawed Vertebrates

All three coding sequences were predicted in the available elephant shark genome and all assigned to a single genomic contig (**Figure 2**) together with two genes bordering the syntenic regions, *Erp27* and *Ddx47*, as identified in other syntenic regions from bony fishes (see **Figure 3**). The identified cDNA sequences of *Mgp1*, *Mgp2*, and *Bgp* could be assigned to a single scaffold in the small-spotted catshark draft genome in synteny with *Ddx47* and *Erp27* (see **Figure 2**). In two batoid genomes (*Amblyraja* and *Pristis*), *Mgp2* and *Bgp* genes could be assigned to a single contig together with *Erp27* and *Ddx47*. However, the *Mgp1* gene was located on another scaffold in the *Amblyraja* genome, outside of the locus identified by the presence of *Erp27* and

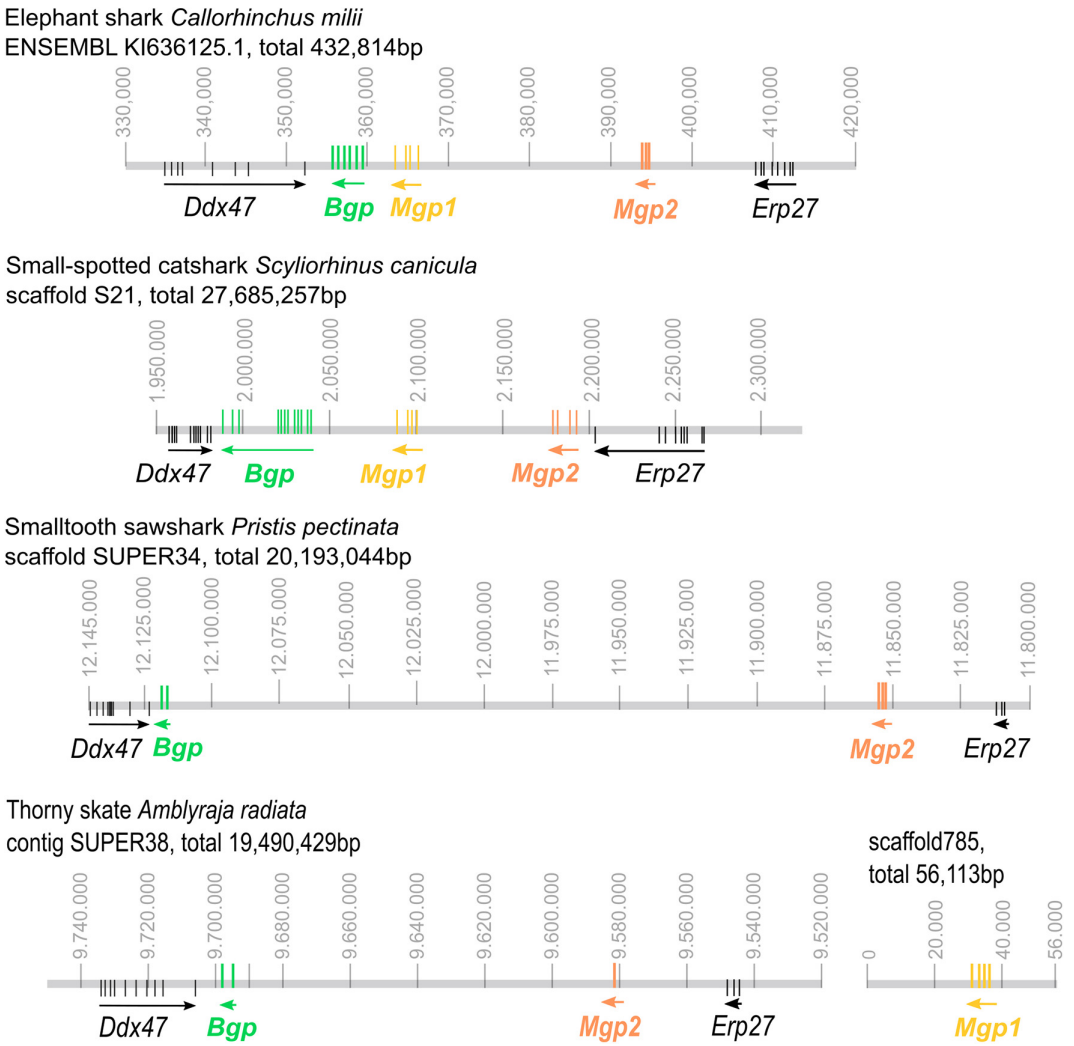

FIGURE 2 | Genomic organization of the Mgp/Bgp gene clusters in reference chondrichthyan genomes: the elephant shark *Callorhinchus milii*; the small-spotted catshark *Scyliorhinus canicula*; the smalltooth sawfish *Pristis pectinata*; the thorny skate *Amblyraja radiata*. *Ddx47* and *Erp27* were included to insure the identification of homologous regions of the genome. Arrows indicate the transcription direction. Vertical colored bars indicate exon position. For *Pristis* and *Amblyraja* genomic mapping, exon position was located by BLASTing cDNA sequences of distant species, so they are putative. Gene colors follow the color code used in **Figure 1**. Position along the genomic scaffold or contig is indicated in base pair (gray numbering).

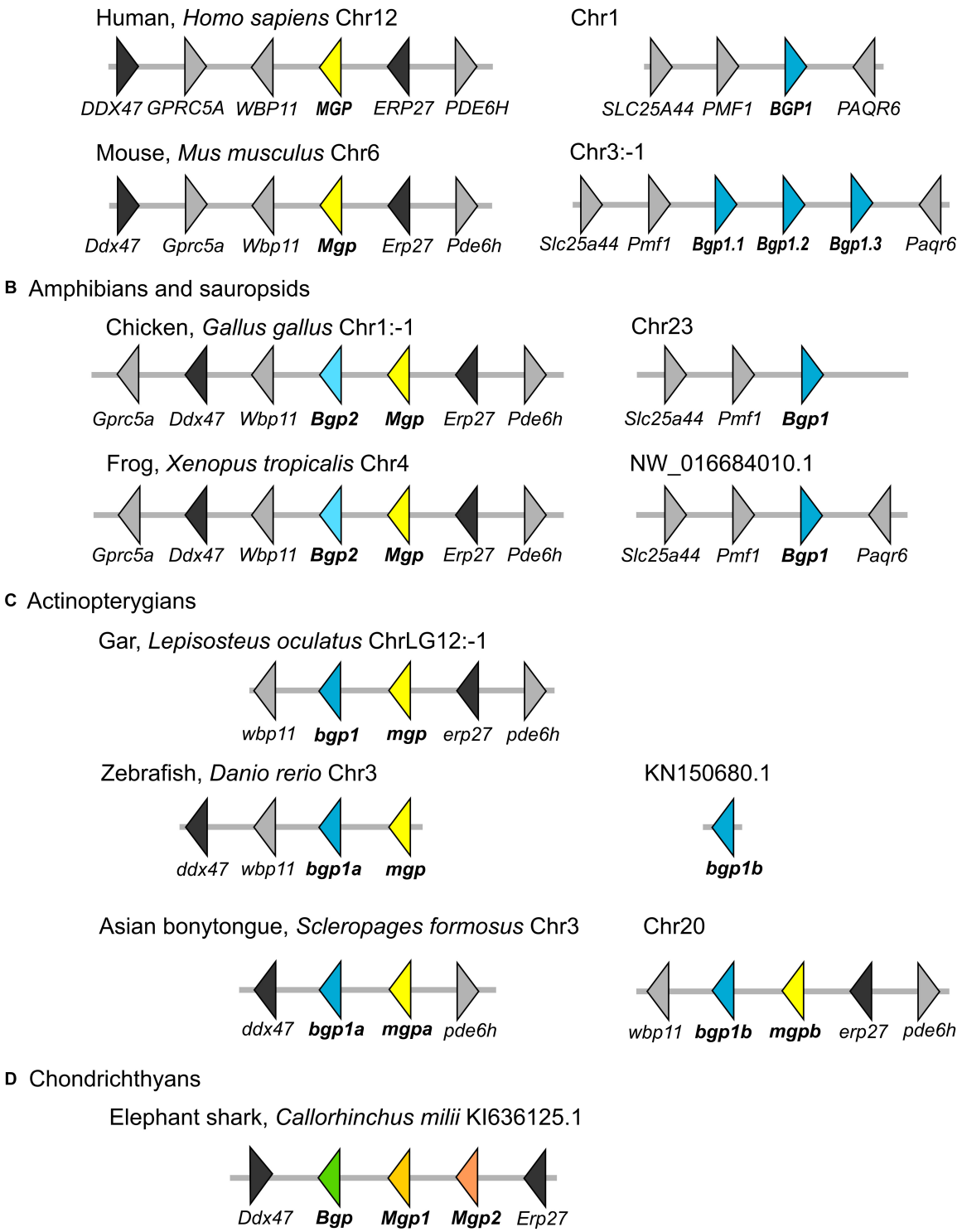

FIGURE 3 | Genomic organization of the *Mgp/Bgp* gene clusters in reference osteichthyan genomes as annotated in currently available databases. **(A)** Two mammalian genomes with separated *Mgp* and *Bgp* loci; **(B)** Two non-mammalian tetrapod genomes with one *Bgp* locus, and one tandem *Bgp* and *Mgp* genes on homologous loci; **(C)** One non-teleost actinopterygian with only one locus where *Mgp* and *Bgp* genes are tandemly organized, and two teleost genomes with two loci, where *mgp* and *bgp* are tandemly organized or single. **(D)** The elephant shark as a representative of chondrichthyans. Several syntenic genes were selected to support the homology of the compared loci. Distance between genes is not to scale. Gene names and corresponding color refer to our phylogenetic analyses, and the correspondence to gene names in databases is found in the **Supplementary Material 1**.

Ddx47 (**Figure 2**), and no *Mgp1* gene could be identified in the *P. pectinata* genome.

The comparison to the genomic data in bony fishes was made in two steps. First, an overview of the genomic locations in tetrapods shows that in the human genome, there are separated loci for the *Mgp* (chromosome 12) and the *Bgp1* (BGLAP on chromosome 1) genes for which we highlighted the position of syntenic genes (**Figure 3**). All occurrences of the tetrapod *Bgp2* gene (as identified in our phylogenetic reconstruction) are in the *Mgp* locus in lissamphibians and sauropsids (**Figure 3**, and verified by BLAST on Ensembl available genomes of *P. sinensis*, *M. unicolor*, and *P. vitticeps*, not shown).

In a second step, we searched the homologous loci in actinopterygians (ray-finned fishes) outside of teleost fishes: the syntenic markers linked to *Bgp1* in tetrapods would not co-localize with any known sequence of either *Bgp* or *Mgp* in actinopterygians (**Figure 3**). The actinopterygian *Bgp1* gene was located in the *Mgp* locus, as defined by the presence of syntenic markers such as *Erp27* and *Ddx47* (**Figure 3**, and verified by BLAST on the available genome of *E. calabaricus*). This *Bgp1* copy is identified as *Bglap* or *Osteocalcin-like* (however, not annotated in the spotted gar) in the available databases (but see **Supplementary Material 1** for predicted gene IDs). Within teleost fishes, the zebrafish *D. rerio* is usually used as a reference species, however, the contig where *bgp1b* is located is very short and does not give syntenic gene markers, while *bgp1a* and *mgp* are located close to each other on chromosome 3 (**Figure 3**). In **Figure 3**, we illustrate the genomic loci in the Asian bonytongue *S. formosus*, where each of the two teleost-specific copies of *bgp1* are found adjacent to one *mgp* gene that we named *mgpa* and *mgpb*, each of these genomic loci with either a sequence coding for *erp27* or *ddx47*, but both regions including a paralog of the *pde6h* gene. In all other teleost genomes that we have screened (see the sequences chosen for the phylogenetic reconstruction, and **Supplementary Material 1**), the *mgp* sequence was found in synteny with the *bgp1a* sequence, together with *ddx47*/*wbp11*, while the *bgp1b* sequence was found with *erp27* but without another copy of *mgp* (not shown).

Protein Domains

The prediction of functional protein domains by InterproScan and SMART led to the recognition of a signal peptide for all sequences, but of a general Gla domain only in Bgp and Mgp1 proteins, excluding the Mgp2 sequences of the small-spotted catshark or elephant shark. The FIMO algorithm also identified a furin cleavage site in the Mgp2 sequence (see **Figure 4**). This was unexpected as it is typical for Bgp proteins but not of Mgp (Laizé et al., 2005). To further describe the presence, absence, and conservation of functional protein domains, we aligned characterized protein sequences of either Mgp or Bgp proteins (from human, mouse or chicken, and zebrafish) to those of the small-spotted catshark and elephant shark (**Supplementary Material 6** and **7**) and identified the expected location of specific functional domains of Mgp and Bgp proteins as previously described (Laizé et al., 2005).

The central motif for the Gla domain ExxxExC could be identified in the Mgp2, as well as in Mgp1 and Bgp sequences (**Figure 4**). However, the C-terminal part of the Gla domain was poorly aligned in the Mgp2 sequences, suggesting a divergent Gla domain in the Mgp2 paralog. In addition, no phosphorylation site could be identified in the Mgp2 sequences.

Mgp1 sequences (both from the small-spotted catshark and elephant shark) displayed well-conserved signal peptide, phosphorylation site, and general Gla domain (**Figure 4**). The expected ANxF site upstream to the Gla domain and supposed to participate in the docking site for the gamma-carboxylase (Viegas et al., 2013) was conserved in the elephant shark but modified to AHSF in the small spotted catshark questioning the functionality of this site (**Figure 4**).

In Bgp protein sequences, a signal peptide was also well conserved, followed by a furin cleavage site in the elephant shark that was not predicted in the small spotted catshark sequence because of a modification to KKSKR (**Figure 4**). A well-conserved Gla domain including the highly conserved Gla motif ExxxExC was present in the elephant shark and small-spotted catshark Bgp sequences.

By aligning each cDNA sequence with the genomic locus, we could map the exonic junctions on the full length protein sequences of the small-spotted catshark: *Mgp1* and *Mgp2* display conserved intron/exon structure [four exons, ATG and peptide signal coding sequence in the first exon, docking site coding sequence in the third exon, and Gla domain in the fourth exon: see **Figure 4** and compare to bony fishes (Laizé et al., 2005; Viegas et al., 2013)]. On the other hand, the small-spotted catshark Bgp sequence displayed a divergent exon-intron structure [as compared to bony fishes (Laizé et al., 2005; Viegas et al., 2013)]: 13 exons and a series of imperfect repeat sequences between exons 3 and 12 (exons 3, 5, 7 code for very similar protein sequences), revealing important divergence of the gene structure. Because our cDNA sequence is reconstructed from RNAseq data, we cannot exclude the existence of splicing variants that would not include these extra-exons. Also, the elephant shark sequence does not include these repeated exons so they may be specific for the lesser spotted catshark (so a product of recent evolution).

Gene Expression Patterns in the Embryonic Small-Spotted Catshark *Scyliorhinus canicula*

All three identified *Mgp*/*Bgp* sequences generated distinct expression patterns in the small-spotted catshark embryos by *in situ* hybridization. The selected stages of development were chosen in order to cover one time point before and another after the initiation of mineralization in the developing vertebrae (Enault et al., 2016) and during tooth development.

Mgp1 Expression

In the 6 cm long embryo, the expression of *Mgp1* was detected in the developing vertebrae: in the cartilaginous core of neural arches, in a cartilaginous ring surrounding the notochord and also in notochordal cells (**Figures 5A,B**). At this stage, these zones of expression are not mineralized (**Figure 5C**; see Enault et al., 2016), but neural arches and the cartilage surrounding the notochord will show strong mineralization in

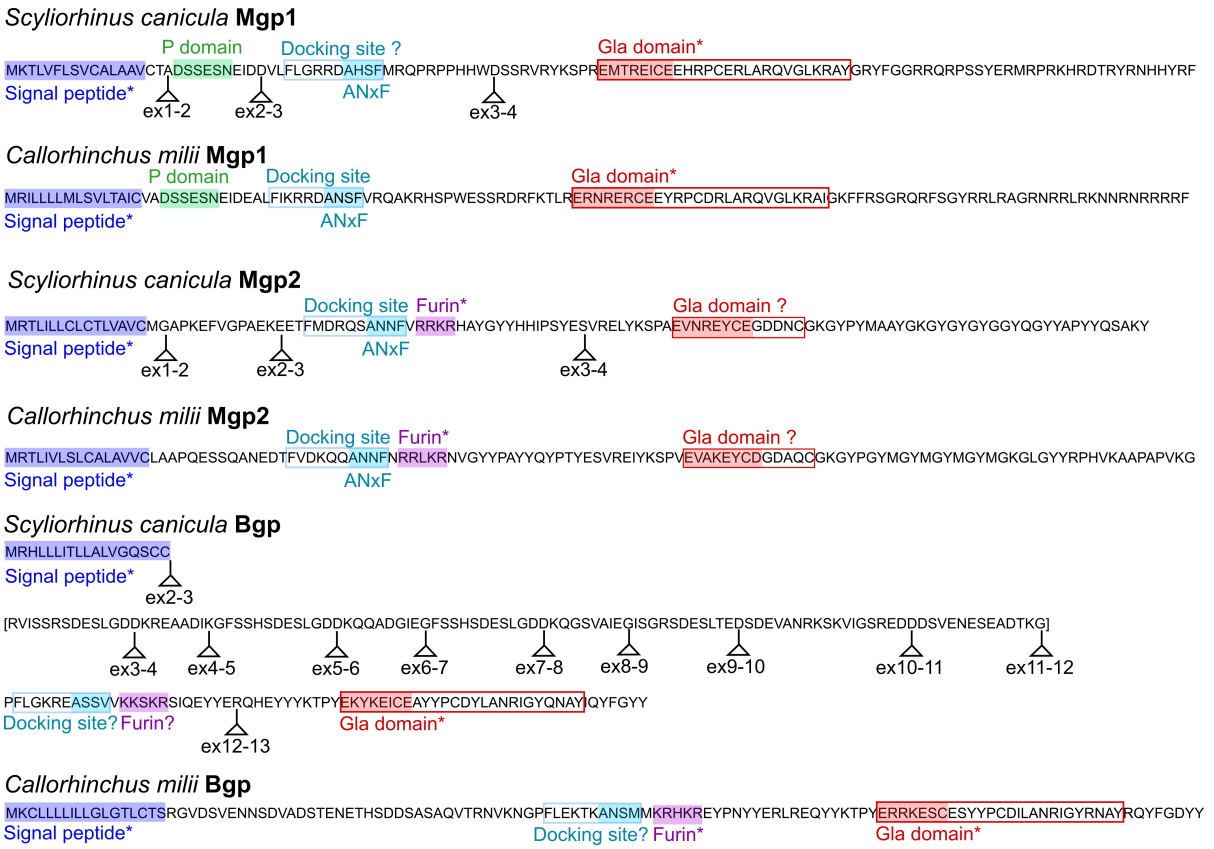

FIGURE 4 | Conserved protein domains in the small-spotted catshark and the elephant shark Mgp/Bgp sequences. The small-spotted catshark Mgp/Bgp sequences are predicted from RNAseq, with location of exonic junctions (ex2–3: junction between exon 2 and exon 3); the elephant shark Mgp/Bgp sequences are predicted from genomic sequences (no exon junction showed). Domains predicted by InterPro, SMART, or FIMO are marked with an asterisk. Other domains are highlighted from their conserved alignment with previously characterized protein domains. Question marks are for domains identified after alignment but showing non-functional mutations. The small-spotted catshark Bgp sequence predicted from exons 3 to 11 is in bracket as it poorly aligns to any other vertebrate Bgp sequences.

embryos measuring 7.7 cm (**Figure 5E**; see Enault et al., 2016). On the 7.7 cm long embryo, the expression of *Mgp1* was no longer detected in neural arches, appeared faint in the cartilage surrounding the notochord, but was still strong in the notochord which is not a site of mineralization (**Figure 5D**). In the Meckel's cartilage, the expression of *Mgp1* was not detected in developing teeth but was detected in a sub-perichondral population of chondrocytes (**Figure 5F**) at a time when no mineralization has started in the lower jaw cartilage (**Figure 5G**), but in a zone prefiguring the site of tesseral mineralization (Enault et al., 2015). Further expression in chondrocytes was detected in the pectoral girdle cartilages in a sub-perichondral layer of chondrocytes located in a contact zone between two cartilages (**Figure 5H**, filled arrowhead). Finally, expression of *Mgp1* was observed in gills, both in the endothelium of the vascular system and in undifferentiated mesenchyme surrounding vascularization (**Figure 5H**).

Mgp2 Expression

The expression of the *Mgp2* gene in the small-spotted catshark was restricted and could be observed with very strong signal in the developing fins, in 6 (**Figures 6A,B**) and 7.7 cm (not shown) long embryos, in the mesenchymal tissue surrounding and most probably synthesizing ceratotrichiae, the semi-rigid fibers that make up the fin support in cartilaginous fishes. Weaker signal was detected in developing unmineralized tooth bud of the lower jaw (**Figure 6C**).

Bgp Expression

Bone Gla protein showed a widespread low-level expression in many connective tissues in the 7.7 cm long embryo (**Figures 7A,B**) but could not be detected in any chondrocyte population, neither in early (data not shown) or late stage vertebrae (**Figure 7B**) nor in Meckel's cartilage (**Figure 7E**). Stronger detection of *Bgp* expression was observed in the cells of the nerve root (**Figure 7B**), the mesenchymal cells of scale buds at a placode stage (**Figure 7C**, filled arrowhead), mesenchymal cells in connective tissues surrounding muscles of the branchial apparatus with strong expression in the zone of attachment between muscle fibers and cartilaginous units (**Figure 7D**, black arrow), few mesenchymal cells of mineralized teeth (**Figure 7E**). Some weaker signal could be detected in the epithelium and

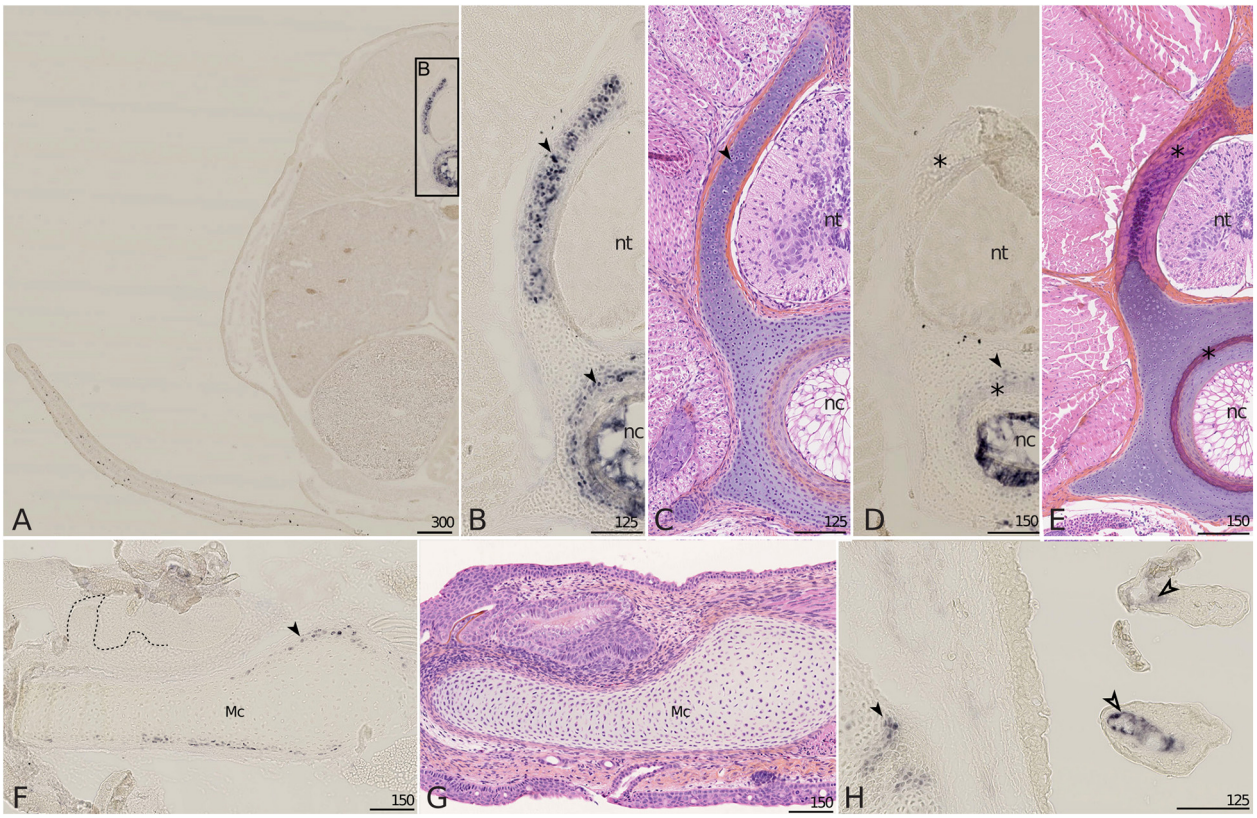

FIGURE 5 | *Mgp1* gene expression on sections of late developing embryos of the small-spotted catshark *Scyliorhinus canicula*. **(A–C)** A total of 6 cm long embryos showing *Mgp1 in situ* hybridization, general **(A)** and closer **(B)** view on transverse sections at the level of the pectoral fin and Hematoxylin-Eosin-Saffron (HES) staining of a comparable zone to **B (C)**. **(D,E,H)** Transverse sections of 7.7 cm long embryos displaying *Mgp1 in situ* hybridization **(D,H)** or HES staining **(E)**. **(F)** *Mgp1 in situ* hybridization on a parasagittal section of the Meckel's cartilage of a hatchling embryo with developing teeth [dotted line separates the epithelial (e) and mesenchymal (m) compartments of teeth]. **(G)** HES staining on a comparable zone to **(F)**. **(H)** Branchial basket with gills. *Mgp1* expression is detected in neural arch and vertebral body chondrocytes (filled arrowheads in **B**,**D**) before but not after mineralization (located with asterisks in **D**,**E**); in chondrocytes in the periphery of the Meckel's cartilage before mineralization (filled arrowhead in **F**) and of other skeletal elements (filled arrowhead in **H**); in the connective tissue cells that surround vasculature in gills (open arrowhead in **H**). Mc, Meckel's cartilage; nc, notochord; nt, neural tube. Scales are in μm.

mesenchyme of non-mineralized tooth buds (**Figure 7E**). *Bgp* expression could also be detected in gill tissues, restricted to the connective mesenchyme that surrounds the vascular system (open arrow), but its expression could not be observed in the vascular endothelium as seen with *Mgp1* (**Figures 7D,F** and compare with **Figure 5H**). Finally, *Bgp* expression was detected in cells of the pectoral fin tip, in the mesenchymal tissue surrounding ceratotrichia in 6 cm long (not shown) and 7.7 cm long embryos (**Figure 7C**, open arrowhead).

Embryonic Patterns of Expression

Total RNA extracts obtained from whole embryos of the small-spotted catshark from stage 18 (end of neurulation) to stage 32 (late organogenesis) (Ballard et al., 1993) allowed the evaluation of relative expression levels for *Bgp, Mgp1,* and *Mgp2* over the course of organogenesis in the small-spotted catshark (**Figure 8**). *Bgp* expression generally tended to be higher than the expression of the Mgp genes during the stages 18–32, to the exception of *Mgp2* expression at stage 32 (**Figure 8**). The results of the one-way ANOVA testing for gene expression variation over developmental stages were non-significant for the genes *Mgp1* and *Bgp*. However, the one-way ANOVA for the *Mgp2* gene indicated a difference between group means at the $P < 0.1$ threshold, probably due to the higher expression level observed at the stage 32. Stage 32 may be the stage of initiation of ceratotrichiae development (there is no sign of ceratotrichiae in pectoral or pelvic fins in stage 30 embryos in Tanaka et al., 2002) explaining the initiation of stronger expression at stage 32.

DISCUSSION

An Evolutionary Scenario for Mgp/Bgp Gene Duplicates

Syntenic and phylogenetic data gathered in this study allow drawing an evolutionary scenario for the genomic organization and diversification of the Mgp/Bgp gene family, under a most-parsimonious model of evolution (**Figure 9** and **Supplementary Material 4**). In the bony fishes, our data allow testing previously

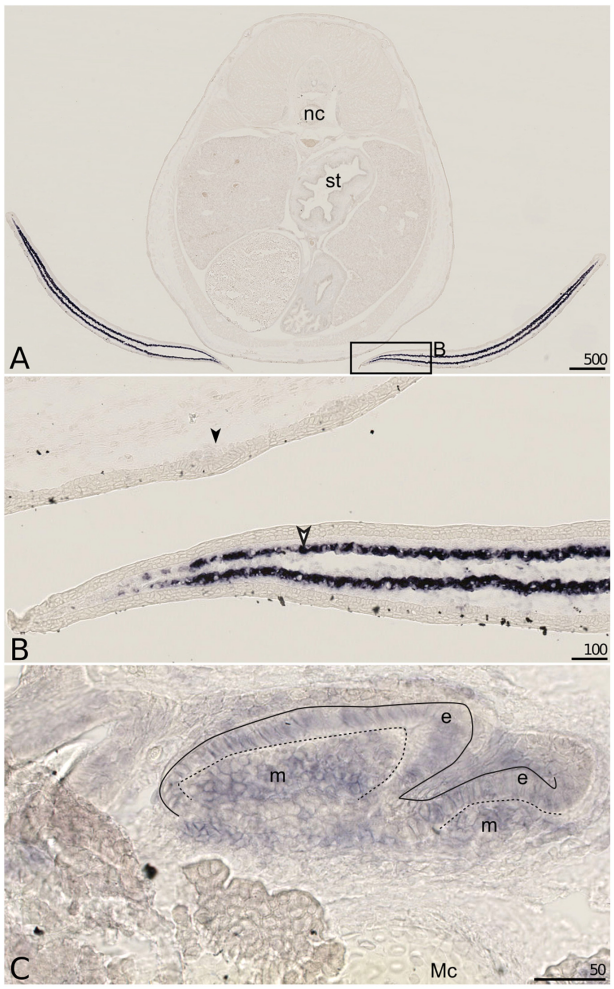

FIGURE 6 | *Mgp2* gene expression on sections of late developing embryos of the small-spotted catshark *Scyliorhinus canicula*. **(A–C)** *Mgp2 in situ* hybridization: general **(A)** and closer **(B)** views on transverse sections of a 6 cm long embryo. **(C)** *Mgp2 in situ* hybridization on a parasagittal section of the Meckel's cartilage (Mc) of a hatchling embryo with developing teeth (e, epithelial compartment; m, mesenchymal compartment of tooth buds; dotted line separates these two compartments). Expression detected in cells surrounding ceratotrichiae (open arrowhead in **B**), epithelial and mesenchymal cells of developing (unmineralized) tooth buds (in **C**). Mc, Meckel's cartilage; nc, notochord; st, stomach. Scales are in μm.

proposed hypotheses. The phylogenetic relationships between Bgp1 and Bgp2 (**Figure 1**) suggest that these two copies emerged from a gene duplication in the last common ancestor of bony fishes which is congruent with previous identification and phylogenetic reconstruction including Bgp2 [previously named OC3 (Cancela et al., 2014)] where data from chondrichthyans were missing. This node (and others) still displays poor robustness when tested with SH-aLRT: these low values may be dependent on the little number of positions in our alignment (129 aa), a tendency which amplifies with higher number of protein sequences in the alignment and which cannot be easily corrected for, due to the small length of the studied proteins.

In addition, we show that a translocation of *Bgp1* most probably occurred in the sarcopterygian or tetrapod stem lineages, while *Bgp2* was lost convergently in actinopterygians and mammals (**Figure 9**). Unfortunately, no sequence homologous to Bgp could be identified in the available genomic databases of the coelacanth (NCBI or Ensembl, by TBLASTN search of the gar Bgp1 sequence), which could have helped in determining more precisely the timing of the *Bgp1* translocation. Finally, our phylogenetic reconstruction and teleost genome data-mining allowed the annotation of the previously named *OC2* gene (Cancela et al., 2014) as one of the two *bgp1* paralogs (**Figures 1**, **9**) generated by the teleost-specific whole-genome duplication (Amores et al., 1998). We also identified two *mpg* co-orthologs in the Asian bonytongue genome, in tandem organization with each of the *bgp1a* and *bgp1b* copies, with two *pde6h* gene copies and located in synteny with either *erp27* or *ddx47* (**Figure 3**), supporting that the duplicated genes could have originated from the teleost-specific genome duplication. However, these two *mgp* copies were found only in one species within the genomes available in Ensembl: only one *mgp*, in synteny with *bgp1a*, is found in all other examined teleost genomes, which would imply a secondary loss of this *mgpb* gene duplicate in all examined taxa. As a consequence, further analysis of the genomic data in teleost fishes is still needed to support this scenario.

In the chondrichthyan lineage, we uncovered a specific tandem duplication in the Mgp locus leading to the *Mgp1* and *Mgp2* genes. Within chondrichthyans, an additional event of translocation may have occurred for the *Mgp1* copy in the batoid lineage (observed in *A. radiata*, **Figure 2**). However, because this is a single observation and because the *Amblyraja Mgp1* copy was identified in a short scaffold, we still cannot rule out the possibility of an assembly artifact. Additional genomic data from batoids are necessary to test the robustness of this observation.

Our results demonstrate that the location of the actinopterygian *Bgp1* and of the chondrichthyan *Bgp* is in the *Ddx47*/*Erp27* locus, which suggests an ancestral location of *Bgp* in this locus, later followed by tandem duplication that generated *Bgp1* and *Bgp2* in bony fishes. The ancestral *Mgp* and *Bgp* genes were, in this scenario, tandem duplicates in the last common ancestor of jawed vertebrates (**Figure 9**). No other closely related genes to Mgp/Bgp family have been reported for jawed vertebrates. In addition, no similar sequence was found in the genomic data of the lamprey (although the *Ddx47*/*Wbp11* locus can be identified on chromosome 3 of the kPetMar1 assembly), nor in Amphioxus nucleotide dataset (NCBI). Taken together, these three last arguments let us hypothesize that the evolution of Mgp/Bgp family cannot be explained by two rounds of whole genome duplications (Ohno, 1970), that occurred before the divergence of jawed vertebrates and resulted in expansion of many gene families from one to four genes located in different paralogons (Dehal and Boore, 2005). The inability to detect closely related gene families might be explained by several scenarios: (i) complete loss of other paralogs, ancestrally to jawed vertebrates [most frequently observed situation (Blomme et al., 2006)], (ii) rapid and extensive evolution of the coding sequences making sequence similarity searches inefficient, and (iii) *de novo*

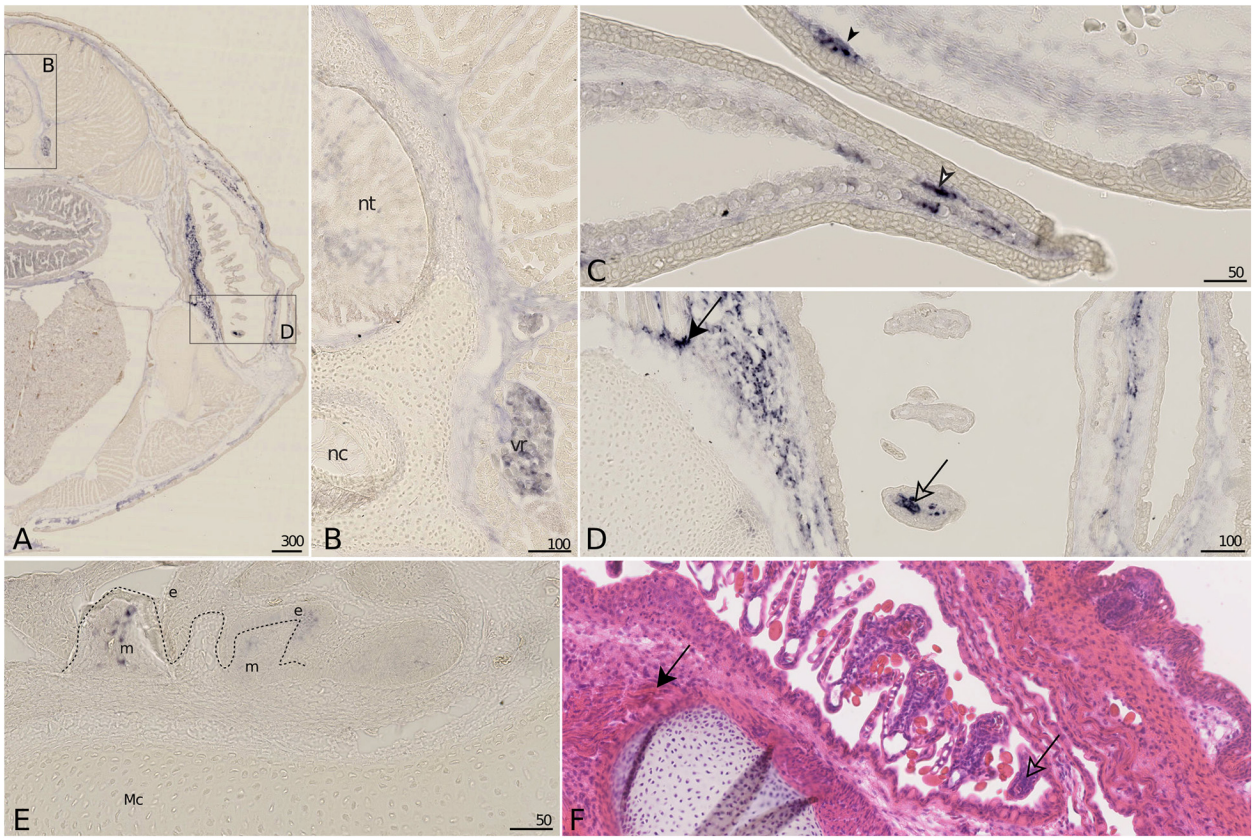

FIGURE 7 | *Bgp* gene expression on sections of late developing embryos of the small-spotted catshark *Scyliorhinus canicula*. **(A–D)** *Bgp in situ* hybridization: general **(A)** and closer **(B–D)** views on transverse sections of a 7.7 cm long embryo. **(E)** *Bgp in situ* hybridization on a parasagittal section of the Meckel's cartilage of a hatchling embryo with developing teeth [dotted line separates the epithelial (e) and mesenchymal (m) compartments of teeth]. **(F)** HES staining of a comparable zone to **(D)**. Expression detected in nerve root **(B)**, cells surrounding ceratotrichiae (open arrowhead in **C**), mesenchymal cells of scale placodes (filled arrowhead in **C**), and mesenchyme of mature (dentin deposition) tooth buds **(E)**, connective tissue at muscle attachment (black arrow in **D**,**F**) and at the tip of vasculature in gills (open arrow in **D**,**F**). Mc, Meckel's cartilage; nc, notochord; nt, neural tube; vr, nerve root. Scales are in μm.

evolution of an ancestral *Bgp*/*Mgp* gene after the two rounds of genome duplication (Van Oss and Carvunis, 2019).

With the evolutionary scenario presented here, the orthology relationships between jawed vertebrate genes of the *Mgp*/*Bgp* family are more complex than usually considered, as the *Bgp* gene found in cartilaginous fishes is not a one-to-one ortholog to the *Bgp* copy (*Bgp1*) found in actinopterygian (non-teleost) fishes or in mammals. In addition, the *Bgp1* copy found in sarcopterygian genomes has gone through a translocation event that may have modified the transcriptional regulation, and therefore the function, of its orthologous copy in sarcopterygian fishes.

Diversity of Expression Patterns in Cartilaginous Fishes and Functional Implications

Previous hypotheses accounting for the evolution of Mgp/Bgp sequences relied on partial sequence data and proposed that only a single *Mgp* gene was present in cartilaginous fishes (Cancela et al., 2014). The survey of transcriptomic and genomic data here reveals the presence of three genes, two *Mgp* genes and one *Bgp*. Few significant aspects of Mgp/Bgp gene evolution in chondrichthyans can be derived from the conservation of functional protein domains. Mgp1, as partly previously described in shark (Price et al., 1994; Rice et al., 1994; Ortiz-Delgado et al., 2006), displays well-conserved signal peptide, phosphorylation sites, carboxylase docking site, and a full Gla domain. This Gla domain is known to be able to bind calcium when secreted in the extracellular matrix and then acts as an inhibitor of mineralization under the condition that Mgp protein is phosphorylated (Schurgers et al., 2007). On the other hand, our data suggest the divergence of the Gla domain in the Mgp2 protein, although the core Gla motif was observed in our alignments, together with a loss of the phosphorylation domain that follows the signal peptide in other Mgp proteins (**Figure 4**). From these observations, we could expect Mgp1 to display a conserved Mgp function as known in bony fishes, while Mgp2 may have undergone partial or complete change of function. These observations suggest that after the *Mgp1*/*Mgp2* duplication event in cartilaginous fishes, the *Mgp2* copy underwent neofunctionalization, while *Mgp1* kept the ancestral function (Ohno, 1970). The chondrichthyan

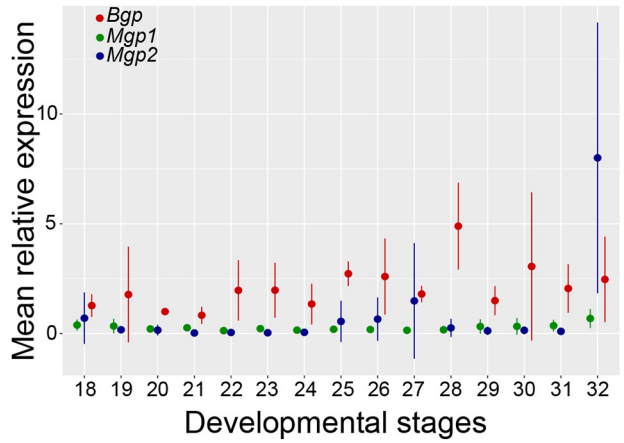

FIGURE 8 | Relative levels of *Mgp1*, *Mgp2,* and *Bgp* mRNA expression in early embryos of the small-spotted catshark (stage 18–32). The value set to 1 was chosen as the *Bgp* mean value at stage 20; for each gene, at each developmental stage, mean values are represented with standard deviation. At each point, $3 < n < 4$.

Bgp preprotein as described from transcriptomic data of the small-spotted catshark shows conserved signal peptide, followed by a long stretch of non-conserved amino-acids that partly originate from repeated sequences through addition of new exons (**Figure 4**). No functional protein domain was predicted in this zone of the protein. It was followed by a putative docking site, and then a better conserved C-terminal sequence including a well conserved Gla domain (**Figure 4**). In the elephant shark, a furin site is conserved in the N-terminal side of the Gla domain. Provided the cleavage site is indeed functional, the mature Bgp protein would then be very similar to Bgp in bony vertebrates: cleavage facilitates carboxylation and as a consequence the affinity of Bgp for hydroxyapatite (Al Rifai et al., 2017).

We also questioned the function of chondrichthyans *Mgp1*, *Mgp2*, and *Bgp* through the survey of their expression patterns in the small-spotted catshark. Some observed expression patterns are shared with bony vertebrates (**Table 1**), but some appear to be specific to cartilaginous fishes. Of course, *in situ* hybridization data show which cells express which genes, but do not help in determining if the protein is produced, where and how much of it is secreted, nor what is the gamma-carboxylation status of the Mgp/Bgp proteins. Further proteomic studies would be necessary to resolve the protein status in terms of post-translational cleavage and carboxylation. As a result, the following discussion only speculates on the functional implications of gene expression patterns in the small-spotted catshark.

A specific site of expression in the small-spotted catshark was found with a very restricted site of expression of *Mgp2* in the developing ceratotrichiae of the pectoral fin, also observed for *Bgp*. These shark ceratotrichiae are massive collagenous fibers that support the distal fin (Kemp, 1977) without being mineralized. Similar collagen-based fibrils named actinotrichia are found in teleost fishes (Durán et al., 2011), and together with lepidotrichiae (bony hemi-segments), they build up the typical fin rays found in actinopterygians fishes. These collagen-based fibers are supposed to be homologous between cartilaginous and actinopterygian fishes (Zhang et al., 2010). To our knowledge, the expression of *Mgp* or *Bgp1* has never been recorded in fish actinotrichia, although the expression of *Bgp1* was detected in the dermal bone of fin rays in several teleost fishes (Stavri and Zarnescu, 2013; Viegas et al., 2013) and in the cartilaginous supports of fins (Gavaia et al., 2006). These data therefore suggest a cartilaginous fish specific site of expression for *Mgp2* and *Bgp* in developing ceratotrichiae, be it an evolutionary innovation in this lineage, or a consequence of secondary loss of this site of expression in bony fish. The fact that this is a shared zone of expression between *Mgp2* and *Bgp* could support the hypothesis of an ancestral feature (that evolved before the duplication of the gene ancestral to *Bgp* and *Mgp*) or a secondary (chondrichthyan-specific) recruitment of both genes that may share regulatory elements, given their genomic proximity. This strong expression in fin ceratotrichiae, that are not mineralized structures, is not congruent with a mineralization function of Bgp proteins in the small-spotted catshark ceratotrichiae.

The remaining range of tissue with expression of the *Bgp* gene in the small-spotted catshark is not congruent either with the hypothesis of a function in the activation of mineralization: it is expressed in several soft tissues such as connective tissues surrounding muscles, nerve root and vasculature of the gills (**Figure 7**). These sites of expression were previously identified in tetrapods and actinopterygian fishes for both *Mgp* and *Bgp* genes (see **Table 1** and discussion below). In most of these soft tissues, the expression of *Mgp* is considered to ensure inhibition of mineralization, but the function of *Bgp* in these tissues is still poorly understood. In the small-spotted catshark, the only site of *Bgp* expression that correlates with tissue mineralization is in the pulp of mineralized teeth, which is similar with other observations in tetrapods and teleost fishes (see **Table 1** for references) but may be linked to non-mineralizing cells in the dental pulp, e.g., vascular system or innervation.

Finally, only the expression of *Mgp1* is strongly linked to the dynamic of skeletal mineralization in the small-spotted catshark: it is found expressed in subpopulations of chondrocytes that are specifically pre-mineralization chondrocytes (before areolar mineralization surrounding the notochord; before the initiation of tesserae mineralization; before globular mineralization in the neural arch (Debiais-Thibaud, 2019); and the expression goes down at the time when mineralization initiates. *Mgp1* is also expressed in the cells of the notochord that never mineralizes. These observations are more congruent with a function of *Mgp1* in the inhibition of mineralization during the maturation of the skeletal tissues in the small-spotted catshark.

Comparative Analyses and the Evolution of Mgp and Bgp Functions

There is currently no possibility to compare the two *Bgp* copies in tetrapods because expression data have been described only for the *Bgp1* copy in the chicken and the tropical clawed frog, and we did not find any description of *Bgp2* expression (see references in **Table 1**).

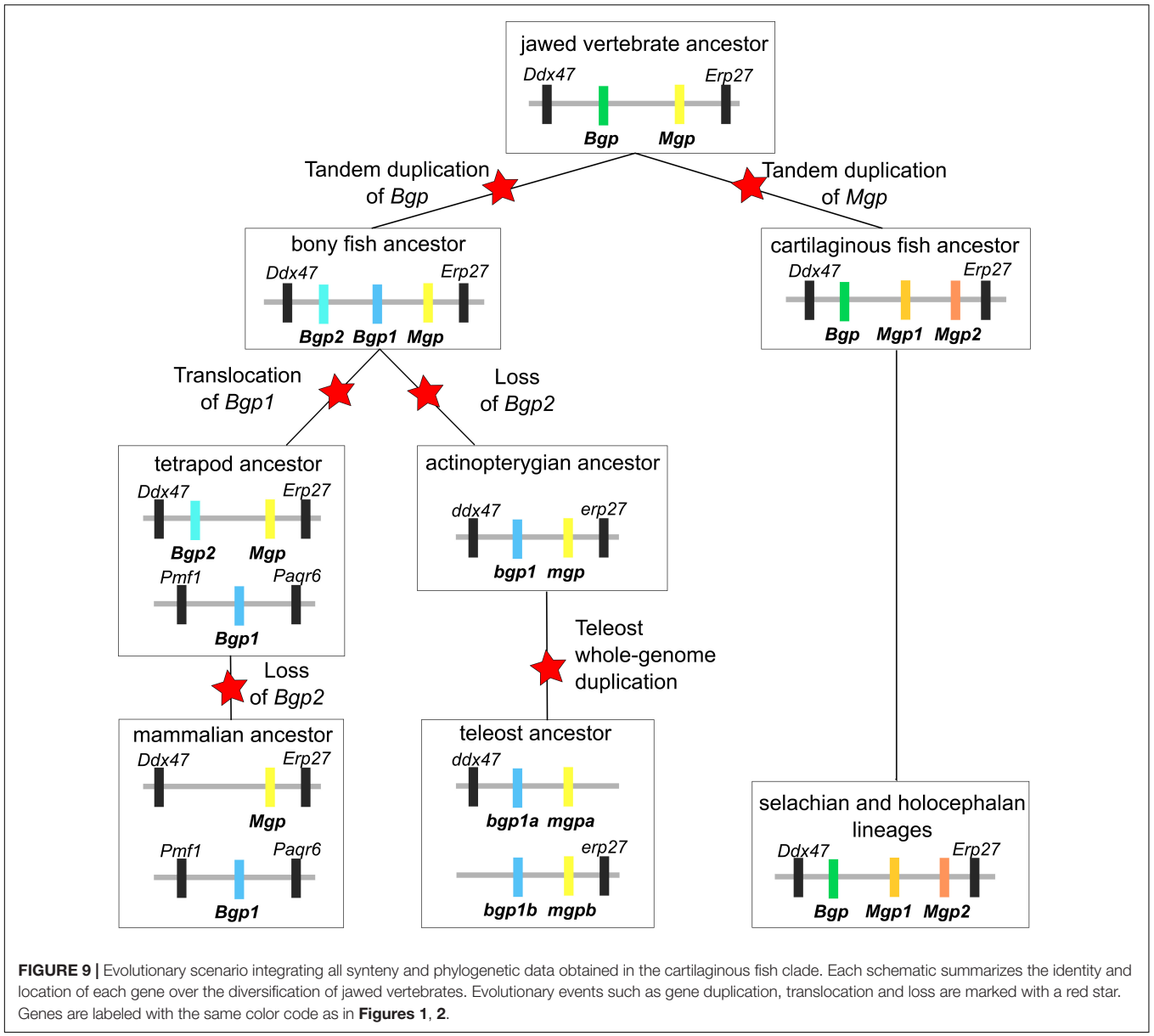

FIGURE 9 | Evolutionary scenario integrating all synteny and phylogenetic data obtained in the cartilaginous fish clade. Each schematic summarizes the identity and location of each gene over the diversification of jawed vertebrates. Evolutionary events such as gene duplication, translocation and loss are marked with a red star. Genes are labeled with the same color code as in **Figures 1**, **2**.

The early and strong embryonic expression detected for *Bgp* in the small-spotted catshark is reminiscent of other studies showing an early expression of *Bgp1* in the zebrafish (Bensimon-Brito et al., 2012), although others detected neither embryonic nor early larval expression of *Bgp1* in other teleost fish (Pinto et al., 2001). On the other hand, *Mgp* genes are also expressed in early embryos: in the vascular system of the avian embryo (Correia et al., 2016) and developing limbs and lungs of the mouse as early as E10.5 (Luo et al., 1995; Gilbert and Rannels, 2004). All these data suggest a shared and ancestral function of Mgp and Bgp proteins during embryogenesis, before tissue and cell differentiation. A function in inhibitory interaction with Bmp proteins was shown for the Mgp protein in human cells (Zebboudj et al., 2002) as well as with the transforming growth factor-β pathway (Oh et al., 2000) which may explain an early expression during morphogenesis. Another conserved aspect of Mgp and Bgp genes is their expression in the tissues surrounding certain muscles and the vasculature along the embryonic and adult period. This zone of expression is shared between *Mgp1* and *Bgp* in the small-spotted catshark, similar to previous descriptions in the zebrafish and mammals (Hao et al., 2004; Simes et al., 2004; Viegas et al., 2013). In these sites of expression, it is accepted that Mgp and Bgp proteins act as mineralization inhibitors, by interacting with the BMP pathway (Yao et al., 2006) or by their properties in their uncarboxylated forms (Schurgers et al., 2005, 2007; Zoch et al., 2016). These two properties might be ancestral characteristics for both Mgp and Bgp in jawed vertebrates, and of the ancestral gene that gave rise to Mgp and Bgp by duplication.

TABLE 1 | Described expression of *Bgp* and *Mgp* genes in selected tissues and selected species of jawed vertebrates compared to data obtained for the small-spotted catshark (this study).

	Small-spotted catshark			Teleost fishes		Xenopus		Mammals		Chicken	
	Mgp1	Mgp2	Bgp	mgp	bgp1a	Mgp	Bgp1	Mgp	Bgp1	Mgp	Bgp1
Embryonic	+	+	+		+ (3)			+ (17)		+ (8)	
Chord	+	−	−		+ (3)					+ (8)	
Chondrocyte	+	−	−	+ (1)	−	+ (10)	− (10)	+ (11)	− (14)	+ (18)	− (12)
Chondrocyte (mineralized matrix)	−	−	−	+ (1)	+ (1)	+ (10)	− (10)	+ (11)	− (14)	+ (18)	+ (12)
Osteoblasts	na	na	na	− (1)	+ (1, 5)	− (10)	+(10)	+ (6)	+ (14)	− (18)	+ (12)
Early tooth/scale bud	−	+	+		+ (15) regeneration				− (13)	na	na
Late (mineralized) tooth/scale	−	−	+	+ (4)	+ (4)				+ (13)	na	na
Muscle and its connective tissue	−	−	+	+ heart (2, 5)	+ heart (5)	− (7)				+ (19)	
Vasculature and its connective tissue	+	−	+ gills	+ heart (2, 5)	+ arteries(5)			+ (11, 16)	+ (16)	+ (8, 18)	
Nerve root	−	−	+						+ (9)		
Ceratotrichia	−	+	+	−	− (1)	na	na	na	na	na	na

Sources: (1) (Gavaia et al., 2006); (2) (Simes et al., 2003); (3) (Bensimon-Brito et al., 2012); (4) (Ortiz-Delgado et al., 2005); (5) (Viegas et al., 2013); (6) (Coen et al., 2009); (7) (Cancela et al., 2001); (8) (Correia et al., 2016); (9) (Ichikawa and Sugimoto, 2002); (10) (Espinoza et al., 2010); (11) (Luo et al., 1997); (12) (Neugebauer et al., 1995); (13) (Bleicher et al., 1999); (14) (Sommer et al., 1996); (15) (Iimura et al., 2012); (16) (Hao et al., 2004); (17) (Gilbert and Rannels, 2004); (18) (Dan et al., 2012); (19) (Wiedemann et al., 1998). na, not applicable (the anatomical structure does not exist in the specified taxon).

Finally, the expression of the small-spotted catshark *Bgp* in the nerve root is also a characteristic previously described in the mouse (Ichikawa and Sugimoto, 2002) and therefore suggests an ancestral role of the *Bgp* copy in the nervous system of jawed vertebrates. The function of Bgp in the nervous system has not been fully uncovered but it has been proposed to be an active neuropeptide in sensory ganglia (Patterson-Buckendahl et al., 2012).

We previously concluded on the putative function of Mgp1 in the inhibition of mineralization during the maturation of the skeletal tissues in the small-spotted catshark. This observation is shared with all described gene expression patterns in skeletal tissues in other jawed vertebrates. As a consequence, it supports the hypothesis of an ancestral involvement of the Mgp/Bgp gene family in the regulation of skeletal mineralization, although limited to the negative regulation of calcium deposition in the cartilage by members of the *Mgp* clade.

CONCLUDING REMARKS

The description of the *Mgp/Bgp* complement in cartilaginous fishes reveals complex dynamic evolution of this gene family during jawed vertebrate evolution. Although previously reported expression of *Mgp* and *Bgp1* in tetrapods was found involved in the regulation of mineralization in skeletal tissues, only *Mgp1* displays association with skeletal tissue differentiation in the small-spotted catshark embryo, and its expression pattern is congruent with an ability to inhibit mineralization in the step preceding precipitation of calcium in the cartilaginous matrix. The ability to activate mineralization in skeletal tissues may finally be a specificity of the *Bgp1* bony fish copy: either because it evolved after the divergence with cartilaginous fishes or because cartilaginous fishes have secondarily lost bone-associated genetic toolkits as they lost bone tissues (Donoghue et al., 2006; Brazeau et al., 2020).

DATA AVAILABILITY STATEMENT

The original contributions presented in this study are included in the article and **Supplementary Material**, further inquiries can be directed to the corresponding authors.

ETHICS STATEMENT

Handling of small-spotted catshark embryos followed all institutional, national, and international guidelines (European Communities Council Directive of 22 September 2010 [2010/63/UE]): no further approval by an ethics committee was necessary as the biological material is embryonic and no live experimental procedures were carried out.

AUTHOR CONTRIBUTIONS

MD-T and TH designed the study, analyzed the data, and drafted the manuscript. NL performed the synteny and phylogenetic analyses. CM-M generated qPCR expression data. SV performed the *in situ* expression experiments. TH performed the genome data mining. All authors contributed to the article and approved the submitted version.

FUNDING

MD-T, CM-M, and NL were supported by the Centre Méditerranéen de l'Environnement et de la Biodiversité (ANR-10-LABX-0004 Skel'Estro project) and TH was supported by the Swedish Research Council (Starting grant 621-2012-4673).

ACKNOWLEDGMENTS

We thank the national infrastructure France-BioImaging and RIO Imaging platform (Montpellier, France, ANR-10-INBS-04, ANR-10-LABX-0020) for nanozoomer acquisitions. We also thank the MBB and GenSeq platforms for help with the transcriptome analyses and the RHEM at the Institute of Cancer Research of Montpellier (IRCM—U1194) for histology data acquisition. We acknowledge Frédéric Delsuc and Céline Scornavacca for our fruitful discussions on phylogenetic analyses.

SUPPLEMENTARY MATERIAL

The Supplementary Material for this article can be found online at: https://www.frontiersin.org/articles/10.3389/fgene.2021.620659/full#supplementary-material

Supplementary Material 1 | References of all sequences used in this manuscript and extracted from open sequence databases or from locally assembled transcriptome data.

Supplementary Material 2 | Protein sequence alignment generated by MAFFT.

Supplementary Material 3 | Protein sequence alignment generated by HmmCleaner automatic cleaning and used to produce the phylogenetic tree reconstruction.

Supplementary Material 4 | Contracted gene and species trees used with Treerecs and the visual output for the maximum parsimony scenario.

Supplementary Material 5 | Unrooted tree obtained after the phylogenetic reconstruction. Colors and gene clade annotations are as in **Figure 1**.

Supplementary Material 6 | Alignment identifying conserved protein regions of Bgp proteins between the human *Homo sapiens*, the chicken *Gallus gallus*, the zebrafish *Danio rerio*, the small spotted catshark *Scyliorhinus canicula*, and the elephant shark *Callorhinchus milii*: signal peptide in the first 22 amino-acids, furin cleavage site in positions 162–166 of the alignment, core Gla domain starting on position 186.

Supplementary Material 7 | Alignment identifying conserved protein regions of Mgp proteins between the human *Homo sapiens*, the zebrafish *Danio rerio*, and both Mgp1 and Mgp2 sequences found in chondrichthyans. Signal peptide is found in the first 20 amino-acids, conserved phosphorylation domain in the Mgp1 sequences in positions 28–36, a partially conserved ANxF domain located in position 48–51 with a F in position 42 (considered as a carboxylase docking site), core Gla domain starting on position 83 with poor conservation of the Mgp2 sequence after position 90. Note the furin cleavage site in positions 53–56 of the alignment, found in *Callorhinchus milii* Mgp2 sequence only.

REFERENCES

Al Rifai, O., Chow, J., Lacombe, J., Julien, C., Faubert, D., Susan-Resiga, D., et al. (2017). Proprotein convertase furin regulates osteocalcin and bone endocrine function. *J. Clin. Invest.* 127, 4104–4117. doi: 10.1172/JCI93437

Amores, A., Force, A., Yan, Y. L., Joly, L., Amemiya, C., Fritz, A., et al. (1998). Zebrafish hox clusters and vertebrate genome evolution. *Science* 282, 1711–1714. doi: 10.1126/science.282.5394.1711

Ballard, W. W., Mellinger, J., and Lechenault, H. (1993). A series of stages for development of *Scyliorhinus canicula* the lesser spotted dogfish (Chondrichthyes: scyliorhinidae). *J. Exp. Zool.* 267, 1–43. doi: 10.1002/jez.1402670309

Bensimon-Brito, A., Cardeira, J., Cancela, M. L., Huysseune, A., and Witten, P. E. (2012). Distinct patterns of notochord mineralization in zebrafish coincide with the localization of Osteocalcin isoform 1 during early vertebral centra formation. *BMC Dev. Biol.* 12:28. doi: 10.1186/1471-213X-12-28

Bleicher, F., Couble, M. L., Farges, J. C., Couble, P., and Magloire, H. (1999). Sequential expression of matrix protein genes in developing rat teeth. *Matrix Biol.* 18, 133–143. doi: 10.1016/S0945-053X(99)00007-4

Blomme, T., Vandepoele, K., De Bodt, S., Simillion, C., Maere, S., and Van de Peer, Y. (2006). The gain and loss of genes during 600 million years of vertebrate evolution. *Genome Biol.* 7:R43. doi: 10.1186/gb-2006-7-5-r43

Bordoloi, J., Dihingia, A., Kalita, J., and Manna, P. (2018). Implication of a novel vitamin K dependent protein, GRP/Ucma in the pathophysiological conditions associated with vascular and soft tissue calcification, osteoarthritis, inflammation, and carcinoma. *Int. J. Biol. Macromol.* 113, 309–316. doi: 10.1016/j.ijbiomac.2018.02.150

Brazeau, M., Giles, S., Dearden, R., Jerve, A., Ariunchimeg, Y. A., Sansom, R., et al. (2020). Endochondral bone in an Early Devonian 'placoderm' from Mongolia. *Nat. Ecol. Evol.* 4, 1477–1484. doi: 10.1038/s41559-020-01290-2

Cancela, M. L., Laizé, V., and Conceição, N. (2014). Matrix Gla protein and osteocalcin: from gene duplication to neofunctionalization. *Arch. Biochem. Biophys.* 561, 56–63. doi: 10.1016/j.abb.2014.07.020

Cancela, M. L., Ohresser, M. C. P., Reia, J. P., Viegas, C. S. B., Williamson, M. K., and Price, P. A. (2001). Matrix gla protein in *Xenopus laevis*: molecular cloning, tissue distribution, and evolutionary considerations. *J. Bone Miner. Res.* 16, 1611–1621. doi: 10.1359/jbmr.2001.16.9.1611

Cavaco, S., Williamson, M. K., Rosa, J., Roberto, V., Cordeiro, O., Price, P. A., et al. (2014). Teleost fish osteocalcin 1 and 2 share the ability to bind the calcium mineral phase. *Fish Physiol. Biochem.* 40, 731–738. doi: 10.1007/s10695-013-9880-9

Coen, G., Ballanti, P., Silvestrini, G., Mantella, D., Manni, M., Di Giulio, S., et al. (2009). Immunohistochemical localization and mRNA expression of matrix Gla protein and fetuin-A in bone biopsies of hemodialysis patients. *Virchows Arch.* 454, 263–271. doi: 10.1007/s00428-008-0724-4

Comte, N., Morel, B., Hasic, D., Guéguen, L., Boussau, B., Daubin, V., et al. (2020). Treerecs: an integrated phylogenetic tool, from sequences to reconciliations. *Bioinformatics* 36, 4822–4824. doi: 10.1093/bioinformatics/btaa615

Correia, E., Conceição, N., Cancela, M. L., and Belo, J. A. (2016). Matrix Gla protein expression pattern in the early avian embryo. *Int. J. Dev. Biol.* 60, 71–76. doi: 10.1387/ijdb.150365jb

Dan, H., Simsa-Maziel, S., Reich, A., Sela-Donenfeld, D., and Monsonego-Ornan, E. (2012). The role of matrix Gla protein in ossification and recovery of the avian growth plate. *Front. Endocrinol. (Lausanne)* 3:79. doi: 10.3389/fendo.2012.00079

Debiais-Thibaud, M., Simion, P., Ventéo, S., Muñoz, D., Marcellini, S., Mazan, S., et al. (2019). Skeletal mineralization in association with Type X collagen expression is an ancestral feature for jawed vertebrates. *Mol. Biol. Evol.* 36, 2265–2276. doi: 10.1093/molbev/msz145

Debiais-Thibaud, M. (2019). "The evolution of endoskeletal mineralisation in chondrichthyan fish," in *Evolution and Development of Fishes*, eds Z. Underwood, C. Richter, and M. Johanson (Cambridge: Cambridge University Press).

Dehal, P., and Boore, J. L. (2005). Two rounds of whole genome duplication in the ancestral vertebrate. *PLoS Biol.* 3:e314. doi: 10.1371/journal.pbio.0030314

D'Errico, J. A., MacNeil, R. L., Takata, T., Berry, J., Strayhorn, C., and Somerman, M. J. (1997). Expression of bone associated markers by tooth root lining cells, in situ and in vitro. *Bone* 20, 117–126. doi: 10.1016/s8756-3282(96)00348-1

Di Franco, A., Poujol, R., Baurain, D., and Philippe, H. (2019). Evaluating the usefulness of alignment filtering methods to reduce the impact of errors

on evolutionary inferences. *BMC Evol. Biol.* 19:21. doi: 10.1186/s12862-019-1350-2

Diegel, C. R., Hann, S., Ayturk, U. M., Hu, J. C. W., Lim, K., Droscha, C. J., et al. (2020). An osteocalcin-deficient mouse strain without endocrine abnormalities. *PLoS Genet.* 16:e1008361. doi: 10.1371/journal.pgen.1008361

Donoghue, P. C. J., and Sansom, I. J. (2002). Origin and early evolution of vertebrate skeletonization. *Microsc. Res. Tech.* 59, 352–372. doi: 10.1002/jemt.10217

Donoghue, P. C. J., Sansom, I. J., and Downs, J. P. (2006). Early evolution of vertebrate skeletal tissues and cellular interactions, and the canalization of skeletal development. *J. Exp. Zool. B. Mol. Dev. Evol.* 306, 278–294. doi: 10.1002/jez.b.21090

Durán, I., Marí-Beffa, M., Santamaría, J. A., Becerra, J., and Santos-Ruiz, L. (2011). Actinotrichia collagens and their role in fin formation. *Dev. Biol.* 354, 160–172. doi: 10.1016/j.ydbio.2011.03.014

Enault, S., Adnet, S., and Debiais-Thibaud, M. (2016). Skeletogenesis during the late embryonic development of the catshark *Scyliorhinus canicula* (Chondrichthyes; Neoselachii). *MorphoMuseuM* 1:e2. doi: 10.18563/m3.1.4.e2

Enault, S., Muñoz, D. N., Silva, W. T. A. F. A. F., Borday-Birraux, V., Bonade, M., Oulion, S., et al. (2015). Molecular footprinting of skeletal tissues in the catshark *Scyliorhinus canicula* and the clawed frog *Xenopus tropicalis* identifies conserved and derived features of vertebrate calcification. *Front. Genet.* 6:283. doi: 10.3389/fgene.2015.00283

Espinoza, J., Sanchez, M., Sanchez, A., Hanna, P., Torrejon, M., Buisine, N., et al. (2010). Two families of *Xenopus tropicalis* skeletal genes display well-conserved expression patterns with mammals in spite of their highly divergent regulatory regions. *Evol. Dev.* 12, 541–551. doi: 10.1111/j.1525-142X.2010.00440.x

Finn, R. D., Attwood, T. K., Babbitt, P. C., Bateman, A., Bork, P., Bridge, A. J., et al. (2017). InterPro in 2017-beyond protein family and domain annotations. *Nucleic Acids Res.* 45, D190–D199. doi: 10.1093/nar/gkw1107

Fraser, J. D., and Price, P. A. (1988). Lung, heart and kidney express high levels of mRNA for the vitamin K-dependent matrix Gla protein. *J. Biol. Chem.* 263, 11033–11036. doi: 10.1016/s0021-9258(18)37912-2

Gavaia, P. J., Simes, D. C., Ortiz-Delgado, J. B., Viegas, C. S. B., Pinto, J. P., Kelsh, R. N., et al. (2006). Osteocalcin and matrix Gla protein in zebrafish (*Danio rerio*) and Senegal sole (*Solea senegalensis*): comparative gene and protein expression during larval development through adulthood. *Gene Expr. Patterns* 6, 637–652. doi: 10.1016/j.modgep.2005.11.010

Gilbert, K. A., and Rannels, S. R. (2004). Matrix GLA protein modulates branching morphogenesis in fetal rat lung. *Am. J. Physiol. Lung Cell. Mol. Physiol.* 286, 1179–1187. doi: 10.1152/ajplung.00188.2003

Grant, C. E., Bailey, T. L., and Noble, W. S. (2011). FIMO: scanning for occurrences of a given motif. *Bioinformatics* 27, 1017–1018. doi: 10.1093/bioinformatics/btr064

Guindon, S., Dufayard, J. F., Lefort, V., Anisimova, M., Hordijk, W., and Gascuel, O. (2010). New algorithms and methods to estimate maximum-likelihood phylogenies: assessing the performance of PhyML 3.0. *Syst. Biol.* 59, 307–321. doi: 10.1093/sysbio/syq010

Hao, H., Hirota, S., Ishibashi-Ueda, H., Kushiro, T., Kanmatsuse, K., and Yutani, C. (2004). Expression of matrix Gla protein and osteonectin mRNA by human aortic smooth muscle cells. *Cardiovasc. Pathol.* 13, 195–202. doi: 10.1016/j.carpath.2004.03.607

Hoang, D. T., Chernomor, O., Haeseler, A., Minh, B. Q., and Vinh, L. S. (2017). UFBoot2: improving the ultrafast bootstrap approximation. *Mol. Biol. Evol.* 35, 518–522. doi: 10.5281/zenodo.854445

Ichikawa, H., and Sugimoto, T. (2002). The difference of osteocalcin-immunoreactive neurons in the rat dorsal root and trigeminal ganglia: co-expression with nociceptive transducers and central projection. *Brain Res.* 958, 459–462.

Iimura, K., Tohse, H., Ura, K., and Takagi, Y. (2012). Expression patterns of runx2, sparc, and bgp during scale regeneration in the goldfish *Carassius auratus*. *J. Exp. Zool. B. Mol. Dev. Evol.* 318, 190–198. doi: 10.1002/jez.b.22005

Ikeda, T., Nomura, S., Yamaguchi, A., Suda, T., and Yoshiki, S. (1992). In situ hybridization of bone matrix proteins in undecalcified adult rat bone sections. *J. Histochem. Cytochem.* 40, 1079–1088. doi: 10.1177/40.8.1619274

Janvier, P. (1996). *Early Vertebrates*. New York: Oxford University Press Inc.

Kaipatur, N. R., Murshed, M., and McKee, M. D. (2008). Matrix Gla protein inhibition of tooth mineralization. *J. Dent. Res.* 87, 839–844. doi: 10.1177/154405910808700907

Katoh, K., Misawa, K., Kuma, K., and Miyata, T. (2002). MAFFT: a novel method for rapid multiple sequence alignment based on fast Fourier transform. *Nucleic Acid Res.* 30, 3059–3066.

Katoh, K., and Standley, D. M. (2013). MAFFT multiple sequence alignment software version 7: improvements in performance and usability. *Mol. Biol. Evol.* 30, 772–780. doi: 10.1093/molbev/mst010

Kemp, N. E. (1977). Banding pattern and fibrillogenesis of ceratotrichia in shark fins. *J. Morphol.* 154, 187–204. doi: 10.1002/jmor.1051540202

Laizé, V., Martel, P., Viegas, C. S. B., Price, P. A., and Cancela, M. L. (2005). Evolution of matrix and bone γ-carboxyglutamic acid proteins in vertebrates. *J. Biol. Chem.* 280, 26659–26668. doi: 10.1074/jbc.M500257200

Letunic, I., Khedkar, S., and Bork, P. (2021). SMART: recent updates, new developments and status in 2020. *Nucleic Acids Res.* 49, D458–D460. doi: 10.1093/nar/gkaa937

Luo, G., D'Souza, R., Hogue, D., and Karsenty, G. (1995). The matrix Gla protein gene is a marker of the chondrogenesis cell lineage during mouse development. *J. Bone Miner. Res.* 10, 325–334. doi: 10.1002/jbmr.5650100221

Luo, G., Ducy, P., McKee, M. D., Pinero, G. J., Loyer, E., Behringer, R. R., et al. (1997). Spontaneous calcification of arteries and cartilage in mice lacking matrix GLA protein. *Nature* 386, 78–81. doi: 10.1038/386078a0

Neugebauer, B. M., Moore, M. A., and Broess, M. (1995). Characterization of structural sequences in the chicken osteocalcin gene: expression of osteocalcin by maturing osteoblasts and by hypertrophic chondrocytes in vitro. *J. Bone Miner. Res.* 10, 157–163.

Nguyen, L. T., Schmidt, H. A., Von Haeseler, A., and Minh, B. Q. (2015). IQ-TREE: a fast and effective stochastic algorithm for estimating maximum-likelihood phylogenies. *Mol. Biol. Evol.* 32, 268–274. doi: 10.1093/molbev/msu300

Oh, S. P., Seki, T., Goss, K. A., Imamura, T., Yi, Y., Donahoe, P. K., et al. (2000). Activin receptor-like kinase 1 modulates transforming growth factor-β1 signaling in the regulation of angiogenesis. *Proc. Natl. Acad. Sci. U.S.A.* 97, 2626–2631. doi: 10.1073/pnas.97.6.2626

Ohno, S. (1970). *Evolution by Gene Duplication*. Berlin: Springer-Verlag.

Omelon, S., Georgiou, J., Henneman, Z. J., Wise, L. M., Sukhu, B., Hunt, T., et al. (2009). Control of vertebrate skeletal mineralization by polyphosphates. *PLoS One* 4:e5634. doi: 10.1371/journal.pone.0005634

Onimaru, K., Marcon, L., Musy, M., Tanaka, M., and Sharpe, J. (2016). The fin-to-limb transition as the re-organization of a Turing pattern. *Nat. Commun.* 7:11582. doi: 10.1038/ncomms11582

Ortiz-Delgado, J. B., Simes, D. C., Gavaia, P. J., Sarasquete, C., and Cancela, M. L. (2005). Osteocalcin and matrix GLA protein in developing teleost teeth: identification of sites of mRNA and protein accumulation at single cell resolution. *Histochem. Cell Biol.* 124, 123–130. doi: 10.1007/s00418-005-0015-y

Ortiz-Delgado, J. B., Simes, D. C., Viegas, C. S. B., Schaff, B. J., Sarasquete, C., and Cancela, M. L. (2006). Cloning of matrix Gla protein in a marine cartilaginous fish, *Prionace glauca*: preferential protein accumulation in skeletal and vascular systems. *Histochem. Cell Biol.* 126, 89–101. doi: 10.1007/s00418-005-0125-6

O'Shaughnessy, K. L., Dahn, R. D., and Cohn, M. J. (2015). Molecular development of chondrichthyan claspers and the evolution of copulatory organs. *Nat. Commun.* 6:6698. doi: 10.1038/ncomms7698

Ota, K. G., Fujimoto, S., Oisi, Y., and Kuratani, S. (2013). Late development of hagfish vertebral elements. *J. Exp. Zool. B. Mol. Dev. Evol.* 320, 129–139. doi: 10.1002/jez.b.22489

Patterson-Buckendahl, P., Sowinska, A., Yee, S., Patel, D., Pagkalinawan, S., Shahid, M., et al. (2012). Decreased sensory responses in osteocalcin null mutant mice imply neuropeptide function. *Cell. Mol. Neurobiol.* 32, 879–889. doi: 10.1007/s10571-012-9810-x

Pinto, J. P., Ohresser, M. C. P., and Cancela, M. L. (2001). Cloning of the bone Gla protein gene from the teleost fish *Sparus aurata*. Evidence for overall conservation in gene organization and bone-specific expression from fish to man. *Gene* 270, 77–91. doi: 10.1016/s0378-1119(01)00426-7

Price, P. A., Rice, J. S., and Williamson, M. K. (1994). Conserved phosphorylation of serines in the Ser-X-Glu / Ser (P) sequences of the vitamin K- dependent matrix Gla protein from shark, lamb, rat, cow, and human. *Protein Sci.* 3, 822–830. doi: 10.1002/pro.5560030511

Rhie, A., Mccarthy, S. A., Fedrigo, O., Damas, J., Formenti, G., London, S. E., et al. (2020). Towards complete and error-free genome assemblies of all vertebrate species. *BioRxiv [Preprint]* doi: 10.1101/2020.05.22.110833

Rice, J. S., Williamson, M. K., and Price, P. A. (1994). Isolation and sequence of the vitamin K-dependent matrix Gla protein from the calcified cartilage of the soupfin shark. *J. Bone Miner. Res.* 9, 567–576. doi: 10.1002/jbmr.5650090417

Schurgers, L. J., Spronk, H. M. H., Skepper, J. N., Hackeng, T. M., Shanahan, C. M., Vermeer, C., et al. (2007). Post-translational modifications regulate matrix Gla protein function: importance for inhibition of vascular smooth muscle cell calcification. *J. Thromb. Haemost.* 5, 2503–2511.

Schurgers, L. J., Teunissen, K. J. F., Knapen, M. H. J., Kwaijtaal, M., Van Diest, R., Appels, A., et al. (2005). Novel conformation-specific antibodies against matrix γ- carboxyglutamic acid (Gla) protein: undercarboitylated matrix Gla protein as marker for vascular calcification. *Arterioscler. Thromb. Vasc. Biol.* 25, 1629–1633. doi: 10.1161/01.ATV.0000173313.46222.43

Simes, D. C., Williamson, M. K., Ortiz-Delgado, J. B., Viegas, C. S. B., Price, P. A., and Cancela, M. L. (2003). Purification of matrix Gla protein from a marine teleost fish, *Argyrosomus regius*: calcified cartilage and not bone as the primary site of mgp accumulation in fish. *J. Bone Miner. Res.* 18, 244–259. doi: 10.1359/jbmr.2003.18.2.244

Simes, D. C., Williamson, M. K., Schaff, B. J., Gavaia, P. J., Ingleton, P. M., Price, P. A., et al. (2004). Characterization of osteocalcin (BGP) and matrix Gla Protein (MGP) fish specific antibodies: validation for immunodetection studies in lower vertebrates. *Calcif. Tissue Int.* 74, 170–180. doi: 10.1007/s00223-003-0079-4

Sommer, B., Bickel, M., Hofstetter, W., and Wetterwald, A. (1996). Expression of matrix proteins during the development mineralized tissues. *Bone* 19, 371–380. doi: 10.1016/s8756-3282(96)00218-9

Stavri, S., and Zarnescu, O. (2013). The expression of alkaline phosphatase, osteopontin, osteocalcin, and chondroitin sulfate during pectoral fin regeneration in *Carassius auratus* gibelio: a combined histochemical and immunohistochemical study. *Microsc. Microanal.* 19, 233–242.

Tan, M., Redmond, A., Dooley, H., Nozu, R., Sato, K., Kuraku, S., et al. (2019). The whale shark genome reveals patterns of vertebrate gene family evolution. *bioRxiv [Preprint]* doi: 10.1101/685743

Tanaka, M., Münsterberg, A., Anderson, W. G., Prescott, A. R., Hazon, N., and Tickle, C. (2002). Fin development in a cartilaginous fish and the origin of vertebrate limbs. *Nature* 416, 527–531. doi: 10.1038/416527a

Van Oss, S. B., and Carvunis, A. R. (2019). De novo gene birth. *PLoS Genet.* 15:e1008150. doi: 10.1371/journal.pgen.1008160

Venkatesh, B., Lee, A. P., Ravi, V., Maurya, A. K., Lian, M. M., Swann, J. B., et al. (2014). Elephant shark genome provides unique insights into gnathostome evolution. *Nature* 505, 174–179. doi: 10.1038/nature12826

Viegas, C. S. B., Simes, D. C., Williamson, M. K., Cavaco, S., Laizé, V., Price, P. A., et al. (2013). Sturgeon osteocalcin shares structural features with matrix Gla protein: evolutionary relationship and functional implications. *J. Biol. Chem.* 288, 27801–27811. doi: 10.1074/jbc.M113.450213

Wen, L., Chen, J., Duan, L., and Li, S. (2018). Vitamin K-dependent proteins involved in bone and cardiovascular health (Review). *Mol. Med. Rep.* 18, 3–15. doi: 10.3892/mmr.2018.8940

Wiedemann, M., Trueb, B., and Belluoccio, D. (1998). Molecular cloning of avian matrix Gla protein. *Biochim. Biophys. Acta Gene Struct. Expr.* 1395, 47–49. doi: 10.1016/S0167-4781(97)00155-3

Yáñez, M., Gil-Longo, J., and Campos-Toimil, M. (2012). Chapter 19: calcium binding proteins. *Adv. Exp. Med. Biol.* 740, 461–482. doi: 10.1007/978-94-007-2888-2

Yao, T., Ohtani, K., Kuratani, S., and Wada, H. (2011). Development of lamprey mucocartilage and its dorsal-ventral patterning by endothelin signaling, with insight into vertebrate jaw evolution. *J. Exp. Zool. B. Mol. Dev. Evol.* 316, 339–346. doi: 10.1002/jez.b.21406

Yao, Y., Zebboudj, A. F., Shao, E., Perez, M., and Boström, K. (2006). Regulation of bone morphogenetic protein-4 by matrix GLA protein in vascular endothelial cells involves activin-like kinase receptor 1. *J. Biol. Chem.* 281, 33921–33930. doi: 10.1074/jbc.M604239200

Zebboudj, A. F., Imura, M., and Boström, K. (2002). Matrix GLA protein, a regulatory protein for bone morphogenetic protein-2. *J. Biol. Chem.* 277, 4388–4394. doi: 10.1074/jbc.M109683200

Zhang, J., Wagh, P., Guay, D., Sanchez-Pulido, L., Padhi, B. K., Korzh, V., et al. (2010). Loss of fish actinotrichia proteins and the fin-to-limb transition. *Nature* 466, 234–237. doi: 10.1038/nature09137

Zhang, Y., Zhao, L., Wang, N., Li, J., He, F., Li, X., et al. (2019). Unexpected role of matrix Gla protein in osteoclasts: inhibiting osteoclast differentiation and bone resorption. *Mol. Cell. Biol.* 39, e00012–e00019.

Zoch, M. L., Clemens, T. L., and Riddle, R. C. (2016). New insights into the biology of osteocalcin. *Bone* 82, 42–49. doi: 10.1016/j.bone.2015.05.046

Conflict of Interest: The authors declare that the research was conducted in the absence of any commercial or financial relationships that could be construed as a potential conflict of interest.

frontiers in Genetics

BRIEF RESEARCH REPORT
published: 07 April 2021
doi: 10.3389/fgene.2021.624533

Carbonic Anhydrases: An Ancient Tool in Calcareous Sponge Biomineralization

Oliver Voigt[1], Benedetta Fradusco[1], Carolin Gut[1], Charalampos Kevrekidis[1], Sergio Vargas[1] and Gert Wörheide[1,2,3]*

[1] Department of Earth and Environmental Sciences, Palaeontology and Geobiology, Ludwig-Maximilians-Universität München, Munich, Germany, [2] GeoBio-Center, Ludwig-Maximilians-Universität München, Munich, Germany, [3] SNSB-Bayerische Staatssammlung für Paläontologie und Geologie, Munich, Germany

Enzymes of the α-carbonic anhydrase gene family (CAs) are essential for the deposition of calcium carbonate biominerals. In calcareous sponges (phylum Porifera, class Calcarea), specific CAs are involved in the formation of calcite spicules, a unique trait and synapomorphy of this class. However, detailed studies on the CA repertoire of calcareous sponges exist for only two species of one of the two Calcarea subclasses, the Calcaronea. The CA repertoire of the second subclass, the Calcinea, has not been investigated so far, leaving a considerable gap in our knowledge about this gene family in Calcarea. Here, using transcriptomic analysis, phylogenetics, and *in situ* hybridization, we study the CA repertoire of four additional species of calcareous sponges, including three from the previously unsampled subclass Calcinea. Our data indicate that the last common ancestor of Calcarea had four ancestral CAs with defined subcellular localizations and functions (mitochondrial/cytosolic, membrane-bound, and secreted non-catalytic). The evolution of membrane-bound and secreted CAs involved gene duplications and losses, whereas mitochondrial/cytosolic and non-catalytic CAs are evidently orthologous genes. Mitochondrial/cytosolic CAs are biomineralization-specific genes recruited for biomineralization in the last common ancestor of calcareous sponges. The spatial–temporal expression of these CAs differs between species, which may reflect differences between subclasses or be related to the secondary thickening of spicules during biomineralization that does not occur in all species. With this study, we extend the understanding of the role and the evolution of a key biomineralization gene in calcareous sponges.

Keywords: carbonic anhydrases, Porifera: Calcarea, biomineralization and calcification, evolution, spicule formation

OPEN ACCESS

Edited by:
Melanie Debiais-Thibaud, Université de Montpellier, France

Reviewed by:
Helena Ćetković, Rudjer Boskovic Institute, Croatia
Ana Riesgo, Natural History Museum, United Kingdom

****Correspondence:***
Oliver Voigt
oliver.voigt@lmu.de

Specialty section:
This article was submitted to Evolutionary and Population Genetics, a section of the journal Frontiers in Genetics

Received: *31 October 2020*
Accepted: *26 February 2021*
Published: *07 April 2021*

Citation:
Voigt O, Fradusco B, Gut C, Kevrekidis C, Vargas S and Wörheide G (2021) Carbonic Anhydrases: An Ancient Tool in Calcareous Sponge Biomineralization. Front. Genet. 12:624533. doi: 10.3389/fgene.2021.624533

INTRODUCTION

Animal biomineralization is a controlled process and leads to the production of mineral–organic composite materials that considerably differ in shape and material properties from their purely inorganic counterparts. The ability to form functional biominerals, such as endo- and exoskeletons, protective shells, or teeth, had been a significant step in animal evolution. Calcium carbonate

biomineralization, the most widespread type among animal phyla (Murdock and Donoghue, 2011), evolved several times independently, resulting in multiple recruitments of the same genes for biomineralization in different lineages (Murdock, 2020). Among these genes, members of the α-carbonic anhydrase gene family (CAs) are essential for biomineralization (Le Roy et al., 2014). CAs are zinc-binding enzymes that catalyze the reversible conversion of carbon dioxide and water to bicarbonate and one proton (Tripp et al., 2001). The zinc-binding is mediated by three histidine residues essential for the protein's catalytic function (Aspatwar et al., 2014; Kim et al., 2020). CAs are involved in many physiological processes requiring ion regulation or carbon transport (Supuran, 2016), both of which are crucial for the controlled precipitation of carbonate biominerals. In mammals, where they are best studied, 16 different CAs are expressed in specific tissues and active in defined subcellular compartments (Imtaiyaz Hassan et al., 2013). Cytosolic, mitochondrial, membrane-bound, and secreted CA forms can be distinguished, and these groups got expanded and reduced in different animal groups (Le Roy et al., 2014; Voigt et al., 2014). Specific CAs are involved in the carbonate biomineralization in distinct metazoan lineages (reviewed in Le Roy et al., 2014), including sponges (Jackson et al., 2007; Voigt et al., 2014; Germer et al., 2015).

Among extant sponges, only the calcareous sponges (class Calcarea) can produce calcite spicules, whereas other classes' spicules are siliceous. Some lineages among demosponges and a few calcareans have massive calcium carbonate basal skeletons, the so-called coralline sponges or sclerosponges. The biomineralizing CAs used by carbonate-producing demosponges are not orthologous to the CAs involved in the spicule formation of calcareous sponges (Voigt et al., 2014), suggesting that the two biomineralization types evolved independently. This observation agrees with the idea that the formation of calcitic spicules is an evolutionary innovation of calcareous sponges (Manuel, 2006).

The shapes of calcareous sponge spicules are simple compared with the sometimes very elaborate siliceous spicules found in the other sponge classes. With only a few exceptions, calcareous sponge spicules can be of three basic types: monaxonic, two-tipped diactines, triactines with three spicules rays, and four-rayed tetractines. Specialized cells, the sclerocytes, produce these spicules, and only a few sclerocytes interact in the formation of one specific spicule: Two sclerocytes produce a diactine, six sclerocytes form a triactine, and seven a tetractines (Minchin, 1898; Woodland, 1905; Ledger and Jones, 1977). A pair of sclerocytes is involved in the growth of each actine of these spicules. After an initial phase, the so-called founder cell promotes actine elongation, the second, so-called thickener cell in some, but not all species deposit additional calcium carbonate on the actine, as it migrates back toward the founder cell (**Figure 1**, Ledger and Jones, 1977; Ilan et al., 1996). Calcareous sponges can possess only one or any combination of the three spicule types in their body, and in many cases, certain spicule types are restricted to specific body parts. This indicates that spicule formation is under strict genetic control in calcareous sponges, and specific CAs play an essential role in this genetic control (Voigt et al., 2017). Indeed, biomineralizing CAs were identified in Calcaronea, one of the two subclasses of calcareous sponges (Voigt et al., 2014). In each of the two studied species, *Sycon ciliatum* (Sci) and *Leucosolenia complicata* (Lco), sclerocytes express one intracellular CA (SciCA1 and LcoCA1) and one secreted or membrane-bound CA (SciCA2 and LcoCA3) during spicule formation. In *Sycon*, these two CAs have specific spatial and temporal expression patterns during spicule formation: Although early in spicule formation, all sclerocytes express *SciCA1* and *SciCA2*, in later stages, only SciCA2 is produced in the founder cells. Simultaneously, the production of certain spicular matrix proteins is induced in the thickener cells, indicating an orchestrated regulation of biomineralization gene expression during spicule formation (Voigt et al., 2017). In addition to these two sclerocyte-specific CAs, several additional secreted or membrane-bound CA proteins are present in both species (six in *Sycon* and four in *Leucosolenia*) and are not directly involved in the biomineralization process (Voigt et al., 2014). Some of these probably lost their catalytic activity due to substitutions of the zinc-binding histidine residues. Such inactive proteins of the gene family are called carbonic anhydrase-related proteins (CARPs, Aspatwar et al., 2014). Determination of gene orthology is difficult for the secreted CAs because of the several gene duplications and losses during evolution that shaped this gene family (Voigt et al., 2014). Phylogenetic analysis of the CAs from the subclass Calcaronea implied the presence of at least three ancestral CAs in the last common ancestor of this subclass (Voigt et al., 2014). Conclusions about the set of CAs in the last common ancestor of all extant calcareous sponges, however, require the study of additional species from the second calcarean subclass, the Calcinea. To gain further insights into the evolution of these essential biomineralization genes of calcareous sponges, we explored the CA repertoire of four additional species from both subclasses by transcriptomic, phylogenetics, and *in situ* hybridization (ISH) experiments.

METHODS

Sampling, RNA Extraction, and Transcriptome Sequencing

RNA of two species of the subclass Calcinea was extracted. The first species was isolated from our laboratory aquarium system and belonged to the genus *Clathrina sensu lato*. The genus *Clathrina* was recently revised (Klautau et al., 2013), but the species belongs to a yet unnamed clade of calcareous sponges that, in contrast to the new definition of the genus, bears tetractines in addition to triactines. Therefore, in this work, we refer to it as *Clathrina* sp. (Csp) in the sense of *Clathrina sensu lato*. It is an asconoid sponge whose body consists of thin anastomosed tubes. Small living specimens were incubated for 18 h in calcein in seawater to stain spicules produced in this time frame and confirm ongoing biomineralization as described before (Voigt et al., 2014). Other specimens were processed for RNA extraction or fixed for RNA ISH, according to previously described methods (Fortunato et al., 2012).

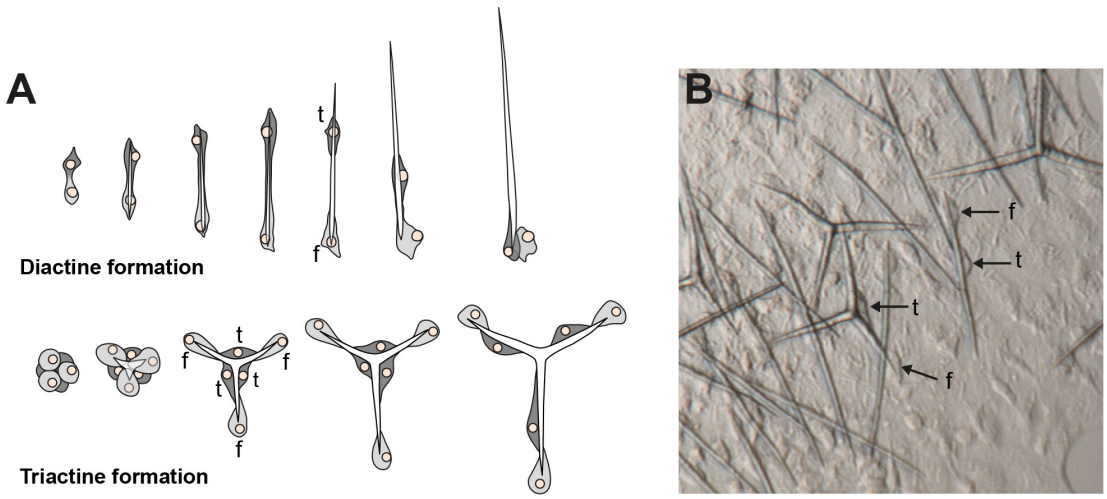

FIGURE 1 | Spicule formation by sclerocytes in calcareous sponges; **(A)** Movement of founder cell (*f*) and thickener (*t*) cells during diactine and triactine formation; **(B)** *in vivo* formation of spicules by sclerocytes (*f* = founder cell, *t* = thickener cell). Modified from Voigt et al. (2017).

The second calcinean species was *Pericharax orientalis* (Por), sampled at the MaRHE center in the Fafuu Atoll in the Maldives. RNA of both species was isolated using Trizol. RNA quality was verified with an Agilent Bioanalyzer 2,100, and transcriptomic libraries were prepared with the Illumina TruSeq2 kit (*Clathrina* s. l.) or the Lexogen SENSE Total RNA-Seq Library Prep Kit. Sequencing was performed on an Illumina Miniseq, NextSeq, and 1,500 HiSeq Sequencer.

Assembly and Identification of α-Carbonic Anhydrases

In addition to the newly sequenced species, published raw reads of two species from a phylogenomic study (Simion et al., 2017), *Clathrina coriacea* (Cco and subclass Calcinea) and *Grantia compressa* (Gco subclass Calcaronea), were downloaded from the GenBank short read archive (SRX1719631 and SRX1719634, respectively). The obtained raw reads were quality controlled, trimmed, and assembled with Trinity (Grabherr et al., 2011); ORFs were predicted for the Trinity contigs with TransDecoder v.5.0.0[1] and used to create a Blast database in Geneious Prime 2019[2]. Raw reads of transcriptomes were submitted to ENA short read archive (Study accession PRJEB41034). Assemblies of transcriptomes are available at LMU Open Data (doi: 10.5282/ubm/data.202).

Protein sequences of *S. ciliatum* CA1 and CA9 (SciCA1, SciCA2, Voigt et al., 2014) were used as BLAST queries against these libraries. Only hits that were confirmed to be CAs by blasting them against Swiss Prot (Katoh and Standley, 2013) were considered further. Of these, we manually corrected some 5′ partial Transdecoder predictions because the potential CDS was close to the 5' end of the contig and comparison with other CAs suggested (see alignments) that the start ATG was included and that the coding sequence was indeed complete (**Supplementary Table 1**). As a measurement of each CA's expression level, their fragments per kilobase million (FPKM) values were obtained with RSEM using Bowtie2 (Li and Dewey, 2011) in a Galaxy environment (Afgan et al., 2018) by mapping the reads back to the obtained transcriptome assemblies. We used SignalP 5.0 (Armenteros et al., 2019) to identify the presence of signal peptides, hence whether a protein is secreted or not. TargetP (Emanuelsson et al., 2000) was used to predict the subcellular localization of calcareous sponge CAs. The presence of a glycosylphosphatidylinositol (GPI) anchor, indicative for membrane-bound CAs, was determined with PredGPI (Pierleoni et al., 2008).

Phylogenetic Analysis

We complemented the dataset of identified CA amino acid sequences with published calcareous sponge CAs from *S. ciliatum* and *L. complicata* and CAs from other sponge classes (**Supplementary Table 2**) and from selected metazoans with sequenced genomes (*Homo sapiens*, *Strongylocentrotus purpurea*, and *Mnemiopsis leidyi*), and the scleractinian coral *Stylophora pistillata*. Non-metazoan CAs (from the green algae *Chlamydomonas* and two Enterobacteria) were added as an outgroup. Sequences were aligned with MAFFT (G-INS-i, gap-opening penalty 3, Katoh and Standley, 2013). We considered one partial CA of each of the transcriptomes of *P. orientalis* and *C. coriacea* to originate from commensals because they did not group with other CAs of calcareous sponges and were only partial transcripts with low FPKM values (**Supplementary Table 1**). We excluded them from further analysis and also some variants of other CAs with FPKM of 0. Gblocks (Castresana, 2000) was used to select 205 sites for the phylogenetic analyses. The final alignment, including the information of the selected sites, is available from LMU Open Data (doi: 10.5282/ubm/data.202) as a mase-file and can be inspected with the Seaview alignment

[1]https://github.com/TransDecoder
[2]https://www.geneious.com

editor (Gouy et al., 2010). A maximum-likelihood tree was calculated with PhyML v3.0 (Guindon et al., 2010) using the best fitting model (LG + G) determined using the AIC in ProTest (Darriba et al., 2011). A Bayesian phylogeny was calculated with MrBayes (Ronquist and Huelsenbeck, 2003) using the same model, two runs and four chains each of five million generations. The temperature setting for the heated chains was decreased from the default of 0.1 to 0.05 to obtain better mixing. Every 1,000th tree was sampled, and a consensus tree was calculated with the sumt command with the first 25% of trees discarded as burn-in. CAs of calcareous sponges that were from the same Trinity sequence cluster but assembled as different "genes" or "isoforms" were considered to be one "gene" and collapsed in the phylogeny as they formed one clade with only short internal branches (**Supplementary Table 1**). Although some of these variants may be true isoforms or real genes, at least some appear to be assembly artifacts because several coded for incomplete proteins or had low FPKM values (**Supplementary Table 1**).

Amplification of α-Carbonic Anhydrases and Preparation of RNA Probes, RNA in situ Hybridization

DNA and RNA were isolated from another specimen of *Clathrina* s. l. using the ZR-Duet^{TM} DNA/RNA MiniPrep (Zymo Research). Complementary DNA was generated using the extracted RNA and the ProtoScript(R) II First-Strand Complementary DNA Synthesis Kit (NEB) and used as a template in PCRs with gene-specific primers to amplify all six *Clathrina* sp. CAs (**Supplementary Table 1**). PCR products were cloned into the pCR4-TOPO vector (Invitrogen) and sequenced to determine the insert orientation (presence of T3 or T7 initiation site on the 3' end of the gene's sense strand). An additional PCR with the corresponding reverse vector primer and a probe-specific forward primer provided the template for the synthesis of DIG-labeled RNA probes (DIG RNA Labeling Mix, Roche) with the corresponding RNA polymerase to generate antisense probes (T3 or T7 polymerase, Promega). RNA ISH was performed as previously described (Fortunato et al., 2014) on fixed tissues of complete small specimens of *Clathrina* sp. The expression patterns of the different CAs were documented using a Leica FM16 stereomicroscope and a Leica DMLB compound microscope. To increase the depth of field, stacks of images were combined with the Auto-Blend-Layers function of Adobe Photoshop 2020.

RESULTS

In the assembled transcriptomes, we identified several complete and incomplete CA genes (in a sense described in M&Ms): Six in *Clathrina* sp. (CspCA1-CspCA6), eight in *P. orientalis* (PorCA1-PorCA8), four in *C. coriacea* (CcoCA1-CcoCA4), and seven in *G. compressa* (GcoCA1–GcoCA7). We arbitrarily labeled them regarding their position in the phylogenetic tree (**Figure 2**), and except for CA1, the numbers do not reflect orthology among the species.

Our ISH experiments with *Clathrina* sp. revealed a sclerocyte-specific expression of *CspCA1* (**Figure 3**) that matches the distribution of active spicule formation expected from the calcein-staining experiments (**Figure 3A** and **Supplementary Figure 3**). Also, different spicule formation stages are recognizable by calcein-staining (**Figures 3B–F**) and the detailed *CspCA1* expression patterns (**Figures 3G–L**).

CspCA1 is not only expressed during early spicule formation stages (**Figures 3G–H**) but additionally in thickener cells during the later stages (**Figures 3J–L**). No sclerocyte-specific expression patterns were observed for *CspCA2*, *CspCA3*, and *CspCA5* (**Supplementary Figure 3**). For *CspCA4* and *CspCA6*, we did not detect a signal in the RNA ISH experiments (**Supplementary Figure 3**). These two CAs showed the lowest expression levels among the CAs of this species (**Supplementary Table 1**).

In the CA phylogeny, many deeper nodes have only low support values (**Figure 2**). The relationship of coral CAs of *S. pistillata* (SpiCA1–16, **Figure 2**) to calcareous sponge CAs, therefore, remains unclear, but they are not specifically closely related. Sponge CAs are not monophyletic. The CAs of the sponge classes Demospongiae and Hexactinellida are each monophyletic. They are sister clades in the ML analysis (with low bootstrap support), but their relationships to each other remain unresolved in the Bayesian reconstruction. CAs of the sponge class Homoscleromorpha occur in three distinct clades. CAs of calcareous sponges fall into four clades (Calcarea clades I–IV, **Figure 2**). Each of these contains CAs with predominantly the same subcellular localization and is subdivided into monophyletic clades of calcinean and calcaronean CAs.

Clade I comprises catalytic CAs (**Supplementary Table 1**) without signal peptide (**Supplementary Table 2**) and, except for LcoCA1, with a mitochondrial targeting sequence. A single CA of each species is present. In addition to CspCA1 (see discussion earlier), a sclerocyte-specific expression is documented for SciCA1 and LcoCA1 (Voigt et al., 2014), suggesting a direct involvement of clade I CAs in biomineralization. Compared with CAs of the other clades, the protein sequences of clade I are more conserved, with a sequence identity between species ranging between 52 and 82% (**Supplementary Figure 1**).

Clades II and III together form a monophyletic clade with high bootstrap and posterior probability support. Most of the complete CAs of clades II and III have an identifiable signal peptide (**Supplementary Table 2**). Two to six CAs per species are found in clade II, and the CAs of each subclass are monophyletic sister clades. Within the subclass clades, the CAs of the species are not monophyletic but intermixed. Intra-clade divergence in clade II is higher compared with the divergence of CAs in clade I (**Supplementary Figure 2**). Besides SciCA6, GcoCA6, and CspCA4, all proteins in this clade have a GPI anchor and therefore are predicted to be membrane-bound. The three zinc-binding histidine residues are generally conserved; only *SciCA4* is probably not catalytic due to a His-Asp replacement of the third catalytic histidine (**Supplementary Table 2**). Clade II includes two calcaronean CAs with a demonstrated expression in sclerocytes (SciCA2, LcoCA3, Voigt et al., 2014).

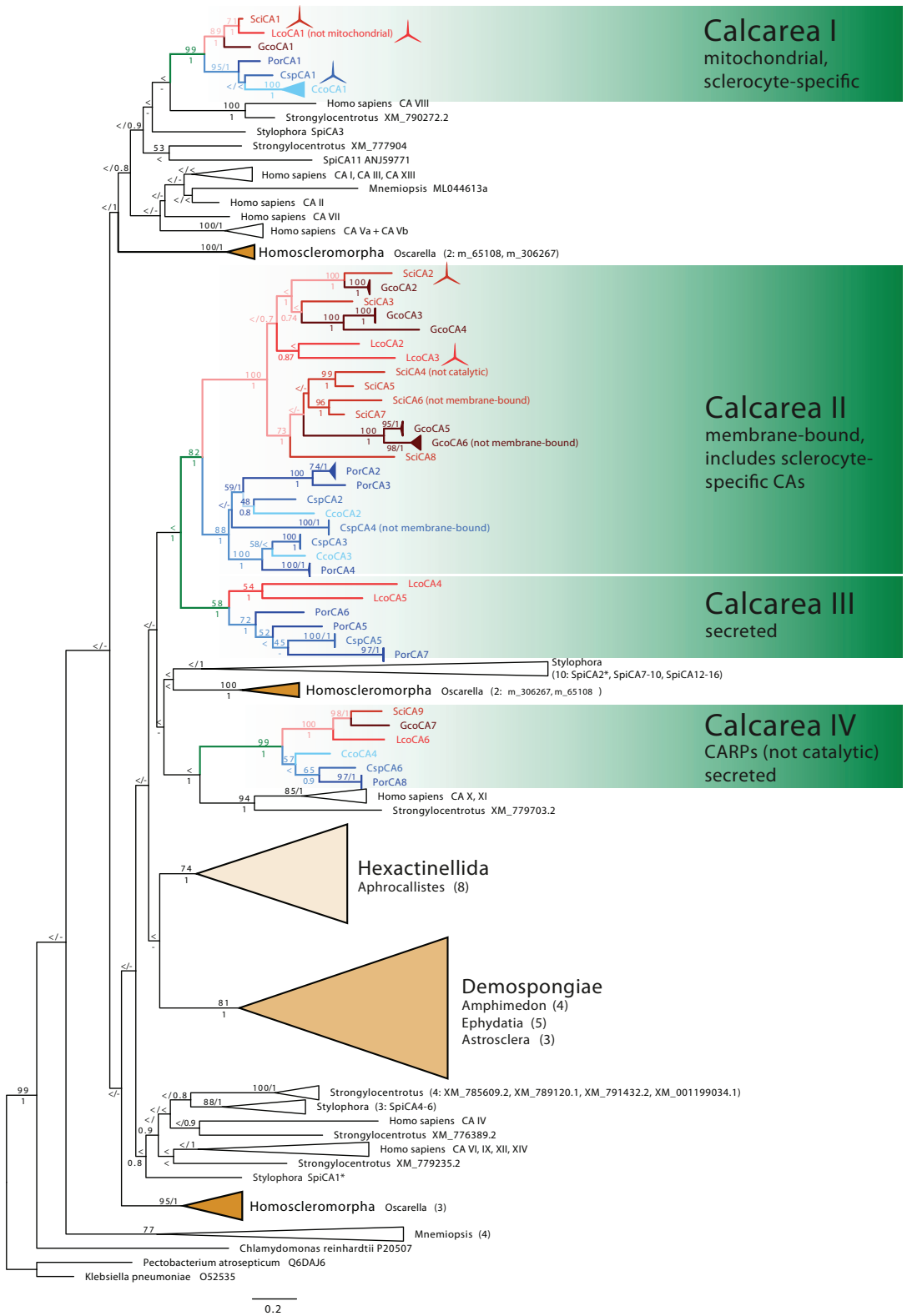

FIGURE 2 | Phylogenetic tree (ML) of CAs. Sponge CAs are highlighted in color: Class Calcarea: green, subclass Calcaronea: red, subclass Calcinea: blue, remaining sponge classes shown as triangles representing their diversity. Monophyletic clades of other species' CAs are collapsed (number of CAs is provided in brackets). ML bootstrap (n = 200) >50 and posterior probability >0.5 are displayed at the corresponding nodes. Spicule symbols mark CAs with verified sclerocyte-specific expression.

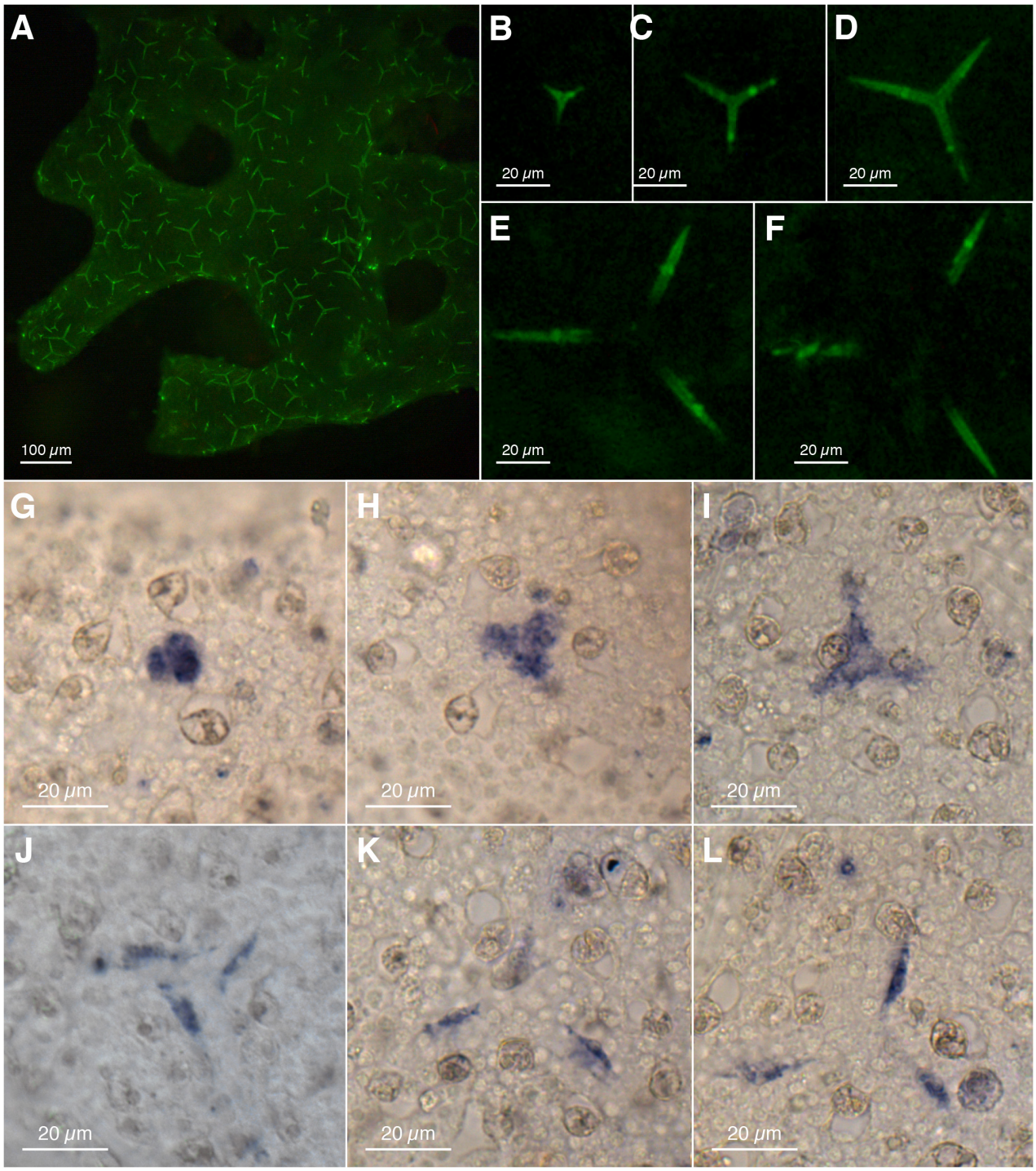

FIGURE 3 | Spicule formation and CA1 expression in *Clathrina* sp.: **(A–F)** spicules formed within 18 h (calcein labeling, fluorescence microscopy); **(A)** Overview, **(B–F)** progressing stages of spicule formation, isolated from **(A)** (overlapping fluorescent actines from adjacent spicules retouched for clarity). **(G–L)** Expression of CA1 in sclerocytes with progressing spicule formation (spicules dissolved during ISH). Sclerocytes in **(J–L)** are thickener cells on the site of the spicules' actines.

Clade III contains CAs from both subclasses, but not from all species; CAs from *S. ciliatum*, *G. compressa*, and *C. coriacea* are missing. These CAs possess a signal peptide but lack GPI anchors and therefore are secreted. The three zinc-binding residues are present in all CAs in this clade, so they are likely catalytic.

Clade IV forms a sister clade to a clade containing the *H. sapiens* CA X and XI and a CA from the urchin

Strongylocentrotus. In clade IV, each species possesses a single protein, which falls into two subclass-specific clades. Besides the previously described *SciCA9* and *LcoCA6* (Voigt et al., 2014), sequences of these clades' CAs are partial. Where detectable, a signal peptide is present, and no GPI anchor was predicted, suggesting clade IV CAs are secreted (**Supplementary Table 1**). The three zinc-binding histidine positions are not conserved because the first histidine is substituted with arginine and the third histidine with glutamine in the sequences that cover this region of the protein. Therefore, the proteins of this clade likely lost their catalytic function and can be considered to represent CARPs.

DISCUSSION

The inclusion of additional CAs from both calcareous sponge subclasses revealed four CA clades with a specific subcellular localization: Clade I with sclerocyte-specific, mitochondrial, or cytosolic CAs, clade II with (mostly) membrane-bound CAs, including, at least for Calcaronea, sclerocyte-specific proteins, clade III with secreted CAs, not present in some species, and clade IV, a clade of secreted calcareous sponge CARPs.

The fact that each of these functional CA clades contains CAs of both subclasses suggests that the last common ancestor of calcareous sponges already possessed ancestral CA proteins belonging to each clade. The phylogeny agrees with the previously reported three clades of calcaronean CAs (Voigt et al., 2014), but now a clear subdivision of clades II and III is evident.

However, especially deeper nodes in the tree are only weakly supported by either bootstrap, posterior probabilities, or both, hampering understanding of the relationship of poriferan and coral CAs. The difficulties in obtaining robust phylogenies for animal CAs are known (Le Roy et al., 2014) and probably not surprising for such a single gene-family dataset, considering that even phylogenomic studies with thousands of genes produce conflicting relationships among animal phyla (King and Rokas, 2017). Nonetheless, the phylogeny of CAs again suggests that CAs were independently recruited for biomineralization in non-Bilateria. None of the CAs that have been suggested to be directly involved in biomineralization in the stony coral *Stylophora* (SpiCA1, SpiCA2: Moya et al., 2008; Bertucci et al., 2011) or in the coralline demosponge *Astrosclera* (Jackson et al., 2007) is particularly closely related to the sclerocyte-specific CAs we report in the clades I and II. We focus our further discussion on the four clades of calcareous sponge CAs, which show moderate to good support values.

Gene orthology is most evident in clades I and IV, in which only one CA per species was observed. Clade I CAs display a conserved role in biomineralization, showing sclerocyte-specific expression in Calcinea (CspCA1, **Figures 3G–L**) and Calcaronea (Voigt et al., 2014). It seems, therefore, that the involvement of mitochondrial CAs in biomineralization in calcareous sponges is an ancient feature dating back to the origin of this subclass's key innovation, i.e., the formation of calcitic spicules. Whether the lack of an identifiable mitochondrial target sequence in one species (*Leucosolenia*) is due to limitations in the prediction of such motifs or a modification of the basic pattern in Calcaronea remains an open question. In this CA group, some variation in the temporal–spatial expression patterns between species appears to have evolved. In *Clathrina* sp., thickener cells in later spicule formation stages also express this CA (**Figures 2J–L**). In the calcaronean *S. ciliatum*, however, thickener cells in later spicule formation stages cease CA expression, in agreement with the observations that these cells deposit little or no calcite in this species (Woodland, 1905; Ledger and Jones, 1977). In contrast, our observations in *Clathrina* sp. implies that thickener cells continue depositing calcite on the actines. Such thickening activity may be specific for this species or possibly for Calcinea in general.

In clade II, multiple gene-duplications and losses occurred in both Calcaronea and Calcinea. However, the fact that CAs of both subclasses are sister groups suggests that the duplication/loss events detected in this clade postdated the split of the two subclasses. The secreted, membrane-bound CAs SciCA2 of *Sycon* and LcoCA3 of *Leucosolenia* are sclerocyte-specific and involved directly in biomineralization (Voigt et al., 2014). We cannot yet identify a calcinean CA with a sclerocyte-specific expression in this clade. Thus, possibly, the recruitment for biomineralization of secreted CAs happened only in the subclass Calcaronea. Alternatively, our ISH experiments, which were limited by material availability, failed to provide a clear signal, hindering the interpretation of the expression patterns in this subclass. Additional experiments, including also other species of Calcinea, are required to address this question.

Clade III (secreted CAs) lacks CAs of *Sycon*, *Grantia*, and *C. coriacea*. In the two latter species, of course, CAs of this clade may not have been expressed in the sampled specimens hampering their detection in the transcriptomes. However, in the genome of *S. ciliatum*, a CA of this clade is also missing, pointing to a loss of secreted CAs in some calcareous sponge species. In this context, it seems relevant that for both, *Sycon* and *Grantia*, one CA in clade II (SciCA6, GcoCA6, respectively) lacks a GPI anchor, that is typical for other CAs of this clade, so these two CAs seem to be secreted. Possibly, they could have functionally replaced the now missing secreted CAs of clade III.

Calcareous sponge CARPs (clade IV) are easily identifiable orthologous proteins (one gene per species) whose catalytic function was already lost in the common ancestor of calcareous sponges. We conclude this from the observation that two of the zinc-binding histidines were replaced with the same amino acids in all CAs in this clade, supporting the hypothesis of a single loss of the CA activity in these CAs. CARPs of other invertebrates also show the same amino acid replacement (Le Goff et al., 2016), although they are not phylogenetically closely related. The function of CARPs in calcareous sponges remains unknown. In the fully grown sponges studied here, CARPs had low expression levels compared with most other CAs in the same species, and the obtained sequences were incomplete (**Supplementary Table 2**). However, in *Sycon*, expression of the CARP *SciCA9* peaks during early post-settlement stages, suggesting a role of these calcareous sponge CARP proteins in early post-larval life stages (Voigt et al., 2014).

In stony corals, the best-studied non-bilaterian animals regarding their biomineralization, only a few CAs have a documented expression in the calcifying tissues. In *Stylophora*, for example, two carbonic anhydrases, SpiCA1 and SpiCA2 (**Figure 2**), are expressed by calcifying cells (Moya et al., 2008; Bertucci et al., 2011). Because both of these have a signal peptide (Del Prete et al., 2019) and SpiCA2 was also found in the coral skeletal matrix (Drake et al., 2013), these CAs seem to be secreted or membrane-bound forms. The cytosolic SpiCA3 is expressed ubiquitously in all tissues, not only in calcifying cells (Del Prete et al., 2019). Although the role of this intracellular CA in coral biomineralization remains uncertain (Del Prete et al., 2019), our results confirm that intracellular mitochondrial/cytosolic CAs are an essential component of the calcareous sponge's biomineralization tool kit. Accordingly, mitochondrial or cytosolic carbonic anhydrases (clade I) were recruited for biomineralization in the last common ancestor of extant calcareous sponges. This suggests that metabolic carbon may be an important constituent of the calcareous sponge spicule's carbonate. The expression pattern in later stages of spicule formation may be subclass-specific and may be correlated to the deposition of calcite by thickener cells on the growing spicules. Secreted, membrane-bound CAs involved in biomineralization only were identified in Calcaronea, but further studies are required to investigate their role in calcification in Calcinea. Future studies could investigate the detailed role of CAs in the biomineralization process of calcareous sponges, for example, by comparing the enzymatic activity of biomineralizing versus non-biomineralizing CAs and tracing the carbon source of the molecules that are transformed by these enzymes.

DATA AVAILABILITY STATEMENT

The data presented in this study are deposited in the European Nucleotide Archive (ENA), study accession PRJEB41034, and in the LMU Open data repository (doi: 10.5282/ubm/data.202).

AUTHOR CONTRIBUTIONS

OV conceived the study and drafted the manuscript. BF generated the data. OV, CG, and CK performed the ISH experiments. OV and SV analyzed the data. GW provided the resources. SV and GW revised the manuscript. All authors contributed to the article and approved the submitted version.

FUNDING

This work was supported by the German Research Foundation (DFG, project VO 2238/1-1).

ACKNOWLEDGMENTS

We thank Gabrielle Büttner for her assistance in library constructions and Helmut Blum and Stefan Krebs for their help in transcriptome sequencing at the Gene Center LMU. Warren R. Francis provided assistance in transcriptome and provided comments to improve the manuscript. We are grateful for support during the fieldwork by the staff of the University of Milano-Bicocca Marine Research and High Education (MaRHE) Centre at Magoodhoo, Faafu Atoll. We would like to acknowledge the Ministry of Fisheries and Agriculture in Malé of the Republic of Maldives for permitting the research end export of samples of *P. orientalis* [permit IDs: (OTHR)30-D/INDIV/2017/377, (OTHR)30-D/INDIV/2018/137, (OTHR)30-D/INDIV/2017/399, and (OTHR)30-D/INDIV/2018/378].

SUPPLEMENTARY MATERIAL

The Supplementary Material for this article can be found online at: https://www.frontiersin.org/articles/10.3389/fgene.2021.624533/full#supplementary-material

REFERENCES

Afgan, E., Baker, D., Batut, B., van den Beek, M., Bouvier, D., Cech, M., et al. (2018). The Galaxy platform for accessible, reproducible and collaborative biomedical analyses: 2018 update. *Nucleic Acids Res.* 46, W537–W544.

Armenteros, J. J. A., Tsirigos, K. D., Sønderby, C. K., Petersen, T. N., Winther, O., Brunak, S., et al. (2019). SignalP 5.0 improves signal peptide predictions using deep neural networks. *Nat. Biotechnol.* 37, 420–423. doi: 10.1038/s41587-019-0036-z

Aspatwar, A., Tolvanen, M. E. E., Ortutay, C., and Parkkila, S. (2014). "Carbonic anhydrase related proteins: molecular biology and evolution," in *Carbonic Anhydrase: Mechanism, Regulation, Links to Disease, and Industrial Applications Subcellular Biochemistry*, eds S. C. Frost and R. McKenna (Dordrecht: Springer Netherlands), 135–156. doi: 10.1007/978-94-007-7359-2_8

Bertucci, A., Tambutté, S., Supuran, C. T., Allemand, D., and Zoccola, D. (2011). A new coral carbonic anhydrase in Stylophora pistillata. *Mar. Biotechnol.* 13, 992–1002. doi: 10.1007/s10126-011-9363-x

Castresana, J. (2000). Selection of conserved blocks from multiple alignments for their use in phylogenetic analysis. *Mol. Biol. Evol.* 17, 540–552. doi: 10.1093/oxfordjournals.molbev.a026334

Darriba, D., Taboada, G. L., Doallo, R., and Posada, D. (2011). ProtTest 3: fast selection of best-fit models of protein evolution. *Bioinformatics* 27, 1164–1165. doi: 10.1093/bioinformatics/btr088

Del Prete, S., Bua, S., Alasmary, F. A. S., AlOthman, Z., Tambutté, S., Zoccola, D., et al. (2019). Comparison of the sulfonamide inhibition profiles of the α-carbonic anhydrase iIsoforms (SpiCA1, SpiCA2 and SpiCA3) encoded by the genome of the scleractinian coral *Stylophora pistillata*. *Mar. Drugs* 17:146. doi: 10.3390/md17030146

Drake, J. L., Mass, T., Haramaty, L., Zelzion, E., Bhattacharya, D., and Falkowski, P. G. (2013). Proteomic analysis of skeletal organic matrix from the stony coral *Stylophora pistillata*. *Proc. Natl. Acad. Sci. U.S.A.* 110, 3788–3793. doi: 10.1073/pnas.1301419110

Emanuelsson, O., Nielsen, H., Brunak, S., and von Heijne, G. (2000). Predicting subcellular localization of proteins based on their N-terminal amino acid sequence. *J. Mol. Biol.* 300, 1005–1016. doi: 10.1006/jmbi.2000.3903

Fortunato, S., Adamski, M., Bergum, B., Guder, C., Jordal, S., Leininger, S., et al. (2012). Genome-wide analysis of the sox family in the calcareous sponge *Sycon ciliatum*: multiple genes with unique expression patterns. *Evodevo* 3:14. doi: 10.1186/2041-9139-3-14

Fortunato, S. A., Adamski, M., Ramos, O. M., Leininger, S., Liu, J., Ferrier, D. E., et al. (2014). Calcisponges have a ParaHox gene and dynamic expression of dispersed NK homeobox genes. *Nature* 514, 620–623. doi: 10.1038/nature13881

Germer, J., Mann, K., Wörheide, G., and Jackson, D. J. (2015). The skeleton forming proteome of an early branching metazoan: a molecular survey of the biomineralization components employed by the coralline sponge *Vaceletia* sp. *PLoS One* 10:e0140100. doi: 10.1371/journal.pone.0140100

Gouy, M., Guindon, S., and Gascuel, O. (2010). SeaView version 4: a multiplatform graphical user interface for sequence alignment and phylogenetic tree building. *Mol. Biol. Evol.* 27, 221–224. doi: 10.1093/molbev/msp259

Grabherr, M. G., Haas, B. J., Yassour, M., Levin, J. Z., Thompson, D. A., Amit, I., et al. (2011). Full-length transcriptome assembly from RNA-Seq data without a reference genome. *Nat. Biotechnol.* 29, 644–652. doi: 10.1038/nbt.1883

Guindon, S., Dufayard, J.-F., Lefort, V., Anisimova, M., Hordijk, W., and Gascuel, O. (2010). New algorithms and methods to estimate maximum-likelihood phylogenies: assessing the performance of PhyML 3.0. *Syst. Biol.* 59, 307–321. doi: 10.1093/sysbio/syq010

Ilan, M., Aizenberg, J., and Gilor, O. (1996). Dynamics and growth patterns of calcareous sponge spicules. *Proc. Royal Soc. Lond. B Biol. Sci.* 263, 133–139. doi: 10.1098/rspb.1996.0021

Imtaiyaz Hassan, M., Shajee, B., Waheed, A., Ahmad, F., and Sly, W. S. (2013). Structure, function and applications of carbonic anhydrase isozymes. *Bioorg. Med. Chem.* 21, 1570–1582. doi: 10.1016/j.bmc.2012.04.044

Jackson, D. J., Macis, L., Reitner, J., Degnan, B. M., and Wörheide, G. (2007). Sponge paleogenomics reveals an ancient role for carbonic anhydrase in skeletogenesis. *Science* 316, 1893–1895. doi: 10.1126/science.1141560

Katoh, K., and Standley, D. M. (2013). MAFFT multiple sequence alignment software version 7: improvements in performance and usability. *Mol. Biol. Evol.* 30, 772–780. doi: 10.1093/molbev/mst010

Kim, J. K., Lee, C., Lim, S. W., Adhikari, A., Andring, J. T., McKenna, R., et al. (2020). Elucidating the role of metal ions in carbonic anhydrase catalysis. *Nat. Commun.* 11:4557.

King, N., and Rokas, A. (2017). Embracing uncertainty in reconstructing early animal evolution. *Curr. Biol.* 27, R1081–R1088.

Klautau, M., Azevedo, F., Cóndor-Luján, B., Rapp, H. T., Collins, A., and de Moraes Russo, C. A. (2013). A molecular phylogeny for the order Clathrinida rekindles and refines Haeckel's taxonomic proposal for calcareous sponges. *Integr. Comp. Biol.* 53, 447–461. doi: 10.1093/icb/ict039

Le Goff, C., Ganot, P., Zoccola, D., Caminiti-Segonds, N., Allemand, D., and Tambutté, S. (2016). Carbonic anhydrases in cnidarians: novel perspectives from the octocorallian *Corallium rubrum*. *PLoS One* 11:e0160368. doi: 10.1371/journal.pone.0160368

Le Roy, N., Jackson, D. J., and Marie, B. (2014). The evolution of metazoan α-carbonic anhydrases and their roles in calcium carbonate biomineralization. *Front. Zool.* 11:75. doi: 10.1186/s12983-014-0075-8

Ledger, P. W., and Jones, W. C. (1977). Spicule formation in calcareous sponge *Sycon ciliatum*. *Cell Tissue Res.* 181, 553–567.

Li, B., and Dewey, C. N. (2011). RSEM: accurate transcript quantification from RNA-Seq data with or without a reference genome. *BMC Bioinformatics* 12:323. doi: 10.1186/1471-2105-12-323

Manuel, M. (2006). Phylogeny and evolution of calcareous sponges. *Can. J. Zool.* 84, 225–241. doi: 10.1139/z06-005

Minchin, E. (1898). Memoirs: materials for a monograph of the Ascons.–I. On the origin and growth of the triradiate and quadriradiate spicules in the family Clathrinidae. *Q. J. Microsc. Sci.* 40:469.

Moya, A., Tambutté, S., Bertucci, A., Tambutté, E., Lotto, S., Vullo, D., et al. (2008). Carbonic anhydrase in the scleractinian coral *Stylophora pistillata*: characterization, localization, and role in biomineralization. *J. Biol. Chem.* 283, 25475–25484. doi: 10.1074/jbc.m804726200

Murdock, D. J. E. (2020). The "biomineralization toolkit"and the origin of animal skeletons. *Biol. Rev. Camb. Philos. Soc.* 95, 1372–1392. doi: 10.1111/brv.12614

Murdock, D. J. E., and Donoghue, P. C. J. (2011). Evolutionary origins of animal skeletal biomineralization. *Cells Tissues Organs* 194, 98–102. doi: 10.1159/000324245

Pierleoni, A., Martelli, P. L., and Casadio, R. (2008). PredGPI: a GPI-anchor predictor. *BMC Bioinformatics* 9:392. doi: 10.1186/1471-2105-9-392

Ronquist, F., and Huelsenbeck, J. P. (2003). MrBayes 3: bayesian phylogenetic inference under mixed models. *Bioinformatics* 19, 1572–1574. doi: 10.1093/bioinformatics/btg180

Simion, P., Philippe, H., Baurain, D., Jager, M., Richter, D. J., Di Franco, A., et al. (2017). A large and consistent phylogenomic dataset supports sponges as the sister group to all other animals. *Curr. Biol.* 27, 958–967. doi: 10.1016/j.cub.2017.02.031

Supuran, C. T. (2016). Structure and function of carbonic anhydrases. *Biochem. J.* 473, 2023–2032. doi: 10.1042/bcj20160115

Tripp, B. C., Smith, K., and Ferry, J. G. (2001). Carbonic anhydrase: new insights for an ancient enzyme. *J. Biol. Chem.* 276, 48615–48618. doi: 10.1074/jbc.r100045200

Voigt, O., Adamska, M., Adamski, M., Kittelmann, A., Wencker, L., and Wörheide, G. (2017). Spicule formation in calcareous sponges: coordinated expression of biomineralization genes and spicule-type specific genes. *Sci. Rep.* 7:45658.

Voigt, O., Adamski, M., Sluzek, K., and Adamska, M. (2014). Calcareous sponge genomes reveal complex evolution of α-carbonic anhydrases and two key biomineralization enzymes. *BMC Evol. Biol.* 14:230. doi: 10.1186/s12862-014-0230-z

Woodland, W. (1905). Memoirs: studies in spicule formation: I.–the development and structure of the spicules in Sycons: with remarks on the conformation, modes of disposition and evolution of spicules in calcareous sponges generally. *Q. J. Microsc. Sci.* 49, 231–282.

Conflict of Interest: The authors declare that the research was conducted in the absence of any commercial or financial relationships that could be construed as a potential conflict of interest.

The reviewer AR declared a past co-authorship with one of the authors GW to the handling editor.

frontiers in Ecology and Evolution

ORIGINAL RESEARCH
published: 22 April 2021
doi: 10.3389/fevo.2021.660767

Diversity and Evolution of Mineralized Skeletal Tissues in Chondrichthyans

Fidji Berio[1,2]*, *Morgane Broyon*[3,4], *Sébastien Enault*[1], *Nelly Pirot*[3,4], *Faviel A. López-Romero*[5] *and Mélanie Debiais-Thibaud*[1]*

[1] ISEM, CNRS, EPHE, IRD, Univ. Montpellier, Montpellier, France, [2] University of Lyon, ENS Lyon, CNRS, Université Claude Bernard Lyon 1, Institut de Génomique Fonctionnelle de Lyon, UMR 5242, Lyon, France, [3] BCM, CNRS, INSERM, Univ. Montpellier, Montpellier, France, [4] IRCM, ICM, INSERM, Univ. Montpellier, Montpellier, France, [5] Department of Palaeontology, University of Vienna, Vienna, Austria

The diversity of skeletal tissues in extant vertebrates includes mineralized and unmineralized structures made of bone, cartilage, or tissues of intermediate nature. This variability, together with the diverse nature of skeletal tissues in fossil species question the origin of skeletonization in early vertebrates. In particular, the study of skeletal tissues in cartilaginous fishes is currently mostly restrained to tessellated cartilage, a derived form of mineralized cartilage that evolved at the origin of this group. In this work, we describe the architectural and histological diversity of neural arch mineralization in cartilaginous fishes. The observed variations in the architecture include tessellated cartilage, with or without more massive sites of mineralization, and continuously mineralized neural arches devoid of tesserae. The histology of these various architectures always includes globular mineralization that takes place in the cartilaginous matrix. In many instances, the mineralized structures also include a fibrous component that seems to emerge from the perichondrium and they may display intermediate features, ranging from partly cartilaginous to mostly fibrous matrix, similar to fibrocartilage. Among these perichondrial mineralized tissues is also found, in few species, a lamellar arrangement of the mineralized extracellular matrix. The evolution of the mineralized tissues in cartilaginous fishes is discussed in light of current knowledge of their phylogenetic relationships.

Keywords: cartilaginous fishes (chondrichthyes), gnathostomes, lamellar mineralization, neural arches, perichondrium, tesserae

OPEN ACCESS

Edited by:
Alessandro Minelli, University of Padua, Italy

Reviewed by:
Zerina Johanson, Natural History Museum, United Kingdom
Ann Huysseune, Ghent University, Belgium

***Correspondence:**
Fidji Berio
fidji.berio@umontpellier.fr
Mélanie Debiais-Thibaud
melanie.debiais-thibaud@umontpellier.fr

Specialty section:
This article was submitted to Evolutionary Developmental Biology, a section of the journal Frontiers in Ecology and Evolution

Received: *29 January 2021*
Accepted: *23 March 2021*
Published: *22 April 2021*

Citation:
Berio F, Broyon M, Enault S, Pirot N, López-Romero FA and Debiais-Thibaud M (2021) Diversity and Evolution of Mineralized Skeletal Tissues in Chondrichthyans. Front. Ecol. Evol. 9:660767. doi: 10.3389/fevo.2021.660767

1. INTRODUCTION

The classical view in vertebrate skeletal biology is mainly driven by the extensive work made in tetrapod species, in which clear distinctions are made between several cartilaginous and bony tissues (Hall, 2015). According to this classical view, cartilaginous tissues are retained in only a few sites in the adult skeleton and are classified into hyaline, elastic, and fibro-cartilages that display various assemblages of collagen fibers (Wachsmuth et al., 2006). Hyaline cartilage appears as a transparent tissue whose extracellular matrix does not display histologically observable fibers. The extracellular matrix of hyaline cartilage is characterized by type II collagen running through high contents of proteoglycans with acidic glycosaminoglycans that sequestrate water (Hall, 2015). Bone is defined by the deposition of type I collagen-rich extracellular matrix with little to no acidic glycosaminoglycans deposited, which undergoes mineralization through the activity of osteocytes (Hall, 2015).

Molecular and paleontological evidence has allowed the elaboration of a timeframe for the emergence of the various vertebrate skeletal tissues. Hyaline cartilage is ancestral to vertebrates (Zhang and Cohn, 2006) and most probably evolved earlier than vertebrates (Tarazona et al., 2016), while dermal and perichondrial bone, but also globular mineralized cartilage, is found in early agnathan vertebrates (Donoghue and Sansom, 2002). Among jawed vertebrates, the skeleton of extant cartilaginous fishes (chondrichthyans) is considered to be made exclusively of cartilage, with different types of mineralization that were described in early classical works (Hasse, 1879; Ridewood and MacBride, 1921; Ørvig, 1951; Applegate, 1967). Cartilage mineralization in chondrichthyans mainly occurs under the form of tesserae that are small articulated units of cartilage impregnated with apatite and are a shared derived character of this group (reviewed in Maisey et al., 2020). Paleontological evidence, therefore, implies that cartilaginous fishes have lost dermal and perichondrial bone more than 400 million years ago (Donoghue and Sansom, 2002). Several genetic data were interpreted in light of this evolutionary framework for skeletal tissues, however, our knowledge of chondrichthyan genomes remains scarce (Ryll et al., 2014; Enault et al., 2015; Debiais-Thibaud et al., 2019; Leurs et al., 2021).

More recent studies have reassessed the diversity of poorly described features of mineralization in cartilaginous fishes (Eames et al., 2007; Enault et al., 2015; Seidel et al., 2017, 2020; Atake et al., 2019; Debiais-Thibaud, 2019; Smith et al., 2019; Chaumel et al., 2020; Pears et al., 2020), raising new questions on the origin and evolution of mineralized tissues in this clade and therefore in vertebrates. Comparative studies of skeletal tissues in non-tetrapods have uncovered a wide range of skeletal tissues that had remained unknown from the sole study of tetrapods (discussed by Witten and Huysseune, 2009 and Hall and Witten, 2019). Teleost fishes display for example a wide variety of skeletal tissues with intermediate features (e.g., hyaline, elastic, fibrous, whether mineralized or not) of what is classically associated to either bone or cartilage and for which standard characterization by histology has been proposed (Witten et al., 2010; Hall and Witten, 2019). A wider description of the diversity of skeletal tissues in non-tetrapod species is therefore still needed to understand the origin and the diversification of mineralized tissues in vertebrates. In this study, we chose to focus on the comparative analysis of mineralized cartilage in the neural arches of chondrichthyans.

Extant chondrichthyans include three major clades. Holocephalans are divided into the three extant families Callorhinchidae, Chimaeridae, and Rhinochimaeridae and have long been considered to have a non-mineralized cartilaginous endoskeleton but are now recognized to have tesserae (Finarelli and Coates, 2014; Maisey et al., 2020; Pears et al., 2020; Seidel et al., 2020). Sister to holocephalans, elasmobranchs include selachians (sharks) that are grouped into Galeomorphii (orders: Carcharhiniformes, Heterodontiformes, Lamniformes, and Orectolobiformes) and Squalomorphii (orders: Hexanchiformes, Pristiophoriformes, Squaliformes, Squatiniformes, and the family Echinorhinidae) and batoids (rays, guitarfishes, skates, and sawfishes) that are divided into Myliobatiformes, Rhinopristiformes, Rajiformes, and Torpediniformes (Naylor et al., 2012; Ebert et al., 2013; Last et al., 2016). Most cartilaginous endoskeletal elements of selachians and batoids are covered by tesserae (e.g., the jaws, fins, and most vertebral elements) (Dean et al., 2009; Chaumel et al., 2020). The tesseral body (the internal part of a tessera) contains type II collagen, round cells enclosed in lacunae, and Liesegang lines typical of globular mineralization (Kemp and Westrin, 1979; Seidel et al., 2017; Chaumel et al., 2020). The tesseral cap zone (the external part of a tessera) is located on the perichondrial side and is characterized by flatter cells engulfed in a type I collagen matrix (Ørvig, 1951; Kemp and Westrin, 1979; Seidel et al., 2017; Chaumel et al., 2020). This cap zone has been discussed as a remnant, or derived version of an ancestral bony tissue in jawed vertebrates (Kemp and Westrin, 1979; Seidel et al., 2017).

Less studied than tesserae are two other mineralized tissues, also reported in the elasmobranch endoskeleton by Ørvig (1951), and reviewed by Dean and Summers (2006) and Debiais-Thibaud (2019). On the one hand, areolar mineralization characterizes the vertebral centra of elasmobranchs (Ridewood and MacBride, 1921). On the other hand, a type of lamellar mineralization has been identified only in the vertebral neural arches and repeatedly compared to bone tissue (Peignoux-Deville et al., 1982; Eames et al., 2007; Atake et al., 2019). Until now, this lamellar mineralization, or bone-like tissue, was reported in two shark species within Carcharhiniformes [the small-spotted catshark *Scyliorhinus canicula* (Peignoux-Deville et al., 1982) and the swellshark *Cephaloscyllium ventriosum* (Eames et al., 2007)], and in two batoid species belonging to Rajiformes [the Eaton's skate *Bathyraja eatonii* and the little skate *Leucoraja erinacea* (Atake et al., 2019)]. The similarity between lamellar mineralization and bone tissue was raised several times—it was first termed osseous tissue by Peignoux-Deville et al. (1982)—because of the occurrence of elongated cells similar to osteoblasts in bone (Peignoux-Deville et al., 1982) that express type I collagen genes (Enault et al., 2015) and because these cells are enclosed in a type I collagen-rich extracellular matrix, which is able to mineralize (Eames et al., 2007). This type of mineralization differs from the classical globular mineralization described in the cartilage of fossils (Ørvig, 1951) and the body zone of tesserae (Kemp and Westrin, 1979; Seidel et al., 2017).

In this study, we first provide microCT images to visualize the architecture of mineralized tissues in the neural arches in ten orders of elasmobranchs and one holocephalan family. We then use classical histology to illustrate cell shape and extracellular matrix characteristics (e.g., fibrous or hyaline nature, presence of acidic proteoglycans) to describe the mineralized tissues. The results provide insights into the evolutionary history of endoskeletal mineralization among chondrichthyans and question the nature of the mineralized tissues described in early gnathostomes and vertebrates.

2. MATERIALS AND METHODS

2.1. Biological Sampling

The dataset includes 19 specimens from 16 species of chondrichthyans (**Table 1**) and covers six of the eight orders

TABLE 1 | Chondrichthyan samples used for histology and microCT scanning.

Subclass	Superorder	Order	Family	Species	Growth stage	Fixation	Decalcification	Section
Elasmobranchii	Galeomorphii	Heterodontiformes	Heterodontidae	*Heterodontus francisci*	Subadult (Meese and Lowe, 2020)	80% ethanol	Yes	posterior
Elasmobranchii	Galeomorphii	Orectolobiformes	Hemiscyllidae	*Chiloscyllium punctatum*	Juvenile (Compagno, 1984)	4% PFA	No	anterior
Elasmobranchii	Galeomorphii	Lamniformes	Odontaspididae	*Carcharias taurus*	Sexually mature (Lucifora et al., 2002)	4% PFA	Yes	anterior
Elasmobranchii	Galeomorphii	Carcharhiniformes	Triakidae	*Galeorhinus galeus*	Juvenile (Lucifora et al., 2004)	80% ethanol	Yes	anterior
Elasmobranchii	Galeomorphii	Carcharhiniformes	Carcharhinidae	*Prionace glauca*	Juvenile (Bustamante and Bennett, 2013)	100% ethanol	Yes	posterior
Elasmobranchii	Galeomorphii	Carcharhiniformes	Scyliorhinidae	*Scyliorhinus canicula*	Embryo (Enault et al., 2016)	4% PFA	No	anterior
Elasmobranchii	Galeomorphii	Carcharhiniformes	Scyliorhinidae	*Scyliorhinus canicula*	Juvenile (Capapé et al., 2008)	4% PFA	No	anterior
Elasmobranchii	Galeomorphii	Carcharhiniformes	Sphyrnidae	*Sphyrna lewini*	Juvenile (Bejarano-Álvarez et al., 2011)	80% ethanol	Yes	posterior
Elasmobranchii	Squalomorphii	Squaliformes	Somniosidae	*Centroscymnus crepidater**	Juvenile (Moore et al., 2013)	70% ethanol	No	posterior
Elasmobranchii	Squalomorphii	Squaliformes	Etmopteridae	*Etmopterus spinax**	Juvenile (Porcu et al., 2014)	70% ethanol	No	posterior
Elasmobranchii	Squalomorphii	Squatiniformes	Squatinidae	*Squatina californica*	Sexually mature (Romero-Caicedo et al., 2016)	80% ethanol	Yes	posterior
Elasmobranchii	Batoidea	Myliobatiformes	Gymnuridae	*Gymnura micrura**	Sexually mature (Yokota et al., 2012)	70% ethanol	Yes	posterior
Elasmobranchii	Batoidea	Rhinopristiformes	Rhinobatidae	*Pseudobatos productus*	Sexually mature (Márquez-Farías, 2007)	80% ethanol	Yes	posterior
Elasmobranchii	Batoidea	Rhinopristiformes	Rhinidae	*Rhina ancylostoma*	147 cm TL	4% PFA	Yes	posterior
Elasmobranchii	Batoidea	Torpediniformes	Torpedinidae	*Torpedo* sp.*	16 cm DW	70% ethanol	Yes	posterior
Elasmobranchii	Batoidea	Rajiformes	Rajidae	*Raja clavata*	Hatchling	4% PFA	No	ant, posterior
Elasmobranchii	Batoidea	Rajiformes	Rajidae	*Raja clavata*	Juvenile (Capapé et al., 2007)	70% ethanol	No	posterior
Holocephali	–	Chimaeriformes	Chimaeridae	*Hydrolagus colliei*	Hatchling	100% ethanol	No	anterior (sy)
Holocephali	–	Chimaeriformes	Chimaeridae	*Hydrolagus colliei**	Juvenile (Barnett et al., 2009)	70% ethanol	No	anterior (sy)

DW, disc width; PFA, paraformaldehyde; sy, synarcual; TL, total length. When no literature data are available on the size at sexual maturity for a species, the TL or DW are indicated. Asterisks indicate the specimens that have been preserved in ethanol for several decades.

of extant sharks, the four orders of extant batoids, and one of the three families of extant Chimaeriformes (Naylor et al., 2012; Ebert et al., 2013; Last et al., 2016). The samples were kindly provided by the University of Montpellier, by the Aquarium of Montpellier (Planet Ocean Montpellier), or were bought at fish markets. No handling of live specimens was necessary for this study. The ontogenetic stages were determined based on literature data, using the total length (TL) or disc width (DW) as proxies (**Table 1**). When no data were available about the ontogenetic stages of the species sampled, the TL, DW, or both were provided (**Table 1**). When fresh or frozen material was available, the vertebra or neural arch were sampled and fixed in 4% paraformaldehyde in Phosphate-Buffered Saline 1X (PBS 1X). Anterior and posterior vertebrae were sampled anterior and posterior to the pelvic girdle, respectively. Samples made from long-term stored material were first rinsed in fresh ethanol for 48 h before further processing (note that some specimens come from collections in ethanol that date back from the 90's, see details in **Table 1**).

2.2. Histological Staining

Alizarin Red S staining on thick (circa 1 mm) slices was performed overnight in a potassium hydroxide (KOH) 0.5% solution with a concentration of Alizarin Red S of 0.005% for samples of *S. canicula* and the thornback ray *Raja clavata*, or 0.05% for samples of the spotted ratfish *Hydrolagus colliei*. Stained samples were progressively equilibrated in 25% glycerol in KOH 0.5%, 50% glycerol in KOH 0.5%, 75% glycerol in KOH 0.5%, and glycerol 100% before being imaged under a binocular (Leica Microsystems). Only samples fixed in paraformaldehyde were used for this staining procedure.

A double Alizarin Red S and Alcian Blue staining was performed on a 14 μm-thick cryostat section made in a non-demineralized portion of the anterior vertebral column of an embryonic lesser spotted catshark fixed in 4% PFA. The section was rinsed in PBS 1X, then in KOH 0.5% before a bath of Alizarin Red S 0.005% in KOH 0.5% for 1 min. The slide was rinsed once in PBS 1X, incubated for 2 min in a 0.02% Alcian blue 8G solution (8:2 ethanol/glacial acetic acid), washed once in EtOH 100%, and once in PBS 1X before being mounted in Mowiol.

For other histological staining protocols, samples exhibiting strong vertebral mineralization were first rehydrated and then demineralized with Thermo Scientific Shandon TBD-2 decalcifier during 24–48 h before the embedding process (**Table 1**). Samples were progressively dehydrated in 70, 96, and 100% ethanol before paraffin embedding. Paraffin-embedded tissue was cut into 7 μm-thick sections, mounted on slides in an alternate consecutive fashion, and dried at 37 °C overnight. Tissue sections were stained with Hematoxylin, Eosin, and Saffron with HMS 740 autostainer (MM France) for preliminary analysis. The Hematoxylin-Eosin-Saffron (HES) protocol stains basophilic components in deep violet [nuclei and basophilic extracellular matrices (H)], cytoplasm in pink (E), and collagen fibers in bright orange (S), allowing a fine description of cell and matrix morphologies. HES has poor staining contrast on hyaline cartilage (gray or beige uniform staining) but allows contrasting the cartilaginous matrix with perichondrial tissue because of the eosinophilic and Saffron-positive staining of the fibrous matrix (Hilton et al., 2005). The modified cartilaginous extracellular matrix in cartilage mineralizing zones is also contrasted in HES (Mayoral et al., 2014), possibly because it is basophilic. Tissue sections were also stained with PAS-AB, which associates the standard Alcian blue method (AB, pH 2.5, standard staining for acid mucins in hyaline cartilage matrix, blue staining) with the Periodic Acid Schiff (PAS) technique to distinguish with neutral mucins (magenta staining). PAS-AB staining is a standard for the detection of hyaline cartilage matrix, as the staining is associated with the acidic glycosaminoglycan content of the matrix (Whiteman, 1973). Previous work has shown that Alcian blue stains best in the proliferative and resting chondrocyte zone of endochondral bone, while the PAS magenta stains both the fibrous perichondrium and the hypertrophic chondrocyte zones (Xiong et al., 2005). Some variation in the intensity and color of HES and PAS-AB assays between samples are observed, which most probably results from variations in the fixation, decalcification, and storage solutions, but also from an important variation in the storage time of our samples. Despite these variations, cell shape was still well-preserved and there was good correspondence between the locations of mineralization (as defined by microCT images) and the places of modified staining with HES in the cartilaginous and fibrous extracellular matrices. Mounted histological slides were scanned with a Hamamatsu NanoZoomer 2.0-HT scanner in the local MRI platform and images were visualized with the NDP.view software (v1.2.47).

2.3. Micro-Computed Tomography

Micro-computed tomography (microCT) was performed on selected vertebral samples preserved in alcohol with EasyTom 150 and reconstructed with the Xact software (v11025). The images were subsequently analyzed with the Avizo Lite software (v2019.3).

2.4. Ancestral Character State Reconstruction

For each character identified in our results, we built a character matrix and used phylogenetic relationships from Licht et al. (2012), Naylor et al. (2012), and Last et al. (2016). We reconstructed the ancestral state for each character (globular mineralization, fibrous mineralization, and lamellar mineralization: presence/absence; mineralization architecture: continuous/semi-discontinuous/discontinuous (tessellated or reduced) with Mesquite (v3.61) (Maddison and Maddison, 2019).

3. RESULTS

3.1. Anatomical and Histological Features of Neural Arches in Three Reference Species

We first selected reference species among the three main chondrichthyan clades: *S. canicula* (Carcharhiniformes, Galeomorphii) (**Figures 1**, **2**), *R. clavata* (Rajiformes, Batoidea) (**Figure 3**), and *H. colliei* (Chimaeriformes, Holocephali)

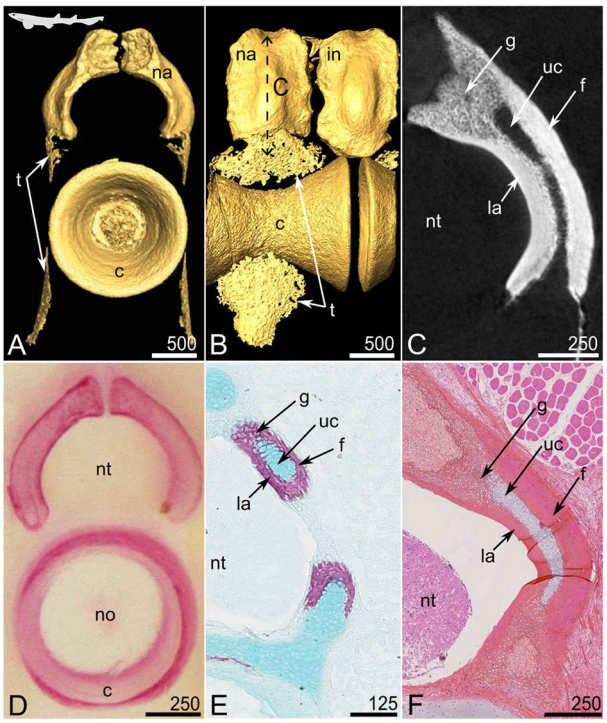

FIGURE 1 | Mineralized tissues in the anterior vertebrae of the small-spotted catshark *Scyliorhinus canicula* at juvenile stages [20 cm TL in **(A–C)** and 31 cm TL in **(F)**] and embryonic stages [8.4 cm TL in **(D)** and 8.0 cm TL in **(E)**]. **(A–C)** Micro-computed tomography imaging, frontal view **(A)** and lateral view **(B)** of 3D isosurfaces and virtual section (**C**, as located by the double sided dashed arrow on **B**). **(D)** Alizarin Red S staining of a thick section. **(E)** Alizarin Red S and Alcian Blue double staining on a cryostat section. **(F)** HES, histological staining; c, centrum; f, fibrous perichondrial mineralization; g, globular mineralized cartilage; in, interneural element; la, lamellar perichondrial mineralization; na, neural arch; no, notochord; nt, neural tube; t, tesserae; uc, unmineralized cartilage. Scale bars are in μm.

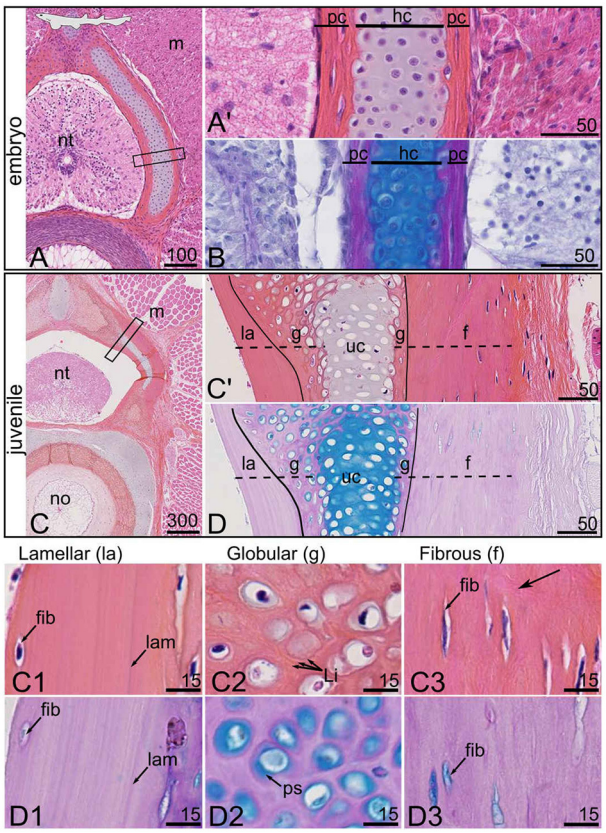

FIGURE 2 | Histological characterization of the mineralized tissues in the anterior vertebrae of the small-spotted catshark *Scyliorhinus canicula* at an embryonic stage [7 cm TL in **(A,B)**] and a juvenile stage [31 cm TL in **(C,D)**]. Serial sections were stained with HES **(A,C)** and PAS-AB **(B,D)**. **(A',C')** Close-ups of the boxed zones in **(A,C)**, respectively. Close-up on the lamellar (la), globular (g), and fibrous (f) mineralized tissues: **(C1–C3,D1–D3)** are details of **(C',D)**, respectively. f, fibrous perichondrial mineralization; fib, fibrocyte-shaped cell; g, globular mineralized cartilage; hc, hyaline cartilage; la, lamellar perichondrial mineralization; lam, lamella; Li, Liesegang lines; m, muscle tissue; no, notochord; nt, neural tube; pc, perichondrium; ps, pericellular space; uc, unmineralized cartilage. Vertical lines in **(C',D)** delimit the fibrous and hyaline cartilaginous matrices. Dashed lines in **(C',D)** locate the zones of mineralized matrix. Black arrow points to fibrous extracellular matrix. Scale bars are in μm.

(**Figure 4**). The description of the vertebrae of these species is provided first because of their representativeness in the chondrichthyan phylogeny, also because literature data shows a strong variation in the type of mineralized tissues in their neural arches (Debiais-Thibaud, 2019), and because we had specimens of successive ontogenetic stages allowing developmental comparisons.

3.1.1. Neural Arch Mineralization in *Scyliorhinus canicula*

Each anterior (thoracic) vertebra of *S. canicula* includes a mineralized, hourglass-shaped, centrum (**Figures 1A,B**). Each centrum is dorsally overlaid by a mineralized neural arch that alternates with interneural elements, both (neural and interneural elements) appearing similar in shape but interneurals are located dorsal to the junction between two centra (**Figures 1A,B**). The vertebral body surface also shows thin zones of mineralization (lace-like mineralization, **Figures 1A,B**) that are small tesserae (see details below and in **Figure 5**). The neural arches and interneural elements externally appear as continuously mineralized structures (**Figures 1A,B**) but the virtual (microCT) and histological sections reveal that the mineralized layer encloses an inner core of unmineralized tissue (**Figures 1C,E,F**) of cartilaginous nature (**Figures 1E,F**). In the following, we used HES and PAS-AB histological staining protocols to characterize cells and their extracellular matrix in each vertebral tissue. We previously successfully used HES staining to characterize cartilaginous matrix mineralization in chondrichthyans (Enault et al., 2015; Debiais-Thibaud, 2019). Mineralized zones (stained with Alizarin Red S in **Figure 1D**) appear dark pink in comparison to the unmineralized matrix (**Figure 1F**, compare g with uc zones), probably because of an eosinophilic nature. The comparison between the virtual and

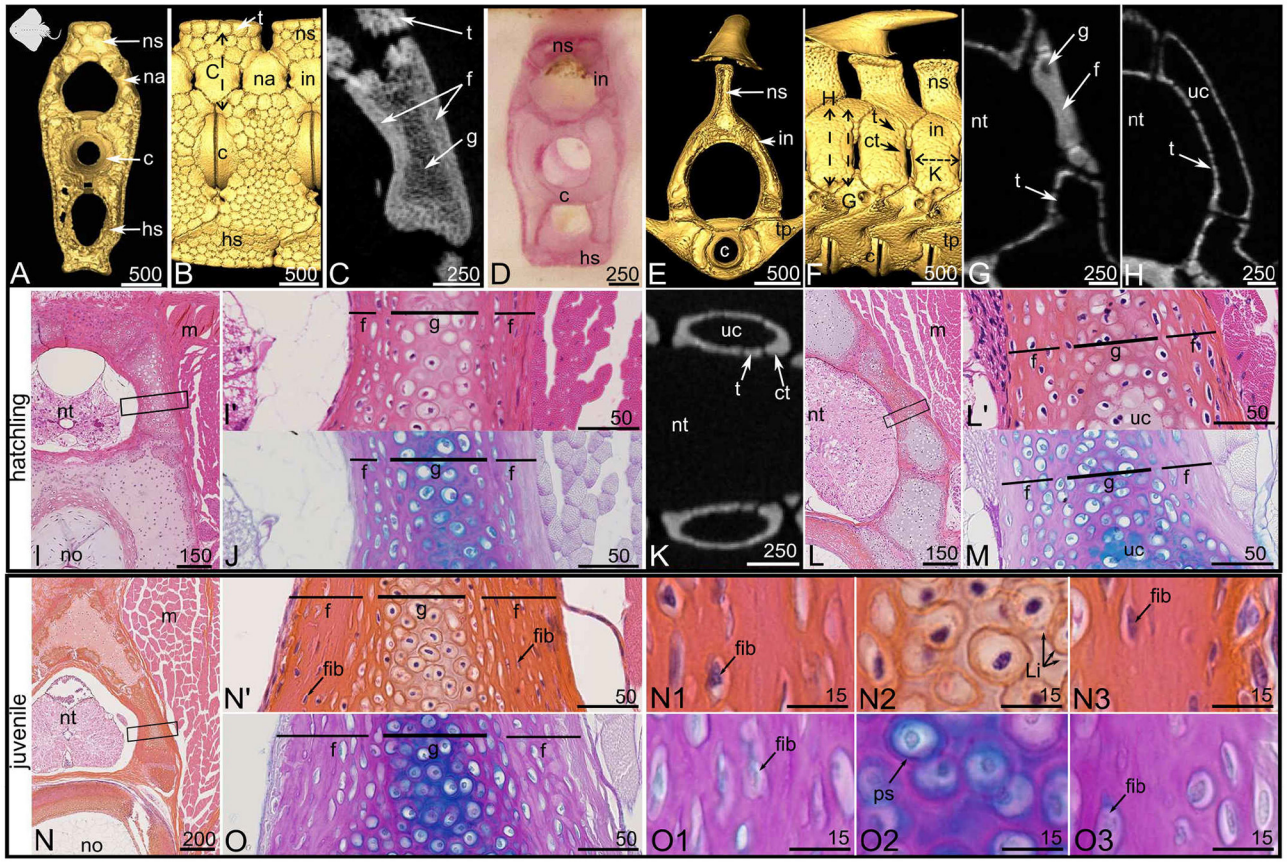

FIGURE 3 | Mineralized tissues in the vertebrae of the thornback ray *Raja clavata* at hatching [8.0 cm DW **(A–M)**] and juvenile stage [13.0 cm DW **(N,O)**]. **(A–D,I,J,N,O)** Posterior vertebrae, **(E–H,K–M)** anterior vertebrae. **(A–C,E–H,K)** Micro-computed tomography imaging, frontal views **(A,E)** and lateral views **(B,F)** of 3D isosurfaces and closer views on virtual sections (**C**: as located by the double sided dashed arrow on **B**; **G,H,K**: as located by the double sided dashed arrows on **F**). **(D)** Alizarin Red S staining of a thick section. **(I,J,L–O)** Histological staining on serial sections with HES **(I,L,N)** and PAS-AB **(J,M,O)**. **(I',L',N')** Close-ups of the boxed zones in **(I,L,N)**, respectively. Cellular details from the proximal **(N1,O1)**, central **(N2,O2)**, and distal **(N3,O3)** zones are zooms taken from the sample in **(N',O)**. c, centrum; ct, corner tessera; f, fibrous perichondrial mineralization; fib, fibrocyte-shaped cell; g, globular mineralized cartilage; hs, hemal spine; in, interneural element; Li, Liesegang lines; m, muscle tissue; na, neural arch; no, notochord; ns, neural spine; nt, neural tube; ps, pericellular space; t, tesserae; tp, transverse process; uc, unmineralized cartilage. Scale bars are in μm.

histological sections (**Figures 1C,F**) allows identifying several types of mineralized tissue. First, there is a zone displaying cell spherical lacunae, where mineralization is less dense (lower gray level in **Figure 1C**), and that is located in the dorsal-most zone of the cartilaginous core (g in **Figure 1**). Denser mineralized zones (deeper white in **Figure 1C**) cover the inner unmineralized cartilage rod (uc in **Figure 1**). These perichondrial zones are further differentiated in the proximal perichondrium (facing the neural tube, la in **Figure 1**) and the distal perichondrium (facing the thoracic muscles, f in **Figure 1**) through the HES and PAS-AB staining protocols.

In the embryonic developing neural arches (**Figures 2A,B**), at a stage when mineralization initiates (Enault et al., 2016), the fibrous perichondrial tissue is characterized by flat cells enclosed in a fibrous extracellular matrix (pc in **Figure 2A'**), while the internal cartilaginous tissue stains positive for Alcian blue (hc in **Figure 2B**).

In the juvenile specimen in which structures are fully mineralized, the neural arch is organized as a central, unmineralized cartilaginous rod (uc in **Figures 2C',D**). This internal cartilaginous rod is no more than 100 μm wide in the juvenile specimen, which is similar to what is observed in the hatchling specimen, suggesting that this internal tissue does not significantly grow between these ontogenetic stages (**Figures 2A,C**). In continuity with this cartilaginous unmineralized rod, the most dorsal and ventral aspects appear mineralized (**Figures 1C,E,F**, **2C',D**) together with the contact surface with the perichondrium (g in **Figures 2C',D**). The perichondrium is characterized by low to absent Alcian blue staining in the PAS-AB assay (**Figure 2D**) and by elongated cells engulfed in a Saffron stained extracellular matrix in the HES assay (**Figure 2C'**). Several differences in cell density and matrix organization can be detected when comparing the distal mineralized perichondrium (toward the trunk muscles) with the

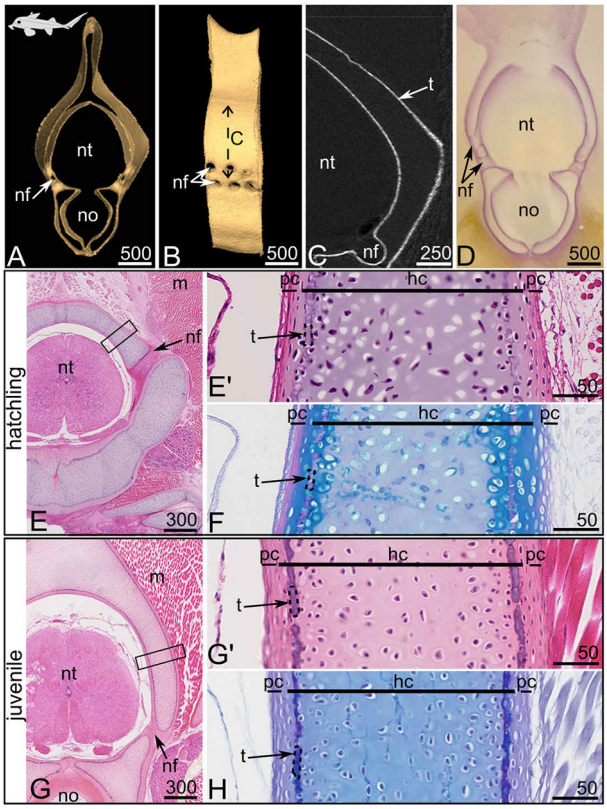

FIGURE 4 | Anterior synarcual mineralization in the spotted ratfish *Hydrolagus colliei* at hatchling [9.5 cm TL, **(A–F)**] and juvenile [14.0 cm TL **(G,H)**] stages. **(A–C)** Micro-computed tomography imaging, frontal view **(A)** and lateral view **(B)** of 3D isosurfaces and virtual section on a closer view (**C**, as located by the double sided dashed arrow on **B**). **(D)** Alizarin Red S staining of a thick section. **(E–H)** Histological staining on serial sections with HES **(E,E',G,G')** and PAS-AB **(F,H)**. **(E',G')** are close-ups of the boxed zones in **(E,G)**, respectively. hc, hyaline cartilage; m, muscle tissue; nf, nerve foramina; no, notochord; nt, neural tube; pc, perichondrium; t, tesserae (dashed contours delineate single tessera). Scale bars are in μm.

proximal mineralized perichondrium (facing the neural tube) (compare **Figures 2C1,C3,D1,D3**).

As a result, three mineralized histotypes can be described in the neural arch of *S. canicula*. The first one is superficial lamellar mineralization that arises from the perichondrium located in the proximal side of the neural arch. The mineralized matrix displays a lamellar organization, cell density appears very low, and the few cells found in the mineralized matrix are elongated (**Figures 2C1,D1**). The second type is globular mineralization, which occurs in the matrix surrounding chondrocytes in the dorsal part of the neural arch and the contact zone with perichondrial mineralized tissues. HES staining in the mineralized matrix shows concentric rings around the chondrocyte lacunae that we interpret as the marks of previously described Liesegang lines (**Figure 2C2**), typical of globular mineralization in hyaline cartilage (Ørvig, 1951; Peignoux-Deville et al., 1982; Seidel et al., 2016). The pericellular space is positive for Alcian blue (ps in **Figure 2D2**). The third type is a fibrous mineralized tissue in the perichondrium that is located in the distal side of the neural arch. The cells also appear elongated as expected with fibrocytes and their matrix is characterized by loosely arranged fibers that stain with Saffron (arrows in **Figure 2C3**). The thin pericellular space is positive for Alcian blue (**Figure 2D3**).

3.1.2. Neural Arch Mineralization in *Raja clavata*

The posterior vertebrae of *R. clavata* are composed of a centrum associated with one neural arch located dorsally, at the junction between two neural spine-interdorsal complexes (**Figures 3A,B**). The neural arches and interneural elements are not covered by tesserae, as opposed to the neural spines (**Figure 3B**). The virtual section shows that the whole depth of the posterior neural arches is mineralized (**Figure 3C**). In both hatchling and juvenile specimens, this architecture is similar in the posterior vertebral column (not shown). HES histological staining highlights the presence of subspherical cells in the center of these neural arches (**Figures 3I',J,N',O,N2,O2**). Their extracellular matrix displays Liesegang lines with HES and an Alcian blue positive pericellullar space with PAS-AB, making this zone similar to the globular mineralization observed in *S. canicula* (**Figures 3N2,O2**). This internal mineralized cartilaginous rod does not seem to differ in size between the hatchling and juvenile specimens, suggesting little growth of this internal zone between the corresponding ontogenetic stages (**Figure 3**, compare the g zone in I' with N').

Surrounding this mineralized cartilage core is a tissue with fibrocyte-shaped cells, engulfed in a fibrous matrix devoid of Alcian blue staining except for a thin pericellular matrix (**Figures 3I',J,N',O,N1,N3,O1,O3**). This mineralized fibrous tissue lines both the proximal and distal sides of the neural arch and is thicker in the juvenile than in the hatchling specimen (compare **Figures 3I',N'**). We assume this tissue to have a perichondrial nature, and it appears similar to the fibrous mineralization in the distal perichondrium of the *S. canicula* neural arches. Similar to the observations in *S. canicula*, perichondrial mineralization appears denser than globular cartilage mineralization (**Figure 3C**). In contrast to *S. canicula*, no lamellar organization of the extracellular matrix was observed in either the proximal or distal perichondrium of *R. clavata* (**Figures 3N1,N3,O1,O3**). In *S. canicula*, the architecture of neural arch mineralization is the same along the anterior-posterior axis of the vertebral column (no difference is observed between the anterior and posterior vertebrae) although the timing of centrum mineralization differs between these regions (Enault et al., 2016). In *R. clavata*, the mineralization architecture in the neural arches differs between anterior and posterior vertebrae (**Figures 3B,F**). In anterior vertebrae, we identified only interneural elements, located dorsal to the junctions between two centra and that were partly covered with tesserae (**Figures 3F,H**), while more massive mineralized units cover the anterior and posterior faces of the interneural elements (**Figures 3F,K**). A longitudinal frontal section in an interneural element shows that these massive units have a U-shape delineating the anterior and posterior faces of each interneural element (**Figure 3K**). As such, we considered them to be "corner tesserae" as previously proposed in the jaw of

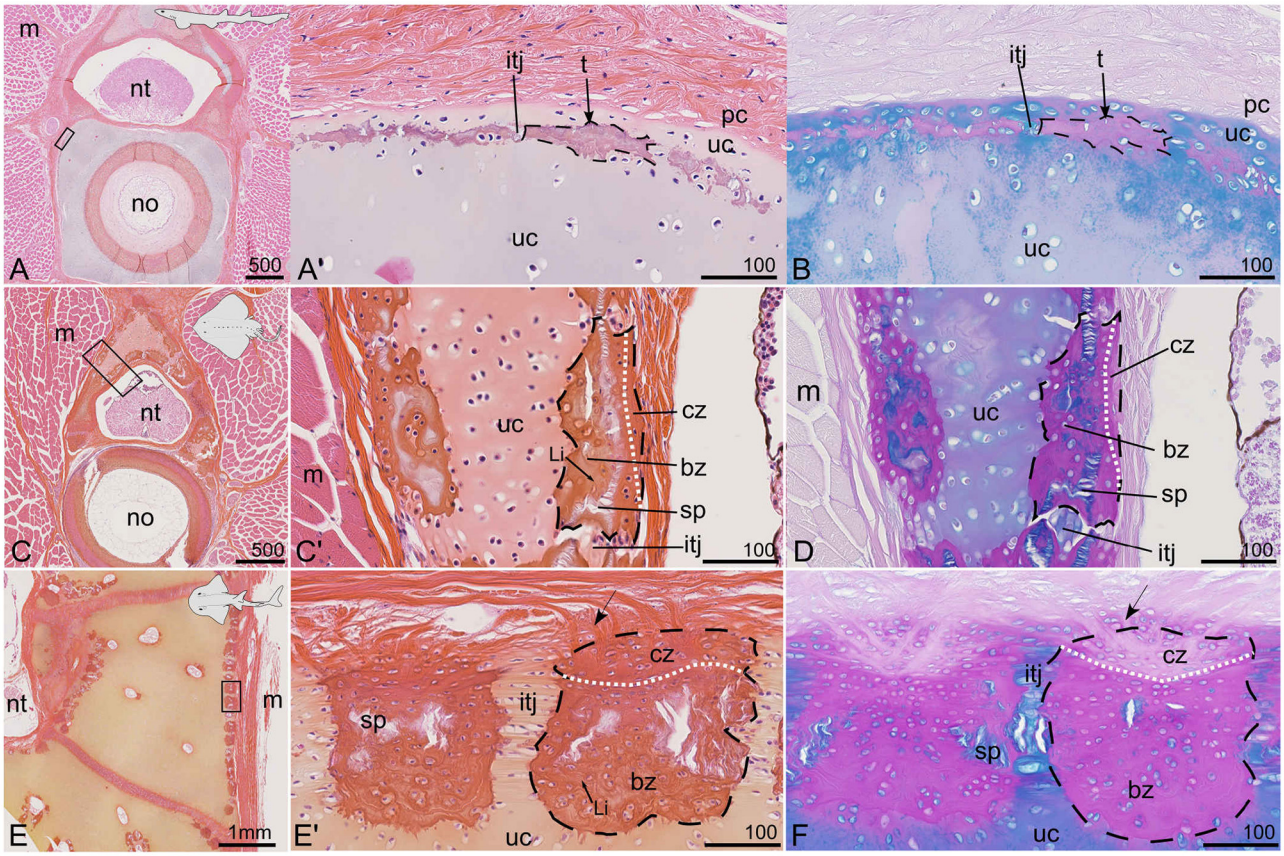

FIGURE 5 | Vertebral tissues with various tesseral mineralization patterns in selected species stained with HES **(A,C,E)** and PAS-AB **(B,D,F)**. **(A,B)** Subperichondrial tesserae in the cartilaginous vertebral body of a juvenile (20 cm TL) small-spotted catshark *S. canicula*; anterior vertebra. **(C,D)** Tesserae in the neural spine of a juvenile (13 cm DW) thornback ray *R. clavata*; posterior vertebra. **(E,F)** Tesserae in the neural arch of a (147 cm TL) bowmouth guitarfish *Rhina ancylostoma*; posterior vertebra. bz, body zone of a tessera; cz, cap zone of a tessera; itj, intertesseral joint; Li, Liesegang lines; m, muscle tissue; no, notochord; nt, neural tube; pc, perichondrium; t, tesserae (dashed contours delineate single tessera); sp, spoke; uc, unmineralized cartilage. The white dotted line separates bz and cz. Arrows point to Sharpey's fibers. **(A',B,C',D,E',F)** are close-ups of the zones located by the rectangles in **(A,C,E)**, respectively. Scale bars are in μm except in **(E)**.

the Haller's round ray *Urobatis halleri* (Dean et al., 2009), although their size relative to the closest tesserae is higher than that of previously observed "corner tesserae" (**Figure 3F**). Histological staining showed the occurrence of mineralized globular cartilage in the center of these elements and layers of fibrous perichondrial mineralization on their proximal and distal surface (**Figures 3L,M**).

As a consequence, the interneural elements and neural arches of *S. canicula* and *R. clavata* in the caudal zone of the vertebral column display continuous mineralization, while the anterior vertebrae of *R. clavata* (immediately posterior to the synarcual) display a combination of tesserae and massive "corner tesserae". All these mineralized structures are characterized by a mineralized perichondrial tissue that covers a partly (*S. canicula*) or more extensively (*R. clavata*) mineralized cartilaginous rod. Perichondrial mineralization occurs as lamellar mineralization only in the proximal zone of the neural arches of *S. canicula* and as fibrous mineralization in all other occurrences.

3.1.3. Synarcual Mineralization in *Hydrolagus colliei*

The synarcual of *H. colliei* is a post-cranial element pierced by dorsal and ventral nerve foramina (**Figures 4A,B**) that develops from the fusion of successive embryonic vertebrae and that does not display discrete neural arch or interneural elements (Johanson et al., 2015). The equivalent zone of elasmobranch neural arches in the synarcual is considered to be the zone dorsal to a ventral foramen (Goodrich, 1930; Eames et al., 2007; Criswell et al., 2017). We hypothesized a similar situation for chimaeras, and focused on the portion of the synarcual located dorsally to a ventral foramen, although our observations were similar in all other parts of the synarcual (including in the vertebral body, see **Figures 4A,D,E,G**). Previous studies showed poorly developed cartilaginous tissue in the posterior vertebrae of juvenile *H. colliei*, where histology displayed no sign of modified cartilaginous matrix that could be linked to cartilage mineralization (Debiais-Thibaud, 2019). However, more recent publications pointed out the thin layer of mineralized matrix in the synarcual of the elephant shark *Callorhinchus milii* (Pears

et al., 2020) and recognized thin tesserae in the adult *C. milii* and rabbit fishes *Chimaera monstrosa* (Pears et al., 2020; Seidel et al., 2020). In our *H. colliei* sample, we detect a similar thin layer of mineralized tissue in the synarcual of a hatchling and a juvenile specimen (**Figures 4A,G**). This pattern is found as a peripheral delineation of the ventral part (corresponding to the vertebral body) and the dorsal part (corresponding to the neural arches) of the synarcual, but also in the inner contact with the notochord (**Figures 4A,D,G**). Most tesserae are not more than 10 μm wide in their chondral-perichondrial axis (**Figures 4E',F,G',H**). The line of modified cartilaginous matrix can be observed at the hatching stage and is more obvious in the juvenile specimen (**Figures 4E–H**). The matrix stains deep purple with HES (**Figures 4E',G'**) and does not stain with Alcian blue (**Figures 4F,H**), suggesting a difference in the glycosaminoglycan content at this mineralization location. This site of mineralization is located in the subperichondrial zone of the cartilaginous unit. The cells located on the perichondrial side of this line are enclosed in lacunae in a matrix of cartilaginous nature [as supported by positive Alcian blue staining (**Figures 4F,H**)], although the cells are flattened (**Figures 4E',G'**). Moreover, no cells can be observed fully embedded in the mineralized cartilaginous matrix, either at the hatching or juvenile stage and the mineralized layer appears discontinuous (**Figures 4G',H**), supporting the presence of aligned tesserae as described in other holocephalan species (Pears et al., 2020).

3.1.4. Diverse Combinations of Histotypes in Chondrichthyan Tesserae

To better compare our observations with literature data on tesserae, these mineralized structures were also illustrated in selected species (**Figure 5**). As previously noted, focal cartilage mineralization is detected with microCT outside the neural arches and surrounding the vertebral body of *S. canicula* (**Figures 1A,B**). Such sites also appear on histology sections, they are stained dark pink with HES and purple with PAS-AB and occur in a subperichondrial location within the cartilaginous matrix (**Figures 5A,B**). Although poorly developed, these sites can be interpreted as thin tesserae engulfing chondrocytes and display intertesseral joint regions (**Figures 5A',B**), as previously described (Seidel et al., 2016). The tesserae are separated from the perichondrium by a subperichondrial and unmineralized cartilaginous layer (**Figures 5A',B**). They are comparable to the discontinuous pattern of mineralization described in *H. colliei* (**Figures 4G',H**) but are thicker (up to 50 μm) and engulf chondrocytes in the mineralized matrix (**Figure 5A'**) in *S. canicula*.

The neural spines of *R. clavata*, as well as the neural arches of the bowmouth guitarfish *Rhina ancylostoma* are covered by tesserae (**Figures 3B**, **5C–F**). The tesserae are separated by unmineralized intertesseral joints (itj in **Figures 5C',D,E',F**) and display internal spokes (sp in **Figures 5C',D,E',F**) as defined by Seidel et al. (2016). Two zones can further be distinguished in the tesserae that correspond to the previously defined body and cap zones of a tessera (Kemp and Westrin, 1979; Seidel et al., 2016, 2017). In both species, the cap zone is characterized by flat cells, a higher content in collagen fibers, and a matrix poorly stained by Alcian blue except in the pericellular layer (**Figures 5D,F**). The cells in the body zone are subspherical and surrounded by an extracellular matrix displaying Liesegang lines with HES staining (**Figures 5C',E'**). In both batoids (*R. clavata* and *R. ancylostoma*), the maximum width of a tessera (tangential axis) is about 200 μm and does not seem to depend on the specimen body size as *R. clavata* is a young juvenile of 13 cm DW and 21 cm TL, while *R. ancylostoma* is 147 cm long. However, the depth of the tesserae (along the chondral-perichondrial axis) is less than 100 μm in *R. clavata*, while it is more than 200 μm in *R. ancylostoma* (compare **Figures 5D,F**). There are no obvious Sharpey's fibers radiating from the tesserae of *R. clavata*, whereas they are well-defined in the tesserae of *R. ancylostoma* (**Figures 5C',D,E'F**). Sharpey's fibers are thick collagenous fibers previously described in tesserae (Kemp and Westrin, 1979; Seidel et al., 2017).

3.2. Neural Arch Mineralization and Elasmobranch Diversity

In the following, we describe the variation of neural arch mineralized histotypes and architectures in several species covering a broad part of the elasmobranch taxonomic diversity.

3.2.1. Batoids

Most of the neural arch of the smooth butterfly ray *Gymnura micrura* and *Torpedo* sp. is covered by tesserae that are 250 μm wide in their tangential axis (**Figures 6A,B,E,F**). Two larger mineralized elements are found on the anteriormost and posteriormost surfaces of each neural arch, similar to the corner tesserae described in *R. clavata*. These elements are more than 500 μm in their longer dimension (**Figures 6A,E**). The virtual sections made through the center of the neural arches show regular-sized tesserae on the neural arch surface (**Figures 6B,F**). The histological sections made through the corner tesserae (**Figures 6C,G**) show a central zone of globular mineralized cartilage covered by fibrous mineralization (**Figures 6C',D,G',H**).

The neural arches of the shovelnose guitarfish *Pseudobatos productus* are covered by classically organized tesserae with no massive corner tesserae (**Figure 6I**). The tesserae of the neural arch reach 400 μm long (in their tangential axis) and 100 μm wide (along the chondral-perichondrial axis, **Figure 6J**) and display intertesseral joints (**Figures 6K',L**). The cap zone of a tessera contains elongated cells in a fibrous (Saffron-positive) matrix with little acidic glycosaminoglycan content (**Figures 6K',L**), while cells in the body zone are similar in shape to chondrocytes in the unmineralized matrix (**Figures 6K',L**). The neural arch of *R. ancylostoma* also is covered by standard tesserae only (**Figures 6E,F**) without enlarged elements (data not shown).

3.2.2. Selachians, Squalomorphs, Order: Squaliformes

In both the velvet belly *Etmopterus spinax* and the longnose velvet dogfish *Centroscymnus crepidater*, the neural arches display thin zones of mineralization dorsal to the centra (**Figures 7A,B,E,F**). Virtual sections passing through the neural arches show a thin, discontinuous layer of mineralization (**Figures 7B,F**). The histological staining results show that the

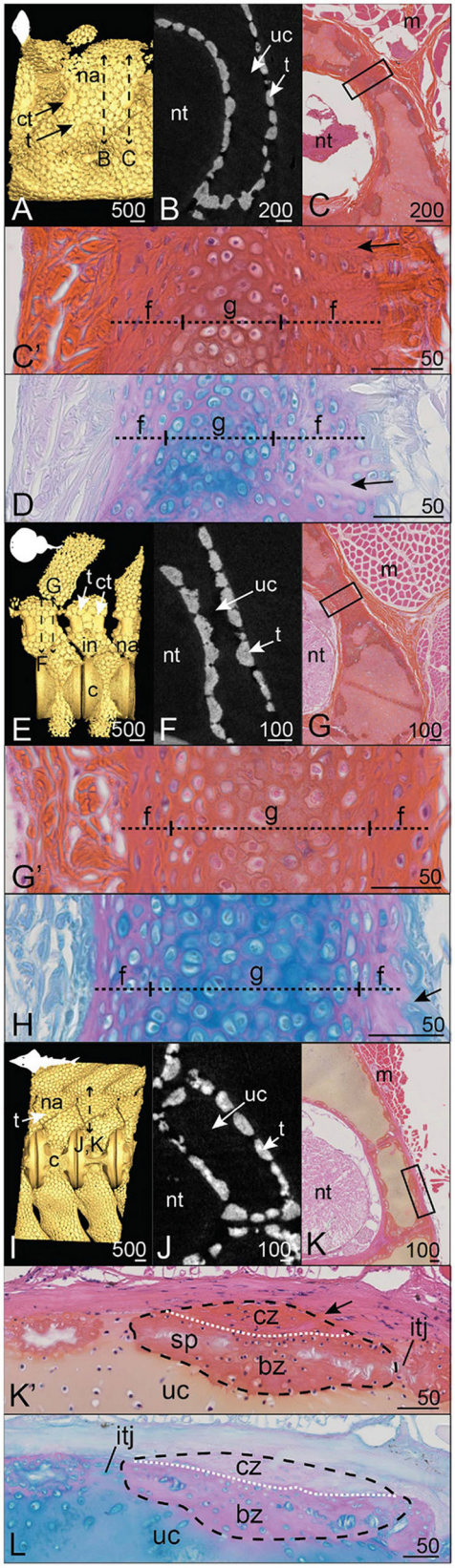

FIGURE 6 | (Continued)

FIGURE 6 | Mineralization patterns in the neural arches of posterior vertebrae in batoids. **(A–D)** Smooth butterfly ray *Gymnura micrura* (40.5 cm DW). **(E–H)** *Torpedo* sp. (16 cm DW). **(I–L)** Shovelnose guitarfish *Pseudobatos productus* (60 cm TL). **(A,E,I)** 3D isosurfaces. **(B,F,J)** Virtual cross sections following the plane indicated by the double sided dashed arrow in **(A,E,I)**. **(C,G,K)** HES staining on transverse sections following the plane indicated by the double sided dashed arrow in **(A,E,I)**. **(C',G',K')** Close-ups of the boxes in **(C,G,K)**. **(D,H,L)** PAS-AB staining of similar zones as in **(C',G',K')**, respectively. Legends as in **Figures 1**–**5**.

thin mineralization layer is both proximal (facing the neural tube) and subperichondrial (**Figures 7C,D,G,H**). Although the majority of the neural arch is composed of unmineralized cartilage matrix containing round chondrocytes (**Figures 7D,H**), the HES staining shows thin purple-stained blocks within the cartilaginous matrix that do not embed any cells (**Figures 7C',G'**), similar to the thin tesserae described in *H. colliei*. The tesserae are 10 μm wide (in their chondral-perichondrial axis, **Figures 7C',G'**) and are separated from the neural tube by a layer of cartilaginous matrix in *C. crepidater* (**Figure 7G'**), while it occurs in contact with the very thin perichondrium in *E. spinax* (**Figure 7C'**).

3.2.3. Selachians, Squalomorphs, Order: Squatiniformes

In the Pacific angelshark *Squatina californica*, the dorsal neural arches and interneural elements appear as continuously mineralized structures that are contiguous with the tesserae covering the neural spine and the basidorsal and basiventral elements (**Figure 8I**). The virtual section of the *S. californica* vertebra shows an internal variation in the mineral density of this structure, with denser peripheral mineralization than in the core (**Figure 8J**). On the histological sections, the cartilaginous tissue core contains round chondrocytes in a modified matrix (**Figures 8K',L**), similar to our previous description of globular mineralization. This central cartilaginous zone is covered proximally and distally by a fibrous mineralized tissue that contains flattened cells, similar to what we already described for fibrous mineralization of the perichondrium (**Figures 8K',L**).

3.2.4. Selachians, Galeomorphs, Order: Carcharhiniformes

In all three Carcharhiniformes considered in the following, neural arch and interneural mineralization builds up continuous structures (**Figures 8A,E,I**). Neural arch mineralization is ventrally contiguous with tesserae from the vertebral body in the tope shark *Galeorhinus galeus* and the scalloped hammerhead *Sphyrna lewini* (**Figures 8A,B,E,F**).

The continuously mineralized elements of *G. galeus* and *S. lewini* include neural arches and interneural elements (**Figures 8A,E**). In both species, neural arch mineralization encloses an unmineralized core and appears denser on the proximal and distal faces than on the dorsal zone (**Figures 8B,F**). The dorsal zone and the contact zone with the mineralized perichondrium are composed of globular mineralization (g in **Figures 8C',D,G',H**). The perichondrial layer of the mineralized tissue is similar to the fibrous mineralization sites described in the

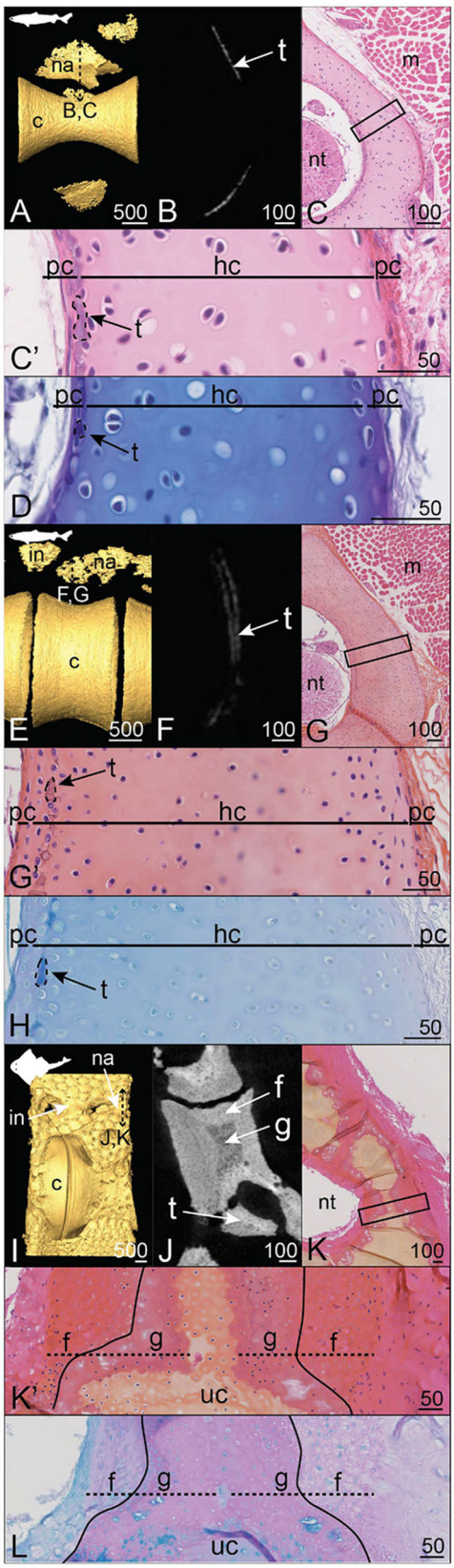

FIGURE 7 | (Continued)

FIGURE 7 | Mineralization patterns in the neural arches of posterior vertebrae in Squaliformes. **(A–D)** Velvet belly *Etmopterus spinax* (23 cm TL). **(E–H)** Longnose velvet dogfish *Centroscymnus crepidater* (31 cm TL). **(I–L)** Pacific angelshark *Squatina californica* (75 cm TL). **(A,E,I)** 3D isosurfaces. **(B,F,J)** Virtual cross sections following the plane indicated in **(A,E,I)**, respectively. **(C,G,K)** HES staining on transverse sections following the plane indicated in **(A,E,I)**. **(C',G',K')** Close-ups of the boxes in **(C,G,K)**. **(D,H,L)** PAS-AB staining of similar zones as in **(C',G',K')**, respectively. Legends as in **Figures 1**–**5**.

distal side of the *S. canicula* neural arch, with enclosed fibrocyte-shaped cells and no observable lamellae (**Figures 8C',D,G',H**).

In the blue shark *Prionace glauca*, neural arch and interneural mineralization sites alternate dorsal to the large centrum and no tesserae can be observed on the whole vertebral unit (**Figure 8I**). Mineralization is very restricted to the dorsoventral axis of the neural arch. The neural arch mineralization is superficial to only one location of the unmineralized cartilaginous neural arch (**Figure 8K**). The mineralized tissue includes globular mineralization in its innermost zone, together with outer perichondrial layers on both proximal and distal sides of the neural arch (**Figures 8K',L**). These perichondrial layers are not homogeneous because the cells undergo a morphological transition from flat—in the contact zone with globular mineralization—to subspherical—in the external zone (**Figures 8K',L**). Besides, the extracellular matrix of the external zone shows HES and Alcian blue staining similar to unmineralized cartilage, suggesting the presence of hyaline cartilaginous matrix in this perichondrial zone (**Figures 8K',L**). However, this external layer also displays numerous bundles of collagen fibers similar to Sharpey's fibers (**Figure 8K'**). The progressive centrifugal transition from a fibrous to a cartilaginous nature of the outer layers corresponds to a progressive decrease of mineralization, as shown in the virtual section (**Figure 8J**).

3.2.5. Selachians, Galeomorphs, Orders: Heterodontiformes, Orectolobiformes, and Lamniformes

In the horn shark *Heterodontus francisci* and the brownbanded bambooshark *Chiloscyllium punctatum*, alternate neural arches and interneural elements display a fully mineralized surface (**Figures 9A,E**). Tesseral mineralization is also located ventral to the neural and interneural elements of *H. francisci* (**Figure 9A**). In both species, the neural arch displays an unmineralized central core (**Figures 9B,F**) made of cartilage (**Figures 9C',G'**). However, globular mineralization is detected in the cartilaginous core in contact with the mineralized perichondrial layers (**Figures 9C',G'**). In *H. francisci*, the perichondrial mineralized layers are highly fibrous, in particular in the distal layer where numerous Sharpey's fibers are observed and incorporate numerous flattened cells (arrows, **Figures 9C',D**). On the contrary, the proximal perichondrium of the *C. punctatum* neural arch contains very few cells and the matrix is arranged in lamellae (**Figures 9G',H**). Overall, the organization and composition of the *C. punctatum* neural arch are very similar to what is observed in the *S. canicula* neural arch (compare with **Figures 1C, 2A',B,C',D**).

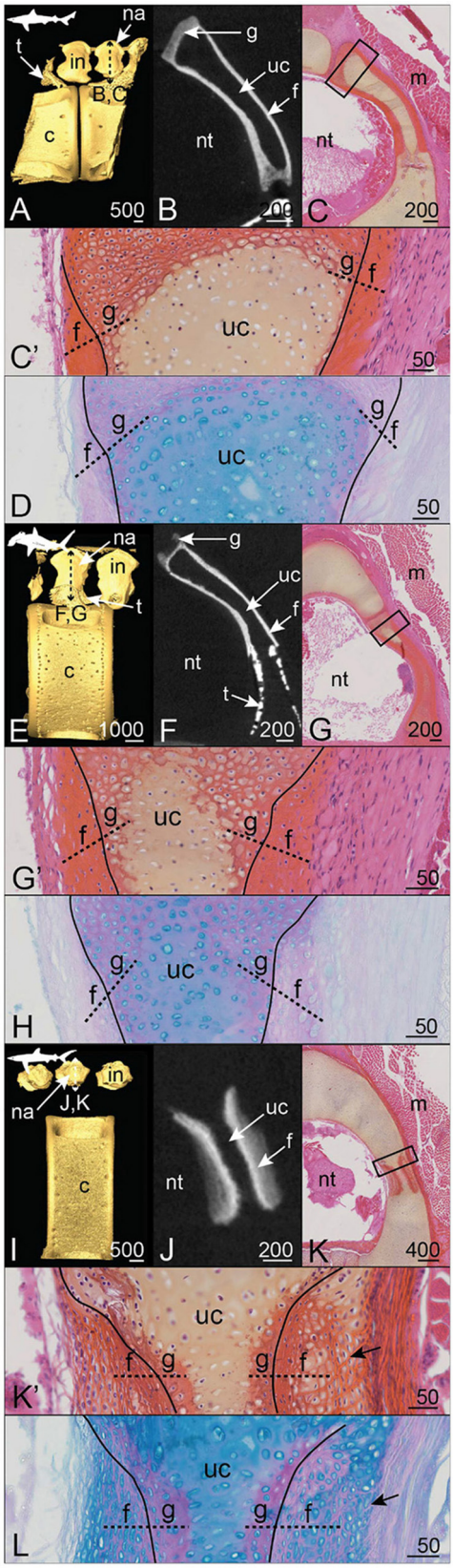

FIGURE 8 | (Continued)

FIGURE 8 | Mineralization patterns of the neural arches in Carcharhiniformes. **(A–D)** Anterior vertebra of a tope shark *Galeorhinus galeus* (50 cm TL). **(E–H)** Posterior vertebra of a scalloped hammerhead *Sphyrna lewini* (60 cm TL). **(I–L)** Posterior vertebra of a blue shark *Prionace glauca* (80 cm TL). **(A,E,I)** 3D isosurfaces. **(B,F,J)** virtual cross sections following the plane indicated in **(A,E,I)**. **(C,G,K)** HES staining on transverse sections following the plane indicated in **(A,E,I)**. **(C',G',K')** Close-ups of the boxes in **(C,G,K)**. **(D,H,L)** PAS-AB staining of similar zones as in **(C',G',K')**, respectively. Legends as in **Figures 1**–**5**.

The neural arch of the bull shark *Carcharias taurus* displays superficial mineralization in the form of standard size tesserae, while the core of the neural arch remains unmineralized (**Figures 9I,J**) and cartilaginous (**Figure 9K**). The tesserae are about 300 μm long (tangential axis) and 150 μm wide (along the chondral-perichondrial axis, **Figures 9K',L**). The cap and body zones cannot be properly distinguished from our sample, probably because of a tilted section plan (**Figures 9K',L**). However, we observe Sharpey's fibers anchoring the tesserae to the distal fibrous layer of the neural arch (arrows, **Figures 9K',L**) and unmineralized intertesseral joints (**Figures 9K',L**).

4. DISCUSSION

In the following, we discuss our results at two scales of organization, as previously defined by Dean and Summers (2006). The description of the cells and extracellular matrices involved in the mineralization (microscale description) allows defining three histotypes: globular mineralization (as reported by Ørvig, 1951), fibrous mineralization, and lamellar mineralization (as reported by Peignoux-Deville et al., 1982). On the other hand, the description of the whole skeletal elements (mesoscale description) provides insights into three mineralization architectures: discontinuous with tessellated cartilage, continuous over the whole neural arch, and semi-discontinuous in which tesserae are found associated with larger elements that we herein named corner tesserae.

4.1. Microscale Characterization of the Diversity of the Chondrichthyan Mineralized Tissues

In this work, we described the distribution of three histotypes in the neural arches of a wide taxonomic range of cartilaginous fishes. These results highlight the combined contribution of cartilaginous and perichondrial tissues in building the mineralized skeletal units of most chondrichthyans.

First, we identified globular mineralization that initiates in the hyaline cartilaginous matrix of the neural arches of all sampled species, in all architectures. It occurs in poorly developed tesserae of a holocephalan and the two Squaliformes examined in this study, in the body zone of tesserae of several elasmobranch species, in the most internal layer of the corner tesserae, and in the continuously mineralized neural arches of the other species. The classical description of tessellated cartilage includes such globular mineralization in the body zone (Kemp and Westrin, 1979; Seidel et al., 2016, 2017; Maisey et al., 2020), where the

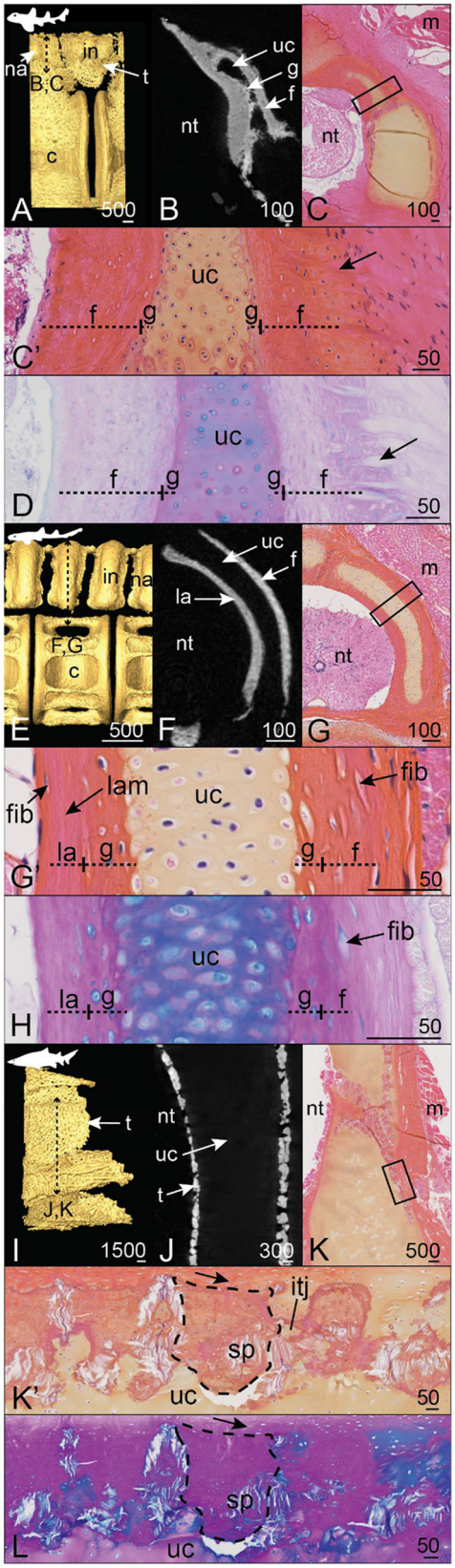

FIGURE 9 | (Continued)

FIGURE 9 | Mineralization patterns of the neural arches in galeomorphs (excluding Carcharhiniformes). **(A–D)** posterior vertebra of a horn shark *Heterodontus francisci* (55 cm TL). **(E–H)** Anterior vertebra of a brownbanded bambooshark *Chiloscyllium punctatum* (19.3 cm TL). **(I–L)** Anterior vertebra of a bull shark *Carcharias taurus* (270 cm TL). **(A,E,I)** 3D isosurfaces. **(B,F,J)** Virtual cross sections following the plane indicated in **(A,E,I)**. **(C,G,K)** HES staining on transverse sections following the plane indicated in **(A,E,I)**. **(C',G',K')** Close-ups of the boxes in **(C,G,K)**. **(D,H,L)** PAS-AB staining of similar zones as in **(C',G',K')**, respectively. Legends as in **Figures 1**–**5**.

surrounding matrix is hyaline and cells display a chondrocyte morphology with some shape variations (Chaumel et al., 2020). In both standard and corner tesserae, our observations are consistent with globular mineralization, from the observation of heterogeneous staining marking the presence of Liesegang lines. Although the exact nature of these Liesegang lines is not clear, they were hypothesized to be produced by the rhythmic activity of chondrocytes in their matrix (Kemp and Westrin, 1979). Because chondrocytes are not embedded in the mineralized matrix of the poorly developed tesserae of *E. spinax*, *C. crepidater*, and *H. colliei*, we could not detect Liesegang lines. However, Liesegang lines have been described in the thin tesserae of other holocephalan species (Pears et al., 2020; Seidel et al., 2020), defining these tesserae as sites of globular mineralization. Previous studies also showed that fully developed tesserae first appear only as subperichondrial focal mineralization sites (Enault et al., 2015; Seidel et al., 2016). This suggests that tesserae remain in an "under-developed" stage in holocephalan species as they do not engulf chondrocytes and are devoid of cap zone mineralization (Pears et al., 2020; Seidel et al., 2020), although chondrocytes in the mineralized matrix were described at an early stage of tesseral growth in *C. milii* (Pears et al., 2020). Our findings extend the occurrence of this thin globular mineralization outside of holocephalans, in selachian species with secondarily poorly mineralized skeletons (*E. spinax* and *C. crepidater*) but also in sites of poor development of these tesserae (in the *S. canicula* vertebral body).

Although they did not study and precisely describe neural arches, Ridewood and MacBride (1921) first illustrated several transverse sections of vertebrae that showed the diversity of mineralized tissues in elasmobranchs. More recent studies have interpreted some aspects of the mineralized neural arch tissues as "bone-like" in few elasmobranch species (Eames et al., 2007; Enault et al., 2015; Atake et al., 2019). Here we show that such tissues may be of at least two different types that we both hypothesize to be of perichondrial origin. Of these two types, fibrous mineralization is found in all occurrences of a continuously mineralized neural arch, is defined by the presence of fibrocyte-shaped cells enclosed in a fibrous matrix often crossed by Sharpey's fibers, and stands in continuity with the peripheral unmineralized connective tissue that links the neural arches to the surrounding muscles. Our histological results support a perichondrial nature of the tissue and therefore a growth by external apposition, as previously suggested (Atake et al., 2019). Also, we show that the inner cartilaginous core keeps a stable thickness in embryonic and

juvenile stages of development, supporting the fact that growth of the outer layers of the neural arches is generated through the activity of perichondrial cells (**Figures 2**, **3**). In our histological assays, there is no staining difference between the fibrous continuous mineralization in neural arches and the cap zone of fully developed tesserae. The cap zone has classically been described as a tissue with a derived type of mineralization (prismatic mineralization in Ørvig, 1951). Because prismatic mineralization can only be identified through polarized light microscopy, our sample preparation does not allow identifying the prismatic nature of the observed mineralization. However, the perichondrial characteristics of the cap zone have also been discussed recurrently in both the continuous neural arch tissues and the cap zone of tesserae because of the presence of type I collagen fibers and the observation of fibrocyte-shaped cells (Kemp and Westrin, 1979; Dean and Summers, 2006; Seidel et al., 2017). Further comparison to bone tissue was also often raised about the cap zone because of its dense mineralization and because of its topological location, similar to the perichondrial bone described in early vertebrates (Ørvig, 1951; Donoghue and Sansom, 2002). In our microCT images, we also detected internal variation of mineral density, suggesting lower density in globular mineralization as compared to fibrous mineralization. A more detailed tissue characterization, including recognition of cellular and lacunar shape or density, would have involved microCT scans of a much higher resolution than those analyzed here.

The third mineralized tissue identified in our samples is another type of perichondrial tissue that we named lamellar mineralization and that is only observed on the proximal side of the neural arches of *S. canicula* and *C. punctatum*. This lamellar tissue in *C. punctatum* is thin and our sampled individual was a young juvenile (19.3 cm TL) so it remains difficult to be properly compared to our observation in *S. canicula*. In *S. canicula*, the extracellular matrix content of this tissue appears more linearly organized than in fibrous mineralization (hence the lamellar denomination). The cell density is extremely low as compared to both cartilaginous and fibrous tissues and the rare cells observed in the matrix are similar to fibrocytes encased in the lamellar matrix, which is particularly visible in the elder *S. canicula* sample (**Figures 1C',D,C1,D1**). The growth of this tissue has to be appositional from cells located on the proximal surface of the neural arch, facing the neural tube, where no thick unmineralized perichondrium was apparent in our samples but only a monolayer of fibrocytes (see **Figure 9G'**). This observation highlights the potential for very different growth processes between the fibrous and lamellar mineralized tissues, as cells do not seem to behave similarly, being either engulfed and kept alive (distal side) or dead or excluded from the mineralized matrix (proximal side).

4.2. Mesoscale Mineralization Patterns: Continuous vs. Discontinuous Architectures

At mesoscale, we chose to classify our observations into several types. We defined the mineralization architecture as discontinuous when the neural surface is covered by tesserae of homogeneous size, either fully developed with a body and cap zones (Dean et al., 2009; Seidel et al., 2020) as in *C. taurus* and in Rhinopristiformes, or reduced in size and acellular (Maisey et al., 2020; Pears et al., 2020) as in Squaliformes and in *H. colliei* (**Table 2** and **Figure 10**, yellow silhouettes). We further observed discontinuous architecture in the neural arches of the posterior vertebrae of another batoid (in the white-blotched river stingray *Potamotrygon leopoldi*, data not shown). On the opposite extreme, we termed continuous architecture the neural arch surface that is mineralized as a whole (**Figure 10**, green silhouettes). Continuous mineralization involves globular, fibrous, and eventually lamellar mineralizations and is reported in Squatiniformes, Rajiformes, and all galeomorphs except in Lamniformes (**Table 2** and **Figure 10**, green silhouettes).

The third mesoscale architectural pattern is characterized by the co-occurrence of homogeneous tesserae covering most of the neural arch surface in addition to two larger elements located on the anteriormost and posteriormost sides of the neural arch, which we named corner tesserae after Dean et al. (2009). From histology, these large elements are comparable both to tesserae and to continuously mineralized neural arches because they involve an internal (chondral) globular mineralization and an external (perichondrial) fibrous mineralization. However, they differ from standard tesserae because of their size and also because they cover the surface of the proximo-distal face of the element, in addition to having two parallel faces, one on the proximal surface and the other one on the distal surface of the neural arch, making them U-shaped in their anterior-posterior axis (**Figure 3K**). As a result, they could be interpreted either as highly modified and enlarged tesserae, or as continuous mineralization that is restricted to only part of the neural arch surface. We termed this situation a semi-discontinuous architecture, considering it an intermediate state between discontinuous and continuous architectures (**Figure 10**, red silhouettes).

We described the semi-discontinuous architecture only in batoids, in the posterior vertebrae of *G. micrura* (Myliobatiformes) and *Torpedo* sp. (Torpediniformes) (**Table 2** and **Figure 10**, red silhouettes). Besides, we report its occurrence in the anterior vertebrae of *R. clavata* (Rajiformes), whereas the posterior vertebrae displayed continuous mineralization. Within Rajiformes, a semi-discontinuous architecture was reported in the Eaton's skate anterior vertebrae *Bathyraja eatonii* (Rajiformes) (Atake et al., 2019), while continuously mineralized neural arches were observed in the little skate posterior vertebrae *Leucoraja erinacea* (Criswell et al., 2017). The co-occurrence of continuous and semi-discontinuous architectures in *R. clavata* calls for more complete descriptions of the mineralized structures in vertebral columns in a wider range of Rajiformes, and other batoids, to allow making any inference on the ancestral state of mineralization architecture in this group.

4.3. Prospects on the Evolution of Mineralized Histotypes in Vertebrates

4.3.1. The Putative Nature of Fibrous Mineralization

Our work provides a histological examination in an unprecedented taxonomic range of elasmobranch fishes. We uncover the occurrence of fibrous mineralization in

TABLE 2 | Description and categorization of the mineralized tissues in the neural arches of the chondrichthyan species examined in this study.

Species	Order	Mineralization histotypes (microscale)			Mineralization architecture (mesoscale)
		Globular (c)	Fibrous (pc)	Lamellar (pc)	
S. canicula	Carcharhiniformes	+	+, dist	+, prox	Continuous
C. punctatum	Orectolobiformes	+	+, dist	+, prox	
P. glauca	Carcharhiniformes	+	+	–	
G. galeus	Carcharhiniformes	+	+	–	
S. lewini	Carcharhiniformes	+	+	–	
H. francisci	Heterodontiformes	+	+	–	
S. californica	Squatiniformes	+	+	–	
R. clavata	Rajiformes	+	+	–	Continuous and semi-discontinuous (corner tesserae)
G. micrura	Myliobatiformes	+	+	–	Semi-discontinuous (corner tesserae)
Torpedo sp.	Torpediniformes	+	+	–	
R. ancylostoma	Rhinopristiformes	+, t	+, t	–	Discontinuous (tessellated)
P. productus	Rhinopristiformes	+, t	+, t	–	
C. taurus	Lamniformes	+, t	+, t	–	
H. colliei	Chimaeriformes	+, t	–	–	Discontinuous (reduced)
C. crepidater	Squaliformes	+, t	–	–	
E. spinax	Squaliformes	+, t	–	–	

+ indicates that the mineralized tissue is detected, as opposed to –, t indicates that the tissue is located within a tessera, and prox and dist are specified when the tissue is restricted to the proximal (facing the neural tube) and distal (facing muscular attachments) sides of the neural arch, respectively. c, cartilage; pc, perichondrium.

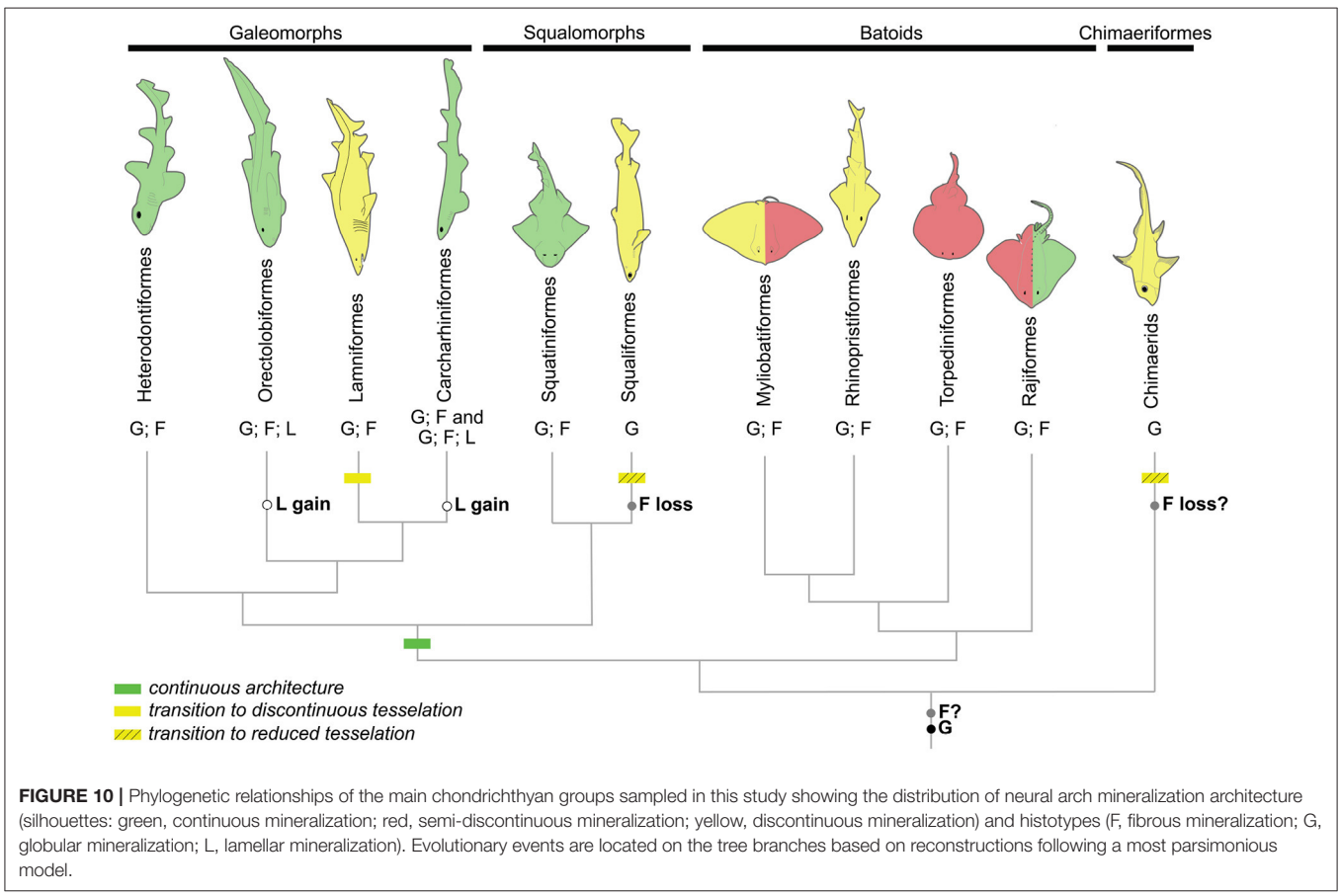

FIGURE 10 | Phylogenetic relationships of the main chondrichthyan groups sampled in this study showing the distribution of neural arch mineralization architecture (silhouettes: green, continuous mineralization; red, semi-discontinuous mineralization; yellow, discontinuous mineralization) and histotypes (F, fibrous mineralization; G, globular mineralization; L, lamellar mineralization). Evolutionary events are located on the tree branches based on reconstructions following a most parsimonious model.

continuously mineralized neural arches in an Heterodontiform, a Squatiniform, most Carcharhiniformes examined in this study, and a Rajiform (**Figure 10**). Fibrous mineralization is also identified in the perichondrial zone of both corner and standard tesserae (**Table 2**). Here we wish to discuss the hypothesis of fibrous mineralization to be naturally mineralizing fibrocartilage, as previously suggested by Ørvig (1951) and Eames et al. (2007). Mineralized fibrocartilages were described in tetrapod entheses that join tendons to bones (Benjamin and Ralphs, 1998) and surrounding rib cartilage (Claassen et al., 1996). Fibrocartilage histology shows strong variation, ranging from almost hyaline to highly fibrous (similar to tendons) in mammals (Wachsmuth et al., 2006) and bony fishes (Benjamin, 1990). Similar variation is observed in our sample, where fibrous mineralization resembles more hyaline-type cartilage crossed by fibers in *P. glauca* (**Figures 8K,L**). This hypothesis would also explain the presence of type II collagen and a thin layer identified as "supra-tesseral cartilage" in the perichondrial surface of tesserae in some species (Seidel et al., 2017). Further histochemical, histological, and cellular characterization is therefore needed to better define the nature of this tissue and compare it to tetrapod tissues.

Beyond the nature of this tissue, we show that perichondrial fibrous mineralization is widely present in skeletal tissues of elasmobranchs. Ancestral character state reconstruction by a most-parsimonious model (**Supplementary Material 1** and summarized in **Figure 10**) suggests that this histotype is ancestral to elasmobranchs (as previously hypothesized by Atake et al., 2019). This scenario implies a secondary loss of fibrous mineralization in *C. crepidater* and *E. spinax*. Considering the secondary loss of mineralization observed in extant holocephalans (Maisey et al., 2020; Pears et al., 2020), it is also plausible that fibrous mineralization is ancestral to all chondrichthyans but lost in holocephalans. Fibrous mineralization may then be a remnant of forms of mineralization found in early vertebrates. As a consequence, a review of the paleontological data is needed, especially in stem gnathostomes and agnathan taxa where several forms of perichondrial bone (cellular or acellular, as described in placoderm taxa Ørvig, 1951 or galeaspid and osteostracan taxa, as reviewed by Donoghue and Sansom, 2002) may be revised in light of this fibrous mineralization that covers cartilaginous skeletal units. Further comparison with extant and extinct taxa of bony fishes may also uncover similar tissues outside of chondrichthyans. Only this information may shed light on the evolution of fibrous mineralization and its significance to the evolution of a mineralized skeleton in vertebrates.

4.3.2. Lamellar Mineralization and Putative Bone in Cartilaginous Fishes

The continuous architecture always includes fibrous mineralization in the distal part of the neural arch but we identified lamellar, instead of fibrous, mineralization in the proximal side of the neural arch of two galeomorph species (**Table 2**). The fibrous and lamellar mineralizations histologically differ in that the former contains numerous cells, as opposed to the latter where only very few cells are observed, and by the arrangement of fibers. Another difference is the lack of a thick unmineralized connective tissue surrounding the lamellar mineralization (see **Figure 2C'**, as opposed to the situation in other galeomorphs, see **Figures 9G',K'**). Bone-like tissue was previously reported in the neural arches of Carcharhiniformes (Peignoux-Deville et al., 1982; Eames et al., 2007) and Rajiformes (Atake et al., 2019). These previous studies did not distinguish the cellular from almost acellular tissues and the histological staining results in the work of Atake et al. (2019) better support the presence of fibrous mineralization in both the proximal and distal sides of the neural arches of *L. erinacea* and *B. eatonii*. As a consequence, the lamellar mineralized pattern as defined in our work has only been described so far in *S. canicula* and most probably in *C. ventriosum* (Eames et al., 2007) (both Carcharhiniformes), and in *C. punctatum* (Orectolobiformes). Considering these results, ancestral character state reconstruction with a most-parsimonious model suggests parallel evolution of this lamellar pattern in Carcharhiniformes and Orectolobiformes (**Supplementary Material 2**, summarized in **Figure 10**). Still, our observations and hypothesis need to be confirmed with broader sampling among Orectolobiform species, including older specimens. As a broader conclusion, our results support a recent evolution of this trait, making it unlikely to be homologous to any bone type found in early vertebrates.

4.4. Concluding Remarks

Tessellated cartilage is considered a synapomorphy of chondrichthyans (reviewed in Maisey, 2013) and displays a high variety of tessera morphologies and spatial arrangements (Summers et al., 1998; Seidel et al., 2016; Maisey et al., 2020; Pears et al., 2020). What could be considered classical, polygonal and flat tesserae as described in extant batoids are assumed to be the ancestral morphology of chondrichthyan tesserae and to have further undergone size and shape alterations during the evolution of different groups, including strong size regression as found in holocephalans (Pears et al., 2020). Here we have described other mineralization architectures in elasmobranchs, where cartilage surfaces can be continuously mineralized or covered by a combination of tesserae and larger mineralized elements. The reconstruction of an ancestral state for the architecture character under maximum parsimony only suggests that mineralization of the neural arches was ancestrally continuous in selachians, considering a secondary reduction of mineralization in our sampled Lamniform (**Supplementary Material 3**). More samples are necessary to generate hypotheses on chondrichthyans and elasmobranchs.

Besides, we never observed any complete absence of mineralization in our samples. What could be considered a minimal state of mineralization was located in a subperichondrial zone of the hyaline cartilaginous matrix of neural arches (in *H. colliei*, *E. spinax*, and *C. crepidater*). This zone was previously considered as the initiator for further mineralization that would propagate from the hyaline cartilage toward the perichondrium (Ørvig, 1951). It is plausible that the process and pattern of tissue mineralization in elasmobranchs (microscale analysis) might be completely independent of the process of architecture regulation (mesoscale analysis) that has led to

the derived evolution of tesserae in chondrichthyans. As a consequence, if mineralized tissues are comparable in continuous and discontinuous mineralized architectures, evolution between these two states may simply entail a variation in the intensity of one regulatory signal (as suggested by Maisey et al., 2020) that would constrain the size of the mineralized elements, from tesserae as minimal objects to fully mineralized structures, with intermediate states involving the massive elements described in some neural arches of batoids.

Finally, the occurrence of a reduced tessellated pattern in phylogenetically distant groups (Squaliformes and holocephalans) questions the existence of ecological signals able to drive such convergent evolution. Deep-water shark species are known to display reduced mineralization of the endoskeleton as compared to shallower species (Dean et al., 2015; Seidel et al., 2016). *H. colliei* is not restricted to deep water habitats (Barnett et al., 2012) but holocephalans are characterized by a reduction of mineralized structures (Pears et al., 2020) and are the chondrichthyan group found in deepest waters (Priede and Froese, 2013). As a conclusion, ecological constraints, such as deep-water habitat may have convergently driven loss of mineralization in chondrichthyans. It is assumed that such a reduced amount of mineralization could contribute to energetic trade-offs by impacting buoyancy and metabolic costs of locomotion (Blaxter et al., 1971; Blaxter, 1980), however, more data on chondrichthyans are needed to challenge this hypothesis.

DATA AVAILABILITY STATEMENT

The original contributions presented in the study are included in the article/**Supplementary Material**, further inquiries can be directed to the corresponding author/s.

ETHICS STATEMENT

Ethical review and approval was not required for the animal study because no handling of live specimens was necessary for this study.

AUTHOR CONTRIBUTIONS

FB and MD-T designed the experimental setup, prepared the samples, imaged and analyzed the results, and drafted the manuscript. SE, MB, and NP performed the histological sections and staining. FAL-R collected the samples. All authors agree to be accountable for the content of the work.

FUNDING

NP and MB are members of the Réseau d'Histologie Expérimentale de Montpellier (RHEM) facility, supported by SIRIC Montpellier Cancer (Grant INCa Inserm DGOS 12553), the European regional development foundation and the occitanian region (FEDER-FSE 2014-2020 Languedoc Roussillon).

ACKNOWLEDGMENTS

We thank Sylvain Adnet, Henri Cappetta, and Guillaume Guinot from the Institut des Sciences de l'Evolution de Montpellier and the aquaria Planet Ocean, Montpellier (Nicolas Hirel) and Marineland Parcs, Antibes (Jean-Philippe Cateau) for providing biological samples. We thank Renaud Lebrun for his help with microCT scans and Camille Martinand-Mari, Nicolas Leurs, and Yann Bayle for insightful proofreading. 3D data acquisitions (microCT facilities) and slide scanning (nanozoomer) are hosted in the MRI platform, a member of the national infrastructure France-BioImaging supported by the French National Research Agency (ANR-10-INBS-04, Investments for the future), and of the Labex CEMEB (ANR-10-LABX-0004) and NUMEV (ANR-10-LABX-0020).

SUPPLEMENTARY MATERIAL

The Supplementary Material for this article can be found online at: https://www.frontiersin.org/articles/10.3389/fevo.2021.660767/full#supplementary-material

REFERENCES

Applegate, S. (1967). "A survey of shark hard parts," in *Sharks, Skates and Rays*, eds P. Gilbert, R. Mathewson, and D. Rall (Baltimore, MD: The Johns Hopkins Press), 37–67.

Atake, O. J., Cooper, D. M. L., and Eames, B. F. (2019). Bone-like features in skate suggest a novel elasmobranch synapomorphy and deep homology of trabecular mineralization patterns. *Acta Biomater.* 84, 424–436. doi: 10.1016/j.actbio.2018.11.047

Barnett, L. A., Earley, R. L., Ebert, D. A., and Cailliet, G. M. (2009). Maturity, fecundity, and reproductive cycle of the spotted ratfish, *Hydrolagus colliei*. *Mar. Biol.* 156, 301–316. doi: 10.1007/s00227-008-1084-y

Barnett, L. A. K., Ebert, D. A., and Cailliet, G. M. (2012). Evidence of stability in a chondrichthyan population: case study of the spotted ratfish *Hydrolagus colliei* (Chondrichthyes: Chimaeridae). *J. Fish Biol.* 80, 1765–1788. doi: 10.1111/j.1095-8649.2011.03216.x

Bejarano-Álvarez, M., Galván-Magaña, F., and Ochoa-Báez, R. I. (2011). Reproductive biology of the scalloped hammerhead shark *Sphyrna lewini* (Chondrichthyes: Sphyrnidae) off southwest Mexico. *Aqua Int. J. Ichthyol.* 17, 11–22.

Benjamin, M. (1990). The cranial cartilages of teleosts and their classification. *J. Anat.* 169, 153–172.

Benjamin, M., and Ralphs, J. R. (1998). Fibrocartilage in tendons and ligaments–an adaptation to compressive load. *J. Anat.* 193, 481–494. doi: 10.1046/j.1469-7580.1998.19340481.x

Blaxter, J. H. S. (1980). "The effect of hydrostatic pressure on fishes," in *Environmental Physiology of Fishes. NATO Advanced Study Institutes Series (Series A: Life Science)*, Vol. 35, ed M. A. Ali (Boston, MA: Springer). doi: 10.1007/978-1-4899-3659-2_13

Blaxter, J. H. S., Wardle, C. S., and Roberts, B. L. (1971). Aspects of the circulatory physiology and muscle systems of deep-sea fish. *J. Mar. Biol. Assoc.* 51, 991–1006. doi: 10.1017/S0025315400018105

Bustamante, C., and Bennett, M. B. (2013). Insights into the reproductive biology and fisheries of two commercially exploited species, shortfin mako (*Isurus oxyrinchus*) and blue shark (*Prionace glauca*), in the south-east Pacific Ocean. *Fish. Res.* 143, 174–183. doi: 10.1016/j.fishres.2013.02.007

Capapé, C., Guélorget, O., Siau, Y., Vergne, Y., and Quignard, J. P. (2007). Reproductive biology of the thornback ray *Raja clavata* (Chondrichthyes: Rajidae) from the coast of Languedoc (southern France, northern Mediterranean). *Vie Milieu* 57, 83–90.

Capapé, C., Reynaud, C., Vergne, Y., and Quignard, J. P. (2008). Biological observations on the smallspotted catshark *Scyliorhinus canicula* (Chondrichthyes: Scyliorhinidae) off the Languedocian coast (southern France, northern Mediterranean). *Pan Am. J. Aquat. Sci.* 3, 282–289.

Chaumel, J., Schotte, M., Bizzarro, J. J., Zaslansky, P., Fratzl, P., Baum, D., et al. (2020). Co-aligned chondrocytes: zonal morphological variation and structured arrangement of cell lacunae in tessellated cartilage. *Bone* 134:115264. doi: 10.1016/j.bone.2020.115264

Claassen, H., Kampen, W. U., and Kirsch, T. (1996). Localization of collagens and alkaline phosphatase activity during mineralization and ossification of human first rib cartilage. *Histochem. Cell Biol.* 105, 213–219. doi: 10.1007/BF01462294

Compagno, L. J. V. (1984). Sharks of the world: an annotated and illustrated catalogue of shark species known to date. *FAO Species Catalog. Fish. Purposes* 2, 175–176.

Criswell, K. E., Coates, M. I., and Gillis, J. A. (2017). Embryonic development of the axial column in the little skate, *Leucoraja erinacea*. *J. Morphol.* 278, 300–320. doi: 10.1002/jmor.20637

Dean, M. N., Ekstrom, L., Monsonego-Ornan, E., Ballantyne, J., Witten, P. E., Riley, C., et al. (2015). Mineral homeostasis and regulation of mineralization processes in the skeletons of sharks, rays and relatives (Elasmobranchii). *Semin. Cell Dev. Biol.* 46, 51–67. doi: 10.1016/j.semcdb.2015.10.022

Dean, M. N., Mull, C. G., Gorb, S. N., and Summers, A. P. (2009). Ontogeny of the tessellated skeleton: insight from the skeletal growth of the round stingray *Urobatis halleri*. *J. Anat.* 215, 227–239. doi: 10.1111/j.1469-7580.2009.01116.x

Dean, M. N., and Summers, A. P. (2006). Mineralized cartilage in the skeleton of chondrichthyan fishes. *Zoology* 109, 164–168. doi: 10.1016/j.zool.2006.03.002

Debiais-Thibaud, M. (2019). "The evolution of endoskeletal mineralisation in chondrichthyan fish," in *Evolution and Development of Fishes, Chapter 6*, eds Z. Johanson, C. Underwood, and M. Richter (Cambridge: Cambridge University Press), 110–125. doi: 10.1017/9781316832172.007

Debiais-Thibaud, M., Simion, P., Ventéo, S., Muñoz, D., Marcellini, S., Mazan, S., et al. (2019). Skeletal mineralization in association with type x collagen expression is an ancestral feature for jawed vertebrates. *Mol. Biol. Evol.* 36, 2265–2276. doi: 10.1093/molbev/msz145

Donoghue, P. C. J., and Sansom, I. J. (2002). Origin and early evolution of vertebrate skeletonization. *Microsc. Res. Tech.* 59, 352–372. doi: 10.1002/jemt.10217

Eames, B. F., Allen, N., Young, J., Kaplan, A., Helms, J. A., and Schneider, R. A. (2007). Skeletogenesis in the swell shark *Cephaloscyllium ventriosum*. *J. Anat.* 210, 542–554. doi: 10.1111/j.1469-7580.2007.00723.x

Ebert, D. A., Fowler, S., and Compagno, L. J. V. (2013). *Sharks of the World: A Fully Illustrated Guide*. Plymouth: Wild Nature Press.

Enault, S., Adnet, S., and Debiais-Thibaud, M. (2016). Skeletogenesis during the late embryonic development of the catshark *Scyliorhinus canicula* (Chondrichthyes; Neoselachii). *MorphoMuseuM* 1:e2. doi: 10.18563/m3.1.4.e2

Enault, S., Muñoz, D. N., Silva, W. T. A. F., Borday-birraux, V., Bonade, M., Oulion, S., et al. (2015). Molecular footprinting of skeletal tissues in the catshark Scyliorhinus canicula and the clawed frog *Xenopus tropicalis* identifies conserved and derived features of vertebrate calcification. *Front. Genet.* 6:283. doi: 10.3389/fgene.2015.00283

Finarelli, J. A., and Coates, M. I. (2014). Chondrenchelys problematica (Traquair 1888) redescribed: a Lower Carboniferous, eel-like holocephalan from Scotland. *Earth Environ. Sci. Trans. R. Soc. Edinb.* 105, 35–59. doi: 10.1017/S1755691014000139

Goodrich, E. S. (1930). *Studies on the Structure & Development of Vertebrates*. London: Macmillan and Co.

Hall, B. K. (2015). *Bones and Cartilage, 2nd Edn*. Oxford: Elsevier-Academic Press.

Hall, B. K., and Witten, P. E. (2019). "Plasticity and variation of skeletal cells and tissues and the evolutionary development of actinopterygian fishes," in *Evolution and Development of Fishes, Chapter 7*, eds Z. Johanson, C. Underwood, and M. Richter (Cambridge: Cambridge Université Press), 126–143. doi: 10.1017/9781316832172.008

Hasse, C. (1879). *Das natürliche System der Elasmobranchier auf Grundlage des Baues und der Entwicklung ihrer Wirbelsäule*, Vol. I Allgemei. Jena: Eine morphologische und paläontologische Studie.

Hilton, M. J., Tu, X., Cook, J., Hu, H., and Long, F. (2005). Ihh controls cartilage development by antagonizing Gli3, but requires additional effectors to regulate osteoblast and vascular development. *Development* 132, 4339–4351. doi: 10.1242/dev.02025

Johanson, Z., Boisvert, C. A., Maksimenko, A., Currie, P., and Trinajstic, K. (2015). Development of the synarcual in the elephant sharks (Holocephali; Chondrichthyes): implications for vertebral formation and fusion. *PLoS ONE* 10:e0135138. doi: 10.1371/journal.pone.0135138

Kemp, N. E., and Westrin, S. K. (1979). Ultrastructure of calcified cartilage in the endoskeletal tesserae of sharks. *J. Morphol.* 160, 75–109. doi: 10.1002/jmor.1051600106

Last, P., Naylor, G., Séret, B., White, W., de Carvalho, M., and Stehmann, M. (2016). *Rays of the World*. Clayton South, VIC: CSIRO Publishing.

Leurs, N., Martinand-Mari, C., Vento, S., Haitina, T., and Debiais-Thibaud, M. (2021). Evolution of matrix gla and bone gla protein genes in jawed vertebrates. *Front. Genet.* 12:245. doi: 10.3389/fgene.2021.620659

Licht, M., Schmuecker, K., Huelsken, T., Hanel, R., Bartsch, P., and Paeckert, M. (2012). Contribution to the molecular phylogenetic analysis of extant holocephalan fishes (Holocephali, Chimaeriformes). *Organ. Divers. Evol.* 12, 421–432. doi: 10.1007/s13127-011-0071-1

Lucifora, L. O., Menni, R. C., and Escalante, A. H. (2002). Reproductive ecology and abundance of the sand tiger shark, *Carcharias taurus*, from the southwestern Atlantic. *ICES J. Mar. Sci.* 59, 553–561. doi: 10.1006/jmsc.2002.1183

Lucifora, L. O., Menni, R. C., and Escalante, A. H. (2004). Reproductive biology of the school shark, *Galeorhinus galeus*, off Argentina: support for a single south western Atlantic population with synchronized migratory movements. *Environ. Biol. Fishes* 71, 199–209. doi: 10.1007/s10641-004-0305-6

Maddison, W. P., and Maddison, D. R. (2019). *Mesquite: A Modular System for Evolutionary Analysis*. Available online at: http://www.mesquiteproject.org

Maisey, J. G. (2013). The diversity of tessellated calcification in modern and extinct chondrichthyans. *Rev. Paléobiol.* 32, 355–371.

Maisey, J. G., Denton, J. S. S., Burrow, C., and Pradel, A. (2020). Architectural and ultrastructural features of tessellated calcified cartilage in modern and extinct chondrichthyan fishes. *J. Fish Biol.* 98, 919–941. doi: 10.1111/jfb.14376

Márquez-Farías, J. F. (2007). Reproductive biology of shovelnose guitarfish Rhinobatos productus from the eastern Gulf of California México. *Mar. Biol.* 151, 1445–1454. doi: 10.1007/s00227-006-0599-3

Mayoral, E. E., Schultz, R., Rosemberg, S., Suzuki, L., Nunes de Oliveira, L. A., and Kay, F. U. (2014). Thanatophoric dysplasia : case report of an autopsy complemented by postmortem computed tomographic study. *Autopsy Case Rep.* 4, 35–41. doi: 10.4322/acr.2014.019

Meese, E. N., and Lowe, C. G. (2020). Environmental effects on daytime sheltering behaviors of California horn sharks (*Heterodontus francisci*). *Environ. Biol. Fishes* 103, 703–717. doi: 10.1007/s10641-020-00977-6

Moore, D. M., Neat, F. C., and McCarthy, I. D. (2013). Population biology and ageing of the deep water sharks *Galeus melastomus*, *Centroselachus crepidater* and *Apristurus aphyodes* from the Rockall Trough, north-east Atlantic. *J. Mar. Biol. Assoc.* 93, 1941–1950. doi: 10.1017/S0025315413000374

Naylor, G. J. P., Caira, J. N., Jensen, K., Rosana, K. A. M., Straube, N., and Lakner, C. (2012). "Elasmobranch phylogeny: a mitochondrial estimate based on 595 species," in *Biology of Sharks and Their Relatives, Chapter 2, 2nd Edn.*, eds J. C. Carrier, J. A. Musick, and M. R. Heithaus (Boca Raton, FL: CRC Press), 31–56. doi: 10.1201/b11867-4

Ørvig, T. (1951). Histologic studies of Placoderms and fossil Elasmobranchs. I: the endoskeleton, with remarks on the hard tissues of lower vertebrates in general. *Arkiv Zool.* 2:322.

Pears, J., Johanson, Z., Trinajstic, K., Dean, M. N., and Boisvert, C. A. (2020). Mineralization of the callorhinchus vertebral column (Holocephali; Chondrichthyes). *Front. Genet.* 11:1477. doi: 10.3389/fgene.2020.571694

Peignoux-Deville, J., Lallier, F., and Vidal, B. (1982). Evidence for the presence of osseous tissue in dogfish vertebrae. *Cell Tissue Res.* 222, 605–614. doi: 10.1007/BF00213858

Porcu, C., Marongiu, M. F., Follesa, M. C., Bellodi, A., Mulas, A., Pesci, P., et al. (2014). Reproductive aspects of the velvet belly *Etmopterus spinax*

(Chondrichthyes: Etmopteridae), from the central western Mediterranean Sea. Notes on gametogenesis and oviducal gland microstructure. *Mediterr. Mar. Sci.* 15, 313–326. doi: 10.12681/mms.559

Priede, I. G., and Froese, R. (2013). Colonization of the deep sea by fishes. *J. Fish Biol.* 83, 1528–1550. doi: 10.1111/jfb.12265

Ridewood, W. G., and MacBride, E. W. (1921). VIII. On the calcification of the vertebral centra in sharks and rays. *Philos. Trans. R. Soc. Lond. B* 210, 311–407. doi: 10.1098/rstb.1921.0008

Romero-Caicedo, A. F., Galván-Magaña, F., Hernández-Herrera, A., and Carrera-Fernández, M. (2016). Reproductive parameters of the Pacific angel shark *Squatina californica* (Selachii: Squatinidae). *J. Fish Biol.* 88, 1430–1440. doi: 10.1111/jfb.12920

Ryll, B., Sanchez, S., Haitina, T., Tafforeau, P., and Ahlberg, P. E. (2014). The genome of Callorhinchus and the fossil record: a new perspective on scpp gene evolution in gnathostomes. *Evol. Dev.* 16, 123–124. doi: 10.1111/ede.12071

Seidel, R., Blumer, M., Chaumel, J., Amini, S., and Dean, M. N. (2020). Endoskeletal mineralization in chimaera and a comparative guide to tessellated cartilage in chondrichthyan fishes (sharks, rays and chimaera). *J. R. Soc. Interface* 17:20200474. doi: 10.1098/rsif.2020.0474

Seidel, R., Blumer, M., Pechriggl, E.-J., Lyons, K., Hall, B. K., Fratzl, P., et al. (2017). Calcified cartilage or bone? Collagens in the tessellated endoskeletons of cartilaginous fish (sharks and rays). *J. Struct. Biol.* 200, 54–71. doi: 10.1016/j.jsb.2017.09.005

Seidel, R., Lyons, K., Blumer, M., Zaslansky, P., Fratzl, P., Weaver, J. C., et al. (2016). Ultrastructural and developmental features of the tessellated endoskeleton of elasmobranchs (sharks and rays). *J. Anat.* 229, 681–702. doi: 10.1111/joa.12508

Smith, M. M., Underwood, C., Goral, T., Healy, C., and Johanson, Z. (2019). Growth and mineralogy in dental plates of the holocephalan *Harriotta raleighana* (Chondrichthyes): novel dentine and conserved patterning combine to create a unique chondrichthyan dentition. *Zool. Lett.* 5, 1–30. doi: 10.1186/s40851-019-0125-3

Summers, A. P., Koob, T. J., and Brainerd, E. L. (1998). Stingray jaws strut their stuff. *Nature* 395, 450–451. doi: 10.1038/26649

Tarazona, O. A., Slota, L. A., Lopez, D. H., Zhang, G., and Cohn, M. J. (2016). The genetic program for cartilage development has deep homology within Bilateria. *Nature* 533, 86–89. doi: 10.1038/nature 17398

Wachsmuth, L., Söder, S., Fan, Z., Finger, F., and Aigner, T. (2006). Immunolocalization of matrix proteins in different human cartilage subtypes. *Histol. Histopathol.* 21, 477–485. doi: 10.14670/HH-21.477

Whiteman, P. (1973). The quantitative measurement of Alcian Blue-glycosaminoglycan complexes. *Biochem. J.* 131, 343–350. doi: 10.1042/bj1310343

Witten, P. E., and Huysseune, A. (2009). A comparative view on mechanisms and functions of skeletal remodelling in teleost fish, with special emphasis on osteoclasts and their function. *Biol. Rev. Camb. Philos. Soc.* 84, 315–346. doi: 10.1111/j.1469-185X.2009.00077.x

Witten, P. E., Huysseune, A., and Hall, B. K. (2010). A practical approach for the identification of the many cartilaginous tissues in teleost fish. *J. Appl. Ichthyol.* 26, 257–262. doi: 10.1111/j.1439-0426.2010.01416.x

Xiong, H., Rabie, A. B. M., and Hagg, U. (2005). Mechanical strain leads to condylar growth in adult rats. *Front. Biosci.* 10, 65–73. doi: 10.2741/1507

Yokota, L., Goitein, R., Gianeti, M. D., and Lessa, R. T. (2012). Reproductive biology of the smooth butterfly ray *Gymnura micrura*. *J. Fish Biol.* 81, 1315–1326. doi: 10.1111/j.1095-8649.2012.03413.x

Zhang, G., and Cohn, M. J. (2006). Hagfish and lancelet fibrillar collagens reveal that type II collagen-based cartilage evolved in stem vertebrates. *Proc. Natl. Acad. Sci. U.S.A.* 103, 16829–16833. doi: 10.1073/pnas.0605630103

Conflict of Interest: The authors declare that the research was conducted in the absence of any commercial or financial relationships that could be construed as a potential conflict of interest.

frontiers in Genetics

REVIEW
published: 11 May 2021
doi: 10.3389/fgene.2021.672433

Evolution of the Avian Eggshell Biomineralization Protein Toolkit – New Insights From Multi-Omics

*Nathalie Le Roy[1], Lilian Stapane[1], Joël Gautron[1] and Maxwell T. Hincke[2,3]**

[1] INRAE, Université de Tours, Nouzilly, France, [2] Department of Innovation in Medical Education, University of Ottawa, Ottawa, ON, Canada, [3] Department of Cellular and Molecular Medicine, University of Ottawa, Ottawa, ON, Canada

The avian eggshell is a remarkable biomineral, which is essential for avian reproduction; its properties permit embryonic development in the desiccating terrestrial environment, and moreover, are critically important to preserve unfertilized egg quality for human consumption. This calcium carbonate ($CaCO_3$) bioceramic is made of 95% calcite and 3.5% organic matrix; it protects the egg contents against microbial penetration and mechanical damage, allows gaseous exchange, and provides calcium for development of the embryonic skeleton. In vertebrates, eggshell occurs in the Sauropsida and in a lesser extent in Mammalia taxa; avian eggshell calcification is one of the fastest known $CaCO_3$ biomineralization processes, and results in a material with excellent mechanical properties. Thus, its study has triggered a strong interest from the researcher community. The investigation of eggshell biomineralization in birds over the past decades has led to detailed characterization of its protein and mineral constituents. Recently, our understanding of this process has been significantly improved using high-throughput technologies (i.e., proteomics, transcriptomics, genomics, and bioinformatics). Presently, more or less complete eggshell proteomes are available for nine birds, and therefore, key proteins that comprise the eggshell biomineralization toolkit are beginning to be identified. In this article, we review current knowledge on organic matrix components from calcified eggshell. We use these data to analyze the evolution of selected matrix proteins and underline their role in the biological toolkit required for eggshell calcification in avian species. Amongst the panel of eggshell-associated proteins, key functional domains are present such as calcium-binding, vesicle-binding and protein-binding. These technical advances, combined with progress in mineral ultrastructure analyses, have opened the way for new hypotheses of mineral nucleation and crystal growth in formation of the avian eggshell, including transfer of amorphous $CaCO_3$ in vesicles from uterine cells to the eggshell mineralization site. The enrichment of multi-omics datasets for bird species is critical to understand the evolutionary context for development of $CaCO_3$ biomineralization in metazoans, leading to the acquisition of the robust eggshell in birds (and formerly dinosaurs).

Keywords: birds, eggshell, calcium carbonate biomineralization, organic matrix, multi-omics tools, evolution

OPEN ACCESS

Edited by:
Frederic Marin, Délégation Centre-Est, Center for the National Scientific Research, France

Reviewed by:
Paula Ramos-Silva, Naturalis Biodiversity Center, Netherlands
Marie Arul, Muséum National d'Histoire Naturelle, France

***Correspondence:**
Maxwell T. Hincke
mhincke@uottawa.ca

Specialty section:
This article was submitted to Evolutionary and Population Genetics, a section of the journal Frontiers in Genetics

Received: *25 February 2021*
Accepted: *08 April 2021*
Published: *11 May 2021*

Citation:
Le Roy N, Stapane L, Gautron J and Hincke MT (2021) Evolution of the Avian Eggshell Biomineralization Protein Toolkit – New Insights From Multi-Omics. Front. Genet. 12:672433. doi: 10.3389/fgene.2021.672433

INTRODUCTION

The avian eggshell is a calcitic biomineral that surrounds the telolecithal egg (i.e., possessing an uneven distribution of vitellus). The eggshell is essential to prevent desiccation during embryonic development and to regulate metabolic gas exchange. The shell is a remarkable physical barrier to protect the embryo against pathogens and mechanical shocks (Hincke et al., 2012; Gautron et al., 2021); moreover, the shell is a source of calcium for embryonic bone mineralization (Hincke et al., 2019). The egg is an autonomous source of all nutritive elements for embryo development, and therefore the unfertilized chicken egg is a high quality nutrient in the human diet. The study of the eggshell calcification process is of great importance to provide new insights into mechanisms of biomineralization, and to provide new tools to ensure the quality of the egg and its food safety for human consumption.

The oviduct is the organ of egg production in birds; it consists of six distinctly specialized segments that secrete the constituents of each egg compartment: infundibulum (vitelline membrane to enclose the egg yolk), magnum (secretion of egg white), white isthmus (elaboration of eggshell membranes), red isthmus (initiation of shell mineralization on mammillary cores), uterus (eggshell formation, cuticle deposition) and vagina (expulsion of mature egg). After ovulation of the ovocyte and its egg yolk, the egg white is secreted and deposited around the forming egg while it transits through the magnum segment. The eggshell membranes are deposited in the isthmus, and the calcitic eggshell is mineralized while it remains in the uterus (Nys et al., 2004). Eggshell mineralization takes place in an acellular uterine fluid secreted by uterine tissue, which contains mineral and organic precursors essential for shell mineralization (Gautron et al., 1997; Jonchère et al., 2012). *In vitro* crystallization tests using chicken uterine fluid have shown that this fluid strongly modifies the kinetics of calcite crystal formation and the resulting crystal morphology (Dominguez-Vera et al., 2000; Hernandez-Hernandez et al., 2008b). Finally, shell biomineralization is arrested with deposition of the phosphate-rich cuticle and the egg is laid. Eggshell mineralization follows five major stages: briefly, (1) amorphous calcium carbonate (ACC) is deposited on the entire surface of the outer eggshell membranes, which then (2) transforms into calcite at organic matrix clusters (mammillary cores); (3) calcite crystals nucleate from these sites and (4) grow rapidly with their *c*-axis becoming increasingly perpendicular to the eggshell surface. Two hours before egg expulsion, (5) mineralization is arrested and a thin layer of organic cuticle is deposited that covers the calcified layer and plugs the respiratory pores (Nys et al., 2004; Rodríguez-Navarro et al., 2015). For more detail regarding eggshell mineralization, the reader is referred to a new review by Gautron et al. (2021).

The avian eggshell is the result of an exceptional evolutionary strategy. Since the Late Devonian geological period (∼360 MYA – million years ago), the conquest of the terrestrial landscape challenged vertebrates to fulfill various vital functions such as breathing, locomotion and reproduction. Birds belong to the Sauropsida clade (that includes modern and extinct reptiles – turtles, lizards, snakes, crocodiles etc. – and birds) that appeared 315 MYA (Falcon-Lang et al., 2007). While amphibians have retained a need to lay their eggs in water, birds produce an impervious calcified barrier around the egg that they lay in terrestrial nests. Amongst laying-egg animals, birds possess the most solid eggshell; the soft-shelled eggs of turtles, lizards and snakes are less mineralized than bird eggshells, whereas crocodiles produce intermediate hard-shelled eggs (Choi et al., 2018). According to the fossil record, the first evidence of a calcified eggshell occurred at the Late Triassic/Early Jurassic, and belonged to a crocodilian (Bonaparte and Vince, 1979; Carpenter, 2000). In dinosaurs, the groups from which birds emerged, the oldest eggshells have been identified in the Early Jurassic, for which microstructural studies reveal a very thin shell (Garcia et al., 2006; Stein et al., 2019). According to numerous observations, the microstructure of dinosaur and bird eggshells is highly similar, with calcareous crystals forming an inner mammillary zone and outer palisade structure (Mikhailov, 1991). A recent study provided evidence for the independent evolution of calcified eggs in dinosaurs, with soft-shelled eggs as the ancestral character and the occurrence of at least three hard-shelled egg events (Norell et al., 2020).

Much knowledge of eggshell biomineralization has been obtained from studies utilizing the chicken egg. For decades, a combination of physical and biological approaches has led to increased understanding of this process. Microscopies (SEM and TEM), infrared and Raman spectroscopies, and X-ray diffraction have characterized the mineral phase (Rodríguez-Navarro et al., 2015; Pérez-Huerta and Dauphin, 2016; Choi et al., 2019). Protein purification, immunochemistry (Western blotting, colloidal gold immunocytochemistry) and proteomics were essential to identify occluded organic matrix constituents (Hincke et al., 2012; Gautron et al., 2021). Hundreds of proteins have been identified in eggshell proteomes from a small number of species (**Table 1**). Amongst this protein cortege, major functions have been assigned such as calcium-binding, matrix-organization, antimicrobial function, and so on (Marie et al., 2015a). The present review aims to describe six major proteins that have been identified as key actors in eggshell mineralization: Ovocalyxin-32 (OCX-32), Ovocalyxin-36 (OCX-36), Ovocleidin-116 (OC-116), Osteopontin (OPN), EGF (epidermal growth factor)-like repeats and discoidin domains 3 (EDIL3), and Ovocleidin-17 and its homologs (OC-17 and XCA). These six proteins possess essential functions (antimicrobial properties, regulation of $CaCO_3$ crystallization or vesicular transport of ACC) and are present in significant abundance to be considered as major members of the eggshell biomineralization toolkit (**Figure 1**); it is likely that they were recruited during evolutionary acquisition of eggshell formation.

AVIAN EGGSHELL: AN EXCEPTIONAL VERTEBRATE CALCIUM CARBONATE BIOMINERAL

The bird eggshell is a remarkable bioceramic that demonstrates exceptional mechanical properties; the eggshell appeared in the last common ancestor of amniotes around 326 MYA

TABLE 1 | List of eggshell proteomes and the presence of transcriptome/genome in bird and reptile species.

Species	Common name	Eggshell proteins	Uterine transcriptome/genome	Proteome references
Neognathae → Galloanserae				
Gallus gallus	Chicken	904	Yes/yes	Mann et al., 2006; Marie et al., 2015a
Meleagris gallopavo	Turkey	697	No/yes	Mann and Mann, 2013
Numida meleagris	Guinea fowl	154	Yes/no	Le Roy et al., 2019
Coturnix japonica	Japanese quail	622	Yes/yes	Mann and Mann, 2015
Anas platyrhynchos	Mallard duck	484	Yes/yes	Zhu et al., 2019
Neognathae → Neoaves				
Taeniopygia guttata	Zebra finch	475	No/yes	Mann, 2015
Palaeognathae				
Struthio camelus	Common ostrich	2	No/yes	Mann and Siedler, 2004
Dromaius novaehollandiae	Emu	2	No/yes	Mann and Siedler, 2006
Rhea americana	Greater rhea	2	No/yes	Mann and Siedler, 2006
Crocodilia				
Crocodylus siamensis	Siamese crocodile	58	No/no	Mikšík et al., 2018

Hundreds of proteins have been identified in eggshell proteomes in a small number of species. The presence of uterine transcriptome characterization and/or genome annotation in these species was checked in NCBI databases.

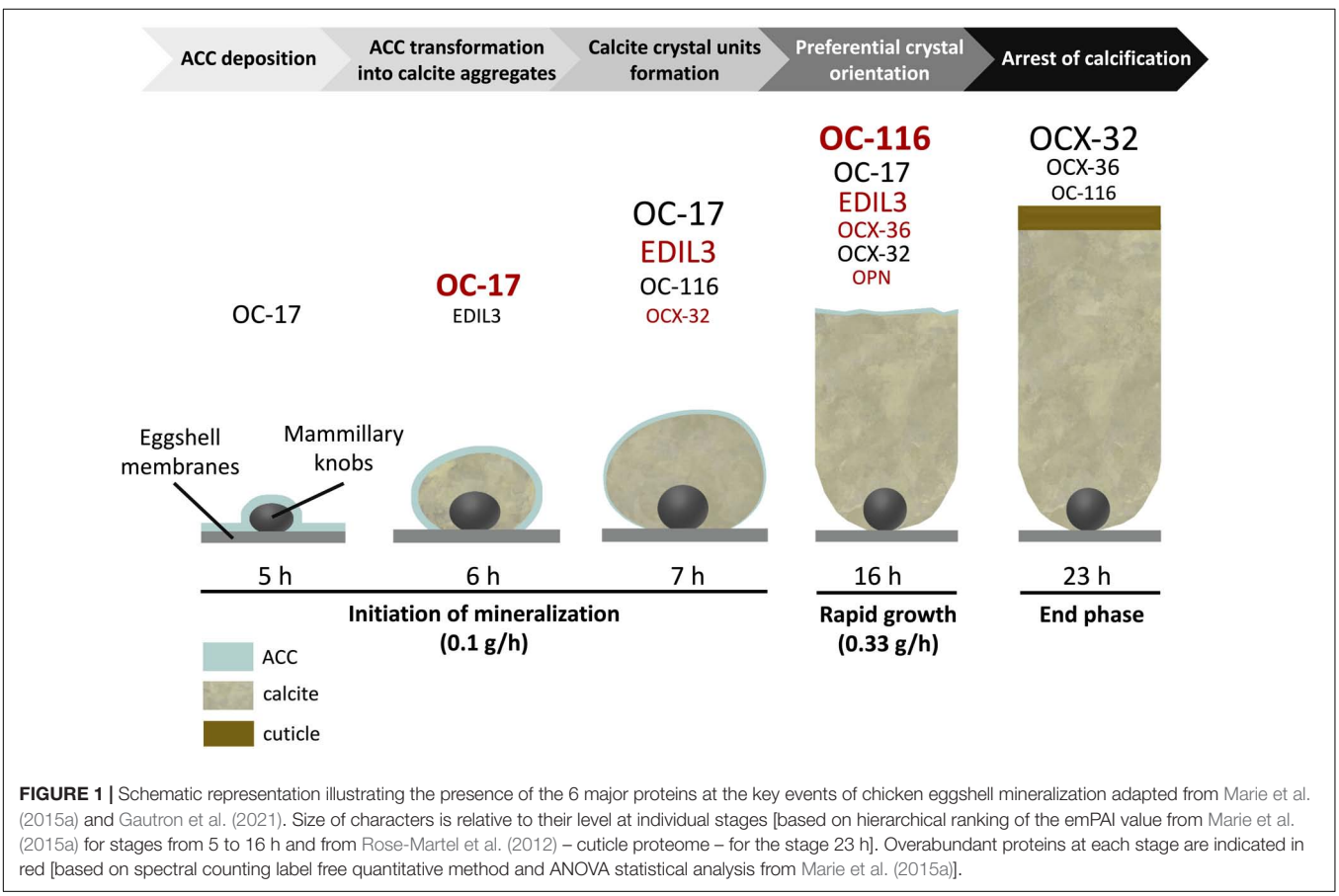

FIGURE 1 | Schematic representation illustrating the presence of the 6 major proteins at the key events of chicken eggshell mineralization adapted from Marie et al. (2015a) and Gautron et al. (2021). Size of characters is relative to their level at individual stages [based on hierarchical ranking of the emPAI value from Marie et al. (2015a) for stages from 5 to 16 h and from Rose-Martel et al. (2012) – cuticle proteome – for the stage 23 h]. Overabundant proteins at each stage are indicated in red [based on spectral counting label free quantitative method and ANOVA statistical analysis from Marie et al. (2015a)].

(Blair and Hedges, 2005; Ford and Benson, 2020). Across various bird species, eggshell strength is positively correlated with egg weight (Ar et al., 1979). Guinea fowl shows an elevated strength (**Figure 2**), which is related to its unique shell texture (Pérez-Huerta and Dauphin, 2016). In general, calcium carbonate crystal units of the bird eggshell palisade layer are parallel to each other and grow following the c-axis, i.e., perpendicular to the eggshell membranes and eventual eggshell

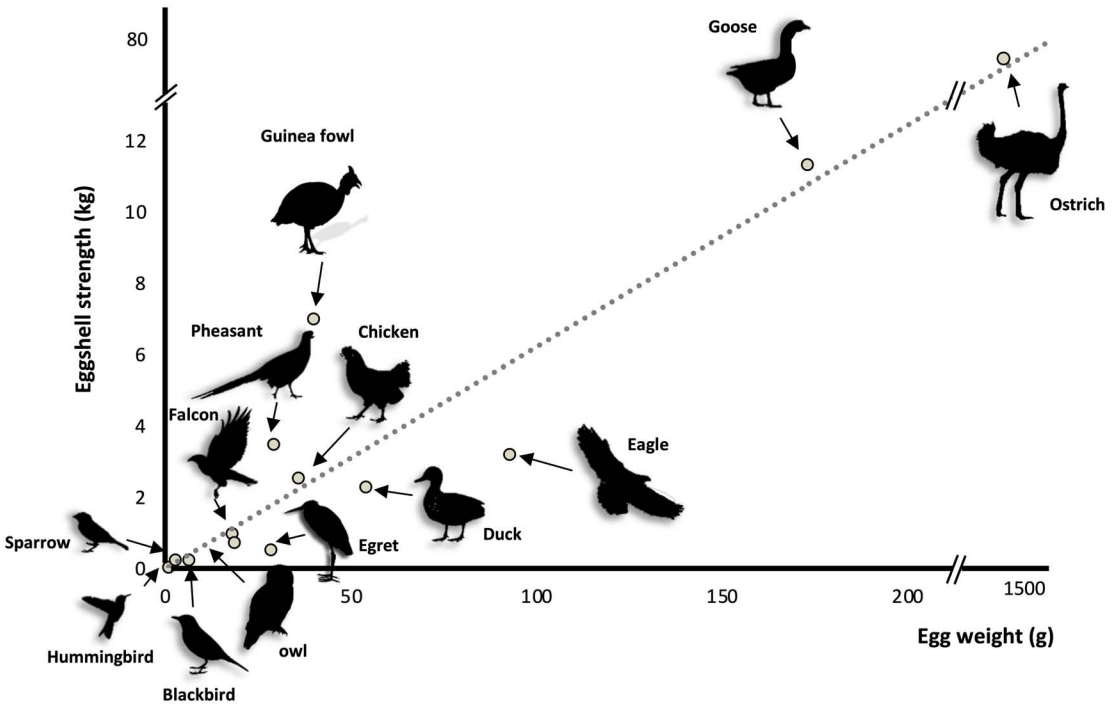

FIGURE 2 | Eggshell strength as function of egg weight in thirteen bird species [adapted from Ar et al. (1979)].

surface (Hernandez-Hernandez et al., 2008a,b; Rodríguez-Navarro et al., 2015). This organization is also observed in fossilized dinosaur eggshells (Mikhailov, 1991; Voris et al., 2018; Dawson et al., 2020). In Guinea fowl (*Numida meleagris*), the first third of deposited shell is similar in structure to that of other species, whereas the outer two-thirds are composed of smaller crystal units with varying crystallographic orientations that form an intricate interlacing pattern that greatly improves shell strength (Petersen and Tyler, 1966; Panheleux et al., 1999a; Song et al., 2000; Pérez-Huerta and Dauphin, 2016). These animals are endemic to Central Africa and lay their eggs on the ground. The elevated breaking strength of their eggshell is likely the result of a specific adaptation to their environment (e.g., predation). A recent microstructural study of other bird eggshells suggested that Guinea fowl is not the only avian species to demonstrate this peculiar feature, since Rhea eggshell also has a similar crystalline organization (Choi et al., 2019). Since both are ground-nesting species, it is tempting to correlate their vulnerable nest location to the interlaced crystalline organization of their strengthened eggshell, which could better protect the egg. However, in other ground-nesting species, such as ostrich, chicken, turkey, etc., the eggshell ultrastructure is columnar.

The ultrastructure, polymorph and nucleation/growth of calcium carbonate crystals are controlled by a specific macromolecular toolkit, the organic matrix (OM) (Chien et al., 2008; Hernandez-Hernandez et al., 2008a,b; Zhao et al., 2013; Gautron et al., 2019, 2021). The bird eggshell OM represents 3.5% of the total shell weight including shell membranes. In the calcified part, the OM represents 1.5–2% of the overall contents (Panheleux et al., 2000). This eggshell OM is composed of proteins and proteoglycans, and has been studied for several decades, especially in chicken, *Gallus gallus* (Leach, 1982; Hincke et al., 1995, 2012; Pines et al., 1995; Gautron et al., 1997, 2021; Nys et al., 1999; Panheleux et al., 1999b; Arias and Fernandez, 2001). Eggshell membranes are the physical support for initiation of shell formation and are composed of a collagen-rich network of fibers (Wong et al., 1984; Arias et al., 1991; Ahmed et al., 2017). As in other metazoan biomineralization systems (e.g., molluscan shell, coral exoskeleton, echinoderm skeleton, etc.), the proteins of the OM possess various functional domains that regulate the matrix organization and control mineral formation (Marie et al., 2010; Ramos-Silva et al., 2013; Gautron et al., 2021). In addition, antimicrobial activities have been identified in avian eggshell that reinforce protection of the embryo against pathogens (Wellman-Labadie et al., 2008a,b,c; Cordeiro et al., 2013; Marie et al., 2015a,b; Gautron et al., 2021). Multiple studies of the evolution of calcium carbonate biomineralization in metazoans have demonstrated that certain homologous proteins were independently recruited to support this process, such as carbonic anhydrases and C-type lectins (Blank et al., 2003; Matsubara et al., 2008; Moya et al., 2008; Le Roy et al., 2014; Voigt et al., 2014; Karakostis et al., 2016; Weber et al., 2016). In other cases, newly arisen genes became specific and essential in the biomineralization process; for instance, the *Enam* gene product (Enamelin) in mammals is involved in dental enamel mineralization. This gene either emerged in mammals after

the mammal/bird divergence or was lost in birds (Kawasaki et al., 2007). There are other examples of taxon-specific proteins involved in metazoan biomineralization, such as scleritin in the calcitic skeleton of octocorals (Conci et al., 2019; Le Roy et al., 2021), galaxin in the calcitic and aragonitic skeleton of corals (Conci et al., 2020), and pearlin in nacre of pearl oysters (Marie et al., 2011).

MULTI-OMICS: A SIGNIFICANT CONTRIBUTION TO THE IDENTIFICATION OF EGGSHELL ORGANIC MATRIX PROTEINS

In the past few years, a huge enrichment of the genomic and transcriptomic databases in Aves has widely contributed to the identification of eggshell OM proteins in diverse species. The current Ensembl database[1] contains genomes from 40 bird and 18 reptile species (**Figure 3A**), while NCBI lists genome assemblies from 507 bird (487 Neognathae and 20 Palaeognathae) and 64 reptile species. The 10,000 Genomes Project (B10K[2]) recently reported the genomes for 363 bird species including 267 new genomes, establishing a new pipeline to analyze the unprecedented scale of genomic data, and illustrating how these resources give improved resolution for genomic evolution analyses (Feng et al., 2020). The recent enrichment of genomic databases provides a critical tool for identification of bird eggshell proteome constituents by high-throughput mass spectrometry analysis (**Figure 3B**) (Mann et al., 2006, 2007a; Rose-Martel et al., 2012, 2015; Mann and Mann, 2013, 2015; Mann, 2015; Marie et al., 2015a; Gautron, 2019; Gautron et al., 2019, 2021; Le Roy et al., 2019; Zhu et al., 2019). Accurate gene annotation is critical to support proteomic approaches. For example, more than 1,300 chicken eggshell protein sequences with different identifiers were aligned to eliminate all redundancies; with this approach, 904 unique proteins were identified in the eggshell layers including membranes and cuticle (Gautron, 2019; Gautron et al., 2019). Another integrated analysis of chicken eggshell matrix enumerated a total of 676 eggshell matrix proteins in the mineralized shell (Yang et al., 2020). Additional bird eggshell proteomes have been studied quite extensively, identifying 697, 622, 475, and 484 proteins in the mineralized eggshell of turkey (*Meleagris gallopavo*), quail (*Coturnix japonica*), zebra finch (*Taeniopygia guttata*) and mallard (*Anas platyrhynchos*) eggshells, respectively (Mann and Mann, 2013, 2015; Mann, 2015;

[1]http://www.ensembl.org/index.html
[2]https://b10k.genomics.cn/index.html

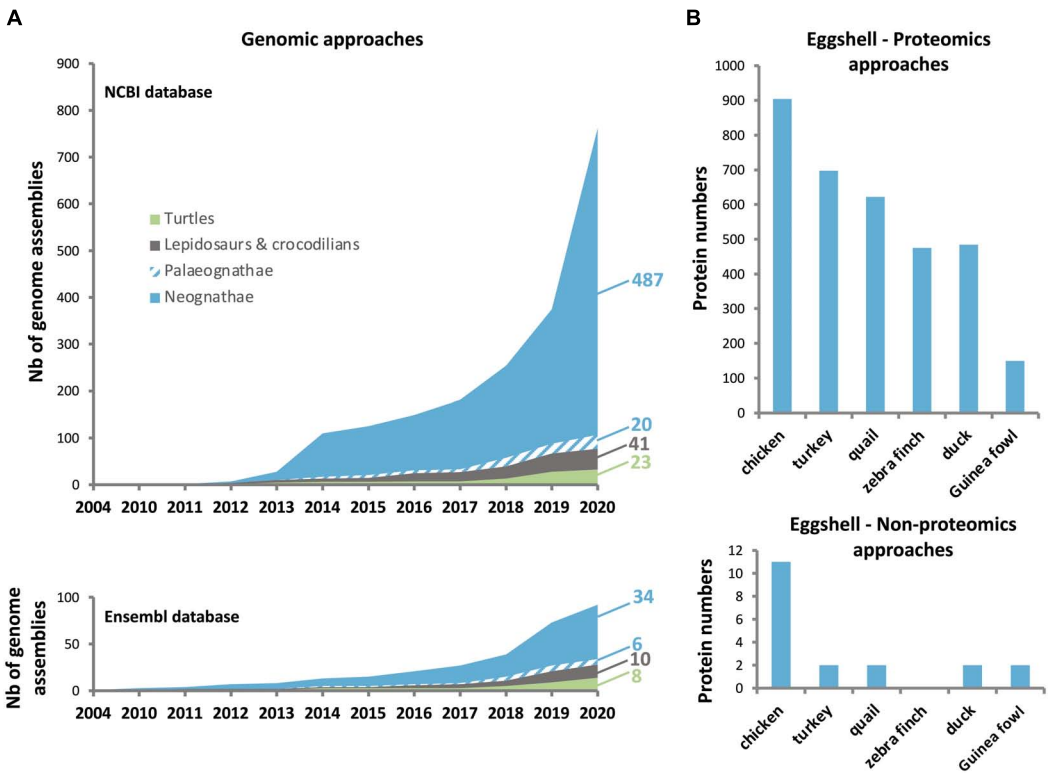

FIGURE 3 | Number of genomes sequenced in birds and reptiles, and the proteins identified in eggshell of different avian species. **(A)** Increase in number of bird and reptile genomes available in NCBI (upper: https://www.ncbi.nlm.nih.gov/), and Ensembl (lower: http://www.ensembl.org/index.html) databases since the chicken genome assembly in 2004. **(B)** Number of identified proteins using proteomics (upper) and non-proteomics (lower) approaches. Data were compiled from Hincke et al. (1995, 1999), Panheleux et al. (1999b), Gautron et al. (2001, 2007),Mann et al. (2006), Mann and Mann (2013, 2015), Mann (2015), Marie et al. (2015a), Zhu et al. (2019), and Le Roy et al. (2019).

Zhu et al., 2019), and 149 proteins in the entire eggshell of Guinea fowl (*Numida meleagris*) (Le Roy et al., 2019). This low number of identified proteins in Guinea fowl eggshell is possibly due to incomplete annotation of its genome (NumMel1.0.).

The next section will describe the evolutionary context for six major proteins that have been identified as key actors in chicken eggshell mineralization (OCX-36, OCX-32, OC-116, OPN, EDIL3, and OC-17/XCA).

VERTEBRATE PROTEINS RECRUITED IN THE EGGSHELL BIOMINERALIZATION PROCESS

Ovocalyxin-32: An Antimicrobial Protein That Influences Eggshell Quality

Ovocalyxin-32 (OCX-32) was originally identified in chicken as an eggshell-specific protein, and its gene is highly expressed in the uterus and the isthmus regions of the oviduct (Gautron et al., 2001). This last study localized OCX-32 in the outer shell (outer palisade layer, the vertical crystal layer and the cuticle). Proteomic analyses revealed abundant OCX-32 in the uterine fluid during the initial phase of mineralization, and its relative enrichment in the palisade region of the eggshell (Marie et al., 2015b,a). OCX-32 was also identified in the proteome of the insoluble fraction of the chicken eggshell organic matrix (Mikšík et al., 2007). OCX-32 possesses 32% identity with mammalian carboxypeptidase inhibitors, latexin and the retinoic acid receptor-responder 1 (RARRES1). Recombinant OCX-32 inhibited bovine carboxypeptidase and the growth of *Bacillus subtilis* (Xing et al., 2007), suggesting an antimicrobial role for OCX-32 in providing protection to the developing avian embryo. Proteomic analysis of the chicken eggshell cuticle demonstrated that OCX-32 is one of the most abundant constituents of this non-mineralized region, and could play a major role in the antimicrobial properties of the cuticle (Rose-Martel et al., 2012; Bain et al., 2013). Polymorphisms in the gene coding for OCX-32, *RARRES1* (gene synonym*: OCX32*), are significantly associated with egg production traits (Uemoto et al., 2009; Romé and Le Roy, 2016). In another study, the quantitative trait loci (QTLs) on chromosome 9 were investigated in an F2 generation that was an intercross between two chicken lines divergently selected for eggshell strength (Takahashi et al., 2010). *RARRES1/OCX32* was identified as a candidate gene influencing eggshell quality (e.g., egg weight, egg dimensions and eggshell weight), and *RARRES1*/*OCX32* SNPs (single-nucleotide polymorphisms) are associated with eggshell quality and mammillary knob layer thickness (Dunn et al., 2008). Trait association studies of non-synonymous SNPs also revealed a significant effect of OCX-32 on shell color in white egg lines and line-specific significant effects on albumen height, early egg weight, puncture score, and yolk weight (Fulton et al., 2012).

Recent proteomics analyses failed to identify OCX-32 in the turkey and quail eggshell (Mann and Mann, 2013, 2015). Nevertheless, in addition to the chicken eggshell organic matrix, this protein has been identified in the eggshell proteome of zebra finch, Guinea fowl and mallard duck (Mann, 2015; Le Roy et al., 2019; Zhu et al., 2019). Synteny analysis of the *RARRES1/OCX32* gene using NCBI database, demonstrates that it is homologous from fishes to mammals (**Figure 4**), suggesting a common ancestor in vertebrates. In addition, the chromosomal location of the *RARRES1/OCX32* gene is highly conserved in a syntenous gene locus from fishes to mammals (**Figure 4**). Therefore, while OCX-32 is highly conserved and may be an important member of the eggshell mineralization toolkit, it does not appear to be present in all eggshell proteomes, nor is it unique to calcium carbonate biomineralizing organisms.

The LBP/BPI/PLUNC Family Protein, Ovocalyxin-36

Ovocalyxin-36 (OCX-36) is a protein belonging to the bactericidal/permeability-increasing (BPI), lipopolysaccharide-binding proteins (LBP), and palate, lung and nasal epithelial clone (PLUNC) protein family (Chiang et al., 2011; Krasity et al., 2011; Baron et al., 2013). OCX-36 was first identified in the chicken eggshell; expression of its gene was detected in the uterus and to a lesser degree in red isthmus, which are located where eggshell mineralization occurs (Gautron et al., 2007). This protein is detected in uterine fluid and throughout the entire eggshell, especially at the inner part of the shell and at the mammillary layer (Gautron et al., 2007; Mikšík et al., 2007). Purification of OCX-36 revealed its antimicrobial activity against *Staphylococcus aureus,* and ability to bind lipopolysaccharide (LPS) from *Escherichia coli* and *S. aureus* lipoteichoic acid (LTA) (Cordeiro et al., 2013). These results support the proposed involvement of OCX-36 in the innate immune response, similar to other homologous members of the BPI/LBP/PLUNC family (Gautron et al., 2007, 2011). The OCX-36 protein sequence is composed of two lipid-binding domains BPI1 (BPI/LBP/CETP N-terminal domain) and BPI2 (BPI/LBP/CETP C-terminal domain) of about 200 amino acids each (**Supplementary Figure 1**) (Gautron et al., 2007). OCX-36 was initially thought to be eggshell-specific since this protein was first identified in chicken eggshell membranes and eggshell organic matrix. However, in addition to the distal oviduct, it is also expressed in the chicken intestine (Gautron et al., 2007; Tian et al., 2010; Chiang et al., 2011).

The BPI/LBP/PLUNC protein family belongs to the TULIP (tubular lipid-binding) superfamily, which split into two groups before the last eukaryote common ancestor: SMP-like proteins (synaptotagmin-like, mitochondrial and lipid-binding proteins) and BPI-like proteins (Alva and Lupas, 2016). The BPI/LBP/PLUNC family is only present in animals (Alva and Lupas, 2016). Indeed, members of this gene family are found in both vertebrate and invertebrate species (Solstad et al., 2007; Chiang et al., 2011; Krasity et al., 2011). In vertebrates, although 20–30% of amino acid identity was observed between chicken OCX-36 and other BPI family B proteins (also called LPLUNCs) (**Supplementary Table 1**), the similar organization of exons/introns in members of this gene family strongly suggests a common origin by multiple duplication events (Gautron et al., 2007; Tian et al., 2010). Synteny analysis of this gene family

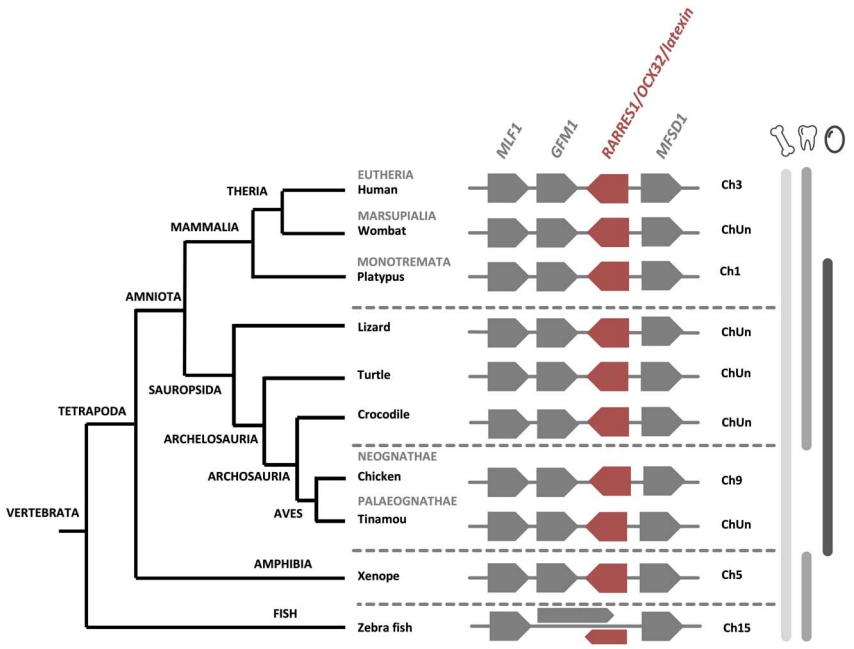

FIGURE 4 | Synteny of *RARRES1/OCX32* genes in vertebrates. The *RARRES1/OCX32* gene is represented by a red box and the flanking genes *MLF1* (myeloid leukemia factor 1), *GFM1* (G elongation factor mitochondrial 1) and *MFSD1* (major facilitator superfamily domain containing 1) are represented by gray boxes. ChUn, chromosome unknown. Gene IDs are listed in **Supplementary Table 2**. The left part of the figure depicts the phylogenetic relationship between vertebrate species (adapted from www.tolweb.org and Kapusta et al., 2017).

confirms a common ancestor for the genes encoding chicken OCX-36, *BPIFB3* (gene synonym: *OCX36*) and other *BPI family B* members (Tian et al., 2010; Gautron et al., 2011) (**Figure 5** and **Supplementary Table 1**). Since these previous analyses were performed, substantial new genomic and transcriptomic data has enriched this story. The synteny presented in **Figure 5** shows the presence of a *BPIFB3*/*OCX36* orthologous gene in reptiles (turtle and alligator), and other bird species from Palaeognathae (kiwi), Neoaves (zebra finch), and Galloanserae (duck). In addition, analysis of the platypus genome (*Ornithorhynchus anatinus*), an egg-laying mammal (Monotremata), reveals the presence of *BPIFB4-like* gene at the same location as *BPIFB3/OCX36* in birds and reptiles (**Figure 5**). Identity and similarity levels are higher between platypus BPIFB4-like and chicken OCX-36 than between chicken OCX-36 and other chicken BPIFB paralogs (**Supplementary Table 1**), suggesting that platypus BPIFB4-like is the ortholog of avian OCX-36. Phylogenetic analysis of OCX-36 and its relatives shows a first cluster containing chicken OCX-36, BPIFB4-like from other birds, OCX-36-like from reptiles and BPIFB4-like from platypus (**Figure 6**). This cluster, in addition to the results of synteny analysis, strongly suggests that all these genes are orthologs of chicken OCX-36. These new inputs expand the presence of *BPIFB3/OCX36* orthologous genes to Archelosauria (turtles, crocodiles, and birds) and Monotremata (egg-laying mammals) phyla. Finally, these new insights invalidate the previous hypothesis that *BPIFB3*/*OCX36* arose after the divergence of birds and mammals (Tian et al., 2010; Chiang et al., 2011; Gautron et al., 2011). The phylogenetic tree coupled with synteny strongly support that *BPIFB3*/*OCX36* appeared before the divergence of birds and mammals, which was likely lost in therian mammals (placentals and marsupials) (**Figures 5**, **6**). This phylogeny indicates that another member, *TENP* (transiently expressed in neural precursors), is the oldest gene in the BPI/LBP/LPLUNC family, and that the *BPIFB3/OCX36* gene is the result of three duplication events before tetrapod diversification and one event in amniotes.

New support for the specificity of OCX-36 protein orthologs to eggshell should be sought by investigation of diverse eggshell proteomes such as ratites, reptiles and monotremes. In the shell proteome of a crocodilian egg, an OCX-36 ortholog was not identified, but, as in birds, its paralog TENP-like is present in the shell organic matrix (Mann et al., 2006; Mikšík et al., 2018). In chicken, TENP is also found in egg white, vitelline membranes and egg yolk (Guérin-Dubiard et al., 2006; Mann, 2007; D'Ambrosio et al., 2008; Mann and Mann, 2008; Farinazzo et al., 2009). Apparently, TENP was recruited to the egg immune system in birds, while mammalian orthologs, BPIL1/BPIFB2/LPLUNC2, were recruited in ORL (olfactory epithelium, larynx, and tongue) tissue immunity (Andrault et al., 2003).

Co-option of SIBLING Bone Proteins, Osteopontin (OPN/SPP1) and Ovocleidin-116 (OC-116/MEPE) in Eggshell Biomineralization

OPN is a phosphoprotein (SPP1, secreted phosphoprotein 1, is the mammalian ortholog) found in both avian bone and

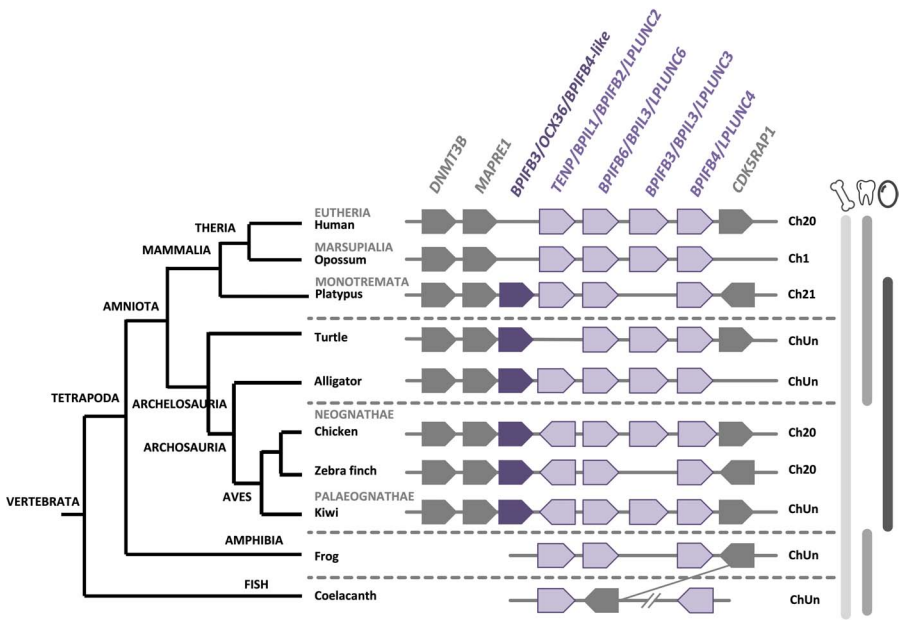

FIGURE 5 | Synteny of *BPIFB3/OCX36* genes in birds and its relatives in vertebrates. The *BPIFB3/OCX36* gene is represented by a dark purple box and its relatives are represented by light purple boxes. Flanking genes DNA (cytosine-5)-methyltransferase 3B (*DNMT3B*), Microtubule-associated protein RP/EB family member 1 (*MAPRE1*) and Mitochondrial tRNA methylthiotransferase (*CDK5RAP1*) are represented by gray boxes. ChUn, chromosome unknown. Gene IDs are listed in **Supplementary Table 2**. The left part of the figure depicts the phylogenetic relationship between vertebrate species (adapted from www.tolweb.org and Kapusta et al., 2017).

eggshell, as well as a variety of other tissue and cell types (Moore et al., 1991; Pines et al., 1995; Sodek et al., 2000; Fernandez et al., 2003; Chien et al., 2009; Hincke et al., 2012). In mice, OPN is strongly implicated in bone remodeling and fracture healing (McKee et al., 2011). In chicken, the oviduct expression of the OPN gene (*SPP1*) is entirely uterine-specific and is temporally associated with eggshell calcification through mechano-transcriptomic coupling of physical distension of the uterine wall to *SPP1* expression (Pines et al., 1995; Lavelin et al., 1998). Moreover, unusual patterns of uterine *SPP1* expression are associated with eggshell mineralization defects (Arazi et al., 2009). Localization by colloidal gold immunocytochemistry shows that OPN is concentrated in the palisade layer of the eggshell, where it is associated with parallel protein sheets of organic matrix, and more diffusely with the (104) crystallographic faces of eggshell calcite (Chien et al., 2008, 2009; Hincke et al., 2008). Specific OPN binding to the growing (104) crystal face during mineralization could modify the resistance of the shell to fracture along this plane. A functional interaction between OPN and the (104) eggshell calcite faces was supported by *in vitro* studies where synthetic calcite crystal growth at the (104) face was inhibited by added OPN (Chien et al., 2008). Nanoindentation and atomic force microscopy measurements suggest that OPN influences eggshell hardness and nanostructure, which in turn control the mechanical properties of the shell (Athanasiadou et al., 2018). SNPs in chicken *SPP1* are associated with eggshell fracture toughness (Dunn et al., 2009; Romé and Le Roy, 2016), which supports a regulatory role for OPN in mineralization. From fishes to mammals, OPN possesses a poly-aspartate motif, which is able to bind calcium and mediates binding to the mineral surface (**Supplementary Figure 2**; Sodek et al., 2000; Athanasiadou et al., 2018; Weber, 2018). However, in birds and reptiles, the OPN protein sequence exhibits a unique feature, a histidine-rich region that is suspected to originate from a microbial gene *via* a horizontal gene transfer event in early reptiles (**Supplementary Figure 2**; Weber, 2018). In mollusk shell, perlinhibin is a histidine-rich protein that inhibits calcium carbonate crystallization (Mann et al., 2007b), suggesting that this motif in eggshell OPN could play a similar calcite-specific role. In addition to the histidine-rich region, the C-terminal region is different between reptiles and non-reptilian vertebrates. In reptiles, the C-terminus is highly conserved, which supports a specialization of this protein with an important functional role in this vertebrate group (**Supplementary Figure 2**).

Ovocleidin-116 (OC-116; MEPE, matrix extracellular phosphoglycoprotein, is the mammalian ortholog) is a major component of the chicken uterine fluid, and is the most abundant matrix protein in the eggshell (Hincke et al., 1999; Mann et al., 2002, 2006; Marie et al., 2015a). It is an eggshell dermatan sulfate proteoglycan, which also possesses two *N*-glycosylated sites as well as *N*-glycan structures with fucosylated LacdiNAc (Nimtz et al., 2004). Immunostaining of the decalcified eggshell demonstrated the presence of OC-116 throughout the palisade layer and in the mammillary cone layer (Hincke et al., 1999). OC-116 is present in both soluble and insoluble fractions of the chicken eggshell matrix (Mann et al., 2002, 2006; Mikšík et al., 2007). Proteomics studies have identified OC-116 in the eggshell of chicken, turkey, quail, mallard duck and Guinea fowl, where

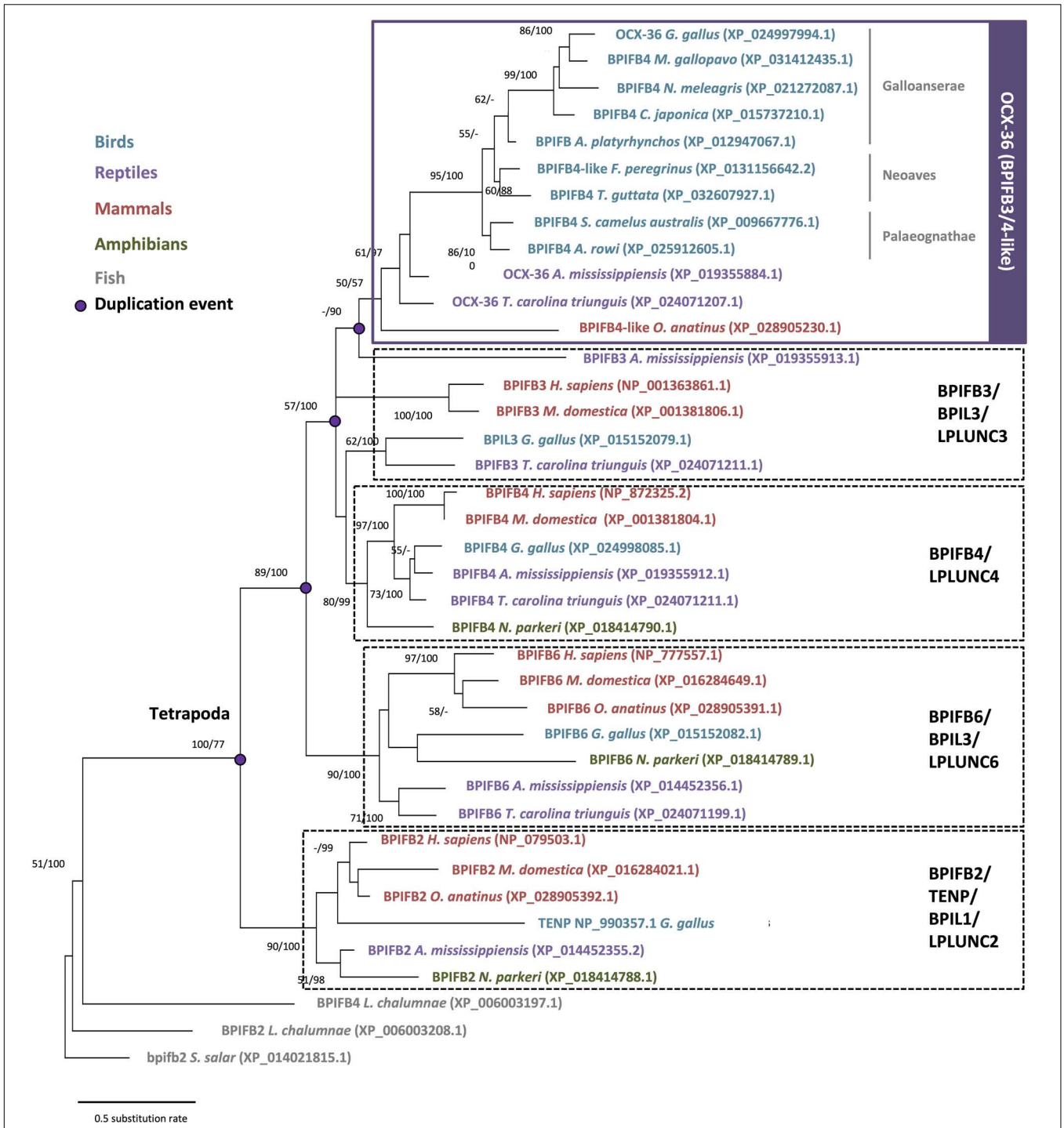

FIGURE 6 | Phylogenetic reconstruction of OCX-36 and its orthologs and paralogs in vertebrates. For phylogeny multiple alignment was performed using ClustalW and Gblocks (www.phylogeny.fr). Model of protein evolution used is JTT + G (MEGAX v10.1.8; https://www.megasoftware.net/). Topology of the tree corresponds to maximum likelihood method with 100 repetitions (MEGAX v10.1.8). Bootstrap values from maximum likelihood/Bayesian inference are indicated at each node when value is >50.

it is one of the most abundant eggshell constituent (Mann and Mann, 2013, 2015; Marie et al., 2015a; Le Roy et al., 2019; Zhu et al., 2019). In addition to the eggshell, OC-116 was reported in the chicken cortical and medullary bone (Horvat-Gordon et al., 2008). SNP analysis revealed that the *MEPE/OC116* gene is associated with shell thickness, elastic modulus and egg shape

(Dunn et al., 2009; Romé and Le Roy, 2016). The mammalian ortholog MEPE is involved in bone and teeth mineralization (Bardet et al., 2010a). Inactivation of the *Mepe* gene in mouse causes an increase in bone mass and mineralization due to an increase in osteoblast number and activity (Gowen et al., 2003). The role of OC-116/MEPE in mineralization is supported by the ASARM (acidic serine-aspartate rich MEPE-associated motif) sequence located at the C-terminus of the protein. When ASARM is phosphorylated, it inhibits mineralization by binding to hydroxyapatite crystals (Addison et al., 2008). This peptide is also involved in phosphatemia regulation (Rowe et al., 2004). Multiple sequence alignment of OC-116/MEPE proteins shows a high conservation of the ASARM peptide throughout tetrapods (**Figure 7**). The presence of numerous putative phosphorylation sites (7 in bird orthologs) suggests that its role in mineralization is also conserved in both bone and eggshell.

Both OPN/SPP1 and OC-116/MEPE belong to the SIBLING (small integrin-binding ligand N-linked glycoprotein) family, with three other protein members: integrin-binding sialoprotein (IBSP), dentin sialophosphoprotein (DSPP) and dentin matrix protein 1 (DMP1). Genes coding for these five proteins are clustered together through tetrapods (**Figure 8A**), and they all have a role in biomineralization (Rowe, 2012); however, none of them appears to be specific to calcium carbonate (eggshell) or calcium phosphate (bone, teeth) mineralization. They possess similar molecular properties such as integrin-binding and calcium-binding (Bardet et al., 2010b). Among the five SIBLING members, OPN and OC-116 have been widely studied in the chicken eggshell, as described above. Moreover, DMP1 and IBSP were detected in the eggshell matrix (by proteomics and Western blotting), and their genes are expressed in uterine tissue (Mann et al., 2006; Horvat-Gordon et al., 2008); however, *DSPP* gene, involved in dentin formation, was secondarily lost in ancestors of birds during late Cretaceous when they become toothless (**Figure 8A**) (Kawasaki and Weiss, 2008; Sire et al., 2008; Mcknight and Fisher, 2009; Kawasaki, 2011; Sire and Kawasaki, 2012). It has been suggested that the entire SIBLING gene family, including OC-116/MEPE and OPN/SPP1, which were initially involved in bone formation, was co-opted for the eggshell calcium carbonate mineralization process in birds (Sire and Kawasaki, 2012). In the phylogenetic reconstruction of OC-116 and OPN, the distribution of both proteins follows the accepted phylogenetic relationships in tetrapods, with a clear split between mammals and reptiles including birds (**Figures 8B,C**). In the Aves clade, Palaeognathae is the basal group; while in Neognathae, Neoaves sequences are well separated from Galloanserae for OPN, and from Galliformae for OC-116. In the recent crocodilian eggshell proteome, OC-116 was identified but not OPN (Mikšík et al., 2018), suggesting the recruitment of OC-116, at least for eggshell mineralization, in the Archosauria linage (Aves and Crocodylia). In seven turtle species and platypus (*O. anatinus*, the only monotreme genome in NCBI database), although gene coding for SPP1 is present, synteny analysis reveals the absence of *MEPE/OC116* from the SIBLING locus (**Figure 8A**), which implies a loss of this gene in these two lineages.

The Glycoprotein EDIL3: A Novel Candidate for Calcium Carbonate Delivery in Eggshell Mineralization

The glycoprotein EDIL3 (EGF-like repeats and discoidin domains 3) was identified in the chicken eggshell by proteomics analysis (Mann et al., 2006; Marie et al., 2015a). The EDIL3 sequence contains three EGF-like domains and two F5/8C (discoidin) domains; it was first identified as an extracellular matrix protein involved in embryonic vascular development in mouse (Hidai et al., 1998). The three EGF-like domains are present in EDIL3 orthologs in all vertebrates except in fishes (Stapane et al., 2019), and the third domain possesses a calcium-binding site, which suggests a potential role of EDIL3 in calcium carbonate crystallization (Marie et al., 2015a). In addition, an RGD (arginine, glycine, and aspartate) motif is present in the second EGF-like domain, through which it can bind integrins (Stapane et al., 2019). Integrins are transmembrane proteins involved in cell-cell and cell-extracellular matrix interactions, and vesicular trafficking (Théry et al., 1999; Hynes, 2002; Gatti et al., 2005; Bridgewater et al., 2012). The second F5/8C domain exhibits a phospholipid-binding site, which give to the protein the ability to complex vesicle and/or cell membranes (**Supplementary Figure 3A**; Stapane et al., 2019). In the EDIL3 sequence of some bird species (*G. gallus*, *A. platyrhynchos*, *Aquila chrysaetos*, *Dromaius novaehollandiae*, etc.), the first EGF-like domain also contains an RGD motif suggesting an even higher affinity of the protein for integrins (**Supplementary Figure 3B**). Proteomics demonstrate the presence of EDIL3 in bird and crocodile eggshell (Marie et al., 2015a; Mikšík et al., 2018; Le Roy et al., 2019). However, in the eggshell proteome of *Crocodylus siamensis*, EDIL3 protein was identified with six peptides matching with EDIL3 from *Alligator mississippiensis* (NCBI accession KYO21076.1) (Mikšík et al., 2018). Surprisingly, amongst the six peptides, only one matched with a domain present in EDIL3 proteins (first F5/8C domain); however, the five other peptides matched with the IG-like (immunoglobulin-like) and LINK_2 domain (hyaluronan-binding region) that is found in HAPLN1 (hyaluronan and proteoglycan link protein 1). Moreover, the annotated *A. mississippiensis* EDIL3 protein is 843 aa in length instead of about 480 aa for the other EDIL3 proteins, and seems to be composed of both EDIL3 and HAPLN1 protein features (**Supplementary Figure 3C**). Indeed, the N-terminal part of alligator EDIL3 shows 53.8% of identity with chicken EDIL3 and the C-terminal part of alligator EDIL3 possesses 54.3% of identity with chicken HAPLN1. These contradictions indicate that the potential identification of the EDIL3 ortholog in crocodilian eggshell requires confirmation (**Supplementary Figure 3**). In chicken, EDIL3 is not an eggshell-specific protein, although it exhibits a high relative abundance in the shell OM (Marie et al., 2015a). According to the emPAI (exponentially modified protein abundance index) values of proteins from chicken eggshell proteome at four calcification stages, EDIL3 is the fifth most abundant protein at the early stages of biomineralization, corresponding to the transformation of ACC into calcite crystals (Marie et al., 2015a).

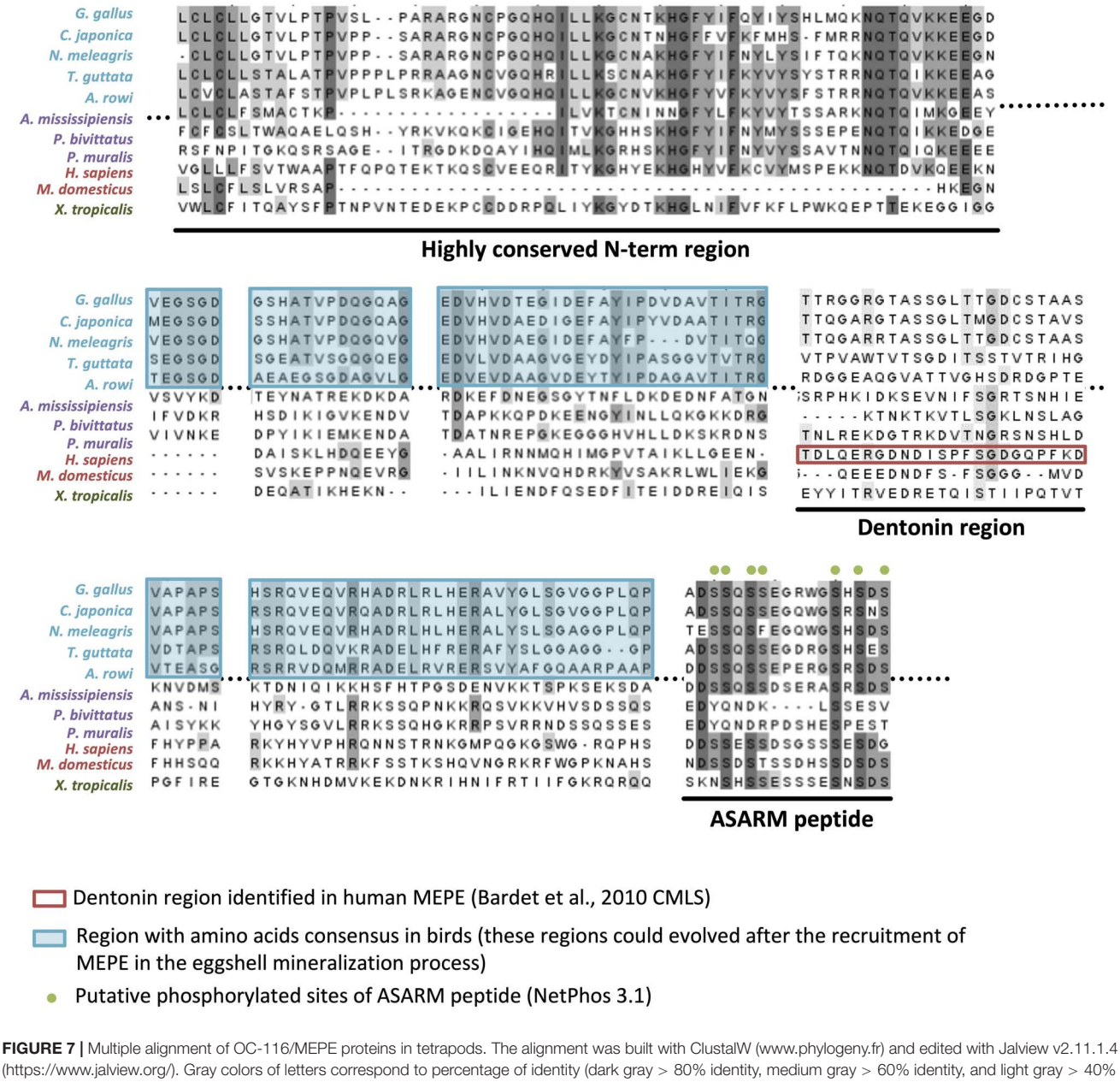

FIGURE 7 | Multiple alignment of OC-116/MEPE proteins in tetrapods. The alignment was built with ClustalW (www.phylogeny.fr) and edited with Jalview v2.11.1.4 (https://www.jalview.org/). Gray colors of letters correspond to percentage of identity (dark gray > 80% identity, medium gray > 60% identity, and light gray > 40% identity). The dentonin region identified in human MEPE, and regions with amino acid consensus in birds, are, respectively, framed in red and blue. Putative phosphorylated sites of the ASARM (acidic, serine, and aspartic acid-rich motif) peptide are indicated by green dots above the alignment. Sequences aligned are from *Gallus gallus* (AAF00982.3), *Coturnix japonica* (XP_015716951.1), *Numida meleagris* (XP_021251779.1), *Taeniopygia guttata* (XP_030127798.1), *Apteryx rowi* (XP_025920573.1), *Alligator mississippiensis* (XP_019343676.1), *Python bivittatus* (XP_025029286.1), *Podarcis muralis* (XP_028598766.1), *Homo sapiens* (XP_006714341.1), *Monodelphis domestica* (XP_007495981.1), and *Xenopus tropicalis* (XP_002938672.2).

In chicken, *EDIL3* gene expression is up-regulated in isthmus and uterus compared with bone, duodenum, kidney, liver and magnum, and is significantly higher in the oviduct segments at early stages (6 and 7 h post-ovulation, initiation of mineralization) than at 16 h post-ovulation (mid-calcification) (Stapane et al., 2019, 2020). Immunohistochemistry in uterine cross-sections confirms the presence of high levels of EDIL3 at the early stages of mineralization in tubular gland cells (5 and 6 h post-ovulation) (Stapane et al., 2020). Moreover, proteomics and Western blot analyses revealed the presence of EDIL3 in extracellular vesicles isolated from chicken uterine fluid (Stapane et al., 2019, 2020). These vesicles are proposed to mediate the transportation of ACC to the mineralization site. Indeed, vesicles have been demonstrated to play roles in ACC stabilization in invertebrate biomineralization models such as sea urchins, molluscan shell and coral skeleton (Levi-Kalisman et al., 2002;

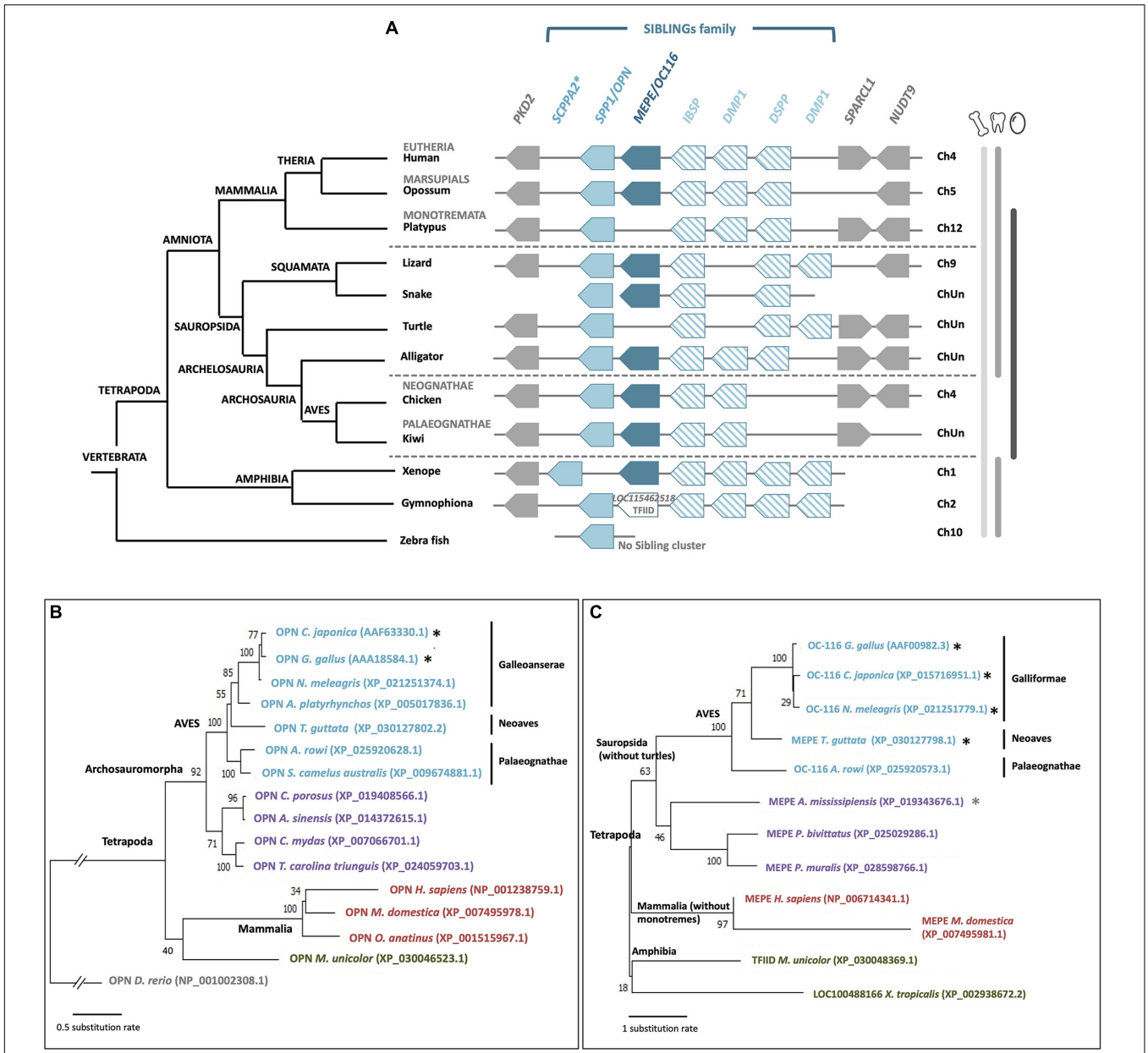

FIGURE 8 | Synteny and phylogeny of *OPN/SPP1* and *MEPE/OC116* genes and corresponding proteins in vertebrates. **(A)** *OPN/SPP1* is represented by a light blue box and *MEPE/OC116* is represented by a dark blue box. The other SIBLING genes are integrin-binding sialoprotein (*IBSP*), dentin sialophosphoprotein (*DSPP*) and dentin matrix protein 1 (*DMP1*), which are represented by empty boxes with oblique blue lines. In Gymnophiona (amphibian), instead of *MEPE* we observed the presence of the transcription initiation factor TFIID subunit 1-like gene (*LOC115462518*, XP_030048369.1). Flanking genes are polycystin 2 (*PKD2*), SPARC-like 1 (*SPARCL1*) and nudix hydrolase 9 (*NUDT9*), which are represented by gray boxes. ChUn: Chromosome Unknown. Blue asterisk indicates that *SCPPA2* is a hypothetical ortholog of *spp1* (Kawasaki, 2011). Gene IDs are listed in **Supplementary Table 2**. In the left part, the phylogenetic tree for vertebrate species is represented (adapted from www.tolweb.org and Kapusta et al., 2017). **(B)** Phylogeny of OPN/SPP1 in vertebrates, which was reconstructed using multiple alignment performed with ClustalW and Gblocks (www.phylogeny.fr) and JTT + G model of protein evolution (MEGAX v10.1.8; https://www.megasoftware.net/). Topology of the tree corresponds to maximum likelihood method (MEGAX v10.1.8). Bootstrap values from maximum likelihood are indicated at each node. The symbol//indicates a gap of 0.8 substitution rate to add to the basal branch. Black asterisks indicate species where the protein was identified in the eggshell. **(C)** Phylogenetic reconstruction of OC-116/MEPE in vertebrates was performed using multiple alignment constructed with ClustalW and Gblocks (www.phylogeny.fr) and JTT + G + F model of protein evolution (MEGAX v10.1.8). Topology of the tree corresponds to maximum likelihood method (MEGAX v10.1.8). Bootstrap values from maximum likelihood are indicated at each node. Black asterisks indicate species where the protein was identified in the eggshell and the gray asterisk indicates a related species (*C. siamensis*) where the protein was identified in the eggshell.

Addadi et al., 2003; Weiner and Dove, 2003; Mass et al., 2017). In chicken uterus samples examined by transmission electron microscopy, extracellular vesicles are observed in uterine cells and fluid, and vesicles are seen budding from cells into the uterine lumen. Energy-dispersive electron spectroscopy and selected area electron diffraction revealed the presence of ACC in extracellular vesicles purified from the uterine fluid (Stapane et al., 2020). Based on these and other results, extracellular vesicles are proposed to play a role in ACC-mediated calcification of the eggshell. EDIL3 is proposed to bind vesicle membrane (phospholipid-binding site/integrin-binding site) and to guide these vesicles from uterine cell cytosol to the mineralization site (calcium-binding site/integrin-binding site) in the uterine fluid of chicken (Stapane et al., 2019, 2020).

The gene *EDIL3* is highly conserved in vertebrates (**Supplementary Figure 4**) (Stapane et al., 2019). The flanking genes in this locus are versican (*VCAN*) and hyaluronan and proteoglycan link protein 1 (*HAPLN1*). Phylogenetic analysis of EDIL3 and its paralog MFGE8 in animals demonstrates the appearance of both proteins after a duplication event in vertebrates 480 MYA (Stapane et al., 2019). EDIL3 was subsequently recruited to the eggshell mineralization process, at least in the Aves phylum. Interestingly, its paralog MFGE8 is also detected in the eggshell proteome of birds; however, its abundance is much lower than EDIL3, and *MFGE8* expression is not specific to tissues responsible for eggshell mineralization or to the initial stages of mineralization (Stapane et al., 2019).

A PROTEIN SPECIFIC TO THE EGGSHELL BIOMINERALIZATION PROCESS

C-Type Lectin Proteins in Eggshell Organic Matrix: Ovocleidin-17 Homologs

The C-type lectin protein Ovocleidin-17 (OC-17) is an eggshell-specific protein, which was first purified and partially sequenced from the chicken eggshell (Hincke et al., 1995). The mRNA sequence was determined only recently by *de novo* transcriptomic assembly (Zhang et al., 2014). OC-17 contains a C-type lectin (CTL) domain and possesses two phosphorylated serine residues (Mann, 1999; Mann and Siedler, 1999). The CTL proteins are a huge family of proteins including at least seven subgroups such as hyalectans, asialoglycoprotein receptors, collectins, selectins, natural killer group transmembrane receptors, macrophage mannose receptors and simple lectins (Zelensky and Gready, 2005). OC-17 and its homologs correspond to a simple lectin, with a short amino acid sequence (about 150 aa) and only one CTL domain. Proteomics analysis demonstrated that OC-17 is a highly abundant protein in the eggshell matrix in chicken and Guinea fowl (Marie et al., 2015a; Le Roy et al., 2019). Moreover, CTL proteins that are homologs of OC-17 have been identified in eggshells of many bird species, including ostrich, emu, and rhea (Mann and Siedler, 2004, 2006). In each of these ratites, two homologous CTL eggshell proteins were identified and named according to the bird species: Struthiocalcin-1 and 2 (SCA-1 and -2) for ostrich, Dromaiocalcin-1 and -2 (DCA-1 and -2) for emu and Rheacalcin-1 and -2 (RCA-1 and -2) for rhea. For easier reading in the present review, we have termed these proteins XCA-1 and XCA-2. In contrast, only one CTL protein (OC-17) is present in chicken eggshell, which aligns with the XCA-2 group of other bird species.

C-type lectin proteins have been identified in the biomineralization process of invertebrates. For instance, in the sea urchin *Strongylocentrotus purpuratus*, SM50 is a protein containing a C-type lectin domain in addition to glycine-rich and proline-rich regions. The study of this C-type lectin domain revealed that it influences the biomineralization of $CaCO_3$ (Rao et al., 2013). In the same manner, in the freshwater pearl mussel, a C-type lectin protein called perlucin, already identified in the shell proteomes of mollusks, is involved in nacre formation (Lin et al., 2013). Purified OC-17 modifies calcite crystallization *in vitro* (Reyes-Grajeda et al., 2004). *In silico* molecular dynamics simulations suggest three protein configurations of OC-17, which is able to bind calcium carbonate surfaces through its positively charged guanidino group of specific arginine residues (Freeman et al., 2010, 2011). Thus, CTL proteins could play a role in eggshell formation by binding to specific calcite crystal faces (Wallace and Schiffbauer, 2016). In addition, chicken OC-17 and its goose ortholog (ansocalcin) exhibit an antimicrobial activity, and could play a potential role in innate immunity of the avian embryo (Wellman-Labadie et al., 2008a). Although the presence of one versus two OC-17 paralogs in the eggshell of Palaeognathae birds has been proposed to correlate with eggshell thickness (Mann and Mann, 2015), there is currently no experimental evidence to support this hypothesis.

Synteny, protein multiple alignment and phylogenetic analysis of XCA-1, XCA-2 and OC-17-like confirm that XCA-2 is ortholog to OC-17-like and XCA-1 is paralog to OC-17-like/XCA-2 (**Figures 9**, **10**, and **Supplementary Figure 5**). OC-17-like and XCAs are also similar to other vertebrate C-type lectin (CTL) proteins, such as REG4 (Regenerating Islet-derived protein 4) and Lithostathine (also known as REG1A and REG1B) in humans. REG1 is a pancreatic CTL protein involved in the inhibition of $CaCO_3$ precipitation in the bicarbonate-rich pancreatic juice (Bernard et al., 1992). The gene encoding REG1/Lithostathine is not found in the genome of reptiles and birds, whereas *REG4* is present in numerous bird and crocodilian species. The OC-17-like/XCAs gene symbol in reptiles and birds is different for each species (i.e., *LOC numbers*; **Supplementary Table 3**); in order to simplify our discussion, we use the arbitrary nomenclature *OC17-like/XCA2* and *XCA1*. Synteny analysis shows that the *REG4* gene is located on a different chromosome than the *OC17-like/XCA2* and *XCA1* gene locus (e.g., in tufted duck *REG4* is located on chromosome 8 and *OC17-like/XCA2* and *XCA1* are located on chromosome 1; **Figure 9**). *REG4* is flanked by the same genes in crocodiles, birds and in mammals, but it is absent in turtles and lepidosaurs (lizards, snakes, etc.) at the same locus. On the other hand, *OC17-like/XCA2* and/or *XCA1* genes are clustered together and flanked by the same genes in birds and reptiles; however, they are absent from the same locus in mammalian and amphibian genomes. These data support the hypothesis that OC-17-like/XCA-2 and XCA-1 are eggshell specific proteins and that

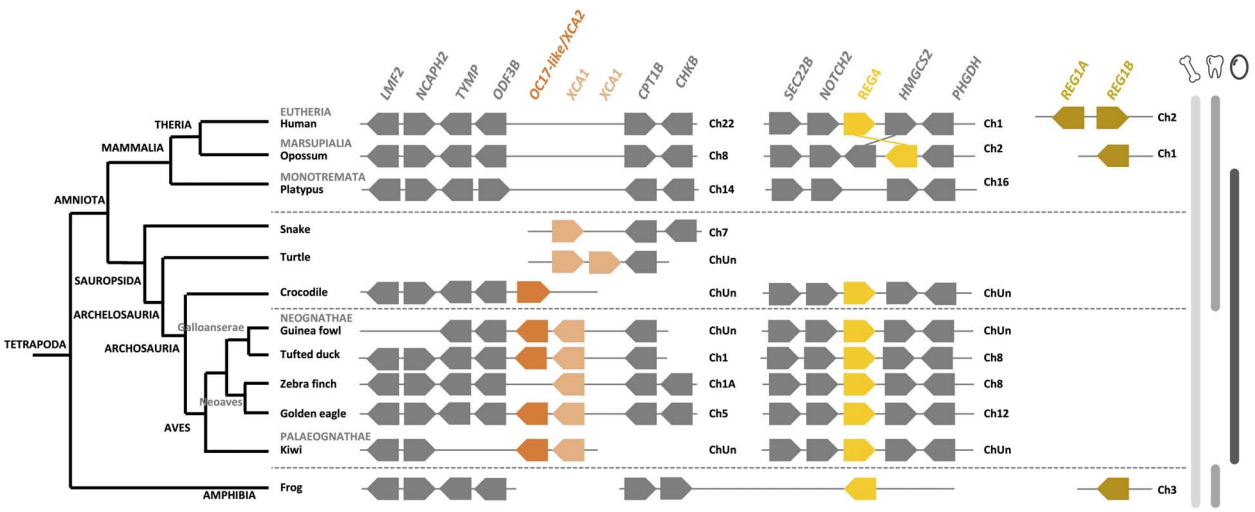

FIGURE 9 | Synteny of *OC17-like*, *XCA* and *REG* orthologs and paralogs in birds and its relatives in vertebrates. *OC17-like/XCA2* is represented by a dark orange box and *XCA1* by a light orange box. *REG4* (regenerating Islet-derived protein 4) is represented by a yellow box and *REG1 A* and *B* (Lithostathine) are represented by a brown box. Flanking genes are represented by gray boxes: lipase maturation factor 2 (*LMF2*), condensing-2 complex subunit H2 (*NCAPH2*), thymidine phosphorylase (*TYMP*), outer dense fiber protein 3B (*ODF3B*), carnitine *O*-palmitoyltransferase 1 (*CPT1B*), choline/ethanolamine kinase (*CHKB*), vesicle-trafficking protein (*SCE22B*), neurogenic locus notch homolog protein 2 (*NOTCH2*), hydroxymethylglutaryl-CoA synthase (*HMGCS2*) and D-3-phosphoglycerate dehydrogenase (*PHGDH*). Gene IDs are listed in **Supplementary Table 2**. The left part of the figure depicts the phylogenetic relationship between vertebrate species (adapted from www.tolweb.org and Kapusta et al., 2017).

these genes are specific to vertebrates that produce a calcitic shell; however, no ortholog has yet been identified in the crocodilian eggshell proteome (Mikšík et al., 2018). Deeper investigation needs to be done in crocodilian eggshells, but also in other reptile eggshells (e.g., snakes, lizards, and turtles), in order to determine if OC-17-like/XCA-2 and/or XCA-1 are widespread in reptile and bird eggshells or if they strictly correspond to the bird eggshell biomineralization process.

The pairwise alignment of chicken REG4 and OC-17 amino acid sequences exhibits 29.2% identity (58.4% similarity), which supports a common origin of both proteins (**Supplementary Table 4**). Phylogenetic reconstruction shows that REG4 and OC-17-like/XCAs are divided into two distinct groups (**Figure 10**). Regarding these observations, the phylogeny indicates that OC-17-like/XCAs arose from a duplication event in Sauropsida. In this clade, squamates (lizards and snakes) are in basal position with only one form of XCA. Then, three groups split: bird OC-17-like/XCA-2 (including crocodilian XCA-2), turtle XCA-1 and bird XCA-1 (**Figure 10**). The synteny of *OC17-like/XCA2* and *XCA1* shows that duplication of the ancestral gene occurred on the same chromosome and the phylogeny suggests that *XCA1* is closer to the ancestral form of the duplicated gene. These observations might indicate that *OC17-like/XCA2* is the result of a duplication event in archosaurs with a loss of *XCA1* in crocodilians. In turtles, two *XCA1* paralogs are also present but they are clustered together suggesting an independent duplication event in the turtle phylum.

In birds, XCA paralogs are present in both Neognathae (Neoaves and Galloanserae), and Palaeognathae (ratites) phyla. Nevertheless, in Neognathae, each bird species does not possess the two paralogs inside sub groups. In Neoaves we notice that only XCA-1 is present in common starling (*Sturnus vulgaris*), falcons (*Falco cherrug* and *Falco rusticolis*) and zebra finch (*Taeniopygia guttata*), whereas both paralogs are present in golden eagle (*A. chrysaetos chrysaetos*) (**Supplementary Figure 6**). In Galloanserae, some species exhibit one paralog such as chicken (*G. gallus*) and pheasant (*Phasianus colchicus*) (Mann et al., 2006; Marie et al., 2015a), for which the genome position is unknown. Conversely, other Galloanserae species possess both paralogs such as Guinea fowl, black swan (*Cygnus atratus*) and tufted duck (*Athya fuligula*) (**Supplementary Figure 6**) (Le Roy et al., 2019). The mallard duck eggshell proteome demonstrated the presence of an ortholog to chicken OC-17 protein (Zhu et al., 2019), which may correspond to mallard SCA-2-like protein translated from the newly submitted (December 2020) mallard genome in NCBI (Accession XP_038024161.1; Gene ID: 119713911). In this genome, the gene coding for SCA-2-like is located next to RCA-1-like (Gene ID: 119713283) in the same gene cluster containing *OC17-like/XCA2* and *XCA1*, as observed in other birds (**Figure 9** and **Supplementary Figure 6**). In Palaeognathae, both paralogs are present in emu, ostrich and rhea eggshells, but in two *Apteryx* species (kiwis), for which eggshell proteomes are not available, one species exhibits two adjacent paralogs and the other species has only one paralog in its genome (**Supplementary Figure 6**). Nevertheless, the lack of genome data (gene sequencing and scaffolding genome assembly) is possibly the reason for the absence of the second paralog in all these species of birds, crocodilian etc. Indeed, the chicken OC-17 transcript has a very high GC content (72.17%), which could account for the observed difficulty to sequence this gene in the chicken genome

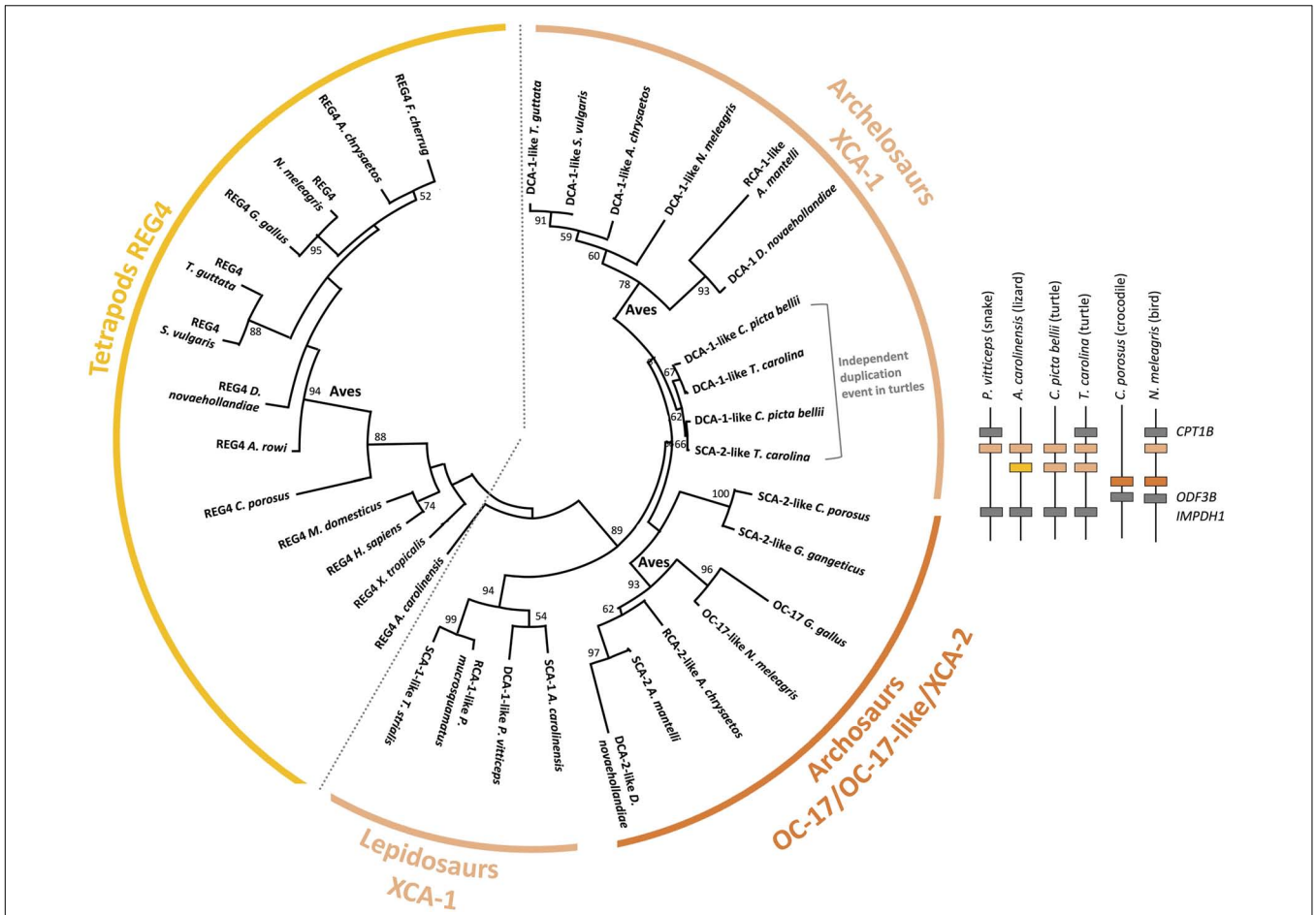

FIGURE 10 | Phylogenetic reconstruction of OC-17 and its orthologs and paralogs in vertebrates. Phylogeny was performed using the maximum likelihood method with 100 repetitions (MEGAX v10.1.8; https://www.megasoftware.net/) using ClustalW multiple alignment and Gblocks (www.phylogeny.fr), and the WAG + G model of protein evolution. Bootstrap values from maximum likelihood are indicated at each node when value is >50. Synteny of *OC-17-like/XCA-2* and *XCA-1* genes is represented for five reptilian species (*Pogona vitticeps*, *Anolis carolinensis*, *Chrysemys picta bellii*, *Terrapene carolina triunguis,* and *Crocodylus porosus*) and one bird (*Numida meleagris*).

and in genome projects of other bird species. Hence, this lack of *OC17-like/XCAs* annotation in bird genomes reduces the possibility to identify orthologous OC-17 peptides using proteomics approaches. This is the case in turkey and quail eggshell proteomes (Mann and Mann, 2013; Mann, 2015). In the Guinea fowl, OC-17-like (71.56% GC) and DCA-1-like (72.01% GC) were detected in its eggshell proteome, likely because the genome assembly of *Numida meleagris* that is available in the NCBI database (NumMel1.0) was built using the *G. gallus* genome.

EVOLUTION OF ORGANIC MATRIX PROTEINS IN EGGSHELL BIOMINERALIZATION

During amniote evolution, reproduction was freed from reliance on the aquatic environment with the emergence of two possible reproductive strategies: egg-laying vs. placentation. In sauropsids and some mammals (Monotremata), the egg-laying strategy was based on a soft or hard-shelled egg to protect the embryo. This adaptation has reached its most advanced development in birds that emerged 102 MYA. The avian eggshell proteome exhibits both co-opted proteins and eggshell-specific proteins. Over the last several decades, the development of high-throughput technologies has helped to characterize and enumerate the complexity of the organic matrices in multiple avian species. The evolution of the eggshell reproductive strategy in sauropsids was accompanied by (1) the recruitment of existing genes for eggshell biomineralization (OCX-32, EDIL3, OC-116/MEPE, and OPN), and (2) the birth of new genes from duplication events, which are highly specialized for this process (XCA-1 and OCX-36; **Figure 11**). It is intriguing that avian OPN orthologs appear to have acquired a His-rich domain which may be related to calcitic biomineralization. Therefore, insight into the common eggshell toolkit which is responsible for eggshell mineralization in birds is emerging.

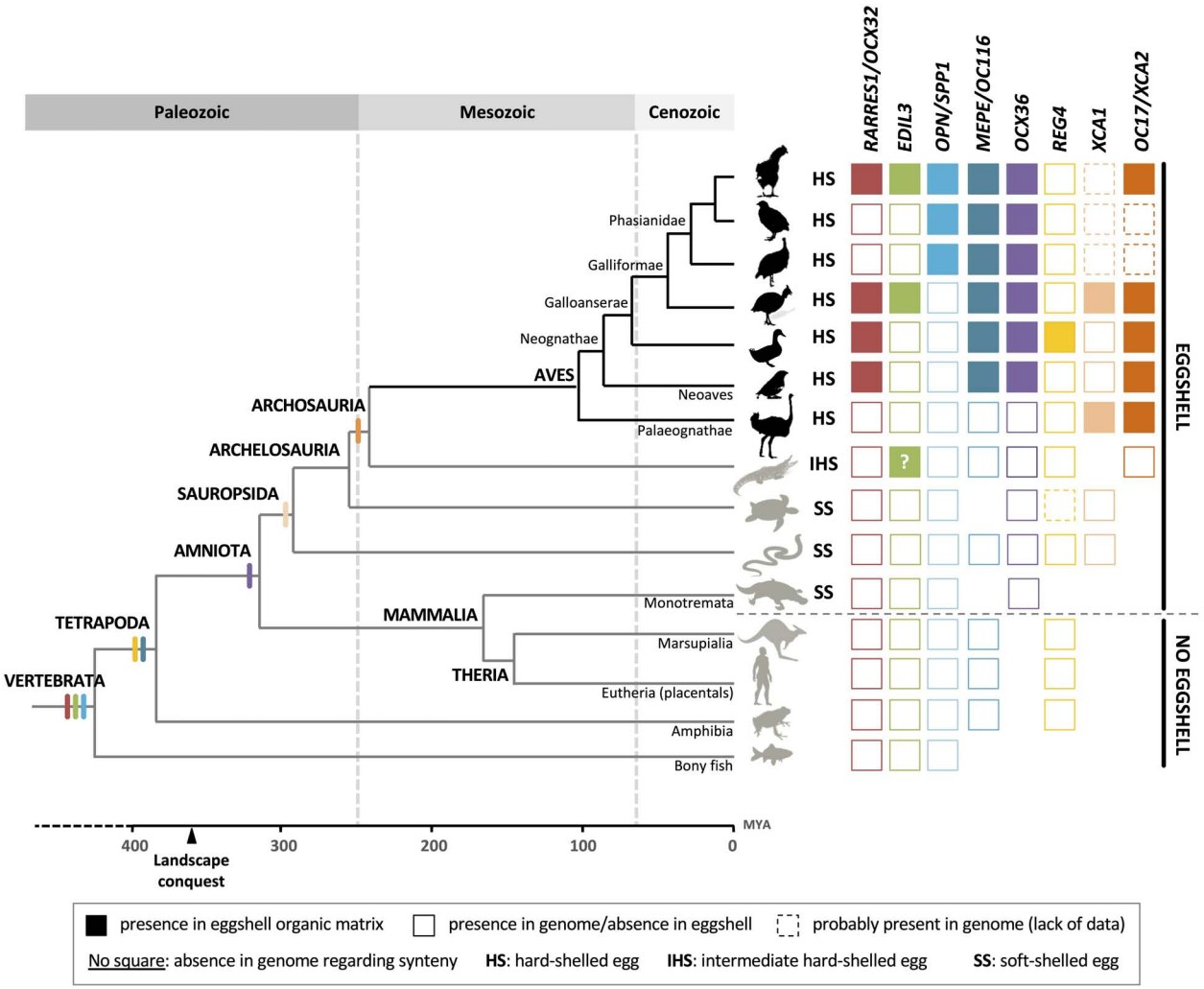

FIGURE 11 | Schematic summary of the presence of genes encoding investigated proteins in vertebrate genomes and the identification of their related proteins in Sauropsida eggshells. Filled squares indicate the presence of the protein in eggshell organic matrix whereas empty squares indicate the presence in genome but the absence in eggshell. Squares with a dotted line indicate a putative presence in genome (lack of data). The absence of square in the figure illustrates an absence in genome with respect to synteny. The "?" in the crocodilian EDIL3 square indicates the uncertainty of true identification of this protein in the crocodilian eggshell proteome (see **Supplementary Figure 3**). Genomic data can come from different species inside the same apical group. The divergent times and topology of the tree are from (www.tolweb.org; Warren et al., 2008; Phillips et al., 2009; Shen et al., 2011; Jarvis et al., 2014; Kapusta et al., 2017).

The huge outpouring of genomic data for bird species from the Bird 10,000 Genomes Project (2015–2020) is of vital importance to better understand the evolution of genes coding for eggshell proteins inside Aves (Palaeognathae vs. Neognathae; Neoaves vs. Galloanserae). In addition, this genomic database enrichment is crucial for future eggshell proteome studies in other bird groups (especially in Palaeognathae, for which only 2 proteins – the paralogs XCA-1 and XCA-2 – have yet been identified in the eggshell organic matrix). Finally, in order to enrich the evolutionary perspective, expanded analysis of eggshell proteomes should be performed in several reptilian species for which genomic/transcriptomic dataset are available, and in monotreme species such as platypus. Although the only crocodilian eggshell proteome exhibits common proteins with bird eggshell proteomes, it suffers from a very low number of identified proteins (58 against 904 for the chicken eggshell proteome), likely due to the absence of genomic/transcriptomic data for this species and incomplete annotation of genomic datasets of other crocodilians. And finally, the eggshell matrix databases must be enriched with post-translational modification (PTM) information, especially phosphorylation and glycosylation, which will permit cross-species comparisons for further insight. Currently, this information only exists in a comprehensive manner for the chicken eggshell phospho-proteome (Mann et al., 2007a).

This review identifies challenges and proposes new strategies to better understand the evolution of eggshell biomineralization, such as the multiplication of eggshell proteomics analyses in

basal birds (ratites), sister groups of birds (crocodiles, turtles, squamates), and in more distant groups (monotremes).

AUTHOR CONTRIBUTIONS

MH and NL coordinated writing of the manuscript and edited the review. JG and LS contributed to the manuscript, wrote part of the review, and approved the final version. All authors contributed to the article and approved the submitted version.

FUNDING

MH acknowledges funding from NSERC (RGPIN-2016-04410) and is grateful to Le STUDIUM for support during the preparation of this manuscript. He is a Le STUDIUM Research Fellow, Loire Valley Institute for Advanced Studies, Orleans-Tours, and BOA, INRAE, Centre Val de Loire, Nouzilly, France. JG thanks the Agence Nationale de la Recherche for funding (Impact project ANR-13-BSV-0007-01). The postdoctoral position of NL was funded by an Agreenskills fellowship. LS acknowledges the University of Tours and the "Region Centre" for financial support during his doctoral thesis.

SUPPLEMENTARY MATERIAL

The Supplementary Material for this article can be found online at: https://www.frontiersin.org/articles/10.3389/fgene.2021.672433/full#supplementary-material

REFERENCES

Addadi, L., Raz, S., and Weiner, S. (2003). Taking advantage of disorder: amorphous calcium carbonate and its roles in biomineralization. *Adv. Mater.* 15, 959–970. doi: 10.1002/adma.200300381

Addison, W. N., Nakano, Y., Loisel, T., Crine, P., and McKee, M. D. (2008). MEPE-ASARM peptides control extracellular matrix mineralization by binding to hydroxyapatite: an inhibition regulated by PHEX cleavage of ASARM. *J. Bone Miner. Res.* 23, 1638–1949. doi: 10.1359/jbmr.080601

Ahmed, T. A. E., Suso, H. P., and Hincke, M. T. (2017). In-depth comparative analysis of the chicken eggshell membrane proteome. *J. Proteomics* 155, 49–62. doi: 10.1016/j.jprot.2017.01.002

Alva, V., and Lupas, A. N. (2016). The TULIP superfamily of eukaryotic lipid-binding proteins as a mediator of lipid sensing and transport. *Biochim. Biophys. Acta* 1861, 913–923. doi: 10.1016/j.bbalip.2016.01.016

Andrault, J. B., Gaillard, I., Giorgi, D., and Rouquier, S. (2003). Expansion of the BPI family by duplication on human chromosome 20: characterization of the RY gene cluster in 20q11.21 encoding olfactory transporters/antimicrobial-like peptides. *Genomics* 82, 172–184. doi: 10.1016/S0888-7543(03)00102-2

Ar, A., Rahn, H., and Paganelli, C. V. (1979). The avian egg: mass and strength. *Condor* 81, 331–337. doi: 10.2307/1366955

Arazi, H., Yoselewitz, I., Malka, Y., Kelner, Y., Genin, O., and Pines, M. (2009). Osteopontin and calbindin gene expression in the eggshell gland as related to eggshell abnormalities. *Poult. Sci.* 88, 647–653. doi: 10.3382/ps.2008-00387

Arias, J. L., and Fernandez, M. S. (2001). Role of extracellular matrix molecules in shell formation and structure. *Worlds. Poult. Sci. J.* 57, 353–357. doi: 10.1079/wps20010024

Arias, J. L., Fernandez, M. S., Dennis, J. E., and Caplan, A. I. (1991). The fabrication and collagenous substructure of the eggshell membrane in the isthmus of the hen oviduct. *Matrix* 11, 313–320. doi: 10.1016/S0934-8832(11)80202-7

Athanasiadou, D., Jiang, W., Goldbaum, D., Saleem, A., Basu, K., Pacella, M. S., et al. (2018). Nanostructure, osteopontin, and mechanical properties of calcitic avian eggshell. *Sci. Adv.* 4:eaar3219. doi: 10.1126/sciadv.aar3219

Bain, M. M., McDade, K., Burchmore, R., Law, A., Wilson, P. W., Schmutz, M., et al. (2013). Enhancing the egg's natural defence against bacterial penetration by increasing cuticle deposition. *Anim. Genet.* 44, 661–668. doi: 10.1111/age.12071

Bardet, C., Delgado, S., and Sire, J. Y. (2010a). MEPE evolution in mammals reveals regions and residues of prime functional importance. *Cell. Mol. Life Sci.* 67, 305–320. doi: 10.1007/s00018-009-0185-1

Bardet, C., Vincent, C., Lajarille, M. C., Jaffredo, T., and Sire, J. Y. (2010b). OC-116, the chicken ortholog of mammalian MEPE found in eggshell, is also expressed in bone cells. *J. Exp. Zool. B Mol. Dev. Evol.* 314, 653–662. doi: 10.1002/jez.b.21366

Baron, O. L., van West, P., Industri, B., Ponchet, M., Dubreuil, G., Gourbal, B., et al. (2013). Parental transfer of the antimicrobial protein LBP/BPI protects Biomphalaria glabrata eggs against oomycete infections. *PLoS Pathog.* 9:e1003792. doi: 10.1371/journal.ppat.1003792

Bernard, J. P., Adrich, Z., Montalto, G., De Caro, A., De Reggi, M., Sarles, H., et al. (1992). Inhibition of nucleation and crystal growth of calcium carbonate by human lithostathine. *Gastroenterology* 103, 1277–1284. doi: 10.1016/0016-5085(92)91516-7

Blair, J. E., and Hedges, S. B. (2005). Molecular phylogeny and divergence times of deuterostome animals. *Mol. Biol. Evol.* 22, 2275–2284. doi: 10.1093/molbev/msi225

Blank, S., Arnoldi, M., Khoshnavaz, S., Treccani, L., Kuntz, M., Mann, K., et al. (2003). The nacre protein perlucin nucleates growth of calcium carbonate crystals. *J. Microsc.* 212, 280–291. doi: 10.1111/j.1365-2818.2003.01263.x

Bonaparte, J. F., and Vince, M. (1979). El hallazgo del primer nido de dinosaurios triásicos, (*Saurischia*, *Prosauropoda*), Triásico Superior de Patagonia, Argentina. *Ameghiniana* 16, 173–182.

Bridgewater, R. E., Norman, J. C., and Caswell, P. T. (2012). Integrin trafficking at a glance. *J. Cell Sci.* 125, 3695–3701. doi: 10.1242/jcs.095810

Carpenter, K. (2000). *Eggs, Nests, and Baby Dinosaurs: A Look at Dinosaur Reproduction*. Bloomington, IN: Indiana University Press, doi: 10.5860/choice.38-4

Chiang, S. C., Veldhuizen, E. J. A., Barnes, F. A., Craven, C. J., Haagsman, H. P., and Bingle, C. D. (2011). Identification and characterisation of the BPI/LBP/PLUNC-like gene repertoire in chickens reveals the absence of a LBP gene. *Dev. Comp. Immunol.* 35, 285–295. doi: 10.1016/j.dci.2010.09.013

Chien, Y. C., Hincke, M. T., and McKee, M. D. (2009). Avian eggshell structure and osteopontin. *Cells Tissues Organs.* 189, 38–43. doi: 10.1159/000151374

Chien, Y. C., Hincke, M. T., Vali, H., and McKee, M. D. (2008). Ultrastructural matrix-mineral relationships in avian eggshell, and effects of osteopontin on calcite growth in vitro. *J. Struct. Biol.* 163, 84–99. doi: 10.1016/j.jsb.2008.04.008

Choi, S., Han, S., Kim, N. H., and Lee, Y. N. (2018). A comparative study of eggshells of gekkota with morphological, chemical compositional and crystallographic approaches and its evolutionary implications. *PLoS One* 13:e0199496. doi: 10.1371/journal.pone.0199496

Choi, S., Han, S., and Lee, Y. N. (2019). Electron backscatter diffraction (EBSD) analysis of maniraptoran eggshells with important implications for microstructural and taphonomic interpretations. *Palaeontology* 62, 777–803. doi: 10.1111/pala.12427

Conci, N., Lehmann, M., Vargas, S., and Wörheide, G. (2020). Comparative proteomics of octocoral ans cleractinian skeletomes and the evolution of coral calcification. *Genome Biol. Evol.* 12, 1623–1635.

Conci, N., Wörheide, G., and Vargas, S. (2019). New non-bilaterian transcriptomes provide novel insights into the evolution of coral skeletomes. *Genome Biol. Evol.* 11, 3068–3081. doi: 10.1093/gbe/evz199

Cordeiro, C. M. M., Esmaili, H., Ansah, G., and Hincke, M. T. (2013). Ovocalyxin-36 is a pattern recognition protein in chicken eggshell membranes. *PLoS One* 8:e84112. doi: 10.1371/journal.pone.0084112

D'Ambrosio, C., Arena, S., Scaloni, A., Guerrier, L., Boschetti, E., Mendieta, M. E., et al. (2008). Exploring the chicken egg white proteome with combinatorial peptide ligand libraries. *J. Proteome Res.* 7, 3461–3474. doi: 10.1021/pr800193y

Dawson, R. R., Field, D. J., Hull, P. M., Zelenitsky, D. K., Therrien, F., and Affek, H. P. (2020). Eggshell geochemistry reveals ancestral metabolic thermoregulation in Dinosauria. *Sci. Adv.* 6, 9361–9375. doi: 10.1126/sciadv.aax9361

Dominguez-Vera, J. M., Gautron, J., Garcia-Ruiz, J. M., and Nys, Y. (2000). The effect of avian uterine fluid on the growth behavior of calcite crystals. *Poult. Sci.* 79, 901–907. doi: 10.1093/ps/79.6.901

Dunn, I. C., Joseph, N. T., Bain, M., Edmond, A., Wilson, P. W., Milona, P., et al. (2008). Polymorphisms in eggshell organic matrix genes are associated with eggshell quality measurements in pedigree Rhode Island Red hens. *Anim. Genet.* 40, 110–114. doi: 10.1111/j.1365-2052.2008.01794.x

Dunn, I. C., Wilson, P. W., Lu, Z., Bain, M. M., Crossan, C. L., Talbot, R. T., et al. (2009). New hypotheses on the function of the avian shell gland derived from microarray analysis comparing tissue from juvenile and sexually mature hens. *Gen. Comp. Endocrinol.* 163, 225–232. doi: 10.1016/j.ygcen.2009.03.006

Falcon-Lang, H. J., Benton, M. J., and Stimson, M. (2007). Ecology of earliest reptiles inferred from basal Pennsylvanian trackways. *J. Geol. Soc.* 164, 1113–1118. doi: 10.1144/0016-76492007-015

Farinazzo, A., Restuccia, U., Bachi, A., Guerrier, L., Fortis, F., Boschetti, E., et al. (2009). Chicken egg yolk cytoplasmic proteome, mined via combinatorial peptide ligand libraries. *J. Chromatogr. A.* 1216, 1241–1252. doi: 10.1016/j.chroma.2008.11.051

Feng, S., Stiller, J., Deng, Y., Armstrong, J., Fang, Q., Reeve, A. H., et al. (2020). Dense sampling of bird diversity increases power of comparative genomics. *Nature* 587, 252–257. doi: 10.1038/s41586-020-2873-9

Fernandez, M. S., Escobar, C., Lavelin, I., Pines, M., and Arias, J. L. (2003). Localization of osteopontin in oviduct tissue and eggshell during different stages of the avian egg laying cycle. *J. Struct. Biol.* 143, 171–180. doi: 10.1016/j.jsb.2003.08.007

Ford, D. P., and Benson, R. B. J. (2020). The phylogeny of early amniotes and the affinities of *Parareptilia* and *Varanopidae*. *Nat. Ecol. Evol.* 4, 57–65. doi: 10.1038/s41559-019-1047-3

Freeman, C. L., Harding, J. H., Quigley, D., and Rodger, P. M. (2010). Structural control of crystal nuclei by an eggshell protein. *Angew. Chem. Int. Ed. Engl.* 49, 5135–5137. doi: 10.1002/anie.201000679

Freeman, C. L., Harding, J. H., Quigley, D., and Rodger, P. M. (2011). Simulations of ovocleidin-17 binding to calcite surfaces and its implications for eggshell formation. *J. Phys. Chem. C.* 115, 8175–8183. doi: 10.1021/jp200145m

Fulton, J. E., Soller, M., Lund, A. R., Arango, J., and Lipkin, E. (2012). Variation in the ovocalyxin-32 gene in commercial egg-laying chickens and its relationship with egg production and egg quality traits. *Anim. Genet.* 43, 102–113. doi: 10.1111/j.1365-2052.2012.02384.x

Garcia, G., Marivaux, L., Pélissié, T., and Vianey-Liaud, M. (2006). Earliest laurasian sauropod eggshells. *Acta Palaeontol. Pol.* 51, 99–104.

Gatti, J.-L., Métayer, S., Belghazi, M., Dacheux, F., and Dacheux, J.-L. (2005). Identification, proteomic profiling, and origin of ram epididymal fluid exosome-like vesicles. *Biol. Reprod.* 72, 1452–1465. doi: 10.1095/biolreprod.104.036426

Gautron, J. (2019). Proteomics analysis of avian eggshell matrix proteins: toward new advances on biomineralization. *Proteomics* 19, 2. doi: 10.1002/pmic.201900120

Gautron, J., Guyot, N., Brionne, A., and Réhault-Godbert, S. (2019). "Bioactive minor egg components," in *Eggs as Functional Foods and Nutraceuticals for Human Health*, ed. J. Wu (London: Royal Society of Chemistry), 259–284.

Gautron, J., Hincke, M. T., Mann, K., Panheleux, M., Bain, M., McKee, M. D., et al. (2001). Ovocalyxin-32, a novel chicken eggshell matrix protein. isolation, amino acid sequencing, cloning, and immunocytochemical localization. *J. Biol. Chem.* 276, 39243–39252. doi: 10.1074/jbc.M104543200

Gautron, J., Hincke, M. T., and Nys, Y. (1997). Precursor matrix proteins in the uterine fluid change with stages of eggshell formation in hens. *Connect. Tissue Res.* 36, 195–210. doi: 10.3109/03008209709160220

Gautron, J., Murayama, E., Vignal, A., Morisson, M., McKee, M. D., Réhault, S., et al. (2007). Cloning of ovocalyxin-36, a novel chicken eggshell protein related to lipopolysaccharide-binding proteins, bactericidal permeability-increasing proteins, and plunc family proteins. *J. Biol. Chem.* 282, 5273–5286. doi: 10.1074/jbc.M610294200

Gautron, J., Réhault-Godbert, S., Pascal, G., Nys, Y., and Hincke, M. T. (2011). Ovocalyxin-36 and other LBP/BPI/PLUNC-like proteins as molecular actors of the mechanisms of the avian egg natural defences. *Biochem. Soc. Trans.* 39, 971–976. doi: 10.1042/BST0390971

Gautron, J., Stapane, L., Le Roy, N., Nys, Y., Rodriguez-Navarro, A. J., and Hincke, M. T. (2021). Avian eggshell biomineralization: an update on its structure, mineralogy and protein tool kit. *BMC Mol. Cell Biol.* 22:11. doi: 10.1186/s12860-021-00350-0

Gowen, L. C., Petersen, D. N., Mansolf, A. L., Qi, H., Stock, J. L., Tkalcevic, G. T., et al. (2003). Targeted disruption of the osteoblast/osteocyte factor 45 gene (Of45) results in increased bone formation and bone mass. *J. Biol. Chem.* 278, 1998–2007. doi: 10.1074/jbc.M203250200

Guérin-Dubiard, C., Pasco, M., Mollé, D., Désert, C., Croguennec, T., and Nau, F. (2006). Proteomic analysis of hen egg white. *J. Agric. Food Chem.* 54, 3901–3910. doi: 10.1021/jf0529969

Hernandez-Hernandez, A., Gomez-Morales, J., Rodriguez-Navarro, A. B., Gautron, J., Nys, Y., and Garcia Ruiz, J. M. (2008a). Identification of some proteins in the process of hen eggshell formation. *Cryst. Growth Des.* 8, 4330–4339. doi: 10.1021/cg800786s

Hernandez-Hernandez, A., Vidal, M. L., Gomez-Morales, J., Rodriguez-Navarro, A. B., Labas, V., Gautron, J., et al. (2008b). Influence of eggshell matrix proteins on the precipitation of calcium carbonate (CaCO3). *J. Cryst. Growth* 310, 1754–1759. doi: 10.1016/j.jcrysgro.2007.11.170

Hidai, C., Zupancic, T., Penta, K., Mikhail, A., Kawana, M., Quertermous, E. E., et al. (1998). Cloning and characterization of developmental endothelial locus-1: an embryonic endothelial cell protein that binds the αvβ3 integrin receptor. *Genes Dev.* 12, 21–33. doi: 10.1101/gad.12.1.21

Hincke, M. T., Chien, Y.-C., Gerstenfeld, L. C., and McKee, M. D. (2008). Colloidal-gold immunocytochemical localization of osteopontin in avian eggshell gland and eggshell. *J. Histochem. Cytochem.* 56, 467–476. doi: 10.1369/jhc.2008.950576

Hincke, M. T., Da Silva, M., Guyot, N., Gautron, J., McKee, M. D., Guabiraba-Brito, R., et al. (2019). Dynamics of structural barriers and innate immune components during incubation of the avian egg: critical interplay between autonomous embryonic development and maternal anticipation. *J. Innate Immun.* 11, 111–124. doi: 10.1159/000493719

Hincke, M. T., Gautron, J., Tsang, C. P. W., McKee, M. D., and Nys, Y. (1999). Molecular cloning and ultrastructural localization of the core protein of an eggshell matrix proteoglycan, ovocleidin-116. *J. Biol. Chem.* 274, 32915–32923. doi: 10.1074/jbc.274.46.32915

Hincke, M. T., Nys, Y., Gautron, J., Mann, K., Rodriguez-Navarro, B., and McKee, M. D. (2012). The eggshell: structure, composition and mineralization. *Front. Biosci.* 17:1266–1280. doi: 10.2741/3985

Hincke, M. T., Tsang, C. P. W., Courtney, M., Hill, V., and Narbaitz, R. (1995). Purification and immunochemistry of a soluble matrix protein of the chicken eggshell (ovocleidin 17). *Calcif. Tissue Int.* 56, 578–583. doi: 10.1007/BF00298593

Horvat-Gordon, M., Yu, F., Burns, D., and Leach, R. M. (2008). Ovocleidin (OC 116) is present in avian skeletal tissues. *Poult. Sci.* 87, 1618–1623. doi: 10.3382/ps.2008-1

Hynes, R. O. (2002). Integrins: bidirectional, allosteric signaling machines. *Cell* 110, 673–687. doi: 10.1016/s0092-8674(02)00971-6

Jarvis, E. D., Mirarab, S., Aberer, A. J., Li, B., Houde, P., Li, C., et al. (2014). Whole-genome analyses resolve early branches in the tree of life of modern birds. *Science* 346, 1320–1331. doi: 10.1126/science.1253451

Jonchère, V., Brionne, A., Gautron, J., and Nys, Y. (2012). Identification of uterine ion transporters for mineralisation precursors of the avian eggshell. *BMC Physiol.* 12:10. doi: 10.1186/1472-6793-12-10

Kapusta, A., Suh, A., and Fescotte, C. (2017). Dynamics of genome size evolution in birds and animals. *Proc. Natl. Acad. Sci. U. S. A.* 114, E1460–E1469. doi: 10.1073/pnas.1616702114

Karakostis, K., Costa, C., Zito, F., Brümmer, F., and Matranga, V. (2016). Characterization of an alpha type carbonic anhydrase from Paracentrotus lividus sea urchin embryos. *Mar. Biotechnol.* 18, 384–395. doi: 10.1007/s10126-016-9701-0

Kawasaki, K. (2011). The SCPP gene family and the complexity of hard tissues in vertebrates. *Cells Tissues Organs.* 194, 108–112. doi: 10.1159/000324225

Kawasaki, K., Buchanan, A. V., and Weiss, K. M. (2007). Gene duplication and the evolution of vertebrate skeletal mineralization. *Cells Tissues Organs.* 186, 7–24. doi: 10.1159/000102678

Kawasaki, K., and Weiss, K. M. (2008). SCPP gene evolution and the dental mineralization continuum. *J. Dent. Res.* 87, 520–531. doi: 10.1177/154405910808700608

Krasity, B. C., Troll, J. V., Weiss, J. P., and McFall-Ngai, M. J. (2011). LBP/BPI proteins and their relatives: conservation over evolution and roles in mutualism. *Biochem. Soc. Trans.* 39, 1039–1044. doi: 10.1042/BST0391039

Lavelin, I., Yarden, N., Ben-Bassat, S., Bar, A., and Pines, M. (1998). Regulation of osteopontin gene expression during egg shell formation in the laying hen by mechanical strain. *Matrix Biol.* 17, 615–623. doi: 10.1016/s0945-053x(98)90112-3

Le Roy, N., Combes-Soia, L., Brionne, A., Labas, V., Rodriguez-Navarro, A. B., Hincke, M. T., et al. (2019). Guinea fowl eggshell quantitative proteomics yield new findings related to its unique structural characteristics and superior mechanical properties. *J. Proteomics* 209:103511. doi: 10.1016/j.jprot.2019.103511

Le Roy, N., Ganot, P., Aranda, M., Allemand, D., and Tambutté, S. (2021). The skeletome of the red coral *Corallium* rubrum indicates an independent evolution of biomineralization process in octocorals. *BMC Evol. Biol.* 21:1. doi: 10.1186/s12862-020-01734-0

Le Roy, N., Jackson, D. J., Marie, B., Ramos-Silva, P., and Marin, F. (2014). The evolution of metazoan α-carbonic anhydrases and their roles in calcium carbonate biomineralization. *Front. Zool.* 11:75. doi: 10.1186/s12983-014-0075-78

Leach, R. M. (1982). Biochemistry of the organic matrix of the eggshell. *Poult. Sci.* 61, 2040–2047. doi: 10.3382/ps.0612040

Levi-Kalisman, Y., Raz, S., Weiner, S., Addadi, L., and Sagi, I. (2002). Structural differences between biogenic amorphous calcium carbonate phases using X-ray absorption spectroscopy. *Adv. Funct. Mater.* 12, 43–48.

Lin, J. Y., Ma, K. Y., Bai, Z. Y., and Le Li, J. (2013). Molecular cloning and characterization of perlucin from the freshwater pearl mussel, *Hyriopsis cumingii*. *Gene* 526, 210–216. doi: 10.1016/j.gene.2013.05.029

Mann, K. (1999). Isolation of a glycosylated form of the chicken eggshell protein ovocleidin and determination of the glycosylation site. Alternative glycosylation/phosphorylation at an N-glycosylation sequon. *FEBS Lett.* 463, 12–14. doi: 10.1016/S0014-5793(99)01586-0

Mann, K. (2007). The chicken egg white proteome. *Proteomics* 7, 3558–3568. doi: 10.1002/pmic.200700397

Mann, K. (2015). The calcified eggshell matrix proteome of a songbird, the zebra finch (*Taeniopygia guttata*). *Proteome Sci.* 13, 29. doi: 10.1186/s12953-015-0086-1

Mann, K., Hincke, M. T., and Nys, Y. (2002). Isolation of ovocleidin-116 from chicken eggshells, correction of its amino acid sequence and identification of disulfide bonds and glycosylated Asn. *Matrix Biol.* 21, 383–387. doi: 10.1016/S0945-053X(02)00031-8

Mann, K., Maèek, B., and Olsen, J. V. (2006). Proteomic analysis of the acid-soluble organic matrix of the chicken calcified eggshell layer. *Proteomics* 6, 3801–3810. doi: 10.1002/pmic.200600120

Mann, K., and Mann, M. (2008). The chicken egg yolk plasma and granule proteomes. *Proteomics* 8, 178–191. doi: 10.1002/pmic.200700790

Mann, K., and Mann, M. (2013). The proteome of the calcified layer organic matrix of turkey (*Meleagris gallopavo*) eggshell. *Proteome Sci.* 11:40. doi: 10.1186/1477-5956-11-40

Mann, K., and Mann, M. (2015). Proteomic analysis of quail calcified eggshell matrix: a comparison to chicken and turkey eggshell proteomes. *Proteome Sci.* 13:22. doi: 10.1186/s12953-015-0078-1

Mann, K., Olsen, J. V., Macek, B., Gnad, F., and Mann, M. (2007a). Phosphoproteins of the chicken eggshell calcified layer. *Proteomics* 7, 106–115. doi: 10.1002/pmic.200600635

Mann, K., Siedler, F., Treccani, L., Heinemann, F., and Fritz, M. (2007b). Perlinhibin, a cysteine-, histidine-, and arginine-rich miniprotein from abalone (*Haliotis laevigata*) nacre, inhibits in vitro calcium carbonate crystallization. *Biophys. J.* 93, 1246–1254. doi: 10.1529/biophysj.106.100636

Mann, K., and Siedler, F. (1999). The amino acid sequence of ovocleidin-17, a major protein of the avian eggshell calcified layer. *Biochem. Mol. Biol. Int.* 47, 997–1007. doi: 10.1080/15216549900202123

Mann, K., and Siedler, F. (2004). Ostrich (*Struthio camelus*) eggshell matrix contains two different C-type lectin-like proteins. Isolation, amino acid sequence, and posttranslational modifications. *Biochim. Biophys. Acta.* 1696, 41–50. doi: 10.1016/j.bbapap.2003.09.006

Mann, K., and Siedler, F. (2006). Amino acid sequences and phosphorylation sites of emu and rhea eggshell C-type lectin-like proteins. *Comp. Biochem. Physiol. - B Biochem. Mol. Biol.* 143, 160–170. doi: 10.1016/j.cbpb.2005.11.003

Marie, B., Le Roy, N., Zanella-Cléon, I., Becchi, M., and Marin, F. (2011). Molecular evolution of mollusc shell proteins: insights from proteomic analysis of the eddible mussel Mytilus. *J. Mol. Evol.* 72, 531–546. doi: 10.1007/s00239-011-9451-6

Marie, B., Marie, A., Jackson, D. J., Dubost, L., Degnan, B. M., Milet, C., et al. (2010). Proteomic analysis of the organic matrix of the abalone *Haliotis* asinina calcified shell. *Proteome Sci.* 8:54. doi: 10.1186/1477-5956-8-54

Marie, P., Labas, V., Brionne, A., Harichaux, G., Hennequet-Antier, C., Rodríguez-Navarro, A. B., et al. (2015a). Quantitative proteomics provides new insights into chicken eggshell matrix protein functions during the primary events of mineralisation and the active calcification phase. *J. Proteomics* 126, 140–154. doi: 10.1016/j.jprot.2015.05.034

Marie, P., Labas, V., Brionne, A., Harichaux, G., Hennequet-Antier, C., Nys, Y., et al. (2015b). Quantitative proteomics and bioinformatic analysis provide new insight into protein function during avian eggshell biomineralization. *J. Proteomics* 113, 178–193. doi: 10.1016/j.jprot.2014.09.024

Mass, T., Giuffre, A. J., Sun, C. Y., Stifler, C. A., Frazier, M. J., Neder, M., et al. (2017). Amorphous calcium carbonate particles form coral skeletons. *Proc. Natl. Acad. Sci. U. S. A.* 114, E7670–E7678. doi: 10.1073/pnas.1707890114

Matsubara, H., Hayashi, T., Ogawa, T., Muramoto, K., Jimbo, M., and Kamiya, H. (2008). Modulating effect of acorn barnacle C-type lectins on the crystallization of calcium carbonate. *Fish. Sci.* 74, 418–424. doi: 10.1111/j.1444-2906.2008.01539.x

McKee, M. D., Pedraza, C. E., and Kaartinen, M. T. (2011). Osteopontin and wound healing in bone. *Cells Tissues Organs.* 194, 313–319. doi: 10.1159/000324244

Mcknight, D. A., and Fisher, L. W. (2009). Molecular evolution of dentin phosphoprotein among toothed and toothless animals. *BMC Evol. Biol.* 9:299. doi: 10.1186/1471-2148-9-299

Mikhailov, K. (1991). Classification of fossil eggshells of amniotic vertebrates. *Acta Palaeontol. Pol.* 36, 193–238.

Mikšík, I., Eckhardt, A., Sedláková, P., and Mikulikova, K. (2007). Proteins of insoluble matrix of avian (*Gallus Gallus*) eggshell. *Connect. Tissue Res.* 48, 1–8. doi: 10.1080/03008200601003116

Mikšík, I., Paradis, S., Eckhardt, A., and Sedmera, D. (2018). Analysis of siamese crocodile (*Crocodylus siamensis*) eggshell proteome. *Protein J.* 37, 21–37. doi: 10.1007/s10930-017-9750-x

Moore, M. A., Gotoh, Y., Rafidi, K., and Gerstenfeld, L. C. (1991). Characterization of a cDNA for chicken osteopontin: expression during bone development, osteoblast differentiation, and tissue distribution. *Biochemistry* 30, 2501–2508. doi: 10.1021/bi00223a029

Moya, A., Tambutté, S., Bertucci, A., Tambutté, E., Lotto, S., Vullo, D., et al. (2008). Carbonic anhydrase in the scleractinian coral Stylophora pistillata: characterization, localization, and role in biomineralization. *J. Biol. Chem.* 283, 25475–25484. doi: 10.1074/jbc.M804726200

Nimtz, M., Conradt, H. S., and Mann, K. (2004). LacdiNAc (GalNAcβ1-4GlcNAc) is a major motif in N-glycan structures of the chicken eggshell protein ovocleidin-116. *Biochim. Biophys. Acta.* 1675, 71–80. doi: 10.1016/j.bbagen.2004.08.007

Norell, M. A., Wiemann, J., Fabbri, M., Yu, C., Marsicano, C. A., Moore-Nall, A., et al. (2020). The first dinosaur egg was soft. *Nature* 583:7816. doi: 10.1038/s41586-020-2412-8

Nys, Y., Gautron, J., Garcia-Ruiz, J. M., and Hincke, M. T. (2004). Avian eggshell mineralization: biochemical and functional characterization of matrix proteins. *CR Palevol.* 3, 549–562. doi: 10.1016/j.crpv.2004.08.002

Nys, Y., Hincke, M. T., Arias, J. L., Garcia-Ruiz, J. M., and Solomon, S. E. (1999). Avian eggshell mineralization. *Poult. Avian Biol. Rev.* 10, 143–166.

Panheleux, M., Kälin, O., Gautron, J., and Nys, Y. (1999a). Features of eggshell formation in guinea fowl: kinetics of shell deposition, uterine protein secretion and uterine histology. *Br. Poult. Sci.* 40, 632–643. doi: 10.1080/00071669987025

Panheleux, M., Bain, M., Fernandez, M. S., Morales, I., Gautron, J., Arias, J. L., et al. (1999b). Organic matrix composition and ultrastructure of eggshell: a comparative study. *Br. Poult. Sci.* 40, 240–252. doi: 10.1080/00071669987665

Panheleux, M., Nys, Y., Williams, J., Gautron, J., Boldicke, T., and Hincke, M. T. (2000). Extraction and quantification by ELISA of eggshell organic matrix proteins (ovocleidin-17, ovalbumin, ovotransferrin) in shell from young and old hens. *Poult. Sci.* 79, 580–588. doi: 10.1093/ps/79.4.580

Pérez-Huerta, A., and Dauphin, Y. (2016). Comparison of the structure, crystallography and composition of eggshells of the guinea fowl and graylag goose. *Zoology* 119, 52–63. doi: 10.1016/j.zool.2015.11.002

Petersen, J., and Tyler, C. (1966). The strength of guinea fowl (*Numida meleagris*) egg shells. *Br. Poult. Sci.* 7, 291–296. doi: 10.1080/00071666608415635

Phillips, M. J., Bennett, T. H., and Lee, M. S. (2009). Molecules, morphology, and ecology indicate a recent, amphibious ancestry for echidnas. *Proc. Natl. Acad. Sci. U. S. A.* 106, 17089–17094. doi: 10.1073/pnas.0904649106

Pines, M., Knopov, V., and Bar, A. (1995). Involvement of osteopontin in egg shell formation in the laying chicken. *Matrix Biol.* 14, 765–771. doi: 10.1016/S0945-053X(05)80019-8

Ramos-Silva, P., Kaandorp, J., Huisman, L., Marie, B., Zanella-Cléon, I., Guichard, N., et al. (2013). The skeletal proteome of the coral *Acropora* millepora: the evolution of calcification by co-option and domain shuffling. *Mol. Biol. Evol.* 30, 2099–2112. doi: 10.1093/molbev/mst109

Rao, A., Seto, J., Berg, J. K., Kreft, S. G., Scheffner, M., and Cölfen, H. (2013). Roles of larval sea urchin spicule SM50 domains in organic matrix self-assembly and calcium carbonate mineralization. *J. Struct. Biol.* 183, 205–215. doi: 10.1016/j.jsb.2013.06.004

Reyes-Grajeda, J. P., Moreno, A., and Romero, A. (2004). Crystal structure of ovocleidin-17, a major protein of the calcified Gallus gallus eggshell: implications in the calcite mineral growth pattern. *J. Biol. Chem.* 279, 40876–40881. doi: 10.1074/jbc.M406033200

Rodríguez-Navarro, A. B., Marie, P., Nys, Y., Hincke, M. T., and Gautron, J. (2015). Amorphous calcium carbonate controls avian eggshell mineralization: a new paradigm for understanding rapid eggshell calcification. *J. Struct. Biol.* 190, 291–303. doi: 10.1016/j.jsb.2015.04.014

Romé, H., and Le Roy, P. (2016). Régions chromosomiques influençant les caractères de production et de qualité des oeufs de poule TT - chromosomal regions influencing egg production and egg quality traits in hens. *INRA Prod. Anim.* 29, 117–128. doi: 10.20870/productions-animales.2016.29.1.2521

Rose-Martel, M., Du, J., and Hincke, M. T. (2012). Proteomic analysis provides new insight into the chicken eggshell cuticle. *J. Proteomics* 75, 2697–2706. doi: 10.1016/j.jprot.2012.03.019

Rose-Martel, M., Smiley, S., and Hincke, M. T. (2015). Novel identification of matrix proteins involved in calcitic biomineralization. *J. Proteomics* 116, 81–96. doi: 10.1016/j.jprot.2015.01.002

Rowe, P. S. N. (2012). The chicken or the egg: PHEX, FGF23 and SIBLINGs unscrambled. *Cell Biochem. Funct.* 30, 355–375. doi: 10.1002/cbf.2841

Rowe, P. S. N., Kumagai, Y., Gutierrez, G., Garrett, I. R., Blacher, R., Rosen, D., et al. (2004). MEPE has the properties of an osteoblastic phosphatonin and minhibin. *Bone* 34, 303–319. doi: 10.1016/j.bone.2003.10.005

Shen, X.-X., Liang, D., Wen, J.-Z., and Zhang, P. (2011). Multiple genome alignments facilitate development of NPCL markers: a case study of tetrapod phylogeny focusing on the position of turtles. *Mol. Biol. Evol.* 28, 3237–3252. doi: 10.1093/molbev/msr148

Sire, J. Y., Delgado, S. C., and Girondot, M. (2008). Hen's teeth with enamel cap: from dream to impossibility. *BMC Evol. Biol.* 8:246. doi: 10.1186/1471-2148-8-246

Sire, J.-Y., and Kawasaki, K. (2012). "Origin and evolution of bone and dentin, and of their phosphorylated, acid-rich matrix proteins," in *Phosphorylated Extracellular Matrix Proteins of Bone and Dentin*, ed. M. Goldberg (Sharjah: Bentham Science), 3–60.

Sodek, J., Ganss, B., and McKee, M. D. (2000). Osteopontin. *Crit. Rev. Oral Biol. Med.* 11, 279–303. doi: 10.1177/10454411000110030101

Solstad, T., Stenvik, J., and Jørgensen, T. (2007). mRNA expression patterns of the BPI/LBP molecule in the Atlantic cod (Gadus morhua L.). *Fish Shellfish Immunol.* 23, 260–271. doi: 10.1016/j.fsi.2006.10.002

Song, K. T., Choi, S. H., and Oh, H. R. (2000). A comparison of egg quality of pheasant, chukar, quail and guinea fowl. *Asian-Australas. J. Anim. Sci.* 13, 986–990. doi: 10.5713/ajas.2000.986

Stapane, L., Le Roy, N., Ezagal, J., Rodriguez-Navarro, A. B., Labas, V., Combes-Soia, L., et al. (2020). Avian eggshell formation reveals a new paradigm for vertebrate mineralization via vesicular amorphous calcium carbonate. *J. Biol. Chem.* 295, 15853–15869. doi: 10.1074/jbc.ra120.014542

Stapane, L., Le Roy, N., Hincke, M. T., and Gautron, J. (2019). The glycoproteins EDIL3 and MFGE8 regulate vesiclemediated eggshell calcification in a new model for avian biomineralization. *J. Biol. Chem.* 294, 14526–14545. doi: 10.1074/jbc.RA119.009799

Stein, K., Prondvai, E., Huang, T., Baele, J. M., Sander, P. M., and Reisz, R. (2019). Structure and evolutionary implications of the earliest (Sinemurian, Early Jurassic) dinosaur eggs and eggshells. *Sci. Rep.* 9:4424. doi: 10.1038/s41598-019-40604-8

Takahashi, H., Sasaki, O., Nirasawa, K., and Furukawa, T. (2010). Association between ovocalyxin-32 gene haplotypes and eggshell quality traits in an F2 intercross between two chicken lines divergently selected for eggshell strength. *Anim. Genet.* 41, 541–544. doi: 10.1111/j.1365-2052.2010.02034.x

Théry, C., Regnault, A., Garin, J., Wolfers, J., Zitvogel, L., Ricciardi-Castagnoli, P., et al. (1999). Molecular characterization of dendritic cell-derived exosomes: selective accumulation of the heat shock protein hsc73. *J. Cell Biol.* 147, 599–610. doi: 10.1083/jcb.147.3.599

Tian, X., Gautron, J., Monget, P., and Pascal, G. (2010). What makes an egg unique? Clues from evolutionary scenarios of egg-specific genes. *Biol. Reprod.* 83, 893–900. doi: 10.1095/biolreprod.110.085019

Uemoto, Y., Suzuki, C., Sato, S., Sato, S., Ohtake, T., Sasaki, O., et al. (2009). Polymorphism of the ovocalyxin-32 gene and its association with egg production traits in the chicken. *Poult. Sci.* 88, 2512–2517. doi: 10.3382/ps.2009-00331

Voigt, O., Adamski, M., Sluzek, K., and Adamska, M. (2014). Calcareous sponge genomes reveal complex evolution of α-carbonic anhydrases and two key biomineralization enzymes. *BMC Evol. Biol.* 14:230. doi: 10.1186/s12862-014-0230-z

Voris, J. T., Zelenitsky, D. K., Therrien, F., and Tanaka, K. (2018). Dinosaur eggshells from the lower Maastrichtian St. Mary River Formation of southern Alberta, Canada. *Can. J. Earth Sci.* 55, 272–282. doi: 10.1139/cjes-2017-0195

Wallace, A., and Schiffbauer, J. (2016). Proteins from the past. *Elife* 5:e20877. doi: 10.7554/eLife.17092

Warren, W. C., Hillier, L. W., Graves, J. A. M., Birney, E., Ponting, C. P., Grützner, F., et al. (2008). Genome analysis of the platypus reveals unique signatures of evolution. *Nature* 453, 175–183. doi: 10.1038/nature06936

Weber, E., Weiss, I. M., Cölfen, H., and Kellermeier, M. (2016). Recombinant perlucin derivatives influence the nucleation of calcium carbonate. *CrystEngComm* 18, 8439–8444. doi: 10.1039/c6ce01878e

Weber, G. F. (2018). The phylogeny of osteopontin - analysis of the protein sequence. *Int. J. Mol. Sci.* 19:2557. doi: 10.3390/ijms19092557

Weiner, S., and Dove, P. M. (2003). An overview of biomineralization processes and the problem of the vital effect. *Rev. Mineral. Geochem.* 54, 1–29. doi: 10.2113/0540001

Wellman-Labadie, O., Lakshminarayanan, R., and Hincke, M. T. (2008a). Antimicrobial properties of avian eggshell-specific C-type lectin-like proteins. *FEBS Lett.* 582, 699–704. doi: 10.1016/j.febslet.2008.01.043

Wellman-Labadie, O., Picman, J., and Hincke, M. T. (2008b). Antimicrobial activity of cuticle and outer eggshell protein extracts from three species of domestic birds. *Br. Poult. Sci.* 49, 133–143. doi: 10.1080/00071660802001722

Wellman-Labadie, O., Picman, J., and Hincke, M. T. (2008c). Antimicrobial activity of the Anseriform outer eggshell and cuticle. *Comp. Biochem. Physiol. B Biochem. Mol. Biol.* 149, 640–649. doi: 10.1016/j.cbpb.2008.01.001

Wong, M., Hendrix, M. J. C., Von der Mark, K., Little, C., and Stern, R. (1984). Collagen in the egg shell membranes of the hen. *Dev. Biol.* 104, 28–36. doi: 10.1016/0012-1606(84)900332

Xing, J., Wellman-Labadie, O., Gautron, J., and Hincke, M. T. (2007). Recombinant eggshell ovocalyxin-32: expression, purification and biological activity of the glutathione S-transferase fusion protein. *Comp. Biochem. Physiol. B Biochem. Mol. Biol.* 147, 172–177. doi: 10.1016/j.cbpb.2007.01.015

Yang, R., Geng, F., Huang, X., Qiu, N., Li, S., Teng, H., et al. (2020). Integrated proteomic, phosphoproteomic and N-glycoproteomic analyses of chicken eggshell matrix. *Food Chem.* 330:127167. doi: 10.1016/j.foodchem.2020.127167

Zelensky, A. N., and Gready, J. E. (2005). The C-type lectin-like domain superfamily. *FEBS J.* 272, 6179–6217. doi: 10.1111/j.1742-4658.2005.05031.x

Zhang, Q., Liu, L., Zhu, F., Ning, Z., Hincke, M. T., Yang, N., et al. (2014). Integrating de novo transcriptome assembly and cloning to obtain chicken ovocleidin-17 full-length cDNA. *PLoS One* 9:e93452. doi: 10.1371/journal.pone.0093452

Zhao, K., Wang, M., Wang, X., Wu, C., Xu, H., and Lu, J. R. (2013). Crystal growth of calcite mediated by ovalbumin and lysozyme: atomic force microscopy study. *Cryst. Growth Des.* 13, 1583–1589. doi: 10.1021/cg301820w

Zhu, F., Zhang, F., Hincke, M., Yin, Z. T., Chen, S. R., Yang, N., et al. (2019). iTRAQ-based quantitative proteomic analysis of duck eggshell during biomineralization. *Proteomics* 19:e1900011. doi: 10.1002/pmic.201900011

Conflict of Interest: The authors declare that the research was conducted in the absence of any commercial or financial relationships that could be construed as a potential conflict of interest.

frontiers in Genetics

ORIGINAL RESEARCH
published: 08 June 2021
doi: 10.3389/fgene.2021.674539

The 'Shellome' of the Crocus Clam *Tridacna crocea* Emphasizes Essential Components of Mollusk Shell Biomineralization

Takeshi Takeuchi[1], Manabu Fujie[2], Ryo Koyanagi[2], Laurent Plasseraud[3], Isabelle Ziegler-Devin[4], Nicolas Brosse[4], Cédric Broussard[5], Noriyuki Satoh[1] and Frédéric Marin[6]**

[1] Marine Genomics Unit, Okinawa Institute of Science and Technology Graduate University, Onna, Okinawa, Japan, [2] DNA Sequencing Section, Okinawa Institute of Science and Technology Graduate University, Onna, Okinawa, Japan, [3] Institut de Chimie Moléculaire de l'Université de Bourgogne, UMR CNRS 6302, Faculté des Sciences Mirande, Université de Bourgogne - Franche-Comté (UBFC), Dijon, France, [4] LERMAB, Faculté des Sciences et Technologies - Campus Aiguillettes, Université de Lorraine, Vandoeuvre-Lès-Nancy, France, [5] 3P5 Proteomic Platform, Cochin Institute, University of Paris, INSERM U1016, CNRS UMR 8104, Paris, France, [6] UMR CNRS 6282 Biogéosciences, Bâtiment des Sciences Gabriel, Université de Bourgogne - Franche-Comté (UBFC), Dijon, France

OPEN ACCESS

Edited by:
Jacob A. Tennessen, Harvard University, United States

Reviewed by:
Benjamin Marie, Centre National de la Recherche Scientifique (CNRS), France
Zhi Liao, Zhejiang Ocean University, China

***Correspondence:**
Frédéric Marin
frederic.marin@u-bourgogne.fr
Takeshi Takeuchi
t.takeuchi@oist.jp

Specialty section:
This article was submitted to Evolutionary and Population Genetics, a section of the journal Frontiers in Genetics

Received: *01 March 2021*
Accepted: *13 May 2021*
Published: *08 June 2021*

Citation:
Takeuchi T, Fujie M, Koyanagi R, Plasseraud L, Ziegler-Devin I, Brosse N, Broussard C, Satoh N and Marin F (2021) The 'Shellome' of the Crocus Clam Tridacna crocea Emphasizes Essential Components of Mollusk Shell Biomineralization. Front. Genet. 12:674539. doi: 10.3389/fgene.2021.674539

Molluscan shells are among the most fascinating research objects because of their diverse morphologies and textures. The formation of these delicate biomineralized structures is a matrix-mediated process. A question that arises is what are the essential components required to build these exoskeletons. In order to understand the molecular mechanisms of molluscan shell formation, it is crucial to identify organic macromolecules in different shells from diverse taxa. In the case of bivalves, however, taxon sampling in previous shell proteomics studies are focused predominantly on representatives of the class Pteriomorphia such as pearl oysters, edible oysters and mussels. In this study, we have characterized the shell organic matrix from the crocus clam, *Tridacna crocea*, (Heterodonta) using various biochemical techniques, including SDS-PAGE, FT-IR, monosaccharide analysis, and enzyme-linked lectin assay (ELLA). Furthermore, we have identified a number of shell matrix proteins (SMPs) using a comprehensive proteomics approach combined to RNA-seq. The biochemical studies confirmed the presence of proteins, polysaccharides, and sulfates in the *T. crocea* shell organic matrix. Proteomics analysis revealed that the majority of the *T. crocea* SMPs are novel and dissimilar to known SMPs identified from the other bivalve species. Meanwhile, the SMP repertoire of the crocus clam also includes proteins with conserved functional domains such as chitin-binding domain, VWA domain, and protease inhibitor domain. We also identified BMSP (Blue Mussel Shell Protein, originally reported from *Mytilus*), which is widely distributed among molluscan shell matrix proteins. *Tridacna* SMPs also include low-complexity regions (LCRs) that are absent in the other molluscan genomes, indicating that these genes may have evolved in specific lineage. These results highlight the diversity of the organic molecules – in particular proteins – that are essential for molluscan shell formation.

Keywords: biomineralization, transcriptome, proteome, Mollusca, Bivalvia, *Tridacna crocea*, shell formation

INTRODUCTION

The shell of mollusks represents a major biological innovation that largely contributed to the great evolutionary and ecological success of the phylum throughout Phanerozoic times. As the shell offered a robust shelter against predation and an effective protection against desiccation, it allowed mollusks to conquer – from shallow epicontinental marine seas – all kinds of habitats, including deep-sea hydrothermal vents, brackish and freshwater domains or a large array of terrestrial environments: in this latter case, even the most hostile ones like deserts, caves, polar territories and high mountains were colonized and still are.

Beside complex genetic equipment involved in development, the formation of mollusk shell is a highly regulated process that requires a large set of macromolecules, i.e., proteins, polysaccharides and lipids, secreted from the dorsal mantle tissue, and which self-assemble into an organic matrix, the framework for shell mineralization. These macromolecules – in particular shell matrix proteins, defined here as SMPs - also play crucial role in nucleation and growth of calcium carbonate crystal. They are in addition considered to be key-players for controlling shell microstructures and mineralogy (Marin et al., 2007).

Our knowledge of mollusk SMP repertoires is rapidly expanding, due to the combined use of transcriptomics on calcifying mollusk mantle tissues and proteomics on shell macromolecular extracts (Joubert et al., 2010; Marie et al., 2011a; Marin et al., 2013). Accumulating data of shell matrix proteomes - referred to as 'shellomes' – from different species highlights extensive but unsuspected diversification of SMP repertoires, in particular in bivalves, the most studied mollusk class from a biomineralization viewpoint (Kocot et al., 2016; Marin, 2020). This diversity expresses not only from genus to genus but also between different shell microstructures of a single shell. For instance, the pearl oysters (genus *Pinctada*) synthesize nacreous aragonitic layer in the inner side of their shells and a calcitic prismatic one in the outer part. To this end, they secrete two different SMP repertoires from corresponding mantle region (Marie et al., 2012; Zhao et al., 2018). Furthermore, to render the situation more complex, it has been shown that larval shell SMP repertoires are almost entirely different from that of adult shells (Zhao et al., 2018). Beside this diversity, some common characteristics can be identified: they include the presence of shared functional domains and the abundance of low complexity regions, referred to as LCRs (Kocot et al., 2016; Marie et al., 2017). These conserved elements may be a clue to understand the evolutionary origin of shell biomineralization. In order to draw a general view of biomineralization process and its evolutionary origin, it is essential to compile a "dictionary" of SMPs that is identified from diverse range of taxa.

To date, shell matrix proteomes, 'shellomes,' were reported from 20 bivalve genera (Marin, 2020). Among them, half belong to Pteriomorphia sub-class, including the pearl oysters *Pinctada margaritifera*, *Pinctada maxima*, and *Pinctada fucata* (Joubert et al., 2010; Marie et al., 2012; Liu et al., 2015; Zhao et al., 2018), the Pacific cupped oyster *Crassostrea gigas* (Zhang et al., 2012; Arivalagan et al., 2017; Zhao et al., 2018), the edible mussels including *Mytilus edulis*, *Mytilus galloprovincialis*, *Mytilus californianus*, *Mytilus coruscus*, and *Perna viridis* (Marie et al., 2011a; Gao et al., 2015; Liao et al., 2015, 2019; Arivalagan et al., 2017), and the king scallop *Pecten maximus* (Arivalagan et al., 2017). In contrast, SMPs of sub-classes Palaeoheterodonta and Heterodonta (Plazzi and Passamonti, 2010) have been far less studied. To our knowledge, the shell proteomes supported by a transcriptome of 3 Palaeoheterodonta species have been analyzed in detail, corresponding to unionoid freshwater mussels: *Hyriopsis cumingii*, *Elliptio complanata,* and *Villosa lienosa* (Berland et al., 2013; Marie et al., 2017). For Heterodonta *sensu lato* (including Anomalodesmata), "shellomic" data supported by transcriptome are scarce too: they include that of the clams *Venerupis philippinarum* (Marie et al., 2011b), *Mya truncata* (Arivalagan et al., 2016), and *Laternula elliptica* (Sleight et al., 2015). Despite the increasing list of SMPs, it should be noted that our present view of biomineralization process in bivalves is extremely partial, given the size of this class (12,000 living species). Entire clades, like heterodont or protobranch bivalves, remain to be investigated.

To this end, we analyzed the shell organic components of the crocus clam, *Tridacna crocea*, a heterodont bivalve and one of the modest-sized representatives of the giant clam taxon. Giant clams, in particular *T. gigas*, are one of the most fascinating models in biomineralization research since they produce the largest and heaviest shells among mollusks. All *Tridacna* species produce thick, dense and rigid shells mostly of crossed lamellar microstructure (Taylor, 1973; Dauphin and Denis, 2000; Agbaje et al., 2017; Gannon et al., 2017). As the giant clams continue to grow their shells throughout the life, shells are precise recorders of environmental conditions such as seawater temperature (Arias-Ruiz et al., 2017; Yan et al., 2020). The longevity of giant clams allows the shells to archive long-term environmental conditions, with a resolution ranging from century to month, or even higher (Yan et al., 2020).

The crocus clam, *T. crocea*, is distributed in tropical seawaters spreading from the western Pacific (Japan, New Caledonia) to the eastern Indian Ocean (Lucas, 1988). *T. crocea* hosts photosymbiotic dinoflagellate algae (Hirose et al., 2006; Ikeda et al., 2017) and they acquire nutrition from both filter-feeding and photosynthesis via zooxanthellae, allowing their fast growth. Despite their ability to produce large amount of calcium carbonate shells, the molecular basis underlying their shell formation has never been explored. In this study, we conducted a biochemical characterization of *T. crocea* organic shell matrix and furthermore identified SMPs constituting the 'shellomes' of the crocus clam by using a combination of proteomics on shell extracts and transcriptomics on mantle tissue. Our results highlight essential components for shell formation in this peculiar crossed-lamellar bivalve model.

MATERIALS AND METHODS

Sample Collection

An adult of *T. crocea* (approx. 8 cm in length) was collected at the Onna fisheries corporation, Okinawa, Japan. Soft tissues were separated from the shells and the mantle tissues were

immediately used for RNA extraction (see below). The two valves were immersed in 1% NaOCl solution for 24 h (initial bleaching), mechanically cleaned to remove remaining tissues, superficial epibionts and periostracum and rinsed with deionized water (DI water, 18 MΩ). The shells were crushed into ∼2 mm fragments with a Jaw-crusher (Retsch BB200), followed by incubating in 1% NaOCl for 60 h (second bleaching). The fragments were then washed twice with DI water, dried, and powdered using a mortar grinder (Frisch Pulverisette 2). The powder (81.6 g) was sieved (pore size <200 μm) and separated into two batches. The first was subsequently decalcified, while the second was bleached for an additional 16 h in 1% NaOCl solution (third bleaching), then thoroughly washed (DI water) and air-dried at 37°C before decalcification.

Extraction of Shell Matrices

The cleaned powder samples (second or third bleaching, approx. 40 g each) were suspended in cold water and decalcified overnight at 4°C by progressively adding (100 μL every 5 s.) cold dilute acetic acid (10% vol/vol) with an electronic burette (Titronic Universal, Schott, Mainz, Germany). The solution was centrifuged at 3,900 *g* for 30 min to separate the supernatant and the pellet. The supernatant was filtered (5 μm) on a Nalgene filtration apparatus and concentrated by ultrafiltration (Amicon stirred cell 400 mL) on a 10 kDa cutoff membrane (Millipore, ref. PLGC07610). The concentrated solution (approx. 16 mL) was dialyzed 4 days against MilliQ water with several water changes, and lyophilized to obtain the acid-soluble matrix (ASM). The pellet was resuspended in Milli-Q water, centrifuged, and the supernatant discarded. After three cycles of resuspension-centrifugation-supernatant discarding, the pellet was lyophilized, forming the acid-insoluble matrix (AIM).

SDS-PAGE

AIM and ASM were suspended in 1× Laemmli sample buffer (Laemmli, 1970) containing β-mercaptoethanol. Samples were denatured for 5 min at 99°C, cooled on ice and briefly centrifuged. Note that for AIM only a fraction of this matrix can be dissolved in Laemmli buffer. This soluble matrix is referred to as LS-AIM (Laemmli-soluble – Acid-insoluble matrix). Then, supernatant were run on precast 4–20% gradient polyacrylamide mini-gels (Bio-Rad) in mini-Protean III system. Gels were stained with silver nitrate (Morrissey, 1981), Stains-all for putative calcium-binding proteins (Campbell et al., 1983; Marin et al., 2005) and Alcian blue, for polyanionic macromolecules/sulfated sugars (Thornton et al., 1996) at pH 1.0.

FT-IR Spectroscopy

FT-IR spectra were acquired on all AIM extracts and on the different cleaned shell powders. In this latter case (not illustrated here), we verified that the powders were all aragonitic, with the double absorption band at 700–712 cm^{-1}, the one at 857 cm^{-1}, the thin low amplitude absorption band at 1,083 cm^{-1} and the main absorption band at 1,474 cm^{-1}. All samples were measured using a Bruker Vector 22 FT-IR spectrometer (Bruker Optics Sarl, Marne la Vallée, France) equipped with a Specac Golden Gate Attenuated Total Reflectance (ATR) device (Specac Ltd., Orpington, United Kingdom) in the wavenumber range 4,000–500 cm^{-1} (12 scans at a spectral resolution of 4 cm^{-1}). The background was recorded before each measurement. The qualitative assignment of absorption bands was performed manually by comparison with previously described spectra, carried out by our group or available in the bibliography.

Monosaccharide Analysis

Monosaccharide quantification of AIMs after two or three bleaching steps was performed according to the HPAE-PAD technology (High Pressure Anion-Exchange - Pulsed Amperometric Detection) on an ICS-3000, Dionex system equipped with a Dionex CarboPac^{TM} PA-20 (3 mm × 150 mm) analytical column. In short, lyophilized samples were hydrolyzed in 2 M trifluoroacetic acid at 105°C for 4 h (100 μg/100 μL), and the solution was neutralized with sodium hydroxide. Hydrolytic conditions deacetylate *N*-acetyl-glucosamine and *N*-acetyl-galactosamine, which are subsequently analyzed as glucosamine and galactosamine, respectively. Filtered samples (20 μL) were eluted at 0.4 mL/min (35°C) using the following sodium hydroxide gradient: pure water 99.2%/250 mM NaOH 0.8%: 0 ∼ 20 min; pure water 75%/250 mM NaOH 20%/NaOAc (1M)- NaOH (20 mM) 5%: 20 ∼ 37 min; pure water 40%/250 mM NaOH 20%/NaOAc (1M)-NaOH (20 mM) 40%: 37 ∼ 41 min. Each elution was followed by a wash and subsequent equilibration time. External sugar and uronic acids standards were used for calibration (7 points per curve): fucose, glucose, xylose, galactose, mannose, rhamnose, arabinose, glucosamine, galactosamine, galacturonic acid, and glucuronic acid (all provided by Sigma-Aldrich).

Enzyme-Linked Lectin Assay (ELLA)

Enzyme Linked Lectin Assay (ELLA) was conducted as described previously (Immel et al., 2016; Takeuchi et al., 2018) on ASM fractions only. Briefly, 96-well plates (MaxiSorp, Nunc/Thermo Scientific, Nunc A/S, Roskilde, Denmark) were coated with ASM (50 ng/well) and incubated for 90 min at 37°C. They were washed three times with a solution of TBS/Tween-20 (0.5 mL Tween 20 per L) spread using a manual microplate 8-channel washer (Nunc Immuno Wash), and subsequently blocked with Carbo-free blocking solution (Vector Laboratories, ref. SP-5040) for 60 min at 37°C. Three sets of 7 biotinylated lectins were used (Vector Laboratories, Peterborough, United Kingdom, ref. BK-1000, BK-2000, and BK-3000). Lectins were applied to the wells (dilution to 10 μg/mL) and incubated for 90 min at 37°C. Unbound lectins were washed five times with TBS/Tween-20. Then, a solution containing alkaline phosphatase-conjugated avidin (Avidin-AP, Sigma A7294, St. Louis, MO, United States) diluted 70,000 times was added (100 μL per well) and incubated for 90 min at 37°C. Microplates were washed again and incubated with ELISA substrate solution (10% vol/vol diethanolamine in Milli-Q water, pH 9.8) containing phosphatase substrate [0.5 mg/mL, 4-nitrophenyl phosphate disodium salt hexahydrate (pNPP) tablet, Sigma, ref. UN3500-A] at 37°C. They were read every 15 min at 405 nm using a Bio-Rad Model 680 micro-plate reader. Results were normalized and converted to percentage of reactivity by subtracting the background (negative control comprising ASM

without lectin but with Avidin-AP) from all values and by considering the highest response as 100%. The test was repeated three times. For detailed information on the saccharidic target binding-sites of each lectin, see one of our previous references (Immel et al., 2016).

Mantle Transcriptome

Total RNA of *T. crocea* was extracted from an adult mantle tissue using Trizol reagent (Invitrogen) and purified using an RNeasy micro kit with DNase (QIAGEN). RNA-seq libraries were prepared using a TruSeq RNA sample Prep Kit v2 (Illumina) following the manufacture's protocol and sequenced with the Illumina GAIIx platform. Raw sequences were quality filtered and trimmed with Trimmomatic 0.36 (Bolger et al., 2014). Reads were then assembled using Trinity version r20140413p1 (Grabherr et al., 2011).

Shell Proteome

Proteomic analyses were conducted on the bulk ASM and AIM matrices (obtained after two and three bleaching treatments) after an in-gel digestion with trypsin, as previously published (Immel et al., 2016). For MS and MS/MS ORBITRAP, analyses were performed using an Ultimate 3000 Rapid Separation Liquid Chromatographic (RSLC) system (Thermo Fisher Scientific) online with a hybrid LTQ-Orbitrap-Velos mass spectrometer (Thermo Fisher Scientific). All technical details are provided in earlier work (Immel et al., 2016). Database searches were carried out using Mascot version 2.4 and 2.5 (Matrix Science, London, United Kingdom) on the transcriptome of *T. crocea*. The false discovery rate was set to 0.05. Proteins supported by more than one peptide sequence were identified as shell matrix proteins (SMPs) in this study. The most significant results are presented in this study.

Characterization of Protein Sequences

Protein sequences identified through proteomic analysis were analyzed using the InterProscan (ver. 5.14-53.0) platform (Jones et al., 2014) in order to search for functional domains. Signal peptide prediction was conducted with SignalP 4.0 (Petersen et al., 2011). Transmembrane domains were assessed with TMHMM version 2.0 (Krogh et al., 2001). Protein sequences were also Blastp-searched against nr or UniProt databases. Theoretical molecular weights and isoelectric points of the proteins were calculated based on their amino acid sequences using IPC 1.0 (Kozlowski, 2016). Phosphorylation sites in protein sequences were predicted using NetPhos 3.1 (Blom et al., 1999). In order to identify LCRs in protein sequences, we searched polypeptide sequences where majority of the amino acids were composed of one or two amino acids. LCRs were defined based on the following criteria; (i) single amino acid occupies $\geq$50% of the 10 amino acid sequence window in more than 14 successive polypeptides or (ii) the most abundant amino acid occupies $\geq$40% and the second abundant amino acid occupies $\geq$20% of the 10 amino acid sequence window in more than 19 successive polypeptides.

RESULTS

SDS-PAGE

After fractionation on SDS-PAGE, the macromolecules in the ASM and the LS-AIM fractions were characterized using three staining methods: silver nitrate, Stains-all, and Alcian blue staining (**Figure 1**). All three show that the two ASMs (2bl and 3bl) exhibited the same electrophoretic pattern, and the two AIMs (2bl and 3bl) too. However, between ASMs and AIMS, differences were noticed. With silver, 5–7 successive discrete bands were detected between 17 and 43 kDa, with two major ones at 35 and 45 kDa in the ASMs. In the two AIMs, a single band at 70 kDa was observed. A band at high molecular weight (>170 kDa) was also visible in all extracts. The overall signals were, however, dominated by smeary 'polydisperse' macromolecules (**Figure 1A**). With Stains-all staining, a broad blue to purple signal was present from about 17 kDa to high molecular weights (>170 kDa) in both ASM fractions (**Figure 1B**), suggesting that these molecules may bind calcium. In contrast, both AIM fractions were mostly stained pink to red, except a band just below the 70 kDa one, which was slightly stained blue. Note the presence of scaling pattern between 17 and 43 kDa in both AIMs; this scaling pattern was not detected with silver. With Alcian blue staining at low pH (1.0), which detects sulfated polysaccharides and glycosaminoglycans, significant discrete signals were visible at 25 and 50 kDa in ASMs and at 70 kDa in AIMs (**Figure 1C**), in spite of the intense smearing staining in all extracts.

FT-IR

FT-IR spectra of AIM showed typical absorption bands derived from proteins, lipids, and saccharides (**Figure 2**). In 2nd bleaching fraction, major signals of a protein backbone were found at around 3,300–3,400, 1,645, and 1,535 cm^{-1}, which correspond to amide A (ν_{N-H}), amide I ($\nu_{C=O}$), and amide II (ν_{C-N}) bands, respectively. Absorptions in the range of 2,850–2,950 cm^{-1} corresponding to ν_{C-H} stretching vibrations, were also detected and may correspond to lipids. An absorption band specific to carbohydrate was observed near 1,061 cm^{-1} (ν_{C-O}). In addition, peaks are detected at 1,454–1,456 and 1,376–1,377 cm^{-1}, corresponding to adsorptions by carboxylic groups and by ν_{C-H} bending, respectively (Marxen et al., 1998). These sharp signals in AIM 2bl were significantly reduced after 3rd bleaching. In contrast, bands located around 550–640 and 1,150–1,200 cm^{-1} can be attributed to characteristic vibrations of phosphate groups, ν_{P-O} (stretching) and δ_{O-P-O} (bending) respectively (Jastrzębski et al., 2011; Campos et al., 2021), which were sharply highlighted after 3rd bleaching. This result indicates that the proteins, lipids, and saccharides moieties were reduced by the 3rd bleaching while phosphate groups were retained after this last cleaning step.

Saccharide Analyses

Monosaccharide analyses performed on the AIM fractions showed that the relative proportions of each hexose did not vary significantly after 2 or 3rd bleaching steps (**Figure 3**). The four

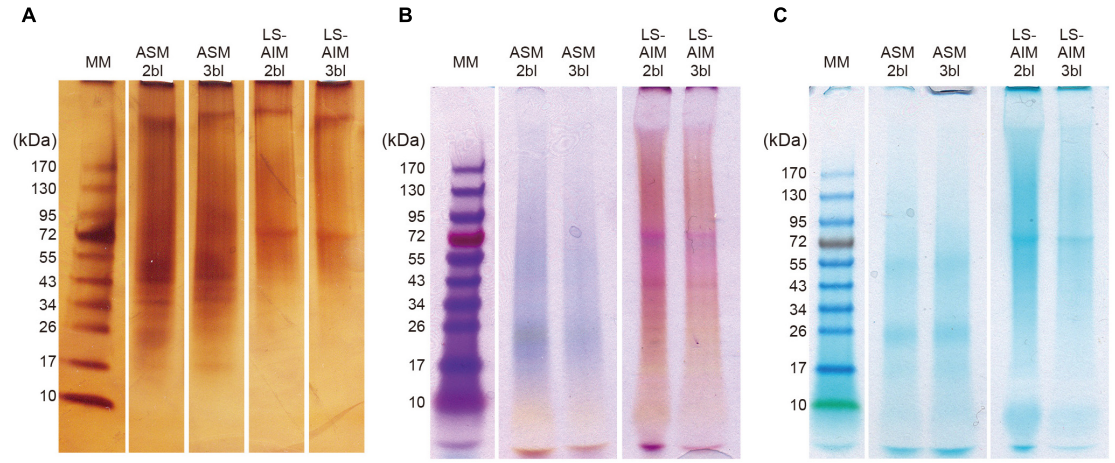

FIGURE 1 | SDS-PAGE of shell organic matrices. **(A)** Silver staining, **(B)** stains-all staining, **(C)** alcian blue staining. Ten microliter of sample solution was loaded in each lane for silver staining and 15 μl for Stains-all staining and alcian blue staining. ASM, acid-soluble matrix. LS-AIM, Laemmli-soluble acid-insoluble matrix. 2bl, second bleaching. 3bl, third bleaching. MM, molecular weight markers.

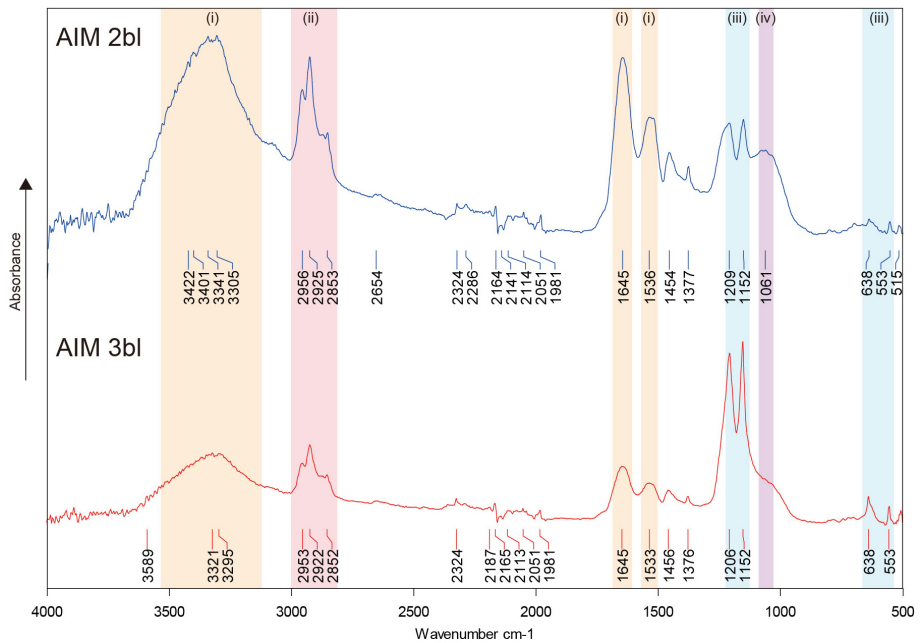

FIGURE 2 | FT-IR spectra of shell organic matrices. The signals in colors indicate the presence of proteins or saccharides (i), lipids (ii), phosphates (iii), and saccharides (iv). AIM, acid-insoluble matrix. 2bl, second bleaching. 3bl, third bleaching.

major monosaccharides in 2bl AIM included xylose (19.4%), galactose (18.9%), glucose (17.7%), and arabinose (12.1%). In the 3bl AIM, each of these monosaccharides represented more than 15% of total amount. Glucosamine and galactosamine showed moderate percentage (around 10%) and mannose and fucose, around 5%. Galacturonic acid was only detected in 3bl fraction. Glucuronic acid was absent from both extracts and rhamnose present in extremely low amounts (<1%). In order to investigate polysaccharidic structure in the ASM fractions, and to obtain their respective lectin-binding signatures, we conducted enzyme-linked lectin assay (ELLA, **Figure 4**). Both ASM fractions showed the strongest affinities for jacalin, and for *Datura stramonium* lectin (DSL). Jacalin is a α-D galactose-binding lectin that is specific of O-linked oligosaccharides while DSL, which binds oligomers and monomers of *N*-acetylglucosamine, is usually considered as a chitin-binding lectin. Signals of weaker amplitude (between 25 and 50% of that of jacalin, for the two extracts) were obtained with LEL, STL, and PSA. The two first are chitin-binding lectins while the third one binds α-linked mannose-containing oligosaccharides. Additional

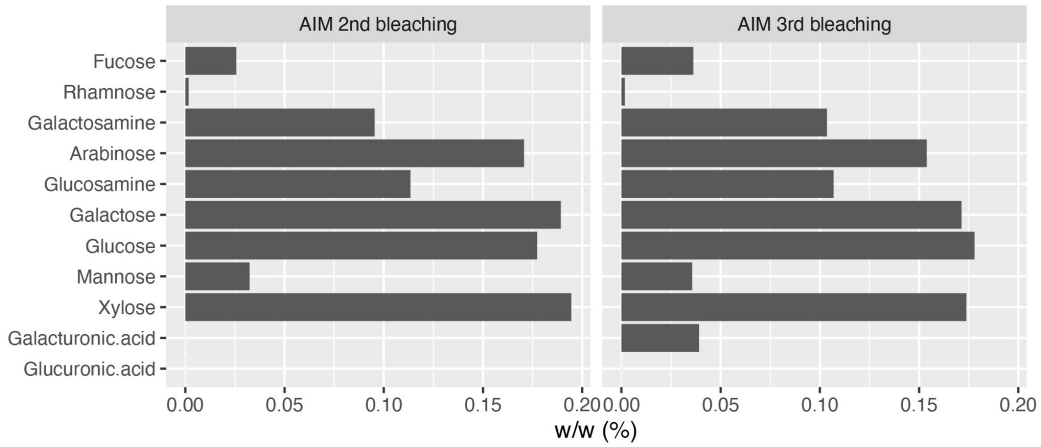

FIGURE 3 | Monosaccharide composition of AIM after two (left) or three (right) bleachings. The third bleaching did not produce any significant change in the relative percentages of monosaccharides in AIM.

lectins (DBA, ConA, SBA, PHA-L, ECL, and GSL-1) gave signals higher than 25% for the 2bl extracts but lower than this value for 3bl one. All the other lectins were almost unreactive with the two extracts. Interestingly, DSL was the single lectin for which a significant increase of the relative intensity was obtained after 3rd bleaching; this signal was maintained for LEL and STL but significantly reduced for all other tested lectins, after 3bl treatment.

Proteomic Analysis

In total, 39 SMPs were identified from the *T. crocea* shells, as shown by the Venn diagram of **Figure 5**. Fourteen SMPs were common to the four extracts, and two additional SMPs to three of the four extracts. Six SMPs were found solely in ASM extracts ("ASM-specific") while 17 were "AIM-specific." We classified these SMPs on the basis of three criteria: the presence of known conserved domains (11 hits), the occurrence of LCRs (19 hits), the absence of these two primary structure characteristics (9 hits). The results are shown in **Table 1**. Conserved domains were sub-categorized according to their putative functions: affinity to polysaccharides (7 hits), enzymatic activities (2 hits), and protease inhibitors (2 hits). Because some of the identified proteins with conserved domains exhibit modular architecture containing LCRs, we are aware that grouping them in three categories is simplistic and may not reflect the fact that they likely exert different molecular functions in biomineralization.

Seven SMPs were characterized by possible affinity to polysaccharides based on functional domain prediction (**Figure 6A** and **Table 1**). These SMPs have one or more chitin-binding domain(s) (ChBD) except for Tcr_713741. Among the ChBD-containing proteins, three SMPs including Tcr_63362, Tcr_684124, and Tcr_684094, also carry functional domains such as Concanavalin-A, von Willebrand factor type A (VWA), and Thrombospondin type-1 (TSP-1) domains. These domains are typically found in proteins of the extracellular matrix (ECM). In particular, a SMP Tcr_684124 exhibits four VWA domains followed by ChBD domain(s), showing the characteristic domain architecture of blue mussel shell proteins, i.e., BMSPs identified in pteriomophid bivalves (**Figure 7**) (Suzuki et al., 2011; Zhao et al., 2018). This is the first report of BMSP ortholog from heterodont bivalves. We consequently name this protein Tcr-BMSP. At last, one SMP (Tcr_713741), which sequence exhibits a calcium-dependent (C-type) lectin fold is also classified in this category (**Figure 6A**).

Our proteomic search also identified 2 SMPs that have conserved functional domain related to enzymatic activity (**Figure 6B** and **Table 1**). The two hits include glycoside hydrolase (Tcr_575573) and tyrosinase copper-binding domains (Tcr_588947). The first one is involved in hydrolyzing glycosidic bonds between two saccharides or between a saccharide and a non-saccharidic moiety. Such domains may be involved in matrix remodeling and reorganization in extracellular environment. The second one, tyrosinase copper-binding domain, catalyzes the hydroxylation of monophenols and the oxidation of *o*-diphenols to *o*-quinols and thus, may be involved either in matrix cross-linking or in shell pigmentation, or both.

At last, two SMPs carried protease inhibitor domains, including trypsin inhibitor Kunitz domain (Tcr_824966) and serine protease inhibitor Kazal domain (Tcr_531040). These domains are known to inhibit the proteolytic activity of a large set of proteases. They are consequently considered as exerting a protective function regarding the shell matrix.

The second category of SMPs comprise 19 proteins characterized by low-complexity regions, abbreviated as LCRs. Hereafter we refer to these proteins as low-complexity region-containing proteins or LCR-CPs. They are all characterized by a significant enrichment of their overall sequence in one or two amino acid residues, as indicated in **Table 1**. The residues involved in the enrichment can be aliphatic (G, A, V, L, I, and P), basic (K and R), hydroxylated (S and T), acidic (D), amidated (Q), sulfur-containing (M), or aromatic (F). Only four LCR-CPs showed partial sequence similarity to known proteins in the public database: Tcr_393634 to serine protease inhibitor (although this SMP did not have the functional

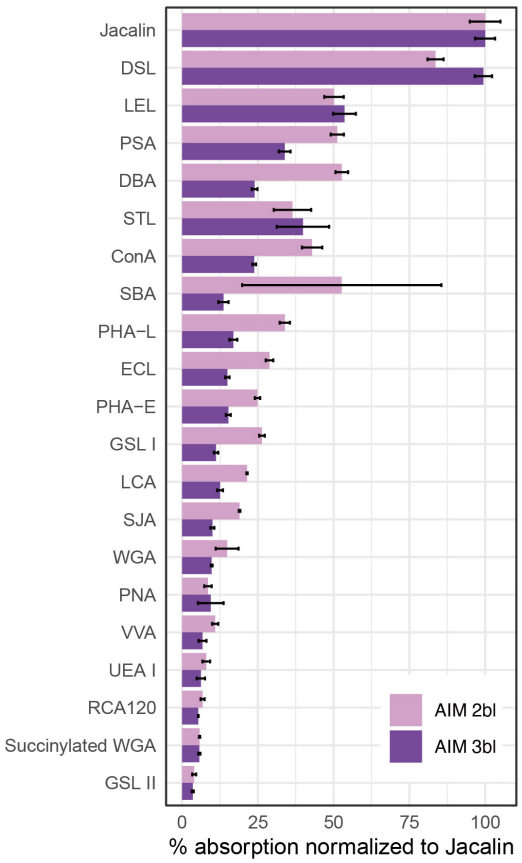

FIGURE 4 | Enzyme-linked lectin assay (ELLA) on ASMs. The test was performed with 21 lectins after two or three bleaching steps. Absorbance values at 405 nm were normalized to the highest value (Jacalin), corresponding to 100% reactivity (n = 3, means ± S.D.). Please refer Table 3 of Kanold et al. (2015) for lectin targets. ConA, concanavalin A; DBA, *Dolichos biflorus* agglutinin; DSL, *Datura stramonium* lectin; ECL, *Erythrina crista-galli* lectin; GSL I, *Griffonia simplicifolia* lectin I; GSL II, *Griffonia simplicifolia* lectin II; LCA, *Lens culinaris* agglutinin; LEL, *Lycopersicon esculentum* lectin; PHA-E, *Phaseolus vulgaris* lectin E; PHA-L, *Phaseolus vulgaris* lectin L; PNA, peanut agglutinin; PSA, *Pisum sativum* agglutinin; RCA, *Ricinus communis* agglutinin; SBA, soybean agglutinin; SJA, *Styphnolobium japonicum* agglutinin; STL, *Solanum tuberosum* lectin; UEA I, *Ulex europaeus* agglutinin I; VVA, *Vicia villosa* agglutinin; WGA,wheat germ agglutinin.

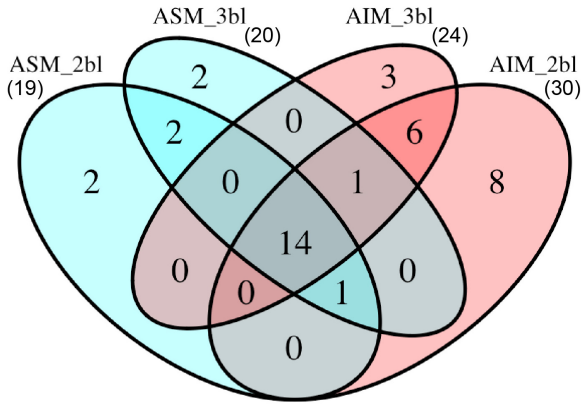

FIGURE 5 | Number of proteins identified from different sample treatments. In total, 39 proteins were identified. ASM, acid-soluble matrix. AIM, acid-insoluble matrix. 2bl, second bleaching. 3bl, third bleaching.

domain), Tcr_589629 to uncharacterized shell matrix protein of *Lottia gigantea* (**Table 1**). Other two proteins (Tcr_529389 and Tcr_564223) were hit to hypothetical proteins. In addition, LCRs were found in 4 ChBD-containing proteins (Tcr_714405, Tcr_356908, Tcr_684209, and Tcr_684124) and in 2 enzymatic domain-containing SMPs (Tcr_824966 and Tcr_531040) (**Table 1** and **Supplementary Table 1**).

Among the LCR-CPs, the most common are those with hydrophobic aliphatic amino (**Table 1**), since they represent 16 hits out of 19. Paired hydrophobic amino acids residues compose LCR in Tcr_325918 (AP-rich), Tcr_402398 (AG-rich), Tcr_393634 (AP-rich), and Tcr_459507 (GP-rich). Acidic LCR is found in one hit only, Tcr_654638, having 2–15 consecutive aspartic acids in its C-terminus (**Table 1** and **Supplementary Table 1**). Its theoretical isoelectric point is 3.44, which classifies this SMP as very acidic. Note that one G- and R-rich protein (Tcr_618259) has a poly-Asp(5) sequence in the C-terminus (**Supplementary Table 2**), although this pattern did not fit to criteria for LCR in this study. Basic LCRs composed of lysin or arginine residues are present in 4 proteins (Tcr_618259, Tcr_366778, Tcr_597367, and Tcr_647748).

Low-complexity regions exhibiting several putative phosphorylation sites on serine or threonine residues were found in 6 LCR-CPs (Tcr_696598, Tcr_438950, Tcr_589629, Tcr_459507, Tcr_647748, and Tcr_467133). T-rich LCRs are also present in 4 ChBD-containing proteins (Tcr_714405, Tcr_356908, Tcr_684209, and Tcr_684124). A computational prediction of phosphorylation sites demonstrated that these S- or T-rich LCRs are often phosphorylated (**Figure 8**). For example, SMP Tcr_459507 exhibited 12 LCRs including a S-rich and a T-rich LCRs, and showed significant phosphorylation probabilities in both the S-rich and T-rich regions (**Figure 8**). Phosphorylation sites were also likely present on S-rich and T-rich LCRs of ChBD-containing proteins such as BMSP.

At last, the third category of *T. crocea* SMPs comprises 9 hits (23% of the SMPs identified here) that did not show any significant similarities to proteins with known conserved domains. One of them (Tcr_311651) exhibits a high similarity with a hypothetical protein of unknown function from the edible oyster *C. gigas*.

DISCUSSION

Here we report the first biochemical and molecular characterization of the shell organic constituents of the Western Pacific crocus clam, *T. crocea*. Our analysis confirms the complex nature of this skeletal matrix, which contains proteins, polysaccharides and lipids; this latter fraction, detected only via FT-IR spectroscopy, was not investigated further. Our discussion focuses, first on the saccharide moiety, secondly on the protein one.

TABLE 1 | Classification of *T. crocea* shell matrix proteins.

Category	Protein ID	Signal peptide	*Trans*-membrane	LCR 1AA*	LCR 2AA*	Pfam/Prositeprofiles/Superfamily
Affinity to polysaccharides	Tcr_63362	Yes	No			Chitin binding domain (PF01607) Concanavalin A-like lectin/glucanase domain (SF49899)
	Tcr_356908	Yes	No	T-rich		Chitin binding domain (IPR002557)
	Tcr_684094	Yes	Yes			TSP1 (PF00090) Chitin binding domain (PF01607) VWA (SSF53300)
	Tcr_684124	Yes	No	P-rich T-rich	GQ-rich GS-rich GT-rich	VWA (PF00092) Chitin binding domain (IPR002557)
	Tcr_684209	No	No	G-rich P-rich T-rich	GM-rich GP-rich	Chitin-binding, domain 3 (PF03067)
	Tcr_713741	Yes	Yes			C-type lectin fold (SSF56436)
	Tcr_714405	Yes	Yes	T-rich		Chitin-binding, domain 3 (PF03067)
Enzymes	Tcr_0.575573	Yes	No			Glycoside hydrolase, family 5 (PF00150)
	Tcr_588947	Yes	No			Tyrosinase copper-binding domain (PF00264)
Protease inhibitors	Tcr_531040	Yes	Yes	P-rich		Kazal domain (IPR002350)
	Tcr_824966	No	No			Pancreatic trypsin inhibitor Kunitz domain (PF00014)
Uncharacterized proteins	Tcr_53656	No	No			–
	Tcr_292514	Yes	No			–
	Tcr_311651	Yes	No			–
	Tcr_425966	Yes	No			–
	Tcr_428448	No	No			–
	Tcr_453318	Yes	No			–
	Tcr_526755	Yes	Yes			–
	Tcr_595442	Yes	No			–
	Tcr_652688	Yes	No			–
LCR-containing proteins	Tcr_16185	Yes	Yes	G-rich	GY-rich PQ-rich	–
	Tcr_83017	Yes	Yes	G-rich		–
	Tcr_325918	Yes	No	P-rich	AP-rich	–
	Tcr_366778	Yes	No	K-rich	PT-rich	–
	Tcr_393634	Yes	No	A-rich	AP-rich	–
	Tcr_402398	No	No		AG-rich GS-rich	–
	Tcr_438950	No	Yes	T-rich		–
	Tcr_459507	Yes	Yes	A-rich G-rich P-rich S-rich T-rich	AG-rich GP-rich KV-rich	–
	Tcr_467133	No	No	P-rich T-rich		–
	Tcr_529389	No	No		GM-rich GP-rich GQ-rich	–
	Tcr_564223	Yes	No	Q-rich		–
	Tcr_589629	No	No		GS-rich	–
	Tcr_597367	Yes	No	G-rich K-rich	GM-rich PV-rich	–
	Tcr_618259	No	Yes	G-rich R-rich	GI-rich RS-rich	–
	Tcr_647748	Yes	No	K-rich T-rich	RS-rich	–
	Tcr_654638	No	Yes	D-rich	DK-rich DL-rich DN-rich	–
	Tcr_675074	Yes	Yes	L-rich	GR-rich	–
	Tcr_696598	Yes	Yes	L-rich T-rich		–
	Tcr_714321	Yes	No	GM-rich		–

**Low complexity region composed of one (1AA) or two (2AA) major amino acid(s).*

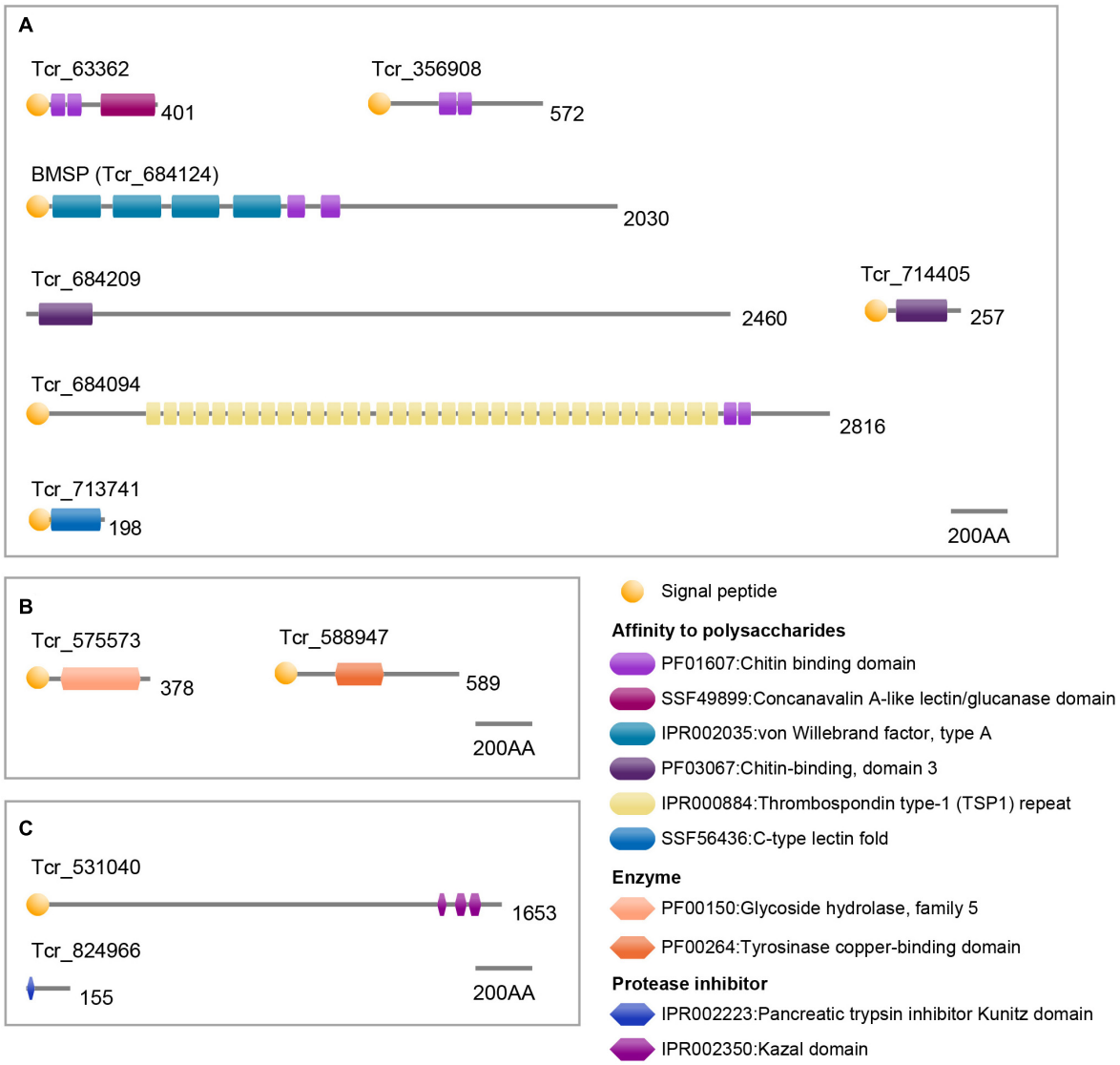

FIGURE 6 | Functional domain architecture of *T. crocea* SMPs. **(A)** Affinity to polysaccharides. **(B)** Enzymes. **(C)** Protease inhibitors. Lengths of amino acid sequences are shown at the right of each protein.

Saccharide Moiety

Both AIMs exhibit peculiar monosaccharide composition, with xylose, galactose, glucose and arabinose as the main residues. Note that xylose is not frequently represented in such proportions in matrices associated to CaCO3 skeletons (Cuif et al., 1996). The case of glucosamine should be emphasized: the detection of this residue can result from the hydrolysis of glucosamine-containing polysaccharides or can ensue from the deacetylation of *N*-acetyl-glucosamine - the monomer of chitin – during hydrolysis. Thus, glucosamine in skeletal matrices is often interpreted as a marker of chitin. In our AIM characterization, glucosamine, although relatively abundant, is not dominant, suggesting that the saccharide moiety consists of a mixture of chitin and other types of saccharides of unknown primary structure. This finding is confirmed by ELLA test on ASM where jacalin, the most reactive lectin, indicates the prominence of D-galactose or of *O*-linked oligosaccharides. DSL, the second most reactive lectin, marks the presence of monomers/oligomers of *N*-acetylglucosamine, suggesting that soluble derived products of chitin are present in the ASM. We suppose that the release of such soluble components ensue from the partial hydrolysis and solubilization of chitin by bleach, similarly to what occurs in a chitin-rich biomineral (Oudot et al., 2020). This also suggests that chitin - accessible to bleach – is *intercrystalline*.

The presence of chitin in shells has been reported among several pteriomorph 'nacro-prismatic' bivalves: histochemical studies detected chitin in the prismatic layer of the pearl oyster *P. fucata* (Suzuki et al., 2007), in the nacreous layer of the winged oyster *Pteria hirundo* (Osuna-Mascaró et al., 2015), and in the larval shell of the Mediterranean mussel *M. galloprovincialis*

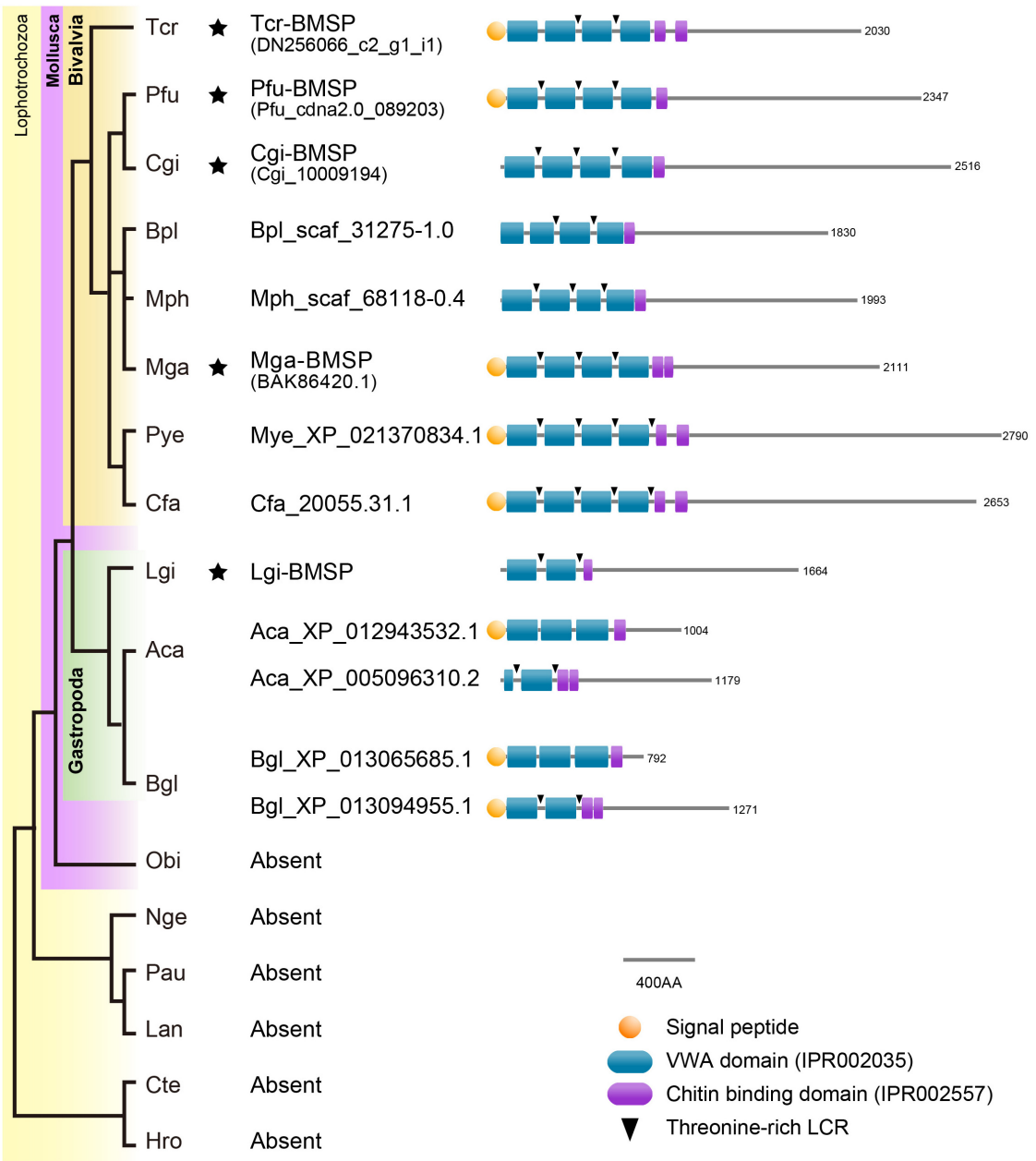

FIGURE 7 | Conserved domain architecture of BMSPs in mollusks. BMSPs carry more than one VWA domain at their N-termini, immediately followed by one or more chitin-binding domains. This domain architecture is only found in molluscan genomes. Asterisks indicate that proteomic analyses confirmed the presence of BMSP in the shells. Species name abbreviation: Aca, *Aplysia californica*, Bgl, *Biomphalaria glabrata*, Bpl, *Bathymodiolus platifrons*, Cfa, *Chlamys farreri*, Cgi, *Crassostrea gigas*, Cte, *Capitella teleta*, Hro, *Helobdella robusta*, Lan, *Lingula anatina*, Lgi, *Lottia gigantea*, Mga, *Mytilus galloprovincialis*, Mph, *Modiolus philippinarum*, Mye, *Mizuhopecten yessoensis*, Nge, *Notospermus geniculatus*, Obi, *Octopus bimaculoides*, Pau, *Phoronis australis*, Pfu, *Pinctada fucata*, Tca, *Tridacna crocea*.

(Weiss and Schönitzer, 2006). A recent study found chitin and its derivative, chitosan, in the crossed lamellar shell layer of two heterodont bivalves, the thin-ribbed cockle *Fulvia tenuicostata* and the giant clam *T. gigas*, a closely-related species to *T. crocea* (Agbaje et al., 2019). Our results obtained by two different techniques (HPAE-PAD and ELLA) confirms this latter finding: the presence of chitin in a 'non-pteriomorph,' crossed-lamellar bivalve model, where it is believed to participate – via the formation of chitin-protein complexes - to the 3D-structuring of the organic framework. Recent data (Agbaje et al., 2018; Oudot et al., 2020) show that chitin, which importance in shell formation is commonly admitted, is not universally distributed in this exoskeleton. Understanding its exact role in mineral deposition, analyzing its distribution and abundance across the Mollusca and

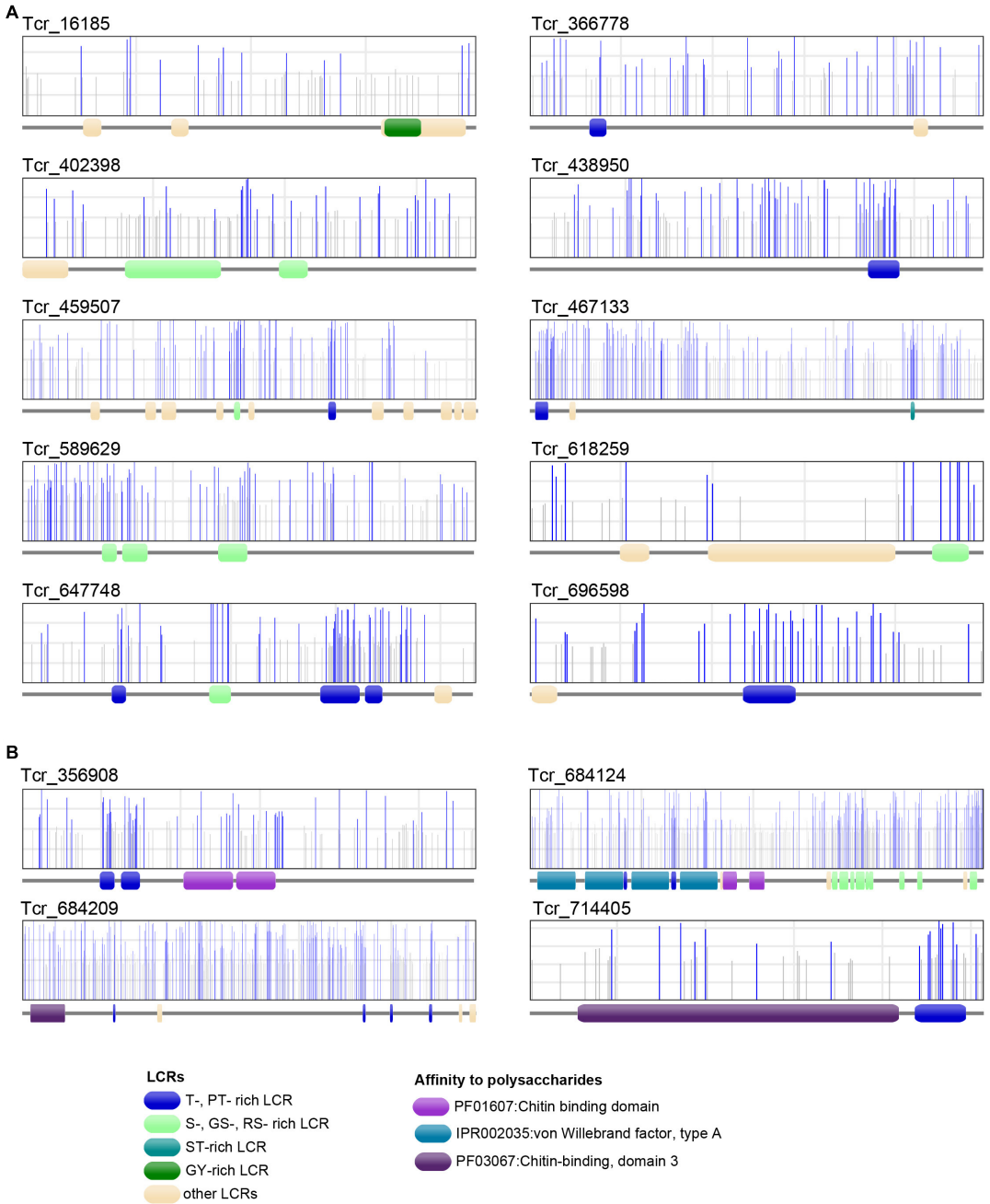

FIGURE 8 | Phosphorylation sites of 10 *T. crocea* SMPs. Each protein primary structure corresponds to the gray horizontal trait with figurations symbolizing conserved functional domains (LCRs, VWA, and ChBDs) dispersed along the sequence. In the rectangles above, vertical lines (gray or blue) represent the positions of putative phosphorylation sites along the sequences, as predicted by NetPhos 3.1. Blue bars indicate likely phosphorylation sites (probability > 0.5), and gray lines, unlikely phosphorylation sites. **(A)** Six LCR-containing proteins. **(B)** Four Chitin-binding domain-containing proteins. Note that the protein regions with the highest density of likely phosphorylation sites often correspond to T-, MT-, PT-, S-, GS-, ST-rich LCRs.

detecting which polymer replaced it functionally in chitin-less shells are major evolutionary questions that deserve attention.

Proteins of the Shell Matrix

Our proteomic data give a snapshot of the protein composition of the crocus clam's shell matrix. Thirty-nine proteins were identified, they divide in three groups: those with one or more well identified domain (like enzymatic domains, protease inhibitors or domains interacting with chitin), those with Low Complexity Regions (LCRs), and finally, uncharacterized proteins, i.e., proteins that cannot be affiliated to any of these two categories. Our data give a glimpse on the

macroevolution of shell mineralizing matrices in a poorly investigated bivalve clade.

Chitin and Chitin-Binding Proteins

While sugar analyses strongly suggests the presence of chitin in the matrix of *T. crocea*, another major clue is the proteomic identification of six shell proteins that contain chitin-binding domains (ChBDs). Formerly, several proteome analyses detected several ChBD-containing proteins in bivalve shells (Arivalagan et al., 2017; Marie et al., 2017; Zhao et al., 2018). Despite their commonality, their evolutionary relationships are not clarified because their sequence similarity is restricted to the ChBD, and their overall primary structures are highly divergent, due to their modular architectures. Interestingly, we have identified, in the *T. crocea* shell proteome, an ortholog of BMSP, a ChBD-containing protein originally identified in the blue mussel shell (Suzuki et al., 2011). The BMSP family members are clearly distinguishable from other ChBD-containing proteins from their primary structure, by exhibiting four N-terminal VWA domains in tandem followed by one or two ChBDs (Suzuki et al., 2011). Genes encoding proteins with such domain architecture (**Figure 7**) are exclusively found in bivalve genomes (Zhao et al., 2018). In contrast, gastropod genomes have one or more putative BMSP gene homologs that encode proteins with only two or three VWA domains followed by one/two ChBDs (Zhao et al., 2018). Many SMPs, in particular those with LCDs or RLCDs, show rapid molecular evolutionary rate (McDougall et al., 2013; Kocot et al., 2016) and putative extensive domain shuffling (Marin et al., 2007). The finding of *T. crocea* BMSP shows that the architecture of the four tandem N-terminal VWA domains was established before the split between Pteriomorphia and Heterodonta sub-classes, an event that dates back to 500 Mya (Plazzi and Passamonti, 2010). The intact conserved domain architecture of BMSPs in two phylogenetically distant bivalve clades indicates that these secreted proteins play likely essential role in shell formation, and that strong functional constraints have maintained the domain architecture of bivalve BMSPs across the Phanerozoic eon. In summary, besides fast-evolving SMPs, 'shellomes' also contain SMPs that are remarkably evolutionarily conserved.

In addition to SMPs with ChBDs, LCR-containing proteins may also be involved in binding chitin, such as the GY-rich LCR of Prismalin-14, identified in the calcitic prismatic layer of *P. fucata* (Suzuki et al., 2004; Suzuki and Nagasawa, 2007). In the *T. crocea* shell proteome, Tcr_16185 contains a GY-rich LCR in its C-terminus that may display similar function. Interestingly, GY-rich sequences that putatively bind chitin were also found in pearl oyster SMPs like MSI31 (Sudo et al., 1997), shematrins (Yano et al., 2006), or KRMPs (Liang et al., 2015). So far, the chitin-binding ability of these SMPs has not been tested yet *in vitro*.

Enzymes and Protease Inhibitors

Tyrosinases represent a family of copper-containing enzymes that oxidize phenol groups of tyrosine into *o*-quinones to induce cross-links. They are responsible for melanogenesis in diverse organisms. They are incorporated as SMPs in the prismatic and nacreous layers on *P. fucata* shells (Nagai et al., 2007; Liu et al., 2015) and nacre of unionoid shells (Marie et al., 2017). Tyrosinases are also identified from different bivalve shell microstructures, including that of three pteriomorphid and one heterodont species (Arivalagan et al., 2017). The presence of tyrosinase in the crossed lamellar shell of *T. crocea* (**Figure 6**) underlines the widespread utilization of this protein family for shell formation in bivalves, where it works in hardening the organic matrix (cross-linking), in innate immunity, in wound healing and not solely in shell pigmentation (Nagai et al., 2007). Tyrosinases are probably part of an ancient toolkit in mollusk evolution, recruited early for shell mineralization: it was shown that this gene family has undergone complex evolutionary history, with multiple independent evolutions and gene expansion, inactivation or loss in different bivalve lineages (Aguilera et al., 2014).

Protease inhibitors become a 'recurrent theme' in mollusc shell proteomes as proteins with protease inhibitor domains have been detected in several shell matrices (Marie et al., 2012; Arivalagan et al., 2017). In *T. crocea* SMPs, we identified two protease inhibitors, a trypsin inhibitor with a Kunitz domain (Tcr_824966) and a serine protease inhibitor with Kazal domains (Tcr_531040). It is generally believed that such proteins are part of a protective mechanism of the calcifying matrix during its secretion, by preventing its premature degradation by proteolytic enzymes in the extracellular environment. We cannot exclude that such domains perform additional unsuspected functions in the context of shell mineralization.

LCR-Containing Proteins

Despite the prevalence of LCRs in SMPs, the function of most of them in shell formation is still elusive. Among the compositionally biased amino acids in LCRs, hydrophobic aliphatic amino acids (alanine and glycine) are common, as shown by **Table 1**. Gly-rich or Ala-rich domains are usually considered to exert 'structural' (cement between crystal units) or 'mechanical' (enhancer of fracture toughness) functions. Because of their hydrophobicity, they may also play a completely different role by expelling water molecules from the system, catalyzing the conversion of amorphous transient water-rich minerals to a crystalline stable form, aragonite. Proline-rich domains are also to be noted because they provide rigid rod-like structures (such as in mucins), but their functional significance is unknown. Basic domains (lysine-rich and arginine-rich) are found in 4 SMPs and their functions give rise to different hypotheses. Two families of basic domain-containing shell proteins have been identified in pteriomorphid bivalves, KRMPs (Liang et al., 2015) and shematrins (Yano et al., 2006). In KRMPs, the basic domains are suspected to inhibit the precipitation of calcium carbonate, to interact with calcite and modify its morphology and to inhibit the growth of aragonite (Liang et al., 2015). We may suggest additional roles: interaction with bicarbonate ions, anchoring of polyanionic polymers via electrostatic interactions. However, these putative functions need to be tested *in vitro*. At last, **Table 1** lists a couple of proteins with glutamine-rich domains. Proteins with similar property have been detected in the shell matrix of the gastropod *Haliotis asinina* (Marie et al., 2010)

and it has been proposed that they might be involved in protein aggregation. Here again, this hypothesis requires *in vitro* experimental evidences.

Acidic Proteins

Acidic proteins, i.e., polyanionic proteins in physiological pH conditions, are key components of calcification process: they are indeed supposed to be involved in nucleation, inhibition, and orientation of crystal growth (Addadi and Weiner, 1985; Albeck et al., 1993; Marin and Luquet, 2008). In particular, Asp-/Glu-rich or poly-Asp/poly-Glu domains – a special case of LCRs – are usually considered as regions that bind high amount of Ca^{2+} ions with a moderate affinity, via the negatively charged side chains of Asp/Glu residues (Hare, 1963; Weiner and Hood, 1975; Takeuchi et al., 2008; Suzuki et al., 2009). Bulk amino acid composition demonstrated that Asp was significantly enriched in bivalve shell matrices (Weiner and Hood, 1975; Weiner, 1979, 1983). However, to date, few acidic SMPs with high proportion of acidic AA residues (Asp + Glu >20%) and low theoretical pI (<3.5) have been identified from pteriomorph bivalves: they include MSP-1 and MSP-2 of the scallop *Patinopecten yessoensis* (Sarashina and Endo, 1998, 2001; Hasegawa and Uchiyama, 2005), Aspein of the Japanese pearl oyster *P. fucata* (Tsukamoto et al., 2004; Isowa et al., 2012) and a collection of isoforms, the Asprich family of the rigid pen shell *Atrina rigida* (Gotliv et al., 2005). The shell matrix of *T. crocea* conforms, to a certain extent, to the concepts outlined above on acidic shell proteins. Firstly, it exhibits polyanionic properties, as shown by Alcian blue staining (ASM + AIM) and has the likely ability to bind calcium ions, as indicated by Stains-all (ASM, only). Secondly, we have identified the full sequence of a novel acidic protein (Tcr_654638, pI = 3.44, Asp + Glu = 32.4%) with a D-rich LCR in its C-terminus (**Table 1** and **Supplementary Table 2**), which does not show any significant sequence similarity to known proteins in public databases. This suggests its independent origin from pteriomorph D-rich proteins (MSP-1, Aspein) and possibly, a clade-specific recruitment within heterodont bivalves.

In addition to the presence of acidic residues, phosphorylation may contribute to the acidic nature of some SMPs (Marin and Luquet, 2007). Phosphate groups are detected in matrices associated to calcium carbonate biominerals of diverse metazoan animals such as the sea urchin *Arbacia lixula* (Kanold et al., 2015), the zebra mussel *Dreissena polymorpha* (Immel et al., 2016), or the scleractinian coral *Porites australiensis* (Takeuchi et al., 2018). Our FT-IR result showed that phosphate groups are retained in the matrices (AIMs) after intense bleach, suggesting their strong affinity with the biomineral (**Figure 2**).

Phosphorylated proteins, in particular those with Ser-rich/Thr-rich LCRs, are found in various biominerals. In vertebrates, they include osteopontin, a bone matrix protein (Gericke et al., 2005) but also dentin matrix protein (DMP-1) and phosphophoryn (aka DMP2) two highly phosphorylated teeth proteins (George et al., 1993; He et al., 2005). Phosphorylation is crucial for both proper folding and calcium binding ability of phosphophoryn (He et al., 2005). Among non-vertebrate calcium carbonate biominerals, Orchestin (Hecker et al., 2003) and CAP-1 (Inoue et al., 2003) are phosphorylated proteins involved in calcium storage during ecdysis in crustaceans, and their calcium-binding ability depends on phosphorylation. Phosphorylated acidic proteins (phosphodontin) were found in the teeth system (Aristotle's lantern) of the sea urchin *Strongylocentrotus purpuratus* (Mann et al., 2010).

In the *T. crocea* shell proteome, 10 SMPs have S- or T-rich LCRs that are likely phosphorylated (**Figure 8**). Four ChBD-containing proteins including BMSP exhibit putative phosphorylated LCRs, which certainly increase their affinity to calcium ions. We suggest that the combination of ChBDs and T-rich LCRs in some SMP sequences may be an essential requisite to form a molecular bridge between chitin and calcium carbonate. Phosphorylation may also change the conformation of SMPs to build proper structure in the shell organic framework. Our results highlight the phosphorylation of SMPs as an alternative mechanism to 'acidify' the shell organic matrix, regardless of the presence of Asp-rich proteins.

CONCLUSION

In this study, we conducted a biochemical characterization of the crossed lamellar shell of *T. crocea*, the crocus clam. We identified 39 proteins that show little homology with that of other bivalves studied so far. Beside evolutionary aspects, the SMP repertoire of *T. crocea* provides a large set of molecular markers, usable to check how this species reacts to environmental stress, in particular ocean acidification, known to induce deleterious effects on shell calcification. We have every reason to think that these effects may be quantifiable by analyzing the SMP gene expression.

At last, the SMP repertoire of living *T. crocea* opens a window on the shell repertoire of similar fossil shell materials. Recently, we have identified SMPs from well-dated (2,880 ± 30 BC) *Tridacna* sp. subfossils of French Polynesia (Marin et al., 2018). Our study shows the good potential for preservation of some SMPs across archaeological times. It consequently paves the road of an emerging discipline, 'palaeoshellomics' (Wallace and Schiffbauer, 2016; Sakalauskaite et al., 2020).

DATA AVAILABILITY STATEMENT

The data presented in the study are deposited in the Dryad repository, accession number https://doi.org/10.5061/dryad.4mw6m9094.

AUTHOR CONTRIBUTIONS

TT and FM conceived and designed the experiments. TT, MF, RK, LP, IZ-D, NB, and CB performed the experiments and analyzed the data. TT, NS, and FM wrote the manuscript. All authors reviewed and approved the manuscript.

FUNDING

This study was supported by internal funds from the Okinawa Institute of Science and Technology (OIST).

Complementary funds were obtained via annual recurrent budget of UMR CNRS Biogeosciences, Dijon (FM).

ACKNOWLEDGMENTS

We thank Munekazu Mekaru (Onna Fisheries Corporation, Okinawa), Yuna Zayasu (OIST), and Chuya Shinzato (The University of Tokyo) for preparing the animals. A part of the experimental work of TT was performed at Biogeosciences research unit via a 6-month post-doctorate.

SUPPLEMENTARY MATERIAL

The Supplementary Material for this article can be found online at: https://www.frontiersin.org/articles/10.3389/fgene.2021.674539/full#supplementary-material

REFERENCES

Addadi, L., and Weiner, S. (1985). Interactions between acidic proteins and crystals: stereochemical requirements in biomineralization. *PNAS* 82, 4110–4114. doi: 10.1073/pnas.82.12.4110

Agbaje, O. B. A., Ben Shir, I., Zax, D. B., Schmidt, A., and Jacob, D. E. (2018). Biomacromolecules within bivalve shells: is chitin abundant? *Acta Biomater.* 80, 176–187. doi: 10.1016/j.actbio.2018.09.009

Agbaje, O. B. A., Thomas, D. E., Dominguez, J. G., Mclnerney, B. V., Kosnik, M. A., and Jacob, D. E. (2019). Biomacromolecules in bivalve shells with crossed lamellar architecture. *J. Mater. Sci.* 54, 4952–4969. doi: 10.1007/s10853-018-3165-8

Agbaje, O. B. A., Wirth, R., Morales, L. F. G., Shirai, K., Kosnik, M., Watanabe, T., et al. (2017). Architecture of crossed-lamellar bivalve shells: the southern giant clam (*Tridacna derasa*, Röding, 1798). *R. Soc. Open Sci.* 4:170622. doi: 10.1098/rsos.170622

Aguilera, F., McDougall, C., and Degnan, B. M. (2014). Evolution of the tyrosinase gene family in bivalve molluscs: independent expansion of the mantle gene repertoire. *Acta Biomater.* 10, 3855–3865. doi: 10.1016/j.actbio.2014.03.031

Albeck, S., Aizenberg, J., Addadi, L., and Weiner, S. (1993). Interactions of various skeletal intracrystalline components with calcite crystals. *J. Am. Chem. Soc.* 115, 11691–11697. doi: 10.1021/ja00078a005

Arias-Ruiz, C., Elliot, M., Bézos, A., Pedoja, K., Husson, L., Cahyarini, S. Y., et al. (2017). Geochemical fingerprints of climate variation and the extreme La Niña 2010–11 as recorded in a Tridacna Squamosa shell from Sulawesi, Indonesia. *Palaeogeogr. Palaeoclimatol. Palaeoecol.* 487, 216–228. doi: 10.1016/j.palaeo.2017.08.037

Arivalagan, J., Marie, B., Sleight, V. A., Clark, M. S., Berland, S., and Marie, A. (2016). Shell matrix proteins of the clam, *Mya truncata*: roles beyond shell formation through proteomic study. *Mar. Genom.* 27, 69–74. doi: 10.1016/j.margen.2016.03.005

Arivalagan, J., Yarra, T., Marie, B., Sleight, V. A., Duvernois-Berthet, E., Clark, M. S., et al. (2017). Insights from the shell proteome: biomineralization to adaptation. *Mol. Biol. Evol.* 34, 66–77. doi: 10.1093/molbev/msw219

Berland, S., Ma, Y., Marie, A., Andrieu, J.-P., Bedouet, L., and Feng, Q. (2013). Proteomic and profile analysis of the proteins laced with aragonite and vaterite in the freshwater mussel hyriopsis cumingii shell biominerals. *Protein Peptide Lett.* 20, 1170–1180. doi: 10.2174/0929866511320100012

Blom, N., Gammeltoft, S., and Brunak, S. (1999). Sequence and structure-based prediction of eukaryotic protein phosphorylation sites. *J. Mol. Biol.* 294, 1351–1362. doi: 10.1006/jmbi.1999.3310

Bolger, A. M., Lohse, M., and Usadel, B. (2014). Trimmomatic: a flexible trimmer for illumina sequence data. *Bioinformatics* 30, 2114–2120. doi: 10.1093/bioinformatics/btu170

Campbell, K. P., MacLennan, D. H., and Jorgensen, A. O. (1983). Staining of the Ca2+-binding proteins, calsequestrin, calmodulin, troponin C, and S-100, with the cationic carbocyanine dye "Stains-all". *J. Biol. Chem.* 258, 11267–11273. doi: 10.1016/s0021-9258(17)44413-9

Campos, P. V., Albuquerque, A. R. L., Angélica, R. S., and Paz, S. P. A. (2021). FTIR spectral signatures of amazon inorganic phosphates: igneous, weathering, and biogenetic origin. *Spectrochim. Acta Part A Mol. Biomol. Spectrosc.* 251:119476. doi: 10.1016/j.saa.2021.119476

Cuif, J., Dauphin, Y., Denis, A., Gautret, A., and Marin, F. (1996). The organo-mineral structure of coral skeletons: a potential source of new criteria for Scleractinian taxonomy. *Bull. Institut. Océanogr. Monaco* 14, 359–367.

Dauphin, Y., and Denis, A. (2000). Structure and composition of the aragonitic crossed lamellar layers in six species of Bivalvia and Gastropoda. *Comp. Biochem. Physiol. Part A Mol. Integr. Physiol.* 126, 367–377. doi: 10.1016/S1095-6433(00)00213-0

Gannon, M. E., Pérez-Huerta, A., Aharon, P., and Street, S. C. (2017). A biomineralization study of the Indo-Pacific giant clam *Tridacna gigas*. *Coral Reefs* 36, 503–517. doi: 10.1007/s00338-016-1538-5

Gao, P., Liao, Z., Wang, X.-X., Bao, L.-F., Fan, M.-H., Li, X.-M., et al. (2015). Layer-by-layer proteomic analysis of *Mytilus galloprovincialis* shell. *PLoS One* 10:e0133913. doi: 10.1371/journal.pone.0133913

George, A., Sabsay, B., Simonian, P. A., and Veis, A. (1993). Characterization of a novel dentin matrix acidic phosphoprotein. Implications for induction of biomineralization. *J. Biol. Chem.* 268, 12624–12630. doi: 10.1016/s0021-9258(18)31434-0

Gericke, A., Qin, C., Spevak, L., Fujimoto, Y., Butler, W. T., Sørensen, E. S., et al. (2005). Importance of phosphorylation for osteopontin regulation of biomineralization. *Calcif. Tissue Int.* 77, 45–54. doi: 10.1007/s00223-004-1288-1

Gotliv, B.-A., Kessler, N., Sumerel, J. L., Morse, D. E., Tuross, N., Addadi, L., et al. (2005). Asprich: a novel aspartic acid-rich protein family from the prismatic shell matrix of the bivalve *Atrina rigida*. *ChemBioChem* 6, 304–314. doi: 10.1002/cbic.200400221

Grabherr, M. G., Haas, B. J., Yassour, M., Levin, J. Z., Thompson, D. A., Amit, I., et al. (2011). Full-length transcriptome assembly from RNA-Seq data without a reference genome. *Nat. Biotechnol.* 29, 644–652. doi: 10.1038/nbt.1883

Hare, P. E. (1963). Amino acids in the proteins from aragonite and calcite in the shells of *Mytilus californianus*. *Science* 139, 216–217. doi: 10.1126/science.139.3551.216

Hasegawa, Y., and Uchiyama, K. (2005). cDNA clonings of shell matrix proteins from scallop shell. *Fish Sci.* 71, 1174–1178. doi: 10.1111/j.1444-2906.2005.01078.x

He, G., Ramachandran, A., Dahl, T., George, S., Schultz, D., Cookson, D., et al. (2005). Phosphorylation of phosphophoryn is crucial for its function as a mediator of biomineralization. *J. Biol. Chem.* 280, 33109–33114. doi: 10.1074/jbc.M500159200

Hecker, A., Testenière, O., Marin, F., and Luquet, G. (2003). Phosphorylation of serine residues is fundamental for the calcium-binding ability of Orchestin, a soluble matrix protein from crustacean calcium storage structures. *FEBS Lett.* 535, 49–54. doi: 10.1016/s0014-5793(02)03856-5

Hirose, E., Iwai, K., and Maruyama, T. (2006). Establishment of the photosymbiosis in the early ontogeny of three giant clams. *Mar. Biol.* 148, 551–558. doi: 10.1007/s00227-005-0119-x

Ikeda, S., Yamashita, H., Kondo, S.-N., Inoue, K., Morishima, S.-Y., and Koike, K. (2017). Zooxanthellal genetic varieties in giant clams are partially determined by species-intrinsic and growth-related characteristics. *PLoS One* 12:e0172285. doi: 10.1371/journal.pone.0172285

Immel, F., Broussard, C., Catherinet, B., Plasseraud, L., Alcaraz, G., Bundeleva, I., et al. (2016). The shell of the invasive bivalve species dreissena polymorpha: biochemical, elemental and textural investigations. *PLoS One* 11:e0154264. doi: 10.1371/journal.pone.0154264

Inoue, H., Ohira, T., Ozaki, N., and Nagasawa, H. (2003). Cloning and expression of a cDNA encoding a matrix peptide associated with calcification in the exoskeleton of the crayfish. *Comp. Biochem. Physiol. Part B Biochem. Mol. Biol.* 136, 755–765. doi: 10.1016/S1096-4959(03)00210-0

Isowa, Y., Sarashina, I., Setiamarga, D. H. E., and Endo, K. (2012). A comparative study of the shell matrix protein aspein in pterioid bivalves. *J. Mol. Evol.* 75, 11–18. doi: 10.1007/s00239-012-9514-3

Jastrzębski, W., Sitarz, M., Rokita, M., and Bułat, K. (2011). Infrared spectroscopy of different phosphates structures. *Spectrochim. Acta Part A Mol. Biomol. Spectrosc.* 79, 722–727. doi: 10.1016/j.saa.2010.08.044

Jones, P., Binns, D., Chang, H.-Y., Fraser, M., Li, W., McAnulla, C., et al. (2014). InterProScan 5: genome-scale protein function classification. *Bioinformatics* 30, 1236–1240. doi: 10.1093/bioinformatics/btu031

Joubert, C., Piquemal, D., Marie, B., Manchon, L., Pierrat, F., Zanella-Cléon, I., et al. (2010). Transcriptome and proteome analysis of *Pinctada margaritifera* calcifying mantle and shell: focus on biomineralization. *BMC Genomics* 11:613. doi: 10.1186/1471-2164-11-613

Kanold, J. M., Guichard, N., Immel, F., Plasseraud, L., Corneillat, M., Alcaraz, G., et al. (2015). Spine and test skeletal matrices of the Mediterranean sea urchin Arbacia lixula – a comparative characterization of their sugar signature. *FEBS J.* 282, 1891–1905. doi: 10.1111/febs.13242

Kocot, K. M., Aguilera, F., McDougall, C., Jackson, D. J., and Degnan, B. M. (2016). Sea shell diversity and rapidly evolving secretomes: insights into the evolution of biomineralization. *Front. Zool.* 13:23. doi: 10.1186/s12983-016-0155-z

Kozlowski, L. P. (2016). IPC – isoelectric point calculator. *Biol. Direct* 11:55. doi: 10.1186/s13062-016-0159-9

Krogh, A., Larsson, B., von Heijne, G., and Sonnhammer, E. L. (2001). Predicting transmembrane protein topology with a hidden Markov model: application to complete genomes. *J. Mol. Biol.* 305, 567–580. doi: 10.1006/jmbi.2000.4315

Laemmli, U. K. (1970). Cleavage of structural proteins during the assembly of the head of bacteriophage T4. *Nature* 227, 680–685. doi: 10.1038/227680a0

Liang, J., Xu, G., Xie, J., Lee, I., Xiang, L., Wang, H., et al. (2015). Dual roles of the lysine-rich matrix protein (KRMP)-3 in shell formation of *Pearl oyster*, *Pinctada fucata*. *PLoS One* 10:e0131868. doi: 10.1371/journal.pone.0131868

Liao, Z., Bao, L.-F., Fan, M.-H., Gao, P., Wang, X.-X., Qin, C.-L., et al. (2015). In-depth proteomic analysis of nacre, prism, and myostracum of *Mytilus shell*. *J. Proteom.* 122, 26–40. doi: 10.1016/j.jprot.2015.03.027

Liao, Z., Jiang, Y.-T., Sun, Q., Fan, M.-H., Wang, J.-X., and Liang, H.-Y. (2019). Microstructure and in-depth proteomic analysis of *Perna viridis* shell. *PLoS One* 14:e0219699. doi: 10.1371/journal.pone.0219699

Liu, C., Li, S., Kong, J., Liu, Y., Wang, T., Xie, L., et al. (2015). In-depth proteomic analysis of shell matrix proteins of *Pinctada fucata*. *Sci. Rep.* 5:17269. doi: 10.1038/srep17269

Lucas, J. S. (1988). *Giant Clams in Asia and the Pacific*. Canberra: Australian Centre for International Agricultural Research.

Mann, K., Poustka, A. J., and Mann, M. (2010). Phosphoproteomes of *Strongylocentrotus purpuratus* shell and tooth matrix: identification of a major acidic sea urchin tooth phosphoprotein, phosphodontin. *Proteome Sci.* 8:6. doi: 10.1186/1477-5956-8-6

Marie, B., Arivalagan, J., Mathéron, L., Bolbach, G., Berland, S., Marie, A., et al. (2017). Deep conservation of bivalve nacre proteins highlighted by shell matrix proteomics of the Unionoida Elliptio complanata and *Villosa lienosa*. *J. R. Soc. Interface* 14:20160846. doi: 10.1098/rsif.2016.0846

Marie, B., Joubert, C., Tayalé, A., Zanella-Cléon, I., Belliard, C., Piquemal, D., et al. (2012). Different secretory repertoires control the biomineralization processes of prism and nacre deposition of the pearl oyster shell. *PNAS* 109, 20986–20991. doi: 10.1073/pnas.1210552109

Marie, B., Marie, A., Jackson, D. J., Dubost, L., Degnan, B. M., Milet, C., et al. (2010). Proteomic analysis of the organic matrix of the abalone Haliotis Asinina calcified shell. *Proteome Sci.* 8:54. doi: 10.1186/1477-5956-8-54

Marie, B., Roy, N. L., Zanella-Cléon, I., Becchi, M., and Marin, F. (2011a). Molecular evolution of mollusc shell proteins: insights from proteomic analysis of the edible mussel mytilus. *J. Mol. Evol.* 72, 531–546. doi: 10.1007/s00239-011-9451-6

Marie, B., Trinkler, N., Zanella-Cleon, I., Guichard, N., Becchi, M., Paillard, C., et al. (2011b). Proteomic identification of novel proteins from the calcifying shell matrix of the manila clam venerupis philippinarum. *Mar. Biotechnol.* 13, 955–962. doi: 10.1007/s10126-010-9357-0

Marin, F. (2020). Mollusc shellomes: past, present and future. *J. Struct. Biol.* 212:107583. doi: 10.1016/j.jsb.2020.107583

Marin, F., Amons, R., Guichard, N., Stigter, M., Hecker, A., Luquet, G., et al. (2005). Caspartin and calprismin, two proteins of the shell calcitic prisms of the Mediterranean fan mussel *Pinna nobilis*. *J. Biol. Chem.* 280, 33895–33908. doi: 10.1074/jbc.M506526200

Marin, F., Chmiel, A., Takeuchi, T., Bundeleva, I., Durlet, C., Samankassou, E., et al. (2018). "Skeletal organic matrices in molluscs: origin, evolution, diagenesis," in *Biomineralization*, eds K. Endo, T. Kogure, and H. Nagasawa (Berlin: Springer), 325–332. doi: 10.1007/978-981-13-1002-7_34

Marin, F., and Luquet, G. (2007). Unusually acidic proteins in biomineralization. *Handb. Biomineral.* 1, 273–290. doi: 10.1002/9783527619443.ch16

Marin, F., and Luquet, G. (2008). "Unusually acidic proteins in biomineralization," in *Handbook of Biomineralization*, eds K. Endo, T. Kogure, and H. Nagasawa (Hoboken, NJ: John Wiley & Sons, Ltd), 273–290. doi: 10.1002/9783527619443.ch16

Marin, F., Luquet, G., Marie, B., and Medakovic, D. (2007). "Molluscan shell proteins: primary structure, origin, and evolution," in *Current Topics in Developmental Biology*, ed. G. Schatten (Cambridge, MA: Academic Press), 209–276. doi: 10.1016/s0070-2153(07)80006-8

Marin, F., Marie, B., Ben Hamada, S., Ramos-Silva, P., Le Roy, N., Guichard, N., et al. (2013). "'Shellome': proteins involved in mollusk shell biomineralization - diversity, functions," in *Recent Advances in Pearl Research*, ed. H. N. S. Watabe (Tokyo: Terrapub), 149–166.

Marxen, J. C., Hammer, M., Gehrke, T., and Becker, W. (1998). Carbohydrates of the organic shell matrix and the shell-forming tissue of the snail *Biomphalaria glabrata* (Say). *Biol. Bull.* 194, 231–240. doi: 10.2307/1543052

McDougall, C., Aguilera, F., and Degnan, B. M. (2013). Rapid evolution of pearl oyster shell matrix proteins with repetitive, low-complexity domains. *J. R. Soc. Interface* 10:20130041. doi: 10.1098/rsif.2013.0041

Morrissey, J. H. (1981). Silver stain for proteins in polyacrylamide gels: a modified procedure with enhanced uniform sensitivity. *Anal. Biochem.* 117, 307–310. doi: 10.1016/0003-2697(81)90783-1

Nagai, K., Yano, M., Morimoto, K., and Miyamoto, H. (2007). Tyrosinase localization in mollusc shells. *Comp. Biochem. Physiol. Part B Biochem. Mol. Biol.* 146, 207–214. doi: 10.1016/j.cbpb.2006.10.105

Osuna-Mascaró, A. J., Cruz-Bustos, T., Marin, F., and Checa, A. G. (2015). Ultrastructure of the interlamellar membranes of the nacre of the bivalve pteria hirundo, determined by immunolabelling. *PLoS One* 10:e0122934. doi: 10.1371/journal.pone.0122934

Oudot, M., Shir, I. B., Schmidt, A., Plasseraud, L., Broussard, C., Neige, P., et al. (2020). A nature's curiosity: the argonaut "shell" and its organic content. *Crystals* 10:839. doi: 10.3390/cryst10090839

Petersen, T. N., Brunak, S., von Heijne, G., and Nielsen, H. (2011). SignalP 4.0: discriminating signal peptides from transmembrane regions. *Nat. Methods* 8, 785–786. doi: 10.1038/nmeth.1701

Plazzi, F., and Passamonti, M. (2010). Towards a molecular phylogeny of Mollusks: bivalves' early evolution as revealed by mitochondrial genes. *Mol. Phylogenet. Evol.* 57, 641–657. doi: 10.1016/j.ympev.2010.08.032

Sakalauskaite, J., Marin, F., Pergolizzi, B., and Demarchi, B. (2020). Shell palaeoproteomics: first application of peptide mass fingerprinting for the rapid identification of mollusc shells in archaeology. *J. Proteomics* 227:103920. doi: 10.1016/j.jprot.2020.103920

Sarashina, I., and Endo, K. (1998). Primary structure of a soluble matrix protein of scallop shell; implications for calcium carbonate biomineralization. *Am. Mineral.* 83, 1510–1515. doi: 10.2138/am-1998-11-1239

Sarashina, I., and Endo, K. (2001). The complete primary structure of molluscan shell protein 1 (MSP-1), an acidic glycoprotein in the shell matrix of the scallop *Patinopecten yessoensis*. *Mar. Biotechnol.* 3, 362–369. doi: 10.1007/s10126-001-0013-6

Sleight, V. A., Thorne, M. A. S., Peck, L. S., and Clark, M. S. (2015). Transcriptomic response to shell damage in the Antarctic clam, *Laternula elliptica*: time scales and spatial localisation. *Mar. Genom.* 20, 45–55. doi: 10.1016/j.margen.2015.01.009

Sudo, S., Fujikawa, T., Nagakura, T., Ohkubo, T., Sakaguchi, K., Tanaka, M., et al. (1997). Structures of mollusc shell framework proteins. *Nature* 387, 563–564. doi: 10.1038/42391

Suzuki, M., Iwashima, A., Tsutsui, N., Ohira, T., Kogure, T., and Nagasawa, H. (2011). Identification and characterisation of a calcium carbonate-binding protein, blue mussel shell protein (BMSP), from the nacreous layer. *ChemBioChem* 12, 2478–2487. doi: 10.1002/cbic.201100317

Suzuki, M., Murayama, E., Inoue, H., Ozaki, N., Tohse, H., Kogure, T., et al. (2004). Characterization of Prismalin-14, a novel matrix protein from the prismatic layer of the Japanese pearl oyster (*Pinctada fucata*). *Biochem. J.* 382, 205–213. doi: 10.1042/BJ20040319

Suzuki, M., and Nagasawa, H. (2007). The structure–function relationship analysis of Prismalin-14 from the prismatic layer of the Japanese pearl oyster, *Pinctada fucata*. *FEBS J.* 274, 5158–5166. doi: 10.1111/j.1742-4658.2007.06036.x

Suzuki, M., Sakuda, S., and Nagasawa, H. (2007). Identification of chitin in the prismatic layer of the shell and a chitin synthase gene from the Japanese *Pearl oyster*, *Pinctada fucata*. *Biosci. Biotechnol. Biochem.* 71, 1735–1744. doi: 10.1271/bbb.70140

Suzuki, M., Saruwatari, K., Kogure, T., Yamamoto, Y., Nishimura, T., Kato, T., et al. (2009). An acidic matrix protein, pif, is a key macromolecule for nacre formation. *Science* 325, 1388–1390. doi: 10.1126/science.1173793

Takeuchi, T., Plasseraud, L., Ziegler-Devin, I., Brosse, N., Shinzato, C., Satoh, N., et al. (2018). Biochemical characterization of the skeletal matrix of the massive coral, Porites Australiensis – The saccharide moieties and their localization. *J. Struct. Biol.* 203, 219–229. doi: 10.1016/j.jsb.2018.05.011

Takeuchi, T., Sarashina, I., Iijima, M., and Endo, K. (2008). In vitro regulation of CaCO(3) crystal polymorphism by the highly acidic molluscan shell protein Aspein. *FEBS Lett.* 582, 591–596. doi: 10.1016/j.febslet.2008.01.026

Taylor, J. D. (1973). The structural evolution of the bivalve shell. *Palaeontology* 16, 519–534.

Thornton, D. J., Carlstedt, I., and Sheehan, J. K. (1996). Identification of glycoproteins on nitrocellulose membranes and gels. *Mol. Biotechnol.* 5, 171–176. doi: 10.1007/BF02789065

Tsukamoto, D., Sarashina, I., and Endo, K. (2004). Structure and expression of an unusually acidic matrix protein of pearl oyster shells. *Biochem. Biophys. Res. Commun.* 320, 1175–1180. doi: 10.1016/j.bbrc.2004.06.072

Wallace, A. F., and Schiffbauer, J. D. (2016). Proteins from the past. *eLife* 5:e20877. doi: 10.7554/eLife.20877

Weiner, S. (1979). Aspartic acid-rich proteins: major components of the soluble organic matrix of mollusk shells. *Calcif. Tissue Int.* 29, 163–167. doi: 10.1007/BF02408072

Weiner, S. (1983). Mollusk shell formation: isolation of two organic matrix proteins associated with calcite deposition in the bivalve *Mytilus californianus*. *Biochemistry* 22, 4139–4145. doi: 10.1021/bi00286a023

Weiner, S., and Hood, L. (1975). Soluble protein of the organic matrix of mollusk shells: a potential template for shell formation. *Science* 190, 987–989. doi: 10.1126/science.1188379

Weiss, I. M., and Schönitzer, V. (2006). The distribution of chitin in larval shells of the bivalve mollusk *Mytilus galloprovincialis*. *J. Struct. Biol.* 153, 264–277. doi: 10.1016/j.jsb.2005.11.006

Yan, H., Liu, C., An, Z., Yang, W., Yang, Y., Huang, P., et al. (2020). Extreme weather events recorded by daily to hourly resolution biogeochemical proxies of marine giant clam shells. *PNAS* 117, 7038–7043. doi: 10.1073/pnas.1916784117

Yano, M., Nagai, K., Morimoto, K., and Miyamoto, H. (2006). Shematrin: a family of glycine-rich structural proteins in the shell of the pearl oyster *Pinctada fucata*. *Comp. Biochem. Physiol. B Biochem. Mol. Biol.* 144, 254–262. doi: 10.1016/j.cbpb.2006.03.004

Zhang, G., Fang, X., Guo, X., Li, L., Luo, R., Xu, F., et al. (2012). The oyster genome reveals stress adaptation and complexity of shell formation. *Nature* 490, 49–54. doi: 10.1038/nature11413

Zhao, R., Takeuchi, T., Luo, Y.-J., Ishikawa, A., Kobayashi, T., Koyanagi, R., et al. (2018). Dual gene repertoires for larval and adult shells reveal molecules essential for molluscan shell formation. *Mol. Biol. Evol.* 35, 2751–2761. doi: 10.1093/molbev/msy172

Conflict of Interest: The authors declare that the research was conducted in the absence of any commercial or financial relationships that could be construed as a potential conflict of interest.

frontiers in Genetics

ORIGINAL RESEARCH
published: 25 November 2021
doi: 10.3389/fgene.2021.788346

Divergent Expression of *SPARC*, *SPARC-L*, and *SCPP* Genes During Jawed Vertebrate Cartilage Mineralization

Adrian Romero[1†], *Nicolas Leurs*[2†], *David Muñoz*[1], *Mélanie Debiais-Thibaud*[2*] and *Sylvain Marcellini*[1*]

[1]Laboratory of Development and Evolution (LADE), University of Concepción, Concepción, Chile, [2]Institut des Sciences de l'Evolution de Montpellier, ISEM, Univ Montpellier, CNRS, IRD, EPHE, Montpellier, France

While cartilage is an ancient tissue found both in protostomes and deuterostomes, its mineralization evolved more recently, within the vertebrate lineage. *SPARC*, *SPARC-L*, and the *SCPP* members (Secretory Calcium-binding PhosphoProtein genes which evolved from *SPARC-L*) are major players of dentine and bone mineralization, but their involvement in the emergence of the vertebrate mineralized cartilage remains unclear. We performed *in situ* hybridization on mineralizing cartilaginous skeletal elements of the frog *Xenopus tropicalis* (*Xt*) and the shark *Scyliorhinus canicula* (*Sc*) to examine the expression of *SPARC* (present in both species), *SPARC-L* (present in *Sc* only) and the *SCPP* members (present in *Xt* only). We show that while mineralizing cartilage expresses *SPARC* (but not *SPARC-L*) in *Sc*, it expresses the *SCPP* genes (but not *SPARC*) in *Xt*, and propose two possible evolutionary scenarios to explain these opposite expression patterns. In spite of these genetic divergences, our data draw the attention on an overlooked and evolutionarily conserved peripheral cartilage subdomain expressing *SPARC* or the *SCPP* genes and exhibiting a high propensity to mineralize.

Keywords: *SPARC*, *SPARC-L*, *SCPP*, cartilage mineralization, *Xenopus tropicalis*, *Scyliorhinus canicula*, vertebrate evolution

OPEN ACCESS

Edited by:
Claudio Oliveira,
São Paulo State University, Brazil

Reviewed by:
Anthony K. Redmond,
Trinity College Dublin, Ireland
Andrew Jheon,
University of California, San Francisco, United States

***Correspondence:**
Mélanie Debiais-Thibaud
melanie.debiais-thibaud@umontpellier.fr
Sylvain Marcellini
smarcellini@udec.cl

[†]*These authors have contributed equally to this work*

Specialty section:
This article was submitted to Evolutionary and Population Genetics, a section of the journal Frontiers in Genetics

Received: *02 October 2021*
Accepted: *10 November 2021*
Published: *25 November 2021*

Citation:
Romero A, Leurs N, Muñoz D, Debiais-Thibaud M and Marcellini S (2021) Divergent Expression of SPARC, SPARC-L, and SCPP Genes During Jawed Vertebrate Cartilage Mineralization. Front. Genet. 12:788346. doi: 10.3389/fgene.2021.788346

INTRODUCTION

The evolution of a mineralized skeleton occurred in early vertebrates, in a variety of tissues including superficial dermal scales and teeth, together with internal cartilages, and perichondral bones (Ørvig, 1951; Donoghue and Sansom, 2002). In the internal skeleton, several cell types are associated with biomineralization, and the most studied cell model in mammalian organisms is the osteoblast active in the endochondral ossification process (Long and Ornitz, 2013). These osteoblasts are derived from periosteal tissues or from hypertrophic transdifferentiated chondrocytes (Tsang et al., 2015). The process of endochondral ossification, or replacement of cartilage matrix by bone marrow and bone trabeculae, is absent from chondrichthyans and has long been thought to be a derived feature specific to osteichthyans (reviewed in Donoghue and Sansom, 2002; Hirasawa and Kuratani, 2015), although recent paleontological data has challenged this view (Brazeau et al., 2020). Also known to mineralize their matrix are the chondrocytes, not only at the ossification front of endochondral bone growth (in the case of hyaline cartilage), but also in stable forms of mineralized cartilage such as fibrocartilages and other forms of cartilage displaying striking similarities to bony tissues (Beresford, 1981; Dyment

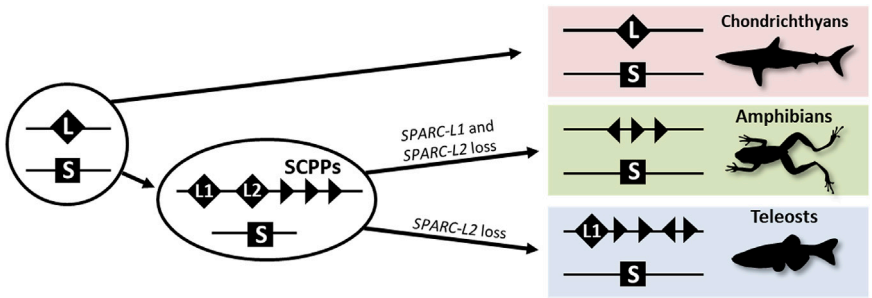

FIGURE 1 | A simplified evolutionary scenario for the *SPARC/SPARC-L/SCPP* family. Vertebrate-specific whole genome duplications produced the ancestral *SPARC* (S) and *SPARC-L* (L) paralogues. These loci were not overtly altered in the chondrichthyan lineage as both genes are clearly identifiable in sharks. In the osteichthyan lineage, local duplications at the *SPARC-L* locus produced *SPARC-L1* (L1), *SPARC-L2* (L2) and the *SCPP* members (triangles). Triangles in different orientations symbolize the fact that *SCPP* genes are subject to independent local duplications events and a high rate of evolutionary divergence, hindering homology relationships. *SPARC-L2* was independently lost in tetrapods and teleosts and *SPARC-L1* was also lost in amphibians. See text for details and references.

et al., 2015; Paul et al., 2016; Pears et al., 2020; Berio et al., 2021). Even though both perichondral bones and cartilaginous tissues displayed mineralization in the earliest forms of mineralized internal skeletons (Ørvig, 1951; Min and Janvier, 1998; Donoghue et al., 2006; Johanson et al., 2010, 2012; Pears et al., 2020), mineralizing cartilages have been understudied from a genetic and evolutionary perspective in extant vertebrates. A better understanding of the genetic underpinning of the mineralizing chondrocytes is therefore necessary to understand the early steps of the evolution of endoskeletal mineralization in vertebrates.

The evolution of vertebrate endoskeletal mineralization has been discussed in the light of the two rounds of whole-genome duplication (2Rs). These duplications occurred before the diversification of extant jawed vertebrates (Nakatani et al., 2021) and generated gene families with diverging gene functions which may have produced the genetic toolkit required for the cellular ability to mineralize an extracellular matrix (Zhang and Cohn, 2008). The evolution of the *SPARC/SPARC-L/SCPP* gene family has been of great interest in this perspective (Kawasaki and Weiss, 2003; Kawasaki et al., 2005; Kawasaki, 2009; Bertrand et al., 2013; Enault et al., 2018), and is summarized in **Figure 1**. *SPARC-L* and *SPARC* are two paralogues having originated from the 2Rs (Kawasaki and Weiss, 2003; Kawasaki et al., 2005; Kawasaki, 2009; Bertrand et al., 2013; Enault et al., 2018). In bony fishes, independent local duplications at the *SPARC-L* locus generated *SPARC-L1* and *SPARC-L2* and a variable number of tandemly located genes coding for Secretory Calcium-binding PhosphoProteins (SCPPs) that have evolved rapidly since their origin (see **Supplementary Figure S1** and Kawasaki and Weiss, 2003; Kawasaki et al., 2005; Enault et al., 2018). Hence outside of amniotes, homology relationships between *SCPP* duplicates are obscured by independent gene gains and losses together with a high rate of sequence divergence (Kawasaki, 2009). No *SCPP* genes have been identified in cartilaginous fish genomes, making the chondrichthyan *SPARC-L* gene the single orthologue to all *SCPP* genes of bony vertebrates (see **Figure 1**, **Supplementary Figure S1** and Ryll et al., 2014; Venkatesh et al., 2014; Enault et al., 2018).

The *SPARC* gene (Secreted Protein Acidic and Rich in Cysteine, formerly coined *Osteonectin*) encodes a matricellular protein which is one of the most abundant non-collagenous matrix proteins in mammalian and teleost bone (Schreiweis et al., 2007; Kessels et al., 2014). Secreted by osteoblasts, the SPARC protein functions in mineralized tissues by binding both collagen fibrils and calcium, but also by signaling to bone cells (reviewed by Rosset and Bradshaw, 2016). In osteichthyans, the expression of *SPARC* is evolutionary conserved in osteoblasts as well as in odontoblasts (Holland et al., 1987; Li et al., 2009; Espinoza et al., 2010; Enault et al., 2018). In chondrichthyans having secondarily lost the bone tissue (and the osteoblast cell type), *SPARC* is highly expressed in odontoblasts (Enault et al., 2018). The single *SPARC-L* gene in cartilaginous fishes is expressed in enameloid secreting cells in teeth and scales of the catshark *Scyliorhinus canicula* (Enault et al., 2018). In osteichthyans it seems that *SPARC-L1* and *SPARC-L2* are not specifically expressed nor functionally required in the skeleton (McKinnon et al., 2000; Bertrand et al., 2013). In addition, *SPARC-L2* was independently lost in tetrapods and teleosts, and *SPARC-L1* was also lost in amphibians (see **Figure 1** and Kawasaki et al., 2007; Bertrand et al., 2013; Enault et al., 2018), suggesting that these two genes are functionally dispensable. Rather, in osteichthyans, *SCPP* family members are key players of skeletal mineralization. Within amniote *SCPP* genes, *Bone sialoprotein* (*BSP*), *Osteopontin* (*OPN* or *SPP1*) and *Dentin matrix protein 1* (*DMP1*) are strongly expressed by osteoblasts and their protein products are stored in the mineral phase of bone tissue (Ustriyana et al., 2021). Most members of this family are also expressed and functional during tooth development in mammals (either in the production of enamel or/and dentin, reviewed by Nikoloudaki, 2021). In the clawed frog *Xenopus tropicalis* and the zebrafish *Danio rerio* the expression of distinct *SCPP* members has been reported in ameloblasts, odontoblasts, and osteoblasts (Kawasaki et al., 2005; Kawasaki, 2009; Espinoza et al., 2010; Enault et al., 2018). Overall, our knowledge of the evolution of the expression of *SPARC*, *SPARC-L* and the *SCPP* members during

cartilage mineralization remains limited, and, in this study, we examined the expression of these genes during endoskeletal development in *Xenopus tropicalis* and *Scyliorhinus canicula*.

METHODS

Specimens, Histological Staining and Cryo-Sections

Lesser spotted catshark (*Scyliorhinus canicula*) embryos were maintained at 17°C at the University of Montpellier, France, until they reached development stage 32 (Ballard et al., 1993; Maxwell et al., 2008). Embryos were taken out of their eggshell, anesthetized and subsequently euthanized by overdose of MS-222 (Sigma) following European animal-care specifications. As substantial growth occurs during stage 32, each individual was measured before fixation and classified into early, intermediate and late stages whose body length measured respectively 5.3, 6.6, and 8.5 cm for histological analyses, and respectively 5.0, 6.3, and 7.9 cm for the Alizarin red S and *in situ* hybridization procedures. Abdominal vertebral portions were fixed 48 h in PFA 4% in PBS 1× at 4°C and were subsequently transferred in ethanol and stored at − 20°C until needed.

Adult *Xenopus tropicalis* were maintained following standard protocols established for this species, at the University of Concepcion. Embryos and tadpoles were raised after natural mating and staged according to the Nieuwkoop and Faber developmental table (Nieuwkoop and Faber, 1967). Anesthesia of tadpoles was performed with a MS-222 (Sigma) solution at 2 mg/ml and each specimen was subsequently decapitated in agreement with international bioethical recommendations (Close et al., 1996; Ramlochansingh et al., 2014).

Dissected organs of both species were embedded in paraffin to generate 7 μm-thick histological sections that were stained with standard protocols [eosin, hematoxylin and safran reaction for catshark (RHEM platform at IRCM, Montpellier); hematoxylin and chromotrope 2R (C3143 Sigma) for frog sections]. The von Kossa protocol was used on paraffin sections of *Xenopus tropicalis* to detect calcium on tissue sections (#10241, Diapath, Italy) following the manufacturer's instruction. Briefly, the von Kossa method is based on the transformation of calcium ions, bound to phosphates, into silver ions brought by a solution of silver nitrate.

Spotted catshark alizarin red S and *in situ* hybridizations were performed on serial, 14 μm thick cryostat sections, cut transversal in the body trunk, at the level of the pectoral fins. Parts of the specimens that were not used for this study were conserved in ethanol at − 20°C for further studies on gene expression. Alizarin red S staining was used to detect calcium deposits with a single bath of 0.05% Alizarin Red S (Sigma) in KOH 0.5%, 5 min, before mounting in Mowiol. All slides generated with catshark samples were scanned on a Hamamatsu nanozoomer.

In situ Hybridizations

All probes and *in situ* hybridization procedures used here with *Scyliorhinus canicula* and *Xenopus tropicalis* were previously described (Espinoza et al., 2010; Enault et al., 2018), except for the frog *SCPPA2* gene (GenBank EU642617) for which a 968 bp product was amplified and cloned into pBluescript using the following primers (5′ to 3′) Forward- GAG TCA TAC TAC AGG ACC TGC, Reverse-CAT GCA ACT CAG CCA AAG CT.

RESULTS

SPARC and *SPARC-L* Expression in the Development of Vertebrae in the Lesser Spotted Catshark *Scyliorhinus canicula*

The catshark vertebral tissue mineralizes at the level of the neural arches and of the vertebral body (Enault et al., 2015). In the neural arches, mineralization occurs at two juxtaposed sites: the matrix of the most peripheral chondrocytes and the fibrous perichondrial tissue surrounding each neural arch (**Figures 2A–H**). In the neural arch peripheral cartilage, a faint Alizarin red-positive signal is observable in early stage 32 embryos (**Figures 2A,B,E,F**), and becomes more intense in intermediate and late stage 32 embryos (**Figures 2C,D,G,H**). Note that neural arch mineralization never extends to the center of the cartilaginous scaffold (**Figures 2A–H** and Berio et al., 2021). In addition, the fibrous perichondrial tissue surrounding each neural arch displays a robust mineralization in intermediate and late stage 32 embryos. In the vertebral body, a mineralization ring appears in the cartilage surrounding the notochord of intermediate stage 32 embryos and becomes more mineralized in late stage 32 embryos (**Figures 2F–H**).

The expression of the *SPARC* gene was detected in the neural tube and several connective tissues such as the dermis and perimysium at all tested developmental stages (**Figures 2I–L**). We report three major sites of *SPARC* expression in the *Sc* developing vertebrae: the neural arch chondrocytes, the neural arch fibrous perichondrium, and the vertebral body. In the neural arches of early stage 32 embryos, *SPARC* expression localizes to peripheral chondrocytes (*i.e.*, specifically to the mineralizing cartilage) and to the cells of the fibrous perichondrium (**Figures 2I,J**). In intermediate stage 32 embryos *SPARC* expression extends to most chondrocytes of the neural arches (**Figure 2K**). Cells of the mineralized fibrous perichondrial tissue surrounding the neural arches also express *SPARC* in intermediate and late stage 32 embryos (**Figures 2J,K**). In the vertebral body from early and intermediate stage 32 embryos, *SPARC* is detected as a ring of expression in chondrocytes surrounding the notochord (**Figures 2I–K**). Our results on late stage 32 embryos show little gene expression of *SPARC* in the vertebral tissues, as only a faint signal was observed in some chondrocytes, (**Figure 2L**), revealing that the expression of this gene is dynamic and transient in relation to the mineralization processes. We had previously shown that *SPARC* is expressed in developing scales (Enault et al., 2018), and the expected signal in odontoblasts presents on the same section strongly argues against a possible technical problem for the detection method in late stage 32 embryos (**Figure 2L**, inset).

On the other hand, the expression of *SPARC-L* could not be detected in any endoskeletal tissues, while its expression in the epithelium (*i.e.*, the ameloblast layer) of developing and mineralized scales was observable at all stages (**Figures 2M–P**), as expected (Enault et al., 2018).

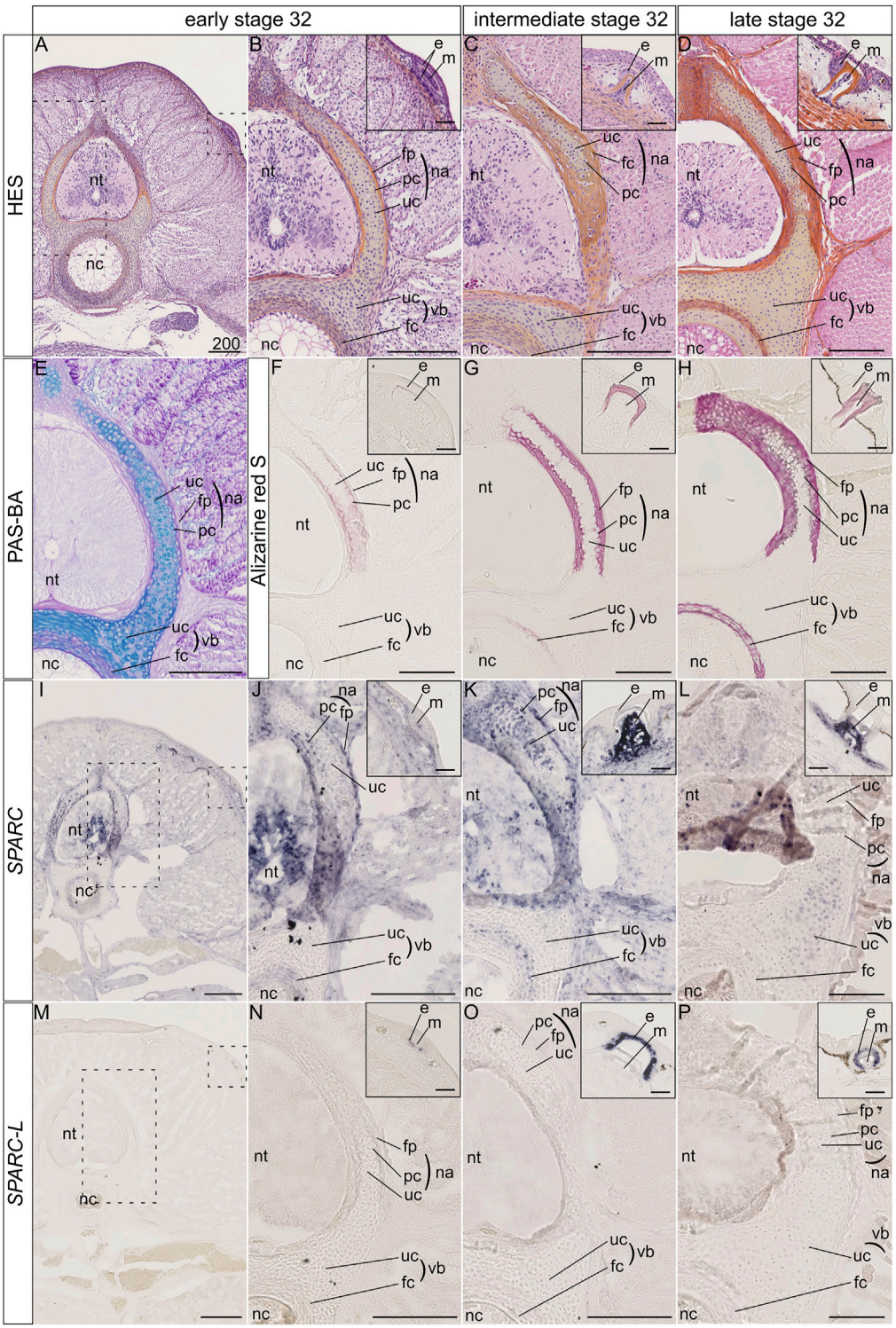

FIGURE 2 | Histology, mineralization dynamics and *SPARC* and *SPARC-L* expression pattern in the vertebrae and scales of the small-spotted catshark *Scyliorhinus canicula*. **(A–D)** Hematoxylin-Eosin Safran (HES) histological staining on transverse sections at the level of thoracic vertebrae: A, general view with location of the neural tube (nt) and notochord (nc); B-D, closer views on vertebral tissues as boxed in A, with identification of the fibrous perichondrium (fp), unmineralized cartilage (uc) and peripheral chondrocytes (pc) of the neural arch (na), as well as the unmineralized cartilage (uc) and fibrous cartilage (fc) of the vertebral body (vb); insets in B-D, closer view of the dorsal scales as boxed in A, indicating the location of the epithelial (e) and mesenchymal (m) compartments of scale buds. Stage 32 embryos were staged according to their total length into "early," "intermediate," and "late" categories as described in the Material and Method section. **(E)** Periodic Acid Schiff-Alcian

(*Continued*)

FIGURE 2 | Blue (PAS-BA) histological staining of a section consecutive to A: BA (blue) stains the acid glycosaminoglycans of the hyaline cartilage and PAS (pink) stains the fibrous content of the perichondrium. **(F–H)** Alizarin red S staining locates calcium deposits in mineralizing matrices [of the peripheral chondrocytes (pc), fibrous perichondrium (fp) or fibrous cartilage (fc), and scale enameloid/dentin], in embryos of similar total length as A-D. **(I–L)** *SPARC* gene expression patterns, for sections that are consecutive to those shown in **(F–H)** respectively. **(M–P)** *SPARC-L* gene expression patterns for sections that are consecutive to those shown in **(F–H)** respectively. Scales represent 200 μm, except in scale insets where they represent 50 μm.

SPARC and *SCPPs* Expression in the Development of Limbs and Vertebrae in the Western Clawed Frog *Xenopus tropicalis*

We examined gene expression in NF58 *Xt* limbs because at this stage hypertrophic cartilage is in its most mature state and becomes eliminated and replaced by bone marrow at the diaphysis (**Figure 3A**). von Kossa staining showed an intense signal in the bone matrix and revealed that the *Xt* hypertrophic cartilage does not mineralize at the diaphysis of NF58 femoral bones (**Figure 3B**). *SPARC* transcripts were specifically detected in osteocytes and in osteoblasts of the periosteum and endosteum, but not in the cartilage (**Figures 3C,D**). A similar situation was observed for *BSP* (**Figure 3E**). *DMP1* was detected in osteocytes as well as in some chondrocytes of the diaphysis (**Figure 3F**). Transcripts from the *SCPPA2* gene were detected in osteocytes and some osteoblasts, and in many chondrocytes located at the cartilage to bone marrow transition and in the vicinity of the bone matrix of the diaphysis (**Figure 3G**) and of the epiphysis (**Figure 3G′**).

Stage NF58 vertebrae (**Figure 4A**) were subjected to von Kossa staining, revealing cartilage mineralization in the dorsal region of the neural arches (**Figures 4B,C**), as well as in the ventral region located between the neural tube and the notochord (**Figures 4B′,C′**), in agreement with previous observations performed with Alizarin red S (Enault et al., 2015). We found that each of the examined genes displays a distinctive expression pattern. *SPARC* is specifically expressed in osteoblasts of the dorsal neural arches and of the ventral region, but not in chondrocytes (**Figures 4D,D′,E,E′**). *BSP* is expressed in osteoblasts and chondrocytes of both regions, albeit its expression is much stronger in the cartilage of the ventral vertebrae (**Figures 4F,F′**). *DMP1* is expressed in osteocytes and in chondrocytes located close to the bone matrix of the dorsal neural arch, but is not expressed in the ventral vertebra at this stage (**Figures 4G,G′**). *SCPPA2* is moderately expressed in some osteocytes and osteoblasts of the dorsal neural arch, and very strongly in chondrocytes of the mineralizing cartilage of both vertebral regions (**Figures 4H,H′**).

DISCUSSION

Our findings in *Xt* reveal an evolutionary conservation of the cartilaginous expression of the *SCPP* genes in tetrapods. Indeed, similarly to the situation in *Xt*, *SPARC* is not expressed in mouse chondrocytes (Holland et al., 1987). Rather, *SCPP* genes such as *DMP1* and *BSP* are expressed and required for mouse cartilage development (Chen et al., 1991; Ye et al., 2005; Bouleftour et al., 2014; Fujikawa et al., 2015). As indicated by other studies (Yagami et al., 1999; Bandyopadhyay et al., 2008), gene expression in cartilaginous elements can be subdivided in two distinct domains which we will use to discuss our results. First, *SCPP* genes become activated at late stages of hypertrophy, when the cartilage matrix becomes replaced by bone marrow at the mammalian diaphysis (Chen et al., 1991; Fujikawa et al., 2015). Likewise, in *Xt*, *DMP1* is exclusively expressed at the diaphysis (**Figure 3F**), and *SCPPA2* exhibits a much stronger expression at the diaphysis than the epiphysis region (**Figures 3G,G′**). A similar situation is observed at the level of the *Xt* vertebrae, where the expression of *SCPP* genes tightly correlates with cartilage maturation and mineralization in the neural arch (for *BSP*, *DMP1*, and *SCPPA2*) as well as in the ventral vertebral region (for *BSP* and *SCPPA2*). Second, the *SCPP* genes harbor a stronger expression in the non-mineralized peripheral cartilage, as observed in mouse for *osteopontin* (Heilig et al., 2016) and *DMP1* (Fujikawa et al., 2015). This situation is similar to the expression of *Xt SSCP* genes in chondrocytes located in the vicinity of the bone matrix in long bones and vertebrae (**Figures 3**, **4**). Such a peripheral cartilage domain expresses specific genes, as reported in chick (Bandyopadhyay et al., 2008), and undergoes ectopic mineralization in mutant mouse animals for the *Mgp* (Marulanda et al., 2017) and *Trps1* (Napierala et al., 2008) genes. In summary, *SCPP* genes from frog and mouse are expressed in the mature cartilage of the diaphysis and neural arches, as well as in peripherally located chondrocytes.

Available expression analyses did not report any cartilaginous expression for *SCPP* genes in teleosts (Kawasaki et al., 2005; Kawasaki, 2009; Weigele et al., 2015). Rather, the expression of the *SPARC* gene has been associated to cartilage development in zebrafish, gilthead seabream and the cichlid mouth breeder (Estevao et al., 2005; Redruello et al., 2005; Rotllant et al., 2008; Estevao et al., 2011; Weigele et al., 2015), albeit not in medaka, at least at the examined stages (Renn et al., 2006). Hence the reported cartilaginous expression patterns in teleosts (*SPARC* positive and *SCPP* negative) are opposite to the tetrapod situation (*SPARC* negative and *SCPP* positive), which might be related to drastic difference in the mode of endochondral ossification between these two groups (Cervantes-Diaz et al., 2017). In this respect, our data in the chondrichthyan representative *Sc* is instrumental to understand the evolution of the expression of these genes in the jawed vertebrate endoskeleton.

As no *SCPP* genes have been reported in chondrichthyan genomes to date, we focused on the evolutionarily related gene *SPARC-L* (Kawasaki and Weiss, 2003; Bertrand et al., 2013; Venkatesh et al., 2014; Enault et al., 2018). Our finding that *Sc SPARC-L* is not expressed in the vertebral cartilage is further confirmed by the robust and expected *Sc SPARC-L* expression in the odontodes present on the same sections and serving as convenient internal positive controls (Enault et al., 2018). By

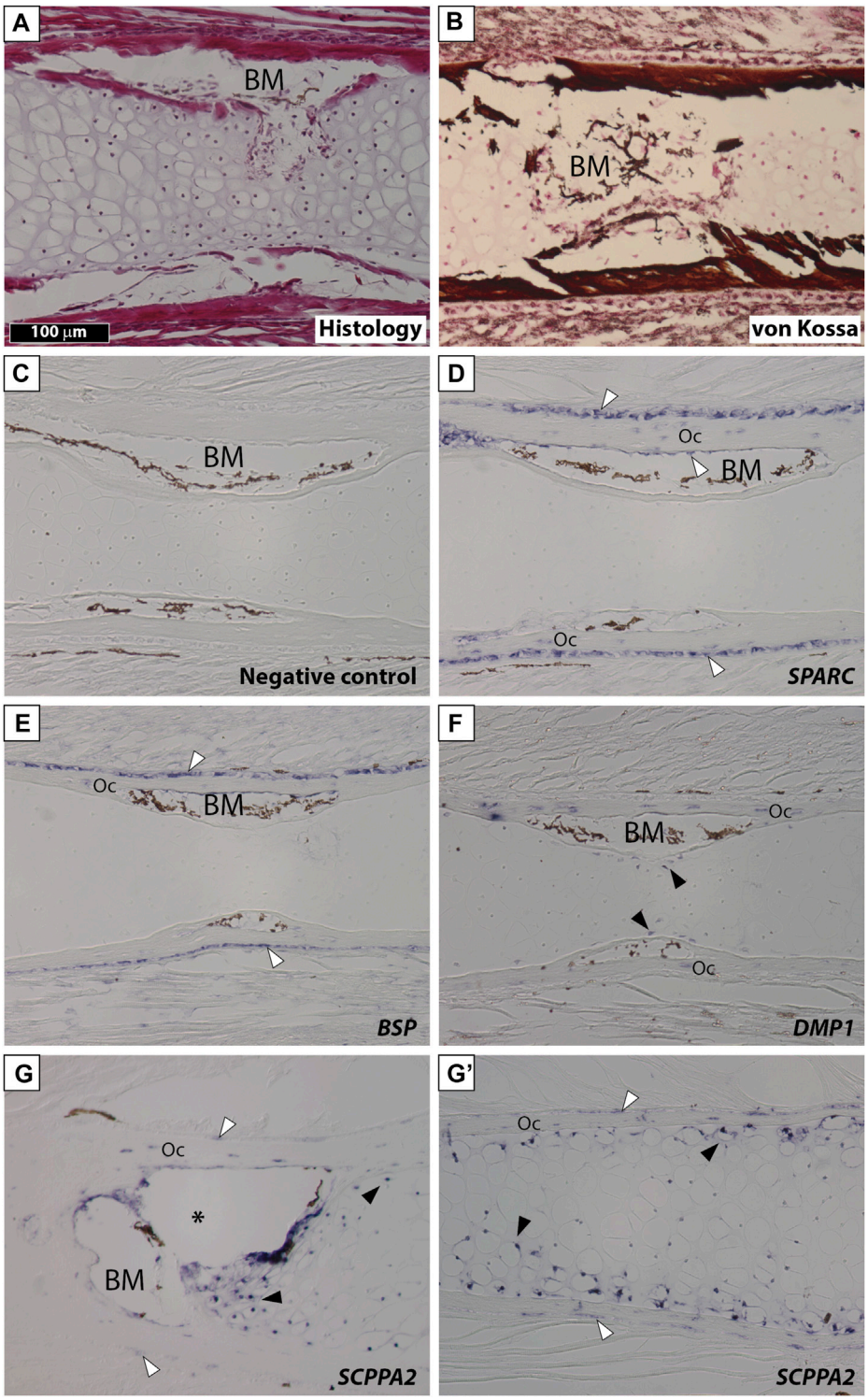

FIGURE 3 | *SPARC* and *SCPP* gene expression in *Xenopus tropicalis* stage NF58 hindlimbs. Longitudinal sections of *Xenopus tropicalis* stage NF58 femoral bones were subjected to Hematoxylin-Eosin staining **(A)**, von Kossa staining **(B)**, or *in situ* hybridization using a negative control [*SPARC* sense probe, **(C)**] or an antisense probe for *SPARC* **(D)**, *BSP* **(E)**, *DMP1* **(F)**, and *SCPPA2* **(G, G')**. Pictures show the diaphysis in **(A–G)** and the epiphysis in **(G')**. White and black arrowheads show *in situ* hybridization signal in osteoblasts and chondrocytes, respectively. Abbreviations: BM, bone marrow, Oc osteocytes showing *in situ* hybridization signal. Scale bar in **(A)** represents 100 μm and applies to all panels. The asterisk shows an artifact due to the cartilage which teared apart and contracted in this region of the section.

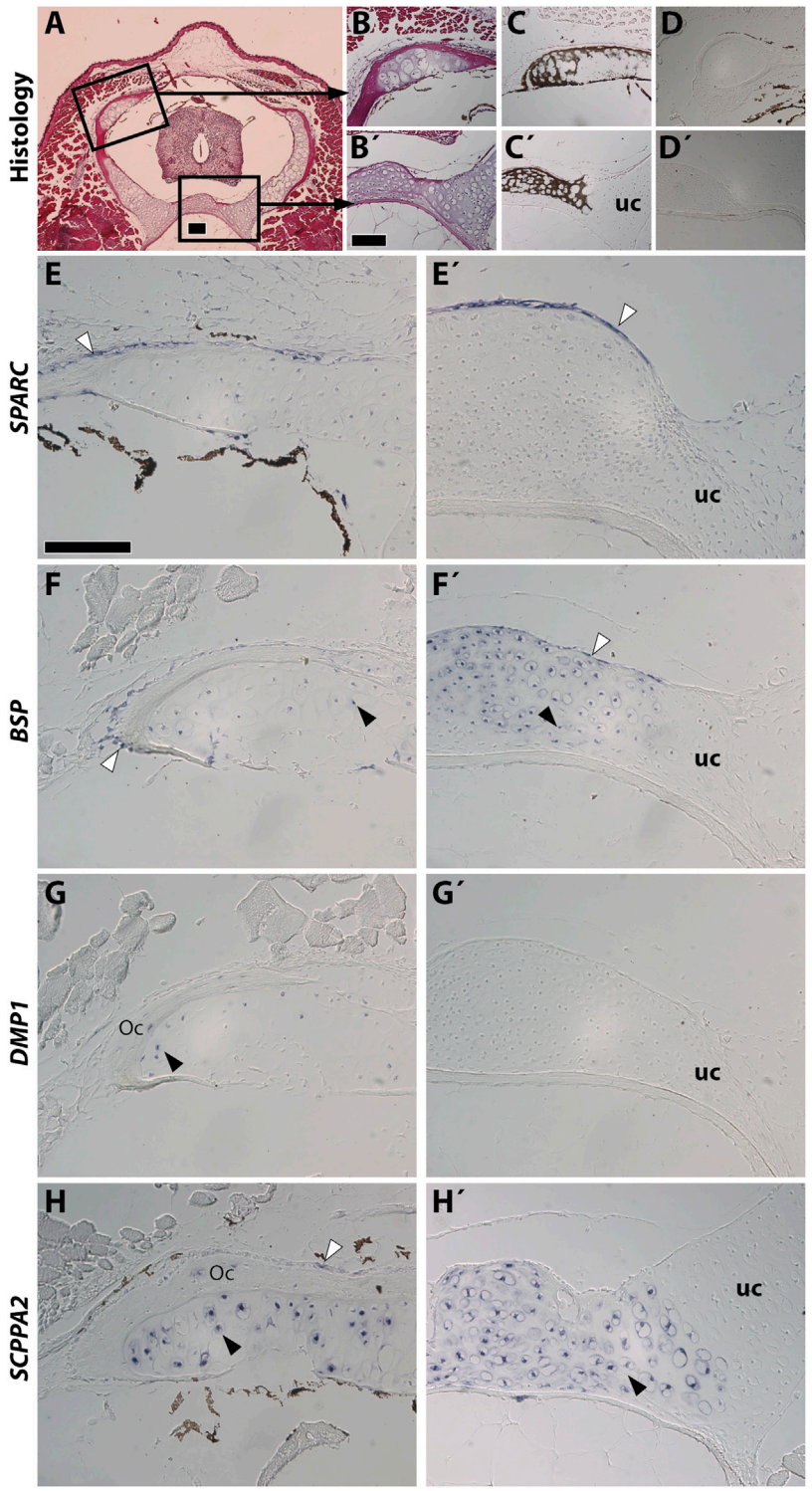

FIGURE 4 | *SPARC* and *SCPP* gene expression in *Xenopus tropicalis* stage NF58 vertebrae. Transversal sections of *Xenopus tropicalis* stage NF58 vertebrae were subjected to Hematoxylin-Eosin staining **(A,B,B′)**, von Kossa staining **(C,C′)**, or *in situ* hybridization using a negative control [*SPARC* sense probe, **(D,D′)**] or an antisense probe for *SPARC* **(E,E′)**, *BSP* **(F,F′)**, *DMP1* **(G, G′)**, and *SCPPA2* **(H,H′)**. Pictures are orientated with dorsal to the top and show the whole vertebrae **(A)**, the neural arch **(B–H)** or the vertebral body **(B′–H′)**. White and black arrowheads show *in situ* hybridization signal in osteoblasts and chondrocytes, respectively. Abbreviations: uc, unmineralized cartilage, Oc osteocytes showing *in situ* hybridization signal. Scale bars: **(A)**, 100 μm; **(B)**, 100 μm in **(B–D′)**; **(E)**, 50 μm in **(E–H′)**.

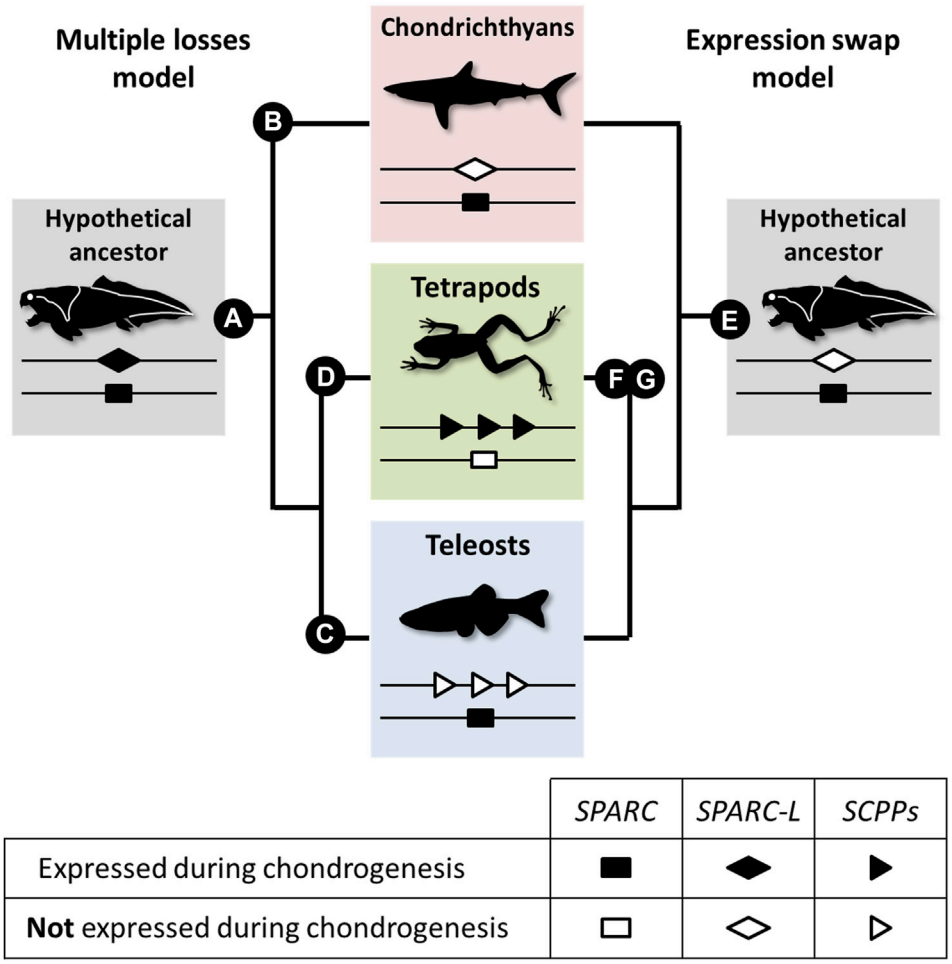

FIGURE 5 | A model for the evolution of the *SPARC/SPARC-L/SCPP* cartilaginous expression in jawed vertebrates. Evolutionary changes are polarized onto vertebrate cladograms. According to the "multiple losses" model **(left)**, the mineralizing cartilage of the jawed vertebrate last common ancestor expressed both the *SPARC* and *SPARC-L* ancestral genes **(A)**. This expression was inherited by the *SCPP* members when they evolved through *SPARC-L* local duplications. Expression losses occurred at least three times independently in distinct lineages: *SPARC-L* expression was lost in chondrichthyans **(B)**, *SCPP* expression was lost in teleosts **(C)** and *SPARC* expression was lost in tetrapods **(D)**. According to the "expression swap" model **(right)**, the mineralizing cartilage of the jawed vertebrate last common ancestor only expressed *SPARC* **(E)**, a situation which remained unchanged in the chondrichthyan and teleost lineages. However, the tetrapod lineage experienced drastic regulatory changes at both loci, leading to the activation of the *SCPP* genes **(F)** and the repression of *SPARC* **(G)** in chondrocytes.

contrast, *SPARC* expression clearly co-localizes with sites of vertebral mineralization. In the neural arches of early stage 32 embryos, *SPARC* is restricted to the mineralizing peripheral cartilage matrix, thereby paralleling the expression of *SCPP* genes in frog (**Figures 2**, **4**) and mouse (Fujikawa et al., 2015; Heilig et al., 2016). Hence, we uncover a novel evolutionarily conserved cartilage domain, as defined by peripherally located chondrocytes expressing *SPARC* in chondrichthyans and the *SCPP* genes in tetrapods. One difference is that this domain mineralizes in chondricthyans, but not in tetrapods. We propose that dosage variations between pro- and anti-mineralizing proteins might explain evolutionary differences between vertebrate lineages, as might be the case for instance for MGP which is a well-conserved cartilage mineralization inhibitor (Yagami et al., 1999; Espinoza et al., 2010; Viegas et al., 2013; Marulanda et al., 2017; Leurs et al., 2021). By examining the centrum of *Sc* specimens from different developmental stages we show that a ring of *SPARC* expression is already present in Alizarin red-negative early stage 32 embryos, suggesting that the presence of the *SPARC* protein plays a crucial role in the initiation of mineralization. The functional interaction between the mammalian *SPARC* and collagen 1 proteins is important for mineralization (Termine et al., 1981). However, as the shark chondrocytes embedded within a mineralizing cartilage matrix neither expresses *collagen 1a1* nor *collagen 1a2* (Enault et al., 2015), *Sc SPARC* function might be related to other aspects of matrix mineralization, such as its interaction with calcium and hydroxyapatite crystals (Engel et al., 1987; Maurer et al., 1995; Fujisawa et al., 1996).

Our data suggest that chondrichthyans are more similar to teleosts than to tetrapods because the *Sc* mineralizing cartilage is *SPARC* positive and *SPARC-L* negative. Here, we propose two

evolutionary models to explain these divergent expression patterns (see **Figure 5** and **Supplementary Figure S1**). Both models are based on the assumption that *SPARC*, *SPARC-L*, and *SCPP* share some level of functional redundancy, at least during chondrogenesis, as suggested by the fact that both *SPARC* and *SCPP* proteins are extracellular transglutaminase substrates (Aeschlimann et al., 1995; Forsprecher et al., 2011) and bind calcium ions (Engel et al., 1987; Chen et al., 1992; Maurer et al., 1995; Klaning et al., 2014). The "multiple losses" model is reminiscent of the Duplication Degeneration Complementation (DDC) phenomenon (Force et al., 1999) and involves at least three independent changes which abrogated the cartilaginous expression of *SPARC*, of *SPARC-L* or of the *SCPP* genes in distinct lineages (**Figure 5**, left panel). The "expression swap" model involves two changes and implies that, in the tetrapod lineage, cartilaginous expression was gained for the *SCPP* genes and lost for *SPARC* (**Figure 5**, right panel). While the *SPARC*/*SPARC-L*/*SCPP* family exhibit a unique evolutionary trajectory (Bertrand et al., 2013; Enault et al., 2018), the "expression swap" model would be similar to the dynamic expression turnover observed between members of the *Keratin*, *Vitellogenin*, and *Globin* vertebrate families (Finn et al., 2009; Vandebergh and Bossuyt, 2012; Opazo et al., 2015). Both scenarios imply regulatory changes that switched off ("multiple losses model") or on ("expression swap model") several *SCPP* genes (**Figure 5**). From a regulatory perspective, the idea of coordinated change in the expression of tandemly located *SCPP* genes is consistent with the fact that *BSP* and *DMP1* are included within the same topological association domain in human chromatin (Krietenstein et al., 2020), and that multiple genes can be co-regulated by the same enhancer (reviewed in Zheng and Xie, 2019). To the best of our knowledge, current experimental evidence is not sufficient to discriminate between the two models shown in **Figure 5**. Hence, a detailed analysis of the expression and regulation of *SPARC*/*SPARC-L*/*SCPP* genes in chondrocyte from a broader array of chondrichthyan and osteichthyan species will be required to shed light on the genetic mechanisms involved in the evolution of cartilage mineralization that originated deep in the vertebrate lineage (Min and Janvier, 1998; Donoghue et al., 2006; Johanson et al., 2010; 2012).

DATA AVAILABILITY STATEMENT

The raw data supporting the conclusion of this article will be made available by the authors, without undue reservation.

ETHICS STATEMENT

Handling of small-spotted catshark embryos followed all institutional, national, and international guidelines [European Communities Council Directive of September 22, 2010 (2010/63/UE)]: no further approval by an ethics committee was necessary as the biological material is embryonic and no live experimental procedures were carried out. The Ethics Committee of the University of Concepcion (Concepcion, Chile) approved all experimental procedures carried out on *Xenopus tropicalis* tadpoles during this study, which were performed following the guidelines outlined in the Biosafety and Bioethics Manual of the National Commission of Scientific and Technological Research (CONICYT, Chilean Government).

AUTHOR CONTRIBUTIONS

AR and DM performed the histological analyses and *in situ* hybridization procedures in *Xenopus tropicalis*. NL and MD-T performed the histological analyses and *in situ* hybridization procedures in *Scyliorhinus canicula*. SM and MD-T wrote the manuscript and prepared the figures. All authors analyzed and interpreted the data and read and approved the manuscript.

FUNDING

We acknowledge the MRI platform, member of the national infrastructure France-BioImaging supported by the French National Research Agency (ANR-10-INBS-04, «Investments for the future»), the labex CEMEB (ANR-10-LABX-0004), and NUMEV (ANR-10-LABX-0020). We also wish to acknowledge the "Réseau d'Histologie Expérimentale de Montpellier"—RHEM facility supported by the SIRIC Montpellier Cancer (Grant INCa_Inserm_DGOS_12553), the european regional development foundation and the occitanian region (FEDER-FSE 2014-2020 Languedoc Roussillon) for processing our animal tissues, histology techniques, and expertise. This study was partially funded by the IRP (LIA) MAST (CNRS). Fondecyt 1190926 to SM. AR and DM were ANID fellows 21170393 and 21160069 respectively.

ACKNOWLEDGMENTS

We thank Stéphanie Ventéo and Camille Martinand-Mari for their help with the biological material and *in situ* hybridization technique.

SUPPLEMENTARY MATERIAL

The Supplementary Material for this article can be found online at: https://www.frontiersin.org/articles/10.3389/fgene.2021.788346/full#supplementary-material

REFERENCES

Aeschlimann, D., Kaupp, O., and Paulsson, M. (1995). Transglutaminase-catalyzed Matrix Cross-Linking in Differentiating Cartilage: Identification of Osteonectin as a Major Glutaminyl Substrate. *J. Cel Biol* 129, 881–892. doi:10.1083/jcb.129.3.881

Ballard, W., Mellinger, J., and Lechenault, H. (1993). A Series of Stages for Development of *Scyliorhinus canicula* the Lesser Spotted Dogfish (Chondrichthyes: Scyliorhinidae). *J. Exp. Zool* 267, 1–43. doi:10.1002/jez.1402670309

Bandyopadhyay, A., Kubilus, J. K., Crochiere, M. L., Linsenmayer, T. F., and Tabin, C. J. (2008). Identification of Unique Molecular Subdomains in the Perichondrium and Periosteum and Their Role in Regulating Gene Expression in the Underlying Chondrocytes. *Develop. Biol.* 321, 162–174. doi:10.1016/j.ydbio.2008.06.012

Beresford, W. A. (1981). Chondroid Bone, Secondary Cartilage, and Metaplasia. *The American Journal of Surgical Pathology* 5, 405.

Berio, F., Broyon, M., Enault, S., Pirot, N., López-Romero, F. A., and Debiais-Thibaud, M. (2021). Diversity and Evolution of Mineralized Skeletal Tissues in Chondrichthyans. *Front. Ecol. Evol.* 9, 1–19. doi:10.3389/fevo.2021.660767

Bertrand, S., Fuentealba, J., Aze, A., Hudson, C., Yasuo, H., Torrejon, M., et al. (2013). A Dynamic History of Gene Duplications and Losses Characterizes the Evolution of the SPARC Family in Eumetazoans. *Proc. R. Soc. B.* 280, 20122963. doi:10.1098/rspb.2012.2963

Bouleftour, W., Boudiffa, M., Wade-Gueye, N. M., Bouët, G., Cardelli, M., Laroche, N., et al. (2014). Skeletal Development of Mice Lacking Bone Sialoprotein (BSP) - Impairment of Long Bone Growth and Progressive Establishment of High Trabecular Bone Mass. *PLoS One* 9, e95144. doi:10.1371/journal.pone.0095144

Brazeau, M. D., Giles, S., Dearden, R. P., Jerve, A., Ariunchimeg, Y., Zorig, E., et al. (2020). Endochondral Bone in an Early Devonian 'placoderm' from Mongolia. *Nat. Ecol. Evol.* 4, 1477–1484. doi:10.1038/s41559-020-01290-2

Cervantes-Diaz, F., Contreras, P., and Marcellini, S. (2017). Evolutionary Origin of Endochondral Ossification: the Transdifferentiation Hypothesis. *Dev. Genes Evol.* 227, 121–127. doi:10.1007/s00427-016-0567-y

Chen, J., Shapiro, H. S., Wrana, J. L., Reimers, S., Heersche, J. N. M., and Sodek, J. (1991). Localization of Bone Sialoprotein (BSP) Expression to Sites of Mineralized Tissue Formation in Fetal Rat Tissues by *In Situ* Hybridization. *Matrix* 11, 133–143. doi:10.1016/s0934-8832(11)80217-9

Chen, Y., Bal, B. S., and Gorski, J. P. (1992). Calcium and Collagen Binding Properties of Osteopontin, Bone Sialoprotein, and Bone Acidic Glycoprotein-75 from Bone. *J. Biol. Chem.* 267, 24871–24878. doi:10.1016/s0021-9258(18)35844-7

Close, B., Banister, K., Baumans, V., Bernoth, E.-M., Bromage, N., Bunyan, J., et al. (1996). Recommendations for Euthanasia of Experimental Animals: Part 1. *Lab. Anim.* 30, 293–316. doi:10.1258/002367796780739871

Donoghue, P. C. J., Sansom, I. J., and Downs, J. P. (2006). Early Evolution of Vertebrate Skeletal Tissues and Cellular Interactions, and the Canalization of Skeletal Development. *J. Exp. Zool.* 306B, 278–294. doi:10.1002/jez.b.21090

Donoghue, P. C. J., and Sansom, I. J. (2002). Origin and Early Evolution of Vertebrate Skeletonization. *Microsc. Res. Tech.* 59, 352–372. doi:10.1002/jemt.10217

Dyment, N. A., Breidenbach, A. P., Schwartz, A. G., Russell, R. P., Aschbacher-Smith, L., Liu, H., et al. (2015). Gdf5 Progenitors Give Rise to Fibrocartilage Cells that Mineralize via Hedgehog Signaling to Form the Zonal Enthesis. *Develop. Biol.* 405, 96–107. doi:10.1016/j.ydbio.2015.06.020

Enault, S., Muñoz, D. N., Silva, W. T. A. F., Borday-Birraux, V., Bonade, M., Oulion, S., et al. (2015). Molecular Footprinting of Skeletal Tissues in the Catshark *Scyliorhinus canicula* and the Clawed Frog Xenopus Tropicalis Identifies Conserved and Derived Features of Vertebrate Calcification. *Front. Genet.* 6, 283. doi:10.3389/fgene.2015.00283

Enault, S., Muñoz, D., Simion, P., Ventéo, S., Sire, J.-Y., Marcellini, S., et al. (2018). Evolution of Dental Tissue Mineralization: an Analysis of the Jawed Vertebrate SPARC and SPARC-L Families. *BMC Evol. Biol.* 18, 127. doi:10.1186/s12862-018-1241-y

Engel, J., Taylor, W., Paulsson, M., Sage, H., and Hogan, B. (1987). Calcium Binding Domains and Calcium-Induced Conformational Transition of SPARC/BM-40/osteonectin, an Extracellular Glycoprotein Expressed in Mineralized and Nonmineralized Tissues. *Biochemistry* 26, 6958–6965. doi:10.1021/bi00396a015

Espinoza, J., Sanchez, M., Sanchez, A., Hanna, P., Torrejon, M., Buisine, N., et al. (2010). Two Families of Xenopus Tropicalis Skeletal Genes Display Well-Conserved Expression Patterns with Mammals in Spite of Their Highly Divergent Regulatory Regions. *Evol. Dev.* 12, 541–551. doi:10.1111/j.1525-142X.2010.00440.x

Estêvão, M. D., Redruello, B., Canario, A. V. M., and Power, D. M. (2005). Ontogeny of Osteonectin Expression in Embryos and Larvae of Sea Bream (Sparus Auratus). *Gen. Comp. Endocrinol.* 142, 155–162. doi:10.1016/j.ygcen.2004.11.018

Estêvão, M. D., Silva, N., Redruello, B., Costa, R., Gregório, S., Canário, A. V. M., et al. (2011). Cellular Morphology and Markers of Cartilage and Bone in the marine Teleost Sparus Auratus. *Cell Tissue Res* 343, 619–635. doi:10.1007/s00441-010-1109-y

Finn, R., Kolarevic, J., Kongshaug, H., and Nilsen, F. (2009). Evolution and Differential Expression of a Vertebrate Vitellogenin Gene Cluster. *BMC Evol. Biol.* 9, 2. doi:10.1186/1471-2148-9-2

Force, A., Lynch, M., Pickett, F. B., Amores, A., Yan, Y.-l., and Postlethwait, J. (1999). Preservation of Duplicate Genes by Complementary, Degenerative Mutations. *Genetics* 151, 1531–1545. doi:10.1093/genetics/151.4.1531

Forsprecher, J., Wang, Z., Goldberg, H. A., and Kaartinen, M. T. (2011). Transglutaminase-mediated Oligomerization Promotes Osteoblast Adhesive Properties of Osteopontin and Bone Sialoprotein. *Cell Adhes. Migration* 5, 65–72. doi:10.4161/cam.5.1.13369

Fujikawa, K., Yokohama-Tamaki, T., Morita, T., Baba, O., Qin, C., and Shibata, S. (2015). An *In Situ* Hybridization Study of Perlecan, DMP1, and MEPE in Developing Condylar Cartilage of the Fetal Mouse Mandible and Limb Bud Cartilage. *Eur. J. Histochem.* 59, 2553. doi:10.4081/ejh.2015.2553

Fujisawa, R., Wada, Y., Nodasaka, Y., and Kuboki, Y. (1996). Acidic Amino Acid-Rich Sequences as Binding Sites of Osteonectin to Hydroxyapatite Crystals. *Biochim. Biophys. Acta (Bba) - Protein Struct. Mol. Enzymol.* 1292, 53–60. doi:10.1016/0167-4838(95)00190-5

Heilig, J., Paulsson, M., and Zaucke, F. (2016). Insulin-like Growth Factor 1 Receptor (IGF1R) Signaling Regulates Osterix Expression and Cartilage Matrix Mineralization during Endochondral Ossification. *Bone* 83, 48–57. doi:10.1016/j.bone.2015.10.007

Hirasawa, T., and Kuratani, S. (2015). Evolution of the Vertebrate Skeleton: Morphology, Embryology, and Development. *Zoolog. Lett* 1. doi:10.1186/s40851-014-0007-7

Holland, P. W., Harper, S. J., Mcvey, J. H., and Hogan, B. L. (1987). *In Vivo* expression of mRNA for the Ca++-Binding Protein SPARC (Osteonectin) Revealed by *In Situ* Hybridization. *J. Cel Biol* 105, 473–482. doi:10.1083/jcb.105.1.473

Johanson, Z., Kearsley, A., Den Blaauwen, J., Newman, M., and Smith, M. M. (2010). No Bones about it: An Enigmatic Devonian Fossil Reveals a New Skeletal Framework-A Potential Role of Loss of Gene Regulation. *Semin. Cel Develop. Biol.* 21, 414–423. doi:10.1016/j.semcdb.2009.10.011

Johanson, Z., Kearsley, A., Den Blaauwen, J., Newman, M., and Smith, M. M. (2012). Ontogenetic Development of an Exceptionally Preserved Devonian Cartilaginous Skeleton. *J. Exp. Zool.* 318B, 50–58. doi:10.1002/jez.b.21441

Kawasaki, K., Buchanan, A. V., and Weiss, K. M. (2007). Gene Duplication and the Evolution of Vertebrate Skeletal Mineralization. *Cells Tissues Organs* 186, 7–24. doi:10.1159/000102678

Kawasaki, K., Suzuki, T., and Weiss, K. M. (2005). Phenogenetic Drift in Evolution: the Changing Genetic Basis of Vertebrate Teeth. *Proc. Natl. Acad. Sci.* 102, 18063–18068. doi:10.1073/pnas.0509263102

Kawasaki, K. (2009). The SCPP Gene Repertoire in Bony Vertebrates and Graded Differences in Mineralized Tissues. *Dev. Genes Evol.* 219, 147–157. doi:10.1007/s00427-009-0276-x

Kawasaki, K., and Weiss, K. M. (2003). Mineralized Tissue and Vertebrate Evolution: the Secretory Calcium-Binding Phosphoprotein Gene Cluster. *Proc. Natl. Acad. Sci.* 100, 4060–4065. doi:10.1073/pnas.0638023100

Kessels, M. Y., Huitema, L. F. A., Boeren, S., Kranenbarg, S., Schulte-Merker, S., Van Leeuwen, J. L., et al. (2014). Proteomics Analysis of the Zebrafish Skeletal Extracellular Matrix. *PLoS One* 9, e90568. doi:10.1371/journal.pone.0090568

Kläning, E., Christensen, B., Sørensen, E. S., Vorup-Jensen, T., and Jensen, J. K. (2014). Osteopontin Binds Multiple Calcium Ions with High Affinity and

Independently of Phosphorylation Status. *Bone* 66, 90–95. doi:10.1016/j.bone.2014.05.020

Krietenstein, N., Abraham, S., Venev, S. V., Abdennur, N., Gibcus, J., Hsieh, T.-H. S., et al. (2020). Ultrastructural Details of Mammalian Chromosome Architecture. *Mol. Cel* 78, 554–565. e557. doi:10.1016/j.molcel.2020.03.003

Leurs, N., Martinand-Mari, C., Ventéo, S., Haitina, T., and Debiais-Thibaud, M. (2021). Evolution of Matrix Gla and Bone Gla Protein Genes in Jawed Vertebrates. *Front. Genet.* 12, 620659. doi:10.3389/fgene.2021.620659

Li, N., Felber, K., Elks, P., Croucher, P., and Roehl, H. H. (2009). Tracking Gene Expression during Zebrafish Osteoblast Differentiation. *Dev. Dyn.* 238, 459–466. doi:10.1002/dvdy.21838

Long, F., and Ornitz, D. M. (2013). Development of the Endochondral Skeleton. *Cold Spring Harbor Perspect. Biol.* 5, a008334. doi:10.1101/cshperspect.a008334

Marulanda, J., Eimar, H., Mckee, M. D., Berkvens, M., Nelea, V., Roman, H., et al. (2017). Matrix Gla Protein Deficiency Impairs Nasal Septum Growth, Causing Midface Hypoplasia. *J. Biol. Chem.* 292, 11400–11412. doi:10.1074/jbc.M116.769802

Maurer, P., Hohenadl, C., Hohenester, E., Göhring, W., Timpl, R., and Engel, J. (1995). The C-Terminal Portion of BM-40 (SPARC/osteonectin) Is an Autonomously Folding and Crystallisable Domain that Binds Calcium and Collagen IV. *J. Mol. Biol.* 253, 347–357. doi:10.1006/jmbi.1995.0557

Maxwell, E. E., Fröbisch, N. B., and Heppleston, A. C. (2008). Variability and Conservation in Late Chondrichthyan Development: Ontogeny of the winter Skate (*Leucoraja ocellata*). *Anat. Rec.* 291, 1079–1087. doi:10.1002/ar.20719

Mckinnon, P. J., Mclaughlin, S. K., Kapsetaki, M., and Margolskee, R. F. (2000). Extracellular Matrix-Associated Protein Sc1 Is Not Essential for Mouse Development. *Mol. Cel Biol* 20, 656–660. doi:10.1128/mcb.20.2.656-660.2000

Min, Z., and Janvier, P. (1998). The Histological Structure of the Endoskeleton in Galeaspids (Galeaspida, Vertebrata). *J. Vertebr. Paleontol.* 18, 650–654. doi:10.1080/02724634.1998.10011091

Nakatani, Y., Shingate, P., Ravi, V., Pillai, N. E., Prasad, A., Mclysaght, A., et al. (2021). Reconstruction of Proto-Vertebrate, Proto-Cyclostome and Proto-Gnathostome Genomes Provides New Insights into Early Vertebrate Evolution. *Nat. Commun.* 12, 4489. doi:10.1038/s41467-021-24573-z

Napierala, D., Sam, K., Morello, R., Zheng, Q., Munivez, E., Shivdasani, R. A., et al. (2008). Uncoupling of Chondrocyte Differentiation and Perichondrial Mineralization Underlies the Skeletal Dysplasia in Tricho-Rhino-Phalangeal Syndrome. *Hum. Mol. Genet.* 17, 2244–2254. doi:10.1093/hmg/ddn125

Nieuwkoop, P. D., and Faber, J. (1967). *Normal Table of* Xenopus laevis *(Daudin)*. Netherlands: North Holland.

Nikoloudaki, G. (2021). Functions of Matricellular Proteins in Dental Tissues and Their Emerging Roles in Orofacial Tissue Development, Maintenance, and Disease. *Ijms* 22, 6626. doi:10.3390/ijms22126626

Opazo, J. C., Hoffmann, F. G., Natarajan, C., Witt, C. C., Berenbrink, M., and Storz, J. F. (2015). Gene Turnover in the Avian Globin Gene Families and Evolutionary Changes in Hemoglobin Isoform Expression. *Mol. Biol. Evol.* 32, 871–887. doi:10.1093/molbev/msu341

Ørvig, T. (1951). Histologic Studies of Placoderms and Fossil Elasmobranchs. I: the Endoskeleton, with Remarks on the Hard Tissues of Lower Vertebrates in General. *Arkiv Zool* 2.

Paul, S., Schindler, S., Giovannone, D., De Millo Terrazzani, A., Mariani, F. V., and Crump, J. G. (2016). Ihha Induces Hybrid Cartilage-Bone Cells during Zebrafish Jawbone Regeneration. *Development* 143, 2066–2076. doi:10.1242/dev.131292

Pears, J. B., Johanson, Z., Trinajstic, K., Dean, M. N., and Boisvert, C. A. (2020). Mineralization of the Callorhinchus Vertebral Column (Holocephali; Chondrichthyes). *Front. Genet.* 11, 571694. doi:10.3389/fgene.2020.571694

Ramlochansingh, C., Branoner, F., Chagnaud, B. P., and Straka, H. (2014). Efficacy of Tricaine Methanesulfonate (MS-222) as an Anesthetic Agent for Blocking Sensory-Motor Responses in *Xenopus laevis* Tadpoles. *PLoS One* 9, e101606. doi:10.1371/journal.pone.0101606

Redruello, B., Estêvão, M. D., Rotllant, J., Guerreiro, P. M., Anjos, L. I., Canário, A. V., et al. (2005). Isolation and Characterization of Piscine Osteonectin and Downregulation of its Expression by PTH-Related Protein. *J. Bone Miner Res.* 20, 682–692. doi:10.1359/JBMR.041201

Renn, J., Schaedel, M., Volff, J.-N., Goerlich, R., Schartl, M., and Winkler, C. (2006). Dynamic Expression of Sparc Precedes Formation of Skeletal Elements in the Medaka (*Oryzias latipes*). *Gene* 372, 208–218. doi:10.1016/j.gene.2006.01.011

Rosset, E. M., and Bradshaw, A. D. (2016). SPARC/osteonectin in Mineralized Tissue. *Matrix Biol.* 52-54, 78–87. doi:10.1016/j.matbio.2016.02.001

Rotllant, J., Liu, D., Yan, Y.-L., Postlethwait, J. H., Westerfield, M., and Du, S.-J. (2008). Sparc (Osteonectin) Functions in Morphogenesis of the Pharyngeal Skeleton and Inner Ear. *Matrix Biol.* 27, 561–572. doi:10.1016/j.matbio.2008.03.001

Ryll, B., Sanchez, S., Haitina, T., Tafforeau, P., and Ahlberg, P. E. (2014). The Genome of Callorhinchus and the Fossil Record: a New Perspective on SCPP Gene Evolution in Gnathostomes. *Evol. Develop.* 16, 123–124. doi:10.1111/ede.12071

Schreiweis, M. A., Butler, J. P., Kulkarni, N. H., Knierman, M. D., Higgs, R. E., Halladay, D. L., et al. (2007). A Proteomic Analysis of Adult Rat Bone Reveals the Presence of Cartilage/chondrocyte Markers. *J. Cel. Biochem.* 101, 466–476. doi:10.1002/jcb.21196

Termine, J. D., Kleinman, H. K., Whitson, S. W., Conn, K. M., Mcgarvey, M. L., and Martin, G. R. (1981). Osteonectin, a Bone-specific Protein Linking mineral to Collagen. *Cell* 26, 99–105. doi:10.1016/0092-8674(81)90037-4

Tsang, K. Y., Chan, D., and Cheah, K. S. E. (2015). Fate of Growth Plate Hypertrophic Chondrocytes: Death or Lineage Extension? *Develop. Growth Differ.* 57, 179–192. doi:10.1111/dgd.12203

Ustriyana, P., Schulte, F., Gombedza, F., Gil-Bona, A., Paruchuri, S., Bidlack, F. B., et al. (2021). Spatial Survey of Non-collagenous Proteins in Mineralizing and Non-mineralizing Vertebrate Tissues *Ex Vivo*. *Bone Rep.* 14, 100754. doi:10.1016/j.bonr.2021.100754

Vandebergh, W., and Bossuyt, F. (2012). Radiation and Functional Diversification of Alpha Keratins during Early Vertebrate Evolution. *Mol. Biol. Evol.* 29, 995–1004. doi:10.1093/molbev/msr269

Venkatesh, B., Lee, A. P., Ravi, V., Maurya, A. K., Lian, M. M., Swann, J. B., et al. (2014). Elephant Shark Genome Provides Unique Insights into Gnathostome Evolution. *Nature* 505, 174–179. doi:10.1038/nature12826

Viegas, C. S. B., Simes, D. C., Williamson, M. K., Cavaco, S., Laizé, V., Price, P. A., et al. (2013). Sturgeon Osteocalcin Shares Structural Features with Matrix Gla Protein. *J. Biol. Chem.* 288, 27801–27811. doi:10.1074/jbc.M113.450213

Weigele, J., Franz-Odendaal, T. A., and Hilbig, R. (2015). Expression of SPARC and the Osteopontin-like Protein during Skeletal Development in the Cichlid Fish *Oreochromis mossambicus*. *Dev. Dyn.* 244, 955–972. doi:10.1002/dvdy.24293

Yagami, K., Suh, J.-Y., Enomoto-Iwamoto, M., Koyama, E., Abrams, W. R., Shapiro, I. M., et al. (1999). Matrix GLA Protein Is a Developmental Regulator of Chondrocyte Mineralization and, when Constitutively Expressed, Blocks Endochondral and Intramembranous Ossification in the Limb. *J. Cel Biol* 147, 1097–1108. doi:10.1083/jcb.147.5.1097

Ye, L., Mishina, Y., Chen, D., Huang, H., Dallas, S. L., Dallas, M. R., et al. (2005). Dmp1-deficient Mice Display Severe Defects in Cartilage Formation Responsible for a Chondrodysplasia-like Phenotype. *J. Biol. Chem.* 280, 6197–6203. doi:10.1074/jbc.M412911200

Zhang, G., and Cohn, M. J. (2008). Genome Duplication and the Origin of the Vertebrate Skeleton. *Curr. Opin. Genet. Develop.* 18, 387–393. doi:10.1016/j.gde.2008.07.009

Zheng, H., and Xie, W. (2019). The Role of 3D Genome Organization in Development and Cell Differentiation. *Nat. Rev. Mol. Cel Biol* 20, 535–550. doi:10.1038/s41580-019-0132-4

Conflict of Interest: The authors declare that the research was conducted in the absence of any commercial or financial relationships that could be construed as a potential conflict of interest.

Publisher's Note: All claims expressed in this article are solely those of the authors and do not necessarily represent those of their affiliated organizations, or those of the publisher, the editors and the reviewers. Any product that may be evaluated in this article, or claim that may be made by its manufacturer, is not guaranteed or endorsed by the publisher.

frontiers in Genetics

REVIEW
published: 22 December 2021
doi: 10.3389/fgene.2021.762042

Mineralized Cartilage and Bone-Like Tissues in Chondrichthyans Offer Potential Insights Into the Evolution and Development of Mineralized Tissues in the Vertebrate Endoskeleton

*Oghenevwogaga J. Atake and B. Frank Eames**

Department of Anatomy, Physiology, and Pharmacology, University of Saskatchewan, Saskatoon, SK, Canada

The impregnation of biominerals into the extracellular matrix of living organisms, a process termed biomineralization, gives rise to diverse mineralized (or calcified) tissues in vertebrates. Preservation of mineralized tissues in the fossil record has provided insights into the evolutionary history of vertebrates and their skeletons. However, current understanding of the vertebrate skeleton and of the processes underlying its formation is biased towards biomedical models such as the tetrapods mouse and chick. Chondrichthyans (sharks, skates, rays, and chimaeras) and osteichthyans are the only vertebrate groups with extant (living) representatives that have a mineralized skeleton, but the basal phylogenetic position of chondrichthyans could potentially offer unique insights into skeletal evolution. For example, bone is a vertebrate novelty, but the internal supporting skeleton (endoskeleton) of extant chondrichthyans is commonly described as lacking bone. The molecular and developmental basis for this assertion is yet to be tested. Subperichondral tissues in the endoskeleton of some chondrichthyans display mineralization patterns and histological and molecular features of bone, thereby challenging the notion that extant chondrichthyans lack endoskeletal bone. Additionally, the chondrichthyan endoskeleton demonstrates some unique features and others that are potentially homologous with other vertebrates, including a polygonal mineralization pattern, a trabecular mineralization pattern, and an unconstricted perichordal sheath. Because of the basal phylogenetic position of chondrichthyans among all other extant vertebrates with a mineralized skeleton, developmental and molecular studies of chondrichthyans are critical to flesh out the evolution of vertebrate skeletal tissues, but only a handful of such studies have been carried out to date. This review discusses morphological and molecular features of chondrichthyan endoskeletal tissues and cell types, ultimately emphasizing how comparative embryology and transcriptomics can reveal homology of mineralized skeletal tissues (and their cell types) between chondrichthyans and other vertebrates.

Keywords: chondrichthyan endoskeleton, sharks, skates, vertebrate mineralization patterns, skeletal evolution and development (EvoDevo), molecular fingerprints, homology

OPEN ACCESS

Edited by:
Frederic Marin,
Délégation Centre-Est (CNRS), France

Reviewed by:
David Marjanović,
Museum of Natural History Berlin (MfN), Germany
Kevin Stevens,
Ruhr University Bochum, Germany

****Correspondence:***
B. Frank Eames
b.frank@usask.ca

Specialty section:
This article was submitted to Evolutionary and Population Genetics, a section of the journal Frontiers in Genetics

Received: *20 August 2021*
Accepted: *30 November 2021*
Published: *22 December 2021*

Citation:
Atake OJ and Eames BF (2021) Mineralized Cartilage and Bone-Like Tissues in Chondrichthyans Offer Potential Insights Into the Evolution and Development of Mineralized Tissues in the Vertebrate Endoskeleton. Front. Genet. 12:762042. doi: 10.3389/fgene.2021.762042

THE BASAL PHYLOGENETIC POSITION OF CHONDRICHTHYANS CAN PROVIDE UNIQUE INSIGHTS INTO ENDOSKELETAL EVOLUTION AMONG VERTEBRATES

Many organisms utilize biominerals to harden the deep (endo-) or more superficial (exo-) supporting skeleton through a process termed biomineralization. Specialized cell types (generally referred to as scleroblasts) drive biomineralization by synthesizing and secreting both the biominerals and the organic extracellular matrices into which they are incorporated (Moss, 1964; Francillon-Vieillot et al., 1990; Checa, 2018). In vertebrates, biomineralization occurs by deposition of biological apatite into collagen-/amelogenin-rich matrices, and this process gives rise to the main types of mineralized (or calcified) tissues: bone, mineralized cartilage, dentine, enamel, and enameloid (Hall, 1975; Kemp, 1989; Donoghue et al., 2006). Given that these mineralized tissue types were already distinct in ancestral vertebrates, later-diverged vertebrate groups mostly modified ancestral mineral and organic components in order to mineralize their skeletal tissues (Enlow and Brown, 1958; Francillon-Vieillot et al., 1990).

The representation of mineralized tissues in the fossil record has fleshed out the evolutionary history of vertebrates (Janvier, 1996). Chondrichthyans (sharks, skates, rays, and chimaeras) and osteichthyans (bony fishes and tetrapods) are the only vertebrate groups with extant (living) representatives that have a mineralized skeleton. Paleontological and molecular analyses have led to the recognition of chondrichthyans as phylogenetically basal to all living jawed vertebrates (Janvier, 1996; Venkatesh et al., 2001; Kikugawa et al., 2004). Thus, the basal phylogenetic position of chondrichthyans makes them excellent model organisms for revealing the evolution of mineralized endoskeletal tissues among vertebrate groups. Extant chondrichthyans are subdivided into two groups: elasmobranchs (sharks, skates, and rays) and holocephalans (chimaeras), which last shared a common ancestor at least 385 million years ago (Janvier and Pradel, 2015; Frey et al., 2019; Cohen et al., 2021). Despite their predominantly cartilaginous endoskeleton, chondrichthyans exhibit a great diversity of derived and ancestral mineralized tissues. For example, tesserae, which are discrete blocks of mineralized tissue lining endoskeletal elements, are a derived and unique skeletal feature of chondrichthyans (Kemp and Westrin, 1979; Dean and Summers, 2006). The centrum (i.e., vertebral body) of chimaeras exhibits an unconstricted perichordal sheath, considered an ancestral vertebrate feature (Miles, 1970; Schmitz, 1998). On the other hand, structural and developmental features of chondrichthyan teeth are considered homologous to those of other vertebrates and likely reflect the ancestral state of jawed vertebrates (Gillis and Donoghue, 2007; Rasch et al., 2016; Rücklin et al., 2021). In this review, we consider how recent analyses of chondrichthyan tesserae and centra shed light upon the evolution of mineralized tissues in the vertebrate endoskeleton, including examining whether chondrichthyans make bone, but first we briefly summarize some basic concepts in skeletal biology (mostly from studies of tetrapods).

MINERALIZATION PATTERNS AND DEVELOPMENTAL PROCESSES OF BONE AND CARTILAGE

A common approach to characterize bone and generally the morphological diversity of vertebrate mineralized tissues is based on their spatial patterns (herein referred to as mineralization patterns). Mineralization patterns of the vertebrate skeleton are often described at the gross anatomical level (i.e., patterns of skeletal elements across the whole skeleton), at the macro- or micro-structural level (i.e., patterns of discrete skeletal tissues), and at the nanostructural level (e.g., patterns of collagen fibrils) (Francillon-Vieillot et al., 1990; Rho et al., 1998). Mineralization patterns at the gross anatomical and nanostructural levels have been reviewed elsewhere (Kemp, 1984; Maisey, 1988; Katz et al., 1989; Huysseune and Sire, 1998; Wiesmann et al., 2005), so we will focus mainly on mineralization patterns of skeletal tissues, particularly that of bone and mineralized cartilage.

Bone is a pervasive endoskeletal tissue that exhibits two basic mineralization patterns: compact and trabecular (Francillon-Vieillot et al., 1990; Rho et al., 1998). The compact mineralization pattern is continuous and smooth, whereas the trabecular pattern has many branching, rod-like struts with unmineralized regions between them (**Figures 1A–C**). Compact and trabecular mineralization patterns are commonly used to characterize the microstructure of bone, but they also can apply to other vertebrate mineralized tissues, such as dentine or mineralized cartilage (Ørvig, 1951; Sire and Huysseune, 2003).

Osteoblasts are the scleroblast type that form vertebrate bone, and the process of bone formation can be either direct from isolated mesenchyme (intramembranous ossification) or indirect using a cartilage template (endochondral and/or perichondral ossification) (Olsen et al., 2000; Galea et al., 2021). In a polarized fashion, osteoblasts synthesize osteoid, the organic component of bone extracellular matrix (ECM), which contains abundant type 1 collagen (Col1) (Rossert and de Crombrugghe, 2002). Osteoblasts also secrete vesicles that initiate bone ECM mineralization (Anderson et al., 2005; Golub, 2009). Osteoblasts are usually trapped in bone ECM where they mature into osteocytes (Franz-Odendaal et al., 2006), but some bony fishes (e.g., teleosts) have acellular (anosteocytic) bone, where osteoblasts are located at the bone ECM surface. In cellular bone, osteocytes extend cytoplasmic extensions through the bone ECM in a network of nano-channels (called canaliculi) that act as mechanosensors and communication channels between neighbouring osteocytes (Aarden et al., 1994; Kamioka et al., 2001; Kerschnitzki et al., 2011).

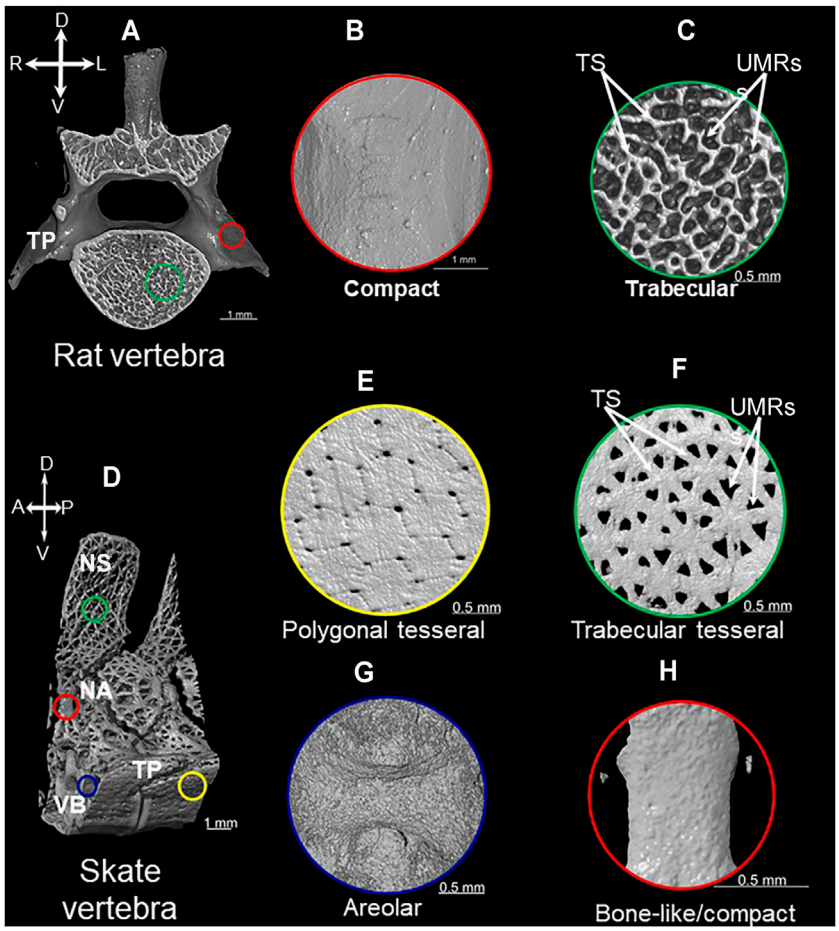

FIGURE 1 | Mineralization patterns of vertebrate mineralized tissues. 3D rendered images of micro-CT scan of vertebrae from rat **(A)** and little skate (*Leucoraja erinacea*) **(D)** showing compact **(B)**, trabecular **(C)**, polygonal tesseral **(E)**, trabecular tesseral **(F)**, areolar **(G)**, and bone-like/compact **(H)** mineralization patterns. Abbreviations: TS = trabecular struts; UMRs = unmineralized regions; NS = neural spine; NA = neural arch; TP = transverse process; VB = vertebral body; A = anterior; P = posterior; R = right; L = left.

Compared to bone, mineralized cartilage is less abundant in most vertebrate endoskeletons, found in such places as the growth plate of bones forming by endochondral ossification, articular surfaces between bones, medial portions of reptilian and mammalian ribs, and mammalian thyroid cartilages (Lohmander and Hjerpe, 1975; Ballock and O'Keefe, 2003; Claassen et al., 2017). In growth plates and thyroid cartilages, mineralized cartilage can exhibit a trabecular mineralization pattern containing wave-like running lines (termed Liesegang lines) resulting from rhythmic deposition of biological apatite in the cartilage ECM (Gerstenfeld and Shapiro, 1996; Kimpel et al., 1999; Sawae et al., 2003; Claassen et al., 2014; Jaroszewicz et al., 2016; Claassen et al., 2017; Estefa et al., 2021). Specifically, the trabecular pattern of mineralization in the growth plate involves rod-like mineralized struts of cartilage that run the longitudinal length of the skeletal element alongside columns of hypertrophic chondrocytes (Sawae et al., 2003; Jaroszewicz et al., 2016). During endochondral ossification, mineralized cartilage also can serve as a scaffold for the formation of trabecular-patterned endochondral bone (Gerstenfeld and Shapiro, 1996; Rauch, 2005; Touaitahuata et al., 2014), but the patterning relationships between these events are unclear.

Chondrocytes are the scleroblast type that form vertebrate cartilage, and the process of cartilage formation (chondrogenesis) is exemplified during endochondral ossification. During chondrogenesis, mesenchymal cells are converted to chondrocytes with a very transient chondroblast stage, because as soon as they begin to differentiate, they immerse themselves immediately in cartilage ECM, which contains abundant type 2 collagen (Col2) (Goldring et al., 2006). During endochondral ossification, chondrocytes form the cartilage template for subsequent bone formation and undergo a specific process called chondrocyte maturation (Eames et al., 2003). Morphologically, chondrocyte maturation includes hypertrophy (i.e., increase in cell size) and mineralization of the cartilage ECM, such as noted above in growth plates. Perhaps in an identical fashion to osteoblasts, mature chondrocytes secrete vesicles that initiate cartilage ECM mineralization (Anderson, 2003; Bottini et al., 2018).

Molecularly, expression of Runt-related transcription factor 2 (Runx2) and Indian hedgehog (Ihh) in mature chondrocytes links developing cartilage to surrounding bone (Lefebvre and Smits, 2005). Runx2 induces *Ihh* expression in mature chondrocytes, and Ihh diffuses to adjacent perichondral cells, inducing differentiation of osteoblasts to form compact-patterned perichondral bone (Lefebvre and Smits, 2005; Komori, 2011). We will discuss the possibility that these basic skeletal biology concepts, largely derived from studies of tetrapods, apply to chondrichthyan endoskeletal tissues below.

WHAT HISTOLOGICAL REGIONS OF TESSERAE PRODUCE TESSERAL MINERALIZATION PATTERNS?

Tesserae are a defining feature of the extant chondrichthyan endoskeleton, and recent work leads toward a new view on how mineralization patterns of tesserae are organized in discrete histological compartments. Traditionally, tesserae were described as a distinctive polygonal mineralization pattern in chondrichthyans that is unique among vertebrates (**Figures 1D,E**; Kemp and Westrin, 1979; Maisey, 2013; Maisey et al., 2021). This polygonal mineralization pattern forms a superficial tiled structure beneath the perichondrium (i.e., subperichondral) of chondrichthyan endoskeletal elements. In addition to the polygonal pattern, recent work on endoskeletal tissues in Eaton's and little skates revealed a previously-unappreciated trabecular mineralization pattern (Atake et al., 2019).

All chondrichthyan tesserae do not necessarily exhibit a polygonal mineralization pattern, but they all appear to exhibit a trabecular mineralization pattern, characterized by branching, rod-like struts (**Figure 1F**; Atake et al., 2019). The trabecular mineralization pattern (also described as stellate) can occur either underlying the polygonal mineralization pattern or can occur independently in the absence of the traditional polygonal mineralization pattern (Atake et al., 2019; Jayasankar et al., 2020). Large unmineralized regions between mineralized rod-like struts clearly distinguish the trabecular mineralization pattern from the polygonal mineralization pattern (**Figures 1E,F**; Atake et al., 2019). Of note, the exact mineralization patterns of tesserae can vary among endoskeletal elements in the same animal; sometimes the patterns even vary within different regions of the same skeletal element. One example of many is the little skate vertebra, the transverse processes of which exhibit polygonal and trabecular tesseral mineralization patterns, while the neural spine of the vertebra exhibits the trabecular pattern only (**Figures 1D–F**). Recent work highlighting the importance of mechanical forces in shaping the morphology and function of chondrichthyan tesserae might shed light on what actually generates this dimorphism of mineralization patterns (Jayasankar et al., 2020; Seidel et al., 2021).

Histological and molecular analyses of tesserae help clarify the nature of the tissues underlying tesseral mineralization patterns. There are two histological regions in tesserae: the cap zone and the body zone (Kemp and Westrin, 1979). The cap zone is subperichondral while the body zone underlies the cap zone (**Figure 2**). As we discuss in more detail below, cells within the cap zone of tesserae have morphological similarities to osteocytes and seem to secrete Col1 (Kemp and Westrin, 1979; Seidel et al., 2016; Seidel et al., 2017; Atake et al., 2019). By contrast, the body zone of tesserae consists of chondrocytes with round lacunae, large, mineral-dense, acellular regions termed spokes, and a Col2-rich ECM (Enault et al., 2015; Seidel et al., 2017). Prismatic mineralization and globular mineralization are traditional paleontological terms that distinguish biomineralization in the cap zone and body zone, respectively. Prismatic mineralization in the cap zone involves lime-prisms, while globular mineralization in the body zone involves globules of mineralized cartilage enriched in Liesegang lines and acellular spokes (Ørvig, 1951; Kemp and Westrin, 1979; Ørvig, 1989; Dean and Summers, 2006; Seidel et al., 2016). These histological features highlight two distinct regions in tesserae: a cap zone that exhibits bony features and a body zone that contains unmineralized and mineralized cartilage.

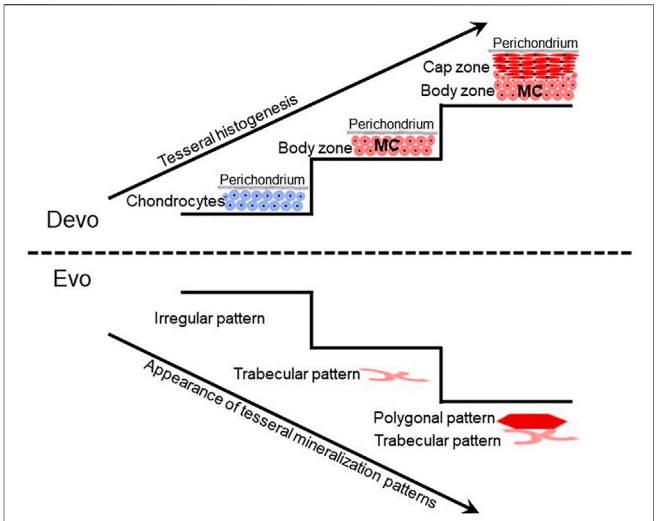

FIGURE 2 | Tesseral development might reflect the evolution of tesseral mineralization patterns. Current limited data suggest that during tesseral development, the body zone of mineralized cartilage (MC) develops first, and the cap zone develops later atop the body zone. The fossil record can test whether this developmental sequence reflects the evolutionary history of tesseral mineralization patterns. Irregular patterns of mineralized cartilage in some acanthodians suggest that ill-defined mineralization patterns preceded well-defined trabecular and polygonal tesseral mineralization patterns in modern chondrichthyans. The emergence of the polygonal tesseral pattern after the trabecular tesseral pattern both in development and evolution needs to be ascertained.

What regions of the tesserae actually produce these two tesseral mineralization patterns? The polygonal mineralization pattern in sharks and skates appears to occur subperichondrally, exclusively within the cap zone (Seidel et al., 2016; Maisey et al., 2021). Current data are not conclusive regarding how the trabecular mineralization pattern relates to histological features of tesserae. The cap zone of polygonal tesserae is much larger than the cap zone of trabecular tesserae (Atake et al., 2019). When

occurring in association with the polygonal pattern, the trabecular pattern either derives from the deep portion of the cap zone or mineralized cartilage in the body zone. When occurring in isolation, the trabecular pattern might derive from the small cap zone or mineralized cartilage in the body zone (Atake et al., 2019). Again, the radiating pattern of acellular, mineral-dense spokes of the deep zone suggest that spokes are strong candidates for the trabecular mineralization pattern (**Figure 1F**; Seidel et al., 2016). Careful measurements correlating mineralized portions with histology can resolve between these two possibilities.

DEVELOPMENTAL STUDIES OF CHONDRICHTHYAN TESSERAE CAN SHED LIGHT ON MINERALIZATION PATTERN EVOLUTION

Recent studies have begun to clarify how morphological features of tesserae are conserved or vary across chondrichthyan clades. Most extant chondrichthyan studies have focussed on elasmobranchs, where polygonal tesserae are widespread (Kemp and Westrin, 1979; Maisey, 2013; Seidel et al., 2016; Seidel et al., 2017; Atake et al., 2019; Marrama et al., 2019). Trabecular (or stellate) tesserae have not been widely described using those terms, but various studies suggest that this mineralization pattern is also widespread among extant elasmobranchs and some fossil chondrichthyans. For example, trabecular/stellate tesserae are present in the propterygium of the round stingray *Urobatis halleri* and in the cranium of the stem-holocephalan *Cladoselache* (Frey et al., 2019; Jayasankar et al., 2020; Maisey et al., 2021).

Studies of the skeleton in chimaeras were extremely limited until the past couple of years, but these recent analyses are providing much-needed data to understand the evolution of the "classical" chondrichthyan trait of tesserae. For example, tesserae in the synarcual of the adult elephant shark *Callorhinchus milii* and in the chondrocranium of the adult rabbit fish *Chimaera monstrosa* do not exhibit either trabecular or polygonal mineralization patterns, instead showing an irregular mineralization pattern (Pears et al., 2020; Seidel et al., 2020). It is unclear which region of tesserae creates the irregular mineralization pattern, because "classical" features of tesserae, such as the cap and body zones, are not discernable. However, histological analyses show that tesserae in chimaeras appear acellular, which is a characteristic of the body zone in elasmobranch tesserae (Debiais-Thibaud, 2018; Pears et al., 2020; Seidel et al., 2020).

Despite these limited data on extant chimaeras, fossil data suggest that the last common ancestor of extant chondrichthyans had polygonal and trabecular tesserae. For example, tesserae in the braincase of fossil chimaeras exhibit polygonal and trabecular mineralization patterns, but their histological features are not known (Finarelli and Coates, 2014; Coates et al., 2017; Pears et al., 2020). Furthermore, recent analyses of tesseral features in fossil chondrichthyans suggest that ill-defined (irregular) patterns of mineralized cartilage, such as those in some acanthodians, might be evolutionary precursors of well-defined trabecular and polygonal mineralization patterns in modern chondrichthyans (**Figure 2**; Burrow et al., 2018; Maisey et al., 2021).

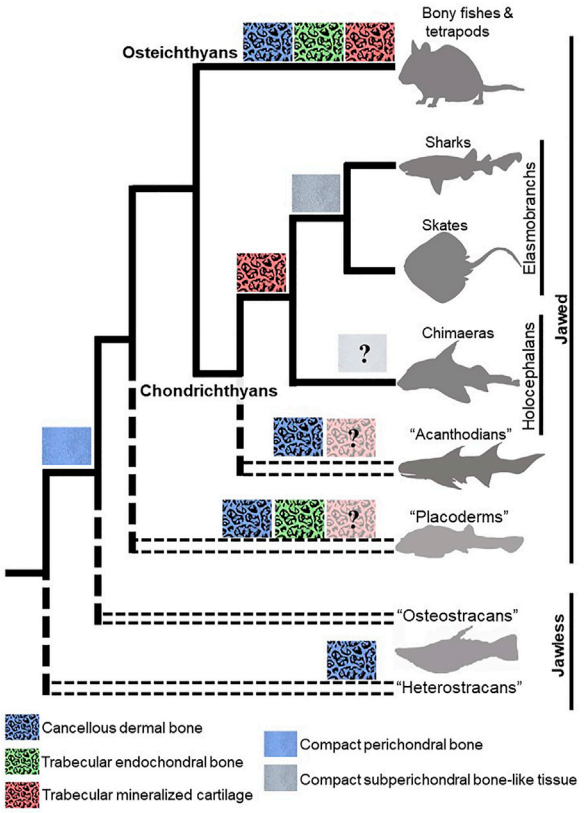

FIGURE 3 | Evolutionary appearances of mineralization patterns of bone and cartilage in vertebrates. Dermal bones in fossil and extant jawless and jawed vertebrates have a cancellous microstructure that is similar to that of trabecular endochondral bone. The recently-described trabecular mineralization pattern of cartilage in chondrichthyans argues that a trabecular mineralization pattern is an ancestral feature of vertebrates, so the presence of trabecular mineralized cartilage should be re-evaluated in ancestral jawless and jawed vertebrates. Compact subperichondral bone-like tissue is an elasmobranch synapomorphy, but endoskeletal tissues in chimaeras need to be examined to ascertain whether this feature would be symplesiomorphic in extant chondrichthyans. The presence of compact perichondral bone in the ancestors of chondrichthyans and osteichthyans suggest that subperichondral bone-like tissue and perichondral bone are homologous. Paraphyletic groups are represented by doubled, dashed lines.

Fossil data argue that the trabecular mineralization pattern recently described in extant chondrichthyans actually appeared very far back during vertebrate evolution. Radiating "trabecles of mineralized cartilage" have been described in tesserae of the stem-elasmobranch *Palaeobates polaris* (**Figure 3**; Ørvig, 1951). Dermal skeletal tissues, such as dentine and dermal bones (i.e., those forming from intramembranous ossification), in the exoskeleton of jawless fishes (e.g., heterostracans) and jawed fishes (e.g., placoderms, acanthodians, and osteichthyans) have a cancellous microstructure similar to the trabecular mineralization pattern (**Figure 3**; Ørvig, 1951; Smith and Hall,

1990; Sanchez et al., 2012; Giles et al., 2013; Keating et al., 2015). The trabecular mineralization pattern in the vertebrate endoskeleton is commonly illustrated by endochondral bone (i.e., bone deposited within a degrading cartilage template), which was long argued to appear first in osteichthyans (Donoghue and Sansom, 2002; Donoghue et al., 2006). New fossil data describe endochondral bone with a trabecular mineralization pattern also in placoderm-like fish (Brazeau et al., 2020), suggesting that the trabecular mineralization pattern is present in the endoskeleton of ancestral vertebrates (**Figure 3**). Given that ostracoderms and placoderms also had mineralized cartilage in their endoskeletons, further work should clarify whether a trabecular mineralization pattern in cartilage was pervasive in these ancestral vertebrates.

Perhaps reflecting shared ancestry, the trabecular mineralization pattern of chondrichthyan tesserae and trabecular bone of other vertebrates share morphological features. In fact, we named the trabecular mineralization pattern of chondrichthyan tesserae after the well-described trabecular bone (i.e., true endochondral bone) that forms during endochondral ossification. Both trabecular tesserae and endochondral bone share morphological similarities, such as trabecular struts and unmineralized regions between them (**Figures 1C,F**). The average thickness of trabecular struts is a relatively constant measure of endochondral bone in tetrapods (Mullender et al., 1996; Swartz et al., 1998; Holzer et al., 2012; Tsegai et al., 2017). Interestingly, trabecular thickness is indistinguishable between trabecular mineralization patterns of chondrichthyan tesserae and endochondral bone in tetrapods (Atake et al., 2019). While both examples of trabecular mineralization patterns have unmineralized regions between them, those regions contain fat (and marrow in tetrapods) in endochondral bone and cartilage in trabecular tesserae. In addition, the trabecular pattern of endochondral bone projects in three dimensions, while the trabecular pattern of trabecular tesserae only extends in two dimensions. Despite these differences, similarities in the mineralization patterns of trabecular tesserae and trabecular bone suggest that, if these mineralization patterns are not homologous, then at least the same set of genes dictating the trabecular patterning process might have been co-opted during evolution of these tissues.

Comparing the development of the trabecular mineralization patterns of endochondral bone and trabecular tesserae will no doubt help to assess any homology between them. Mineralized cartilage is the scaffold upon which endochondral bone is formed, but how endochondral bone derives its trabecular mineralization pattern remains unclear. During endochondral ossification, cartilage ECM in the hypertrophic zone of the growth plate is organized into longitudinal and transverse septa; ECM of the longitudinal septa becomes mineralized, while the transverse septa are unmineralized (Gerstenfeld and Shapiro, 1996; Sawae et al., 2003; Jaroszewicz et al., 2016). Sometimes, trabeculae of mineralized cartilage even persist after cartilage ECM degradation, and osteoblasts deposit bone matrix on these cartilage remnants to form endochondral bone (Rauch, 2005; Touaitahuata et al., 2014). Despite common misunderstanding in the skeletal biology field, studies demonstrate clearly that matrix degradation of growth plate cartilage occurs by proteolytic activity of vascular endothelial cells, not chondro-/osteoclasts (Lewinson and Silbermann, 1992; Lee et al., 1995; Romeo et al., 2019). Molecularly, the Notch pathway in endothelial cells appears to drive the pattern of cartilage degradation, and thus Notch signalling is the only known molecular determinant of trabecular bone patterning (Ramasamy et al., 2014). While previous studies of this process were in 2D (Lewinson and Silbermann, 1992; Gerstenfeld and Shapiro, 1996; Sawae et al., 2003), recent studies using high resolution 3D images will provide unique insights into the trabecular patterning mechanism of endochondral bone (Ramasamy et al., 2014; Jaroszewicz et al., 2016).

Developmental studies of tesserae might reveal evolution of chondrichthyan mineralization patterns. Unfortunately, only limited studies on chondrichthyan skeletal development have been published (Lorch, 1949; Jollie, 1971; Reif, 1980; Miyake et al., 1992; Dahn et al., 2007; Eames et al., 2007; Dean et al., 2009; Gillis et al., 2009a; Gillis et al., 2009b; Gillis et al., 2011; Johanson et al., 2013; Johanson et al., 2015; O'Shaughnessy et al., 2015; Seidel et al., 2016; Criswell et al., 2017; Johanson et al., 2019; Smith et al., 2019; Marconi et al., 2020; Pears et al., 2020; Smith et al., 2020), and none of these has looked carefully at tesseral development. During development of polygonal tesserae in the round stingray, an early stage is deposition of islets of globular mineralized cartilage (Seidel et al., 2016). Given that the body zone of adult tesserae contains globular mineralization, these data support previous speculation that the body zone precedes the cap zone during tesseral development (**Figure 2**; Kemp and Westrin, 1979; Ørvig, 1989). If the trabecular mineralization pattern derives from the body zone, then it would be interesting to reveal if the trabecular mineralization pattern precedes the polygonal mineralization pattern during development. Such a finding might shed light on the evolution of these two mineralization patterns, since traits that appear earlier in development often appear earlier in evolution (**Figure 2**; De Beer, 1930; Haeckel, 1866; Ørvig, 1989). In addition, homology of trabecular mineralization patterns of tesserae and endochondral bone would be strengthened by analyses of Notch signalling during tesseral development.

THE ELASMOBRANCH CENTRUM EXHIBITS A UNIQUE AREOLAR MINERALIZATION PATTERN

In the centrum (mineralized portion of the vertebral body) of sharks and skates, mineralization occurs in concentric rings of the perichordal sheath surrounding the notochord in what is termed an areolar mineralization pattern (Ridewood and MacBride, 1921; Ørvig, 1951; Dean and Summers, 2006). While the areolar mineralization pattern is considered one of the hallmarks of the chondrichthyan endoskeleton, it has never been described in the centra of chimaeras. Unconstricted mineralized perichordal sheaths have been described in some chimaeras (Gadow and Abbott, 1895; Didier, 1995), but whether

they reflect the areolar mineralization pattern and its histological features is yet to be clearly ascertained.

An elastic interna, a middle fibrous sheath, and an elastic externa form the perichordal sheath, which supports the development and mineralization of the centrum (for a review of the different types of vertebral centra, see Gadow and Abbott, 1895; Arratia et al., 2001). During development, migrating mesenchymal cells that will form cartilage of the vertebral body are thought to constrict the perichordal sheath, giving the elasmobranch centrum a biconcave morphology (**Figure 1G**; Gadow and Abbott, 1895). Some mesenchymal cells actually invade the perichordal sheath and help to differentiate the middle fibrous sheath into three distinct layers: inner, middle, and outer (Ridewood and MacBride, 1921; Eames et al., 2007; Criswell et al., 2017). Rounded cell lacunae of the inner and outer centrum layers reflect chondrocytes embedded in cartilage matrix. Cells of the middle centrum layer, which have elongated cell lacunae, are thought to produce the areolar mineralization pattern.

Centra in both elasmobranchs and ray-finned fishes demonstrate a biconcave morphology (Gadow and Abbott, 1895; Laerm, 1976), but they might not be homologous. Like elasmobranch centra, centra in ray-finned fishes also derive their biconcave morphology from the constriction of the perichordal sheath by migrating mesenchymal cells (Gadow and Abbott, 1895). Unlike centrum development in elasmobranchs, however, mesenchymal cells do not invade the perichordal sheath during centrum development in ray-finned fishes (Gadow and Abbott, 1895; Grotmol et al., 2003). Consequently, biconcave centra in elasmobranchs and ray-finned fishes derive from cellular and acellular mineralization of the perichordal sheath, respectively. This difference in the developmental processes of biconcave centra in elasmobranchs and ray-finned fishes has made their homology contentious, and despite tremendous similarities in morphology, centra in these two animal groups are thought to have evolved independently (Arratia et al., 2001; Grotmol et al., 2003; Fleming et al., 2015; Maisey et al., 2021). Developmental differences also suggest that centra evolved independently in different lineages of ray-finned fishes (Laerm, 1982; López-Arbarello and Sferco, 2018).

CHONDRICHTHYAN SUBPERICHONDRAL BONE-LIKE TISSUES MIGHT BE HOMOLOGOUS TO PERICHONDRAL BONE

Bone is one of the novelties characterizing vertebrate evolution (Hyman, 1943; Zhang and Cohn, 2008), and bone was widespread among vertebrates prior to the evolution of jaws (Stensiö, 1927; Janvier, 1990; Smith and Hall, 1990; Min and Janvier, 1998; Keating et al., 2015). Furthermore, the two main extant jawed vertebrate groups, chondrichthyans and osteichthyans, diverged from a common bony ancestor about 420 million years ago (Inoue et al., 2010). Acanthodians have long been recognized as a group of extinct jawed vertebrates with endoskeletal bone, and analyses over the past decade have led to the understanding that some members of this group are actually stem chondrichthyans (Davis et al., 2012; Brazeau and de Winter 2015; Maisey et al., 2021). So, both ancestral jawed vertebrates and stem chondrichthyans had endoskeletal bone. What about living chondrichthyans, which are thought to retain the most ancestral vertebrate features (Criswell and Gillis, 2020; Hirschberger et al., 2021)? Despite all of these phylogenetic data, the chondrichthyan endoskeleton has traditionally been characterized as lacking bone (Ørvig, 1951; Zangerl, 1966; Moss, 1977; Janvier, 1981; Maisey, 1988; Clement, 1992). Like chondrichthyans, Acipenseriformes (sturgeons and paddlefishes) have a predominantly cartilaginous endoskeleton and retain features of ancestral vertebrates (Cheng et al., 2020). The presence of endoskeletal bone in Acipenseriformes is also yet to be clearly demonstrated despite reports of mineralized bone-like tissue in Siberian sturgeons (Leprévost et al., 2017; Warth et al., 2017).

Current data lead to the idea that extant chondrichthyans might not have lost the endoskeletal bone that was present in their ancestors. Two locations within the elasmobranch endoskeleton have received much attention in this respect: the neural arches, which are dorsal extensions from the vertebral body that protect the neural tube (Arratia et al., 2001), and the cap zone of tesserae. Specifically, subperichondral neural arch tissue and the cap zone of tesserae (hereafter referred to as subperichondral bone-like tissues) show histological and molecular features that are consistent with bone. Back in 1932, Wurmbach observed that subperichondral neural arch tissue of some sharks is compact and develops appositionally (Wurmbach, 1932). Subsequent work supported this finding, not only in many species of shark, but also in skates and other batoids, suggesting that this bone-like tissue in the neural arch might at least be an elasmobranch synapomorphy (**Figure 1H**; **Figure 3**; Eames et al., 2007; Atake et al., 2019; Berio et al., 2021). Data on chimaeras are needed in order to understand whether this might be an ancestral trait of all living chondrichthyans. Similarly, Kemp and Westrin proposed that the cap zone of tesserae might also be bone-like (Kemp and Westrin, 1979). The mineralization pattern in polygonal tesserae of both sharks and skates is compact, and as discussed above, new data on chimaera tesserae suggest that they have a somewhat compact mineralization pattern (Pears et al., 2020; Seidel et al., 2020). In sum, morphological data demonstrate that both tesserae and neural arches exhibit bone-like features, and such features might have been present in the last common ancestor to extant chondrichthyans.

Cell morphological and limited molecular studies also support the idea that extant chondrichthyans make endoskeletal bone. In typical vertebrate perichondral bone, osteocyte lacunae demonstrate an elongate morphology, and bone ECM has high levels of Col1 (Rossert and de Crombrugghe, 2002; Currey, 2003; Atkins and Findlay, 2012). Indeed, cell lacunae in chondrichthyan subperichondral bone-like tissues also exhibit an elongate morphology, and histological, immunohistochemical, and electron microscopy analyses show the presence of tightly packed Col1 in the ECM of subperichondral bone-like tissues (Kemp and Westrin, 1979; Peignoux-Deville et al., 1982; Eames et al., 2007; Seidel et al., 2017). Interestingly, similar to osteocyte canaliculi, cell lacunae in subperichondral neural arch tissue of

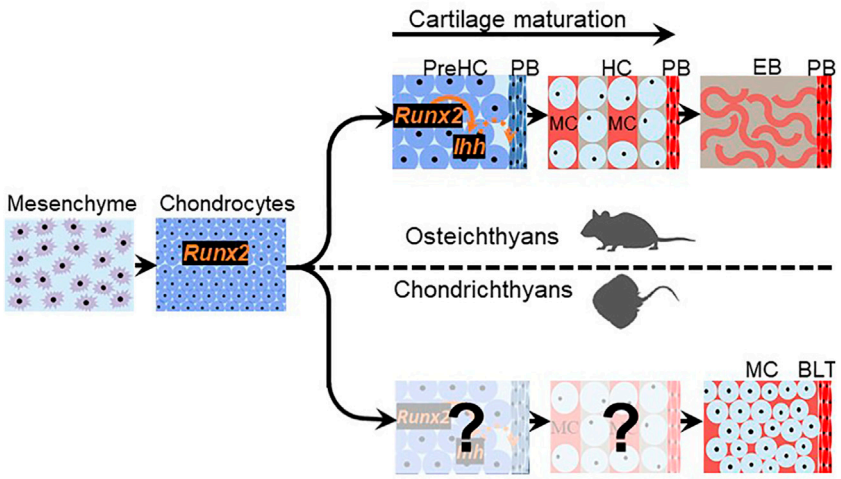

FIGURE 4 | Chondrichthyan subperichondral bone-like tissues and osteichthyan perichondral bone might share a developmental program. Chondrichthyan subperichondral bone-like tissue (BLT) and osteichthyan perichondral bone (PB) develop in association with a cartilage template that expresses *Runx2*. In osteichthyans, the cartilage template undergoes a maturation process involving the creation of mature hypertrophic chondrocytes (HC) and expression of *Ihh*, which induces perichondral bone. If cartilage maturation occurs during the development of chondrichthyan subperichondral bone-like tissues, then the persistence of mineralized cartilage (MC) in chondrichthyans (and early vertebrates outside the gnathostome crown group such as placoderms and ostracoderms) and the additional cartilage degradation step occurring in osteichthyans argues that cartilage maturation is evolvable.

the catshark might be connected by nano-channels (Bordat, 1987). Bone is a metabolically active tissue that undergoes remodelling (Hadjidakis and Androulakis, 2006). While *Sox9/Sox5/Sox6*-expressing perichondral cells were shown recently to mediate cartilage regeneration in the little skate (Marconi et al., 2020), the capability of chondrichthyan bone-like tissues to undergo (cellular- or acellular-mediated) remodelling is currently untested. Nevertheless, morphological, histological, and molecular features suggest that chondrichthyan subperichondral bone-like tissues and perichondral bone are homologous.

Two criteria must be met for chondrichthyan subperichondral bone-like tissues to be homologous with perichondral bone: shared ancestry and shared developmental programs. Homologous characters are classically defined by descent from a common ancestor (Jardine, 1967). Clearly, the last common ancestor of chondrichthyans and osteichthyans had perichondral bone (**Figure 3**; Ørvig, 1951; Donoghue and Sansom, 2002; Donoghue et al., 2006; Maisey, 2013), so extant chondrichthyan subperichondral bone-like tissues might be a modified perichondral bone. Homology of chondrichthyan subperichondral bone-like tissues and perichondral bone should be further assessed by comparative embryology, because homologous characters must share a developmental program, even though each clade might have modified that ancestral program independently (Boyden, 1947; Sachs, 1982; Van Valen, 1982; Roth, 1984; Stevens, 1984; Tomlinson, 1984; Wagner, 1989; Roth, 1991; Gilbert and Bolker, 2001). Perichondral bone formation has been well-studied, but only limited features of chondrichthyan neural arch or tesseral development have been described (Eames et al., 2007; Seidel et al., 2016), so research is desperately needed on the development of chondrichthyan bone-like tissues.

If chondrichthyan subperichondral bone-like tissues and perichondral bone were homologous, then what developmental features might they share? Chondrichthyan subperichondral bone-like tissues appear to develop in association with a cartilage template (Eames et al., 2007), so that aspect seems conserved with perichondral bone (**Figure 4**). Runx2 and Ihh expression during cartilage maturation is required for induction of adjacent perichondral bone in osteichthyans (**Figure 4**; Lanske et al., 1996; Vortkamp et al., 1996; Hoshi et al., 1999; Inada et al., 1999; Kim et al., 1999; St-Jacques et al., 1999; Long et al., 2001; Kronenberg, 2003; Hammond and Schulte-Merker, 2009; Eames et al., 2011). Interestingly, *Runx2* is expressed in developing cartilages of the dogfish shark, and the ability of Runx proteins to induce Hedgehog genes might be an ancestral trait of all chordates (Hecht et al., 2008). However, it remains unclear what molecules drive the differentiation of chondrichthyan subperichondral bone-like tissues. Furthermore, perichondral bone in osteichthyans derives from perichondral osteoprogenitor cells, while some true endochondral bone derives from mature chondrocytes *trans*-differentiating into osteoblasts (Moskalewski and Malejczyk, 1989; Roach, 1992; Hammond and Schulte-Merker, 2009; Zhou et al., 2014; Giovannone et al., 2019). Whether chondrichthyan bone-like tissues derive from the perichondrium or from chondrocyte *trans*-differentiation is unknown.

To summarize, in order to assess correspondence of the developmental programs of chondrichthyan subperichondral

bone-like tissues and perichondral bone, some key aspects of chondrichthyan endoskeletal development must be revealed:

1) Do chondrocytes in the cartilage template of chondrichthyan subperichondral bone-like tissues undergo hypertrophy and express maturation genes, such as *Runx2* and *Ihh*?
2) Does Hedgehog signalling induce bone-like tissues?
3) Do chondrichthyan subperichondral bone-like tissues derive from the perichondrium and/or chondrocytes?

More broadly, elucidating the process of perichondral ossification in ancestral vertebrates would be key to understanding the evolutionary history of perichondral ossification. However, direct assessment of the developmental process of perichondral bone in extinct ancestral jawless and jawed vertebrates is not feasible, unless many fossilized embryos and larvae of different stages are identified, such as the remarkable discoveries of ptyctodontid placoderm embryos and acanthodian larvae (Zidek, 1985; Long et al., 2008; Chevrinais et al., 2017). Also, living jawless vertebrates (lampreys and hagfishes) do not mineralize their skeleton (Shimeld and Donoghue, 2012). Thus, the basal phylogenetic position of chondrichthyans makes their subperichondral bone-like tissues an excellent proxy for assessing the mechanism of perichondral ossification in ancestral vertebrates. In jawless (e.g., osteostracans) and jawed (e.g., placoderms) vertebrates, perichondral bone typically overlies a persistent mineralized cartilage (Ørvig, 1951; Wang et al., 2005; Long et al., 2015). Similarly, subperichondral bone-like tissues in chondrichthyans overlie a persistent mineralized cartilage, which would be the body zone in the case of tesserae and the cartilage core in the case of the neural arches (**Figure 2**; Eames et al., 2007; Seidel et al., 2016; Atake et al., 2019). These data argue that the process of cartilage maturation is highly evolvable as mineralized cartilage persists (and induces perichondral bone?) in stem-pan-gnathostomes (e.g., heterostracans and placoderms), whereas a subsequent cartilage degradation step occurs in crown-gnathostomes (e.g., osteichthyans) to facilitate endochondral bone formation (**Figure 4**).

USING COMPARATIVE TRANSCRIPTOMICS TO TEST FOR CHONDRICHTHYAN BONE

If chondrichthyan bone-like tissues and perichondral bone are homologous, then they would derive from a homologous cell type: the osteoblast. Homologous cell types are evolutionary units defined by descent from a common ancestor (Arendt, 2008; Arendt et al., 2016). Each cell type expresses a characteristic set of genes, termed a molecular fingerprint, which can be conserved across phylogenetic lineages (Sudmant et al., 2015; Liang et al., 2018).

A few candidate genes have been used conventionally to characterize evolution of skeletal cell types, but this approach is very limited. For example, Collagen type 10 alpha 1 (*Col10a1*) is expressed by mature chondrocytes and osteoblasts in teleosts and other ray-finned fishes, including medaka, zebrafish, and spotted gar (Laue et al., 2008; Albertson et al., 2010; Renn and Winkler, 2010; Eames et al., 2012). Only one of six identified duplicates of *Col10a1* in the catshark is expressed specifically by cells in subperichondral neural arch tissue (Debiais-Thibaud et al., 2019). This shared expression of a given gene by osteoblasts, mature chondrocytes, and cells of bone-like tissue highlights some of the limitations in adopting candidate gene approaches to demonstrate cell type homology. Are cells that form chondrichthyan bone-like tissue best characterized as osteoblasts or mineralizing chondrocytes?

Comparative transcriptomics of osteoblasts, mineralizing chondrocytes, and cells forming chondrichthyan bone-like tissues can resolve the molecular fingerprints of cells forming chondrichthyan subperichondral bone-like tissues. Unbiassed transcriptomic profiling of cell types is readily achievable following the advent of deep RNA sequencing. The molecular fingerprint should be revealed by RNA sequencing of a specific cell type at a developmental stage when differentiation genes are highly expressed (Arendt, 2008). Cells that form chondrichthyan bone-like tissues would be best characterized as osteoblasts if they demonstrate the osteoblast molecular fingerprint. However, osteoblasts can evolve in clade-specific fashions (Nguyen and Eames, 2020), so what, if anything, is the vertebrate osteoblast molecular fingerprint to which chondrichthyan data should be compared?

Defining the osteoblast molecular fingerprint must involve transcriptomic profiling of osteoblasts from several vertebrate groups. In addition to unravelling a conserved suite of genes, these data need to be coupled to phylogenetic bioinformatic analyses to estimate the ancestral osteoblast molecular fingerprint. A survey of unbiased transcriptomic profiles of osteoblasts reveals that transcripts have been mainly from studies on mammals (Ayturk, 2019). More efforts are therefore needed to uncover the transcriptome of osteoblasts in non-mammalian vertebrates to enable a comprehensive definition of the vertebrate osteoblast molecular fingerprint. In addition, bioinformatics techniques need to be developed to compare networks of transcriptomic data quantitatively and infer ancestral gene networks (for a recent review, see Ovens et al., 2021).

CONCLUSION

The designation of chondrichthyans as "cartilaginous fishes" was clearly made at a time when research tools were very limited. The advent of high-resolution imaging and contemporary molecular techniques has renewed investigative interests on morphological and molecular features of the chondrichthyan endoskeleton. Unraveling the developmental mechanisms underlying the formation of tesserae and subperichondral bone-like tissues generally will provide tremendous insight into the evolutionary history of endochondral and perichondral bone among vertebrates, guiding future investigations on vertebrate mineralized skeletal tissues. Employing comparative embryology and transcriptomics can robustly test the hypothesis that the chondrichthyan endoskeleton lacks bone. The question "Do sharks and relatives make bone?" has lasted

for many centuries, but for the first time the answers are now within experimental reach.

AUTHOR CONTRIBUTIONS

OJA and BFE wrote and revised the manuscript.

FUNDING

OJA was funded by the College of Medicine at the University of Saskatchewan. The authors' research was funded by Natural Sciences and Engineering Research Council (NSERC) grants RGPIN 435655-201 and RGPIN 2014-05563 to BFE.

REFERENCES

Aarden, E. M., Nijweide, P. J., and Burger, E. H. (1994). Function of Osteocytes in Bone. *J. Cel. Biochem.* 55, 287–299. doi:10.1002/jcb.240550304

Albertson, R. C., Yan, Y.-L., Titus, T. A., Pisano, E., Vacchi, M., Yelick, P. C., et al. (2010). Molecular Pedomorphism Underlies Craniofacial Skeletal Evolution in Antarctic Notothenioid Fishes. *BMC Evol. Biol.* 10, 4. doi:10.1186/1471-2148-10-4

Anderson, H. C., Garimella, R., and Tague, S. E. (2005). The Role of Matrix Vesicles in Growth Plate Development and Biomineralization. *Front. Biosci.* 10, 822–837. doi:10.2741/1576

Anderson, H. C. (2003). Matrix Vesicles and Calcification. *Curr. Rheumatol. Rep.* 5, 222–226. doi:10.1007/s11926-003-0071-z

Arendt, D., Musser, J. M., Baker, C. V. H., Bergman, A., Cepko, C., Erwin, D. H., et al. (2016). The Origin and Evolution of Cell Types. *Nat. Rev. Genet.* 17, 744–757. doi:10.1038/nrg.2016.127

Arendt, D. (2008). The Evolution of Cell Types in Animals: Emerging Principles from Molecular Studies. *Nat. Rev. Genet.* 9, 868–882. doi:10.1038/nrg2416

Arratia, G., Schultze, H.-P., and Casciotta, J. (2001). Vertebral Column and Associated Elements in Dipnoans and Comparison with Other Fishes: Development and Homology. *J. Morphol.* 250, 101–172. doi:10.1002/jmor.1062

Atake, O. J., Cooper, D. M. L., and Eames, B. F. (2019). Bone-like Features in Skate Suggest a Novel Elasmobranch Synapomorphy and Deep Homology of Trabecular Mineralization Patterns. *Acta Biomater.* 84, 424–436. doi:10.1016/j.actbio.2018.11.047

Atkins, G. J., and Findlay, D. M. (2012). Osteocyte Regulation of Bone mineral: a Little Give and Take. *Osteoporos. Int.* 23, 2067–2079. doi:10.1007/s00198-012-1915-z

Ayturk, U. (2019). RNA-seq in Skeletal Biology. *Curr. Osteoporos. Rep.* 17, 178–185. doi:10.1007/s11914-019-00517-x

Ballock, R. T., and O'KEEFE, R. J. (2003). The Biology of the Growth Plate. *The J. Bone Jt. Surgery-American Volume* 85, 715–726. https://www.ncbi.nlm.nih.gov/pubmed/12672851. doi:10.2106/00004623-200304000-00021

Berio, F., Broyon, M., Enault, S., Pirot, N., López-Romero, F. A., and Debiais-Thibaud, M. (2021). Diversity and Evolution of Mineralized Skeletal Tissues in Chondrichthyans. *Front. Ecol. Evol.* 9, 223. doi:10.3389/fevo.2021.660767

Bordat, C. (1987). Étude ultrastructurale de l'os des vertèbres du Sélacien *Scyliorhinus canicula* L. *Can. J. Zool.* 65, 1435–1444. doi:10.1139/z87-226

Bottini, M., Mebarek, S., Anderson, K. L., Strzelecka-Kiliszek, A., Bozycki, L., Simão, A. M. S., et al. (2018). Matrix Vesicles from Chondrocytes and Osteoblasts: Their Biogenesis, Properties, Functions and Biomimetic Models. *Biochim. Biophys. Acta (Bba) - Gen. Subjects* 1862, 532–546. doi:10.1016/j.bbagen.2017.11.005

Boyden, A. (1947). Homology and Analogy. A Critical Review of the Meanings and Implications of These Concepts in Biology. *Am. Midland Naturalist* 37, 648–669. doi:10.2307/2421470

Brazeau, M. D., and de Winter, V. (2015). The Hyoid Arch and Braincase Anatomy of Acanthodes Support Chondrichthyan Affinity of 'acanthodians'. *Proc. R. Soc. B.* 282, 20152210. doi:10.1098/rspb.2015.2210

Brazeau, M. D., Giles, S., Dearden, R. P., Jerve, A., Ariunchimeg, Y., Zorig, E., et al. (2020). Endochondral Bone in an Early Devonian 'placoderm' from Mongolia. *Nat. Ecol. Evol.* 4, 1477–1484. doi:10.1038/s41559-020-01290-2

Burrow, C. J., Newman, M., Den Blaauwen, J., Jones, R., and Davidson, R. (2018). The Early Devonian Ischnacanthiform Acanthodian *Ischnacanthus Gracilis* (Egerton, 1861) from the Midland Valley of Scotland. *Acta Geologica Pol.* 68, 335–362. doi:10.1515/agp-2018-0008

Checa, A. G. (2018). Physical and Biological Determinants of the Fabrication of Molluscan Shell Microstructures. *Front. Mar. Sci.* 5. doi:10.3389/fmars.2018.00353

Cheng, P., Huang, Y., Lv, Y., Du, H., Ruan, Z., Li, C., et al. (2020). The American Paddlefish Genome Provides Novel Insights into Chromosomal Evolution and Bone Mineralization in Early Vertebrates. *Mol. Biol. Evol.* 38, 1595–1607. doi:10.1093/molbev/msaa326

Chevrinais, M., Sire, J.-Y., and Cloutier, R. (2017). From Body Scale Ontogeny to Species Ontogeny: Histological and Morphological Assessment of the Late Devonian Acanthodian *Triazeugacanthus Affinis* from Miguasha, Canada. *PLOS ONE* 12, e0174655. doi:10.1371/journal.pone.0174655

Claassen, H., Schicht, M., Fleiner, B., Hillmann, R., Hoogeboom, S., Tillmann, B., et al. (2017). Different Patterns of Cartilage Mineralization Analyzed by Comparison of Human, Porcine, and Bovine Laryngeal Cartilages. *J. Histochem. Cytochem.* 65, 367–379. doi:10.1369/0022155417703025

Claassen, H., Schicht, M., Sel, S., and Paulsen, F. (2014). Special Pattern of Endochondral Ossification in Human Laryngeal Cartilages: X-ray and Light-Microscopic Studies on Thyroid Cartilage. *Clin. Anat.* 27, 423–430. doi:10.1002/ca.22309

Clement, J. (1992). Re-examination of the fine Structure of Endoskeletal Mineralization in Chondrichthyans: Implications for Growth, Ageing and Calcium Homeostasis. *Mar. Freshw. Res.* 43, 157–181. doi:10.1071/mf9920157

Coates, M. I., Gess, R. W., Finarelli, J. A., Criswell, K. E., and Tietjen, K. (2017). A Symmoriiform Chondrichthyan Braincase and the Origin of Chimaeroid Fishes. *Nature* 541, 208–211. doi:10.1038/nature20806

Cohen, K. M., Harper, D. A. T., Gibbard, P. L., and Car, N., 2021. International Chrono Stratigraphic. Chart v2021/07 [Chart]. Available at: http://www.stratigraphy.org/ICSchart/ChronostratChart2021-07.pdf.

Criswell, K. E., Coates, M. I., and Gillis, J. A. (2017). Embryonic Development of the Axial Column in the Little Skate, *Leucoraja erinacea*. *J. Morphol.* 278, 300–320. doi:10.1002/jmor.20637

Criswell, K. E., and Gillis, J. A. (2020). Resegmentation Is an Ancestral Feature of the Gnathostome Vertebral Skeleton. *Elife* 9, e51696. doi:10.7554/eLife.51696

Currey, J. D. (2003). The many Adaptations of Bone. *J. Biomech.* 36, 1487–1495. doi:10.1016/s0021-9290(03)00124-6

Dahn, R. D., Davis, M. C., Pappano, W. N., and Shubin, N. H. (2007). Sonic Hedgehog Function in Chondrichthyan Fins and the Evolution of Appendage Patterning. *Nature* 445, 311–314. doi:10.1038/nature05436

Davis, S. P., Finarelli, J. A., and Coates, M. I. (2012). Acanthodes and Shark-like Conditions in the Last Common Ancestor of Modern Gnathostomes. *Nature* 486, 247–250. doi:10.1038/nature11080

De Beer, G. (1930). *Embryology and Evolution*. Oxford: Clarendon Press.

Dean, M. N., Mull, C. G., Gorb, S. N., and Summers, A. P. (2009). Ontogeny of the Tessellated Skeleton: Insight from the Skeletal Growth of the Round stingrayUrobatis Halleri. *J. Anat.* 215, 227–239. doi:10.1111/j.1469-7580.2009.01116.x

Dean, M. N., and Summers, A. P. (2006). Mineralized Cartilage in the Skeleton of Chondrichthyan Fishes. *Zoology* 109, 164–168. doi:10.1016/j.zool.2006.03.002

Debiais-Thibaud, M., Simion, P., Ventéo, S., Muñoz, D., Marcellini, S., Mazan, S., et al. (2019). Skeletal Mineralization in Association with Type X Collagen Expression Is an Ancestral Feature for Jawed Vertebrates. *Mol. Biol. Evol.* 36, 2265–2276. doi:10.1093/molbev/msz145

Debiais-Thibaud, M. (2018). The Evolution of Endoskeletal Mineralisation in Chondrichthyan Fish, Evolution and Development of Fishes. *Cambridge Univ. Press*, 110–125. doi:10.1017/9781316832172.007

Didier, D. A. (1995). *Phylogenetic Systematics of Extant Chimaeroid Fishes (Holocephali, Chimaeroidei)*. New York: American Museum of Natural History.

Donoghue, P. C. J., Sansom, I. J., and Downs, J. P. (2006). Early Evolution of Vertebrate Skeletal Tissues and Cellular Interactions, and the Canalization of Skeletal Development. *J. Exp. Zool.* 306B, 278–294. doi:10.1002/jez.b.21090

Donoghue, P. C. J., and Sansom, I. J. (2002). Origin and Early Evolution of Vertebrate Skeletonization. *Microsc. Res. Tech.* 59, 352–372. doi:10.1002/jemt.10217

Eames, B. F., Allen, N., Young, J., Kaplan, A., Helms, J. A., and Schneider, R. A. (2007). Skeletogenesis in the Swell Shark *Cephaloscyllium ventriosum*. *J. Anat.* 210, 542–554. doi:10.1111/j.1469-7580.2007.00723.x

Eames, B. F., Amores, A., Yan, Y.-L., and Postlethwait, J. H. (2012). Evolution of the Osteoblast: Skeletogenesis in Gar and Zebrafish. *BMC Evol. Biol.* 12, 27. doi:10.1186/1471-2148-12-27

Eames, B. F., de la Fuente, L., and Helms, J. A. (2003). Molecular Ontogeny of the Skeleton. *Birth Defect Res. C* 69, 93–101. doi:10.1002/bdrc.10016

Eames, B. F., Yan, Y.-L., Swartz, M. E., Levic, D. S., Knapik, E. W., Postlethwait, J. H., et al. (2011). Mutations in Fam20b and Xylt1 Reveal that Cartilage Matrix Controls Timing of Endochondral Ossification by Inhibiting Chondrocyte Maturation. *Plos Genet.* 7, e1002246. doi:10.1371/journal.pgen.1002246

Enault, S., Muñoz, D. N., Silva, W. T. A. F., Borday-Birraux, V., Bonade, M., Oulion, S., et al. (2015). Molecular Footprinting of Skeletal Tissues in the Catshark *Scyliorhinus canicula* and the Clawed Frog *Xenopus Tropicalis* Identifies Conserved and Derived Features of Vertebrate Calcification. *Front. Genet.* 6, 283. doi:10.3389/fgene.2015.00283

Enlow, D. H., and Brown, S. O. (1958). A Comparative Histological Study of Fossil and Recent Bone Tissues. Part III. *Tex. J. Sci.* 10, 187–230.

Estefa, J., Tafforeau, P., Clement, A. M., Klembara, J., Niedźwiedzki, G., Berruyer, C., et al. (2021). New Light Shed on the Early Evolution of Limb-Bone Growth Plate and Bone Marrow. *Elife* 10, e51581. doi:10.7554/eLife.51581

Finarelli, J. A., and Coates, M. I. (2014). *Chondrenchelys Problematica* (Traquair, 1888) Redescribed: a Lower Carboniferous, Eel-like Holocephalan from Scotland. *Earth Environ. Sci. Trans. R. Soc. Edinb.* 105, 35–59. doi:10.1017/S1755691014000139

Fleming, A., Kishida, M. G., Kimmel, C. B., and Keynes, R. J. (2015). Building the Backbone: the Development and Evolution of Vertebral Patterning. *Development* 142, 1733–1744. doi:10.1242/dev.118950

Francillon-Vieillot, H., de Buffrénil, V., Castanet, J., Géraudie, J., Meunier, F., Sire, J., et al. (1990). "Microstructure and Mineralization of Vertebrate Skeletal Tissues," in *Skeletal Biomineralization: Patterns, Processes and Evolutionary Trends*. Editor J. Carter, 175–234.

Franz-Odendaal, T. A., Hall, B. K., and Witten, P. E. (2006). Buried Alive: How Osteoblasts Become Osteocytes. *Dev. Dyn.* 235, 176–190. doi:10.1002/dvdy.20603

Frey, L., Coates, M., Ginter, M., Hairapetian, V., Rücklin, M., Jerjen, I., et al. (2019). The Early Elasmobranch Phoebodus : Phylogenetic Relationships, Ecomorphology and a New Time-Scale for Shark Evolution. *Proc. R. Soc. B.* 286, 20191336. doi:10.1098/rspb.2019.1336

Gadow, H. F., and Abbott, E. (1895). IV. On the Evolution of the Vertebral Column of Fishes. *Phil. Trans. R. Soc. Lond. B* 186, 163–221. doi:10.1098/rstb.1895.0004

Galea, G. L., Zein, M. R., Allen, S., and Francis-West, P. (2021). Making and Shaping Endochondral and Intramembranous Bones. *Dev. Dyn.* 250, 414–449. doi:10.1002/dvdy.278

Gerstenfeld, L. C., and Shapiro, F. D. (1996). Expression of Bone-specific Genes by Hypertrophic Chondrocytes: Implications of the Complex Functions of the Hypertrophic Chondrocyte during Endochondral Bone Development. *J. Cel. Biochem.* 62, 1–9. doi:10.1002/(sici)1097-4644(199607)62:1<1:aid-jcb1>3.0.co;2-x

Gilbert, S. F., and Bolker, J. A. (2001). Homologies of Process and Modular Elements of Embryonic Construction. *J. Exp. Zool.* 291, 1–12. doi:10.1002/jez.1

Giles, S., Rücklin, M., and Donoghue, P. C. J. (2013). Histology of "placoderm" Dermal Skeletons: Implications for the Nature of the Ancestral Gnathostome. *J. Morphol.* 274, 627–644. doi:10.1002/jmor.20119

Gillis, J. A., Dahn, R. D., and Shubin, N. H. (2009a). Chondrogenesis and Homology of the Visceral Skeleton in the Little skate,*Leucoraja erinacea*(Chondrichthyes: Batoidea). *J. Morphol.* 270, 628–643. doi:10.1002/jmor.10710

Gillis, J. A., Dahn, R. D., and Shubin, N. H. (2009b). Shared Developmental Mechanisms Pattern the Vertebrate Gill Arch and Paired Fin Skeletons. *Proc. Natl. Acad. Sci.* 106, 5720–5724. doi:10.1073/pnas.0810959106

Gillis, J. A., and Donoghue, P. C. J. (2007). The Homology and Phylogeny of Chondrichthyan Tooth Enameloid. *J. Morphol.* 268, 33–49. doi:10.1002/jmor.10501

Gillis, J. A., Rawlinson, K. A., Bell, J., Lyon, W. S., Baker, C. V. H., and Shubin, N. H. (2011). Holocephalan Embryos Provide Evidence for Gill Arch Appendage Reduction and Opercular Evolution in Cartilaginous Fishes. *Proc. Natl. Acad. Sci.* 108, 1507–1512. doi:10.1073/pnas.1012968108

Giovannone, D., Paul, S., Schindler, S., Arata, C., Farmer, D. J. T., Patel, P., et al. (2019). Programmed Conversion of Hypertrophic Chondrocytes into Osteoblasts and Marrow Adipocytes within Zebrafish Bones. *Elife* 8, e42736. doi:10.7554/eLife.42736

Goldring, M. B., Tsuchimochi, K., and Ijiri, K. (2006). The Control of Chondrogenesis. *J. Cel. Biochem.* 97, 33–44. doi:10.1002/jcb.20652

Golub, E. E. (2009). Role of Matrix Vesicles in Biomineralization. *Biochim. Biophys. Acta (Bba) - Gen. Subjects* 1790, 1592–1598. doi:10.1016/j.bbagen.2009.09.006

Grotmol, S., Kryvi, H., Nordvik, K., and Totland, G. K. (2003). Notochord Segmentation May Lay Down the Pathway for the Development of the Vertebral Bodies in the Atlantic salmon. *Anat. Embryol.* 207, 263–272. doi:10.1007/s00429-003-0349-y

Hadjidakis, D. J., and Androulakis, I. I. (2006). Bone Remodeling. *Ann. N Y Acad. Sci.* 1092, 385–396. doi:10.1196/annals.1365.035

Haeckel, E. (1866). *Generelle Morphologie der Organismen [General morphology of organisms]*. Berlin: Reimer.

Hall, B. K. (1975). Evolutionary Consequences of Skeletal Differentiation. *Am. Zool* 15, 329–350. doi:10.1093/icb/15.2.329

Hammond, C. L., and Schulte-Merker, S. (2009). Two Populations of Endochondral Osteoblasts with Differential Sensitivity to Hedgehog Signalling. *Development* 136, 3991–4000. doi:10.1242/dev.042150

Hecht, J., Stricker, S., Wiecha, U., Stiege, A., Panopoulou, G., Podsiadlowski, L., et al. (2008). Evolution of a Core Gene Network for Skeletogenesis in Chordates. *Plos Genet.* 4, e1000025. doi:10.1371/journal.pgen.1000025

Hirschberger, C., Sleight, V. A., Criswell, K. E., Clark, S. J., and Gillis, J. A. (2021). Conserved and Unique Transcriptional Features of Pharyngeal Arches in the Skate (*Leucoraja erinacea*) and Evolution of the Jaw. *Mol. Biol. Evol.* 38, 4187–4204. doi:10.1093/molbev/msab123

Hölzer, A., Pietschmann, M. F., Rösl, C., Hentschel, M., Betz, O., Matsuura, M., et al. (2012). The Interrelation of Trabecular Microstructural Parameters of the Greater Tubercle Measured for Different Species. *J. Orthop. Res.* 30, 429–434. doi:10.1002/jor.21525

Hoshi, K., Komori, T., and Ozawa, H. (1999). Morphological Characterization of Skeletal Cells in Cbfa1-Deficient Mice. *Bone* 25, 639–651. doi:10.1016/s8756-3282(99)00223-9

Huysseune, A., and Sire, J. Y. (1998). Evolution of Patterns and Processes in Teeth and Tooth-related Tissues in Non-mammalian Vertebrates. *Eur. J. Oral Sci.* 106 (Suppl. 1), 437–481. doi:10.1111/j.1600-0722.1998.tb02211.x

Hyman, L. H. (1943). *Comparative Vertebrate Anatomy*. University of Chicago Press.

Inada, M., Yasui, T., Nomura, S., Miyake, S., Deguchi, K., Himeno, M., et al. (1999). Maturational Disturbance of Chondrocytes inCbfa1-Deficient Mice. *Dev. Dyn.* 214, 279–290. doi:10.1002/(sici)1097-0177(199904)214:4<279:aid-aja1>3.0.co;2-w

Inoue, J. G., Miya, M., Lam, K., Tay, B.-H., Danks, J. A., Bell, J., et al. (2010). Evolutionary Origin and Phylogeny of the Modern Holocephalans (Chondrichthyes: Chimaeriformes): a Mitogenomic Perspective. *Mol. Biol. Evol.* 27, 2576–2586. doi:10.1093/molbev/msq147

Janvier, P. (1996). *Early Vertebrates*. Oxford University Press.

Janvier, P. (1990). La structure de l'exosquelette des Galeaspida (Vertebrata). Comptes rendus de l'Académie des sciences. Série 2. *Mécanique, Physique, Chim. Sci. de l'univers, Sci. de la Terre* 310, 655–659.

Janvier, P., and Pradel, A. (2015). Elasmobranchs and Their Extinct Relatives: Diversity, Relationships, and Adaptations through Time. *Elsevier*, 1–17. doi:10.1016/b978-0-12-801289-5.00001-8

Janvier, P. (1981). The Phylogeny of the Craniata, with Particular Reference to the Significance of Fossil "Agnathans". *J. Vertebr. Paleontol.* 1, 121–159. doi:10.1080/02724634.1981.10011886

Jardine, N. (1967). The Concept of Homology in Biology. *Br. J. Philos. Sci.* 18, 125–139. doi:10.1093/bjps/18.2.125

Jaroszewicz, J., Kosowska, A., Hutmacher, D., Swieszkowski, W., and Moskalewski, S. (2016). Insight into Characteristic Features of Cartilage Growth Plate as a Physiological Template for Bone Formation. *J. Biomed. Mater. Res.* 104, 357–366. doi:10.1002/jbm.a.35575

Jayasankar, A. K., Seidel, R., Hosny, A., Weaver, J. C., Fratzl, P., Chen, J., et al. (2020). Multi-scale Modeling and Mechanical Performance Characterization of Stingray Skeleton-Inspired Tessellations. *J. Mech. Phys. Sol.* 138, 103906. doi:10.1016/j.jmps.2020.103906

Johanson, Z., Boisvert, C., Maksimenko, A., Currie, P., and Trinajstic, K. (2015). Development of the Synarcual in the Elephant Sharks (Holocephali; Chondrichthyes): Implications for Vertebral Formation and Fusione0135138. *PLOS ONE* 10. doi:10.1371/journal.pone.0135138

Johanson, Z., Martin, K., Fraser, G., and James, K. (2019). The Synarcual of the Little Skate, *Leucoraja erinacea*: Novel Development Among the Vertebrates. *Front. Ecol. Evol.* 7, 12. doi:10.3389/fevo.2019.00012

Johanson, Z., Trinajstic, K., Carr, R., and Ritchie, A. (2013). Evolution and Development of the Synarcual in Early Vertebrates. *Zoomorphology* 132, 95–110. doi:10.1007/s00435-012-0169-9

Jollie, M. (1971). Some Developmental Aspects of the Head Skeleton of the 35-37 mmSqualus Acanthias Foetus. *J. Morphol.* 133, 17–40. doi:10.1002/jmor.1051330103

Kamioka, H., Honjo, T., and Takano-Yamamoto, T. (2001). A Three-Dimensional Distribution of Osteocyte Processes Revealed by the Combination of Confocal Laser Scanning Microscopy and Differential Interference Contrast Microscopy. *Bone* 28, 145–149. doi:10.1016/s8756-3282(00)00421-x

Katz, E. P., Wachtel, E., Yamauchi, M., and Mechanic, G. L. (1989). The Structure of Mineralized Collagen Fibrils. *Connect. Tissue Res.* 21, 149–158. discussion 155-148. doi:10.3109/03008208909050005

Keating, J. N., Marquart, C. L., and Donoghue, P. C. J. (2015). Histology of the Heterostracan Dermal Skeleton: Insight into the Origin of the Vertebrate Mineralised Skeleton. *J. Morphol.* 276, 657–680. doi:10.1002/jmor.20370

Kemp, N. E. (1984). Organic Matrices and mineral Crystallites in Vertebrate Scales, Teeth and Skeletons. *Am. Zool* 24, 965–976. doi:10.1093/icb/24.4.965

Kemp, N. E. (1989). The Phosphatic Mode of Calcification in Ontogeny and Phylogeny of the Integument and Skeleton of Vertebrates Origin. *Evolution, Mod. Aspects Biomineralization Plants Anim. Springer*, 237–249. doi:10.1007/978-1-4757-6114-6_17

Kemp, N. E., and Westrin, S. K. (1979). Ultrastructure of Calcified Cartilage in the Endoskeletal Tesserae of Sharks. *J. Morphol.* 160, 75–101. doi:10.1002/jmor.1051600106

Kerschnitzki, M., Wagermaier, W., Roschger, P., Seto, J., Shahar, R., Duda, G. N., et al. (2011). The Organization of the Osteocyte Network Mirrors the Extracellular Matrix Orientation in Bone. *J. Struct. Biol.* 173, 303–311. doi:10.1016/j.jsb.2010.11.014

Kikugawa, K., Katoh, K., Kuraku, S., Sakurai, H., Ishida, O., Iwabe, N., et al. (2004). Basal Jawed Vertebrate Phylogeny Inferred from Multiple Nuclear DNA-Coded Genes. *BMC Biol.* 2, 3. doi:10.1186/1741-7007-2-3

Kim, I. S., Otto, F., Zabel, B., and Mundlos, S. (1999). Regulation of Chondrocyte Differentiation by Cbfa1. *Mech. Dev.* 80, 159–170. doi:10.1016/s0925-4773(98)00210-x

Kimpel, M., Claassen, H., Fleiner, B., and Tillmann, B. (1999). Vascularization and Cartilage Mineralization of the Thyroid Cartilage of Munich Minipigs and Domestic Pigs. *Anat. Embryol.* 199, 281–290. doi:10.1007/s004290050228

Komori, T. (2011). Signaling Networks in RUNX2-dependent Bone Development. *J. Cel. Biochem.* 112, 750–755. doi:10.1002/jcb.22994

Kronenberg, H. M. (2003). Developmental Regulation of the Growth Plate. *Nature* 423, 332–336. doi:10.1038/nature01657

Laerm, J. (1976). The Development, Function, and Design of Amphicoelous Vertebrae in Teleost Fishes1. *Zoolog. J. Linn. Soc.* 58, 237–254. doi:10.1111/j.1096-3642.1976.tb00830.x

Laerm, J. (1982). The Origin and Homology of the Neopterygian Vertebral Centrum. *J. Paleontol.* 56, 191–202. http://www.jstor.org/stable/1304503.

Lanske, B., Karaplis, A. C., Lee, K., Luz, A., Vortkamp, A., Pirro, A., et al. (1996). PTH/PTHrP Receptor in Early Development and Indian Hedgehog-Regulated Bone Growth. *Science* 273, 663–666. doi:10.1126/science.273.5275.663

Laue, K., Jänicke, M., Plaster, N., Sonntag, C., and Hammerschmidt, M. (2008). Restriction of Retinoic Acid Activity by Cyp26b1 Is Required for Proper Timing and Patterning of Osteogenesis during Zebrafish Development. *Development* 135, 3775–3787. doi:10.1242/dev.021238

Lee, E. R., Lamplugh, L., Shepard, N. L., and Mort, J. S. (1995). The Septoclast, a Cathepsin B-Rich Cell Involved in the Resorption of Growth Plate Cartilage. *J. Histochem. Cytochem.* 43, 525–536. doi:10.1177/43.5.7730591

Lefebvre, V., and Smits, P. (2005). Transcriptional Control of Chondrocyte Fate and Differentiation. *Birth Defect Res. C* 75, 200–212. doi:10.1002/bdrc.20048

Leprévost, A., AzaÏs, T., Trichet, M., and Sire, J.-Y. (2017). Vertebral Development and Ossification in the Siberian Sturgeon (*Acipenser baerii*), with New Insights on Bone Histology and Ultrastructure of Vertebral Elements and Scutes. *Anat. Rec.* 300, 437–449. doi:10.1002/ar.23515

Lewinson, D., and Silbermann, M. (1992). Chondroclasts and Endothelial Cells Collaborate in the Process of Cartilage Resorption. *Anat. Rec.* 233, 504–514. doi:10.1002/ar.1092330403

Liang, C., Musser, J. M., Cloutier, A., Prum, R. O., and Wagner, G. P. (2018). Pervasive Correlated Evolution in Gene Expression Shapes Cell and Tissue Type Transcriptomes. *Genome Biol. Evol.* 10, 538–552. doi:10.1093/gbe/evy016

Lohmander, S., and Hjerpe, A. (1975). Proteoglycans of Mineralizing Rib and Epiphyseal Cartilage. *Biochim. Biophys. Acta (Bba) - Gen. Subjects* 404, 93–109. doi:10.1016/0304-4165(75)90151-8

Long, F., Zhang, X. M., Karp, S., Yang, Y., and McMahon, A. P. (2001). Genetic Manipulation of Hedgehog Signaling in the Endochondral Skeleton Reveals a Direct Role in the Regulation of Chondrocyte Proliferation. *Development* 128, 5099–5108. doi:10.1242/dev.128.24.5099

Long, J. A., Burrow, C. J., Ginter, M., Maisey, J. G., Trinajstic, K. M., Coates, M. I., et al. (2015). Correction: First Shark from the Late Devonian (Frasnian) Gogo Formation, Western Australia Sheds New Light on the Development of Tessellated Calcified Cartilage. *PLOS ONE* 10, e0131502. doi:10.1371/journal.pone.0131502

Long, J. A., Trinajstic, K., Young, G. C., and Senden, T. (2008). Live Birth in the Devonian Period. *Nature* 453, 650–652. doi:10.1038/nature06966

López-Arbarello, A., and Sferco, E. (2018). Neopterygian Phylogeny: the Merger Assay. *R. Soc. Open Sci.* 5, 172337. doi:10.1098/rsos.172337

Lorch, I. J. (1949). The Distribution of Alkaline Phosphatase in Relation to Calcification in *Scyliorhinus canicula*. *J. Cel Sci.* s3-90, 381–390. doi:10.1242/jcs.s3-90.12.381

Maisey, J. G., Denton, J. S. S., Burrow, C., and Pradel, A. (2021). Architectural and Ultrastructural Features of Tessellated Calcified Cartilage in Modern and Extinct Chondrichthyan Fishes. *J. Fish. Biol.* 98, 919–941. doi:10.1111/jfb.14376

Maisey, J. G. (1988). Phylogeny of Early Vertebrate Skeletal Induction and Ossification Patterns. *Evol. Biol.*, 1–36. Springer. doi:10.1007/978-1-4613-0931-4_1

Maisey, J. G. (2013). The Diversity of Tessellated Calcification in Modern and Extinct Chondrichthyans. *Revue de Paléobiologie* 32, 355–371.

Marconi, A., Hancock-Ronemus, A., and Gillis, J. A. (2020). Adult Chondrogenesis and Spontaneous Cartilage Repair in the Skate, *Leucoraja erinacea*. *Elife* 9, e53414. doi:10.7554/eLife.53414

Marramà, G., Schultz, O., and Kriwet, J. (2019). A New Miocene Skate from the Central Paratethys (Upper Austria): the First Unambiguous Skeletal Record for the Rajiformes (Chondrichthyes: Batomorphii). *J. Syst. Palaeontology* 17, 937–960. doi:10.1080/14772019.2018.1486336

Meredith Smith, M., Underwood, C., Goral, T., Healy, C., and Johanson, Z. (2019). Growth and Mineralogy in Dental Plates of the Holocephalan *Harriotta Raleighana* (Chondrichthyes): Novel Dentine and Conserved Patterning Combine to Create a Unique Chondrichthyan Dentition. *Zoolog. Lett* 5, 1–30. doi:10.1186/s40851-019-0125-3

Miles, R. S. (1970). Remarks on the Vertebral Column and Caudal Fin of Acanthodian Fishes. *Lethaia* 3, 343–362. doi:10.1111/j.1502-3931.1970.tb00828.x

Min, Z., and Janvier, P. (1998). The Histological Structure of the Endoskeleton in Galeaspids (Galeaspida, Vertebrata). *J. Vertebr. Paleontol.* 18, 650–654. doi:10.1080/02724634.1998.10011091

Miyake, T., McEachran, J. D., Walton, P. J., and Hall, B. K. (1992). Development and Morphology of Rostral Cartilages in Batoid Fishes (Chondrichthyes: Batoidea), with Comments on Homology within Vertebrates. *Biol. J. Linn. Soc.* 46, 259–298. doi:10.1111/j.1095-8312.1992.tb00864.x

Moskalewski, S., and Malejczyk, J. (1989). Bone Formation Following Intrarenal Transplantation of Isolated Murine Chondrocytes: Chondrocyte-Bone Cell Transdifferentiation. *Development* 107, 473–480. doi:10.1242/dev.107.3.473

Moss, M. L. (1977). Skeletal Tissues in Sharks. *Am. Zool* 17, 335–342. doi:10.1093/icb/17.2.335

Moss, M. L. (1964). "The Phylogeny of Mineralized Tissues," in *International Review of General and Experimental Zoology* (Elsevier), 297–331. doi:10.1016/b978-1-4831-9977-1.50013-4

Mullender, M. G., Huiskes, R., Versleyen, H., and Buma, P. (1996). Osteocyte Density and Histomorphometric Parameters in Cancellous Bone of the Proximal Femur in Five Mammalian Species. *J. Orthop. Res.* 14, 972–979. doi:10.1002/jor.1100140618

Nguyen, J. K. B., and Eames, B. F. (2020). Evolutionary Repression of Chondrogenic Genes in the Vertebrate Osteoblast. *Febs J.* 287, 4354–4361. doi:10.1111/febs.15228

Olsen, B. R., Reginato, A. M., and Wang, W. (2000). Bone Development. *Annu. Rev. Cel Dev. Biol.* 16, 191–220. doi:10.1146/annurev.cellbio.16.1.191

Ørvig, T. (1989). Histologic Studies of Ostracoderms, Placoderms and Fossil Elasmobranchs. 6. Hard Tissues of Ordovician Vertebrates. *Zool Scripta* 18, 427–446. doi:10.1111/j.1463-6409.1989.tb00138.x

Ørvig, T. (1951). *The Endoskeleton, with Remarks on the Hard Tissues of Lower Vertebrates in General, Histologic Studies of Placoderms and Fossil Elasmobranchs*. Stockholm: Almqvist & Wiksell, 321–454.

O'Shaughnessy, K. L., Dahn, R. D., and Cohn, M. J. (2015). Molecular Development of Chondrichthyan Claspers and the Evolution of Copulatory Organs. *Nat. Commun.* 6, 6698. doi:10.1038/ncomms7698

Ovens, K., Eames, B. F., and McQuillan, I. (2021). Comparative Analyses of Gene Co-expression Networks: Implementations and Applications in the Study of Evolution. *Front. Genet.* 12, 695399. doi:10.3389/fgene.2021.695399

Pears, J. B., Johanson, Z., Trinajstic, K., Dean, M. N., and Boisvert, C. A. (2020). Mineralization of the *Callorhinchus* Vertebral Column (Holocephali; Chondrichthyes). *Front. Genet.* 11, 571694. doi:10.3389/fgene.2020.571694

Peignoux-Deville, J., Lallier, F., and Vidal, B. (1982). Evidence for the Presence of Osseous Tissue in Dogfish Vertebrae. *Cell Tissue Res.* 222, 605–614. doi:10.1007/BF00213858

Ramasamy, S. K., Kusumbe, A. P., Wang, L., and Adams, R. H. (2014). Endothelial Notch Activity Promotes Angiogenesis and Osteogenesis in Bone. *Nature* 507, 376–380. doi:10.1038/nature13146

Rasch, L. J., Martin, K. J., Cooper, R. L., Metscher, B. D., Underwood, C. J., and Fraser, G. J. (2016). An Ancient Dental Gene Set Governs Development and Continuous Regeneration of Teeth in Sharks. *Dev. Biol.* 415, 347–370. doi:10.1016/j.ydbio.2016.01.038

Rauch, F. (2005). Bone Growth in Length and Width: the Yin and Yang of Bone Stability. *J. Musculoskelet. Neuronal Interact* 5, 194–201.

Reif, W.-E. (1980). Development of Dentition and Dermal Skeleton in embryonicScyliorhinus Canicula. *J. Morphol.* 166, 275–288. doi:10.1002/jmor.1051660303

Renn, J., and Winkler, C. (2010). Characterization Ofcollagen Type 10a1andosteocalcinin Early and Mature Osteoblasts during Skeleton Formation in Medaka. *J. Appl. Ichthyology* 26, 196–201. doi:10.1111/j.1439-0426.2010.01404.x

Rho, J.-Y., Kuhn-Spearing, L., and Zioupos, P. (1998). Mechanical Properties and the Hierarchical Structure of Bone. *Med. Eng. Phys.* 20, 92–102. doi:10.1016/s1350-4533(98)00007-1

Ridewood, W., and MacBride, E. W. (1921). VIII.—On the Calcification of the Vertebral Centra in Sharks and Rays. *Philosophical Trans. R. Soc. Lond. Ser. B, Containing Pap. a Biol. Character* 210, 311–407.

Roach, H. I. (1992). Trans-differentiation of Hypertrophic Chondrocytes into Cells Capable of Producing a Mineralized Bone Matrix. *Bone Mineral.* 19, 1–20. doi:10.1016/0169-6009(92)90840-a

Romeo, S. G., Alawi, K. M., Rodrigues, J., Singh, A., Kusumbe, A. P., and Ramasamy, S. K. (2019). Endothelial Proteolytic Activity and Interaction with Non-resorbing Osteoclasts Mediate Bone Elongation. *Nat. Cel Biol* 21, 430–441. doi:10.1038/s41556-019-0304-7

Rossert, J., and de Crombrugghe, B. (2002). "Type I Collagen," in *Type I Collagen: Structure, Synthesis, and Regulation, Principles of Bone Biology* (Elsevier), 189–XVIII. doi:10.1016/b978-012098652-1.50114-1

Roth, V. L. (1991). Homology and Hierarchies: Problems Solved and Unresolved. *J. Evol. Biol.* 4, 167–194. doi:10.1046/j.1420-9101.1991.4020167.x

Roth, V. L. (1984). On Homology. *Biol. J. Linn. Soc.* 22, 13–29. doi:10.1111/j.1095-8312.1984.tb00796.x

Rücklin, M., King, B., Cunningham, J. A., Johanson, Z., Marone, F., and Donoghue, P. C. J. (2021). Acanthodian Dental Development and the Origin of Gnathostome Dentitions. *Nat. Ecol. Evol.* 5, 919–926. doi:10.1038/s41559-021-01458-4

Sachs, T. (1982). "A Morphogenetic Basis for Plant Morphology," in *A Morphogenetic Basis for Plant Morphology, Axioms and Principles of Plant Construction* (Springer), 118–131. doi:10.1007/978-94-009-7636-8_6

Sanchez, S., Ahlberg, P. E., Trinajstic, K. M., Mirone, A., and Tafforeau, P. (2012). Three-dimensional Synchrotron Virtual Paleohistology: a New Insight into the World of Fossil Bone Microstructures. *Microsc. Microanal* 18, 1095–1105. doi:10.1017/S1431927612001079

Sawae, Y., Sahara, T., and Sasaki, T. (2003). Osteoclast Differentiation at Growth Plate Cartilage-Trabecular Bone junction in Newborn Rat Femur. *J. Electron Microsc.* 52, 493–502. doi:10.1093/jmicro/52.6.493

Schmitz, R. J. (1998). Comparative Ultrastructure of the Cellular Components of the Unconstricted Notochord in the sturgeon and the Lungfish. *J. Morphol.* 236, 75–104. doi:10.1002/(sici)1097-4687(199805)236:2<75:aid-jmor1>3.0.co;2-n

Seidel, R., Blumer, M., Chaumel, J., Amini, S., and Dean, M. N. (2020). Endoskeletal Mineralization in Chimaera and a Comparative Guide to Tessellated Cartilage in Chondrichthyan Fishes (Sharks, Rays and Chimaera). *J. R. Soc. Interf.* 17, 20200474. doi:10.1098/rsif.2020.0474

Seidel, R., Blumer, M., Pechriggl, E.-J., Lyons, K., Hall, B. K., Fratzl, P., et al. (2017). Calcified Cartilage or Bone? Collagens in the Tessellated Endoskeletons of Cartilaginous Fish (Sharks and Rays). *J. Struct. Biol.* 200, 54–71. doi:10.1016/j.jsb.2017.09.005

Seidel, R., Jayasankar, A. K., and Dean, M. N. (2021). The Multiscale Architecture of Tessellated Cartilage and its Relation to Function. *J. Fish. Biol.* 98, 942–955. doi:10.1111/jfb.14444

Seidel, R., Lyons, K., Blumer, M., Zaslansky, P., Fratzl, P., Weaver, J. C., et al. (2016). Ultrastructural and Developmental Features of the Tessellated Endoskeleton of Elasmobranchs (Sharks and Rays). *J. Anat.* 229, 681–702. doi:10.1111/joa.12508

Shimeld, S. M., and Donoghue, P. C. J. (2012). Evolutionary Crossroads in Developmental Biology: Cyclostomes (Lamprey and Hagfish). *Development* 139, 2091–2099. doi:10.1242/dev.074716

Sire, J.-Y., and Huysseune, A. (2003). Formation of Dermal Skeletal and Dental Tissues in Fish: a Comparative and Evolutionary Approach. *Biol. Rev.* 78, 219–249. doi:10.1017/s1464793102006073

Smith, M., Manzanares, E., Underwood, C., Healy, C., Clark, B., and Johanson, Z. (2020). Holocephalan (Chondrichthyes) Dental Plates with Hypermineralized Dentine as a Substitute for Missing Teeth through Developmental Plasticity. *J. Fish. Biol.* 97, 16–27. doi:10.1111/jfb.14302

Smith, M. M., and Hall, B. K. (1990). Development and Evolutionary Origins of Vertebrate Skeletogenic and Odontogenic Tissues. *Biol. Rev. Camb Philos. Soc.* 65, 277–373. doi:10.1111/j.1469-185x.1990.tb01427.x

St-Jacques, B., Hammerschmidt, M., and McMahon, A. P. (1999). Indian Hedgehog Signaling Regulates Proliferation and Differentiation of Chondrocytes and Is Essential for Bone Formation. *Genes Dev.* 13, 2072–2086. doi:10.1101/gad.13.16.2072

Stensiö, E. A. (1927). *The Downtonian and Devonian Vertebrates of Spitsbergen. I, Family Cephalaspidae*. OSLO: Norske Videnskaps-Akademi.

Stevens, P. F. (1984). Homology and Phylogeny: Morphology and Systematics. *Syst. Bot.* 9, 395–409. doi:10.2307/2418788

Sudmant, P. H., Alexis, M. S., and Burge, C. B. (2015). Meta-analysis of RNA-Seq Expression Data across Species, Tissues and Studies. *Genome Biol.* 16, 287. doi:10.1186/s13059-015-0853-4

Swartz, S. M., Parker, A., and Huo, C. (1998). Theoretical and Empirical Scaling Patterns and Topological Homology in Bone Trabeculae. *J. Exp. Biol.* 201, 573–590. doi:10.1242/jeb.201.4.573

Tomlinson, P. B. (1984). Homology: an Empirical View. *Syst. Bot.* 9, 374–381. doi:10.2307/2418786

Touaitahuata, H., Cres, G., de Rossi, S., Vives, V., and Blangy, A. (2014). The mineral Dissolution Function of Osteoclasts Is Dispensable for Hypertrophic Cartilage Degradation during Long Bone Development and Growth. *Dev. Biol.* 393, 57–70. doi:10.1016/j.ydbio.2014.06.020

Tsegai, Z. J., Skinner, M. M., Pahr, D. H., Hublin, J.-J., and Kivell, T. L. (2018). Systemic Patterns of Trabecular Bone across the Human and Chimpanzee Skeleton. *J. Anat.* 232, 641–656. doi:10.1111/joa.12776

Van Valen, L. M. (1982). Homology and Causes. *J. Morphol.* 173, 305–312. doi:10.1002/jmor.1051730307

Venkatesh, B., Erdmann, M. V., and Brenner, S. (2001). Molecular Synapomorphies Resolve Evolutionary Relationships of Extant Jawed Vertebrates. *Proc. Natl. Acad. Sci.* 98, 11382–11387. doi:10.1073/pnas.201415598

Vortkamp, A., Lee, K., Lanske, B., Segre, G. V., Kronenberg, H. M., and Tabin, C. J. (1996). Regulation of Rate of Cartilage Differentiation by Indian Hedgehog and PTH-Related Protein. *Science* 273, 613–622. doi:10.1126/science.273.5275.613

Wagner, G. P. (1989). The Biological Homology Concept. *Annu. Rev. Ecol. Syst.* 20, 51–69. doi:10.1146/annurev.es.20.110189.000411

Wang, N.-Z., Donoghue, P. C., Smith, M. M., and Sansom, I. J. (2005). Histology of the Galeaspid Dermoskeleton and Endoskeleton, and the Origin and Early Evolution of the Vertebrate Cranial Endoskeleton. *J. Vertebr. Paleontol.* 25, 745–756. doi:10.1671/0272-4634(2005)025

Warth, P., Hilton, E. J., Naumann, B., Olsson, L., and Konstantinidis, P. (2017). Development of the Skull and Pectoral Girdle in Siberian sturgeon,*Acipenser baerii*, and Russian sturgeon,*Acipenser gueldenstaedtii*(Acipenseriformes: Acipenseridae). *J. Morphol.* 278, 418–442. doi:10.1002/jmor.20653

Wiesmann, H. P., Meyer, U., Plate, U., and Höhling, H. J. (2005). Aspects of Collagen Mineralization in Hard Tissue Formation. *Int. Rev. Cytol.* 242, 121–156. doi:10.1016/S0074-7696(04)42003-8

Wurmbach, H. (1932). Das Wachstum des Selachierwirbels und seiner Gewebe. *Zool Jahrb (Abt Anat. Ont Tiere)* 55, 1–136.

Zangerl, R. (1966). *A New Shark of the Family Edestidae,* Ornithoprion Hertwigi, *from the Pennsylvanian Mecca and Logan Quarry Shales of Indiana, Fieldiana: Geology*. Chicago: Field Museum of Natural History, 1–43.

Zhang, G., and Cohn, M. J. (2008). Genome Duplication and the Origin of the Vertebrate Skeleton. *Curr. Opin. Genet. Dev.* 18, 387–393. doi:10.1016/j.gde.2008.07.009

Zhou, X., von der Mark, K., Henry, S., Norton, W., Adams, H., and de Crombrugghe, B. (2014). Chondrocytes Transdifferentiate into Osteoblasts in Endochondral Bone during Development, Postnatal Growth and Fracture Healing in Mice. *Plos Genet.* 10, e1004820. doi:10.1371/journal.pgen.1004820

Zidek, J. (1985). Growth Inacanthodes (Acanthodii: Pisces) Data and Implications. *Paläont. Z.* 59, 147–166. doi:10.1007/bf02986006

Conflict of Interest: The authors declare that the research was conducted in the absence of any commercial or financial relationships that could be construed as a potential conflict of interest.

Publisher's Note: All claims expressed in this article are solely those of the authors and do not necessarily represent those of their affiliated organizations, or those of the publisher, the editors and the reviewers. Any product that may be evaluated in this article, or claim that may be made by its manufacturer, is not guaranteed or endorsed by the publisher.

frontiers in Ecology and Evolution

ORIGINAL RESEARCH
published: 17 March 2022
doi: 10.3389/fevo.2022.794287

Microstructural and Genetic Insights Into the Formation of the "Winter Diffusion Layer" in Japanese Pearl Oyster *Pinctada fucata* and Its Relation to Environmental Temperature Changes

Kei Sato[1,2†], Davin H. E. Setiamarga[3,4†], Hiroshi Yonemitsu[3] and Keita Higuchi[5]*

[1] Department of Earth Sciences, School of Education, Waseda University, Tokyo, Japan, [2] Institute of Liberal Arts and Science, Kanazawa University, Kanazawa, Japan, [3] Department of Applied Chemistry and Biochemistry, National Institute of Technology, Wakayama College, Wakayama, Japan, [4] The University Museum, The University of Tokyo, Tokyo, Japan, [5] Mikimoto Pearl Research Laboratory, Shima, Japan

OPEN ACCESS

Edited by:
Sylvain Marcellini,
University of Concepcion, Chile

Reviewed by:
Felipe Aguilera,
University of Concepcion, Chile
Frederic Marin,
Délégation Centre-Est (CNRS), France

***Correspondence:**
Kei Sato
ksato@staff.kanazawa-u.ac.jp

†ORCID:
Kei Sato
orcid.org/0000-0001-8308-1579
Davin H. E. Setiamarga
orcid.org/0000-0002-3854-4893

Specialty section:
This article was submitted to Evolutionary and Population Genetics, a section of the journal Frontiers in Ecology and Evolution

Received: 13 October 2021
Accepted: 21 January 2022
Published: 17 March 2022

Citation:
Sato K, Setiamarga DHE, Yonemitsu H and Higuchi K (2022) Microstructural and Genetic Insights Into the Formation of the "Winter Diffusion Layer" in Japanese Pearl Oyster Pinctada fucata and Its Relation to Environmental Temperature Changes. Front. Ecol. Evol. 10:794287. doi: 10.3389/fevo.2022.794287

Phenotypic plasticity in molluscan shell microstructures may be related to environmental changes. The "winter diffusion layer," a shell microstructure of the Japanese pearl oyster *Pinctada fucata,* is an example of this phenomenon. In this study, we used *P. fucata* specimens with shared genetic background to evaluate the seasonal plasticity of shell microstructures, at molecular level. To detect the seasonal changes in shell microstructure and mineral composition, shells of multiple individuals were periodically collected and analyzed using scanning electron microscopy and Raman spectrophotometry. Our observations of the winter diffusion layer revealed that this irregular shell layer, located between the outer and middle shell layers, had a sphenoid shape in radial section. This distinct shape might be caused by the internal extension of the outer shell layer resulting from growth halts. The winter diffusion layer could be distinguished from the calcitic outer shell layer by its aragonitic components and microstructures. Moreover, the components of the winter diffusion layer were irregular simple prismatic (the outer and inner sublayers) and homogeneous structures (the middle sublayer). This irregular formation occurred until April, when the animals resumed their "normal" shell formation after hibernation. To check for a correlation between gene expression and the changes in microstructures, we conducted qPCR of seven major biomineralization-related shell matrix protein-coding genes (*aspein*, *prismalin-14*, *msi7*, *msi60*, *nacrein*, *n16*, and *n19*) in the shell-forming mantle tissue. Tissue samples were collected from the mantle edge (tissue secreting the outer shell layer) and mantle pallium (where the middle shell layer is constructed) of the same individuals used for microstructural observation and mineral identification that were collected in January (winter growth break period), April (irregular shell formation period), and August (normal shell formation period). Statistically significant differences in gene expression levels were

observed between mantle edge and mantle pallium, but no seasonal differences were detected in the seasonal expression patterns of these genes. These results suggest that the formation of the irregular shell layer in *P. fucata* is caused by a currently unknown genetic mechanism unrelated to the genes targeted in the present study. Further studies using big data (transcriptomics and manipulation of gene expression) are required to answer the questions herein raised. Nevertheless, the results herein presented are essential to unravel the intriguing mystery of the formation of the winter diffusion layer, which may allow us to understand how marine mollusks adapt or acclimate to climate changes.

Keywords: biomineralization, shell matrix protein, shell microstructure, *Pinctada fucata*, winter diffusion layer, phenotypic plasticity, gene expression pattern, nacreous structure

INTRODUCTION

Biominerals are inorganic minerals precipitated by living organisms that are mainly used to form external hard structures (i.e., exoskeletons and shells) and internal hard tissues (i.e., endoskeletons) (Crenshaw, 1990). Such structures are composed of both minerals and minor organic matrix, and their formation and organization, including at the microscale (e.g., mineral composition, crystallographic axes, and microstructures), seem to be under genetic control, at least to some degree (Carter, 1990). The presence of an external, mineralized shell is one of the defining characteristics of mollusks (Kocot et al., 2016). Calcium carbonate-based biominerals (e.g., aragonite, calcite, and rarely vaterite) are the main components of molluscan shells (Spann et al., 2010; Frenzel and Harper, 2011). Shells are not uniform but composed of few superimposed layers that are characterized by different arrangements – defined as "shell microstructures" – of their elementary crystallites (Marin et al., 2012). Many studies admit that the shell construction in mollusks is an organic matrix-mediated process (Weiner et al., 1983): according to this view, cells or tissues secrete organic biomolecules that self-assemble in framework in which inorganic salts precipitate (Lowenstam, 1981).

Molecular studies on the genetics of shell formation (e.g., its microstructure and mineral composition) have been successful in identifying major shell matrix proteins (SMPs) such as Nacrein (Miyamoto et al., 1996), MSI60, and MSI31 (Sudo et al., 1997). Follow-up functional studies were also conducted to gain insights into their function in the regulation of microstructural formation and crystal polymorphism. For example, Suzuki et al. (2009) conducted knockdown on the Pif coding gene, and their experiment revealed that it is essential for nacre formation. To understand the involvement of Aspein in calcification, Takeuchi et al. (2008) conducted an *in vitro* $CaCO_3$ crystallization experiment, in which they found that it promotes calcite precipitation. Recent developments in gene and protein sequencing have allowed for the accumulation of data on complete gene sequences of novel shell proteins, their molecular evolution, and the comparison of analogs and homologs of various SMPs found in different species with similar shell microstructures (Marie et al., 2011, 2012, 2017; Isowa et al., 2012; Zhang et al., 2018; Setiamarga et al., 2021).

The results of above-mentioned biological studies have indicated that mollusks might have undergone a specific evolution in their shell mineralization process. However, these studies have not tackled the drastic microstructural evolutions that occurred throughout the geological periods. For example, such studies have targeted mollusk species with nacreous structures (mother of pearl) in their shells, partly due to scientific interests stemming from their commercial value. Originally, the nacreous structure was thought to be a symplesiomorphy in Conchiferan mollusks because it is present in the shell microstructures of the group's four major classes (Bivalvia, Gastropoda, Cephalopoda, and Monoplacophora). However, recent findings in paleontology indicate that the nacreous structure might have evolved independently in each class, and thus is probably a result of convergence (Checa et al., 2009; Vendrasco et al., 2011, 2013). Moreover, a recent phylogenetic study of Sato et al. (2020a) showed that in Protobranch bivalves (a basal taxon of bivalves), the nacreous structure was repeatedly lost in various lineages. Most Protobranch lineages that have lost the nacre tend to show a homogeneous structure. A similar pattern of shell microstructural evolution (nacre to homogeneous) was also found in Thraciid bivalves (Anomalodesmata) (Taylor et al., 1973). These examples suggest that even within a class, the nacreous structure is probably not homologous. From group to group, crystallographic variations in the crossed lamellar structure, another major molluscan shell microstructure, may also indicate convergent evolution (Kogure et al., 2014).

Moreover, phenotypic plasticity in the microstructures of molluscan shells among different individuals of the same lineage/species was also observed. One such variation is the thermal dependence of the crystallization and shell microstructures. For example, Höche et al. (2021) reported variations in crystal size in *Arctica islandica* shells depending on water temperature. Füllenbach et al. (2014) reported that the first-order lamellar orientation of the crossed lamellar structure in the freshwater gastropod *Viviparus viviparus* becomes uniform in stable and warm conditions. Gilbert et al. (2017) also reported thermal dependence in the thickness of molluscan nacre tablet crystals. Moreover, variations in the shell microstructure were reported by Lutz and Clark (1984: *Geukensia demissa*) and Nishida et al. (2012, 2015: *Scapharca*

broughtonii). Other than thermal dependence variation, Carter et al. (1998) reported nested occurrences of aragonitic and calcitic microstructures within the same shell layers in some bivalves, which were probably related to habitat conditions. A similar phenomenon was later confirmed by Sato et al. (2020b) in Pectinodontid limpets.

Most of the aforementioned reports on microstructural plasticity were studied in nacreless species. However, a similar phenomenon was observed for species with nacre. Moini et al. (2014) observed that *Nautilus pompilius* in aquaria forms shells with a disordered crystalline structure. Moreover, unique microstructures were observed from the repaired shells of nacre-bearing species (e.g., *Mytilus edulis*, Suzuki and Uozumi, 1979; *Haliotis tuberculata*, Fleury et al., 2008), suggesting that the molluscan mantle is originally capable of controlling microstructural plasticity. A similar phenomenon was also described in the Japanese pearl oyster *Pinctada fucata* by Wada (1961); he reported the formation of the "winter diffusion layer," a layer in the shell microstructure showing an irregular formation of mineral crystals formed only in winter, although he did not provide detailed images. These examples imply that the physiological condition of an animal, which in most cases occurs as a response to environmental changes, might somehow affect shell formation at the microstructural level.

The margaritid Japanese pearl oyster, *P. fucata*, is an important aquaculture species that has been industrially raised and cultured because of its pearl. However, it has been further developed as a model system for biological research, with its whole genome sequenced and published recently (Takeuchi et al., 2012, 2016). Some studies on *P. fucata* have focused on the molecular evolution of its genes (Koga et al., 2013; Setiamarga et al., 2013). The species has also been used as a model organism in several molluscan biomineralization studies (Suzuki et al., 2009). Thus, not only because of the availability of experimental tools, protocols, and a breadth of biological data, but also because it also has a winter diffusion layer, whose formation is probably related to low temperatures in winter, *P. fucata* is an appropriate model system for studying the mechanisms of seasonal phenotypic plasticity in the shell microstructure.

To our knowledge, no study has explicitly addressed the effect of low temperature on gene expression to explain the genetic mechanisms behind the formation of the winter diffusion layer. Therefore, in this study, we focused on the formation of the winter diffusion layer in *P. fucata* and examined its shell microstructure in samples taken in time series throughout the year. We also obtained mantle tissue samples from various months corresponding to seasonal changes throughout the year, and studied the expression patterns of seven shell matrix protein-coding genes. Our study on the expression of the shell matrix protein-coding gene in time series samples allows us to determine whether there is a correlation between possible fluctuations in gene expression and water temperatures caused by seasonal changes, and thus, a glimpse into the mechanisms of microstructural phenotypic plasticity in nacre-bearing Conchiferan mollusks. This also allows us to discuss the possible implications for the evolution of the biomineralized shell in mollusks.

MATERIALS AND METHODS

Materials

This study examined cultured individuals of the Japanese pearl oyster, *P. fucata*, at the MIKIMOTO Pearl Research Laboratory (Mie Prefecture, Japan). Pearl oysters in this institution are bred for commercial purposes. Our specimens were chosen at random from a single congenic breed to standardize their genetic background and placed in Ago Bay in front of the laboratory.

Pinctada fucata has a nacroprismatic shell; the outer shell layer has a calcitic columnar regular simple prismatic structure, the middle layer is of a sheet nacreous structure, the myostracum layer has an irregular simple prismatic structure, and the inner layer is again of a sheet nacreous structure (Taylor et al., 1969; Carter and Sato, 2020). Following the description of Wada (1961, 1972), the seasonal cycle of nacre formation in Japanese pearl oysters was defined for descriptive purposes as follows: (1) Winter growth break: shell formation in *P. fucata* ceases when the seawater temperature falls below 14°C; (2) Brief period of irregular shell formation: *P. fucata* resumes shell formation once the water temperature increases above 14°C; and (3) the normal nacroprismatic shells are secreted at a proper temperature (normal shell formation period). Wada (1961) mentioned that during the period of irregular shell formation, the middle and inner shell layers consist of incondite crystals called "a winter diffusion layer," although their microstructural diagnosis was unclear. Thus, to describe these incondite nacre crystals in detail and then evaluate intraspecific variations in the gene expression profile of the SMPs, five individuals of *P. fucata* were collected at each of the following dates: January 26 (winter growth break period), April 4 (irregular shell formation period), and August 2 (normal shell formation period), 2018. The seawater temperature at the sampling locality (2-m depth) was logged every 2 h on each collection date, and the daily averaged values were recorded as 11.0, 16.7, and 28.4°C, respectively (**Figure 1**). Samples were immediately dissected to collect mantle edges that secrete the calcitic columnar regular simple prismatic structure of the outer shell layer and interior parts of the mantle (mantle pallium), which is essential for the formation of the nacreous structure. Both parts were isolated from the dissected mantle piece based on the visual inspection of their color (mantle edge is brown and mantle pallium is faint yellow). Each mantle was cut into small (up to 5-mm square) pieces and fixed using RNA stabilization reagent (RNAlater, Qiagen, Hilden, Germany), and stored at –80°C until subsequent experiments. Remaining shells were used for shell microstructural observations and mineral identification. Furthermore, three shell samples were collected from each respective population at the end of each month from February to August 2018 for the observation of shell microstructures to assess the accurate period of the incondite nacre crystal formation and any individual specificities (see **Supplementary Table 1** for details of sample use).

Mantle Gene Expression Level Analysis

Total cellular RNA was isolated using the RNeasy Mini Kit (Qiagen, Valencia, CA, United States) from each mantle sample.

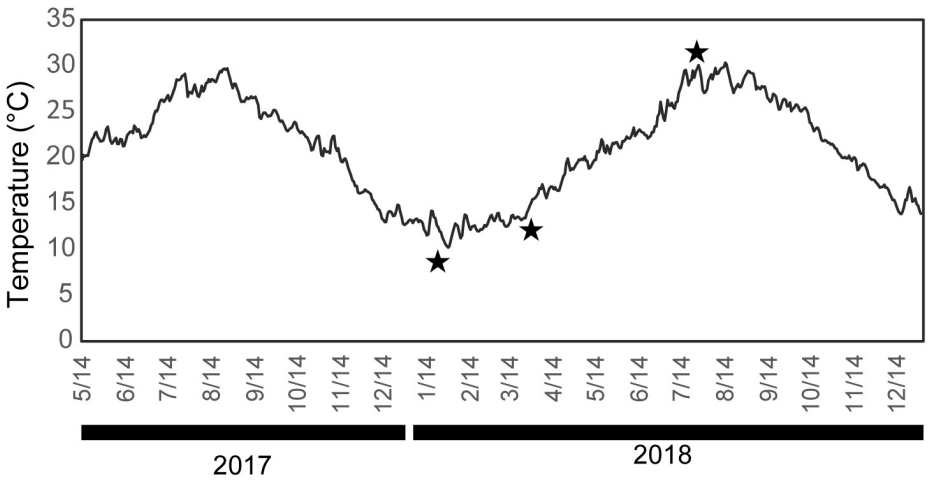

FIGURE 1 | Daily mean water temperature at the sampling point (2-m depth). Stars indicate the sampling dates (January 26, April 4, and August 2, 2018).

RNA was quantified, and its integrity was assessed using a NanoDrop Lite spectrophotometer (NanoDrop Technologies Inc., Wilmington, DE, United States). Then, reverse transcription was carried out using ReverTra Ace qPCR-RT Master Mix Kit (TOYOBO, Osaka, Japan) according to the manufacturer's instructions. The expression levels of seven biomineralization-related (*aspein*, *prismalin-14*, *msi7*, *msi60*, *nacrein*, *n16*, and *n19*) and two housekeeping genes (*gapdh* and *ef1α*) were analyzed by quantitative RT-PCR analysis using a set of forward and reverse primers (**Table 1**). *aspein* (Tsukamoto et al., 2004) and *prismalin-14* (Suzuki et al., 2004) are biomineralization-related shell matrix protein genes, which were discovered from the prismatic structure and are predominantly produced both at the mantle edge and center. Those discovered from nacreous structures such as *msi60* (Sudo et al., 1997), *nacrein* (Miyamoto et al., 1996), and *n16* (Samata et al., 1999) are dominant in the mantle pallium (Kinoshita et al., 2011). In addition, the gene expression level of *n19* (Yano et al., 2007), which is isolated from the nacreous structure, is moderate in the mantle center and high in the pearl sac (Wang et al., 2009). *msi7*, found by Zhang et al. (2003), is produced at both the mantle edge and center. The expression levels of the two housekeeping genes were analyzed to normalize the expression levels of the seven target genes based on the assumption that the expression levels of these housekeeping genes do not exhibit seasonal variation (Lee and Nam, 2016; Li et al., 2019). Quantitative PCR (qPCR) amplification using a Rotor-Gene SYBR Green PCR kit (Qiagen, Hilden, Germany) was carried out on a Rotor-Gene Q real-time PCR cycler (Qiagen, Hilden, Germany), using the following profile, based on the manufacturer's protocol: initial denaturation for 5 min at 95°C, followed by 40 cycles of denaturation for 5 s at 95°C and annealing/extension for 10 s at 60°C. After qPCR, the amplicon melting temperature curve was analyzed to confirm the absence of non-specific products (55–95°C with a heating rate of 1°C for each step, with continuous fluorescence measurement). The comparative threshold cycle (Ct) method was applied to analyze the expression levels of the examined genes using the Rotor-Gene Q Series Software ver. 2.0.2 (Qiagen, Hilden, Germany).

Statistics

Data distribution of the gene expression levels of SMPs from each of the five specimens collected in January, April, and August and two different parts of the mantle (mantle edge/mantle pallial) were analyzed using the Kolmogorov–Smirnov test and two-sample *t*-test, respectively. Then, a non-parametric Kruskal–Wallis test was applied to assess the significant differences among the three groups (January, April, and August). Statistical analyses were performed with EZR version 1.50 (Kanda, 2013), which is a graphical user interface for R version 4.0.2 (R Core Team, 2020), and the statistical tools in Microsoft Excel (version 2008).

Observations of Shell Microstructures and Determining Their Mineralogy

Miyamura and Makido (1958) confirmed that the characteristics of the pearl from various parts of the mantle are more continuous in *P. fucata* than in the freshwater pearl-producing bivalve (*Hyriopsis schlegeli*) (Mizumoto, 1965). Therefore, the posterodorsal parts of the shells were cut into small pieces (approximately 1 × 2 cm square) using a hand cutter and observed under a scanning electron microscope (SEM, Hitachi-S3400N, Tokyo, Japan). The left valves were used for most specimens, but the right valve was used in one specimen (sample ID: 180802-1). Both the inner shell surfaces and polished planes of the radial section of the shells were observed to characterize the shell microstructures around the mineralization front of the nacreous layer (i.e., the boundary between the outer and middle shell layers). The polished planes were filled with epoxy resin (Crystal Resin II super clear, Nisshin Resin Co., Kanagawa, Japan) before cutting using a low-speed saw (Minitom, Struers, Copenhagen, Denmark) and were prepared using a graded series of carborundum powder. After these processes, they were treated through: (1) removal of organic matter contained in the shell

TABLE 1 | Nucleotide sequences of primers used in real-time PCR.

Primer name		Sequence	References
Prismalin14	Forward primer	ATTTCCCGCGTTTCTCCTAT	Takeuchi and Endo, 2006
	Reverse primer	CCTCCGTAACCACCGTTAAA	Takeuchi and Endo, 2006
Aspein	Forward primer	TACTTTCCCAGTGGCTGACC	Takeuchi and Endo, 2006
	Reverse primer	CATCACTGGGCTCCGATACT	Takeuchi and Endo, 2006
MSI7	Forward primer	GATAAAAGGTCGGTGCCCAAC	Zhang and He, 2011
	Reverse primer	AAGGTTGATGCCAGGTCCGTA	Zhang and He, 2011
N16	Forward primer	CTCATACTGCTGGATACCCTACGA	Miyazaki et al., 2010
	Reverse primer	TCATTCCACATCTAAGCCACTCA	Miyazaki et al., 2010
N19	Forward primer	TGGCAACAAAGCAGTCATAACCG	Zhang and He, 2011
	Reverse primer	GGCGTCGTTGTAGCATTGAAGG	Zhang and He, 2011
MSI60	Forward primer	GATCTCCCCACACAACATAGATAGAG	Miyazaki et al., 2010
	Reverse primer	TGAATTGAAGCCTAATACTGGTCTGT	Miyazaki et al., 2010
Nacrein	Forward primer	CTTCATTGCATGTGGAATTGGA	Miyazaki et al., 2010
	Reverse primer	TCGGTTCTGATGATTGGTCACT	Miyazaki et al., 2010
GAPDH	Forward primer	TATTTCTGCACCGTCTGCTG	Takeuchi and Endo, 2006
	Reverse primer	ATCTTGGCGAGTGGAGCTAA	Takeuchi and Endo, 2006
EF1-α	Forward primer	CCTGGCCACAGAGATTTCAT	Takeuchi and Endo, 2006
	Reverse primer	AATTCCCCAACACCAGCAG	Takeuchi and Endo, 2006

with sodium hypochlorite for 30 min, and (2) etching with 0.2% (vol/vol) HCl for 1 min. The surfaces of the polished planes were coated with gold, but some were re-polished after SEM observation or not coated for mineral identification. Raman spectroscopy (inVia RefreX, Renishaw) was used to determine the calcium carbonate phase of the irregular shell layer, using a 532-nm laser with a holographic notch filter as a laser excitation source. The shell surfaces were carefully observed using SEM prior to Raman analysis to verify the position of the irregular shell layer. Each layer was marked by carbon adhesive tape or felt pen immediately after SEM observation (see **Figures 2A,C**). These landmarks were corrected by repeated SEM observations, and minor amendments of their positions were performed. The regions of interest were selected through SEM imaging and subsequently analyzed with Raman spectroscopy. Several spots in a single sample were analyzed to identify the mineralogy of each shell layer. The Raman peaks were identified based on Kontoyannis and Vagenas (2000).

RESULTS

Shell Microstructure Surrounding the Nacre Growth Front

Scanning electron microscope images obtained from the small pieces of *P. fucata* shells collected monthly from January to August 2018 are shown in **Figures 3–5**. Outer calcitic columnar regular simple prismatic and middle sheet nacreous structures were observed in all specimens, and the outer prismatic structure was composed of wide prominent first-order prisms (more than 20 μm on average) perpendicularly aligned to the shell surface (**Figures 3A,B**). Each prism was filled with second-order fine granular to lamella crystals (**Figure 3C**) and ensheathed by the organic wall. Second-order lamella crystals were stacked horizontally or obliquely to the shell surface, and their angle changed depending on the prism (**Figure 3C**). A thin layer (<20 μm in thickness), the so-called initial nacreous layer (Dauphin et al., 2008; Saruwatari et al., 2009), was inserted between the prismatic and nacreous structures in all the observed specimens (**Figure 3C**). This layer was the aggregation of hemispherical prisms with second-order irregularly shaped acicular crystals radiating from the center of the hemisphere (high-angle non-denticular composite prismatic structure). The middle sheet nacreous structure consisted of flattened polygonal column-to-circular cylindrical tablets stacked vertically to the shell surface (**Figures 3D–I**). Their bottom shape varied according to the individuals and/or dorsoventral axes (i.e., the mineralization front of the nacre to the thickened part of the middle shell layer). Regarding the bottom morphology of the nacre tablets near the mineralization front, their shape changed from circular to elliptic from winter to summer (**Figures 3E,F,H,I**).

Another thin sphenoid layer in the radial shell section often lied next to the initial nacreous layer (**Figures 4**, **5**) in the area where the outer prisms were discontinued in a wedge shape (**Figures 4A,D,G,H**). Aragonite was detected in this layer (sample ID 180226-1, **Figures 4A–C**) using Raman spectrometry (**Figure 2**). This layer comprised three components: a middle sublayer consisting of fine-grained crystals (less than 1 μm in diameter) sandwiched between the outer and inner sublayers of irregularly shaped acicular crystals (**Figures 4C,E,I**). The boundary of the initial nacreous layer was sometimes difficult to identify (**Figures 4B,E**). The middle sublayer sometimes did not appear depending on the specimens (aragonitic simple prismatic structure; **Figures 4G,H**). Organic walls stood perpendicular to the shell surface and surrounded the crystals irregularly in this layer at the side close to the outer shell layer (**Figures 4B,E,I**); moreover, they decreased distal to the outer shell layer

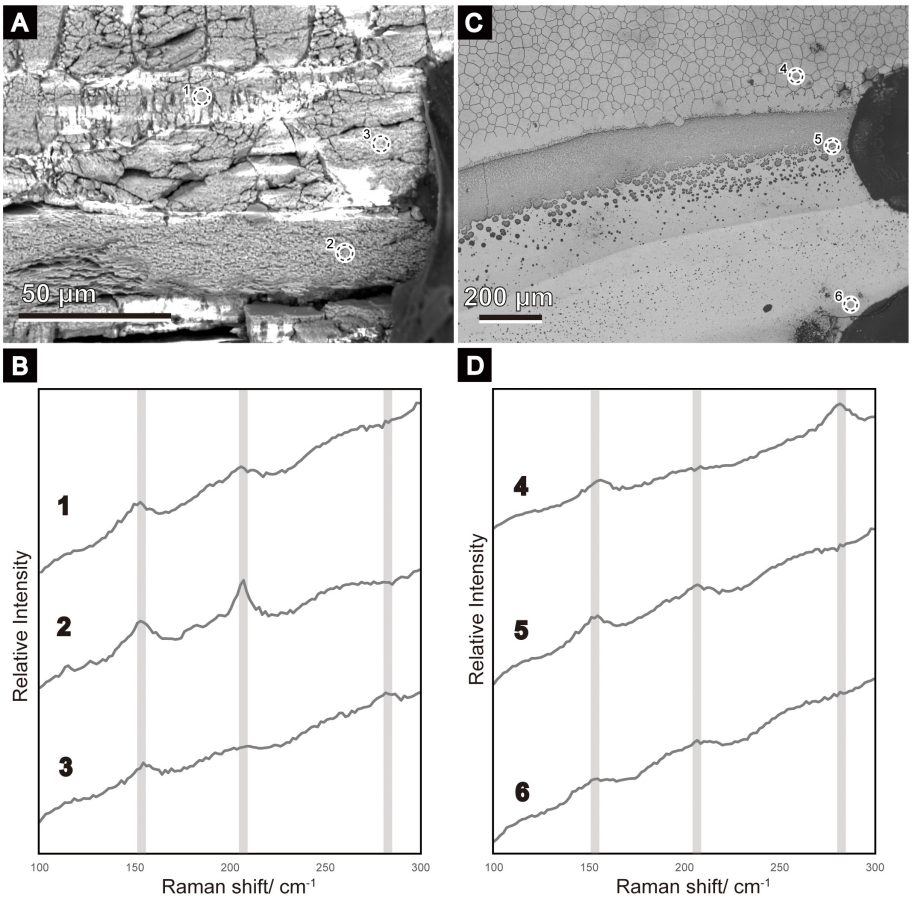

FIGURE 2 | Scanning electron micrographs **(A,C)** of the areas where Raman analyses were conducted, and the resulting Raman spectra **(B,D)**. The broken-lined circle roughly indicates the part from which the Raman spectra were acquired (1–6). **(A)** Radial section of ID 180226-1. A similar position before re-polishing to remove evaporated gold for Raman analysis is shown in **Figure 4B**. A carbon tape was attached to the right as a landmark. **(B)** Inner shell surface of ID 180226-1 (**Figure 5A**). Dots on the right side were used as landmarks. **(B,D)** Raman spectra of calcitic columnar regular simple prismatic structures are indicated by 3 and 4; the sheet nacreous structure is indicated by 2; the winter diffusion layers are indicated by 1, 5, and 6. Aragonite peaks (152, 205) are clear in 1, 2, 5, and 6, whereas calcite peaks (154, 280) are detected in 3 and 4.

(**Figure 4A**). As a result, the appearance of irregular pits (**Figures 5C,E**) at the inner shell surfaces also decreased toward the dorsal side in the middle sublayer, and then this sublayer became analogous to the homogeneous structure because it had no apparent structural unit (**Figures 4C**, **5C**). Discontinued and irregular networks of organic walls (**Figure 5B**) and adjoined or collapsed nacre tablet-shaped prisms (**Figures 5F,G**) were observed on the inner shell surfaces of the outer and inner sublayers. This layer appeared in the inner shell surface of specimens collected from February to April, but it was distant from the nacre mineralization front of the remaining specimens (collected from May to August).

Expression Patterns of Shell Matrix Protein Genes

The expression levels of the seven biomineralization-related genes were analyzed using quantitative real-time PCR (qPCR) (**Figure 6**). Statistically significant differences were observed between mantle edge and mantle pallium in the expression levels of *n16*, *msi60*, and *aspein* in *ef1*α normalized data and of *n16*, *nacrein*, and *aspein* in *gapdh* normalized data. Although not statistically significant, the expression levels of *msi60*, *n16*, and *n19* were higher in mantle pallium than in mantle edges in all three groups (collected in January, April, and August). Conversely, *aspein* and *prismalin-14* were generally expressed significantly in the mantle edge. The expression levels of *nacrein* and *msi7* in the mantle exhibited no clear statistical significances.

Regarding seasonal expression patterns, no statistically significant pattern was noted in any of the analyzed genes. Nonetheless, *msi60* and *n16* expression patterns were lower in April. *n19* had the highest expression levels in the mantle pallium of January individuals and the second-highest in those of April individuals. April individuals had the lowest expression of *prismalin-14* and *aspein* in the mantle edge when considering *ef1*α-normalized data, but their expression was lowest in August individuals considering *gapdh*-normalized data. When considering *ef1*α-normalized data, *nacrein* expression

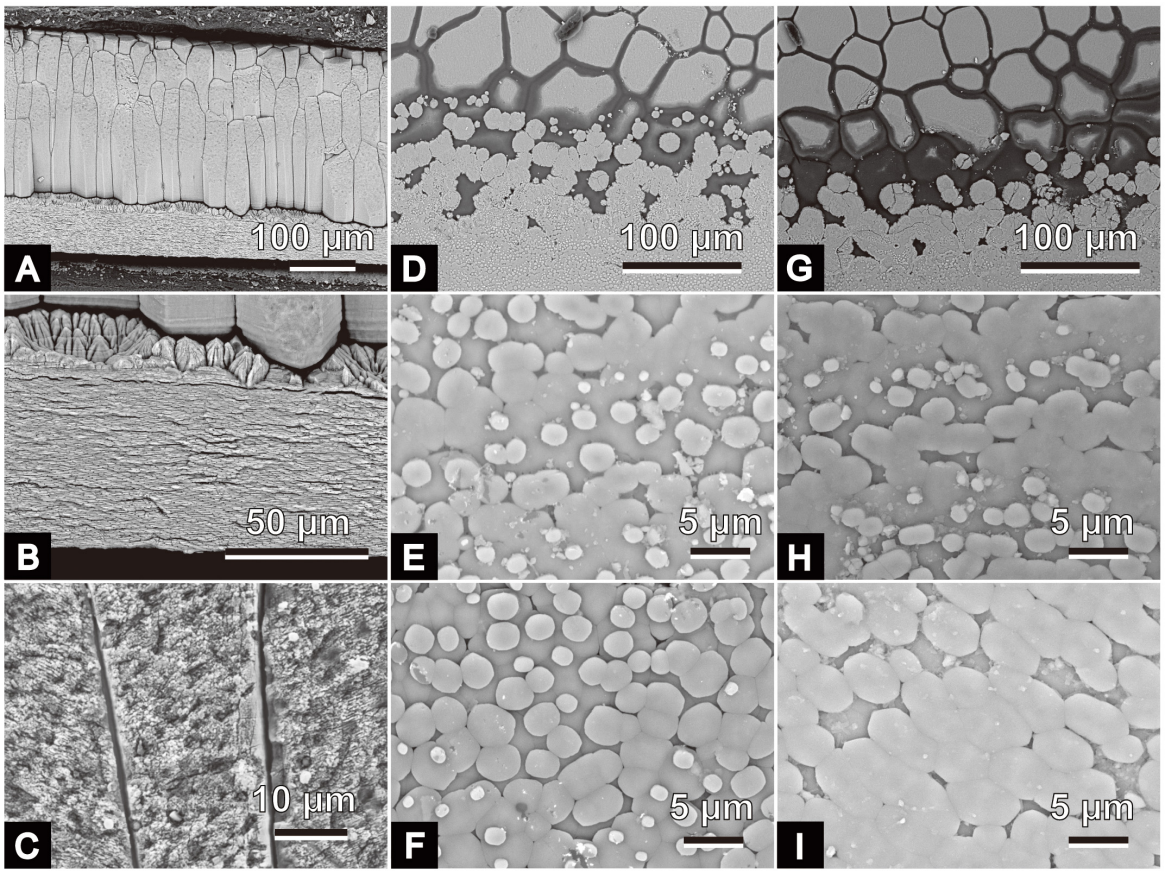

FIGURE 3 | Scanning electron micrographs of microstructures of *Pinctada fucata*. **(A–C)** Radial sections of the polished plane. Growth directions (i.e., direction of the shell margin) are on the right side. **(A)** Outer calcitic columnar regular simple prismatic to middle sheet nacreous structures of a specimen collected on June 26, 2018 (ID: 180626-1). **(B)** Detailed view of panel **(A)**; a thin initial nacreous layer is visible between the outer and middle shell layers. **(C)** Detailed view of the outer shell layer of specimen collected on January 26, 2018; ID: 180126-5). **(D–I)**: growth front of nacre on the inner surfaces and the upper sides of these images indicate the direction of the shell margins. **(D,E)** Specimen collected on May 28, 2018, ID: 180528-1. **(F)** Specimen collected on June 26, 2018, ID: 180626-1; **(G,H)**. Specimen collected on July 25, 2018, ID: 180725-1. **(I)** Specimen collected on August 2, 2018, ID: 180802-1. The outer calcitic columnar regular simple prismatic structure and the middle sheet nacreous structure appear on the upper and lower sides of panels **(D,G)**, respectively.

levels showed a trend similar to those of *msi60* and *n16* in the mantle pallium, with April individuals having the lowest expression levels; however, no clear trend was noted for *nacrein* expression levels when considering *gapdh*-normalized data. The expression levels of *msi7* were the lowest in August.

DISCUSSION

Diagnosis of the Irregular Shell Layer

We carefully described the microstructural characteristics of the irregular shell layer formed within the sheet nacreous structure of the middle shell layer. This layer was found on or close to the inner shell surfaces of cultured *P. fucata* individuals collected from February to April. We consider this seasonal formation to be analogous to that of the "winter diffusion layer" reported by Wada (1961). Our analysis revealed that this irregular layer (1) has a sphenoid shape in the radial section of the shell, (2) is found between the initial and regular nacreous layers, (3) is aragonitic (**Figure 2**), and (4) is composed of three sublayers: outer and inner layers of irregular simple prismatic structures, and middle layer with homogeneous to aragonitic simple prismatic structures (**Figures 4**, **5**). Wada (1961) described the "winter diffusion layer" as being composed of four components: (1) a granular layer constructed before hibernation, (2) a roughened surface resulting from shell dissolution during hibernation, (3) a conchiolin layer constructed immediately after the end of hibernation, and (4) a granular layer constructed after hibernation. The difference between our observations and those of Wada (1961) probably results from the method used, as the latter was mainly conducted on the inner shell surface, which makes the microstructural diagnosis unclear. Although further verification is needed, the granular layers of Wada (1961) probably coincide with our irregular shell layer comprising three sublayers.

The sphenoid shape entering the outer shell layer herein shown is similar to the extension of the outer shell layer into the inner shell layer observed in some unioid bivalves (Checa, 2000). The irregularly layered unioid shells are considered to

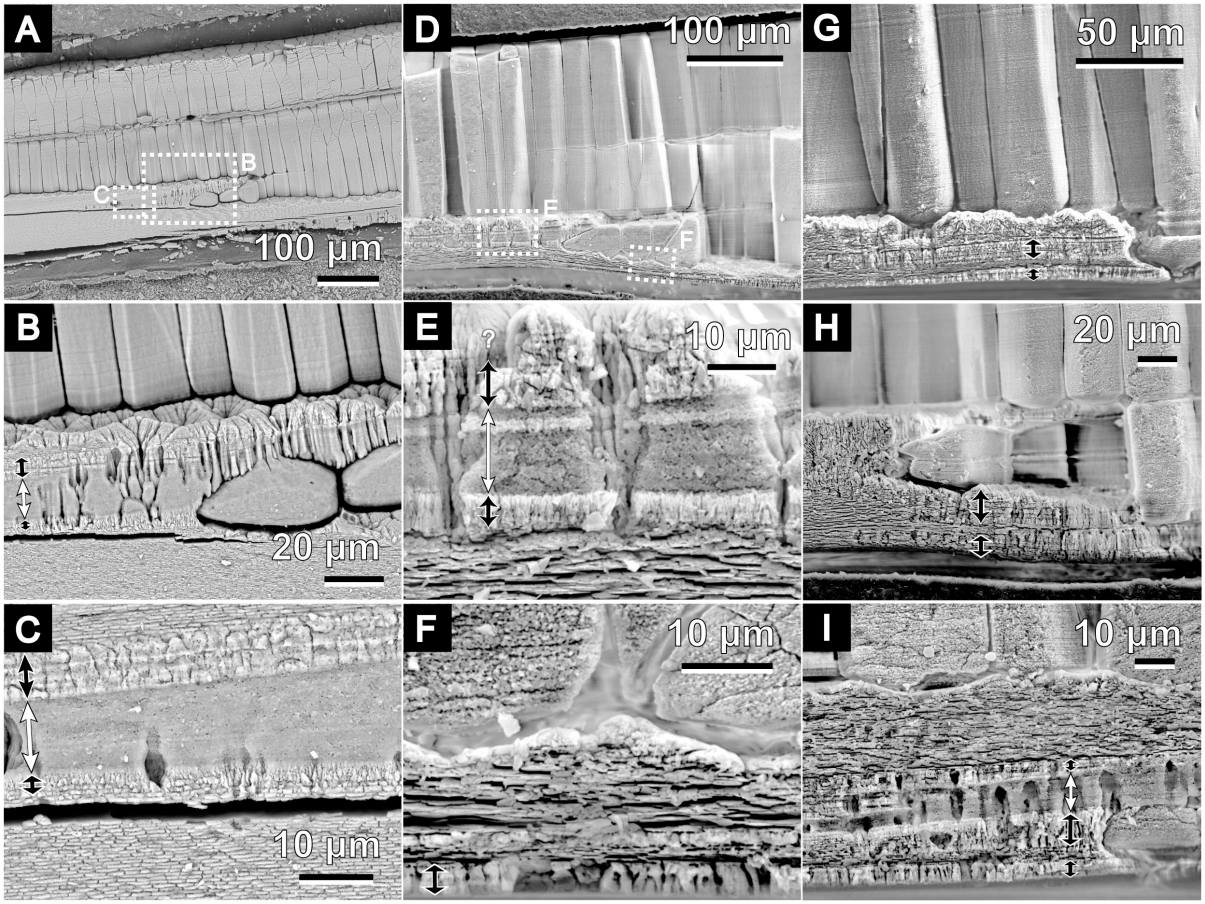

FIGURE 4 | Scanning electron micrographs of the microstructure of the irregular shell layer in *P. fucata*. All images show radial sections in polished planes. Growth direction of the shells are on the right side of images. White double-headed arrows indicate the middle sublayer of the irregular shell layer between the outer and middle layers. Black arrows show the distribution of the outer and inner sublayers. **(A)** Outer to middle shell layers of ID 180226-1, collected on February 26, 2018. Detailed views in panels **(B,C)**. **(D)** Outer to middle shell layers of ID 180404-4, collected on April 4, 2018. Detailed views in panels **(E,F)**. **(G–I)** Show the same structures as in panels **(A,D)**, but are of different individuals collected on April 4, 2018 [ID 180404-1 **(G)**, ID 180404-3 **(H)**, and ID 180404-2 **(I)**].

result from the retraction of the outer mantle fold during annual or semi-annual growth halts [see description by Checa (2000)]. Some arcid bivalves also have an annual sphenoid insertion of the composite prismatic structure into the crossed lamellar structure within the outer shell layer (Kobayashi, 1976a,b; Nishida et al., 2012). Nishida et al. (2015) experimentally confirmed that the variation in thickness of the composite prismatic structure was synchronized with water temperature. A similar physical reaction (i.e., retraction of the mantle due to the low water temperature) is likely to have occurred during the formation of the winter diffusion layer in *P. fucata*; therefore, this layer can be considered a unique type of annual disturbance ring.

Putative Mechanisms of Formation of the Winter Diffusion Layer

Genetic or epigenetic mechanisms might be a component in the formation of peculiar microstructures such as the winter diffusion layer. *In vitro* studies by Takeuchi et al. (2008), genetic manipulation studies by Suzuki et al. (2009), and other biochemical and physicochemical studies (e.g., Olson et al., 2012; Zhang et al., 2018) have strongly suggested that physics and chemistry cannot thoroughly explain the intricate mechanisms of biomineralization in living organisms. Meanwhile, several studies have also examined the expression of some shell matrix protein-coding genes in margaritid bivalves and found a correlation between gene expression patterns and variations in environmental conditions (e.g., food supply and high temperature) (Joubert et al., 2014; Latchere et al., 2017). We hypothesized that the expression pattern of SMPs changes at low temperature, leading to the formation of the winter diffusion layer.

We herein focused on the genes coding for SMPs as they are possibly directly related to the biomineralization process during shell formation, as shown by Suzuki et al. (2009) and Zhang et al. (2018). No information is available on the signaling pathway controlling the expression of SMP-coding genes. However, our working hypothesis was that this does

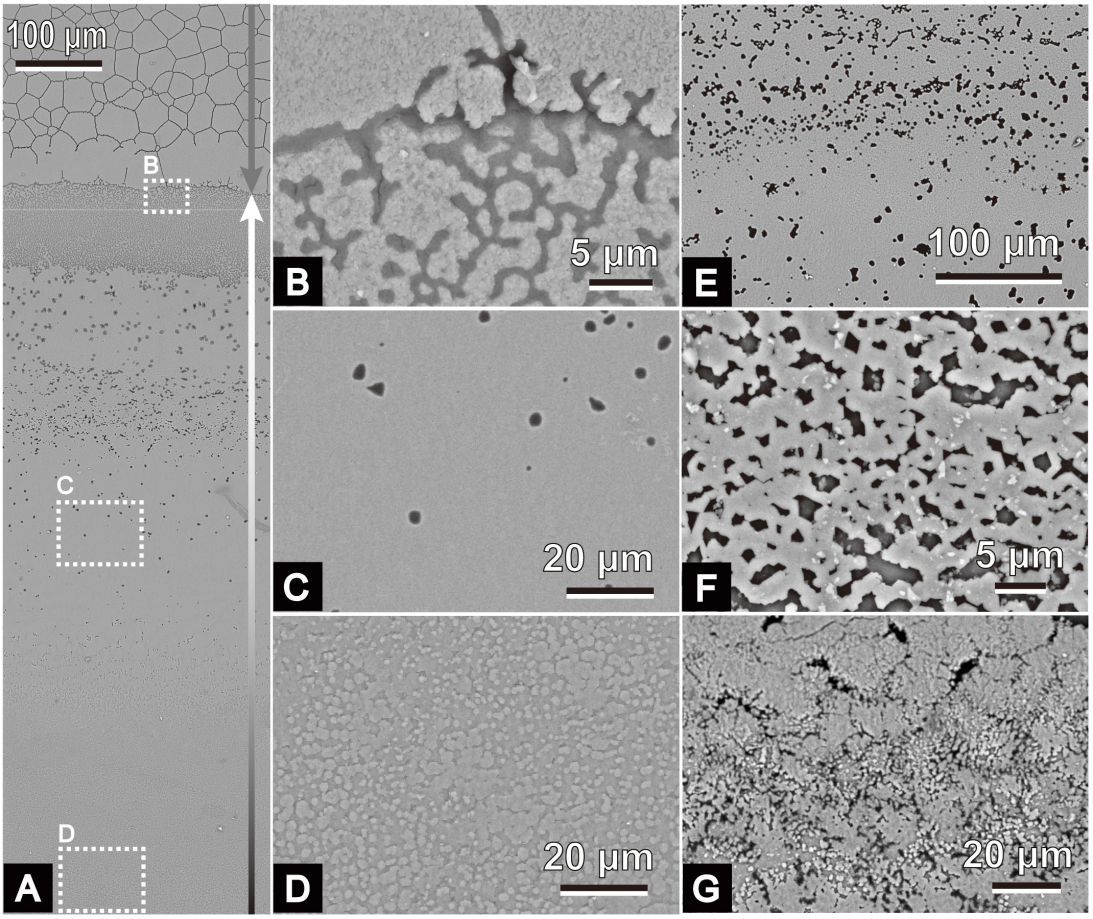

FIGURE 5 | Scanning electron micrographs of the microstructure of the irregular shell layer in *P. fucata*. All images show inner shell surfaces. Shell margins are on the upper sides of the images. **(A)** Inner shell surface of ID 180226-1, collected on February 26, 2018. Gray arrow indicates the outer calcitic columnar regular simple prismatic structure. The irregular shell layer covers the inner surface of the outer layer **(B,C)** and the middle sheet nacreous gradually accumulates **(D)** on it (indicated by the white and black arrow). Variations of the irregular shell layer are shown in panel **(E)** (ID 180424-1, collected on April 24, 2018), **(F)** (ID 180404-1, collected on April 4, 2018), and **(G)** (ID 180404-3, collected on April 4, 2018).

not matter because all upstream mechanisms controlling the expression of the SMP-coding genes must affect the expression of the SMP-coding genes themselves, with a possible feedback loop to the signaling pathways causing possible attenuation or suppression of the downstream genes controlling the phenotypes (Venturelli et al., 2012; Zhang et al., 2012; Liu et al., 2017). Changes in SMP-coding genes must then be translated into the actual biomineralization process. Thus, we examined the expression levels of seven biomineralization-related proteins in specimens collected in different seasons to cover the herein defined seasonal cycle of nacre formation (i.e., winter growth break, irregular shell formation, and normal shell formation). However, no statistical significance was detected in the SMP gene expression levels among seasons, which interestingly shows that these seven SMPs, although important for shell formation, are probably not affected by temperature changes, and are thus not involved in the formation of the winter diffusion layer of *P. fucata*. Nevertheless, whether changes in the expression levels of other SMPs with varying environmental factors influence the formation and irregularities of shell microstructures remains to be tested. Moreover, further experiments using samples cultured in a controlled environment to cancel other parameters (e.g., food supply) that could affect the gene expression of SMPs should be performed. Genetic mechanisms may also be indirectly involved in the formation of irregular microstructures. For example, the increased expression of housekeeping genes as a result of environmental cues might be involved in the subsequent induction of the appropriate expression of upstream genes (regulatory genes and transcription factors) related to development, growth, and cell proliferation (e.g., *dpp*) (Rogulja and Irvine, 2005; Shimizu et al., 2013) or to direct metabolic and physiological responses to such changes (Shinomiya et al., 1999). Although the stability of the expression of downstream genes such as the SMP-coding genes is controlled by homeostasis (as is also suggested by our results), cells expressing SMPs are either physically or chemically different as they respond to environmental cues, which in turn may cause variations in their phenotypes.

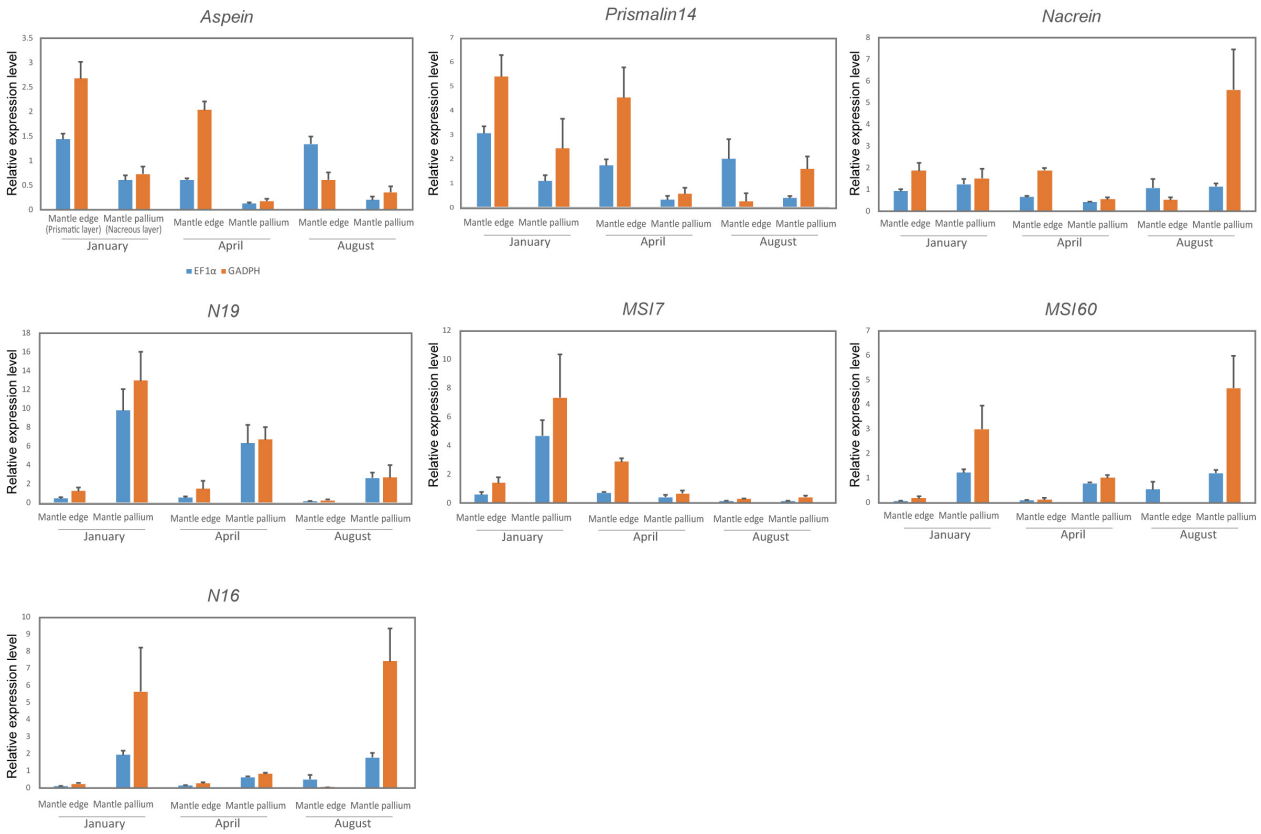

FIGURE 6 | Relative gene expression of biomineralization-related shell matrix genes normalized by housekeeping genes (blue, EF1α; orange, *GAPDH*). Each value represents the mean ± SD of the data analyzed on up to five individuals.

The thermodynamic process is another candidate driving force of the formation of the winter diffusion layer. Olson et al. (2012) hypothesized that the crystallographic axes and morphology of nacre crystals could be related to environmental factors (water temperature and pressure), and Gilbert et al. (2017) demonstrated that the thickness of nacre tablets is correlated with water temperature. Both studies attributed these changes to thermodynamics, whereas Cartwright et al. (2020) considered that changes in nacre thickness were rather a type of biological control determined by the position of the interlamellar membranes, which are secreted before nacre formation. Olson et al. (2012) and Gilbert et al. (2017) also hypothesized that the addition of some proteins to chitin nanocrystals affects the thermally dependent thickening of nacre tablets, besides suggesting the existence of gaps in the knowledge on the role of SMPs on nacre thickness and irregular shell formation, which could be driven by other genetic mechanisms involving transcription factors, cell metabolism-controlling genes, and other upstream genes. We herein observed that the interlamellar membranes surrounding the nacre tablets reduced and showed an irregular distribution or even disappeared, which may have resulted from the low expression of specific insoluble SMPs. Moreover, the downsized and deformed crystals were found in the winter diffusion layer. These may be linked to the change in calcium carbonate deposition and/or nucleation rate; or. from a biological perspective, they may have been caused by the inhibitory activity of SMPs on the crystallization of $CaCO_3$. SMPs other than those herein tested may be directly or indirectly involved in the formation of these microstructural changes. Furthermore, the time gap between our sampling and the animals' irregular shell formation and the number of individuals for statistical analysis should be considered in further studies.

Some of the SMP genes herein tested (*aspein*, *prismalin-14*, *n19*, and *msi7*) had higher expression in the mantle pallium of winter individuals, although these data were not statistically significant. These expression patterns were consistent with the development of nacre tablets. Wada (1972) showed that the (001) planes of aragonite in the middle and inner nacreous layers (i.e., basal planes of nacre tablets) became larger during winter until animal hibernation, when the calcification process was slow. This relationship between nacre growth and SMP expression may be statistically significant in a sampling period larger than that used in the present study. Therefore, future studies with DNA chip analysis and exhaustive exploration of the mantle transcriptome and shell proteomics might provide biological insights into the genetic mechanisms of the formation of the winter diffusion layer in *P. fucata* shells.

The Formation of the Irregular Shell Microstructures and Its Implication to Molluscan Shell Evolution

As previously mentioned, some Protobranchia and Thraciidae bivalves that presented a nacreous structure lost their nacreous shells and acquired a homogeneous structure mostly in the Paleozoic and Mesozoic (Taylor et al., 1973; Sato et al., 2020a). Many studies have suggested that the nacreous structure is costly and has gradually lost its "market share" in the course of molluscan evolution (Cartwright and Checa, 2007; Frýda et al., 2010; Vendrasco et al., 2013). Meanwhile, the similar appearance of a homogeneous structure with an irregular microstructure within the nacreous structure as in winter *P. fucata* has also been reported for *Nautilus pompilius* in the aquarium [see Figure 7 in Moini et al. (2014)]. The phenotypic plasticity of the shells in these two species seems to be triggered by adverse conditions, and may thus be a biological response to produce a low-cost shell. The production cost of molluscan shells can be estimated from their organic content (Palmer, 1992), and the homogeneous structure is presumed to be a low-cost material compared to the nacreous structure (Taylor and Layman, 1972). Consequently, the biomineralization mechanism that controls the phenotypic plasticity from a nacreous to a homogeneous structure also seems to drive shell microstructural evolutions. Therefore, in addition to exploring the genes involved in the formation of the irregular structure of the winter diffusion layer in *P. fucata*, assessing the homology between SMP genes in the homogeneous structure of mollusks (e.g., protobranchs) should be tackled in future paleobiological studies.

DATA AVAILABILITY STATEMENT

The original contributions presented in the study are included in the article/**Supplementary Material**, further inquiries can be directed to the corresponding author.

AUTHOR CONTRIBUTIONS

KS conceived the idea of this study and diagnosed the shell microstructure. KS, DS, and KH conducted the field sampling. KS, DS, and HY performed the gene expression experiments. KS and DS wrote the manuscript. All authors contributed to the discussion and interpretation of the data and read, edited, commented, and confirmed the content of the final version of this manuscript.

FUNDING

This research was supported by Grants-in-Aid for Scientific Research (21K14033) from the Japan Society for the Promotion of Science and Environment Research and Technology Development Fund (5RF-2101) of the Environmental Restoration and Conservation Agency of Japan to KS. DS was partially supported by FY2016 Research Grant for Chemistry and Life Sciences from The Asahi Glass Foundation, Grants-in-Aid for Scientific Research (C) (18K06363), and Grants-in-Aid for Exploratory Research (19K21646). This study was supported by the members of MIKIMOTO Pearl Research Laboratory (MPRL).

ACKNOWLEDGMENTS

We are especially grateful to Kiyohito Nagai and Yasunori Iwahashi for granting us permission to conduct this project in MPRL, besides giving us valuable technical advice. Takenori Sasaki gave technical advice on the anatomy of our sampling. Kazuyoshi Endo gave us valuable advice regarding the direction of our research. Keisuke Shimizu (University of Tokyo) and Akito Ishikawa (University of Tokyo) supported our molecular biology experiments and statistical analyses. Kozue Nishida (Tsukuba University) also gave valuable advice on our statistical analyses. We also thank the members of Setiamarga laboratory [National Institute of Technology (KOSEN), Wakayama College] for their assistance in setting up the environment for our experiments.

SUPPLEMENTARY MATERIAL

The Supplementary Material for this article can be found online at: https://www.frontiersin.org/articles/10.3389/fevo.2022.794287/full#supplementary-material

Supplementary Table 1 | Specimens used for qPCR and shell microstructural observation.

REFERENCES

Carter, J. G. (1990). *Skeletal Biomineralization: Patterns, Processes and Evolutionary Trends*, Vol. I. New York, NY: Van Nostrand & Reinhold.

Carter, J. G., and Sato, K. (2020). Part N, Revised, Chapter 2A: bivalve shell microstructure and mineralogy: shell microstructure terminology. *Treatise Online* 1, 1–81.

Carter, J. G., Barrera, E., and Tevesz, M. J. S. (1998). Thermal potentiation and mineralogical evolution in the bivalvia (Mollusca). *J. Paleontol.* 72, 991–1010.

Cartwright, J. H. E., and Checa, A. G. (2007). The dynamics of nacre self-assembly. *J. R. Soc. Interface* 4, 491–504. doi: 10.1098/rsif.2006.0188

Cartwright, J. H. E., Checa, A. G., and Sainz-Díaz, C. I. (2020). Nacre is a liquid-crystal thermometer of the oceans. *ACS Nano* 14, 9277–9281. doi: 10.1021/acsnano.0c05353

Checa, A. (2000). A new model for periostracum and shell formation in Unionidae (Bivalvia, Mollusca). *Tissue Cell* 32, 405–416. doi: 10.1054/tice.2000.0129

Checa, A. G., Ramírez-Rico, J., González-Segura, A., and Sánchez-Navas, A. (2009). Nacre and false nacre (foliated aragonite) in extant monoplacophorans (=Tryblidiida: Mollusca). *Naturwissenschaften* 96, 111–122. doi: 10.1007/s00114-008-0461-1

Crenshaw, M. A. (1990). "Biomineralization mechanisms," in *Skeletal Biomineralization: Patterns, Processes and Evolutionary Trends*, Vol. I, ed. J. G. Carter (New York, NY: Van Nostrand & Reinhold), 1–3.

Dauphin, Y., Ball, A. D., Cotte, M., Cuif, J. P., Meibom, A., Salomé, M., et al. (2008). Structure and composition of the nacre-prisms transition in the shell of *Pinctada margaritifera* (Mollusca, Bivalvia). *Anal. Bioanal. Chem.* 390, 1659–1669. doi: 10.1007/s00216-008-1860-z

Fleury, C., Marin, F., Marie, B., Luquet, G., Thomas, J., Josse, C., et al. (2008). Shell repair process in the green ormer *Haliotis tuberculata*: a

histological and microstructural study. *Tissue Cell* 40, 207–218. doi: 10.1016/j.tice.2007.12.002

Frenzel, M., and Harper, E. M. (2011). Micro-structure and chemical composition of vateritic deformities occurring in the bivalve *Corbicula fluminea* (Müller, 1774). *J. Struct. Biol.* 174, 321–332. doi: 10.1016/j.jsb.2011.02.002

Frýda, J., Klicnarová, K., Frýdová, B., and Mergl, M. (2010). Variability in the crystallographic texture of bivalve nacre. *Bull. Geosci.* 85, 645–662. doi: 10.3140/bull.geosci.1217

Füllenbach, C. S., Schöne, B. R., and Branscheid, R. (2014). Microstructures in shells of the freshwater gastropod *Viviparus viviparus*: a potential sensor for temperature change? *Acta Biomater.* 10, 3911–3921. doi: 10.1016/j.actbio.2014.03.030

Gilbert, P. U. P. A., Bergmann, K. D., Myers, C. E., Marcus, M. A., DeVol, R. T., Sun, C. Y., et al. (2017). Nacre tablet thickness records formation temperature in modern and fossil shells. *Earth Planet Sci. Lett.* 460, 281–292. doi: 10.1016/j.epsl.2016.11.012

Höche, N., Walliser, E. O., de Winter, N. J., Witbaard, R., and Schöne, B. R. (2021). Temperature-induced microstructural changes in shells of laboratory-grown *Arctica islandica* (Bivalvia). *PLoS One* 16:e0247968. doi: 10.1371/journal.pone.0247968

Isowa, Y., Sarashina, I., Setiamarga, D. H. E., and Endo, K. (2012). A comparative study of the shell matrix protein aspein in pterioid bivalves. *J. Mol. Evol.* 75, 11–18. doi: 10.1007/s00239-012-9514-3

Joubert, C., Linard, C., Le Moullac, G., Soyez, C., Saulnier, D., Teaniniuraitemoana, V., et al. (2014). Temperature and food influence shell growth and mantle gene expression of shell matrix proteins in the pearl oyster *Pinctada margaritifera*. *PLoS One* 9:e103944. doi: 10.1371/journal.pone.0103944

Kanda, Y. (2013). Investigation of the freely available easy-to-use software "EZR" for medical statistics. *Bone Marrow Transpl.* 48, 452–458. doi: 10.1038/bmt.2012.244

Kinoshita, S., Wang, N., Inoue, H., Maeyama, K., Okamoto, K., Nagai, K., et al. (2011). Deep sequencing of ESTs from nacreous and prismatic layer producing tissues and a screen for novel shell formation-related genes in the Pearl Oyster. *PLoS One* 6:e21238. doi: 10.1371/journal.pone.0021238

Kobayashi, I. (1976a). Internal structure of the outer shell layer *Anadara broughtnii* (Schrenck). *Venus* 35, 63–72.

Kobayashi, I. (1976b). The change of internal shell structure of *Anadara ninohensis* (Okuta) during the shell growth. *J. Geol. Soc. Japan* 82, 441–447.

Kocot, K. M., McDougal, C., and Degnan, B. M. (2016). "Developing perspectives on molluscan shells, part 1: introduction and molecular biology," in *Physiology of Molluscs: A Collection of Selective Reviews*, eds S. Saleuddin and S. Mukai (New York, NY: Apple Academic Press), 1–41. doi: 10.1201/9781315207483

Koga, H., Hashimoto, N., Suzuki, D. G., Ono, H., Yoshimura, M., Suguro, T., et al. (2013). A genome-wide survey of genes encoding transcription factors in Japanese pearl oyster *Pinctada fucata*: II. Tbx, Fox, Ets, HMG, NFκ;B, bZIP, and C2H2 Zinc Fingers. *Zoolog. Sci.* 30, 858–867. doi: 10.2108/zsj.30.858

Kogure, T., Suzuki, M., Kim, H., Mukai, H., Checa, A. G., Sasaki, T., et al. (2014). Twin density of aragonite in molluscan shells characterized using x-ray diffraction and transmission electron microscopy. *J. Cryst. Growth* 397, 39–46. doi: 10.1016/j.jcrysgro.2014.03.029

Kontoyannis, C. G., and Vagenas, N. V. (2000). Calcium carbonate phase analysis using XRD and FT-Raman spectroscopy. *Analyst* 125, 251–255. doi: 10.1039/a908609i

Latchere, O., Le Moullac, G., Gaertner-Mazouni, N., Fievet, J., Magré, K., and Saulnier, D. (2017). Influence of preoperative food and temperature conditions on pearl biogenesis in *Pinctada margaritifera*. *Aquaculture* 479, 176–187. doi: 10.1016/j.aquaculture.2017.05.046

Lee, S. Y., and Nam, Y. K. (2016). Evaluation of reference genes for RT-qPCR study in abalone Haliotis discus hannai during heavy metal overload stress. *Fish. Aquat. Sci.* 19, 1–11. doi: 10.1186/S41240-016-0022-Z

Li, Y., Zhang, L., Li, R., Zhang, M., Li, Y., Wang, H., et al. (2019). Systematic identification and validation of the reference genes from 60 RNA-Seq libraries in the scallop Mizuhopecten yessoensis. *BMC Genomics* 20:288. doi: 10.1186/s12864-019-5661-x

Liu, D., Albergante, L., and Newman, T. J. (2017). Universal attenuators and their interactions with feedback loops in gene regulatory networks. *Nucleic Acids Res.* 45, 7078–7093. doi: 10.1093/nar/gkx485

Lowenstam, H. A. (1981). Minerals formed by organisms. *Science* 211, 1126–1131. doi: 10.1126/science.7008198

Lutz, R. A., and Clark, G. R. (1984). Seasonal and geographic variation in the shell microstructure of a salt-marsh bivalve (*Geukensia demissa* (Dillwyn)). *J. Mar. Res.* 42, 943–956. doi: 10.1357/002224084788520684

Marie, B., Arivalagan, J., Mathéron, L., Bolbach, G., Berland, S., Marie, A., et al. (2017). Deep conservation of bivalve nacre proteins highlighted by shell matrix proteomics of the Unionoida *Elliptio complanata* and *Villosa lienosa*. *J. R. Soc. Interface* 14:20160846. doi: 10.1098/rsif.2016.0846

Marie, B., Joubert, C., Tayalé, A., Zanella-Cleón, I., Belliard, C., Piquemal, D., et al. (2012). Different secretory repertoires control the biomineralization processes of prism and nacre deposition of the pearl oyster shell. *Proc. Natl. Acad. Sci. U.S.A.* 109, 20986–20991. doi: 10.1073/pnas.1210552109

Marie, B., Le Roy, N., Zanella-Cléon, I., Becchi, M., and Marin, F. (2011). Molecular evolution of mollusc shell proteins: insights from proteomic analysis of the edible mussel *Mytilus*. *J. Mol. Evol.* 72, 531–546. doi: 10.1007/s00239-011-9451-6

Marin, F., Roy, N. L., and Marie, B. (2012). The formation and mineralizarion of mollusks shell. *Front. Biosci.* 4:1099–1125.

Miyamoto, H., Miyashita, T., Okushima, M., Nakano, S., Morita, T., and Matsushiro, A. (1996). A. carbonic anhydrase from the nacreous layer in oyster pearls. *Proc. Natl. Acad. Sci. U.S.A.* 93, 9657–9660. doi: 10.1073/pnas.93.18.9657

Miyamura, M., and Makido, T. (1958). Quality of the pearl examined in association with the graft tissues taken from various parts of the mantle. *B. Jpn. Soc. Sci. Fish.* 24, 441–444.

Miyazaki, Y., Nishida, T., Aoki, H., and Samata, T. (2010). Expression of genes responsible for biomineralization of *Pinctada fucata* during development. *Comp. Biochem. Physiol. B Biochem. Mol. Biol.* 155, 241–248. doi: 10.1016/j.cbpb.2009.11.009

Mizumoto, S. (1965). "Tansuishinjyu," in *Shinjyu Yousyoku Zensyo Hensui Iinnkai*, ed. Shinjyu Yousyoku Zensho (Tokyo: Zenkoku Shinjyu Yousyoku Gyogyoukumiai Rengoukai), 428–457. [in Japanese].

Moini, M., O'Halloran, A., Peters, A. M., France, C. A. M., Vicenzi, E. P., Dewitt, T. G., et al. (2014). Understanding irregular shell formation of *Nautilus* in aquaria: chemical composition and structural analysis. *Zoo. Biol.* 33, 285–294. doi: 10.1002/zoo.21132

Nishida, K., Ishimura, T., Suzuki, A., and Sasaki, T. (2012). Seasonal changes in the shell microstructure of the bloody clam, *Scapharca broughtonii* (Mollusca: Bivalvia: Arcidae). *Palaeogeogr. Palaeoclimatol. Palaeoecol.* 363–364, 99–108. doi: 10.1016/j.palaeo.2012.08.017

Nishida, K., Suzuki, A., Isono, R., Hayashi, M., Watanabe, Y., Yamamoto, Y., et al. (2015). Thermal dependency of shell growth, microstructure, and stable isotopes in laboratory-reared *Scapharca broughtonii* (Mollusca: Bivalvia). *Geochem. Geophys. Geosys.* 16, 2395–2408. doi: 10.1002/2014GC005634

Olson, I. C., Kozdon, R., Valley, J. W., and Gilbert, P. U. P. A. (2012). Mollusk shell nacre ultrastructure correlates with environmental temperature and pressure. *J. Am. Chem. Soc.* 134, 7351–7358. doi: 10.1021/ja210808s

Palmer, A. R. (1992). Calcification in marine molluscs: how costly is it? *Proc. Natl. Acad. Sci. U.S.A.* 89, 1379–1382. doi: 10.1073/pnas.89.4.1379

R Core Team (2020). *R: A Language and Environment for Statistical Computing*. Vienna: R Foundation for Statistical Computing.

Rogulja, D., and Irvine, K. D. (2005). Regulation of cell proliferation by a morphogen gradient. *Cell* 123, 449–461. doi: 10.1016/j.cell.2005.08.030

Samata, T., Hayashi, N., Kono, M., Hasegawa, K., Horita, C., and Akera, S. (1999). A new matrix protein family related to the nacreous layer formation of *Pinctada fucata*. *FEBS Lett.* 462, 225–229. doi: 10.1016/S0014-5793(99)01387-3

Saruwatari, K., Matsui, T., Mukai, H., Nagasawa, H., and Kogure, T. (2009). Nucleation and growth of aragonite crystals at the growth front of nacres in pearl oyster, *Pinctada fucata*. *Biomaterials* 30, 3028–3034. doi: 10.1016/j.biomaterials.2009.03.011

Sato, K., Kano, Y., Setiamarga, D. H. E., Watanabe, H. K., and Sasaki, T. (2020a). Molecular phylogeny of protobranch bivalves and systematic implications of their shell microstructure. *Zool. Scr.* 49, 458–472. doi: 10.1111/zsc.12419

Sato, K., Watanabe, H. K., Jenkins, R. G., and Chen, C. (2020b). Phylogenetic constraint and phenotypic plasticity in the shell microstructure of vent and seep pectinodontid limpets. *Mar. Biol.* 167:79. doi: 10.1007/s00227-020-03692-z

Setiamarga, D. H. E., Hirota, K., Yoshida, M., Takeda, Y., Kito, K., Ishikawa, M., et al. (2021). Hydrophilic shell matrix proteins of *Nautilus pompilius* and the

identification of a core set of conchiferan domains. *bioRxiv* [Preprint]. doi: 10.1101/2020.11.14.382804

Setiamarga, D. H. E., Shimizu, K., Kuroda, J., Inamura, K., Sato, K., Isowa, Y., et al. (2013). An in-silico genomic survey to annotate genes coding for early development-relevant signaling molecules in the pearl oyster, *Pinctada fucata*. *Zoolog. Sci.* 30, 877–888. doi: 10.2108/zsj.30.877

Shimizu, K., Iijima, M., Setiamarga, D. H. E., Sarashina, I., Kudoh, T., Asami, T., et al. (2013). Left-right asymmetric expression of *dpp* in the mantle of gastropods correlates with asymmetric shell coiling. *Evodevo* 4:15. doi: 10.1186/2041-9139-4-15

Shinomiya, Y., Iwanaga, S., Kohno, K., and Yamaguchi, T. (1999). Seasonal variations in carbohydrate-metabolizing enzyme activity and body composition of Japanese pearl oyster *Pinctada fucata* martensii in pearl culture. *Nippon Suisan Gakkaishi* 65, 294–299. doi: 10.2331/suisan.65.294

Spann, N., Harper, E. M., and Aldridge, D. C. (2010). The unusual mineral vaterite in shells of the freshwater bivalve *Corbicula fluminea* from the UK. *Naturwissenschaften* 97, 743–751. doi: 10.1007/s00114-010-0692-9

Sudo, S., Fujikawa, T., Nagakura, T., Ohkubo, T., Sakaguchi, K., Tanaka, M., et al. (1997). Structures of mollusc shell framework proteins. *Science* 387, 563–564. doi: 10.1038/42391

Suzuki, M., Murayama, E., Inoue, H., Ozaki, N., Tohse, H., Kogure, T., et al. (2004). Characterization of Prismalin-14, a novel matrix protein from the prismatic layer of the Japanese pearl oyster (*Pinctada fucata*). *Biochem. J.* 382, 205–213. doi: 10.1042/BJ20040319

Suzuki, M., Saruwatari, K., Kogure, T., Yamamoto, Y., Nishimura, T., Kato, T., et al. (2009). An acidic matrix protein, Pif, is a key macromolecule for nacre formation. *Science* 325, 1388–1390. doi: 10.1126/science.1173793

Suzuki, S., and Uozumi, S. (1979). The histochemical changes associated with the development of the organic membrane-shell in mussel, *Mytilus edulis* [in Japanese]. *Earth Sci.* 33, 200–207.

Takeuchi, T., and Endo, K. (2006). Biphasic and dually coordinated expression of the genes encoding major shell matrix proteins in the pearl oyster *Pinctada fucata*. *Mar. Biotechnol.* 8, 52–61. doi: 10.1007/s10126-005-5037-x

Takeuchi, T., Kawashima, T., Koyanagi, R., Gyoja, F., Tanaka, M., Ikuta, T., et al. (2012). Draft genome of the pearl oyster *Pinctada fucata*: a platform for understanding bivalve biology. *DNA Res.* 19, 117–130. doi: 10.1093/dnares/dss005

Takeuchi, T., Koyanagi, R., Gyoja, F., Kanda, M., Hisata, K., Fujie, M., et al. (2016). Bivalve-specific gene expansion in the pearl oyster genome: implications of adaptation to a sessile lifestyle. *Zool. Lett.* 2, 1–13. doi: 10.1186/s40851-016-0039-2

Takeuchi, T., Sarashina, I., Iijima, M., and Endo, K. (2008). In vitro regulation of $CaCO_3$ crystal polymorphism by the highly acidic molluscan shell protein Aspein. *FEBS Lett.* 582, 591–596. doi: 10.1016/j.febslet.2008.01.026

Taylor, J. D., and Layman, M. (1972). The mechanical properties of bivalve (Mollusca) shell structure. *Paleontology* 15, 73–87.

Taylor, J. D., Kennedy, W. J., and Hall, A. (1969). The shell structure and mineralogy of the bivalvia. introduction, Nuculacea-Trigonacea. *Bull. Brit. Mus. Nat. His. Zool.* 3, 1–125.

Taylor, J. D., Kennedy, W. J., and Hall, A. (1973). The shell structure and mineralogy of the Bivalvia. II. Lucinacea-Clavagellacea, Conclusions. *Bull. Brit. Mus. Nat. His. Zool.* 22, 253–284.

Tsukamoto, D., Sarashina, I., and Endo, K. (2004). Structure and expression of an unusually acidic matrix protein of pearl oyster shells. *Biochem. Biophys. Res. Commun.* 320, 1175–1180. doi: 10.1016/j.bbrc.2004.06.072

Vendrasco, M. J., Checa, A. G., and Kouchinsky, A. V. (2011). Shell microstructure of the early bivalve *Pojetaia* and the independent origin of nacre within the mollusca. *Palaeontology* 54, 825–850. doi: 10.1111/j.1475-4983.2011.01056.x

Vendrasco, M. J., Checa, A. G., Heimbrock, W. P., and Baumann, S. D. J. (2013). Nacre in molluscs from the ordovician of the Midwestern United States. *Geoscience* 3, 1–29. doi: 10.3390/geosciences3010001

Venturelli, O. S., El-Samad, H., and Murray, R. M. (2012). Synergistic dual positive feedback loops established by molecular sequestration generate robust bimodal response. *Proc. Natl. Acad. Sci. U.S.A* 109, E3324–E3333. doi: 10.1073/pnas.1211902109

Wada, K. (1961). The influence of the life-activity upon pearl formation in the pearl culture of *Pinctada martensii* (Dunker) II. The seasonal changes of crysta1 growth and luster of the pearl. *Bull. Natl. Pearl. Res. Lab.* 6, 586–606.

Wada, K. (1972). Nucleation and growth of aragonite crystals in the nacre of some bivalve molluscs. *Biomineralisation* 6, 141–159.

Wang, N., Kinoshita, S., Riho, C., Maeyama, K., Nagai, K., and Watabe, S. (2009). Quantitative expression analysis of nacreous shell matrix protein genes in the process of pearl biogenesis. *Comp. Biochem. Physiol. B Biochem. Mol. Biol.* 154, 346–350. doi: 10.1016/j.cbpb.2009.07.012

Weiner, S., Talmon, Y., and Traub, W. (1983). Electron diffraction of mollusc shell organic matrices and their relationship to the mineral phase. *Int. J. Biol. Macromol.* 5, 325–328. doi: 10.1016/0141-8130(83)90055-7

Yano, M., Nagai, K., Morimoto, K., and Miyamoto, H. (2007). A novel nacre protein N19 in the pearl oyster *Pinctada fucata*. *Biochem. Biophys. Res. Commun.* 362, 158–163. doi: 10.1016/j.bbrc.2007.07.172

Zhang, H., Chen, Y., and Chen, Y. (2012). Noise propagation in gene regulation networks involving interlinked positive and negative feedback loops. *PLoS One* 7:e51840. doi: 10.1371/journal.pone.0051840

Zhang, L., and He, M. (2011). Quantitative expression of shell matrix protein genes and their correlations with shell traits in the pearl oyster *Pinctada fucata*. *Aquaculture* 314, 73–79. doi: 10.1016/j.aquaculture.2011.01.039

Zhang, R., Xie, L., and Yan, Z. (2018). *Biomineralization Mechanism of the Pearl Oyster, Pinctada fucata*. Singapore: Springer.

Zhang, Y., Xie, L., Meng, Q., Jiang, T., Pu, R., Chen, L., et al. (2003).). A novel matrix protein participating in the nacre framework formation of pearl oyster, *Pinctada fucata*. *Comp. Biochem. Physiol. B Biochem. Mol. Biol.* 135, 565–573. doi: 10.1016/S1096-4959(03)00138-6

Conflict of Interest: The authors declare that the research was conducted in the absence of any commercial or financial relationships that could be construed as a potential conflict of interest.

Publisher's Note: All claims expressed in this article are solely those of the authors and do not necessarily represent those of their affiliated organizations, or those of the publisher, the editors and the reviewers. Any product that may be evaluated in this article, or claim that may be made by its manufacturer, is not guaranteed or endorsed by the publisher.

frontiers | Frontiers in Cell and Developmental Biology

TYPE Original Research
PUBLISHED 12 October 2022
DOI 10.3389/fcell.2022.932341

OPEN ACCESS

EDITED BY
Sylvain Marcellini,
University of Concepcion, Chile

REVIEWED BY
Tatjana Haitina,
Uppsala University, Sweden
Jake Leyhr,
Uppsala University, Sweden, in collaboration with reviewer TH
Jonathan Huie,
George Washington University, United States
Matthew Vickaryous,
University of Guelph, Canada

*CORRESPONDENCE
Mason N. Dean,
mndean@cityu.edu.hk,
mason.dean@mpikg.mpg.de

†These authors have contributed equally to this work and share first authorship

SPECIALTY SECTION
This article was submitted to Evolutionary Developmental Biology, a section of the journal Frontiers in Cell and Developmental Biology

RECEIVED 29 April 2022
ACCEPTED 22 August 2022
PUBLISHED 12 October 2022

CITATION
Clark B, Chaumel J, Johanson Z, Underwood C, Smith MM and Dean MN (2022), Bricks, trusses and superstructures: Strategies for skeletal reinforcement in batoid fishes (rays and skates).
Front. Cell Dev. Biol. 10:932341.
doi: 10.3389/fcell.2022.932341

Bricks, trusses and superstructures: Strategies for skeletal reinforcement in batoid fishes (rays and skates)

Brett Clark[1†], Júlia Chaumel[2†], Zerina Johanson[3], Charlie Underwood[3,4], Moya M. Smith[5] and Mason N. Dean[2,6*]

[1]Image and Analysis Centre, Core Research Labs, London, United Kingdom, [2]Department of Biomaterials, Max Planck Institute of Colloids and Interfaces, Potsdam, Germany, [3]Natural History Museum, London, United Kingdom, [4]Department of Earth and Planetary Sciences, Birkbeck, University of London, London, United Kingdom, [5]Centre for Craniofacial and Regenerative Biology, Dental Institute, King's College, London, United Kingdom, [6]Department of Infectious Diseases and Public Health, City University of Hong Kong, Kowloon Tong, Hong Kong SAR, China

Crushing and eating hard prey (durophagy) is mechanically demanding. The cartilage jaws of durophagous stingrays are known to be reinforced relative to non-durophagous relatives, with a thickened external cortex of mineralized blocks (tesserae), reinforcing struts inside the jaw (trabeculae), and pavement-like dentition. These strategies for skeletal strengthening against durophagy, however, are largely understood only from myliobatiform stingrays, although a hard prey diet has evolved multiple times in batoid fishes (rays, skates, guitarfishes). We perform a quantitative analysis of micro-CT data, describing jaw strengthening mechanisms in *Rhina ancylostoma* (Bowmouth Guitarfish) and *Rhynchobatus australiae* (White-spotted Wedgefish), durophagous members of the Rhinopristiformes, the sister taxon to Myliobatiformes. Both species possess trabeculae, more numerous and densely packed in *Rhina*, albeit simpler structurally than those in stingrays like *Aetobatus* and *Rhinoptera*. *Rhina* and *Rhynchobatus* exhibit impressively thickened jaw cortices, often involving >10 tesseral layers, most pronounced in regions where dentition is thickest, particularly in *Rhynchobatus*. Age series of both species illustrate that tesserae increase in size during growth, with enlarged and irregular tesserae associated with the jaws' oral surface in larger (older) individuals of both species, perhaps a feature of ageing. Unlike the flattened teeth of durophagous myliobatiform stingrays, both rhinopristiform species have oddly undulating dentitions, comprised of pebble-like teeth interlocked to form compound "meta-teeth" (large spheroidal structures involving multiple teeth). This is particularly striking in *Rhina*, where the upper/lower occlusal surfaces are mirrored undulations, fitting together like rounded woodworking finger-joints. Trabeculae were previously thought to have arisen twice independently in Batoidea; our results show they are more widespread among batoid groups than previously appreciated, albeit apparently absent in the phylogenetically basal Rajiformes. Comparisons with several other durophagous and non-durophagous species illustrate that batoid skeletal reinforcement architectures are modular: trabeculae can be variously oriented and are dominant in some species (e.g. *Rhina*, *Aetobatus*), whereas

cortical thickening is more significant in others (e.g. *Rhynchobatus*), or both reinforcing features can be lacking (e.g. *Raja*, *Urobatis*). We discuss interactions and implications of character states, framing a classification scheme for exploring cartilage structure evolution in the cartilaginous fishes.

KEYWORDS

Batoidea, durophagy, jaw, trabeculae, tesserae, tessellated cartilage, skeletal biomaterials

Introduction

Among cartilaginous fishes (Chondrichthyes), the consumption of hard prey (durophagy) is most common in the clade of skates and rays (Batoidea; Elasmobranchii), particularly in the subfamilies Rhinopterinae and Myliobatinae (both Myliobatiformes: Myliobatidae), which contain only durophagous taxa (Figure 1). Durophagy in batoid fishes takes a variety of forms: diets can involve comparatively thin-shelled crustaceans, thick-shelled molluscs and/or prey with softer, tougher exoskeletons (e.g. shrimp or even insects) (Wilga and Motta, 2000; Kolmann et al., 2015b, 2016). Hard prey processing has not been extensively surveyed in batoid fishes, but at least two strategies exist (Figure 1): what we will call "chemical durophagy," where predators rely on low stomach pH or chinitase to break down prey exoskeletons (Fänge et al., 1979; Holmgren and Nilsson, 1999; Cortés et al., 2008; Anderson et al., 2010) and "mechanical durophagy," where predators crush prey before ingestion (Summers, 2000; Summers et al., 2004; Kolmann et al., 2015b; Rutledge et al., 2019; Ajemian et al., 2021). The limited current knowledge of the phylogenetic distribution of these two strategies suggests they could be mutually exclusive in batoid fishes (Figure 1), perhaps also indicating that these prey processing modes demand a level of anatomical and physiological specialization, in gut physiology for chemical durophagy and in skeletal reinforcement for mechanical durophagy.

From an anatomical perspective, mechanical durophagy is a particularly impressive dietary mode for elasmobranch fishes, as shark and ray skeletons are composed predominantly of unmineralized cartilage covered by a mineralized crust of blocks called tesserae, typically arranged in a monolayer merely hundreds of microns thick (Maisey, 2013; Atake and Eames, 2021; Berio et al., 2021; Maisey et al., 2021). A variety of morphological features have been found to be associated with mechanical durophagy (e.g. Summers, 2000; Summers et al., 2004; Dean et al., 2007, 2015; Herbert and Motta, 2018; Rutledge et al., 2019; Seidel et al., 2021; Huie et al., 2022), particularly within durophagous myliobatiform stingrays (Myliobatiformes): flat pavement-like teeth; large adductor muscles; relatively shortened jaws with high leverage, fused at the midline symphysis; and structural reinforcements of the jaw tissues in the form of thickening of the mineralized cortex (the tesseral layer) and/or mineralized struts (trabeculae) coursing through the unmineralized cartilage. Some of these structural features, however, may support functions not associated with durophagy. For example, the cownose ray (*Rhinoptera bonasus*; Myliobatiformes) was previously considered to be an obligate durophage, its jaws bearing all the anatomical indicators of durophagy, yet this species has also been shown to suction feed opportunistically on soft-bodied prey (Collins et al., 2007). Conversely, the jaws of the non-durophagous electric ray, *Narcine brasilinensis* (Torpediniformes) have a thickened cortex and trabeculae, but these features likely support this species' predation on buried polychaetes, preventing the highly protrusible jaws from buckling when they are used in benthic excavation of prey (Dean et al., 2006). The disparate feeding modes and phylogenetic positions of Myliobatiformes and Torpediniformes (Dean et al., 2006, 2007; Aschliman et al., 2012) suggest that reinforcing features such as trabeculae and cortical thickening may be more widespread in Batoidea than currently appreciated (Figure 1).

In the last ~20 years, much of the research into both elasmobranch skeletal biology and the functional morphology of durophagy has centered on myliobatiform stingrays (e.g. Summers, 2000; Summers et al., 2004; Dean et al., 2009; Kolmann et al., 2015a, 2015b; Seidel et al., 2016, 2017, 2021; Rutledge et al., 2019). Yet, batoid taxa offer a valuable diversity of species for exploring links between skeletal anatomy and ecology and clarifying how a cartilage skeleton can be modified through evolution to meet diverse functional demands. In this study, we use X-ray microcomputed tomography (micro-CT) to investigate whether jaw and dentition characters associated with stingray durophagy are also present in two durophagous members of the Rhinopristiformes, sister taxon to the Myliobatiformes (Dean et al., 2007; Aschliman et al., 2012; Aschliman, 2014) (Figure 1). We investigate two rhinopristiform species, *Rhina ancylostoma* (Bowmouth guitarfish; Rhinidae) and *Rhynchobatus australiae* (White-spotted wedgefish; Rhynchobatidae), large-bodied species with small, rounded, and ornamented teeth. In both species, these teeth form an unusual and striking dental battery, where multiple teeth are arrayed into spheroidal "meta-teeth"—bulbous structures constructed from multiple teeth, and particularly massive in *Rhina*—fitting into concave regions in the opposing jaw (Figures 2, 3A, 4A). These undulating dentitions are conspicuously different from the

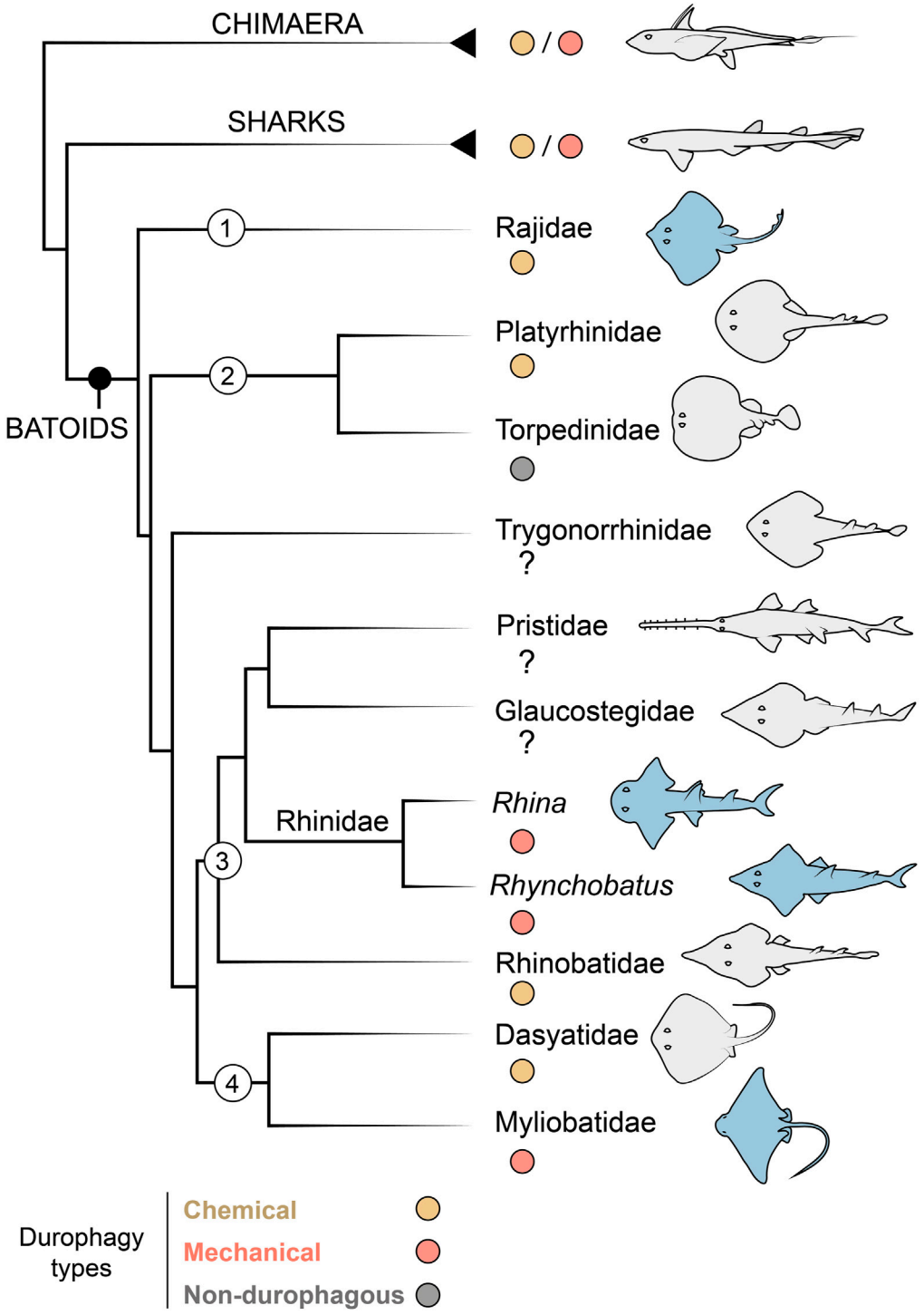

FIGURE 1
Durophagy in Chondrichthyes, with a focus on batoid relationships. Taxa of interest are indicated with numbers as follows: *1*) Rajiformes, *2*) Torpediniformes, *3*) Rhinopristiformes and *4*) Myliobatiformes. The Rhinidae is shown to genus level to indicate the two genera investigated in this study (*Rhina* and *Rhynchobatus*). Species examined in this study are highlighted in blue. In groups with some durophagous members, the most common types are highlighted, either chemical (where shelled prey is digested) or mechanical (where shelled prey is crushed). Groups where it is unclear if durophagy exists are marked with a question mark. Phylogenetic relationships based on (Franklin et al., 2014; Underwood et al., 2015).

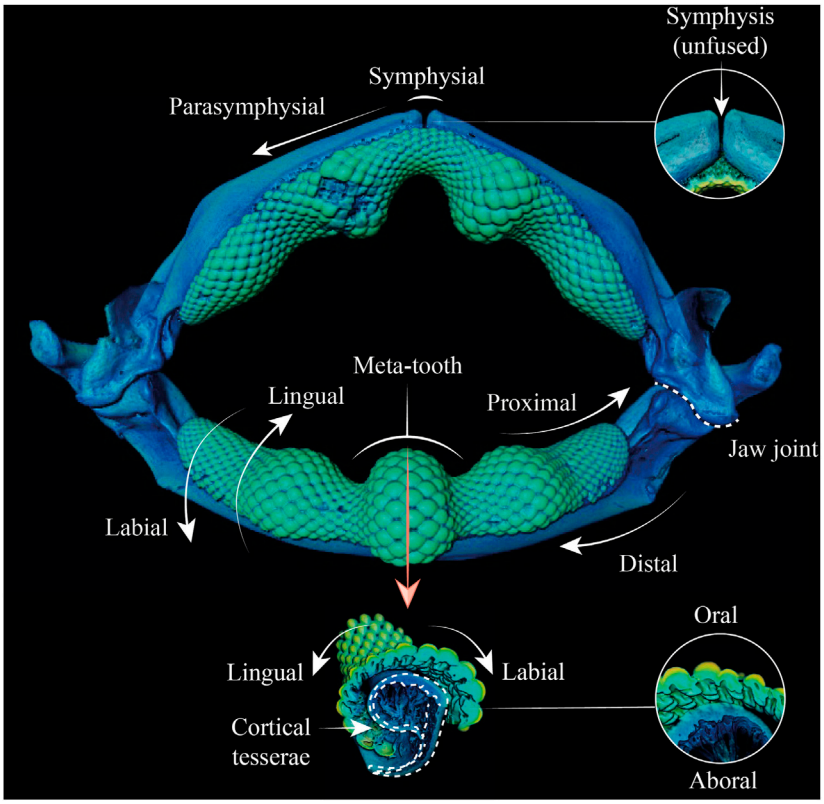

FIGURE 2
Anatomical terminology used in this study. 3D reconstruction (top) and cross-sections of the lower jaw (bottom) of *Rhina* indicate the different anatomical positions and orientation terminology used in the text.

familiar, flat pavements of myliobatiform stingray teeth (e.g. Underwood et al., 2015), suggesting that the Rhinopristiformes may employ alternative anatomical strategies for durophagy.

Given that much previous research into cartilaginous fish durophagy has focused on myliobatiform stingrays, the Rhinopristiformes offer great potential for understanding the degree to which known anatomical modifications for a hard prey diet are group-specific or more general tissue-level modifications. Biomaterials and functional morphology studies (e.g. Summers, 2000; Dean et al., 2006; Liu et al., 2014; Seidel et al., 2019, 2020) have shown that tessellated cartilage (at least in some stingrays) has a distinct multi-scale mechanical anisotropy, with tesserae oriented parallel to the direction of loading (e.g. the biting direction) having a higher stiffness than those oriented perpendicular to it. Similarly, excised blocks of jaw cartilage are stiffer when they contain trabecular struts, and when the struts (and the tesserae forming them) are oriented in-line with the direction of applied load (Summers et al., 1998). The effect of tesserae orientation on skeletal stiffness presents a structural conundrum: the jaws of myliobatiform stingrays must have an appreciably broad, flat area to accommodate their pavement-like dentitions, yet this necessitates a wide skeletal surface where tesserae are oriented perpendicular to the biting load (i.e. in their less stiff orientation). This may explain the incredibly high density of trabeculae supporting the jaws in myliobatiform rays (i.e. buttressing occlusal areas with more tesserae oriented in-line with biting loads), while also suggesting that such supporting mechanisms may be less relevant for those durophagous batoids that lack flattened platform regions on their jaws (e.g. Rhinopristiformes) and/or that structural reinforcement may be accomplished by other means. It is possible, for example, that the shape of tesserae beneath the dentition may be altered, perhaps taking on the dome-like "voussoir" tesserae morphology known to be associated with arched skeletal surfaces (Maisey et al., 2021). Additionally, the jaw's cortex could be reinforced by accessory tesseral layers (>10 have been described in some large species; Dean et al., 2015, 2017). We dissect these options in the current study, providing the first three-dimensional characterization of jaw-strengthening anatomies in batoids, comparing features among the range of durophagous and non-durophagous species examined in this study and previous works, to synopsize the diversity of strategies by which

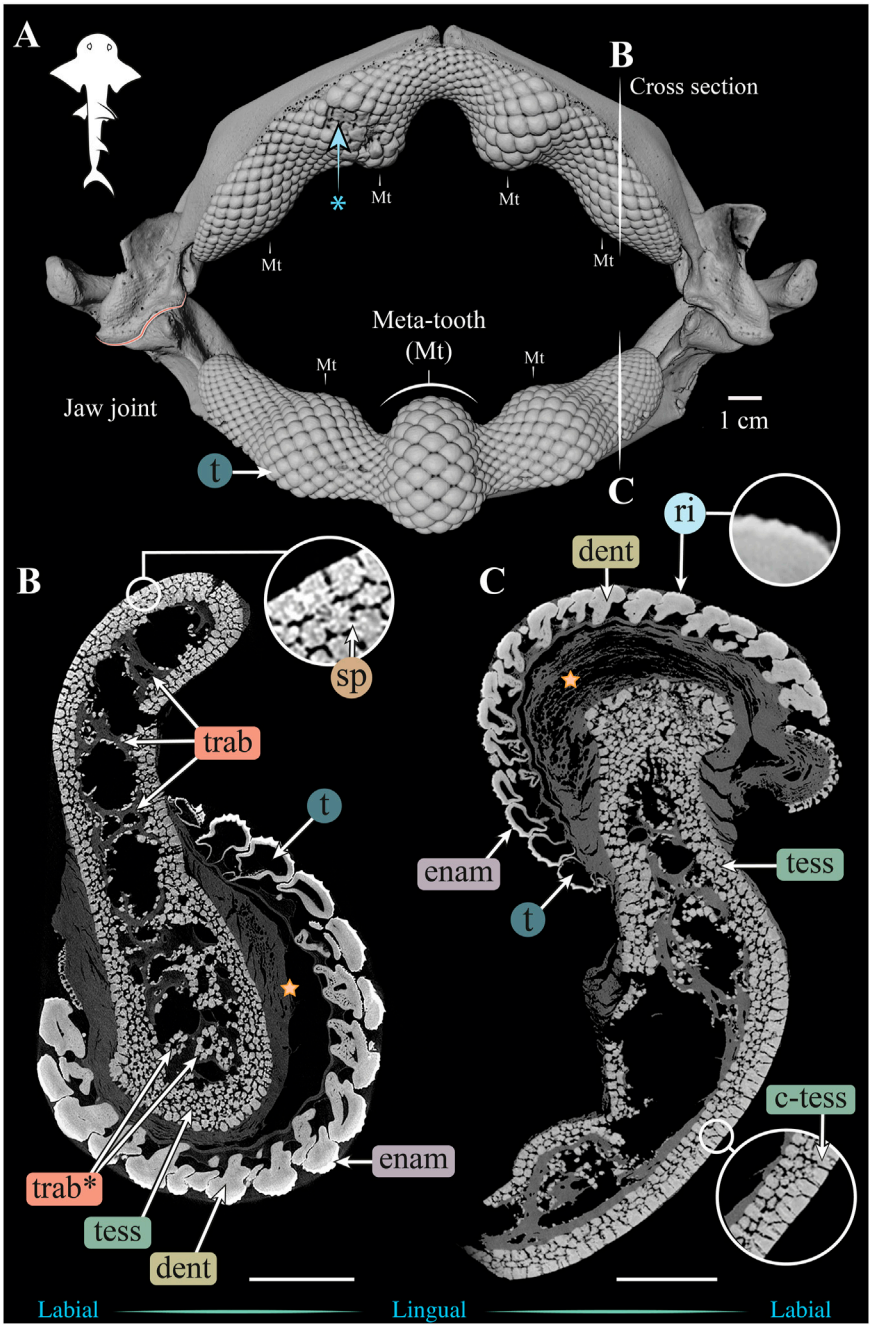

FIGURE 3
3D reconstruction and cross sections of a *Rhina ancylostoma* jaw. **(A)** 3D reconstruction of upper and lower jaws, showing the distinctive undulating dentition and several bulbous "meta-teeth" (Mt) on the upper and lower jaw. Asterisk indicates an area of the jaw with broken teeth. Vertical white lines indicate the position in the jaw of cross sections shown in **(B,C)**. Slices of the upper **(B)** and lower **(C)** jaws show trabeculae running parallel (trab) and perpendicular (trab*) to the section plane. Both globular (tess) and columnar (c-tess) tesserae form the jaw cortex, with hypermineralized "spokes" (sp) visible as regions of higher grayscale intensity, reinforcing the joints between tesserae. Tooth developmental stages can be distinguished in both sections, where newly formed teeth are hollow and progressively filled with mineralized dentin. Teeth typically exhibit surface ornamentation in the form of eight ridges, sculpted from the enameloid of each tooth crown. A bulk of unmineralized connective tissue (including jaw perichondrium and dental ligament) is visible between the teeth and tesserae (star). All scale bars 1 cm. Abbreviations: dent, dentin; enam, enameloid; ri, ridges; sp, spokes; tess, tesserae; c-tess, columnar tesserae; t, tooth; trab, trabeculae. Images from sample BMNH 2015.1.25.5 (24 cm).

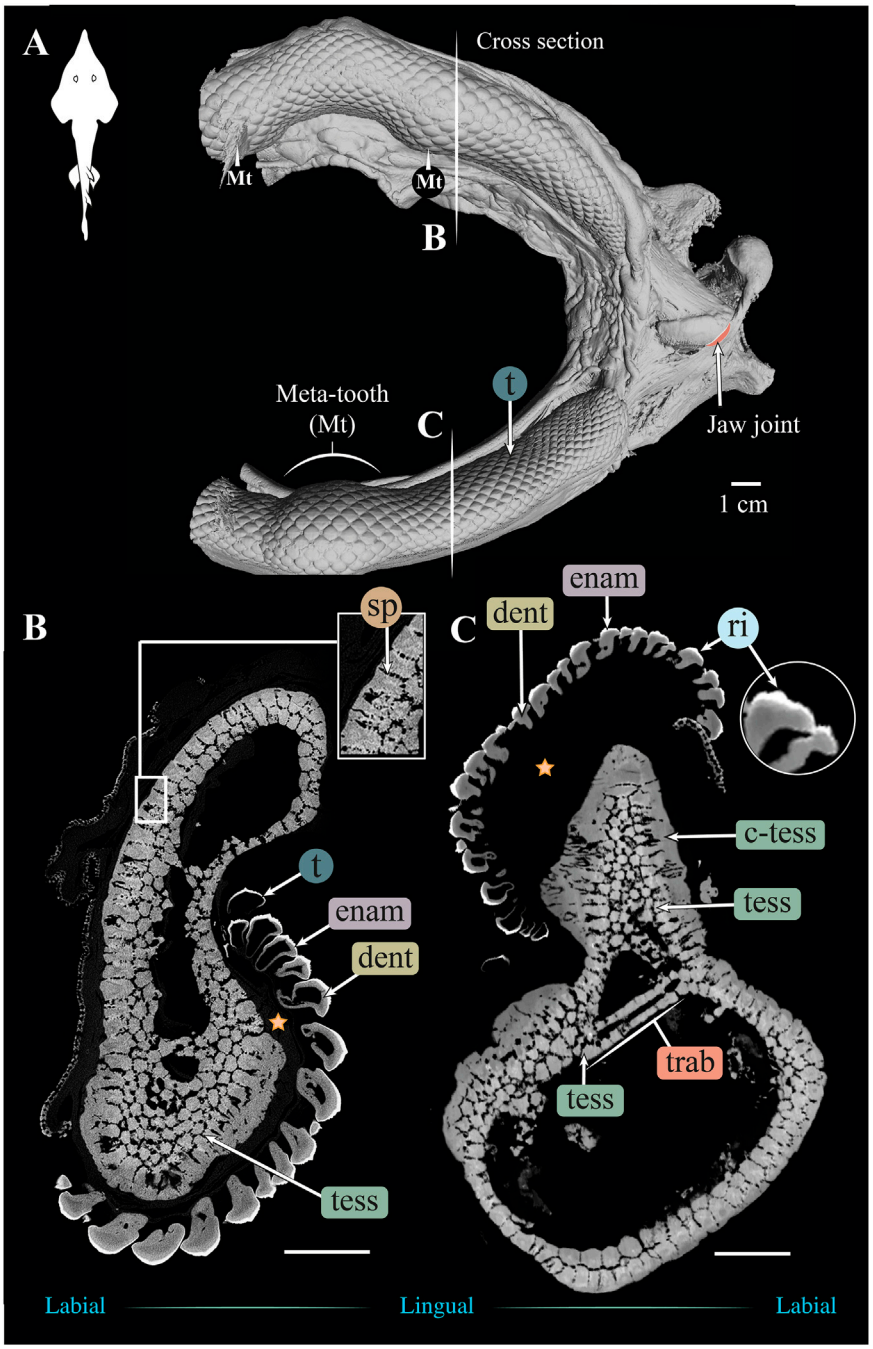

FIGURE 4
3D reconstruction and cross section of a *Rhynchobatus australiae* jaw. **(A)** 3D reconstruction of upper and lower jaws, showing the distinctive undulating dentition and several bulbous "meta-teeth" (Mt) on the upper and lower jaw. Vertical white lines indicate the position in the jaw of cross sections shown in **(B,C)**. Slices of the upper **(B)** and lower **(C)** jaws show trabeculae (trab) running largely parallel to the section plane (compare with the *Rhina* jaw in Figures 3B,C). Both globular (tess) and columnar (c-tess) tesserae form the jaw cortex, with hypermineralized "spokes" (sp) visible as regions of higher grayscale intensity, reinforcing the joints between tesserae (compare with the cortex of the *Rhina* jaw in Figure 3B, constructed from more numerous and smaller tesserae). Tooth developmental stages can be distinguished in both sections, where newly formed teeth are hollow and progressively filled with mineralized dentin. Teeth typically exhibit surface ornamentation in the form of low ridges, sculpted from the enameloid of each tooth crown. A bulk of unmineralized connective tissue (including jaw perichondrium and dental ligament) is visible between the teeth and tesserae (star). All scale bars 1 cm. Abbreviations: dent, dentin; enam, enameloid; ri, ridges; sp, spokes; tess, tesserae; c-tess, columnar tesserae; t, tooth; trab, trabeculae. Images from sample BMNH 2017.7.11.1 (28 cm).

cartilage has been modified throughout elasmobranch evolution to meet varied performance demands.

Materials and methods

Sample selection and X-ray tomography acquisition

The dried jaw specimens examined in this study are from the Life Sciences Collections, Natural History Museum, London (BMNH) (Supplementary Table S1). Two specimens were used for the bulk of detailed analysis—*Rhina ancylostoma* (BMNH 2015.1.25.5) and *Rhynchobatus australiae* (BMNH 2017.7.11.1)—with additional higher-resolution scans focused on the regions of interest at the proximal ends of the lower and upper jaws. Other specimens of different sizes—*Rhina* (BMNH 2014.11.11.1) and *Rhynchobatus* (NHMUK PV P4048 and two unregistered specimens) — were scanned to investigate how tesserae and jaw trabeculae vary with age. The original body sizes of the animals from which specimens came were unknown and so jaw size (i.e. the outer jaw width at the jaw joints) was used as a proxy for age (i.e. larger jaws were assumed to come from larger and therefore older animals). A previous study (Dean et al., 2017) estimated *Rhynchobatus* jaw width to be ~7–11% of total length and our measurements from two intact *Rhina* specimens (95.5 and 147 cm TL) and dried jaws from six specimens from animals of known total length suggest a similar ratio (~11–15% of TL). Based on available size at maturity information for both species (Last et al., 2016; Purushottama et al., 2020), the jaw specimens used in our study (Supplementary Table S1) are likely all from mature individuals, an assertion supported by the high degree of mineralization of the skeleton (Seidel et al., 2016). It should be noted that two of the *Rhynchobatus* jaws could not be confidently identified to species; although available information indicates that all *Rhynchobatus* species include some amount of hard-shelled prey in their diet (e.g. Darracott, 1977; Moazzam and Osmany, 2020; Purushottama et al., 2020). Additionally, for comparative purposes, the upper and lower jaws of the durophagous stingray *Aetobatus* ex. gr. *narinari* (BMNH 2015.1.25.4; Myliobatiformes) and of the non-durophagous skate *Raja clavata* (BMNH 2015.1.25.2; Rajiformes) were scanned and examined.

Micro-CT imaging was performed at the Imaging and Analysis Centre, Natural History Museum, London, using a Nikon Metrology HMX ST 225 with a reflection target. The eight specimens listed above were scanned, as well as several selected regions imaged at smaller voxel sizes in both *Rhina* and *Rhynchobatus*, producing 12 separate data sets. X-ray source conditions ranged from 100 to 190 kV adjusted for field of view differences and sample density. A range of voxel sizes were achieved (26–121 μm), with smaller image pixel sizes utilized for quantifying tesserae dimensions. For a detailed list of micro-CT scan parameters and specimen information, *see* Supplementary Information, Supplementary Table S1.

Image processing

All scans were processed, rendered, and analysed using Avizo/Amira (version 9.4 and above or Amira ZIB Edition). Each acquisition was enhanced using a "low level" non-local means filter to reduce imaging noise from the data. Individual jaw elements were separated (segmented) for comparative analysis, using volume editing tools to isolate the lower jaw (Meckel's cartilage) from the upper jaw (palatoquadrate), and to separate the left and right jaw moieties at the symphyses.

Terminology

Anatomical terminology used is presented visually in Figure 2. "Proximal" indicates a position or direction toward the jaw joint and "distal" toward the jaw symphysis. "Symphyseal" refers to the (distal) midline joint between the two jaw halves, with "parasymphyseal" regions flanking the jaw symphysis laterally (e.g. Underwood et al., 2015). "Oral" is towards the biting surface of the jaw or teeth, with "aboral" indicating the opposing surface. "Labial" refers to the outer surface of the jaw, and "lingual" to the inner (pharyngeal) surface of the jaw. "Cortical" refers to a position or direction toward the jaw's cortex, the outer mineralized rind comprising single or multiple layers of tesserae. "Perichondral" is used similarly, to indicate tesserae or portions of tesserae associated with the unmineralized, collagenous perichondrium that wraps the outer surface of tessellated cartilage skeletons (Seidel et al., 2020, 2021).

Measurements

Cortical and tooth thickness

The thickness of the jaw cortex and the dentition was measured from the full jaws of *Rhina* (Figure 3) and *Rhynchobatus* (Figure 4), on a mesh generated from the segmented volumes of the whole jaw specimen scans. Meshes were generated for the upper and lower jaws, and the upper and lower dentitions for each species; the upper and lower jaw cartilages were analysed independently from the dentition. The use of meshes simplified the process of bulk linear measurements and allowed thickness to be color-coded over the entire jaw surface: meshed surfaces were minimally smoothed and simplified to reduce computational resources needed, then thickness was determined by measuring the distance between two opposing vertices in the mesh that were

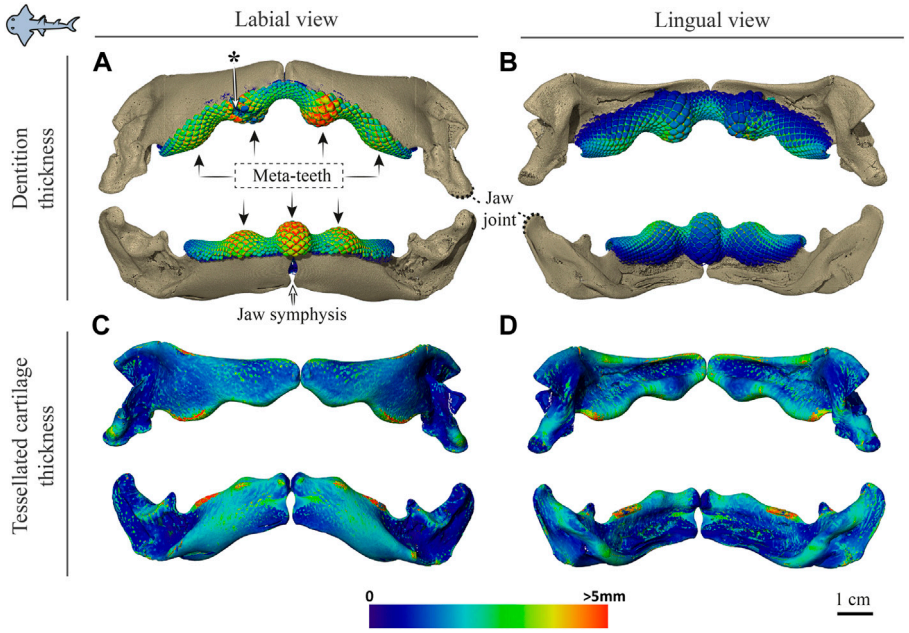

FIGURE 5
Dentition and tessellated cartilage thickness in the jaws of *Rhina ancylostoma*. **(A,B)** Color-coded dentition thickness, and **(C,D)** jaw cortex (tessellated cartilage) thickness. Both upper and lower jaws are shown in labial **(A,C)** and lingual **(B,D)** views. Black arrows in **(A)** indicate the positions of the meta-teeth in the lower and upper jaw. Asterisk in **(A)** indicates a region of tooth breakage (*see* also Figure 3A). Note also the gap between left and right jaw moieties, illustrating the lack of symphyseal fusion. Thickness is represented by a physics color map, with regions in red being thicker than 5 mm. Images from sample BMNH 2015.1.25 (24 cm).

both nearest and parallel (or very close to parallel) to each other. To visualize thickness variation, measurements were then represented by a surface scalar field for each vertex and a physics color map with a range of 0 to >5 mm, with thickness above 5 mm represented as red (Figures 5, 6). This process allowed quantification and visualization of the bulk thickness of the jaw cortex (regardless of the number of tesseral layers) and the dentition (i.e. tooth height, including the contributions of enameloid and dentin). For comparative purposes, additional meshes were generated and similarly quantified for the upper and lower jaw cartilages and dentitions of *Aetobatus* ex. gr. *narinari* (Figure 7) and *Raja clavata* (Figure 8).

Tesserae

Qualitative evaluation of the arrangements and morphologies of tesserae in the jaw cortex were performed on scan slice data and volume-renderings. To quantify aspects of tesseral morphology, the smallest possible voxel size was necessary to resolve tesserae boundaries successfully, but this came at the expense of scan volume: whereas entire jaws could be scanned from smaller specimens (i.e. the two smallest *Rhynchobatus* jaws, 11 and 18 cm [unregistered specimens]), ROI-scans were necessary to quantify tesserae morphometrics in larger specimens (lower right jaws of *Rhynchobatus*, NHMUK PV P4048 and BMNH 2015.1.25.5; lower right jaw of *Rhina*, BMNH 2014.11.11.1 and 2015.1.25.5; Supplementary Table S1). The dimensions of individual tesserae were investigated in the entire jaws of the small specimens and across four ROIs at the proximal ends of both the upper and lower jaws of the larger *Rhina* and *Rhynchobatus* (Figures 9, 10 and Supplementary Table S2); these regions were chosen for their comparatively simple cross-sections and the fact that they could be consistently compared across individuals and species (avoiding the undulating morphologies of the symphyseal regions, which become more pronounced with age). The mineralized tissue was segmented and individual tesserae isolated using the Separate Objects module with a marker extent of "2" (relating to the size of the seeds marking objects for separation). Segmentation of individual tesserae was possible due to the narrow gaps between tesserae (i.e. intertesseral joints) and with a high level of accuracy, particularly where high magnification was achieved. The Separate Objects module applies the Chamfer method which splits volumetric bodies that touch only partially with neighbouring bodies (e.g. at the "intertesseral contact zones," where tesserae abut; Seidel et al., 2016; Jayasankar et al., 2020). Using this method, structures with strong overlap are not separated. In our data, once tesserae were segmented from one another, we recorded their locations (X, Y and Z

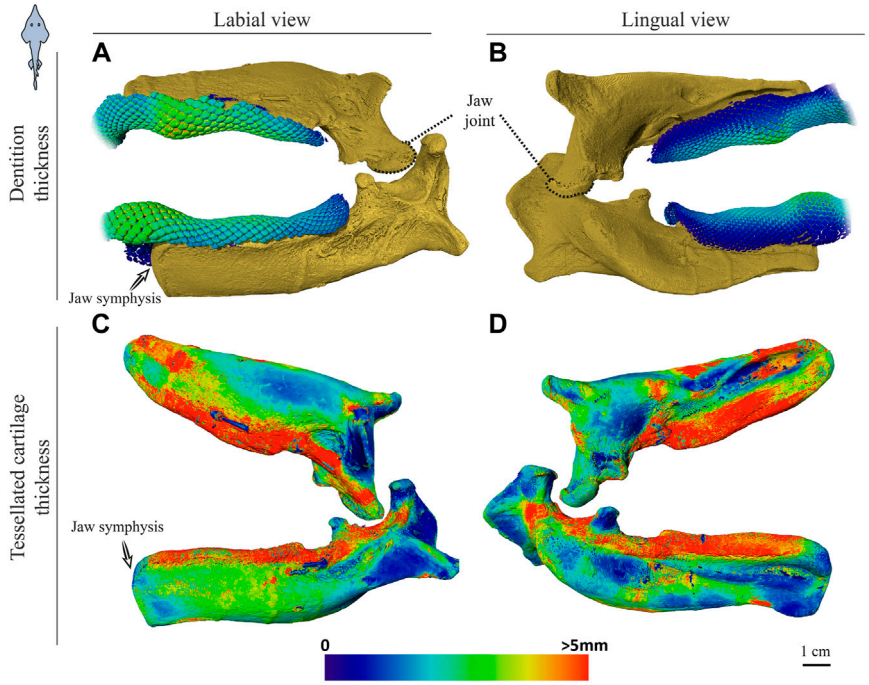

FIGURE 6
Dentition and tessellated cartilage thickness of the left jaw moieties of *Rhynchobatus australiae*. **(A,B)** Color-coded dentition thickness, and **(C,D)** jaw cortex (tessellated cartilage) thickness. Both upper and lower jaws are shown in labial **(A,C)** and lingual **(B,D)** views. As in the *Rhina* jaws (Figures 5C,D), the symphysis is unfused (note the anatomical edge of the jaw halves). Thickness is represented by a physics color map, with regions in red being thicker than 5 mm. Images from sample BMNH 2017.7.11.1 (28 cm).

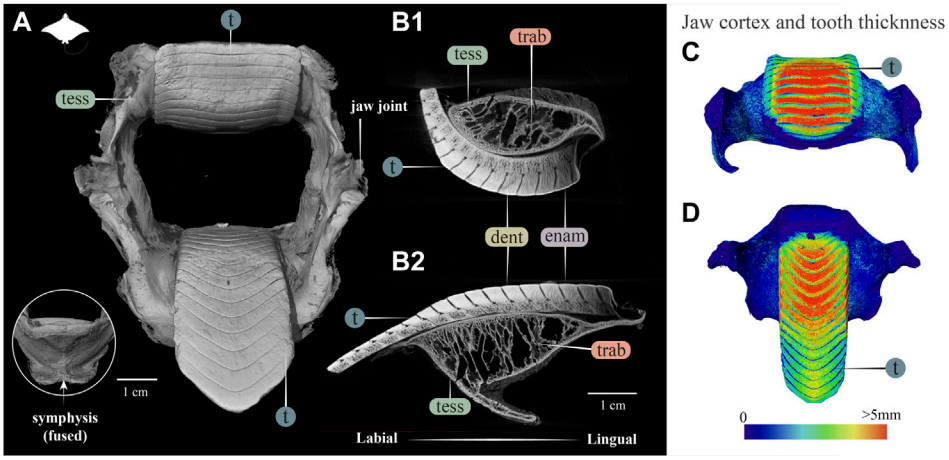

FIGURE 7
3D reconstruction, cross section and thickness analysis of the jaw of an eagle ray jaw (*Aetobatus* ex. gr. *narinari*). **(A)** 3D reconstruction of upper and lower jaw and teeth in labial view. The inset shows the fused symphysis beneath the dentition. **(B)** Slices through the opposing upper **(B1)** and lower **(B2)** jaws, showing a cross section of the jaw skeleton, comprising a cortex of tesserae and internal trabeculae, and surmounted by interlocked teeth. Note that the cortex is comprised of fewer layers of tesserae and trabeculae exhibit more of a hierarchical branching pattern than in the jaws of *Rhina* (Figure 3) and *Rhynchobatus* (Figure 4). A visible progression of teeth development can be seen (moving from right to left in B1 and B2), characterized by a more porous dentin in newly formed teeth, infilled with mineralized dentin as teeth become functional. **(C,D)** Jaw cortex and tooth thickness are represented by a physics color map with regions in red being thicker than 5 mm. Abbreviations: enam, enameloid; dent, dentin; tess, tesserae; t, tooth; trab, trabeculae. Images from sample BMNH 2015.25.4 (7.5 cm).

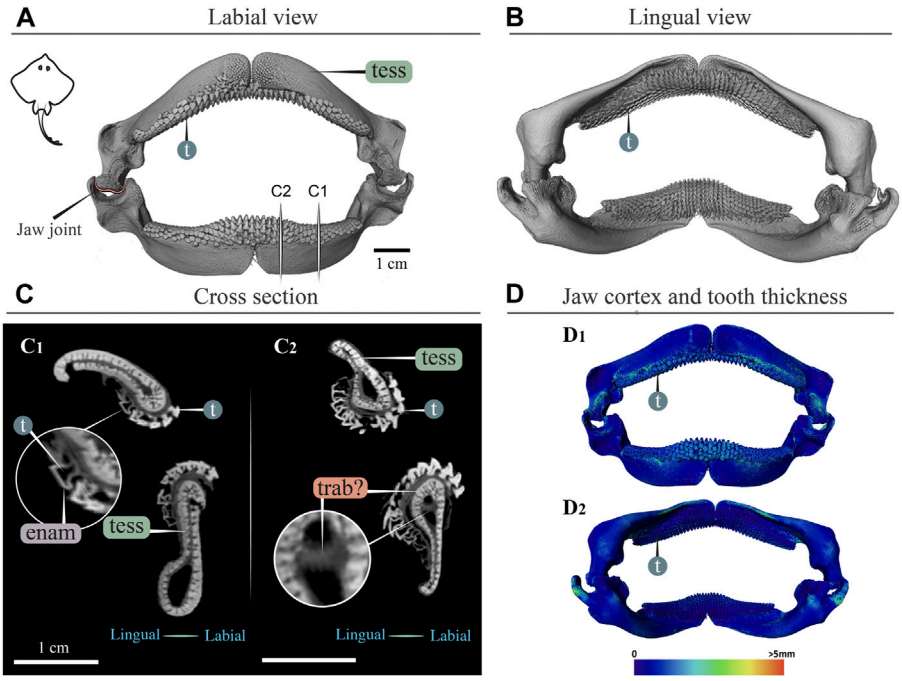

FIGURE 8
3D reconstruction, cross section and thickness analysis of a skate jaw (*Raja clavata*). 3D reconstruction of upper and lower jaw with labial **(A)** and lingual **(B)** views of the jaws and teeth. Vertical white lines in A indicate the position in the jaw of cross sections shown in C1 and C2. **(C)** Slices show cross sections of the upper and lower jaws at two positions **(C1**,**C2)**. Tooth developmental stages can be distinguished in both sections, where newly formed teeth are hollow and progressively filled with mineralized dentin. Note that the cortex comprises only a single layer of tesserae, with a single potential trabecula (trab?) passing through the jaw. **(D)** Jaw cortex and tooth thickness are represented by a physics color map with regions in red being thicker than 5 mm (**D1** labial view, **D2** lingual view). All scale bars 1 cm. Abbreviations: enam, enameloid; dent, dentin; tess, tesserae; t, tooth; trab?, potential trabecula. Images from sample BMNH 2015.25.2 (9 cm).

coordinates of their centroids) and also approximated their sizes by measuring the major, intermediate and minor axis lengths of a bounding box enclosing all of the voxels belonging to each tessera (Supplementary Figure S1). Although this high-throughput size estimation calculates the length, width and thickness of every tessera's bounding box, it does not determine how the bounding box's orientation is linked to the tessera's anatomical orientation. In other words, the method can calculate, for example, the longest dimension of a tessera's bounding box, but not whether this is the tessera's "width" or its "thickness" (i.e. the dimension parallel to the surface of the jaw vs perpendicular to it; *see* Supplementary Figure S1); addressing this challenge requires a method for identifying which tesseral face is associated with the skeletal surface, a feature unavailable in the segmentation and analysis software. As a result, in the current study, we only report the bounding box's smallest linear dimension as an indication of "tesseral size." We found this to be a reliable and usefully conservative general measurement for illustrating local variations in tesseral size, particularly since the longest bounding box dimension is heavily biased by tesseral fusions (*see* Results) and since length is a more anatomically intuitive metric than volume for tesserae. Measured values for tesserae size (Supplementary Table S2) were in reasonable agreement with 2D measurements from previous works (e.g. Dean et al., 2009; Seidel et al., 2016, 2021; Maisey et al., 2021), supporting the validity of our method. Comparisons of the various possible tesseral measurements and the development of methods for anatomical orientation of bounding boxes will be addressed in a future work (B. Yang et al., in preparation). Tesserae size distributions were plotted for all specimens of both species across eight size bins, distributed equally between each species' minimum and maximum tesseral sizes (Figure 11). Tesseral size was also represented in jaw volume renderings with color maps grading from dark red to pale yellow (Figures 9, 10 and Supplementary Figures S1, S2, Supplementary Table S2).

Trabeculae

Trabeculae position and orientation were examined from scan slice data and volume-renderings. In addition, trabeculae were manually segmented from the full jaw scans of both species—the right upper and lower jaw moieties in *Rhina* (BMNH 2015.1.25.5) and the left upper and lower jaw

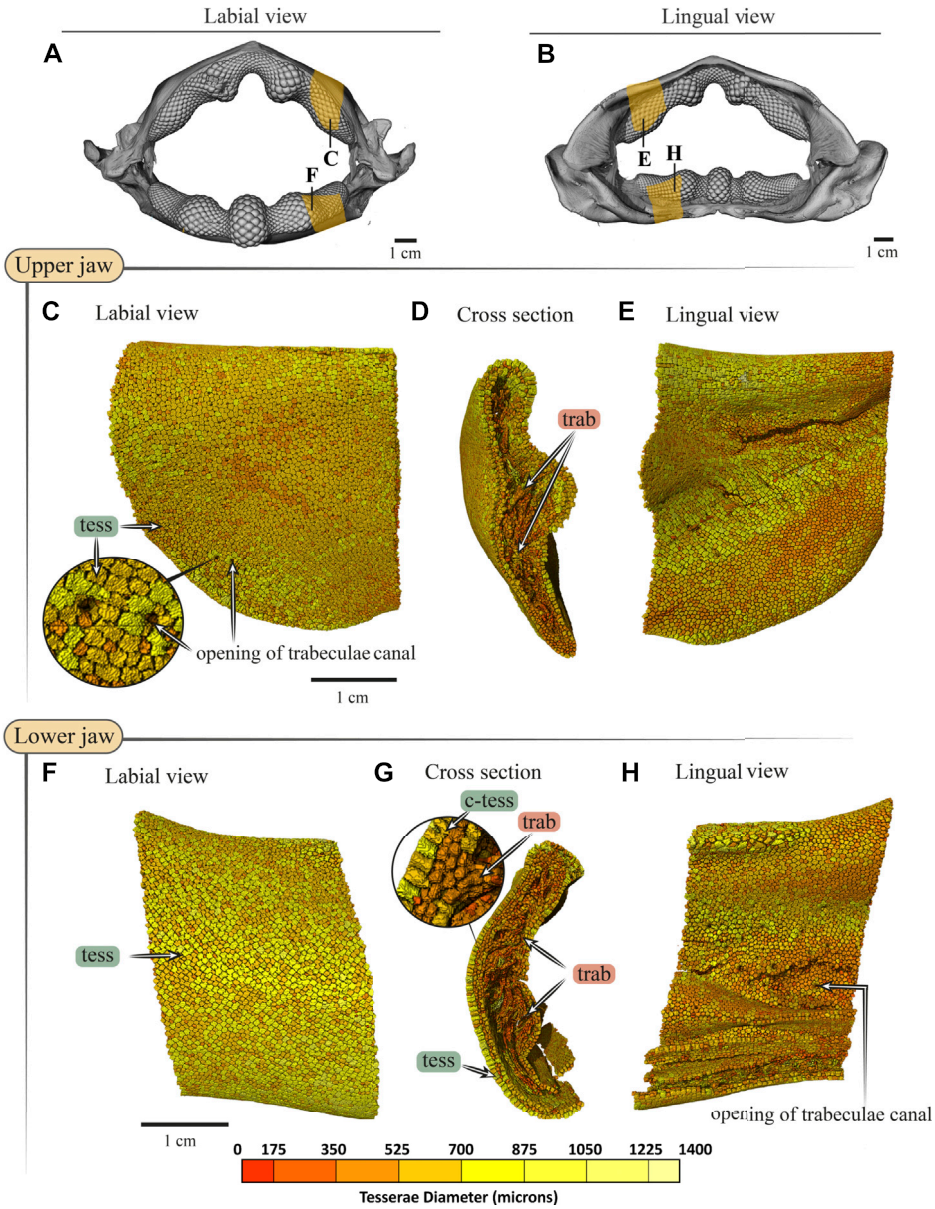

FIGURE 9
Tesserae size variation in the jaws of *Rhina ancylostoma*. **(A,B)** 3D rendering of *Rhina ancylostoma* jaws, in labial **(A)** and lingual **(B)** views, showing the regions of interest (yellow) used for tesserae size analysis. The scale for tesserae size color-coding is shown at the bottom of figure. **(C–E)** Tesserae color-coded according to their size in labial, cross-section and lingual views of the upper **(C–E)** and lower **(F–H)** jaw. The pores visible in the labial cortical surface are openings for trabeculae canals **(C,H)**, and volume-rendered trabeculae can be seen running through the cross-section **(D,G)**. **(F–H)** Columnar tesserae (c-tess) form the superficial portion of the cortex in both upper and lower jaws. Note that tessera size is not uniform, but rather varies across the cortical surface. All scale bars 1 cm. Abbreviations: c-tess, Columnar tesserae; tess, tesserae; trab, trabeculae. Full jaw images are from sample BMNH 2015.1.25.5 (24 cm) and regions of interest images are from sample BMNH 2014.11.11.1 (35 cm).

moieties in *Rhynchobatus* (BMNH 2017.7.11.1) — by combining region-growing and selective thresholding, using a brush tool to separate the trabeculae from the cortical mineralized cartilage. Trabeculae prevalence was then quantified as a percent volume fraction relative to the total volume of mineralized jaw cartilage (including trabeculae; Supplementary Table S3). To further visualize interspecies differences, trabeculae were also volume-rendered using a red to light yellow color map with the remaining (non-trabecular) mineralized tissue (i.e. the jaw cortex) visualised in transparent grayscale (Figure 12).

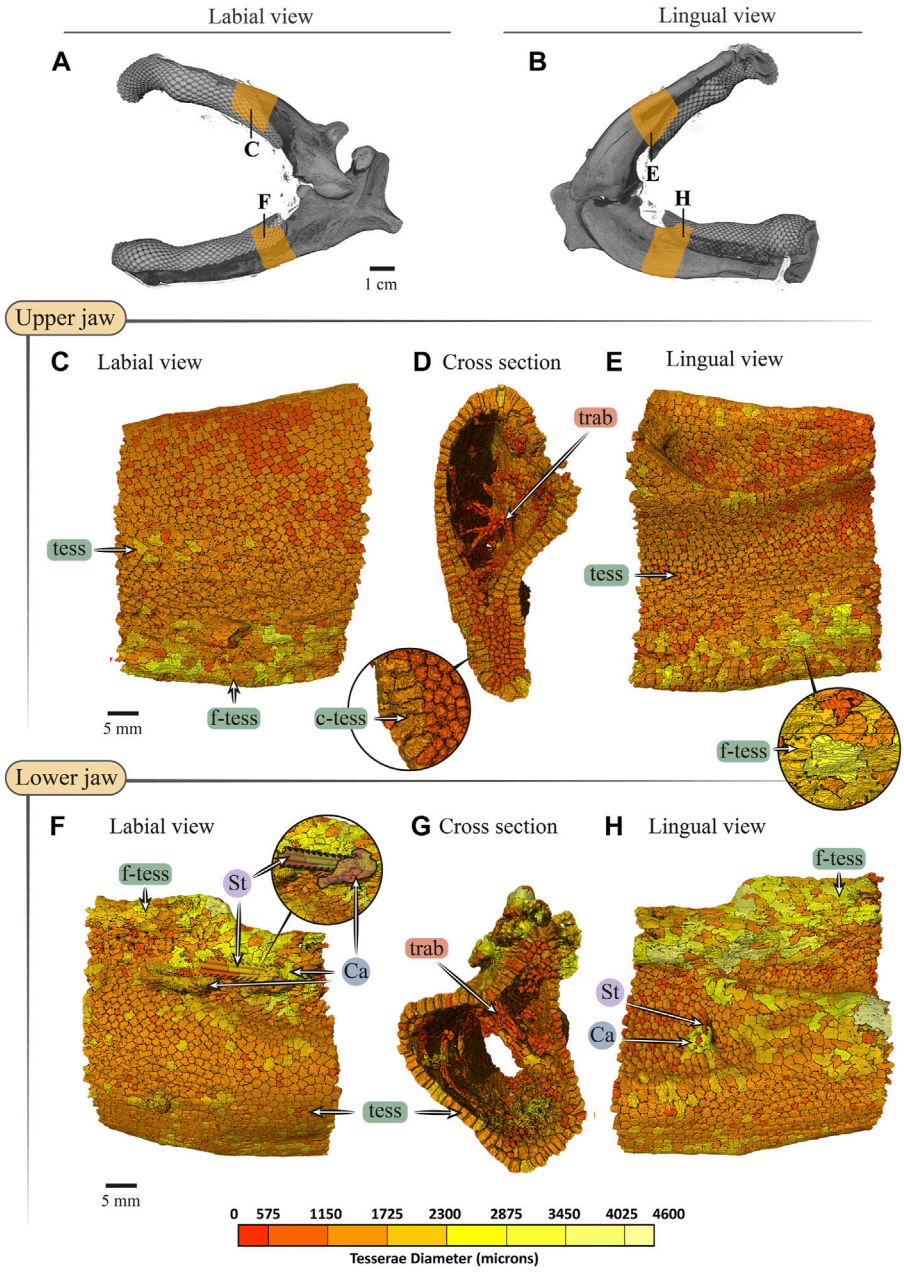

FIGURE 10
Tesserae size variation in the jaws of *Rhynchobatus australiae*. **(A,B)** 3D rendering of *Rhynchobatus australiae* jaws, in labial **(A)** and lingual **(B)** views, showing the regions of interest (yellow) used for tesserae size analysis. Tesserae color-coded according to their size in labial, cross section and lingual views of the upper **(C–E)** and lower **(F–H)** jaw. Volume-rendered trabeculae can be observed running across the cross sections of the upper **(D)** and lower jaws **(G)**. Columnar tesserae (c-tess) form the superficial portion of the cortex **(inset in D,G)**. In labial **(F)** and lingual **(H)** views, a barb/sting from a stingray can be observed embedded in the jaw, being surrounded with a mineralized callus (*see* Dean et al., 2017). Note that tessera size is not uniform, but rather varies across the cortical surface. Abbreviations: Ca, callus; St, sting; tess, tesserae; c-tess, columnar tesserae; f-tess, fused tesserae; trab, trabeculae. Full jaw images are from sample *Unregistered specimen* (11 cm) and region of interest Images are from sample BMNH 2017.7.11.1 (28 cm).

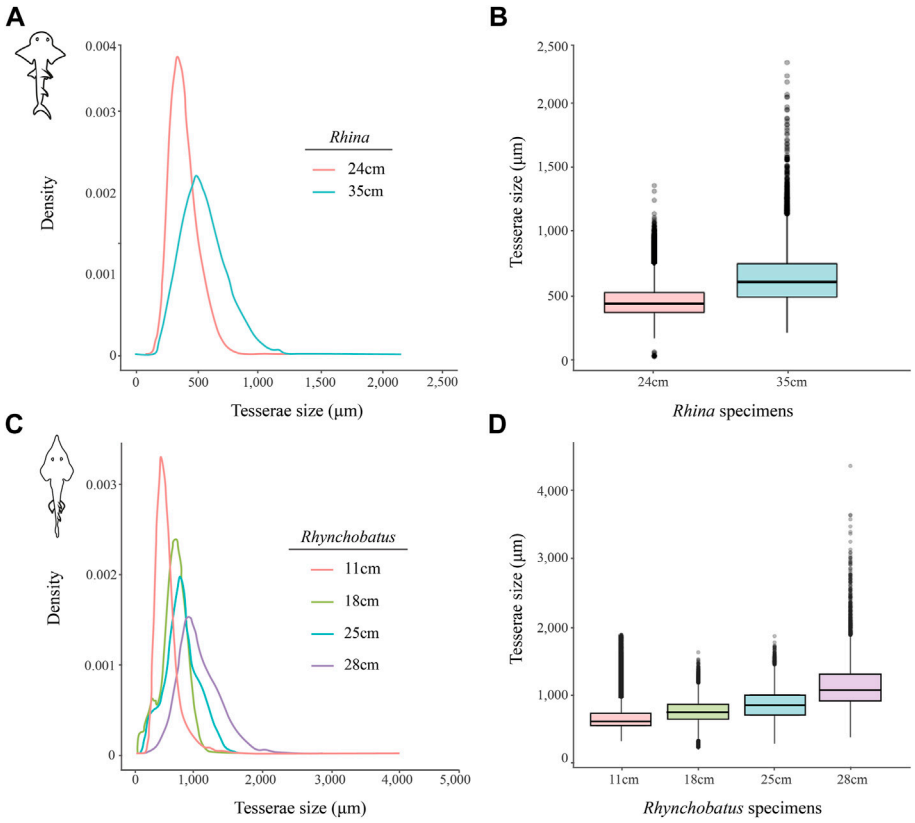

FIGURE 11
Variation of tesserae size across different jaw sizes (ages) in *Rhina* and *Rhynchobatus*. **(A,B)** Density graph **(A)** and boxplot **(B)** showing the distribution differences of tesserae size between two different *Rhina* specimens of different jaw sizes. **(C,D)** Density graph **(C)** and boxplot **(D)** showing the distribution differences of tesserae size among four *Rhynchobatus* specimens of different jaw sizes. All graphs illustrate an increase in tesseral size and a broadening of the size distributions with age. Note the size scale differences between the *Rhina* and *Rhynchobatus* graphs, with relatively larger tesserae in *Rhynchobatus*.

Results

Rhina and *Rhynchobatus*

Gross morphology, jaw cortex and cortical tesserae

Although similar-sized jaws were examined for *Rhina* and *Rhynchobatus*, jaw morphologies and tissue arrangements varied considerably (Figures 3, 4). Our scans revealed that the oral/occlusal edges of both species' jaws echo the undulating morphology of their meta-tooth arrays. The symphyseal regions were exceptions to this, where the largest meta-teeth (on the lower jaw in both species) encircled the unfused symphyseal joint (labeled meta-tooth in Figures 2–4). The symphyseal mandibular meta-tooth was most striking in *Rhina*, forming a robust, denticulate torus around the symphysis (Figure 3). The meta-teeth themselves were not solid masses of mineralized tissue, but rather spheroidal constructions of slightly larger-than-average teeth (*see* section 3.1.3 below), forming a shell around an underlying mass of unmineralized dental ligament and perichondrium (star in Figures 3B,C, 4B,C). In both species, a single ovoid tessellated sesamoid cartilage was seen embedded in the connective tissue of the mandibular meta-tooth, between the tooth layer and symphysis (Figure 12 and Supplementary Figure S1).

Significant differences were also apparent between the species in the thickness of the jaw cortex, how this thickness was constructed, and in the morphologies of the tesserae themselves. The general gross tissue arrangements, however, were similar between the species: beneath the teeth, the jaws were roughly sigmoid or pear-shaped in cross-section, with a pronounced lingual depression housing the youngest portion of the tooth array (hollow, incipient teeth; *see* section 3.1.3 below) and with connective tissue linkages between the tooth array and jaw cortex as described above (dark areas marked with stars in Figures 3B,C, 4B,C). The thickness of the mineralized cortex (composed of tesserae) varied across regions of the jaws in both taxa, in general thickest along the oral jaw surfaces, and thinnest

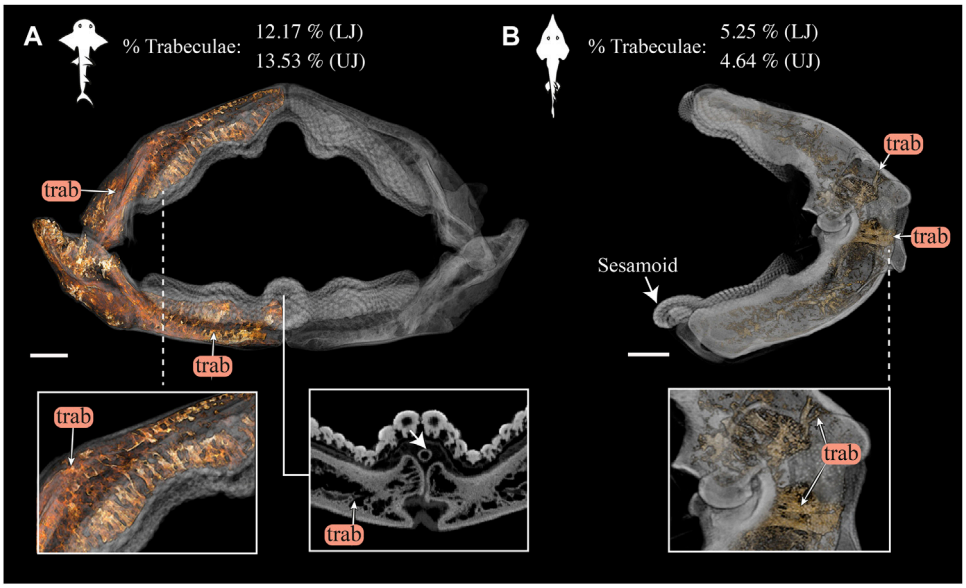

FIGURE 12
3D rendering and volumetric measures of trabeculae in *Rhina* and *Rhynchobatus* jaws. **(A)** 3D rendering of the full jaw of *Rhina ancylostoma*, with trabeculae (trab) highlighted in orange. A higher magnification view (left inset) shows trabeculae of relatively consistent orientation in the parasymphyseal region and a cross-section of the meta-teeth (right inset) shows the sesamoid cartilage (white arrow). **(B)** 3D rendering of the left jaw moiety of *Rhynchobatus australiae*, showing that, although less dense than in *Rhina*, trabeculae are also present, especially in the region surrounding the jaw joint (bottom inset). The mandibular sesamoid of *Rhynchobatus* is visible in the volume rendering in **(B)** (white arrow). The interspecies difference in trabecular density is also quantified in terms of volume percentage of trabeculae at the top of the figure. All scale bars 1 cm. Abbreviations: trab, trabeculae. Images from samples BMNH 2015.1.25.5 (*Rhina ancylostoma,* 24 cm) and BMNH 2017.7.11.1 (*Rhynchobatus australiae,* 28 cm).

near the jaw joint and symphysis (Figures 3B,C, 4B,C, 5C,D, 6C,D). In *Rhina*, the cortex was generally between 0.5 and 1.5 mm thick, however with the cortex visibly thicker along the biting (oral) and contralateral aboral margins (~2–3 mm and up to nearly 5 mm in some areas) (Figures 5C,D). The labial side of the lower jaw was also noticeably thicker than the contralateral lingual face (~2–3 mm; Figures 5C,D), this thickened cortex continuing from the symphysis to the area of the proximal termination of the dentition, approaching the jaw joint. In *Rhynchobatus*, the cortex of the upper and lower jaws was overall notably thicker than in *Rhina* (in most areas >3 mm), with the labial cortex often more than 1 mm thicker than the lingual, and the oral jaw margins strikingly reinforced (>5 mm thick; Figures 6C,D).

In both *Rhina* (Figures 3B,C, Supplementary Figures S2B,C, Supplementary Movies S1, S2) and *Rhynchobatus* (Figures 4B,C, Supplementary Figures S1B,C, Supplementary Movie S3), the jaw cortex is formed from multiple monolayers of tesserae. In virtual sections, a high variation in tesseral shape and size is apparent, with tesserae noticeably larger and fewer in number in *Rhynchobatus* than in *Rhina*, even for jaws of similar sizes (Figures 3B,C versus Figures 4B,C). Unlike the thin plate-like tesserae described for other batoid species (e.g. *see* Fig. 10 in Seidel et al., 2016), in *Rhina* and *Rhynchobatus*, tesserae shapes tended toward columnar (tall and narrow; *c-tess* in Figures 3C, 4C, 9G, 10D) or globular forms (more common; Figures 3B,C, 4B,C), but varied locally across the cross-sections of both species' jaws. In *Rhina*, tesserae in the labial jaw cortex tended to be larger and columnar in shape (Figures 3B,C), in comparison with tesserae of the lingual cortex, which were smaller and arranged in fewer layers, particularly in the lower jaw (Figure 3C). In *Rhynchobatus*, labial and lingual tesserae were more comparable in size (Figures 4B,C).

Within the multiple tesseral layers of the jaw cortex, the outermost/surface layer typically had a more regular morphology (in size and shape) relative to the inner layers, readily distinguishable by eye (*see* below; e.g. Figures 3B,C, 4B,C). Most jaw regions examined in both *Rhina* and *Rhynchobatus* exhibited from three to seven layers of tesserae, with the most numerous tesseral layers observed in association with the jaw's oral surface (beneath the teeth; Figures 3B,C, 4B,C). Oral (sub-dental) multi-layers were observed even in the smallest specimen examined (*Rhynchobatus*, Supplementary Figures 1B,C), although in the largest *Rhina*, the number of oral tesseral layers appeared reduced, compared to the medium *Rhina* (compare Figures 3B,C to Supplementary Figures 2B,C). In sub-dental regions, the number of tesseral layers was challenging to count, as the smaller tesserae there formed a

disorganized scree nearly filling the narrow, labiolingually-compressed interior of the jaw (Figures 3C, 4C, 9D,G, 10D,G). This "tesseral scree" was also occasionally visible in the narrow aboral regions of the jaw (e.g. Figure 4B). Although a multi-layered tesseral cortex was the norm in both taxa, monolayers were present in localized areas of the aboral-lingual margin of the lower jaw of *Rhynchobatus* (Figure 4C). Convex regions of the jaw cortex in all scans had abundant columnar tesserae, often twice as thick as tesserae in flatter areas of the skeleton (Figures 3C, 4C, 9D,G, 10D,G). These tesserae were often somewhat wedge-shaped, slightly wider at their perichondral side.

The tesserae of both species were typically hundreds of micrometers wide, with those of *Rhynchobatus* on average larger than those of *Rhina* (note the scale differences in the color-coding in Figures 9–11 and Supplementary Table S2). Although only region-of-interest scans were performed for larger specimens, all datasets examined included tens of thousands of tesserae (and more than 100,000 tesserae in one case), with the small age series examined exhibiting the same trend for both species: with increasing jaw (and, therefore, animal) size, the distribution of tesseral sizes broadened and shifted toward larger tesserae (Figure 11). Compared to the 24 cm *Rhina* jaw, for example, tesserae in the 35 cm *Rhina* jaw were nearly 40% larger (from 456.8 ± 120.3 μm to 632.3 ± 199.7 μm: mean ± standard deviation; Supplementary Table S2). Similarly, in *Rhynchobatus*, tesserae showed almost a twofold average size increase from the smallest animal to the largest, ranging from 606.6 ± 186.4 μm in the 11 cm jaw to 1086.4 ± 338.6 μm in the 28 cm jaw (Supplementary Table S2). The largest tesserae recorded in both species (2315.4 μm in *Rhina*, 4504.6 μm in *Rhynchobatus*) represent the tesserae we observed beneath the teeth, fused together into mineralized sheets (*see* below; Figures 9, 10).

In jaw cross sections, tesserae showed differences in orientation and connectivity within and among the different tesseral layers (Figures 3B,C, 4B,C and Supplementary Figures S1B,C, S2B,C). In the outermost layer, the contacts between adjacent columnar tesserae appeared tightest peripherally (nearest the perichondrium), especially compared to the looser packing of scree tesserae in deeper layers. Throughout the jaw cortex, minute projections were regularly seen bridging adjacent tesserae (see insets in Figures 3B, 4B); these were often very bright in tomographic slices, indicating they are the hypermineralized "spokes" known to reinforce intertesseral joints in other species (Seidel et al., 2016, 2019, 2020). In *Rhina* and *Rhynchobatus*, multiple spokes could often be seen spanning a single joint space, particularly in the perichondral layer (e.g. Figures 3B, 4B insets). Spokes appeared irregularly distributed in both taxa (i.e. not visible between every tessera in every slice) and were more numerous in *Rhynchobatus*. Spokes were not as apparent in the smallest individual sampled (*Rhynchobatus*, Supplementary Figures 1B,C), nor in the largest (*Rhina*, Supplementary Figures S2B,C). It is unclear from the current data whether this was a function of the spokes being less prevalent (as in younger animals; Seidel et al., 2016), or their presence being masked by the lower resolution resulting from the large field of view needed to scan the largest specimen (Supplementary Table S1).

The density of tesserae (based on gray values, calculated from the attenuation coefficient) appeared generally consistent within datasets, similar to tooth dentin and skin denticles, but less mineral-dense than tooth enameloid (e.g. Figures 3B,C, 4B,C). Whereas smaller specimens of *Rhina* and *Rhynchobatus* showed more consistent density contrast in all tesseral layers (Figures 3B,C and Supplementary Figures S1B,C), in the largest *Rhina* (Supplementary Figures S2B,C) and especially the largest *Rhynchobatus* (Figures 4B,C), tesserae had a visibly lower density in areas directly below the dentition, implying a lower degree of mineralization. In these regions in *Rhynchobatus* and in the very large *Rhina*, tesserae at the oral surface were large and often partially fused together into irregular mineralized masses (e.g. Supplementary Figure S2), in extreme cases resulting in the tesseral pattern being obliterated and replaced by a nearly homogeneous tissue of lower mineral density (Figures 4B,C).

Trabeculae and trabecular tesserae

Trabeculae (reinforcing struts passing through the core of the jaws) were present in both species (Figures 3, 4, 9D,G, 10D,G, 12 and Supplementary Figures 1B,C, 2B,C, Supplementary Movies S1–S3). Trabeculae in *Rhynchobatus* were tessellated tubes with walls one tesseral layer thick (Figures 4B,C, 10D,G). In contrast, in *Rhina*, trabeculae often appeared only partially mineralized (Figures 3B,C), as darker gray (less-mineralized) tubes studded with tesserae. It was impossible to determine, however, the degree to which these trabeculae might have collapsed, lost tesserae, or become degraded as these museum specimens were dried and the internal cartilage pulled away during dehydration.

In both species, trabeculae typically ran between the labial and lingual cortical surfaces (e.g. Figures 3C,D, 4C,D, 12), but with some exceptions (*see* below). The internal canals formed by trabeculae were often open at each end, communicating to the perichondrium through visible pores, particularly in *Rhina* (e.g. Figures 9C,H and Supplementary Figure 2G). In *Rhina*, trabeculae represented 13.6% and 12.2% of the volume of the mineralized tissue in the upper and lower jaws, respectively (Figure 12A and Supplementary Table S3). In contrast, trabeculae were far less dominant in *Rhynchobatus*, representing only 5.2% and 4.7% of the upper and lower jaw volumes, respectively (Figure 12B and Supplementary Table S3). The abundance of trabeculae in *Rhina* was particularly apparent in the distal jaw region associated with teeth, where trabeculae dominated the interior of the jaw, orientated in numerous directions (oral-aboral, labio-lingual; Figures 9D,G, 12A), and even appearing to course parallel to the cortex of the oral surface (i.e. in the proximo-distal direction) in some areas (e.g. circular

trabecular sections in Figures 3B, 12A [*trab**] and Supplementary Movies S1–S3). In contrast, trabeculae in *Rhynchobatus*, tended to be oriented labio-lingually, although some proximo-distal trabeculae were also observed (Figures 4B,C, 10D,G, 12B).

Teeth

Our tomographic slices provided clear views of the process of tooth development in both species (Figures 3B,C, 4B,C and Supplementary Figures S1B,C, 2B,C). New teeth arose at the lingual side of the jaw, appearing in our micro-CT data as hollow shells covered by dense enameloid caps and anchored to the dental lamina by thin dentin bases. As the teeth developed and progressed labially, the enameloid layers became thicker and the interior pulp cavities were gradually filled with mineralized dentin, before the teeth reached their functional positions. In some sections, the enameloid layer of post-functional teeth appeared slightly thinner, suggesting some wear. The enameloid layer was thicker on average in *Rhina* (Figures 3B,C versus Figures 4B,C). Both species showed surface ornamentation on their teeth: a single latero-medial ridge on each tooth crown of *Rhynchobatus* (occasionally with smaller secondary ridges visible in cross section; inset in Figure 4B), in contrast to a series of labio-lingual ridges in *Rhina* (typically eight per tooth; inset in Figure 3C). These ornamentations were sculpted predominantly from enameloid, with only a slight associated undulation of the enameloid-dentin junction. In cross-section, points of direct labio-lingual contact were visible between teeth in a tooth file (labio-lingual series; Figures 3B,C, 4B,C), the teeth touching at only a single point in *Rhynchobatus*, but effectively interlocking in *Rhina*. In both species, points of contact always appeared to be between enameloid-coated tooth regions, not where dentin was exposed.

Teeth in both taxa were largest and the dentitions thickest where associated with the meta-teeth: at the symphysis on the lower jaw and parasymphyseally on the upper jaw in both species, with additional less pronounced meta-teeth also present parasymphyseally on the lower jaw in *Rhina* (Figures 3A,B, 4A,B, 5A,B, 6A,B). Conversely, the concave regions of the undulating dentition (i.e. those that "received" the meta-teeth) were covered by comparatively small teeth. The largest teeth (those forming the meta-teeth) were also slightly more bulbous, whereas the teeth associated with concave regions of the jaws and the proximal end of the dentition were slightly flatter (Figures 3, 4). In jaws of similar size (e.g. Figures 5A,B, 6A,B), the dentition of *Rhina* was more robust (typically ≥1 mm thicker).

Myliobatiformes (*Aetobatus*), Rajiformes (*Raja*)

The dentition of the durophagous stingray *Aetobatus* (Myliobatiformes) consists of a single symphyseal file of elongate teeth in both the upper and lower jaws (Figure 7). *Aetobatus* teeth were much thicker than the jaw's cortex (Figures 7C,D), which bore several tesseral layers in the upper jaw (four to five layers, in some areas), but fewer in the lower jaw (Figures 7B1,B2 and Supplementary Movie S4). As with *Rhina* and *Rhynchobatus*, the regions with the most cortical tesseral layers were directly beneath the functional teeth, although the number of cortical tesseral layers was generally far fewer than in the rhinopristiform taxa. *Aetobatus* tesserae ranged in size from ~100 to 500 µm, with no irregularly-shaped tesserae observed (e.g. the perichondral columnar tesserae of *Rhina* and *Rhynchobatus*). The teeth were capped by a thin layer of enameloid (<300 µm thick), with the bulk of the tooth thickness provided by dentin. As with *Rhina* and *Rhynchobatus*, gray values of micro-CT data show that internal teeth tissues gradually mineralize during development, with the dentin of the newest forming teeth being poorly mineralized, compared to the more highly mineralized functional teeth. In *Aetobatus*, however, older teeth were considerably worn, being only ~10% their starting height (apparently due to removal of both enameloid and dentin). Trabeculae were far more numerous than in either *Rhina* or *Rhynchobatus*, representing 37.1% and 33.2% of the mineralized tissue volume of the upper and lower jaws, respectively. *Aetobatus* trabeculae occurred throughout the jaw (Figures 7B1,B2 and Supplementary Movies S1–S6), running primarily from the oral to aboral jaw surfaces. Trabeculae in this species were also more irregularly-shaped than in either rhinopristiform species, appearing to branch and anastomose toward the oral jaw surface. Although trabeculae were tessellated near the oral surface of the jaw, aborally, trabeculae appeared to lack tesserae (as in *Rhina*, described above).

In *Raja*, the teeth were small and pointed with a thin enameloid cover (Figure 8; a male specimen, in females the teeth are also small, but flatter and rounded; Underwood et al., 2015), and of similar thickness to the jaw cortex (Figure 10D). Tesserae in *Raja* range between 400 and 900 µm in size, having the regular prismatic shape previously described for batoid fishes (Seidel et al., 2020). In cross section, the cortical tesserae appeared thicker than those of *Aetobatus*, although only a single layer was present in *Raja*, except beneath the dentition, where additional layers of smaller tesserae occurred (Figure 8C). Trabeculae were absent, although what appeared to be an unmineralized or poorly mineralized strut was visible in one section (Figure 8C2).

Discussion

The rhinopristiform species investigated here demonstrate multiple strategies for jaw reinforcement against a hard prey diet, indicating species- and order-level differences, while also illustrating that the accepted anatomical correlates of durophagy in elasmobranchs (e.g. Summers, 2000; Dean et al.,

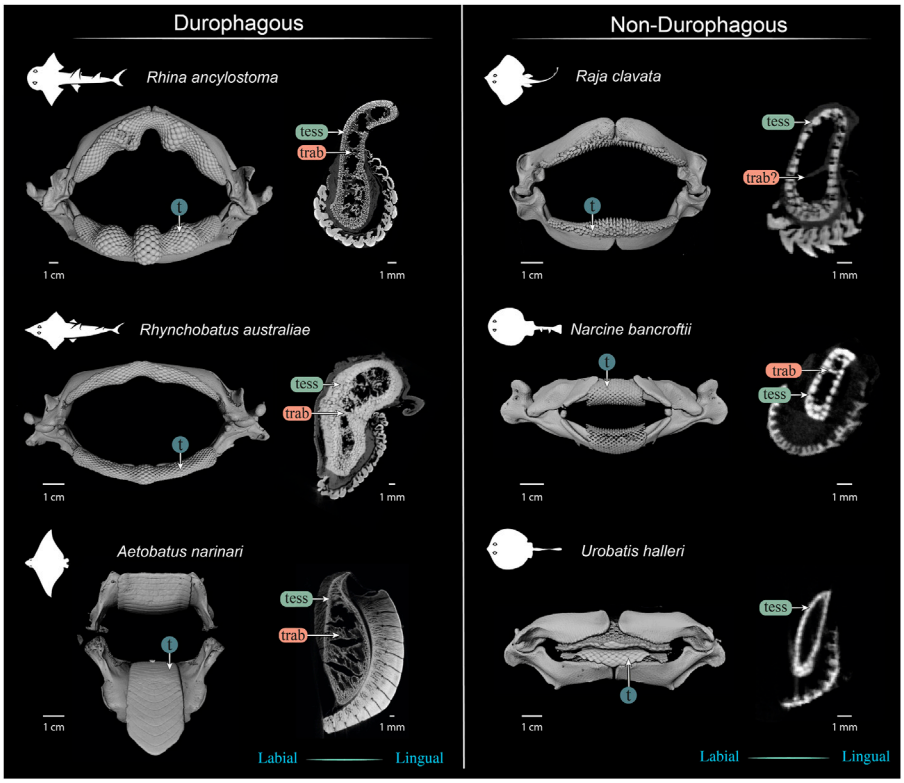

FIGURE 13
Comparison of jaws and upper jaw cross sections of durophagous (left) and non-durophagous batoid species (right). The durophagous batoid jaws shown here are highly "structured," involving large tesserae and/or numerous tesseral layers reinforcing the cortex, and well-defined tessellated trabeculae (trab), but the preponderance of these characters varies among the species shown here. The non-durophagous jaws are simpler in their cross-sectional shape and sheathed mostly in a single layer of tesserae, but some regions bear features previously associated only with durophagous taxa. For example, multiple tesseral layers are visible in the jaw cortex at the oral ends of all jaw cross sections (beneath the teeth) and sparse load-leading trabeculae are visible in the jaws of *Narcine bancroftii* and perhaps in *Raja clavata* (trab?), that of the latter albeit not surrounded by tesserae. In contrast, the jaws of *Urobatis halleri* were entirely devoid of trabeculae and bore a comparatively thin cortex. The *Narcine* and *Urobatis* scans are from unregistered specimens, scanned for other studies.

2006; Seidel et al., 2021) are more varied and modular than previously appreciated.

Tesserae

Although closely related, *Rhina* and *Rhynchobatus* exhibited clear differences in overall thickness of the jaw cortex; in degrees of mineralization in tesserae associated with the jaw cartilage; in size, shape and arrangement of individual tesserae; in number, location, orientation and degree of mineralization of trabeculae; and in thickness of enameloid and the functional dentition (Figures 1, 3, 4). Both species, however, shared an obvious reinforcement of dental and skeletal features in association with the occlusal regions of the jaw. In both taxa, larger jaws exhibit greater cortical thickness distally along the jaw at the oral surface (Figures 5, 6). In *Rhynchobatus*, the cortical thickness below the dentition (in the form of multiple layers of tesserae) can be more than double that of *Rhina* (Figures 3–6, 9, 10). This thickening, however, is not the result of *Rhynchobatus* possessing more layers of tesserae, but rather having larger tesserae overall (Figures 9,10 and Supplementary Table S2). In contrast, in *Rhina*, local cortical thickening is accomplished through assemblies of smaller tesserae arranged into a thickened, disorganized scree (Figure 3).

In the rhinopristiform species we examined, dentition-associated cortical thickening apparently becomes more pronounced with age, suggestive of an adaptive response. Tessellated cartilage is believed to have limited to no remodeling ability (Clement, 1992; Dean et al., 2015; Marconi et al., 2020) and therefore the mineralized layer can only grow through addition of new material (Dean et al., 2009, 2017; Seidel et al., 2016). Across the *Rhina* and *Rhynchobatus* specimens examined, the distribution of tesseral sizes broadens and shifts in the direction of increasingly larger tesserae as animals increase in size (Figure 11 and Supplementary Table S2). These data

therefore provide the first broadscale support of a tessellated cartilage growth hypothesis based previously only on 2D slices from limited numbers of tesserae, arguing that skeletal growth is accomplished (at least in part) by tesserae increasing in size with age (Dean et al., 2009; Seidel et al., 2016, 2019). Growth of the cortex could also be a function of the addition of new (small) tesserae interstitially in the tesseral layer; however, the rightward shifting of our tesseral size distributions away from smaller tesserae argues this mechanism is either not occurring or is comparatively uncommon.

Our data also suggest that tesserae may not be growing at uniform rates. In *Rhynchobatus*, tesseral size appears to become more heterogeneous with age: in comparison with the smaller individuals, tesserae size in the larger *Rhynchobatus* specimen is more variable (Figures 11C, D and Supplementary FigureS1). In both *Rhynchobatus* and *Rhina*, the perichondral (outermost) tesseral layers involve massive tesserae with striking columnar morphologies (Figures 3, 4, 9, 10). Such high-aspect-ratio tesserae have been likened by Maisey et al. (2021) to the "voussoir" stones used by stonemasons to build the curved portions of archways; similarly, most images of voussoir tesserae suggesting they have a quite local distribution, associated with skeletal ridges and the margins of foramina in tessellated cartilage (Seidel et al., 2016; Maisey et al., 2021). Our data, however, show columnar tesserae to be the primary tesseral morphology of the perichondral tesseral layer in the jaws of durophagous *Rhynchobatus* and *Rhina*, not only limited to curved regions. This argues that these large tesserae may be important for resisting high mechanical loads, as well as for constructing strongly curved surfaces (i.e. regions with small radii of curvature). Also, accepting that tesserae increase in size with age, the larger size of voussoir tesserae could indicate that the perichondral tesseral layer is the oldest in the jaw skeleton. This would suggest that the inner (chondral) layers of smaller scree tesserae developed after perichondral tesserae, within the unmineralized cartilage (Maisey et al., 2021), their disorganization perhaps suggesting a more rapid development in response to increased feeding stresses as the animals grew. Alternatively, columnar tesserae might be larger due to more rapid growth (e.g. in response to high mechanical loads) and scree layering could simply be a constructional constraint of building highly curved cross-sections from individual brick-like elements (tesserae). The hypothesis that larger tesserae and/or a thicker jaw cortex develop in response to load (or at least are involved in resisting higher loads) is also supported by the occurrence of thicker tesseral layers below the dentition (in *Rhina* and *Rhynchobatus*, but also in *Aetobatus* and *Raja*) and associated with the jaw joint (*Rhina*, *Rhynchobatus*, *Raja*) (Figures 5C,D, 6C,D, 7C,D, 8D). The presence of tessellated sesamoid cartilages beneath the symphyseal meta-teeth in both rhinopristiform species is further suggestive of high local mechanical stresses (Sarin et al., 1999; Fontenelle et al., 2018).

The largest tesserae we measured were irregular and less-mineralized, observed in the oral cortex of larger *Rhina* and especially *Rhynchobatus* specimens (Figures 9, 10 and Supplementary Figure S2, Supplementary Table S2). We believe these to be the product of fusions of individual tesserae. It is possible that these structures instead represent groups of tesserae with particularly narrow gaps between them (i.e. beyond the resolutions of our scans), but we find this unlikely, given that individual tesserae were successfully resolved in all other scan regions. The irregular shape of these tesserae is a significant departure from the polygonal (or at least symmetrical) tesserae of other batoid taxa (e.g. *Urobatis*, *Aetobatus*, *Raja*; Seidel et al., 2016, 2020, 2021; Atake and Eames, 2021) and of the smaller *Rhina* and *Rhynchobatus* sampled here (Figures 9, 10 and Supplementary Figure S2). Similar irregular tesserae, fused together at their perichondral surfaces, have been observed in the jaw cortices of other species, either in healthy tissues (Maisey, 2013; Maisey et al., 2021) or associated with a callus-building damage response (Dean et al., 2017). Maisey (2013) hypothesized this morphology represented a breakdown of the inhibition of mineralization in the joints between tesserae, noting that this morphology did not always occur in regions of high stress. The similar irregular mineralization we observed in larger *Rhina* and *Rhynchobatus* could therefore be associated with age, however, the lower level of mineralization in these tesserae is more difficult to explain. Perhaps these morphologies indicate tesserae with an especially high organic content (e.g. particularly large Sharpey's fibers; Seidel et al., 2017), as might be needed where the fibrous dental ligament is anchored into the skeleton.

Trabeculae

In addition to surface reinforcements of the skeleton, trabeculae were present in the jaws of all durophagous species examined (*Rhynchobatus*, *Rhina* and *Aetobatus*), but absent in *Raja* and also *Urobatis* (*see* summary diagram, Figure 13). In both *Rhynchobatus* and *Rhina*, trabeculae were simple, relatively linear tubes (Figure 12). Whereas trabeculae were typically covered by a single layer of stout tesserae in *Rhynchobatus*, they apparently bore only a patchy tessellated covering in some regions in *Rhina*, although trabeculae in this species were roughly three times as densely packed as in *Rhynchobatus* (Figures 3, 4 and Supplementary Movies S1–S3). The patchy tessellation of *Rhina* trabeculae is similar to the trabeculae of the *Aetobatus* jaw we examined (Figure 7 and Figures 9, 10 and Supplementary Movie S4), where trabeculae appeared to lack tesserae at their aboral ends (but *see* caveat above about the dried nature of the specimens). In contrast to the rhinopristiform species, the trabeculae of

Aetobatus were hierarchically branched and far more densely populated.

The orientations of trabeculae in all three durophagous species suggest differences in loading patterns associated with feeding. "Load leading" trabeculae (oriented in-line with the bite force; Dean et al., 2006) were situated beneath the dentition in both the upper and lower jaw cartilages of *Rhina* and *Aetobatus*; the durophagous diets of these species can explain the need for such support, preventing collapse of the jaw cortex when exerting the force necessary to fracture invertebrate exoskeletons. The irregular and branching nature of *Aetobatus* trabeculae may compensate for their comparatively thin walls, but may also indicate this species employs more diverse (e.g. multi-axial) prey-processing behaviors. Conversely, the apparent lack of load-leading trabeculae in *Rhynchobatus* may be accounted for by the species' particularly robust jaw cortex. Both *Rhina* and *Rhynchobatus* also exhibited trabeculae oriented perpendicular to the direction of bite force, "truss trabeculae" bridging the labial and lingual jaw cortices (Dean et al., 2006), particularly in narrow regions of the jaw cross-section (Figures 3B,C, 4B,C, 9D,G, 10D,G). As with horizontal tie-bars used to brace and strengthen brickwork walls (e.g. Spina et al., 2004; Zielińska, 2017), truss trabeculae likely help maintain the jaw shape during biting by preventing structural buckling (Dean et al., 2006). Whereas truss trabeculae were largely found in the mid-shaft (parasymphyseal regions) of the jaw in both rhinopristiform species, load-leading trabeculae were absent in *Rhynchobatus* and concentrated closer to the symphysis in *Rhina*, suggesting some local division of labor in the jaws, perhaps associated with the undulating dentitions of these species. A third class of trabeculae was observed in both rhinopristiform species, perpendicular to both load-leading and truss trabeculae, in line with the long (proximo-distal) axis of the jaws (*trab** in Figure 3B and Figures 9, 10 and Supplementary Movies S1–S6). To our knowledge, such trabeculae have not been previously described. Although their role is unclear, their orientation could argue they provide either additional structural support (e.g. like longitudinal bars in steel-reinforced concrete beams) or even a non-mechanical function (e.g. nutrient transport). Mapping the full trabecular network in hydrated samples would help to clarify the true diversity of their functional roles.

Teeth

The teeth of durophagous species are in a battle of contact and fracture mechanics with their prey, working to cause damage to prey shells and exoskeletons, but without tooth materials being damaged in return (Lucas et al., 2008; Amini et al., 2020). The nature of contact between tooth and prey is a deciding factor in which surface is damaged (e.g. tooth or shell) with the radius of curvature of the contacting tooth being hugely important to the type of damage caused (Lucas et al., 2008; Crofts and Summers, 2014). For a given prey item, as teeth become flatter (i.e. with larger radius of curvature), they will tend to cause more far-field damage (at a distance from the contact point) and through-thickness shell failure (Lucas et al., 2008). These are more destructive damage modes than produced by near-contact stresses (Lucas et al., 2008), although smaller indenters, like pointed tooth cusps, can be quite effective in initiating cracks (Crofts and Summers, 2014). Furthermore, for a given tooth diameter and prey item, flat and domed teeth require less force than concave ones to initiate crack propagation in prey exoskeletons, although this is conversely also dependent on the size of the prey item, relative to the concavity (Crofts and Summers, 2014).

The distinctive curved dentitions of *Rhina* and *Rhynchobatus* take advantage of the geometric factors facilitating prey fracture. Although containing smaller teeth with far smaller radii of curvature than myliobatiform stingray dentitions (this study; Kolmann et al., 2015a), the bulbous meta-teeth of the rhinopristiform species, particularly pronounced in *Rhina*, massively increase the radius of curvature of contact with prey items, creating larger "effective cusps" more suited for pulverizing shells. Additionally, although the cross-sectional shape of myliobatiform jaws has been shown to have little impact on shell crushing performance (Kolmann et al., 2015a), the undulating oral jaw surfaces of *Rhina* and *Rhynchobatus* provide a sculptured loading platform for prey items, the biological equivalent of an engineering three-point bending rig, allowing the meta-teeth to act as large, local stress concentrators.

Compared to most other examined batoid fishes, *Rhina* and *Rhynchobatus* have thicker enameloid, comprising a compact outer layer of randomly-orientated crystallites and an inner parallel-organized layer, with crystallites orientated perpendicular to the tooth surface (Enault et al., 2013; Manzanares et al., 2016). This thickened microstructure is believed to impart compression resistance to the enameloid (Gillis and Donoghue, 2006; Enault et al., 2013; Amini et al., 2020). Coupled with teeth being interlocked, and tooth ridges and meta-teeth surely enhancing the grip on prey (particularly in *Rhina*), these dental features create a stabilized platform for crushing behaviors. The comparatively large teeth that comprise meta-teeth (Figures 3–6) and the broken cusps observed in two of our specimens' meta-teeth (asterisk in Figures 3A, 5A) are perhaps indications of the exceptional local stresses generated in these areas. The robust and self-supporting nature of *Rhina* and *Rhynchobatus* dentitions is also demonstrated by their spanning of the jaw symphyses, which we show are unfused and flanked by the distal jaw tips, which have surprisingly thin-walled cortices (Figures 3, 4). This is in stark contrast to the jaws of *Aetobatus*, where the jaw

halves are fused at the midline into stout, single elements (Figure 7). In *Rhina* and *Rhynchobatus*, the dentitions (and perhaps, sesamoid cartilages) must therefore also act as structural girders to support the jaws at the midline, a function not typically attributed to teeth.

Toward a synthesis of elasmobranch durophagy

It is clear that "durophagy" is too general a descriptor for the diverse diets and morphologies of elasmobranch fishes typically placed in this category. For example, whereas the diet of *Aetobatus* is dominated by hard-shelled molluscs (Schluessel et al., 2010), *Rhina* is known to feed on fish, prawns, and cephalopods, in addition to crabs and bivalves (Compagno and Last, 1999; Raje, 2006). The stomach contents of *Rhynchobatus*, by comparison, indicate a predominantly shrimp-based diet, with fish and crabs eaten only by larger individuals (Nasir, 2000; Abdurahiman et al., 2010), while a recent study, based on spines embedded in the jaws (*see* also Figure 10F), suggested that *Rhynchobatus* may also prey on smaller stingrays (Dean et al., 2017). Anyone who has eaten seafood knows that the strategies for crushing mollusc shells differ considerably from those for processing crustaceans like shrimp. Yet to date, no experimental study has looked broadly enough at durophagous feeding anatomy and performance in elasmobranchs to resolve more subtle ecomorphological connections.

Our data, combined with anatomical data from previous works (e.g. Summers, 2000; Kolmann et al., 2015a; Rutledge et al., 2019) begin to frame a more holistic view of elasmobranch durophagy, mapping out a suite of modular morphological characters, which can be diversely combined to reinforce against extreme feeding loads. A comparison of several of the batoid fishes most-studied in anatomical research (Figure 13) illustrates the potential interrelationships of morphological characters, underlining differences in diet, tesseral shape and layering, trabecular presence and orientation, and dentition (including enameloid thickness and surface ornamentation). Cortical tesserae, for example, can vary in their size and shape, and in how orderly and numerous their layers are. Thicker cortices are certainly associated with regions of high load, even in non-durophagous species, but this can be variously achieved, by employing massive tesserae (e.g. perichondral columnar tesserae), numerous tesseral layers, or both. Such reinforcements seem to come with departures from the "typical" polygonal tesseral forms, in perichondral and chondral tesseral layers. Symphyseal fusion, more massive and flatter teeth, and teeth interacting to form superstructures (e.g. meta-teeth) also occur in species experiencing high feeding stresses. Trabeculae, also present in their "truss" (labio-lingual) orientation in non-durophagous species, occur in far higher densities and with telltale load-leading (oral-aboral) alignment in species with molluscs in their diets.

These characters can all be involved in jaw reinforcement for durophagy, yet they appear to trade-off in their preponderance: *Rhynchobatus* possesses a thicker jaw cortex (comprised of fewer, but more massive tesserae, fused into mineralized concretions beneath the teeth), but no load-leading trabeculae, an unfused symphysis, and shorter teeth with a low degree of interlocking and tooth superstructuring (i.e. assembly into meta-teeth). *Rhina*'s unfused symphysis and thinner jaw cortex (from smaller, but more numerous tesserae), is compensated for by thick-walled trabeculae (albeit in some regions only partially tessellated), oriented in line with loading and a more robust dentition, with thicker teeth, thicker enameloid and massive meta-teeth. The jaws of *Aetobatus* have a comparatively thin cortex (comprised of several layers of thin, platelike tesserae), but are filled with a dense stand of load-leading trabeculae (thin-walled, but branching), the jaws fused at the symphysis, and the extremely thick and interlocking teeth creating a monolithic dental plate.

Previous comparisons of durophagous shark and ray species have suggested that elasmobranch lineages invest to different degrees in shape-vs. structure-vs. material-solutions for jaw reinforcement (Summers et al., 2004; Huie et al., 2022). Including our data, these observations of varied reinforcement strategies argue that durophagy is an interestingly multivariate problem in elasmobranchs with diverse solutions, yet the pressures driving the evolution of the different character combinations are unclear. The key to clarifying this is multi-disciplinary: by examining and integrating feeding behavior and mechanics, gut content, anatomical, and biological materials data, we can better resolve the factors that have shaped extreme feeding modes and determine their links to phylogeny, prey co-evolution and biogeography.

Data availability statement

Renderings of the primary microCT datasets are provided in annotated videos in the Supplementary Material. Additional microCT data is available from the authors by request.

Ethics statement

Ethical review and approval was not required for the animal study because all samples examined were fixed or dried specimens from research collections (Natural History Museum, London).

Author contributions

BC, ZJ, MMS, and MD devised the project and experiments. BC, ZJ, and CU procured and scanned specimens and rendered scan data. BC, JC, and MD analyzed data. BC, JC, and ZJ generated the figures and tables. BC, MD, ZJ, and JC wrote the manuscript. All authors edited the manuscript.

Funding

Several of the study's micro-CT scans were performed *via* a SYNTHESYS project collections-based research grant (GB-TAF-6706; http://www.synthesys.info) to MD, financed by the European Community Research Infrastructure Action under the FP7 Integrating Activities Programme.

Acknowledgments

We thank Yannis Papastamatiou and Carol Bucking for insights into elasmobranch digestive enzymes and Matt Kolmann for always-inspiring discussions about elasmobranch durophagy and all things batoid. Frederik Mollen (Elasmobranch Research Belgium) kindly provided *Rhina* specimens to help in estimating maturity from jaw width. Daniel Werner, Binru Yang and Dominique Adriaens helped arrange the *Urobatis* and *Narcine* scans for Figure 13. We also thank James MacLaine, Oliver Crimmen and Emma Bernard (Natural History Museum, London) for access to collections under their care.

Conflict of interest

The authors declare that the research was conducted in the absence of any commercial or financial relationships that could be construed as a potential conflict of interest.

Publisher's note

Supplementary material

The Supplementary Material for this article can be found online at: https://www.frontiersin.org/articles/10.3389/fcell.2022.932341/full#supplementary-material

References

Abdurahiman, K. P., Nayak, T. H., Zacharia, P. U., and Mohamed, K. S. (2010). Trophic organisation and predator–prey interactions among commercially exploited demersal finfishes in the coastal waters of the southeastern Arabian Sea. *Estuar. Coast. Shelf Sci.* 87, 601–610. doi:10.1016/j.ecss.2010.03.002

Ajemian, M. J., Lamboy, C., Ibrahim, A., DeGroot, B. C., Bassos-Hull, K., Mann, D. A., et al. (2021). Capturing shell-crushing by large mobile predators using passive acoustics technology. *J. Exp. Mar. Biol. Ecol.* 535, 151497. doi:10.1016/j.jembe.2020.151497

Amini, S., Razi, H., Seidel, R., White, W., Weaver, J. C., Dean, M. N., et al. (2020). Staying sharp despite erosion: Lessons from the micro-architectural heterogeneities in Port Jackson shark tooth enameloid. *Nat. Commun.* 11, 5971. doi:10.1038/s41467-020-19739-0

Anderson, W. G., Dasiewicz, P. J., Liban, S., Ryan, C., Taylor, J. R., Grosell, M., et al. (2010). Gastro-intestinal handling of water and solutes in three species of elasmobranch fish, the white-spotted bamboo shark, *Chiloscyllium plagiosum*, little skate, *Leucoraja erinacea* and the clear nose skate *Raja eglanteria*. *Comp. Biochem. Physiol. A Mol. Integr. Physiol.* 155, 493–502. doi:10.1016/j.cbpa.2009.09.020

Aschliman, N. C., Claeson, K. M., and McEachran, J. D. (2012). "Phylogeny of Batoidea," in *Biology of sharks and their relatives*. Editors J. C. Carrier, J. A. Musick, and M. R. Heithaus (CRC Press), 57.

Aschliman, N. C. (2014). Interrelationships of the durophagous stingrays (Batoidea: Myliobatidae). *Environ. Biol. Fishes* 97, 967–979. doi:10.1007/s10641-014-0261-8

Atake, O. J., and Eames, B. F. (2021). Mineralized cartilage and bone-like tissues in chondrichthyans offer potential insights into the evolution and development of mineralized tissues in the vertebrate endoskeleton. *Front. Genet.* 12, 762042. doi:10.3389/fgene.2021.762042

Berio, F., Broyon, M., Enault, S., Pirot, N., López-Romero, F. A., and Debiais-Thibaud, M. (2021). Diversity and evolution of mineralized skeletal tissues in chondrichthyans. *Front. Ecol. Evol.* 9, 660767. doi:10.3389/fevo.2021.660767

Clement, J. G. (1992). Re-Examination of the fine structure of endoskeletal mineralization in chondrichthyans: Implications for growth, ageing and calcium homeostasis. *Mar. Freshw. Res.* 43, 157–181. doi:10.1071/mf9920157

Collins, A., Heupel, M., Hueter, R., and Motta, P. J. (2007). Hard prey specialists or opportunistic generalists? An examination of the diet of the cownose ray. *Mar. Freshw. Res.* 58, 135–144. doi:10.1071/mf05227

Compagno, L. J. V., and Last, P. R. (1999). *FAO species identification guide for fishery purposes. The living marine resources of the western central pacific*. Norfolk, Virginia, USA: Food and Agriculture Organization of the United Nations–FAO, 1418

Cortés, E., Papastamatiou, Y. P., Carlson, J. K., Ferry-Graham, L., Wetherbee, B. M., Cyrino, J. E. P., et al. (2008). *An overview of the feeding ecology and physiology of elasmobranch fishes. Feeding and Digestive Functions of Fishes*. London: CRC Press, 393

Crofts, S. B., and Summers, A. P. (2014). How to best smash a snail: The effect of tooth shape on crushing load. *J. R. Soc. Interface* 11, 20131053. doi:10.1098/rsif.2013.1053

Darracott, A. (1977). Availability, morphometrics, feeding and breeding activity in a multi-species, demersal fish stock of the Western Indian Ocean. *J. Fish. Biol.* 10, 1–16. doi:10.1111/j.1095-8649.1977.tb04036.x

Dean, M. N., Bizzarro, J. J., Clark, B., Underwood, C. J., and Johanson, Z. (2017). Large batoid fishes frequently consume stingrays despite skeletal damage. *R. Soc. Open Sci.* 4, 170674–170611. doi:10.1098/rsos.170674

Dean, M. N., Bizzarro, J. J., and Summers, A. P. (2007). The evolution of cranial design, diet, and feeding mechanisms in batoid fishes. *Integr. Comp. Biol.* 47, 70–81. doi:10.1093/icb/icm034

Dean, M. N., Ekstrom, L., Monsonego-Ornan, E., Ballantyne, J., Witten, P. E., Riley, C., et al. (2015). Mineral homeostasis and regulation of mineralization processes in the skeletons of sharks, rays and relatives (Elasmobranchii). *Semin. Cell Dev. Biol.* 46, 51–67. doi:10.1016/j.semcdb.2015.10.022

Dean, M. N., Huber, D. R., and Nance, H. A. (2006). Functional morphology of jaw trabeculation in the lesser electric ray *Narcine brasiliensis*, with comments on the evolution of structural support in the Batoidea. *J. Morphol.* 267, 1137–1146. doi:10.1002/jmor.10302

Dean, M. N., Mull, C. G., Gorb, S. N., and Summers, A. P. (2009). Ontogeny of the tessellated skeleton: Insight from the skeletal growth of the round stingray *Urobatis halleri*. *J. Anat.* 215, 227–239. doi:10.1111/j.1469-7580.2009.01116.x

Enault, S., Cappetta, H., and Adnet, S. (2013). Simplification of the enameloid microstructure of large stingrays (Chondrichthyes: Myliobatiformes): A functional approach. *Zool. J. Linn. Soc.* 169, 144–155. doi:10.1111/zoj.12059

Fänge, R., Lundblad, G., Lind, J., and Slettengren, K. (1979). Chitinolytic enzymes in the digestive system of marine fishes. *Mar. Biol.* 53, 317–321. doi:10.1007/bf00391614

Fontenelle, J. P., Loboda, T. S., Kolmann, M., and De Carvalho, M. R. (2018). Angular cartilage structure and variation in Neotropical freshwater stingrays (Chondrichthyes: Myliobatiformes: Potamotrygonidae), with comments on their function and evolution. *Zool. J. Linn. Soc.* 183, 121–142. doi:10.1093/zoolinnean/zlx054

Franklin, O., Palmer, C., and Dyke, G. (2014). Pectoral fin morphology of batoid fishes (Chondrichthyes: Batoidea): Explaining phylogenetic variation with geometric morphometrics. *J. Morphol.* 275, 1173–1186. doi:10.1002/jmor.20294

Gillis, J. A., and Donoghue, P. C. J. (2006). The homology and phylogeny of chondrichthyan tooth enameloid. *J. Morphol.* 268, 33–49. doi:10.1002/jmor.10501

Herbert, A. M., and Motta, P. J. (2018). Biomechanics of the jaw of the durophagous bonnethead shark. *Zoology* 129, 54–58. doi:10.1016/j.zool.2018.07.001

Holmgren, S., and Nilsson, S. (1999). *Sharks, skates and rays: The biology of elasmobranch fishes*. Editor W. C. Hamlett (Baltimore, London: The Johns Hopkins University Press), 144

Huie, J. M., Summers, A. P., and Kawano, S. M. (2022). SegmentGeometry: A tool for measuring second moment of area in 3D slicer. *Integr. Org. Biol.* 4, obac009. doi:10.1093/iob/obac009

Jayasankar, A. K., Seidel, R., Hosny, A., Weaver, J. C., Fratzl, P., Chen, J., et al. (2020). Multi-scale modeling and mechanical performance characterization of stingray skeleton-inspired tessellations. *J. Mech. Phys. Solids* 138, 103906. doi:10.1016/j.jmps.2020.103906

Kolmann, M. A., Crofts, S. B., Dean, M. N., Summers, A. P., and Lovejoy, N. R. (2015a). Morphology does not predict performance: Jaw curvature and prey crushing in durophagous stingrays. *J. Exp. Biol.* 218, 3941–3949. doi:10.1242/jeb.127340

Kolmann, M. A., Huber, D. R., Motta, P. J., and Grubbs, R. D. (2015b). Feeding biomechanics of the cownose ray, *Rhinoptera bonasus*, over ontogeny. *J. Anat.* 227, 341–351. doi:10.1111/joa.12342

Kolmann, M. A., Welch, K. C., Jr, Summers, A. P., and Lovejoy, N. R. (2016). Always chew your food: Freshwater stingrays use mastication to process tough insect prey. *Proc. Biol. Sci.* 283, 20161392–20161399. doi:10.1098/rspb.2016.1392

Last, P., Naylor, G., Séret, B., White, W., de Carvalho, M., and Stehmann, M. (2016). *Rays of the world*. Australia, New Zealand: Csiro Publishing.

Liu, X., Dean, M. N., Youssefpour, H., Summers, A. P., and Earthman, J. C. (2014). Stress relaxation behavior of tessellated cartilage from the jaws of blue sharks. *J. Mech. Behav. Biomed. Mat.* 29, 68–80. doi:10.1016/j.jmbbm.2013.08.014

Lucas, P., Constantino, P., Wood, B., and Lawn, B. (2008). Dental enamel as a dietary indicator in mammals. *Bioessays* 30, 374–385. doi:10.1002/bies.20729

Maisey, J. G., Denton, J. S. S., Burrow, C., and Pradel, A. (2021). Architectural and ultrastructural features of tessellated calcified cartilage in modern and extinct chondrichthyan fishes. *J. Fish. Biol.* 98, 919–941. doi:10.1111/jfb.14376

Maisey, J. G. (2013). The diversity of tessellated calcification in modern and extinct chondrichthyans. *Rev. Paléobiologie, Genève* 32, 355.

Manzanares, E., Rasskin-Gutman, D., and Botella, H. (2016). New insights into the enameloid microstructure of batoid fishes (Chondrichthyes). *Zool. J. Linn. Soc.* 177, 621–632. doi:10.1111/zoj.12377

Marconi, A., Hancock-Ronemus, A., and Andrew Gillis, J. (2020). Adult chondrogenesis and spontaneous cartilage repair in the skate, *Leucoraja erinacea*. *eLife* 9, e53414. doi:10.7554/elife.53414

Moazzam, M., and Osmany, H. B. (2020). Species composition, commercial landings, distribution and some aspects of biology of guitarfish and wedgefish (Class Pisces: Order Rhinopristiformes) from Pakistan. *J. Biol. Biotechnol.* 17, 469

Nasir, N. A. (2000). The food and feeding relationships of the fish communities in the inshore waters of Khor Al-Zubair, northwest Arabian Gulf. *Cybium Int. J. Ichthyology* 24 (1), 89

Purushottama, G. B., Raje, S. G., -T., Akhilesh, K. V., Kizhakudan, S. J., and Zacharia, P. U. (2020). Reproductive biology and diet composition of *Rhynchobatus laevis* (bloch and schneider, 1801) (Rhinopristiformes: Rhinidae) from the northern Indian ocean. *Indian J. Fish.* 67. doi:10.21077/ijf.2020.67.4.95636-02

Raje, S. G. (2006). Skate fishery and some biological aspects of five species of skates off Mumbai. *Indian J. Fish.* 53, 431

Rutledge, K. M., Summers, A. P., and Kolmann, M. A. (2019). Killing them softly: Ontogeny of jaw mechanics and stiffness in mollusk-feeding freshwater stingrays. *J. Morphol.* 280, 796–808. doi:10.1002/jmor.20984

Sarin, V. K., Erickson, G. M., Giori, N. J., Bergman, A. G., and Carter, D. R. (1999). Coincident development of sesamoid bones and clues to their evolution. *Anat. Rec.* 257, 174–180. doi:10.1002/(SICI)1097-0185(19991015)257:5<174::AID-AR6>3.0.CO;2-O

Schluessel, V., Bennett, M. B., and Collin, S. P. (2010). Diet and reproduction in the white-spotted eagle ray *Aetobatus narinari* from queensland, Australia and the penghu islands, taiwan. *Mar. Freshw. Res.* 61, 1278–1289. doi:10.1071/mf09261

Seidel, R., Blumer, M., Chaumel, J., Amini, S., and Dean, M. N. (2020). Endoskeletal mineralization in chimaera and a comparative guide to tessellated cartilage in chondrichthyan fishes (sharks, rays and chimaera). *J. R. Soc. Interface* 17, 20200474. doi:10.1098/rsif.2020.0474

Seidel, R., Blumer, M., Pechriggl, E.-J., Lyons, K., Hall, B. K., Fratzl, P., et al. (2017). Calcified cartilage or bone? Collagens in the tessellated endoskeletons of cartilaginous fish (sharks and rays). *J. Struct. Biol.* 200, 54–71. doi:10.1016/j.jsb.2017.09.005

Seidel, R., Jayasankar, A. K., and Dean, M. N. (2021). The multiscale architecture of tessellated cartilage and its relation to function. *J. Fish. Biol.* 98, 942–955. doi:10.1111/jfb.14444

Seidel, R., Lyons, K., Blumer, M., Zaslansky, P., Fratzl, P., Weaver, J. C., et al. (2016). Ultrastructural and developmental features of the tessellated endoskeleton of elasmobranchs (sharks and rays). *J. Anat.* 229, 681–702. doi:10.1111/joa.12508

Seidel, R., Roschger, A., Li, L., Zhang, Q., Yin, J., Yang, T., et al. (2019). Mechanical properties of stingray tesserae: High-resolution correlative analysis of mineral density and indentation moduli in tessellated cartilage. *Acta Biomater.* 96, 421–435. doi:10.1016/j.actbio.2019.06.038

Spina, G., Ramundo, F., and Mandara, A. (2004). *Masonry strengthening by metal tie-bars, a case study*. *Structural Analysis of Historical Constructions*. Padova, Italy, 10. Available at: http://www.hms.civil.uminho.pt/sahc/2004/1207.pdf

Summers, A. P., Ketcham, R., and Rowe, T. (2004). Structure and function of the horn shark (*Heterodontus francisci*) cranium through ontogeny - the development of a hard prey specialist. *J. Morphol.* 260, 1–12. doi:10.1002/jmor.10141

Summers, A. P., Koob, T. J., and Brainerd, E. L. (1998). Stingray jaws strut their stuff. *Nature* 395, 450–451. doi:10.1038/26649

Summers, A. P. (2000). Stiffening the stingray skeleton—an investigation of durophagy in myliobatid stingrays (Chondrichthyes, Batoidea, Myliobatidae). *J. Morphol.* 243, 113–126. doi:10.1002/(SICI)1097-4687(200002)243:2<113::AID-JMOR1>3.0.CO;2-A

Underwood, C. J., Johanson, Z., Welten, M., Metscher, B., Rasch, L. J., Fraser, G. J., et al. (2015). Development and evolution of dentition pattern and tooth order in the skates and rays (Batoidea; Chondrichthyes). *PLoS One* 10, e0122553–19. doi:10.1371/journal.pone.0122553

Wilga, C. D., and Motta, P. J. (2000). Durophagy in sharks: Feeding mechanics of the hammerhead *Sphyrna tiburo*. *J. Exp. Biol.* 203, 2781–2796. doi:10.1242/jeb.203.18.2781

Zielińska, M. (2017). Comparative numerical analysis of different strengthening systems of historical brick arches. *Int. J. Appl. Mech. Eng.* 22, 483–491. doi:10.2478/ijame-2017-0032

Frontiers in Genetics

Highlights genetic and genomic inquiry relating to all domains of life

The most cited genetics and heredity journal, which advances our understanding of genes from humans to plants and other model organisms. It highlights developments in the function and variability of the genome, and the use of genomic tools.

Discover the latest Research Topics

See more →

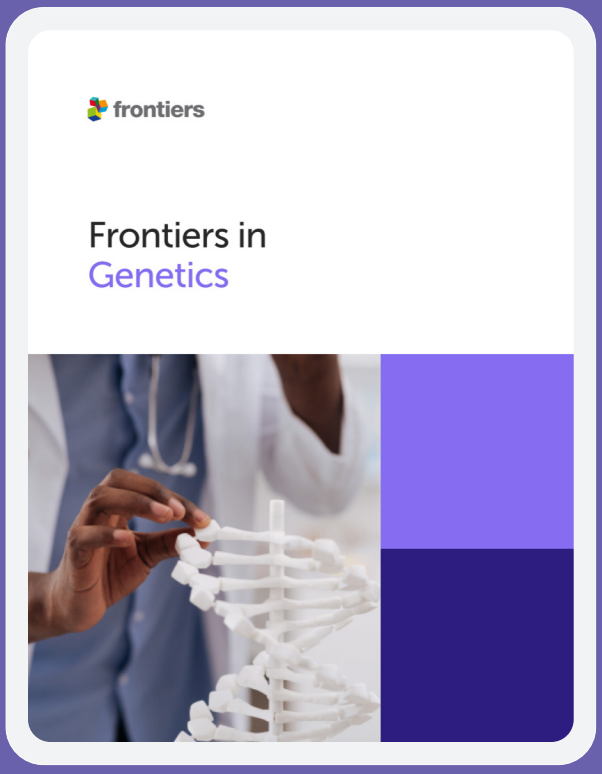

Frontiers

Avenue du Tribunal-Fédéral 34
1005 Lausanne, Switzerland
frontiersin.org

Contact us

+41 (0)21 510 17 00
frontiersin.org/about/contact